UNIVERSITY OF CRETE

DEPARTMENT OF PHYSICS

PhD THESIS

# A multi-wavelength study of the activity in a representative sample of nearby star-forming galaxies

Alexandros Maragkoudakis

---

*Advisor:* *Associate Professor* Andreas Zezas – University of Crete

UNIVERSITY OF CRETE
DEPARTMENT OF PHYSICS

# PhD THESIS

Doctor of Philosophy
of
- Astrophysics -

*Defended by*
Alexandros Maragkoudakis

# A multi-wavelength study of the activity in a representative sample of nearby star-forming galaxies

COMMITTEE

| | | | |
|---|---|---|---|
| *Associate Professor* | Zezas Andreas | – | University of Crete |
| *Professor* | Charmandaris Vasileios | – | University of Crete |
| *Professor* | Papadakis Iossif | – | University of Crete |
| *Professor Emeritus* | Kylafis Nikos | – | University of Crete |
| *Assistant Professor* | Pavlidou Vasiliki | – | University of Crete |
| *Assistant Professor* | Tassis Kostas | – | University of Crete |
| *Senior Researcher* | Xilouris Manolis | – | National Observatory of Athens |

Date of the defense:
27/03/2017

# Περίληψη

Αυτή η διδακτορική διατριβή παρουσιάζει την ταξινόμηση ενός δείγματος γαλαξιών με έντονη εκπομπή στο υπέρυθρο, βάση της δραστηριότητας στον πυρήνα τους. Στόχος μας είναι η διερεύνηση της πυρηνικής δραστηριότητας αλλά και της διαδικασίας αστρογένεσης σε ολόκληρο το γαλαξία συνολικά, καθώς και σε μεμονωμένες περιοχές εντός του γαλαξία.

Αρχικά διερευνούμε τον τρόπο με τον οποίο η πυρηνική ταξινόμηση των γαλαξιών εξαρτάται από το ποσοστό του φωτός από το υπόλοιπο σώμα του γαλαξία, το οποίο υπεισέρχεται στη σχισμή που εξάγεται το πυρηνικό φάσμα των γαλαξιών. Χρησιμοποιούμε φάσματα από φασματογράφο σχισμής καθώς και προσομοιώσεις φασμάτων που έχουν ληφθεί από ελλειπτικές οπές διαφορετικών μεγεθών για την περίπτωση 14 γαλαξιών. Μελετάμε τον τρόπο με τον οποίο οι λόγοι φασματικών γραμμών εκπομπής που χρησιμοποιούνται σε οπτικά διαγνωστικά ταξινόμησης γαλαξιών αλλάζουν και κατ επέκταση επηρεάζουν την ταξινόμηση των γαλαξιών, καθώς όλο και περισσότερο φως από το σώμα του γαλαξία εμπεριέχεται στην σχισμή από την οποία εξάγεται το πυρηνικό φάσμα. Βρίσκουμε ότι οι μέθοδοι αφαίρεσης του αστρικού φωτός από το πυρηνικό φάσμα εκπομπής του γαλαξία μπορούν να περιορίσουν αλλά όχι να αφαιρέσουν απόλυτα την εισχώρηση του φωτός από το σώμα του γαλαξία στην πυρηνική σχισμή. Επιπλέον, γαλαξίες με έντονη εξωπυρηνική αστρογένεση παρουσιάζουν μεγαλύτερους λόγους [O III]λ5007/H$\beta$ καθώς αυξάνεται το μέγεθος της πυρηνικής σχισμής της φασματικής εξαγωγής, σε αντίθεση με την κοινή αντίληψη ότι το επιπρόσθετο φως από το σώμα του γαλαξία θα μειώσει τους λόγους γραμμών εκπομπής του πυρήνα. Τόσο με τη χρήση φασματοσκοπίας σχισμής όσο και οπτικών ινών οι γαλαξίες θα παρουσιάζουν διαφορετική θέση στα διαγνωστικά διαγράμματα και σε κάποιες περιπτώσεις διαφορετική ταξινόμηση καθώς όλο και περισσότερο φως από το σώμα του γαλαξίες υπεισέρχεται στην πυρηνική σχισμή φασματικής εξαγωγής.

Παρουσιάζουμε τα δημογραφικά στοιχεία της πυρηνικής δραστηριότητας γαλαξιών με έντονη εκπομπή στο υπέρυθρο στο κοντινό Σύμπαν, χρησιμοποιώντας το αντιπροσωπευτικό δείγμα του Star Formation Reference Survey (SFRS; Ashby et al. 2011). Το πλαίσιο ταξινόμησης που χρησιμοποιούμε βασίζεται σε ένα συνδυασμό των τριών διαγνωστικών οπτικών γραμμών εκπομπής καθώς και διαγνωστικών υπέρυθρων χρωμάτων. Χρησιμοποιούμε τα συνολικά υπέρυθρα χρώματα των γαλαξιών για να αναγνωρίσουμε περιπτώσεις ενεργών γαλαξιακών πυρήνων (Active Galactic Nuclei: AGN) που είναι καλυμμένα μέσα σε πυκνά στρώματα σκόνης, αλλά επιπλέον χρησιμοποιούμε και τα πυρηνικά υπέρυθρα χρώματα των γαλαξιών για να λάβουμε υπόψιν την εισχώρηση φωτός από το υπόλοιπο σώμα του γαλαξία στον πυρήνα. Χρησιμοποιώντας τα στατιστικά βάρη που έχουν απο-

δοθεί στους γαλαξίες του SFRS σε σχέση με το ευρύτερο δείγμα γαλαξιών PSC$z$ από το οποίο προέκυψαν, υπολογίζουμε τα ποσοστά των διαφορετικών γαλαξιακών πυρηνικών τύπων και μελετούμε τα χαρακτηριστικά των γαλαξιών στα οποία ανήκουν. Βρίσκουμε ότι το PSC$z$ περιέχει 71% γαλαξίες αστρογένεσης H II, 13% γαλαξίες Seyferts, 3% μεταβατικά αντικείμενα, ανδ 13% αντικείμενα πυρηνικών γραμμών εκπομπής χαμηλού ιονισμού (Low-Ionization Nuclear Emission-Line Regions: LINERs). Για τους H II γαλαξίες του SFRS υπολογίζουμε τον ρυθμό αστρογένεσης και την μεταλλικότητα του αερίου στον πυρήνα τους, ενώ για όλους τους γαλαξίες που παρατηρήθηκαν με φασματογράφο σχισμής υπολογίζουμε την μεταλλικότητά στις περιοχές εκτός του πυρήνα τους και υπολογίζουμε βαθμίδες μεταλλικότητας για 12 γαλαξίες. Οι περισσότεροι H II γαλαξίες έχουν ένα μικρό εύρος τιμών μεταλλικότητας κοντά στην ηλιακή και επίπεδες βαθμίδες μεταλλικότητας. Βρίσκουμε με βάση τα χαρακτηρηστικά του σώματος και του πυρήνα των γαλαξιών ότι η κυρίαρχη πηγή παραγωγής ενέργειας για τα SFRS (PSCz) μεταβατικά αντικείμενα είναι η δραστηριότητα αστρογένεσης. Οι LINERs βρίσκονται κατά κύριο λόγο σε γαλαξίες μεγάλης μάζας με χαμηλές τιμές $L(60\mu\mu)$, χαμηλές θερμοκρασίες σκόνης, και χαμηλές τιμές επιφανειακής πυκνότητας $L_{\mathrm{H}\alpha}$, υποδηλώνοντας ως βασική πηγή ιονισμού αστρικούς πληθυσμούς μεγάλης ηλικίας και όχι δραστηριότητα ενεργών γαλαξιακών πυρήνων.

Περιγράφουμε μία κύρια ακολουθία σε διακριτές περιοχές εντός των γαλαξιών (sub-galactic main sequence: SGMS) συσχετίζοντας την επιφανειακή πυκνότητα του ρυθμού αστρογένεσης ($\Sigma_{\mathrm{SFR}}$) και της επιφανειακής πυκνότητας αστρικής μάζας ($\Sigma_\star$) για διακριτές περιοχές γαλαξιών αστρογένεσης, συμπεριλαμβανομένων των πυρήνων τους. Χρησιμοποιούμε ένα δείγμα 246 κοντινών γαλαξιών αστρογένεσης από το δείγμα του SFRS και δείχνουμε ότι η SGMS ορίζεται σε κλίμακες έως και $\sim$1 kpc με κλίση $\alpha = 0.91$ και διασπορά 0.31 dex, παρόμοια με την πρότυπη κυρία ακολουθία (MS) η οποία υπολογίζεται για τον συνολικό ρυθμό αστρογένεσης και την συνολική αστρική μάζα των γαλαξιών. Η κλίση της SGMS εξαρτάται από τη μορφολογία των γαλαξιών, με τους μεταγενέστερου τύπου σπειροειδείς (Sc–Irr) να έχουν κλίση $\alpha = 0.97$ και τους προγενέστερου τύπου σπειροειδείς (Sa–Sbc) να έχουν κλίση $\alpha = 0.81$. Η SGMS η οποία προκύπτει από τις διακριτές περιοχές κάθε γαλαξία ξεχωριστά έχει κατά μέσω όρο τα ίδια χαρακτηριστικά με την SGMS που προκύπτει από όλους τους γαλαξίες μαζί. Η SGMS που σχηματίζεται αποκλειστικά από τους γαλαξιακούς πυρήνες έχει διασπορά όμοια με την συνολική SGMS. Από την ανάλυσή μας προκύπτει ότι δειγματοληψία από περιορισμένο εύρος τιμών του χώρου SFR–$\mathrm{M}_\star$ έχει σαν αποτέλεσμα την υπό- ή υπέρ-γραμμικότητα της κλίσης της SGMS. Σχεδόν για όλους τους γαλαξίες τόσο η επιφανειακή πυκνότητα του ρυθμού αστρογένεσης όσο και της αστρικής μάζας έχει τη μέγιστη τιμή της στον πυρήνα των γαλαξιών, υποδηλώνοντας ότι τα σμήνη γύρω από τον πυρήνα είναι από τα πιο ενεργές περιοχές αστρογένεσης στους

γαλαξίες και οι πιο μαζικές. Ο ρυθμός αστρογένεσης στον πυρήνα συσχετίζεται επίσης και με την συνολική αστρική μάζα των γαλαξιών, δημιουργώντας μια ξεχωριστή ακολουθία από την πρότυπη κυρία ακολουθία (MS) αστρογένεσης. Η πυρηνική κυρία ακολουθία αστρογένεσης θα είναι χρήσιμη για την μελέτη της ανάπτυξης του σφαιροειδούς (bulge) των γαλαξιών καθώ και για τον χαρακτηρισμό διαδικασιών ανάδρασης (feedback) μεταξύ των ενεργών γαλαξιακών πυρήνων και των διαδικασιών αστρογένεσης.

# Abstract

This thesis presents the activity demographics of an Infrared-selected sample of galaxies in the local Universe. Our goal is to investigate the nuclear activity and the star-forming activity in galaxy-wide and sub-galactic (kpc) physical scales.

First, we investigate how activity classification depends on the proportion of the host galaxy's light that is included in the nuclear spectral extraction aperture. We use both observed long-slit spectra and spectra from simulated elliptical apertures of different sizes for a set of 14 galaxies. We examine how the line ratios used in optical activity classification diagnostics, change and possibly influence the resulting classifications as a larger portion of starlight is gradually incorporated in the extracted aperture. We find that starlight subtraction can mitigate but not remove the effect of host galaxy contamination in the nuclear aperture. Furthermore, galaxies with extranuclear star formation can show higher [O III]$\lambda$5007/H$\beta$ ratios with increasing aperture, in contrast to the naive expectation that integrated light will only dilute the nuclear emission lines. Both fiber and long slit spectroscopy ascertain that galaxies will have a different placement in the diagnostic diagrams and on certain occasions a different classification as more starlight is included in the aperture of spectral extraction.

We present activity demographics and host-galaxy properties of IR-selected galaxies in the local Universe, using the representative Star Formation Reference Survey (SFRS; Ashby et al. 2011). Our classification scheme is based on a combination of the three standard optical emission-line diagrams (BPT) and IR-color diagnostics. We employ total IR colors to identify obscured active galactic nuclei (AGN), but furthermore we use also nuclear IR colors to account for host-galaxy light contamination. Using the well defined weights of the SFRS galaxies with respect to the parent PSC$z$ sample, we derive the fractions of different activity types and their respective host-galaxy properties for the parent sample of IR-selected galaxies. We find that the PSC$z$ comprises 71% H II galaxies, 13% Seyferts, 3% Transition Objects, and 13% Low-Ionization Nuclear Emission-Line Regions (LINERs). For the SFRS sample we derive nuclear star-formation rates and gas-phase metallicities for the star-forming galaxies (SFGs $\equiv$ H II), host-galaxy metallicities for all activity types with available long-slit spectroscopy, and measure abundance gradients for a subset of 12 face-on galaxies. The majority of SFGs show a narrow range of metallicities, close to solar, and flat metallicity profiles. We find that based on their host-galaxy and nuclear properties, the dominant ionizing source in

the SFRS (PSCz) transition objects is star-forming activity. LINERs are found mostly in massive hosts with low $L(60\mu\mathrm{m})$, low dust temperatures, and low $L_{\mathrm{H}\alpha}$ surface densities, indicating older stellar populations as their main ionizing source rather than AGN activity.

We describe a sub-galactic main sequence (SGMS) relating star-formation rate surface density ($\Sigma_{\mathrm{SFR}}$) and stellar mass density ($\Sigma_{\star}$) for distinct regions within star forming galaxies, including their nuclei. We use a sample of 246 nearby star-forming galaxies from the SFRS and demonstrate that the SGMS holds down to $\sim$1 kpc scales with a slope of $\alpha = 0.91$ and a dispersion of 0.31 dex, similar to the well-known main sequence (MS) measured for globally integrated star formation rates (SFRs) and stellar masses. The SGMS slope depends on galaxy morphology, with late-type galaxies (Sc–Irr) having a slope $\alpha = 0.97$, and early-type spirals (Sa–Sbc) having $\alpha = 0.81$. The SGMS constructed from sub-regions of individual galaxies has on average the same characteristics as the composite SGMS from all galaxies. The SGMS for galaxy nuclei shows a dispersion similar to that seen for other sub-regions. Our analysis shows that sampling a limited range of the SFR–$\mathrm{M}_{\star}$ space results in either sub-linearity or super-linearity of the SGMS slope. For nearly all galaxies, both the SFR and stellar mass peak in the nucleus, indicating that circumnuclear clusters are among the most actively star-forming regions in the galaxy and the most massive. The nuclear SFR also correlates with total galaxy mass, forming a distinct sequence from the standard MS of star-formation. The nuclear main sequence will be useful for studying bulge growth and for characterizing feedback processes connecting AGN and star formation.



To my family

# Declaration

I hereby declare that the work in this thesis is that of the candidate alone, except where indicated below.

Chapter 3: This Chapter is published in the Monthly Notices of the Royal Astronomical Society as: A. Maragkoudakis, A. Zezas, M. L. N. Ashby., P. Willner., 2014, MNRAS, Vol. 441 2296-2308.

Chapter 4: This Chapter is submitted to the Monthly Notices of the Royal Astronomical Society. This paper is co-authored by A. Zezas, M. L. N. Ashby., P. Willner.

Chapter 5: This Chapter is published in the Monthly Notices of the Royal Astronomical Society as: A. Maragkoudakis, A. Zezas, M. L. N. Ashby., P. Willner., 2017, MNRAS, Vol 466 1192-1204.

Alexandros Maragkoudakis
March 2017

# Acknowledgements

A PhD thesis is not a single person's effort but mostly an "N-body interaction" process. The contribution of each individual, in scientific or emotional level, has been an invaluable asset to me throughout the entire course of this work, and I would like to express my gratitude and attempt to acknowledge them here.

Firstly, I would like to thank my supervisor, Professor Andreas Zezas, for being more of a mentor and a scientific exemplar, than a plain advisor. His support, guidance, patience, and encouragement throughout the years has been immeasurable, and I cannot thank him enough for that.

Special thanks goes to my collaborators at the Smithsonian Center for Astrophysics: Dr. Matthew L. N. Ashby, and Dr. Steven P. Willner, for their valuable scientific guidance and counsel.

I would like to express my gratitude to the Professors of the Astronomy Section at the Physics department of the University of Crete, and especially Professor Emeritus Nikos Kylafis, and Professor & Chairman of the Department Iossif Papadakis, for their inspiring interaction and guidance throughout my MSc studies.

I would also like to thank Dr. Manolis Xilouris for his advise and encouragement to apply to the MSc program in Advanced Physics at the University of Crete, and his alacrity and faith for future collaboration.

Many thanks to the Skinakas Observatory personnel: Anna Steiakaki, Tassos Kougentakis, George Paterakis, Dr. Efthymios Palaiologou, for their overall assistance and the wonderful time we spent observing at Skinakas Observatory.

I'm more than thankful to Grigoris Maravelias, Paolo Bonfini, and Konstantina Anastasopoulou for sharing moments not just at work, but in life.

Many thanks goes to fellow PhD students, MSc students, Post-Docs, which passed through the Department of Physics throughout the years, and especially: Tzina Panopoulou, Alexandros Psychogios, Theodoris Bitsakis, Stergios Kyanidis, Maria Koutoulaki, Ioanna Leonidaki, Ioannis Liodakis.

A very special thanks to my fiancée Maria for her compassion, thoughtfulness (and her incredible chicken pie!), and to my best friend Valantis, both for their continuous support and for all the moments we shared all these years.

I will always be grateful to my family, and especially to my mother Alexandra, for her support and positive thinking all these years. Thanks also to my sister Adamantia who shared all her bizarre dreams and nightmares with me and made me laugh in tough days, and to my beloved 4-months old niece Yiasemi for bringing new light and joy in my life.

# Contents

# List of Figures

# List of Tables

# 1 Introduction

## 1.1 The Central Engine of Ionization in Galaxies

Energy production in galaxies is a manifestation of two major processes: Star formation, and accretion of matter onto the central black hole, commonly referred to as active galactic nuclei (AGN) activity. While star formation is considered as the most common process, the imprints of both star formation and AGN activity are often encountered and compete in the total energy output of galaxies. Star formation is a global process taking place throughout the body of galaxies, predominately in the disk and less actively in bulges, while AGN activity happens in the central parsec-scale regions of galaxies. Distinguishing between these two major processes is not always a trivial task, but it is undoubtedly a crucial and important step towards understanding their respective role in galaxy evolution. In the following sections (1.1.1–1.1.2) we present the basic concepts and properties of these two processes.

### 1.1.1 Star Formation

With the advent of wide-field and multi-wavelength surveys over the past decade, a large amount of high-quality observational data has become available, advancing our knowledge on star formation in all scales. New space and ground-based facilities

has allowed the detailed examination of the wide range of different environments that star formation occurs. The most notable facilities and missions include the Atacama Large Millimeter/sub-millimeter Array (ALMA) observatory, the Spitzer Space Telescope (Werner et al., 2004) and Herschel Space Observatory (Pilbratt et al., 2010), the Hubble Space Telescope (HST), and Galaxy Evolution Explorer (GALEX) satellite mission (Martin et al., 2005). In addition, the Sloan Digital Sky Survey (SDSS, York et al. 2000) is the first digital optical survey covering a substantial fraction of the sky, offering a plethora of high-quality spectrophotometric data for nearby and intermediate redshift galaxies. Complementing the abundance of multi-wavelength observations, new technical innovations in astronomy such as integral field unit (IFU) spectroscopy has allowed the acquisition of pixel-by-pixel spectra for different regions of nearby galaxies, leading to the detailed examination of the physical conditions and stellar population properties in spatially resolved regions within galaxies. The present thesis work utilizes the majority of data from these facilities and surveys to characterize processes of star-formation in the local Universe.

Most of the star formation in galaxies occurs in spiral arms, where large molecular clouds concentrations co-exist with young luminous short-lived O and B-stars (OB associations), and ionized gas regions (H II regions). Due to the complex galactic environments in which star formation takes place, it is evident that it can only be studied at its full context when examined from a multi-wavelength perspective. Stars are born embedded in dark molecular clouds and dusty environments where light is absorbed and obscured, and star-formation activity can be mostly inferred from re-emission of light in longer wavelengths. Figure 1.1.1 shows an example of the spiral galaxy M101 as observed in different wavelengths. Infrared (IR) observations from Spitzer reveal areas of warm dust regions and dust lane structures where stars can form, while the optical HST image shows regions of blue star-forming clumps where new stars have formed. Traces from hot gas emission are visible in X-ray light as revealed in the Chandra image.

While star-formation is primarily a small-scale phenomenon and can be effectively decomposed and understood in resolved scales within the Milky Way, extragalactic studies of star-formation offer the statistical advantage of extended samples of galaxies both in numbers as well as in diversity of environments under which star formation occurs. Extragalactic observations have revealed important scaling laws, such as the correlation between the disk-averaged SFR and gas surface densities in galaxies, known as the Kennicutt-Schmidt (KS) SFR law (Schmidt 1959; Kennicutt 1998b). The KS law is parametrized as $\Sigma_{\rm SFR} \propto \Sigma_{gas}^{1.4}$ and the precise form of this relation depends on

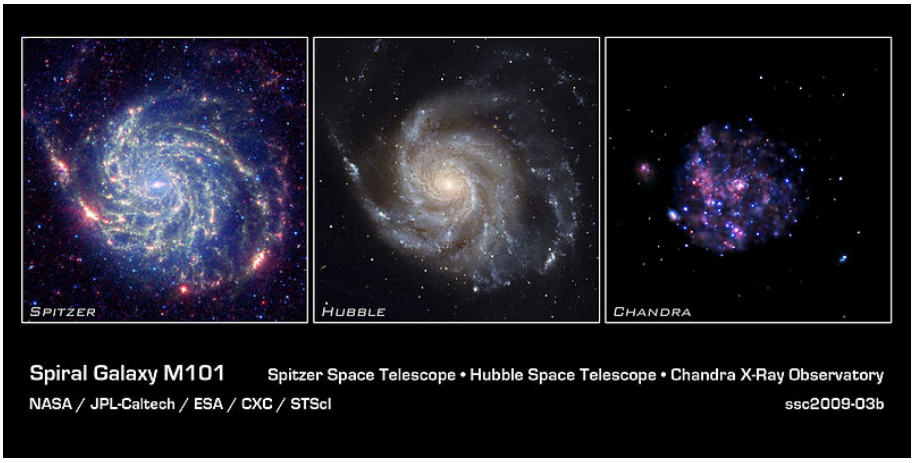


**Figure 1.1.1:** The spiral galaxy Messier 101, as observed from Spitzer Space Telescope (left panel), HST (middle panel), and Chandra X-ray Observatory (right panel). The yellow-green filaments in the Spitzer image are dust lanes where new stars can form, while regions in red is dust warmed by the light of hot, young stars. In the HST image star-forming regions are shown in bright blue clumps, while the older stellar populations in the center have yellow colors. Chandra's image taken in X-ray light shows the high-energy features of M101. Pink emission indicates lower-energy X-rays and the blue higher-energy X-rays. The white dots are X-ray sources that include the remains of exploded stars, but also material colliding at high speeds around black holes. The pink and blue colors are emission from hot gas and massive stars clusters.

assumptions about how $\Sigma_{gas}$ is derived from the observations. Figure 1.1.2 (adopted by Kennicutt & Evans (2012)) shows the KS law using an diverse and enlarged sample of galaxies from that studied by Kennicutt (1998b) with the surface density defined as the total gas mass (molecular plus atomic), and SFRs and gas masses normalized to the radius of the main star-forming disk.

Star-forming galaxies can be categorized based on the mode of the star-formation activity within them. Normal star-forming galaxies like the Milky Way are forming stars with a rate of $\sim 1-3$ $M_{\odot}$/yr, while the so-called starburst galaxies are characterized by a strongly enhanced star-formation rate often larger by a factor of more than a hundred compared to normal star-forming galaxies. On the other hand, the GALEX mission was revealed the detection of low-level star-forming activity in environments often considered to be devoid of star formation, such as early-type galaxies, dwarf galaxies, low-surface-brightness galaxies, and extreme outer disks of normal galaxies. Therefore, studying the entire context of star-formation as encountered in different modes and environments is essential to frame a complete picture of the star forming phenomenon and understand its role in galaxy evolution.

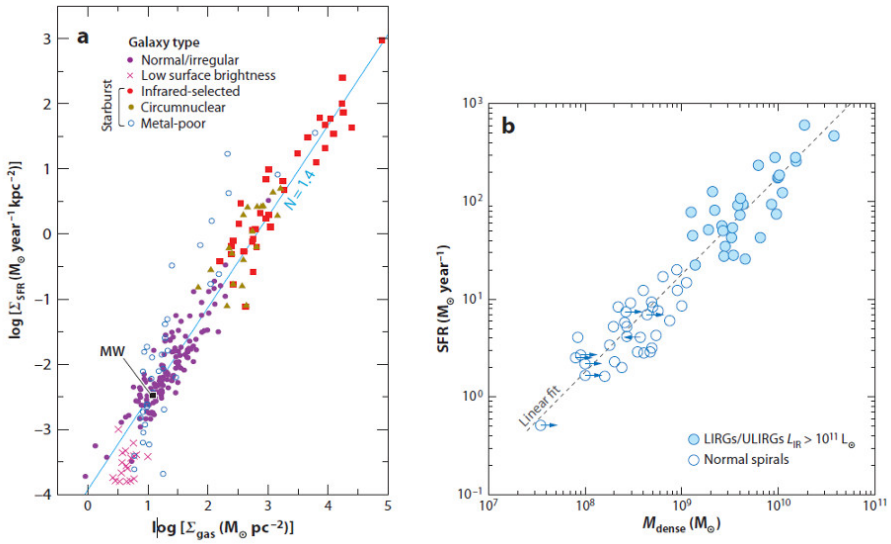


**Figure 1.1.2:** (a) Relationship between the disk-averaged surface densities of star formation and gas (atomic and molecular) for different classes of star-forming galaxies. The light blue line shows a fiducial relation with slope N = 1.4 (not a fit). (b) Corresponding relation between the total (absolute) SFR and the mass of dense molecular gas as traced inHCN. The dashed gray line is a linear fit, which contrasts with the nonlinear fit in panel a. [Adopted from Kennicutt & Evans (2012)]

### 1.1.2 Active Galactic Nuclei

The term active galactic nuclei (AGN) describes the energetic phenomena in the nuclei of galaxies which cannot be attributed clearly and directly to stars. The mechanism responsible for the energetic nuclear regions of AGN is considered to be accretion of cool gas on to a supermassive black hole, originating either from the host galaxy or the extragalactic environment (e.g., cluster gas, companion galaxies). Large-scale gravitational torques, such as those produced by galaxy bars and galaxy interactions have the potential to remove significant amounts of angular momentum and drive the gas into the central regions of galaxies (e.g., García-Burillo et al. 2005). However, the gravitational torques have a limited effect on sub-kpc scales, and due to the conversion of angular momentum the infalling matter does not fall directly into the black hole but forms an accretion disk. During these mass-accretion events large amount of energy is liberated, often producing bolometric luminosities of $L_{bol} \geq 10^{12} L_{\odot}$.

The AGN class encompasses a large range of objects and their characterization and distinction can be made with more than one ways. A widely used classification scheme is based on their optical spectroscopic properties, such as the presence or absence of

broad permitted lines, the degree of ionization of narrow lines, as well as their optical morphologies, e.g., point-like sources (quasars) or clearly visible host galaxies (Seyferts). Similarly, different AGN classes are defined based on their radio properties, such as the presence of radio jets, their radio morphology, or their radio spectrum. Other classification schemes are based on the multi-wavelength variability of the sources or the overall shape of the SED from X-rays to radio. However, among the large number of AGN categories the two major subclasses that are generally recognized are Seyfert galaxies and quasars.

Seyfert galaxies are considered as modest luminosity AGNs (typically between $10^{41} - 10^{44}$erg s$^{-1}$) compared to quasars ($10^{45} - 10^{46}$erg s$^{-1}$), but they are dominated by emission lines of very high excitation. The high excitation energy of some of the observed emission lines requires photons more energetic than photons from young stars. Such high energy photons can be produced by inverse Compton scattering and synchrotron emission processes at the immediate vicinity of the black hole. Seyfert galaxies have a quasar-like nucleus but a clearly detectable host galaxy. A common characteristic in the nuclear spectrum of Seyfert galaxies is the presence of broad-line features that are prominent in the ultraviolet (UV) and optical part of the spectrum. These are known as Type-1 Seyferts (or Seyfert 1). Another set of narrow emission lines are typically superposed on top of the broad lines of Seyferts 1, while Seyfert galaxies showing only narrow lines in their spectra are denoted as Type-2 (or Seyfert 2). In between Seyfert 1 and 2 intermediate classes exist (Seyfert 1.5, 1.8, 1.9) which are defined based on their broad-to-narrow line flux ratio. Figure 1.1.3 shows an example spectrum of the Seyfert 1 galaxy NGC 1275, and Figure 1.1.4 shows the optical spectrum of the Seyfert 2 galaxy NGC 1667.

Quasars belong to the most luminous subclasses of AGN, exceeding the luminosity of normal galaxies by a factor of a thousand, and with a small minority (∼5–10%) being strong radio sources. Quasars are distinguished from Seyferts in that they are in general spatially unresolved. Spectroscopically, quasars have very similar characteristics to type-1 Seyferts with broad permitted emission lines of 10000 km s$^{-1}$ FWHM, and narrow forbidden emission lines with widths of several 100 km s$^{-1}$ which are still broad compared to the typical velocities in normal galaxies (e.g., Blandford et al. 1990). On the other hand quasars, in contrast to Seyferts, show very weak stellar absorption features as a result of the lower contribution of the host-galaxy light.

The wide variety of AGN classes can be explained, at least to a first approximation, by geometric considerations depending on the angle between the accretion disk axis and the line-of-sight to the source (e.g., Antonucci 1993). Figure 1.1.5 displays the

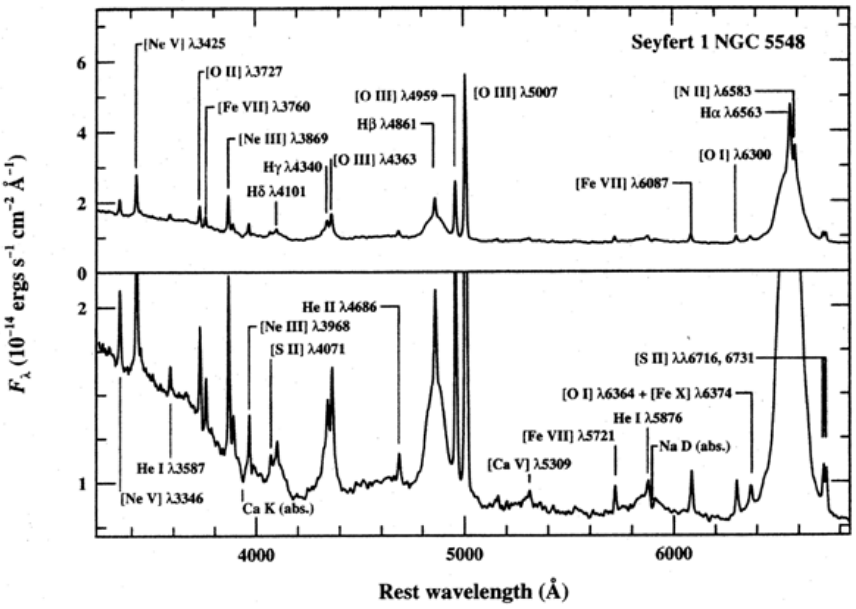


**Figure 1.1.3:** The optical spectrum of the Seyfert 1 galaxy NGC 1275. The prominent broad and narrow emission lines are labeled. The vertical scale is expanded in the lower panel to show the weaker features. The full width at half maximum (FWHM) of the broad components is about 5900 km s$^{-1}$, and the width of the narrow components is about 400 km s$^{-1}$. Adapted from B.M. Peterson An Introduction to Active Galactic Nuclei, Cambridge University Press, (Peterson, 1997)

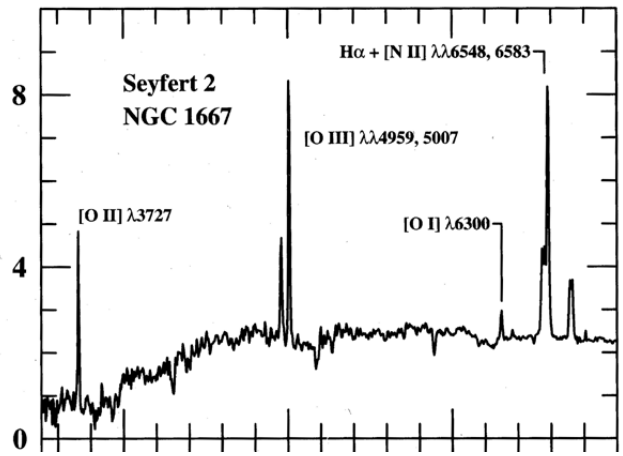


**Figure 1.1.4:** The optical spectrum of the Seyfert 2 galaxy NGC 1667. Adapted from B.M. Peterson An Introduction to Active Galactic Nuclei, Cambridge University Press, (Peterson, 1997)

current widely accepted AGN unification scheme. An accretion disk surrounds the central SMBH emitting the bulk of UV and optical continuum emission. Gas clouds above and below the accretion disk are responsible for the broad emission lines seen in the spectra of Type-1 AGN, and this region is referred to as *broad line region* (BLR). The BLR is surrounded by an optically thick structure most commonly believed to be a dusty molecular torus, though its geometry is probably more complicated. Outside the molecular torus a low-density region exists where narrow forbidden and permitted emission lines are produced, known as the *narrow-line region* (NLR). An observer located near the plane of the disk observing through the dusty molecular torus will not observe the BLR that is obscured by the torus, but will only see narrow emission lines from the NLR gas which is located at much larger distances from the black hole. Jets appear to be characteristic ingredients of all AGNs and are fully visible when they are perpendicular to the observer's line of sight. In contrast, jets are not clearly distinguishable when they are seen face-on and their emission is strongly beamed in the direction of the jet motion, which is the case of blazars and quasars.

AGNs are found in almost all galaxy evolutionary stages, from star-forming galaxies (e.g., Gu et al. 2006; Davies et al. 2007), to "green valley" galaxies which are considered as a transitioning stage from the star-forming blue cloud to the quiescent red sequence loci in the color-magnitude diagram (CMD) of galaxies (e.g., Georgakakis et al. 2008), as well as quiescent elliptical galaxies (e.g., Schawinski et al. 2010). The evolved nature of many AGN host galaxies can be a result of AGN feedback quenching star formation (Nandra et al. 2007; Schawinski et al. 2009). An example of a CMD diagram for different AGN classes is shown in Figure 1.1.6.

### 1.1.3 LINERs and Composite Objects

Among the most intriguing and at the same time complicated cases of galaxy activity types, are those of composite objects and Low-Ionization Nuclear Emission-Line Regions (LINERs; Heckman 1980). The former are considered as galaxies whose energy output is a composition of star-forming and AGN activity, while the central source of ionization in LINERS is still a subject of great dispute and controversy in the literature.

Composite objects, often referred to as transition objects (TO), were identified by Ho et al. (1993) as galaxies whose [OI] strengths are intermediate between those of H II nuclei and LINERs. In standard line-ratio diagrams (e.g., Section 1.2, left-panel plot of Figure 1.2.1), transition objects are empirically defined to be those sources that lie between the loci of H II regions and AGN. The host galaxies of transition nuclei exhibit systematically higher levels of recent star formation. At the same time though,

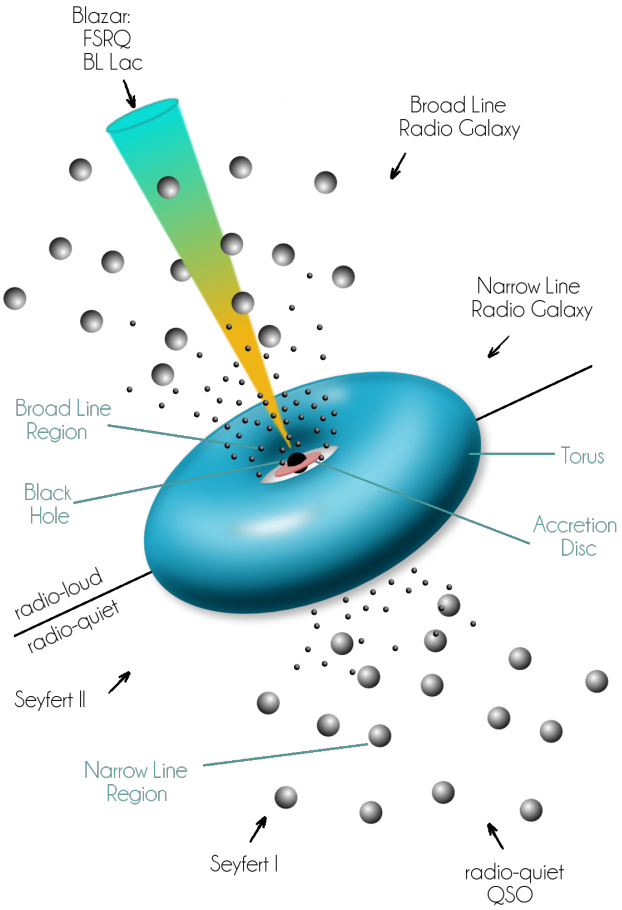


**Figure 1.1.5:** Sketch of the AGN unification scheme. The accretion disk is surrounded by a thick-like structure containing dust clouds obscuring the view to the center of the AGN. When looking from a direction near the plane of the disk the BLR is blocked, whereas it is directly visible from directions closer to the symmetry axis of the disk. The difference between Seyfert 1 and Seyfert 2 can be explained based on the orientation relative to the line-of-sight. If an AGN is seen exactly along the jet axis, it appears as a blazar. Image credit: F. Krauss after Urry & Padovani (1995).

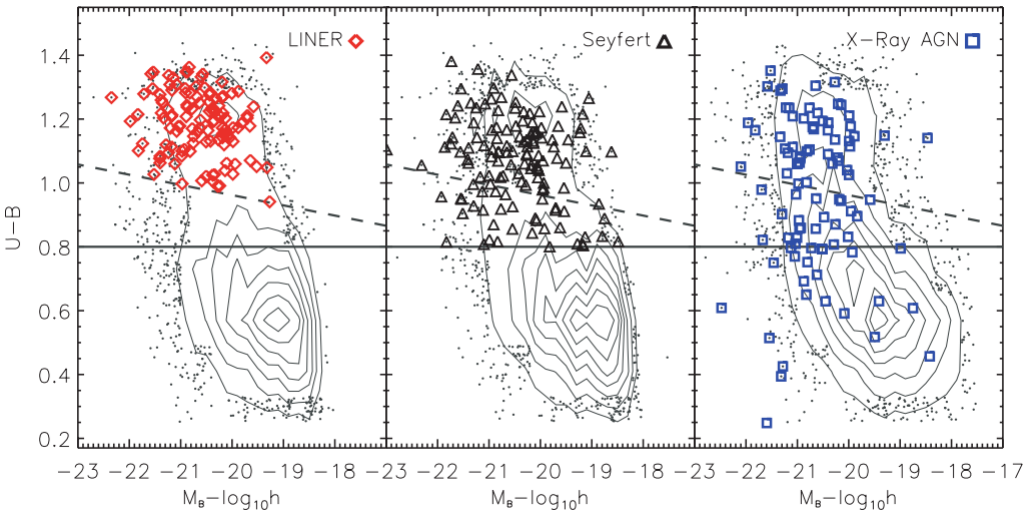


**Figure 1.1.6:** The CMD for LINERs (left-hand panel, red diamonds), Seyferts (middle panel, black triangles) and X-ray AGN (right-hand panel, blue squares), adopted from Montero-Dorta et al. (2009).The demarcations given by the solid and dashed lines represent the conventions adopted to separate the blue cloud from the green valley, and the latter from red sequence objects respectively.

the detection rate of X-ray cores in transition objects is remarkably high and identical to that of LINER 2s and similar to that of Seyfert 2s (Ho, 2008), strongly suggesting that the majority of transition objects indeed do harbor AGNs. Therefore, the class of composite objects appears as the ideal galaxy population for the study of the connection between the star formation and AGN phenomenon.

The activity class of LINERs is much more controversial regarding their main ionizing energy source. LINERs are sometimes considered as the low-luminosity, low-accretion-rate branch of Seyfert galaxies (e.g., Ho et al. 1993; Ho et al. 2003), which is a justified assertion at least for Type-1 LINERs with clear broad H$\alpha$ emission line features. However, it has been also shown that post asymptotic giant branch (post-AGB) stars can produce the required ionizing spectrum necessary to excite LINER-like emission (e.g., Binette et al. 1994; Stasińska et al. 2008), placing serious argument against the AGN nature of LINERs. Furthermore, results from the MaNGA survey (Belfiore et al., 2016b) showed that in LINER galaxies not contaminated by star formation, line ratios sensitive to the ionization parameter ([O III] $\lambda$5007/[O II] $\lambda$3727, and to some extent [O III] $\lambda$5007/H$\beta$) have flat or very shallow profiles over radial scales of tens of kpc, indicating an extended source of ionization consistent with extended starlight, and

at odds with the steeper profiles predicted in the AGN scenario.

## 1.2 Optical activity diagnostics

Standard optical emission-line diagnostic diagrams have been extensively used and calibrated over the past decades to identify the dominant ionizing source of radiation in galaxies, especially in the local universe. The Baldwin, Phillips, and Terlevich emission-line ratio diagnostic of [O III] $\lambda$5007/H$\beta$ against [N II] $\lambda$6583/H$\alpha$ (BPT, Baldwin et al. 1981; Veilleux & Osterbrock 1987) efficiently separates galaxies whose ionizing spectrum is dominated by star formation from those dominated by AGN activity. The extreme ultra-violet (EUV) hard radiation field from the accretion disk of an AGN ionizes the [O III] and [N II] lines, producing larger [O III] $\lambda$5007/H$\beta$ and [N II] $\lambda$6583/H$\alpha$ line ratios than photoionization from young stars, separating star-forming and AGN dominated galaxies in the BPT diagram. Kewley et al. (2001) using stellar population synthesis, photoionization and shock models, defined a theoretical upper bound to the location of star-forming galaxies in the [O III] $\lambda$5007/H$\beta$ versus [N II] $\lambda$6583/H$\alpha$ diagram, above of which the spectrum of galaxies is dominated by AGN processes. Furthermore, Kauffmann et al. (2003) using a sample of 122,808 SDSS galaxies empirically separated galaxies having pure star-forming activity. In between the Kauffmann et al. (2003) and Kewley et al. (2001) lines objects that host both starburst and AGN activity are located, commonly referred to as composite or transition objects. Two more variations of the standard [O III] $\lambda$5007/H$\beta$ against [N II] $\lambda$6583/H$\alpha$ diagram are often used, replacing the [N II] $\lambda$6583/H$\alpha$ ratio with [S II] $\lambda\lambda$6716, 6731/H$\alpha$, or [O I] $\lambda$6300/H$\alpha$. Kewley et al. (2006) refined the [S II] $\lambda\lambda$6716, 6731/H$\alpha$, and [O I] $\lambda$6300/H$\alpha$ diagnostics calculating an empirical separating line in the AGN plane, distinguishing the Seyfert populations from LINERs. In the same context, Schawinski et al. (2007) defined an empirical line in the [N II]/H$\alpha$ BPT diagnostic separating Seyfert from LINER classes.

The BPT diagrams are limited for use in galaxies that lie no further than $z \sim 0.5$, because beyond that redshift the [N II] emission line is shifted into the IR part of the spectrum. To overcome such difficulties, alternative diagnostics have been proposed substituting the horizontal line ratios in the BPT diagrams with other galaxy parameters. Among the most notable examples are the Lamareille (2010) "blue diagram", replacing [N II]/H$\alpha$ with [O II] $\lambda\lambda$3726+3729/H$\beta$, the Mass-Excitation (MEx) diagram (Juneau et al. 2011, Juneau et al. 2014) using total stellar mass (Fig. 1.2.2), and the Color-Excitation (CEx) diagram (Yan et al., 2011) using the rest-frame $U - B$ color. Another approach to identify distant AGN was presented by Trouille et al. (2011) (TBT

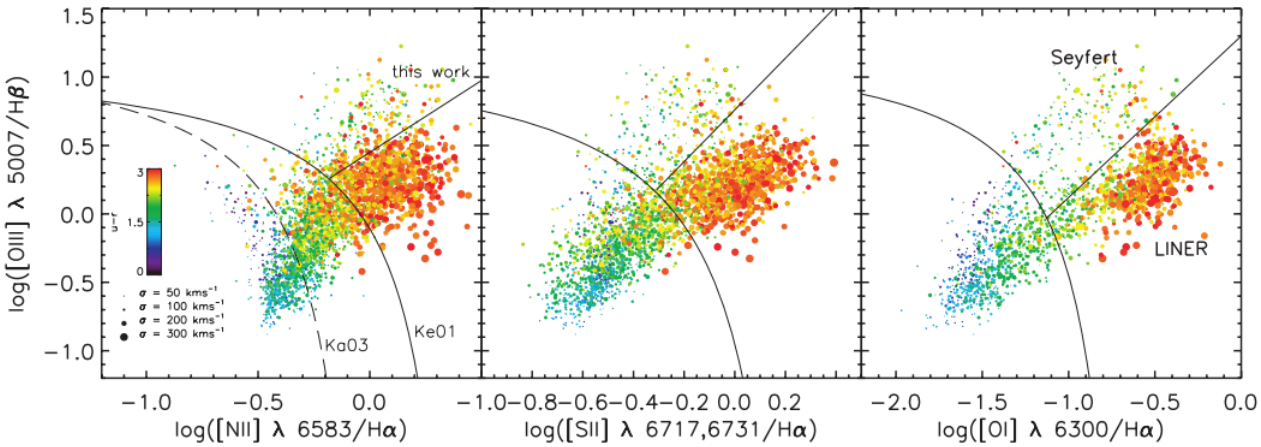


**Figure 1.2.1:** The three variations of the BPT diagrams. The dashed line in the [N II]/H$\alpha$ diagram (left-hand panel) is the empirical star-forming line of Kauffmann et al. (2003), while the solid curve in all three diagrams is the theoretical maximum starburst line from Kewley et al. (2001). The straight black line in all diagrams separates Seyfert nuclei from LINERs. The Seyfert/LINER demarcation line is defined by Schawinski et al. (2007) in the [N II]/H$\alpha$ diagram while for the [S II]/H$\alpha$ and [O III]/H$\beta$ diagrams the lines are defined by Kewley et al. (2006). Each galaxy is colored by its optical $u - r$ color and point sizes scale with the galaxy velocity dispersion. Figure adopted from Schawinski et al. (2007).

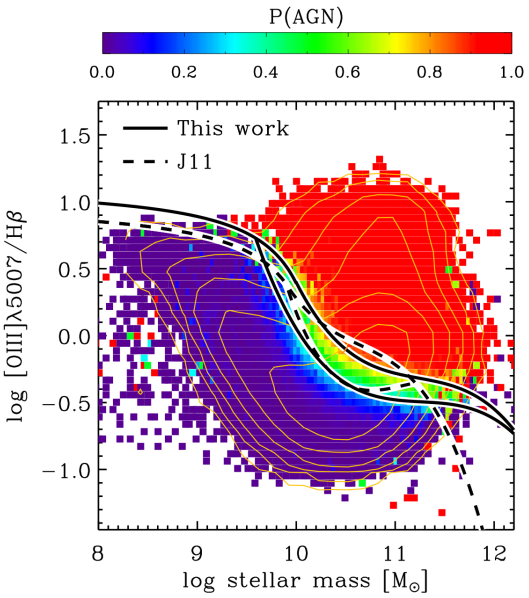


**Figure 1.2.2:** The MEx diagram adopted from Juneau et al. (2014). The color scheme indicates the fraction of galaxies classified as AGN using the BPT-[N II]and [S II] diagnostics, from 0.0 (purple) to 1.0 (red). The demarcation lines separate star-forming from AGN populations, while composite objects are found in between them. The solid lines are based on the Juneau et al. (2014) SDSS DR7 sample used to calibrate the MEx diagram which is the refined version of the Juneau et al. (2011) (J11), shown with dashed lines.

diagram) based on rest-frame $g - z$ color, [Ne III]$\lambda$3869, and [O II] $\lambda\lambda$3726+3729 used for galaxies out to $z < 1.4$. Lastly, Kewley et al. (2013) introduced the "cosmic" BPT diagram using a new redshift-dependent optical classification line for the [O III] /H$\beta$ versus [N II]/H$\alpha$ diagnostic that accounts for how the structure of the ISM changes with redshift, showing that the position of independently confirmed AGN is consistent with the new classification line at $z \sim 2.5$.

## 1.3 Galaxy activity demographics and host-galaxy properties

From the era of the earliest redshift surveys (e.g., Humason et al. 1956, Heckman 1980) it was established that a large fraction of local galaxies contained emission-line nuclei. The physical processes governing the central regions in galaxies responsible for their emission-line spectral characteristics can be very well attributed to star-formation

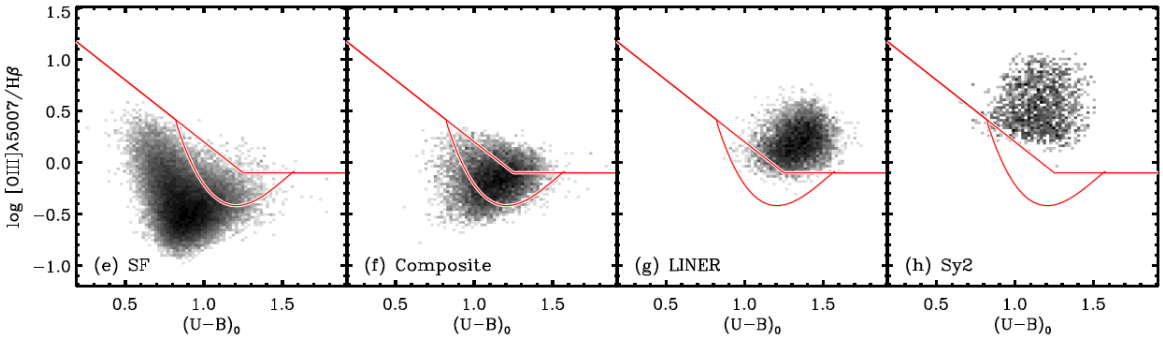


**Figure 1.2.3:** The CEx diagram (Yan et al., 2011) adopted from Juneau et al. (2011). Galaxies are plotted separately for each classification based on the BPT diagrams. The empirical curves separate SFGs from Sy and LINER classes while in between the lines is the region where BPT-SFGs and BPT-composite galaxies overlap.

activity in the circumnuclear regions, as well as to accretion processes onto the central BH, as discussed in Section 1.1.2 . Understanding and distinguishing between the different activity mechanisms is extremely important for the detailed understanding of the respective galaxy populations, their role in galaxy evolution, and gaining insights on the BH and AGN demographics in the local Universe.

The Palomar spectroscopic survey of nearby galaxies (Filippenko & Sargent 1985; Ho et al. 1995; Ho et al. 1997a; Ho et al. 1997b) is arguably among the most important activity demographics surveys, examining in detail the different galaxy subpopulations and their properties. The Palomar survey is an optical, magnitude-limited ($B_T \leq 12.5$ mag) sample of very nearby galaxies at a median distance of 17 Mpc. One of the most interesting results in the series of Palomar survey studies is the fact that the activity class of LINERs (Low-ionization nuclear emission-line regions) constitutes the dominant population of AGNs in the local Universe. Furthermore, these studies found that 15% of the AGN population in the survey has broad H$\alpha$ emission lines, while additionally 11% more have questionable (rather broad) detections concluding that $\sim 20 - 25\%$ of all nearby AGN are type 1 sources.

In terms of host galaxy properties of AGN, the Palomar survey sample concluded that the host galaxies of Seyferts and LINERs display a remarkable degree of homogeneity in their large-scale properties. Specifically, they found that both classes have essentially identical total luminosities, bulge luminosities, sizes, while no obvious differences were found in the integrated optical colors or far-IR luminosities and colors, implying very similar global stellar content and current star-formation rates. In addi-

tion, Ho et al. (2003) examined the stellar absorption-line indices and nuclear continuum colors of the Palomar spectra and deduced that the three categories of AGN have very similar stellar content.

A vastly larger statistical census on the activity demographics and host-galaxy properties of lower and intermediate redshift galaxies was established based on results from the Sloan Digital Sky Survey (SDSS, York et al. 2000). Kauffmann et al. (2003) reported an overall AGN fraction of 40% of which 10% are Seyferts, similar to the 43% and 10% of AGN and Seyferts reported by Ho et al. (1997b) respectively. Furthermore, Kauffmann et al. (2003) found that AGN of all luminosities reside almost exclusively in massive galaxies and have distributions of sizes, stellar surface mass densities and concentrations that are similar to those of ordinary early-type galaxies. However, it should be noted that stellar mass determination were based on mass-to-light ratio $M/L$ calibrations, which for the AGN cases should be only treated as upper limits. Furthermore, SDSS spectra are obtained from $3''-$diameter fibers including substantial contamination from off-nuclear emission, which dilutes and, in same cases, masks the emission from the nucleus. The host-galaxy light contamination may confine the emission-line nuclei identification only to the cases of bright galaxy nuclei, but furthermore light from gas shocked by supernova remnants or diffuse warm ionized plasma can mimic LINER-like spectra, biasing the derived demographics and galaxy properties.

The era of IFU spectroscopy introduced significant observational improvement in galaxy studies, allowing the examination of galaxies and their physical properties within kpc physical scales. The SDSS-IV Mapping Nearby Galaxies at Apache Point Observatory (MaNGA) survey (Bundy et al., 2015), is an ongoing IFU survey that is obtaining spatially resolved spectroscopy for a sample of 10,000 nearby galaxies. Some of the areas explored by the MaNGA survey include the spatially resolved star formation histories in galaxies as a function of galaxy mass and type. Specifically, Goddard et al. (2016) using a sample of 721 galaxies with stellar masses ranging between $10^9 - 10^{11.5}\mathrm{M}_\odot$, showed that stellar age gradients tend to be shallow for both early-type and late-type galaxies. Furthermore, they found that mass-weighted age gradients of early-types are positive pointing to an "outside-in" progression of star formation, while late-type galaxies have negative light-weighted age gradients, suggesting an "inside-out" formation of discs. Metallicity gradient measurements performed by Goddard et al. (2016) revealed negative gradients for both early and late-type morphological classes that are correlated to galaxy mass, with gradients becoming steeper with increasing galaxy mass. However, the above properties have not been yet examined in the context of galaxies hosting AGN activity.

## 1.4 The Starburst–AGN Connection

Several scaling relations between black-hole mass and host galaxy properties such as stellar velocity dispersion, bulge mass, and bulge luminosity imply that black holes grow in parallel with their host galaxies (Kormendy & Richstone 1995; Magorrian et al. 1998; Ferrarese & Merritt 2000; Mullaney et al. 2012). Furthermore, the cosmic evolution of the star-formation rate density and the supermassive black hole mass accretion rate density (e.g., Silverman et al. 2008; Aird et al. 2010) point towards a connection between the evolution of star formation and AGN activity. However, the exact mechanisms under which AGN activity regulates star-formation in the host galaxy, or circumnuclear star-formation affects the accretion activity on the central black hole remain yet unclear (see Kormendy & Ho 2013 for a review).

The growing number of IFU surveys, such as the Calar Alto Legacy Integral Field Area (CALIFA) Survey (Sánchez et al., 2012), and the MaNGA survey of local galaxies can provide statistical analysis of the radial variations in star-formation histories, SFRs and the relative fraction of starburst to AGN energy output in AGN host galaxies. Davies et al. (2014) using four CALIFA galaxies showed that star-formation and the AGN are each responsible for at least 25% of the global H$\alpha$, [OII], and [OIII] luminosities highlighting the need to correct for any AGN contribution when calculating star-formation rates using H$\alpha$ or [OII] tracers. Furthermore, Davies et al. (2016) using IFU data for two AGN host galaxies from the S7 survey (Dopita et al., 2015), showed that many of the spectra extracted from the sample datacubes showed clear evidence of mixing sequences between star formation and AGN activity. The emission line luminosities of $> 85\%$ of these spectra could be reproduced by linear superpositions of the emission line luminosities of one AGN dominated basis spectrum and one star formation dominated basis spectrum.

In this thesis we provide further evidence for a connection between star-formation processes in the central regions of galaxies and their hosts, presenting a correlation between the nuclear SFR and total-stellar mass. This correlation can provide insights on the characterization of the nature of feedback mechanisms, whether it is AGN-driven quenching of star formation (negative feedback), or AGN-driven boosting of star formation (positive feedback) as discussed in Section 5.5.3.

## 1.5 The Galaxy Main Sequence of Star Formation

Advances in space and ground-based missions over the past decade has enabled the study of large samples of galaxies in a wide range of redshifts in great detail. Furthermore, the considerable progress in stellar population synthesis (SPS) modeling (e.g., Bruzual & Charlot 2003 - BC03; Maraston 2005; Conroy & Gunn 2010) has improved the determination of key physical parameters of galaxies, such as SFRs, stellar population properties (masses, ages, metallicities), and dust attenuation among others. The robust determination of these parameters has also revealed a strong correlation between SFR and $M_\star$, known as the "main sequence" (MS) of star-forming galaxies and holds from $z = 0 \sim 6$ (e.g., Brinchmann et al. 2004; Daddi et al. 2007; Elbaz et al. 2007; Whitaker et al. 2012).

The MS implies that higher stellar-mass systems undergo more intense star formation activity than lower mass systems. However, the slope of the MS is non linear and depends both on redshift and sample selection criteria, as discussed in detail in Chapter 5. Figure 1.5.1, adopted from Speagle et al. (2014), shows the evolution of the MS at different redshifts, compiled from 25 MS literature studies. It is evident that galaxies on the MS formed stars at much higher rates in the past than today. This is related to the rapid quenching of star-formation (e.g., Bell et al. 2007; Moustakas et al. 2013) as well as the "downsizing paradigm" for galaxy evolution (Cowie et al., 1988) which describes the movement of star formation from more massive to less massive systems with time. Another important outcome from the study of the MS comes from the fact that the correlation is rather tight, with only ∼0.35 dex of scatter (Speagle et al. 2014 and references within). This is indicative that star formation is regulated predominantly through secular processes rather than stochastic, such as merger-driven star-forming episodes.

The numerous studies dedicated to the MS of star-forming galaxies show large variations between the measured MS slopes and the reported scatter around the best-fit of the SFR–$M_\star$ correlation. The variations with respect to the scatter of the MS are related to the parameters that affect the determination of SFR and $M_\star$, such as the choice of the IMF, $M/L$ conversions, assumed SFH, SSP libraries, SED fitting parameters, while variations in the MS slope are linked mostly to sample selection effects. A choice of actively SFGs produces slopes close to unity, while a mixture of star-forming and passively evolving populations will produce sublinear slopes. The

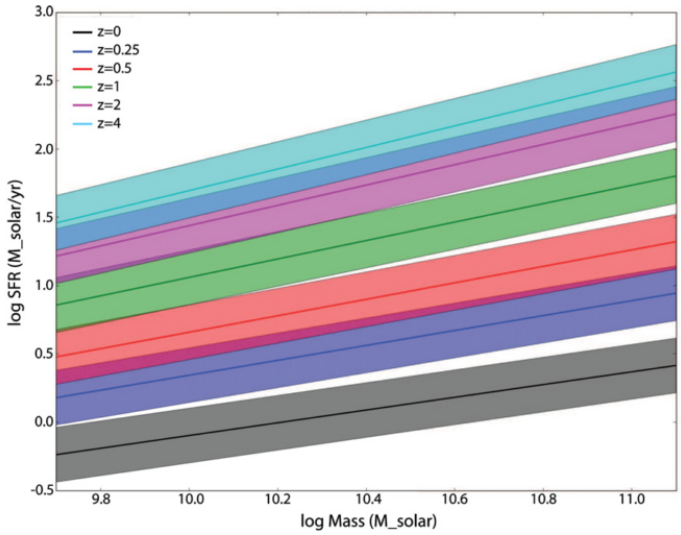


**Figure 1.5.1:** The "main sequence" relations at different redshifts as calculated by Speagle et al. (2014) combining 25 literature studies. The widths of the distributions correspond to $\pm 0.2$ dex. It is evident that the slope of the MS is a function of redshift, and furthermore the SFR at fixed mass evolves $\sim$2 orders of magnitude from $z = 4$ to 0. [Figure adopted from Speagle et al. (2014).]

selection of pure SFG populations and the accurate exclusion of AGN hosts is also a parameter affecting the results reported in various literature works.

Recently, certain works have focused on the study of the MS of star-forming galaxies in sub-galactic scales, showing that a similar MS-like correlation between the SFR surface density and stellar mass surface density for individual regions within galaxies is also present. At intermediate to higher redshifts ($z > 1$) the sub-galactic correlation has been determined with a slope close to unity (e.g., Wuyts et al. 2013, Magdis et al. 2016), while at lower redshifts sublinearity has been reported (e.g., Cano-Díaz et al. 2016). As with the case of the integrated MS, the different choice of parameters used for SFR and stellar-mass estimation as well as the selection criteria affects, the determination of the sub-galactic MS properties.

## 1.6 Thesis overview

In this thesis we aim to study the activity demographics of a representative sample of IR-selected galaxies in the local Universe, and examine their host galaxy properties with

respect to their activity classes. A large sample of 369 galaxies spanning the full range of properties of local star-forming galaxies form the basis of this work. The representative nature of the sample (see Chapter 2) provides an exceptional opportunity for a detailed examination of nearby IR-selected AGN and star-forming galaxies, as well as their host-galaxy properties with respect to their nuclear activity types. High resolution long-slit and optical spectra combined with IR photometric colors from *Spitzer* bands are our primary tools for activity classification.

In Chapter 3 we investigate the impact of host-galaxy starlight contamination to the resulting nuclear activity classification, based on the size of the aperture of spectral extraction. Depending on the sizes and distances of galaxies, as well as the size of the observing aperture, different portions of host-galaxy light is included within the aperture of extraction. Therefore it is crucial to obtain a census on the dilution of optical emission-lines from host-galaxy light, especially in the cases of SDSS fiber spectra that may include substantial contamination from off-nuclear emission. Our analysis of the aperture effects on spectroscopic galaxy activity classification is based on observed long-slit spectra and simulated elliptical-aperture spectra of different sizes.

Chapter 4 presents the activity demographics for our sample of 369 IR-selected galaxies, using a combination of optical emission-line diagnostics and IR color diagrams to account for dust-rich galactic environments. We compare our results using different classification methods used in the literature, and further compare the classification obtained from different observing methods (fiber and long-slit spectroscopy). Furthermore, we derive nuclear star-formation rates and gas-phase metallicities for the star-forming populations, host-galaxy metallicities for all activity types with available long-slit spectroscopy, and measure abundance gradients for a subset of 12 face-on galaxies.

Finally, in Chapter 5 we use 246 star-forming galaxies from our sample and make a detailed study of the "main sequence" of star-forming galaxies in sub-galactic scales. We describe a sub-galactic main sequence relating star-formation rate surface density ($\Sigma_{\rm SFR}$) and stellar-mass density ($\Sigma_{\star}$) for distinct regions within star forming galaxies, including their nuclei. We examine the sub-galactic main sequence characteristics for different morphological groups, and furthermore we investigate the sub-galactic sequence within one galaxy.

# 2

# The Star Formation Reference Survey (SFRS)

The star formation phenomenon is a major and complex field of astrophysics, that despite its extensive examination in both galaxy-wide and (sub-)parsec physical scales it is not yet entirely understood. Star-formation activity manifests in a different manner throughout the cosmic epochs. It has been established by ground-based as well as UV and IR observations from GALEX and Spitzer that star-formation activity was significantly higher in the past (Lilly et al. 1996, Schiminovich et al. 2005, Le Floc'h et al. 2005). More specifically, the cosmic star-formation rate density shows a rise and fall from high redshifts to the present time with a peak sometime between $1 < z < 3$ (Madau & Dickinson 2014, and references therein).

While not capturing the peak of star-formation activity, the local Universe offers the opportunity to study its process in observationally resolved conditions and unprecedented detail. Star formation takes place in a plethora of different galactic environments, and its full description requires samples representative of all the physical conditions in which stars are born. Numerous efforts towards the exploration of star formation in the local Universe have been performed over the past couple decades, with some notable recent examples including the *Spitzer* Infrared Nearby Galaxies Sample (SINGS; Kennicutt et al. 2003), Great Observatories All-sky LIRG Survey (GOALS; Armus et al. 2009), *Herschel* Reference Survey (HRS; Boselli et al. 2010), Key Insights on Nearby Galaxies (KINGFISH (Kennicutt et al., 2011)). These surveys have been

designed to focus mainly on specific aspects of star formation, and therefore do not provide a complete description of star formation in galaxies. For instance, SINGS is comprised of a relatively small number of nearby and extended objects at the low-luminosity end of FIR luminosity function and therefore do not depict star-formation in its whole extent. GOALS on the other hand consists predominantly of Luminous Infrared Galaxies (LIRGs) and a few Ultra-Luminous Infrared Galaxies (ULIRGs), sampling the higher ends of star-formation and galactic activity in general, while the HRS is oriented towards high-density environments.

For a comprehensive study of the star formation phenomenon in a wide range of environments and physical conditions in the local universe, a well defined and representative sample of galaxies is required. To this cause the "Star Formation Reference Survey" (SFRS; Ashby et al. 2011) was established.

## 2.1 Sample Selection

The parent sample of the SFRS is the IRAS Point Source Catalog (PSC$z$; Saunders et al. 2000), a full-sky database of 15,411 nearby star-forming galaxies brighter than 0.6Jy at 60$\mu m$. The selection criteria were defined objectively to guarantee that the sample spans the full range of properties exhibited by star-forming galaxies in the local Universe. Specifically, the SFRS sample was selected to be well defined in the entire range of the three-dimensional space occupied by galaxies in 60$\mu m$ luminosity (L(60$\mu$m)), $F_{60}/K$s flux ratio, and far-IR flux density ratio $F_{60\mu\mathrm{m}}/F_{100\mu\mathrm{m}}$ (Ashby et al., 2011). In this scheme the L(60$\mu$m) serves as an unbiased SFR tracer, because hot young stars illuminate the interstellar material in which they are embedded, and subsequently this radiation is re-emitted to far-infrared wavelengths. The $K$s 2.2$\mu$m flux of the Two Micron All Sky Survey (2MASS; Skrutskie et al. 2006) is a robust proxy for stellar mass, and essentially the ratio of $F_{60}$ and $K-$band flux ($F_{60}/K$s) provides a measurement of the specific SFR (i.e. SFR per unit stellar mass). Finally, the far-IR flux density ratio ($F_{60}/F_{100}$) acts as a measure of dust temperature and monitors star-forming activity, because high color-temperature indicates that dust grains are close to newborn stars, while low color-temperature can be related to ambient radiation field from older populations illuminating dust in the interstellar medium (ISM). Arguably, the SFR, sSFR, and dust temperature are among the most important properties of galaxies, as they represent respectively the ongoing and past star-formation activity, as well as the densities of the regions where stars are born.

This three-dimensional parameter space was binned by decade in 60$\mu m$ luminosity

and by quartiles in both the $60\mu\mathrm{m}/K\mathrm{s}$ and the $F_{60}/F_{100}$ flux density ratio (Fig.2.1.1 adopted from Ashby et al. 2011). This ensured that the sample contains all existing combinations of high- and low-sSFR with far-IR color and luminosity. Objects were selected from the parent sample in a way that ensured representative sampling with good statistics for the entire PSC$z$ catalog (for a detailed description see Ashby et al. 2011). Ultimately, the SFRS consists of 369 galaxies guaranteeing a sample fully representative of the much larger PSC$z$, but most importantly representative of star-forming galaxies in general.

Examining star-formation in all different environments requires an uncensored sample of galaxies, and for this reason the SFRS sample did not exclude galaxies hosting AGN activity. To accurately separate AGN hosts from pure star-forming galaxies, as well as identify intermediate cases of galaxies with composite contribution from AGN and star-forming activity, we employed a set of well calibrated optical activity diagnostics (discussed in detail in Sections 4.4), further supplemented with IR activity diagnostics to account for obscured AGN. Optical fiber spectra from SDSS were available for 210 out of the 369 SFRS galaxies, based on SDSS data release 7 (DR7; Abazajian et al. 2009), at the time the SFRS sample data were assembled. For the remaining galaxies we initiated a long-slit spectroscopic campaign to collect high-resolution optical spectra. The spectra were acquired at the Fred Lawrence Whipple Observatory in Arizona using the 60-inch Tillinghast telescope with the FAST (Fabricant et al., 1998) spectrograph, during the period of 2011–2014.

## 2.2 Multi-wavelength Observations

The SFRS has a wealth of multi-band observations at its arsenal, spanning from the UV to the radio part of the electromagnetic spectrum. Multi-wavelength observations are particularly important for the broadband study of galactic properties (Section 2.2.2), but also for a complete and accurate determination of total SFRs (Section 2.2.1). The available multi-band of the SFRS sample and the fraction for the sample covered in each waveband are summarized in Table 2.2.1.

### 2.2.1 SFR tracers

A complete study of the star-formation activity requires a multi-wavelength approach. The UV emission of galaxies traces directly the emission of young stars, making the UV light one of the most direct tracers of recent/ongoing SFR. However, the primary

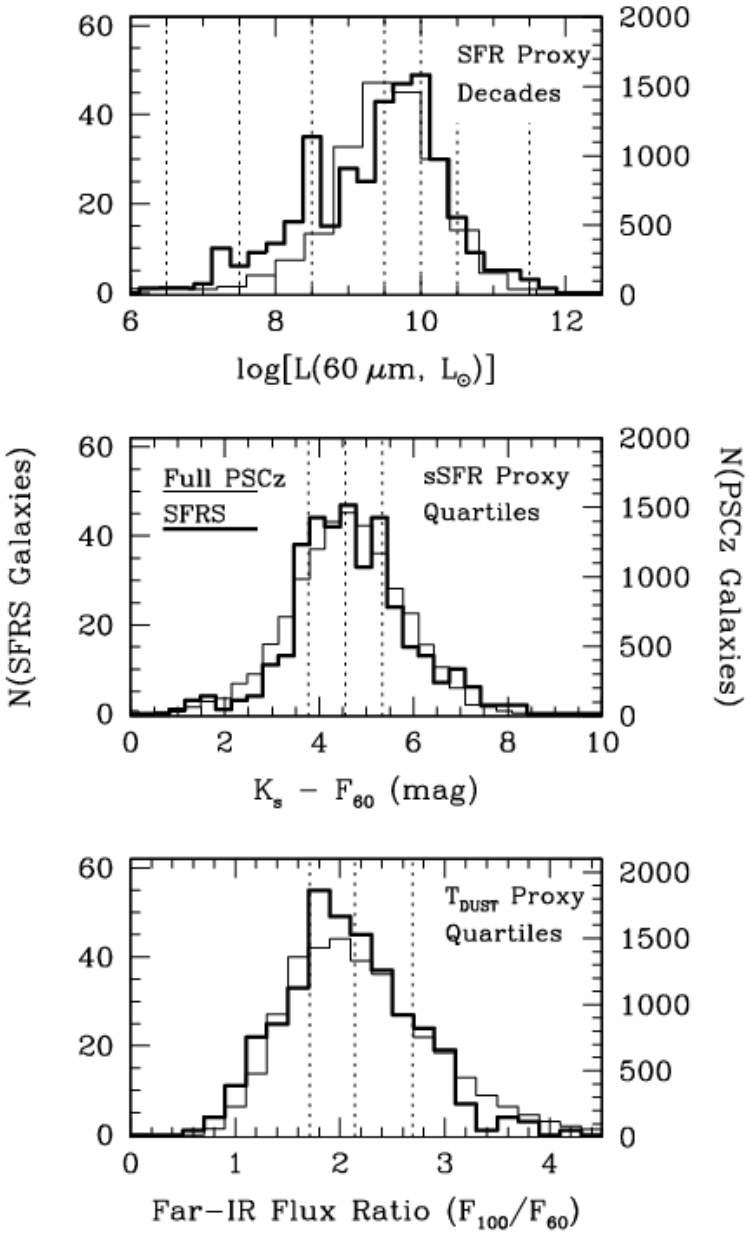


**Figure 2.1.1:** Distributions of the SFRS galaxies in each of the three parameter spaces used to select the sample. Thick histograms indicate the SFRS galaxies and are referenced to the left-hand axes, and thin histograms represent the larger PSCz sample from which the SFRS sample is drawn and are referenced to the right-hand axes. The distributions are very similar in all three panels. The vertical dotted lines in each panel indicate the boundaries defining the bins. [Adopted from Ashby et al. (2011)]

**Table 2.2.1:** Summary of the available photometric and spectroscopic multi-wavelength data for the SFRS sample. (Updated version of Table 3 in Ashby et al. 2011).

| Multi-Wavelength Data For The SFRS Galaxies | | |
|---|---|---|
| Bandpass | Observatory | Sample Coverage |
| 1.4 GHz | VLA/NVSS | 100% |
| 12,25,60,100 $\mu$m | IRAS | 100% |
| 65,90,140,160 $\mu$m | AKARI FIR All-Sky Survey | 95% |
| 12,23 $\mu$m | WISE | 100% |
| 24 $\mu$m | Spitzer/MIPS | 70% |
| 3.6, 4.5, 5.8, 8.0 $\mu$m | Spitzer/IRAC | 100% |
| $JHKs$ | 2MASS | 100% |
| $JHK$ | PAIRITEL/Skinakas | 100% |
| PS1.y | Pan-STARRS | 100% |
| $ugriz$ | SDSS | 100% |
| Optical spectra | SDSS | 57% (210/369) |
| Optical spectra | FAST (long-slit) | 43% (159/369) |
| H$\alpha$ Imaging | Skinakas | 30% (ongoing campaign) |
| 0.13–0.28$\mu$m | GALEX | 90% |
| 0.5–8.0 keV (X-ray) | Chandra, XMM | $> 30\%$ |

disadvantage of UV SFR tracers is their sensitivity to interstellar dust attenuation. ISM dust surrounding star-forming regions absorbs the light from newly formed stars and re-emits it in the IR, constituting IR tracers a necessity in the study of SFR in galaxies. IR SFR calibrations, as all SFR indicators, are subject to important systematics because IR emission does not account for the starlight that is not absorbed by dust. This becomes extremely important in dust-poor dwarf galaxies where the IR emission will systematically underestimate the SFR. Dust is not the only component that reprocesses light in the immediate environment surrounding star-forming regions. Optical (H$\alpha$, [O II]; Kennicutt 1998a) and near-IR emission lines (e.g., [NeII]12.8-$\mu$m and [NeIII]15.6$\mu$m; Ho & Keto 2007) from ionized gas surrounding young stars provide a measure of nearly instantaneous SFR, as these trace stars with lifetimes of $\sim 3-10$ Myr. Similarly to UV tracers though, H$\alpha$ is largely affected by dust attenuation. It is obvious therefore that broadband information is required for a comprehensive determination of the SFR in galaxies.

Composite multi-wavelength tracers have been used to construct dust-corrected SFRs, with the most common prescriptions using UV or H$\alpha$ combined with IR (L(TIR) or L(25$\mu$m)) measurements. Some notable examples of dust-attenuation corrections using combinations of FUV and H$\alpha$ fluxes with various IR and radio tracers are given by Hao et al. (2011) and Kennicutt et al. (2011). However, composite SFR indicators are not without systematic uncertainties of their own, as questions remain regarding the systematic reliability of the independent attenuation calibrations, or the stellar population dependences (Kennicutt & Evans, 2012). Nevertheless, composite tracers are a major improvement over single-wavelength tracers and can be used for calibrating and the uncertainties in the monochromatic indicators (e.g., Boquien et al. 2014, Hayward et al. 2014). The representative nature of the SFRS combined with the availability of multi-frequency observations delivers an excellent opportunity for precise SFR determination, but also for a robust cross-calibration between the different SFR tracers (e.g., Willner et al. in preparation).

### 2.2.2 Robust galaxy properties determination

The wealth of the SFRS multi-wavelength data is arguably an important asset in the determination of host-galaxy properties for galaxies of all activity types in the sample. The modeling of the spectral energy distribution (SED) of galaxies can reveal important information regarding their stellar populations (ages, metallicities), their dust components (composition, geometry), and the relative contribution of AGN and star formation in the total luminosity. Employing the combined power of multi-wavelength

photometry available in the SFRS sample and spectroscopic information gathered from long-slit and fiber observations (see detailed description in Section 6.2.2) will gives us the opportunity to determine precisely the host-galaxy properties for the 369 galaxies in the SFRS sample.

# 3 Aperture effects on spectroscopic galaxy activity classification

This works is published in the Monthly Notices of the Royal Astronomical Society as: A. Maragkoudakis, A. Zezas, M. L. N. Ashby., P. Willner., 2014, MNRAS, Vol. 441 2296-2308.

## 3.1 Introduction

Energy production in galaxies is based on two major processes, sometimes mutually contributing to the total energy output. Star formation is the most common process, taking place throughout galaxies, while accretion of matter onto a supermassive black hole in the nucleus is another, less frequent, mechanism of energy production. The energetic nuclear regions associated with black hole accretion, referred to as Active Galactic Nuclei (AGN), are confined to the centers of galaxies. Understanding these processes is key to understanding galaxy evolution, including black hole growth in the center of galaxies, star formation, and possible correlations between them. Activity classification diagnostics provide tools to reveal the dominant energy production mechanism, signifying either processes of star-formation throughout the galaxy, or accretion in the nucleus. However, the distance dependence of physical size on angular size introduces observational difficulties (including starlight contamination from the host galaxy), making AGN identification a difficult and sometimes complex task. An accu-

rate activity classification scheme that accounts for these complexities is essential to understand energy production in galaxies and subsequently galaxy evolution.

Visible emission-line ratio diagnostics are probably the most widely used and best-calibrated method of galaxy activity classification. Baldwin et al. (1981), hereafter BPT, and later Veilleux & Osterbrock (1987), have shown that emission-line galaxies can be distinguished as star-forming, Seyfert, or Low-ionization nuclear emission-line regions (Heckman, 1980) using the intensity ratios of two pairs of emission lines. Three standard diagnostic diagrams are used, based on [O III] $\lambda$5007/H$\beta$, [N II] $\lambda$6583/H$\alpha$, [S II] $\lambda\lambda$6716, 6731/H$\alpha$, or [O I] $\lambda$6300/H$\alpha$. Because the relative intensity of spectral lines of different excitation energy depends on the hardness of the ionizing continuum, galaxies with different sources of ionizing radiation occupy different locations in the diagrams. Kewley et al. (2001) defined a theoretical upper limit on the location of star-forming galaxies in the BPT diagrams using H II region model spectra. Later Kauffmann et al. (2003) defined an empirical line delineating the pure star-forming galaxies in the [O III]$\lambda$5007/H$\beta$ versus [N II] $\lambda$6583/H$\alpha$ diagnostic diagram based on a sample of 122,808 galaxies from the Sloan Digital Sky Survey (York et al., 2000). In between the empirical pure starburst and the theoretical maximum starburst lines lie the composite or transition objects (TO), introduced by Ho et al. (1993), which may have both star-burst and AGN activities. A refinement of the BPT diagrams was introduced by Kewley et al. (2006), who calculated the distinguishing line that separates Seyferts and LINERs on the standard optical diagnostic diagrams of [S II] $\lambda\lambda$6716, 6731/H$\alpha$ and [O I] $\lambda$6300/H$\alpha$.

The activity classification obtained with visible-light diagnostic diagrams should be treated with caution. In general, the emission-line spectra of galaxy nuclei will be contaminated to some degree by unrelated stellar light that falls in the aperture; the problem is worse at high redshifts. In early-type galaxies in particular, where evolved stars dominate the light from galaxy bulges, absorption features in the stellar spectra will affect the strength of most emission lines. A demonstration of this effect was presented by Moran et al. (2002) for distant galaxies, where their angular diameters were comparable to the widths of the slits used to measure their spectrum. Moran et al. obtained integrated and nuclear spectra of nearby Seyfert 2 galaxies, known to be absorbed X-ray sources, and showed that in their integrated spectra the emission lines were far less prominent or even completely obliterated compared to their respective nuclear spectra. These effects could result in a different activity classification of a galaxy depending on the region used to extract its spectrum. The effect becomes very important in the case of SDSS spectra of distant galaxies, where the 3″ diameter fibers

used by SDSS may include a large portion of host galaxy's starlight or in some cases the whole galaxy's light. It is important to address this issue and examine if starlight subtraction methods are capable of correcting it.

Over the last decade starlight subtraction methods that can estimate and subtract the contamination by the host galaxy have been introduced (e.g., Hao et al. 2005; Sarzi et al. 2007 ). One of the most common approaches for starlight subtraction involves the use of templates, derived from spectra of several different galaxies (e.g., Ho et al. 1997c). More recent methods (e.g., STARLIGHT; Cid Fernandes et al. 2005) fit a model spectrum constructed from population synthesis techniques using a linear combination of stellar libraries. However, due to multiple parameters involved in the fitting process (e.g., metallicity, multiple stellar populations, extinction) along with the complexity of dealing with the AGN component, star formation, and the interstellar medium (ISM), the degree to which starlight subtraction methods can account for the contribution of starlight is still unclear.

Even with optimal starlight subtraction, emission line ratios can still vary with aperture size. One of the major reasons is the presence of extra-nuclear star-forming activity enhancing the integrated flux of emission lines. Another factor can be the metallicity gradient observed in disk galaxies (e.g., Ferguson et al. 1998), as lower-metallicity H II regions in the outer parts of galaxy discs are capable of producing high-excitation emission lines. When observing the integrated spectra of galaxies both effects may impact the line ratios and subsequently galaxy classification.

This paper examines how the BPT activity classification changes as a function of how much of the host galaxy's light that is included in the extraction aperture and the degree to which starlight removal techniques can mitigate the effect of host galaxy light. We use long-slit spectra for different types of galaxies in order to extract spectra of different-sized apertures and measure how the activity classification depends on the amount of host galaxy light included. Section 3.2 presents the study sample and reviews its properties. Section describes the spectral extraction techniques used and the analysis thereof. Section 3.4 summarizes our results and discusses the effectiveness of starlight subtraction, and Section 3.5 presents our conclusions and discusses how spectra of more distant galaxies are affected by aperture effects.

## 3.2 Sample selection

The galaxies used in our analysis were selected from the Star Formation Reference Survey (SFRS; Ashby et al. 2011), an on-going multi-wavelength project studying the

properties of star formation in nearby galaxies. Nearby galaxies with large surface are optimal candidates to test aperture effects by extracting spectra from incrementally increasing aperture widths. Therefore, for this study we excluded point-like sources, while at the same time we avoided galaxies with major axis diameter similar to the spectrograph slit length. The last criterion was introduced in order to avoid sky-subtraction procedures which would require a separate sky exposure, keeping the analysis as simple and unbiased as possible. Because we are examining how activity classification is affected by aperture effects, we included galaxies of different activity classifications, (star-forming, LINER, Seyfert) based on their nuclear spectra (Maragkoudakis et al, in prep). Out of the 50 objects observed so far, 11 fulfill the above criteria.

In order to account for different morphological types the SFRS sample was supplemented by elliptical galaxies, known to host an AGN. The galaxies used were 3C 033, 3C 084, and 3C 296, selected based on the sample of Buttiglione et al. (2009). The basic parameters of the final sample of 14 galaxies used in our study are presented in Table 3.2.1.

With the exception of NGC 4704 at 122.8 Mpc, UGC 9412 at 198.7 Mpc, and 3C 033 at 252 Mpc, the objects in the sample are located within 92 Mpc with a mean distance of 79.8 Mpc. The majority of the galaxies are of spiral morphological types based on NASA/IPAC Extragalactic Database (NED), which is based on de Vaucouleurs system (de Vaucouleurs, 1959). Their integrated photometry was obtained from the SDSS database and corresponds to $g$-band Petrosian magnitudes (Blanton et al., 2001).

## 3.3 Observations and analysis

The long-slit spectra were acquired using the FAST Spectrograph (Fabricant et al., 1998) mounted at the 60-inch Tillinghast telescope at Fred Lawrence Whipple Observatory during the period from March to May 2012. We used a $3''$ wide, $6'$ long slit oriented along the major axis of each galaxy with a 300 l/mm grating providing a dispersion of 1.47 Å pixel$^{-1}$, and resolution of 322 km/s (5.993 Å) as measured from the full width at half maximum (FWHM) of the O I 5577 Å sky line. The exposure times varied from 600 to 1800 seconds, and the spectra were obtained using the 2688 × 512 pixel FAST3 CCD, covering the 3500-7400 Å spectral range.

The spectra were analyzed using IRAF (Image Reduction and Analysis Facility; Tody 1986). All standard initial procedures of bias subtraction and flat fielding as well as wavelength calibration using arc-lamp exposures, were performed on the two-dimensional CCD images. The integrated spectra of all galaxies were extracted at

**Table 3.2.1:** Galaxy Characteristics.

| Galaxy | Morphology | SDSS $m_g$ (mag) | Distance (Mpc) | Exposure (s) | Classification (Nucleus) | D25 (arcmin) |
|---|---|---|---|---|---|---|
| NGC 2608 | SB(s)b | 13.520 ± 0.021 | 36.3 | 1800 | H II | 2.3 (1.7) |
| NGC 2731 | S? | 13.756 ± 0.081 | 35.0 | 900 | H II | 0.8 (0.9) |
| NGC 3306 | SB(s)m? | 14.025 ± 0.007 | 46.6 | 1800 | H II | 1.3 (0.9) |
| NGC 4412 | SB(r)b? pec | 12.972 ± 0.002 | 30.6 | 1200 | Sy2 | 1.4 (1.1) |
| NGC 4491 | SB(s)a | 13.327 ± 0.003 | 16.8 | 600 | H II | 1.7 (1.6) |
| NGC 4500 | SB(s)a | 13.070 ± 0.037 | 52.0 | 600 | H II | 1.6 (0.9) |
| NGC 4704 | SB(rs)bc pec | 14.255 ± 0.004 | 122.8 | 1200 | Sy2 | 1.0 (0.9) |
| NGC 4868 | SAab? | 13.662 ± 0.109 | 74.0 | 600 | H II | 1.6 (1.4) |
| NGC 5660 | SAB(rs)c | 13.358 ± 0.022 | 38.9 | 1800 | H II | 2.8 (1.6) |
| UGC 6732 | S0? | 13.533 ± 0.002 | 53.6 | 600 | LINER | 0.9 (1.6) |
| UGC 9412 | S? | 13.913 ± 0.003 | 198.7 | 1800 | Sy1 | 0.6 (0.4) |
| 3C 033 | – | 15.772 ± 0.005 | 251.8 | 1800 | Sy2 | 0.7 (0.8) |
| 3C 084/NGC 1275 | pec | 12.079 ± 0.659 | 68.2 | 600 | LINER | 2.2 (2.0) |
| 3C 296/NGC 5532 | – | 12.698 ± 0.009 | 91.2 | 900 | Sy2 | 0.6 (0.7) |

Column (1) Galaxy name; Column (2) Morphological types obtained from NED; Column (3) Integrated SDSS G-band apparent magnitudes taken from Ashby et al. (2011); Column (4) Distances in Mpc taken from Ashby et al. for the SFRS sample and NED for the elliptical galaxies; Column (5) Exposure time of each object's observation in seconds; Column (6) Activity classifications based on the nuclear spectra of galaxies (Maragkoudakis et al, in prep); Column (7) D25 angular diameters taken from Ashby et al. (2011) for the SFRS galaxies, and from the Third Reference Catalogue of Bright Galaxies (RC3; de Vaucouleurs et al. 1991) for the elliptical galaxies except for 3C033, which was obtained from 2MASS $K_s$ band survey (Jarrett et al. (2003)). The value in the parentheses is the maximum angular diameter used for spectral extraction.

first using the "APALL" task. Extracting the integrated spectra is an essential part of the analysis in order to obtain their activity classification based on the standard long-slit spectroscopic analysis and also to estimate the full extent of the galaxies along the slit. The size of the extraction aperture was based on the width of the spatial profile of the spectrum and was defined up to the point that the galaxy's luminosity was indistinguishable from the level of the background. The sky subtraction was also performed by "APALL", and the level of the background was defined from regions in the spatial direction of the spectrum that do not contain any light from the source. The uncertainties were also calculated by "APALL" as the square root of the counts in each dispersion-axis bin. Flux calibration was applied using standard star exposures, which were processed in the same way as the galaxy spectra. Lastly, we measured the location of characteristic lines from all galaxy spectra in order to calculate their redshift and correct them to their rest frame.

Our first approach is to examine line ratios along the slits to see how the line ratios change and possibly influence classifications as a larger portion of starlight is gradually incorporated in the extracted spectrum. To achieve this, we began the spectral extraction from a small central aperture (3 pixels (3.51″) wide) and repeated the process by increasing the aperture width in steps of 2 pixels (2.34″) along the major axis until the entire galaxy was covered. The minimum size of the central aperture was determined from the average value of seeing at the time of the observations. We obtained 10 to 42 sub-spectra for each galaxy depending on its apparent size. All the steps of flux calibration and redshift correction were also performed in each individual sub-spectrum of every galaxy before proceeding to measure their emission lines.

The next step in our analysis was to simulate elliptical apertures of various sizes based on the spectra extracted from different apertures along the major axis. This way we produce spectra resembling those obtained with optical fiber spectrographs. To do so we started with a central (3-5 pixels wide along the major axis) aperture. In order to simulate spectra from larger elliptical apertures we incrementally added spectra from emulated elliptical annuli of increasing radius. Each successive annulus was derived from the spectrum of two 2-pixel wide (2.34″) rectangular apertures at equal distance on either side from the center of the galaxy. Then, using G-band images of the galaxies taken from the SDSS DR8 (Aihara et al., 2011), we measured the broadband emission in each of the rectangular apertures as well as in the elliptical annulus with major and minor axes enclosing these regions and position angle equal to that of the long-slit (Figure 3.3.1). The sky background was defined from source-free regions on the SDSS images and then subtracted from the regions of interest. The ratio of the intensity

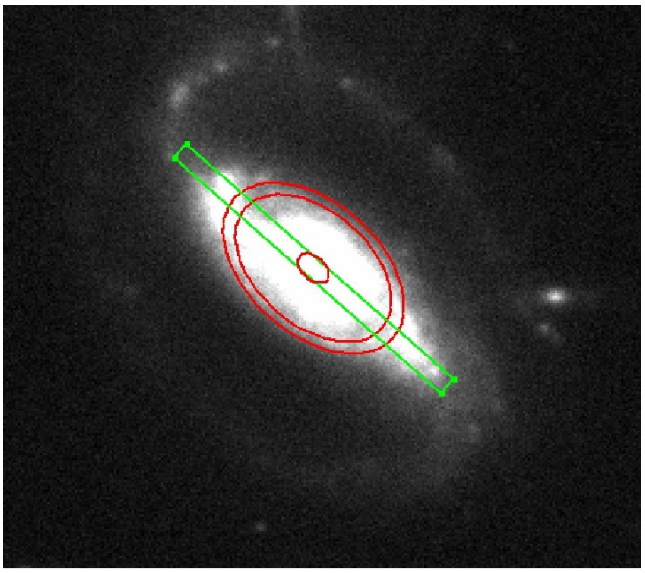

**Figure 3.3.1:** SDSS $g$-band image of NGC 4500. Parallel lines show the long slit, and ellipses show an example annulus, in this case $34''$ in diameter. The intersection of the long slit and the annulus apertures denotes the rectangular regions used to create the spectrum of the elliptical annulus.

in the elliptical annulus to the intensity inside the rectangular apertures provides the multiplicative factor needed to simulate the spectrum of an elliptical annulus based on the spectrum of the rectangular apertures. This way we emulate the spectrum from an elliptical annulus, assuming that the spectrum along the major axis is representative of the spectrum in the rest of the galaxy at the same galactocentric radius. This is an important step in order to account for the increasing area of the galaxy in larger galactocentric radii that is not accounted for in the equal rectangular apertures along the long-slit spectra.

For the central region of each galaxy, we used a single rectangular region to extract the spectrum and an elliptical region around it to calculate the weight and thus create a central elliptical spectrum, similarly to the process described previously. Adding consecutive simulated elliptical annuli spectra gave us the simulated spectra of elliptical apertures of varying sizes.

In order to investigate the efficiency of starlight subtraction and the degree to which it can improve the inclusion of additional extra-nuclear light, we measured emission lines from simulated spectra with and without starlight subtraction. We removed the starlight contribution from all the long-slit and integrated elliptical aperture sub-spectra

of each galaxy using the STARLIGHT v.04 starlight subtraction code. STARLIGHT fits the observed spectrum using linear combinations of simple stellar populations (SSPs) based on the models of Bruzual & Charlot (2003). The fit was performed on emission-line-free regions of the spectrum. The best-fit combination was subtracted, and reddening corrections were performed. The extinction ($A_V$) is a fitted parameter applied to the unreddened stellar models. In our analysis we used the Cardelli reddening law (Cardelli et al., 1989) with $R_v = 3.1$, defined as the ratio of total to selective extinction: $R_v \equiv A_v/E(B-V)$. To fit the starlight components we used a base of 138 SSPs, consisting of populations of 23 ages between 1Myr and 13Gyr and 6 metallicities ranging from 0.005 to 2.5 $Z\odot$.

After starlight subtraction we measured the intensities of the forbidden lines [O III] $\lambda$5007, [N II] $\lambda$6583, [S II] $\lambda\lambda$6716, 6731, [O I] $\lambda$6300/H$\alpha$, and the Balmer H$\beta$ and H$\alpha$ lines for all the galaxies in both cases of long-slit and simulated-elliptical spectra. In the case of the simulated elliptical spectra we also measured emission lines without applying starlight subtraction. For this task we used SHERPA (Freeman et al., 2001), a modeling and fitting application designed for CIAO, the Chandra (X-Ray Observatory) Interactive Analysis of Observations software package (Fruscione et al., 2006). One of the advantages of SHERPA is that we are able to fit complex multi-component models and obtain the uncertainties on all parameters in the fit. The uncertainties were calculated (within $1\sigma$ confidence intervals) by varying a given parameter's value along a grid of values while at the same time the values of all other model parameters were allowed to float to new best-fit values. We measured the emission line intensities by fitting them with a set of Gaussian functions and a constant for the continuum. All three characteristic parameters of each Gaussian (center, intensity, full width at half maximum (FWHM)) were generally free to vary. In many cases, linking parameters such as the FWHM of emission line doublets was required and applied individually in each set of lines. Additionally, in certain cases a broad component was required along with the narrow one in order to fit the Balmer emission lines. Such components can be the result of galaxy rotation or, in the case of Seyfert 1 galaxies, of emission from the broad-line region (BLR), producing line widths up to $10^4$ km/s.

The resulting diagrams are presented in Figures 3.3.2a-d. In NGC 4491 and UGC 6732 we could not measure any emission lines without applying starlight subtraction because they are lost in the stellar absorption features. For both NGC 4491 and NGC 4868, even in the case of starlight subtracted spectra, we were only able to obtain emission line measurements out to approximately half of their semi-major axis. NGC 4704 has a non starlight-subtracted "path" on the BPT diagrams starting at the point where the

diagnostic lines were measurable, approximately at half semi-major axis distance, and extended to its final largest aperture.

The light encompassed in a given aperture depends on radius. To calculate flux as a function of radius and thus the half-light radius, we built a curve of growth from the SDSS $g$-band images. Additionally, we plot on the same graphs the H$\alpha$ and H$\beta$ emission line equivalent widths measured from the non-starlight subtracted spectra in order to have a sense on the continuum change and its impact on the emission lines due to stellar Balmer absorption lines. The results are presented in Figures 3.3.3a-d. In most cases all line ratios tend to vary in the same way as a function of galactocentric radius. However, the range of their actual values differs as a result of the different sources of ionizing photons when moving from the nucleus to the outer parts of galaxies. There are also cases (e.g. NGC 2608, NGC 4500) where the equivalent widths of H$\alpha$ and H$\beta$ as a function of galactocentric radius or encompassed flux appear to show the opposite behavior compared to the BPT line-ratio. This is a good indication that the Balmer lines are those that are driving the trends of the diagnostic line ratios and hence the resulting "path" on the diagrams.

Based on the previous analysis we calculated the dispersion of every diagnostic line ratio for the H II and Seyfert galaxies. This was derived from their individual elliptical sub-spectra with respect to their central aperture. Then, we calculated the mean of the above dispersion for each galaxy class with its corresponding standard deviation. In this way we obtained a sense of the uncertainties of the line-ratios used in the BPT diagrams due to the effect of the host galaxy light, which is particularly useful for higher-$z$ galaxies that are generally unresolved. As we see in Table 4.4.1, the largest scatter is observed in the [O III] $\lambda$5007/H$\beta$ ratio of Seyfert galaxies. This is expected as the higher ionization [O III] $\lambda$5007 line drops abruptly as we move farther out from the center of galaxies with AGN, as discussed in Section 3.4.

# 3.4 Discussion

## 3.4.1 General trends

As slit length or aperture size gradually increases, there is a corresponding increase in the starlight and extra-nuclear line emission in the spectra. We expected to see all emission line intensities decrease as the proportion of starlight in the extraction aperture increased, diluting the nuclear emission (e.g., Moran et al., 2002). In the case of galaxies hosting AGN, as we move farther away from the central regions we

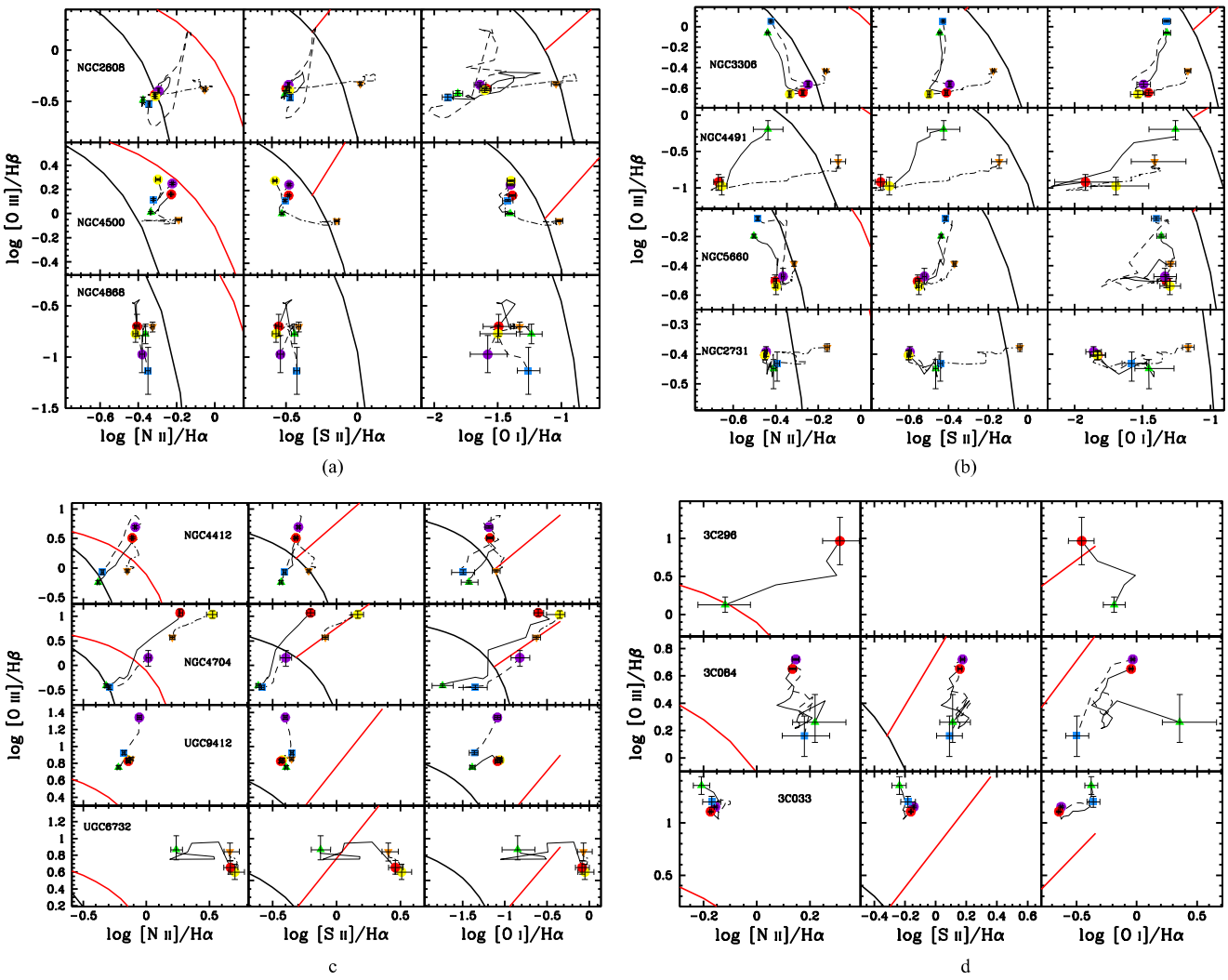


**Figure 3.3.2:** (a) The three line-ratio-diagnostic diagrams for the star-forming galaxies NGC 2608, NGC 4500, and NGC 4868, presenting a small decrease in their line ratios with increasing aperture. The solid line represents the simulated elliptical apertures, starting from the smallest one around the nuclear region(red circle) up to the largest covering the entire galaxy (green triangle). The dashed line shows the ratios without starlight subtraction, with the purple circle indicating the spectrum from the smallest aperture and the blue square the largest one. The ratios based on the long-slit apertures is shown with the dash-dotted line with the yellow circle representing the central aperture, often coincident with the central elliptical aperture, and the upside-down orange triangle the aperture along the full length of the major axis of the galaxy. On some occasions the starting points of the two methods slightly differed, because the central elliptical aperture was often 5 pixels wide and hence encloses more light than the central long-slit aperture, being always 3 pixels wide. (b) The BPT diagrams of star-forming galaxies NGC 3306, NGC 4491, NGC 5660, and NGC 2731, with the three first presenting an upward trend on the [O III] $\lambda$5007/H$\beta$ axis with increasing aperture. (c) The BPT diagrams of the three spiral-Seyfert galaxies NGC 4412, NGC 4704, UGC 9412, and LINER UGC 6732. The line-ratio decrement with increasing aperture is clearly visible in the case of the Seyfert galaxies. (d) The BPT diagrams of the elliptical galaxies 3C 033, 3C 084, and 3C 296, without applying the long-slit method. Galaxy 3C 296 had no visible emission lines without starlight subtraction, while the [S II] $\lambda\lambda$6716, 6731 doublet was not detected even after starlight subtraction; hence, there is no available [S II]/H$\alpha$ BPT diagnostic for this galaxy.

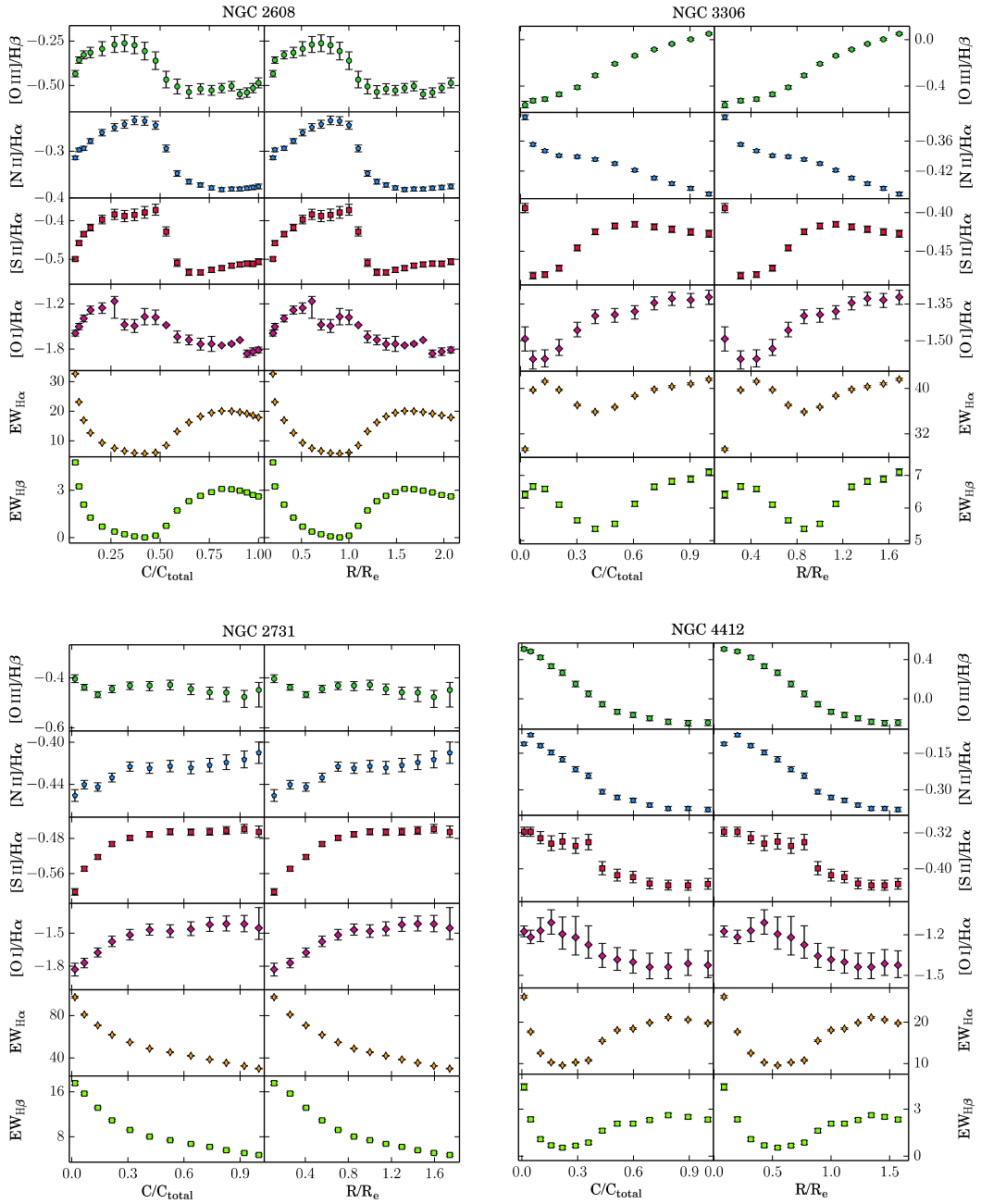


**Figure 3.3.3:** (a) Radial dependence of line ratios and equivalent widths measured in simulated elliptical apertures. On the left-hand side of each panel, the abscissa is light enclosed relative to total light of the galaxy. The right-hand-side abscissas are radius relative to the galaxy's half-light radius. Line ratios are shown after starlight subtraction and given in decimal logarithms. Equivalent widths are in Angstrom units as observed prior to starlight subtraction. The plots of NGC 2608, NGC 2731, NGC 3306, and NGC 4412 are shown here.

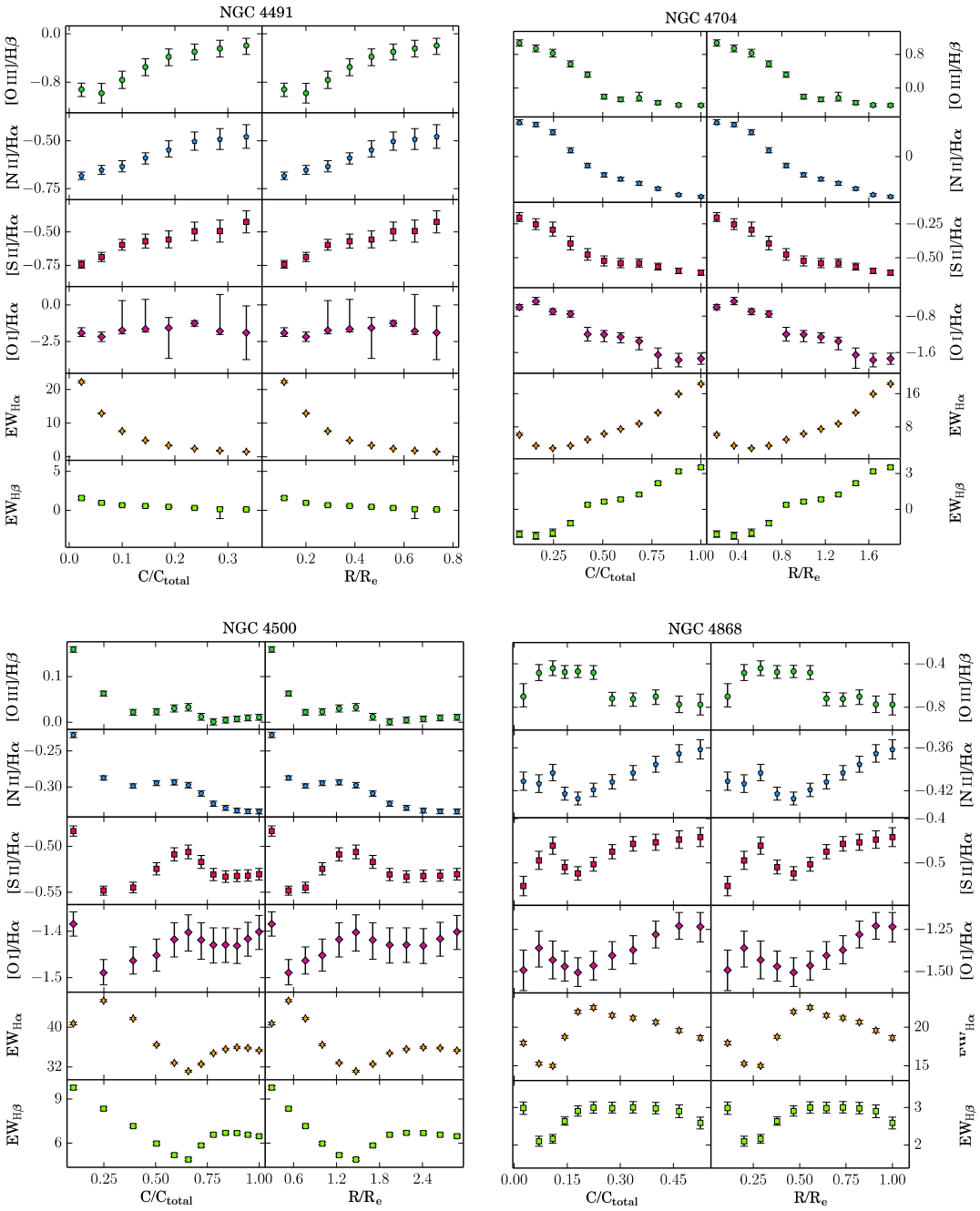


**Figure 3.3.3:** (b) The plots of NGC 4491, NGC 4500, NGC 4704, and NGC 4868.

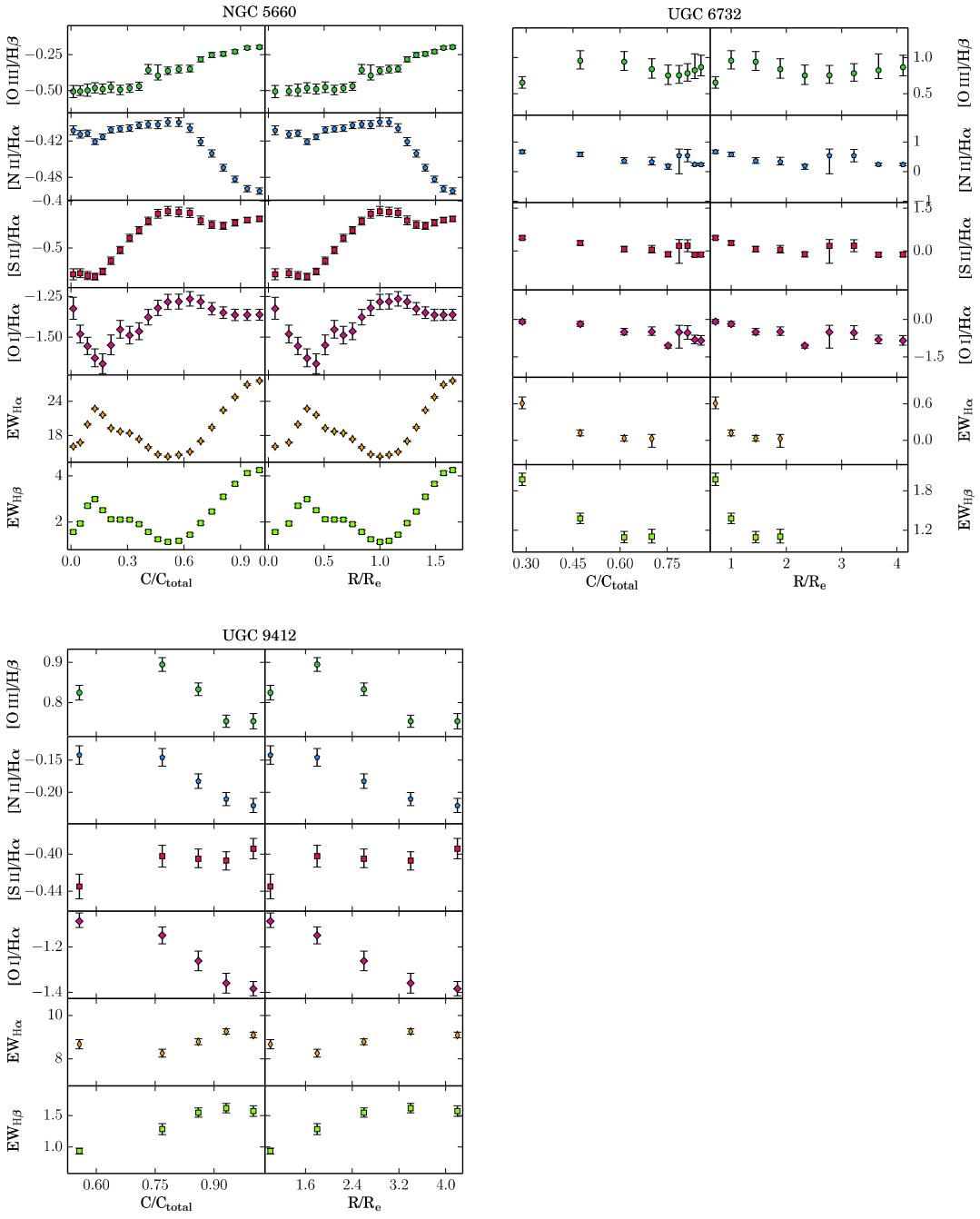


**Figure 3.3.3:** (c) The plots of NGC 5660, UGC 6732, and UGC 9412. In the case of UGC 6732, the equivalent widths of H$\alpha$ and H$\beta$ are plotted up to the point that the lines were visible.

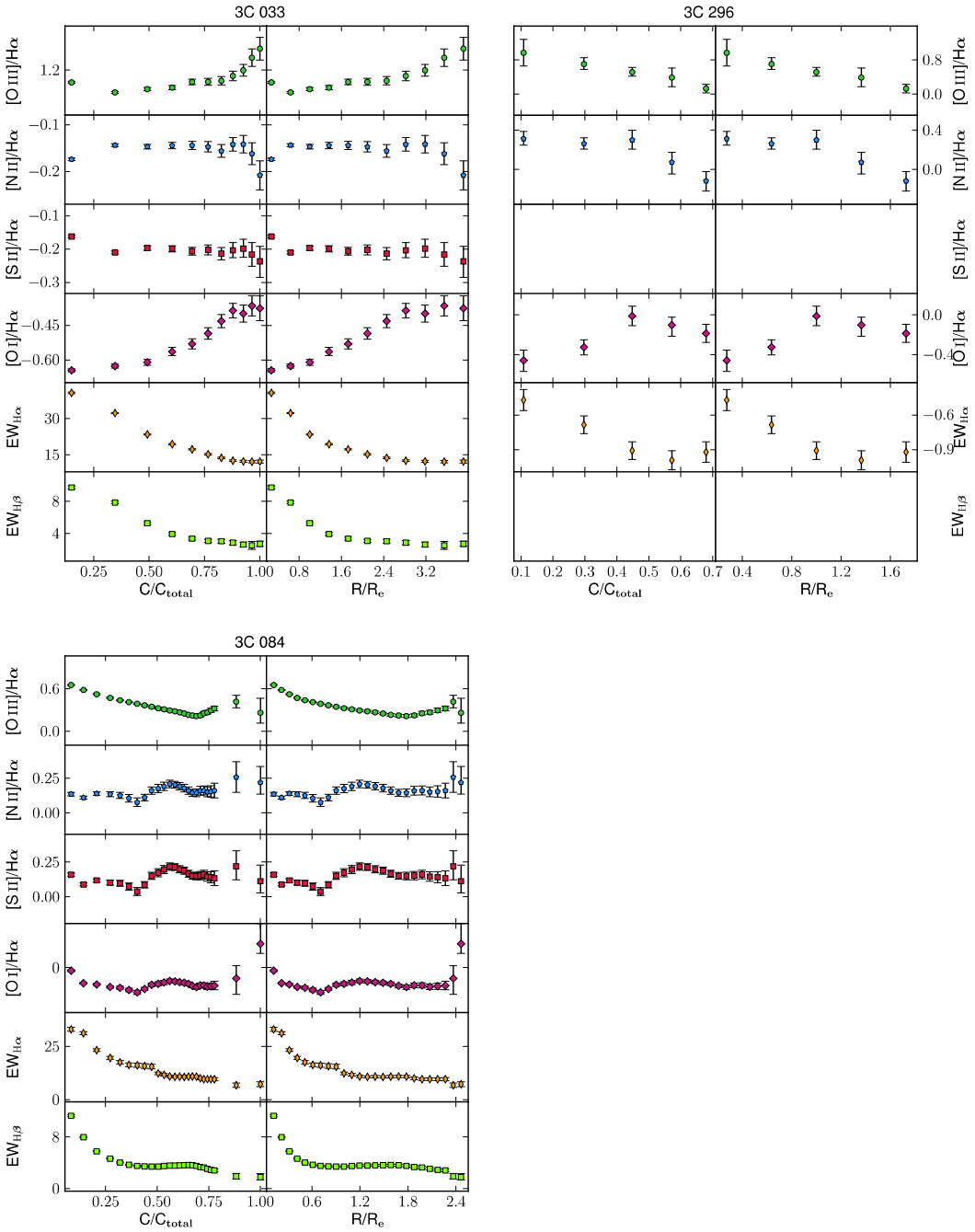


**Figure 3.3.3:** (d) The plots of the elliptical galaxies 3C 033, 3C 084, and 3C 296. No [S II] $\lambda\lambda$6716, 6731 emission lines or H$\beta$ equivalent widths were measured for 3C 296.

**Table 3.3.1:** Diagnostic line ratio dispersion. The mean dispersion $\mu_\sigma$ for the BPT line ratios with its corresponding standard deviation $\sigma$ for the star-forming and Seyfert galaxies in the sample. They are derived from the dispersion of each line ratio in every starlight-subtracted elliptical aperture, with respect to the ratios in the nuclear aperture (see Section 3.3).

| | H II | | Seyfert | |
|---|---|---|---|---|
| Line-Ratio | $\mu_\sigma$ | $\sigma$ | $\mu_\sigma$ | $\sigma$ |
| log([O III] $\lambda$5007/H$\beta$) | 0.21 | 0.16 | 0.45 | 0.49 |
| log([N II] $\lambda$6583/H$\alpha$) | 0.18 | 0.08 | 0.34 | 0.31 |
| log([S II] $\lambda\lambda$6716, 6731/H$\alpha$) | 0.16 | 0.08 | 0.30 | 0.27 |
| log([O I] $\lambda$6300/H$\alpha$) | 0.21 | 0.10 | 0.41 | 0.36 |

expected the intensities of higher ionization lines to drop faster than those of Balmer lines, as the former have usually a higher ionization potential than hydrogen. On the other hand, young or low-metallicity H II regions found further away from the nucleus of late-type galaxies are expected to produce high excitation emission lines. The net result will depend on both the age and the metallicity of the stellar populations on the H II regions. In the first case the intensities of the [O III] $\lambda$5007 and [N II] $\lambda$6583 emission lines should decrease faster compared to the Balmer lines. Consequently, in terms of activity classification, the respective emission-line ratios in an e.g., [O III] $\lambda$5007/H$\beta$ - [N II] $\lambda$6583/H$\alpha$ BPT diagram should gradually decrease when moving from the center to the edge of galaxies. This will produce a classification trend towards the H II region. This is exactly what we observe, both with and without starlight subtraction, in the case of the spiral-Seyfert galaxies NGC 4412, NGC 4704, and less strongly for UGC 9412, in agreement with the results of Moran et al (2002). The same trend in the BPT diagrams is also observed in the case of the elliptical-Seyfert galaxies 3C 084 and 3C 296. Because the ionization potential of [O III] $\lambda$5007 is twice that of the other emission lines of interest, it is expected to drop more abruptly following the reduction of high-energy photon density as we move outwards in the galaxy. Indeed Figures 3.3.2 show the larger variations along the [O III] $\lambda$5007/H$\beta$ axis as opposed to the horizontal axis of the diagrams.

### 3.4.2 Trends in late-type galaxies

For the spiral galaxies, we see two different trends. Some galaxies (NGC 4500, NGC 4868) show lower [O III] $\lambda$5007/H$\beta$ values with increasing aperture, in line with our expectations. On the other hand, four galaxies (NGC 3306, NGC 4491, NGC 5660, and UGC 6732) show ratios moving towards the upper, higher excitation regions of the diagnostic diagrams. This behavior is apparent in all types of analysis (long-slit, elliptical aperture with/without starlight subtraction). Of these galaxies NGC 3306, NGC 4491, and NGC 5660 are classified as star-forming, while UGC 6732 is classified as LINER based on their long-slit spectra of their nuclear (3.5″ or 5.85″ x 3″) regions. Star formation does not occur exclusively in the nuclei of galaxies but is distributed throughout the galactic disk (Kennicutt et al., 1989). Star-formation activity of different ages, occurring in various areas throughout the galaxy, will produce ionizing continua of different shapes with more recent starbursts giving the most energetic photons. As seen in the two-dimensional spectra and the SDSS $g$-band and GALEX near-UV images of galaxies NGC 3306 and NGC 5506 (Figure 3.4.1), several star-forming clumps are present on their spiral arms. Our spectra of these knots shows that their [O III] $\lambda$5007-line intensity is greater than that of the central star-forming region, indicating a harder ionizing continuum and hence younger stellar populations. A similar effect could arise from metallicity gradient observed in galaxies. These effects can explain the increasing excitation of NGC 3306 and NGC 5660 (Figure 3.3.2b). The result highlights how morphology and galaxy structure can affect the analysis and the activity classification even of pure star-forming galaxies even though the line ratios remain within the star-forming range at all radii.

Interarm regions of galaxies should enhance the overall starlight component of the spectrum because interstellar gas is mostly absent from those regions. Even if there is any small amount of gas, the evolved stars present there are not capable of ionizing it. With respect to the integrated spectrum, this means that the spectral absorption features will intensify while the emission lines will remain almost constant. When applying starlight subtraction, the additional stellar populations encountered in the interarm regions can introduce complications to the fit, leading to an overestimation (or underestimation) of the starlight continuum. In turn, this would lead to a larger (or smaller) estimation of the Balmer absorption line equivalent widths, and the resulting subtraction of the stellar continuum would have an impact on the flux of Balmer emission lines. Lower values of the H$\beta$ emission line results in higher placement of the galaxy in all BPT diagrams. Furthermore, when constructing the elliptical aper-

tures, considering that the elliptical annulus size increases as we move towards the outer regions of a galaxy while the rectangular regions always maintain a fixed size, the resulting weight used to multiply the rectangular region's spectrum will increase with respect to the radius. In the case of the interarm regions this will produce a spectrum of intense absorption features and increasing starlight continuum resulting in reduced apparent intensity of the H$\beta$ emission line. This is applicable not only in interarm regions but also in the extra-nuclear regions of galaxies with low star-forming activity in general. This could be the case in NGC 4491, where the quality of the elliptical simulated spectra dropped dramatically as we expanded the apertures towards the galaxy edges, and we were able to measure the emission line ratios out to approximately half of the surface area. This effect could be the source of the apparent (but not significant) upward trend for NGC 4491 on the diagnostic diagrams. Correspondingly, this could also apply for UGC 6732 where the initial (nuclear) and the final (simulated integrated) spectra have similar [O III] $\lambda$5007/H$\beta$ ratio within their uncertainties.

Regarding the behavior of galaxies along BPT horizontal axis, excluding NGC4491 and NGC4868 which give simulated elliptical aperture spectra of lower quality, the rest of the sample tends to move towards the left side on the diagnostics as expected. The lower ionization potential of [N II] $\lambda$6583, [S II] $\lambda\lambda$6716, 6731 and [O I] $\lambda$6300/H$\alpha$, compared to [O III] $\lambda$5007, allows less energetic photons to ionize these species in gaseous regions farther away from the center and hence generate a less dramatic reduction in their line ratios, resulting in smaller shifts along the horizontal axis of all three diagnostic compared to the [O III] $\lambda$5007/H$\beta$ variations.

For three galaxies in the sample (NGC 2608, NGC 4412, and NGC 4704), we observe an actual change in their activity classification based on the elliptical-aperture simulation method in at least one of the three diagnostic diagrams, while three more galaxies (NGC 2731, NGC 4491 and NGC 4500) have a change in their classification based on the varying standard-long-slit method. NGC 4412 and NGC 4704, classified as Seyfert based on their nuclear spectra, fall into the star-forming region of all three diagrams. (If we omit starlight subtraction they fall into the TO region in the $[N_{II}]/H\alpha$ diagnostic). Finally, NGC 2608 along with NGC 4412 and NGC 4704 undergo a change in classification towards the TO region in the [N II] $\lambda$6583/H$\alpha$ diagnostic at an aperture covering approximately half of their surface. This is demonstrating an intermediate stage of the aperture effect that can be encountered when observing with a fiber, where a portion of the galaxy including the nucleus is observed rather than just the central region or the total surface.

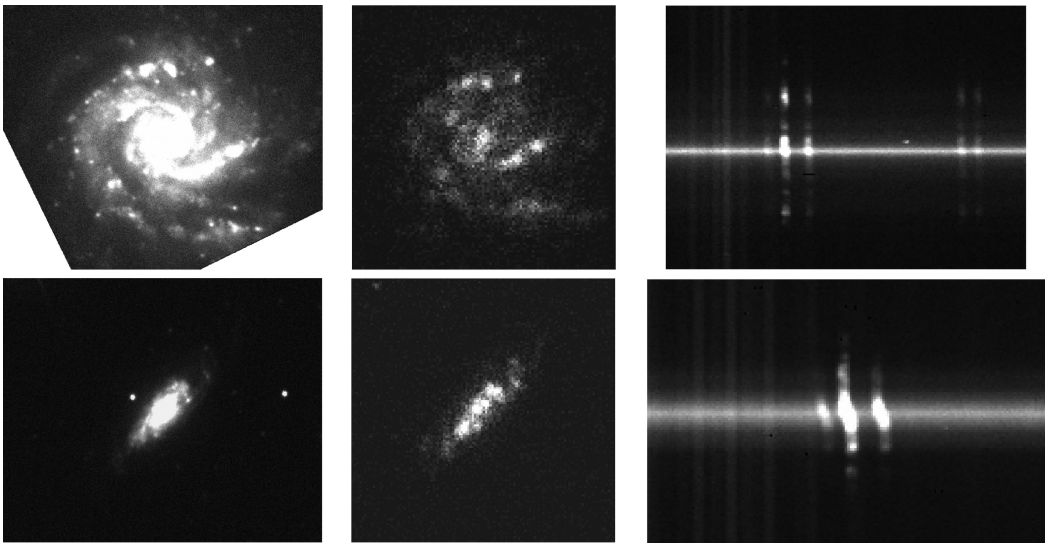

**Figure 3.4.1:** Upper panel: SDSS's G-band (left), GALEX UV (middle), and two-dimensional spectrum around the H$\alpha$ region for galaxy NGC 5560. The optical and UV images show star-formation clumps, while in the two-dimensional spectrum we see emission from regions away from the center. Lower panel: The same information for galaxy NGC 3306.

### 3.4.3 Trends in early-type galaxies

Early type galaxies are nearly devoid of star-forming activity, simplifying in principle the complications found in late-type galaxies with extra-nuclear star formation. The sample of elliptical galaxies follows the same trend as spiral-Seyfert galaxies, that is towards lower excitation with increasing radius (Figure 3.3.2d). Again, the upward tendency of 3C 033 on the optical diagnostic diagrams can be attributed to the uncertainties in the emission-line measurements. 3C 296 appears to have an activity classification change from Seyfert to TO and LINER in the case of [N II]/H$\alpha$ and [O I]/H$\alpha$ diagnostics respectively. For this galaxy, we were not able to measure emission-lines without applying starlight subtraction, and even so the [S II]$\lambda$6716, 6731 doublet was not detected, hence no classification was acquired using the [S II]/H$\alpha$ diagnostic. The most intriguing aspect of this analysis for the elliptical subsample is that even when star-forming activity had no significant impact on the continuum subtraction, the host galaxy's starlight could not be accurately removed. Galaxies fall lower in the BPT diagnostics as aperture increases even when starlight subtraction is applied, revealing the masking of the AGN features by the host galaxy's starlight.

### 3.4.4 The efficiency of starlight subtraction

One might naively expect optimal subtraction of galaxy starlight to place the central and the larger aperture sub-spectra at the same location on the BPT diagrams. The previous Section demonstrates that this is not the case. We attribute this to two different reasons. First, as we showed, star-forming activity occurring outside the nucleus of a galaxy will influence the emission from the interstellar medium and hence the resulting classification in the BPT diagrams. This is a problem that starlight subtraction cannot account for. The second reason is the possible errors of starlight subtraction. Uncovering the actual stellar populations of galaxies responsible for the continuum light diluting the emission lines is a challenging task even in the case of elliptical galaxies, which generally have simpler stellar populations than spiral galaxies. The stellar continuum is the result of the radiation from stars of different ages and metallicities. Due to the known age-metallicity degeneracy (Worthey 1994), different combinations of stellar populations can produce similar continuum shapes. Furthermore, the observed spectral shape and characteristics (e.g., the FWHM of absorption lines) are also affected by the stellar velocity dispersion and extinction, both important parameters used when fitting the actual spectrum of a galaxy. Most importantly the limited number of stellar lines available after excluding the Balmer lines does not allow

for an accurate and unique decomposition of the stellar component. In this respect methods based on fitting elliptical galaxy templates (e.g., Ho et al. 1997c) rather than combination of single stellar population (e.g., STARLIGHT) could be more robust, but they do not ensure a reasonable fit in every case.

Determining all the parameters affecting a galaxy spectrum is not a trivial process. Even small deviations from the actual parameters will produce an inaccurate stellar continuum, meaning that the subtraction from the observed spectrum may not reveal the proper emission-line characteristics. This will lead to the observed displacement in the BPT diagrams between the central and all intermediate and larger aperture spectra.

For galaxies hosting AGN there is an additional parameter influencing the result of the stellar component subtraction, and that is the inclusion or omission of the AGN continuum in the fit. Generally, a power-low component is used to fit the AGN continuum. The proper selection of the power-law index though is not a standard task as it can differ between galaxies. Consequently, without accounting separately for the AGN continuum, it is treated in the fit as part of the stellar continuum. This means that additional stellar populations may be used to supplement for the AGN continuum, producing a less accurate synthetic spectrum for subtraction. This has a major effect in the estimated Balmer absorption lines intensities from the starlight. In particular, the true Balmer absorption depth will be less than the calculated values, and the recombination line fluxes will be over-corrected.

## 3.5 Conclusions

Our analysis indicates that line ratios and consequently activity classification obtained from the SDSS 3″ fibers can be affected by aperture effects. The proportions of nuclear and disk (stellar) light that enter an SDSS fiber depend on galaxy distance. Thus, AGN features' detectability are likewise a function of distance. The result could be a different activity classification than the one obtained from observations specifically from the central regions. This is crucial, because from the AGN identification standpoint one must solely concentrate on the central regions of a galaxy, while on the other hand when tracing star-formation it is essential, as proven in the analysis, that the whole surface must be scanned.

On the whole, both methods, fiber or a standard long slit, ascertain that galaxies will have a different placement in the BPT diagrams and on certain occasions a different classification as more starlight is included in the aperture of spectral extraction. Starlight subtraction does not change significantly this effect, but it helps in some cases

to measure emission lines, especially of higher ionization, that are otherwise completely lost in the stellar continuum. As demonstrated here reality appears to be more complex, with extra-nuclear star-forming activity (which cannot be subtracted) seriously influencing the photometry from large apertures. Low-activity galaxies (Low-luminosity AGN (LLAGN), Starburst, LINERs, and TO) seem to be more affected by star-forming activity throughout the galactic disk, often increasing their lower-ionization emission-line intensities and placing them higher in the activity classification diagrams. A larger sample of galaxies would prove beneficial in order to identify trends in the way galaxies are classified depending on the amount of host galaxy's light that is incorporated during their observations and furthermore examine the importance of their morphology by using as many different morphological types as possible.

# Appendix

## 3.A Galaxy Characteristics

**NGC 2608**: A barred spiral galaxy classified as star-forming based on the standard long-slit analysis of the nuclear spectrum. The galaxy changes its activity classification towards the TO region for intermediate aperture sizes and falls into the LINER region for the largest apertures in the long-slit approach. A large portion of the slit, oriented along the major axis, passes through an extensive interarm region. This could be responsible for the decrement in the flux of the Balmer lines (see the corresponding H$\alpha$ equivalent width plot), producing the upward and towards the right tendency on the BPT diagrams at small to intermediate sized apertures. Then, at larger apertures, the slit falls upon the spiral arm regions where we observe a gradual increase in the Balmer line flux and decrease of the BPT line ratios.

**NGC 2731**: A spiral star-forming galaxy with almost no scatter at the [O III] $\lambda$5007/H$\beta$ axis but with significant variation towards the right side of the BPT diagrams mostly in the long-slit approach. As discussed previously, this is a case where the higher ionization [O III] $\lambda$5007 line incrementally decreases at faster rates compared to lower ionization lines as we move farther out from the nucleus of the galaxy. In the long-slit method the galaxy reaches the TO and LINER region at larger apertures.

**NGC 3306**: This is a barred-spiral galaxy and one of the starbursts in the sample having an upward movement on the BPT diagrams with increasing aperture. Several younger, extra-nuclear star-forming clumps on the spiral arms produce a harder ionizing continuum, which results in the upward behavior observed. Though close to the pure star-forming distinguishing line, it only relocates to the TO region for the largest apertures in the long-slit method.

**NGC 4412**: This is a typical example of a spiral Seyfert-2 galaxy having its AGN features obscured with increasing aperture and starlight. Regarding the change of its activity classification, the galaxy falls into the TO and star-forming regions in both methods and passes through the LINER region for intermediate apertures in the long-

slit method.

**NGC 4491**: An early-type, barred spiral galaxy producing moderate-quality simulated elliptical spectra that have an upward trend on the BPT diagrams. No emission lines were measured without performing starlight subtraction. The two-dimensional spectrum doesn't show any evidence of extra-nuclear star-forming activity, and because the produced elliptical spectra were of moderate-quality it is possible that the applied starlight subtraction could have overestimated the flux on the absorption Balmer lines. This would give a smaller flux on the Balmer emission lines and would result in the observed upward behavior on the diagrams.

**NGC 4500**: Another early-type, barred spiral galaxy maintaining a TO classification in the [N II] $\lambda$6583/H$\alpha$ diagnostic and a star-forming classification in the [S II] $\lambda\lambda$6716, 6731/H$\alpha$, and [O I] $\lambda$6300/H$\alpha$ diagrams. The galaxy only passes into the LINERs' region at the largest apertures of the long-slit approach. Being in the TO region and very close to the maximum starburst line at its smallest aperture, the galaxy's possible AGN fraction appears to decrease with increasing aperture as in the case of Seyferts.

**NGC 4704**: This is a spiral Seyfert-2 galaxy showing a decrement of AGN characteristics with increasing aperture. The galaxy falls into the star-forming region passing through the TOs at intermediate apertures. Without starlight subtraction emission lines emerge approximately at half major semi-axis radius.

**NGC 4868**: An early-type spiral galaxy without notable scatter along all BPT axes, presenting no change of activity classification with increasing aperture. The galaxy's reddish color on the SDSS image and inspection of the two-dimensional spectrum suggests mild star-forming activity and agrees with the star-forming classification and placement towards the lower end of the [O III] $\lambda$5007/H$\beta$ axis.

**NGC 5660**: Another starburst, late-type spiral galaxy presenting an upward movement on the BPTs due to extra-nuclear star-forming activity, as explained previously. Only the largest apertures cross the TO region in the [N II] $\lambda$6583/H$\alpha$ diagnostic for the non-starlight-subtracted elliptical aperture and the standard long-slit methods. In the other two diagnostics the galaxy remains in the star-forming region.

**UGC 6732**: This is a lenticular galaxy classified as LINER based on the long-slit analysis of the nuclear spectrum. It shows a small upward tendency on the BPTs which could be statistically insignificant due to the uncertainties of the emission-line measurements. In the [S II] $\lambda\lambda$6716, 6731/H$\alpha$, and [O I] $\lambda$6300/H$\alpha$ diagnostics, the galaxy crosses the Seyfert region at intermediate apertures. No emission lines were measured without starlight subtraction.

**UGC 9412**: This spiral Seyfert-2 galaxy is the second most distant galaxy in the sample. It moves towards lower values of [O III] $\lambda$5007/H$\beta$ with increasing aperture, an effect diminished when applying starlight subtraction. Despite the decreasing [O III] $\lambda$5007/H$\beta$ values, the galaxy preserves its Seyfert classification. Combined with the fact that it is relatively distant, the galaxy's AGN features seem to be most dominant and least affected by the host galaxy's starlight.

**3C 033**: This is an elliptical Seyfert galaxy having a small upward trend on the BPTs, but within the uncertainties of the emission-line measurements this could be statistically insignificant. Having a quiescent star-formation activity as an early-type galaxy, this small upward placement with increasing aperture is indicative of possible over-subtraction of the stellar continuum.

**3C 084**: An elliptical galaxy classified as LINER and producing the expected decrement of AGN features with increasing aperture in all three diagnostic diagrams.

**3C 296**: This elliptical galaxy is classified as Seyfert based on the analysis of the central elliptical aperture, descending towards the TO region in the [N II] $\lambda$6583/H$\alpha$ diagnostic, and crossing the LINER region in the [O III] $\lambda$5007/H$\beta$ diagnostic with increasing aperture. No emission lines were measured without starlight subtraction, and even so the $[S_{II}]\lambda\lambda 6716, 6731$ doublet did not show any emission.

This work was supported by a "Maria Michail Manasaki" bequest fellowship. A. Maragkoudakis acknowledges partial support by HST grant AR-12621-01-A. A. Zezas acknowledges partial support by NASA grant NNX12AN05G, and Chandra grant AR1-12011X. We would like to thank the referee for his/her useful comments and suggestions which have improved the clarity of this paper. We also thank observers P. Berlind and M. Calkins for performing the FLWO observations. Funding for SDSS-III has been provided by the Alfred P. Sloan Foundation, the Participating Institutions, the National Science Foundation, and the U.S. Department of Energy Office of Science. The SDSS-III web site is http://www.sdss3.org/. SDSS-III is managed by the Astrophysical Research Consortium for the Participating Institutions of the SDSS-III Collaboration including the University of Arizona, the Brazilian Participation Group, Brookhaven National Laboratory, Carnegie Mellon University, University of Florida, the French Participation Group, the German Participation Group, Harvard University, the Instituto de Astrofisica de Canarias, the Michigan State/Notre Dame/JINA Participation Group, Johns Hopkins University, Lawrence Berkeley National Laboratory, Max Planck Institute for Astrophysics, Max Planck Institute for Extraterrestrial Physics, New Mexico State University, New York University, Ohio State University, Pennsylvania State University, University of Portsmouth, Princeton University, the Spanish Participation

Group, University of Tokyo, University of Utah, Vanderbilt University, University of Virginia, University of Washington, and Yale University. This research has made use of the NASA/IPAC Extragalactic Database (NED) which is operated by the Jet Propulsion Laboratory, California Institute of Technology, under contract with the National Aeronautics and Space Administration.

# 4 Activity demographics and host-galaxy properties for Infrared-selected galaxies

## 4.1 Introduction

Distinguishing between the processes of star-formation and active galactic nuclei (AGN) is crucial in the study of energy production in galaxies. The ratio of these processes and their interplay is important on both whole-galaxy and galaxy nucleus scales for understanding their part in galaxy evolution. Several scaling relations between black hole mass ($M_{\rm BH}$), bulge luminosity ($L_{\rm bulge}$), bulge mass ($M_{\rm bulge}$), velocity dispersion ($\sigma$) e.g., $M_{\rm BH} - L_{\rm bulge}$: (Kormendy & Richstone, 1995), $M_{\rm BH} - M_{\rm bulge}$ (Magorrian et al., 1998), $M_{\rm BH} - \sigma$ (Ferrarese & Merritt, 2000), average black hole growth rate, and mean total stellar mass (Mullaney et al., 2012) describe empirical relations between the central regions of galaxies and their hosts. However, the origin and degree of influence of such relations are still debated. (For a review see Kormendy & Ho 2013).

The close similarities between the cosmic evolution of the star-formation rate density and the supermassive black hole (SMBH) mass accretion rate density (e.g., Silverman et al. 2008; Aird et al. 2010) point towards a connection between the evolution of star formation and AGN activity. Davies et al. (2007) provided strong evidence for a starburst–AGN connection by examining the nuclei of nine Seyfert galaxies and show-

ing that the peak of AGN activity occurs 50–100 Myr after the onset of star formation. The delay between star formation and AGN activity indicates that the starburst had a significant impact on fueling the central black hole. Hydrodynamical simulations (e.g., Hobbs et al. 2011) support this scenario by showing that stellar winds and supernovae enhance the black hole mass accretion by injecting turbulence into the surrounding gas disc. However, a complete picture of these processes has not yet been established, and many questions remain open regarding the ways star formation and AGN feedback mechanisms impact and regulate one another considering the different physical conditions at different cosmic epochs.

A complete study of the starburst–AGN connection requires a representative sample of galaxies probing the wide range of different physical conditions that these phenomena engage. The nearby Universe offers the opportunity to study the above processes and overall galaxy properties in observationally resolved conditions. A number of nearby galaxy surveys (e.g., *Spitzer* Infrared Nearby Galaxies Sample−SINGS; Kennicutt et al. 2003, Great Observatories All-sky LIRG Survey−GOALS; Armus et al. 2009, *Herschel* Reference Survey−HRS; Boselli et al. 2010) have approached the subject by focusing mainly on specific aspects of the star formation or AGN processes. For example, SINGS galaxies constitute a relatively small number of nearby and extended objects at the low-luminosity end of FIR luminosity function and therefore do not depict star-formation in its whole extent. Furthermore, powerful AGNs were intentionally excluded from the SINGS sample, thus limiting the diversity of AGN systems available for a comprehensive study of the starburst–AGN connection. GOALS on the other hand consists predominantly of Luminous Infrared Galaxies (LIRGs, $10^{11}L_{\odot} < L < 10^{12}L_{\odot}$) and a few Ultra-Luminous Infrared Galaxies (ULIRGs $L \geq 10^{12}L_{\odot}$), sampling the higher ends of star formation and galactic activity in general, while the HRS is particularly oriented toward high-density environments.

For a comprehensive study of the star formation and AGN phenomenon in a wide range of environments and physical conditions in the local universe, it is imperative to employ a well defined and representative sample of galaxies. To this cause the "Star Formation Reference Survey" (SFRS; Ashby et al. 2011) was established. An initial result from the SFRS sample indicating a connection between the central regions of star-forming galaxies and their hosts (Maragkoudakis et al., 2017) showed a correlation between the nuclear star-formation rate (SFR) and the total stellar mass of the galaxies. This was referred to as the Nuclear Main Sequence of star-forming galaxies.

The current paper presents the activity demographics and the host galaxy properties for the SFRS galaxies and is organized as follows. Section 4.2 describes the SFRS and

gives basic information on the sample properties. Section 4.3 describes the observations, the initial reduction of the spectra, and the measurement of the fluxes of the strong optical emission lines. The activity classification is presented in Section 4.4. Gas-phase metallicities, metallicity gradients, and nuclear SFR measurements are presented in Section 4.5. Section 5.5 provides a detailed discussion of the activity demographics in the local Universe, the different classification methods used, the galaxy properties based on activity type, and the dominant source of ionization in LINERs and transition objects. Finally, we summarize our results in Section 4.7. Throughout the paper the activity class H II (or H II galaxies) is used to describe pure star-forming galaxies (SFGs) that exhibit no fraction of AGN activity.

## 4.2 The SFRS sample

The SFRS galaxies were chosen in order to build a representative sample spanning the full range of properties of local galaxies hosting primarily star-formation activity. The parent sample from which SFRS was drawn is the PSC$z$ (Saunders et al., 2000), a database of 15,411 nearby star-forming galaxies brighter than 0.6 Jy at 60$\mu m$ across 84 per cent of the sky at redshifts $z \leq 0.2$. Selection from the PSC$z$ into the SFRS was based on observational proxies for SFR, specific SFR (sSFR), and dust temperature. Specifically, Ashby et al. (2011) used the IRAS 60 $\mu$m luminosity as a SFR tracer, the flux ratio of $F_{60}$ to 2MASS $K_S$ ($F_{60}/K_S$) as sSFR proxy, and the far-IR flux density ratio of $F_{100}/F_{60}$ as a measure of dust temperature to create a sample of galaxies spanning this three-dimensional parameter space. 369[1] galaxies were selected (Ashby et al., 2011) to explore all existing combinations of these parameters over their entire range. Each SFRS galaxy was assigned a weight reflecting its relative prevalence with respect to the parent population from which the SFRS was defined (Ashby et al., 2011). The overall distribution of SFRS's total infrared (TIR) luminosities is $10^{7.95}-10^{12.25}$L$_\odot$, the $F_{60}/F_{100}$ flux-density ratio distribution is between 0.14–1.64, and the stellar masses range between $10^{7.79} - 10^{12.14}$M$_\odot$ (Maragkoudakis et al., 2017). Thus, the parameter space covered by the SFRS captures the full range of star-forming and AGN conditions and environments, making it an ideal survey for the study of these processes in the local Universe.

Exploring all conditions of star formation requires an uncensored sample of galaxies, and therefore galaxies hosting AGN activity were not discarded from the SFRS. This

[1]Quasar 3C 273 and blazar OJ 287 are excluded from the spectroscopic studies related to star formation but are included in the rest of the SFRS analysis.

also provides the opportunity to examine the AGN contribution to the overall energy output of galaxies and simultaneously investigate the interplay between star formation and AGN mechanisms (i.e., quenching or boosting of star formation). Therefore, we initiated a long-slit spectroscopic campaign to acquire spectra for the SFRS galaxies lacking SDSS spectroscopic coverage and used a combination of optical emission-line and IR diagnostics to identify AGN hosts.

The SFRS has an impressive range of multiband photometric data from UV to radio bands: GALEX FUV–NUV, SDSS $ugriz$, 2MASS $JHKs$, *Spitzer*/IRAC 3.6, 4.5, 5.8, 8.0 $\mu$m, *Spitzer*/MIPS 24 $\mu$m, *AKARI FIR All-Sky Survey*, *IRAS*, VLA/NVSS. Furthermore, there is an ongoing H$\alpha$ imaging campaign at the 1.3-m Ritchey-Crétien telescope at the Skinakas Observatory in Crete. This complete set of multi-wavelength photometry combined with the spectroscopically defined activity classification will allow us to derive fundamental galaxy properties (i.e., SFRs, stellar masses, dust-luminosities) for each galaxy activity class using both luminosity-dependent calibrations as well as spectral energy distribution (SED) fitting techniques.

# 4.3 Observations and analysis

## 4.3.1 SDSS spectra and aperture effects

210 SFRS galaxies had available SDSS spectra as of data release 7 (DR7; Abazajian et al. 2009). These cover a spectral range from 3800 Å to 9200 Å with a resolution $R = 1500$ at 3800 Å and $R = 2500$ at 9000 Å. The spectra refer to a 3″-diameter region of the nucleus of each galaxy. Taking into account that at the median SFRS redshift of 0.024 the fiber diameter correspond to a physical size of approximately 1.5 kpc, the obtained SDSS spectra provide a reasonable representation of the nuclear region of the SFRS galaxies. Because the SDSS fibers are located on the nucleus, and the region of spectral extraction can not be adjusted, we refer to all SDSS classification as nuclear region classification. Thirty six SFRS galaxies are located at redshifts between $0.05 < z < 0.2$, 21 of which have SDSS fiber spectra. The projected aperture diameter at these redshifts is between 3 kpc and 12 kpc, which are closer to global spectra of galaxies rather than nuclear. Maragkoudakis et al. (2014) showed that line ratios and consequently activity classification obtained from SDSS 3″ fibers can be affected by aperture size. Besides AGN spectral features being veiled by the host-galaxy starlight, extranuclear star-forming activity encompassed in the fiber can influence spectral lines, often increasing lower ionization emission-line intensities. Although starlight removal

techniques can mitigate these effects they do not fully remove them, especially the contamination by emission lines from the ionized interstellar medium (ISM) in the host galaxy (Maragkoudakis et al. 2014). However, these galaxies constitute only a very small fraction of the SFRS sample, and they do not change the conclusions of the analysis.

### 4.3.2 Long-slit spectra

Long-slit spectra were acquired at the Fred Lawrence Whipple Observatory in Arizona using the 60-inch Tillinghast telescope with the FAST spectrograph (Fabricant et al., 1998). The target list included 159 galaxies without SDSS spectra plus 19 galaxies observed by SDSS but with insufficient signal-to-noise ratio (S/N) or bad fiber centering. Each galaxy was observed with a $3''$ wide $\times 6'$ long slit visually centered on the nucleus and oriented along the galaxy major axis. The data were collected using the $2688 \times 512$ pixel FAST3 CCD camera. We used two configurations: a) a 600 l mm$^{-1}$ grating giving a spectral coverage of the 3800 – 5700 Å or 5500 – 7800Å wavelength range in the blue and red part of the spectrum respectively with a dispersion of 0.75Å pixel$^{-1}$ b) a 300 l mm$^{-1}$ grating covering the spectral range of 3400 – 7200 Å with a dispersion of 1.47 Å pixel$^{-1}$. The first configuration was used for the observation of 39 galaxies of which 23 also have SDSS spectra. The second configuration provided simultaneous coverage of all diagnostic lines of interest with sufficient resolution and was used for most of the galaxies. The resolution of the 300 l mm$^{-1}$ grating was 5.993 Å as measured from the full width at half maximum (FWHM) of the [O I] 5577 Å sky line. Two to three exposures were acquired for each object to correct for the presence of cosmic rays on the images. The individual exposure times varied between 600 and 1800 seconds in order to achieve a S/N of 40 at the H$\alpha$ emission line. For large galaxies covering a major portion of the slit, separate sky exposures were obtained as close as possible to the location of the galaxies in the sky to allow proper sky subtraction. Spectrophotometric standard-star exposures from the list of Massey et al. (1988) were also obtained during each night and used for flux calibration of the spectra.

The initial reduction of the long-slit spectra was performed with IRAF (Image Reduction and Analysis Facility). Standard procedures of bias subtraction, flat fielding, and wavelength calibration were applied to the two-dimensional CCD images. The different exposures of each galaxy were combined in order to remove cosmic ray imprints on the data. Two types of one-dimensional spectra were extracted with IRAF's APALL task: integrated spectra with aperture size matched to the point where the galaxy's flux reached the level of the background and nuclear spectra, extracted from a $3.5'' \times 3''$

aperture, determined from the average seeing at the time of the observations. The standard star spectra were processed in the same way as the galactic spectra. We identified the strongest lines on the extracted spectra and measured their location with IRAF's SPLOT task. The measured emission-line centroids were used to establish galaxy redshifts and shift all spectra to the rest frame. This step was also performed on the SDSS spectra. During the SFRS long-slit campaign (2010−2014), 45 galaxies with no previous SDSS data were added to the SDSS data releases. We have analyzed these galaxies to examine the agreement, or possible deviations, between long-slit and fiber spectroscopy.

### 4.3.3 Starlight Subtraction

The stellar continuum was removed from both the long-slit (integrated and nuclear) and the SDSS spectra with the STARLIGHT v.04 code (Cid Fernandes et al., 2005). STARLIGHT fits the stellar continuum on emission-line-free regions of the spectrum using linear combinations of simple stellar populations (SSPs) from the Bruzual & Charlot (2003) (hereafter BC03) libraries. We used a base of 138 SSPs with 23 ages ranging between 1 Myr and 13 Gyr and 6 metallicities from 0.005 to $2.5 Z\odot$. The extinction ($A_V$) was also fitted by STARLIGHT, assuming the Cardelli et al. (1989) reddening law with the ratio of total to selective extinction $R_V \equiv A_V/E(B-V) = 3.1$. In order to handle any age mixture biases in the fitting process for galaxies having an excessive blueness when $A_V$ is close to 0, we allowed $A_V$ to take negative values as discussed by Cid Fernandes et al. (2014). Negative $A_V$ was also allowed in studies using different fitting methods (e.g., Kauffmann et al. (2003)). A statistical justification for this unphysical condition is that when $A_V$ is truly $= 0$, unbiased estimates should oscillate around 0, including both negative and positive values. There are only 14 cases showing negative extinctions but very close to zero, with a median of $-0.08$.

An initial assessment of starlight subtraction results can be done by comparing the estimated $A_V$ extinction with the Two-Micron All-Sky Survey (2MASS) $H-K$ colors. It has been recognized for some time that infrared colors could be used to directly measure extinction (e.g., Hyland et al. 1980; Lada et al. 1994). Fig. 4.3.1 shows the theoretical $H-K$ reddening curve for K-type and O-type stars and the fit to STARLIGHT estimated extinction. The observed correlation between the two quantities indicates reasonably good fitting results. Based on the fitted spectra, the range of equivalent widths of H$\alpha$ and H$\beta$ absorption lines are 2.49Å $<$ EW(H$\alpha$) $<$ 4.70Å and 2.05Å $<$ EW(H$\beta$) $<$ 3.04Å. Appendix 4.B.1 shows that the distribution of the F(H$\alpha$) and F(H$\beta$) emission line fluxes measured after subtracting different STARLIGHT best-fit models from different

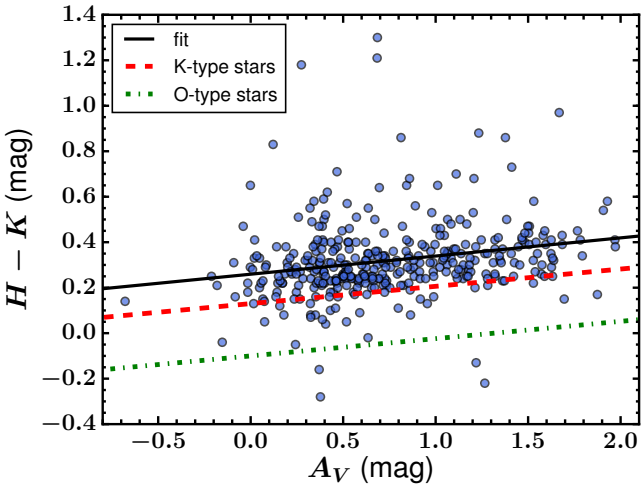


**Figure 4.3.1:** Comparison between the $A_V$ extinction calculated by STARLIGHT and the 2MASS $H-K$ colors in Vega magnitudes. The black solid line is the fit to the data. The red dashed line is the theoretical $H-K$ reddening curve (Cardelli et al., 1989), assuming intrinsic $(H-K)_o = 0.1$ for K-type stars (Blum et al., 2000). Similarly, the green dash-dot line is the theoretical $H-K$ reddening curve, assuming intrinsic $(H-K)_o = -0.1$ based on the O-type stars calibrations by Martins & Plez (2006), representing the bluest possible stellar populations. NGC 4688 is the galaxy with $A_V = -0.68$ also reported with $E(B-V) = 0$ by Ho et al. (1997a).

STARLIGHT runs, is always smaller than their measured uncertainties, and therefore the uncertainties introduced by STARLIGHT have no impact on our results.

STARLIGHT also provides physical parameters such as the dominant stellar populations in the host galaxies, their corresponding metallicities, stellar ages, and masses. However adopting these parameters as the actual or most representative parameters of the input galaxies is not a trivial matter, as many degeneracies are involved in the fitting process and cannot be neglected. (See Appendix 4.B.) Despite the uncertainties in the parameters of the stellar populations, STARLIGHT appears to be robust in measuring, fitting, and removing the stellar features (continuum and absorption lines) in our spectra. We reached this result by fitting the same spectra using different sets of stellar population.

Figure 4.3.2 shows an example of the observed, STARLIGHT-fitted, and starlight-subtracted spectra of NGC 2712. All the SFRS galaxy spectra are available online from MNRAS.

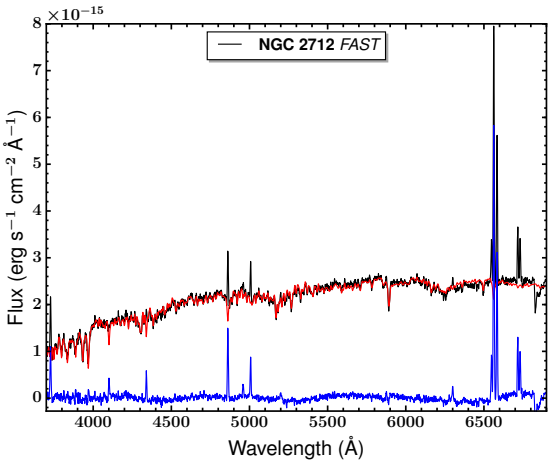


**Figure 4.3.2:** The observed (black line), STARLIGHT-fitted (red line), and starlight-subtracted (blue line) spectra of NGC 2712 observed with the FAST spectrograph.

### 4.3.4 Emission Line Measurements

The emission lines of interest were fitted with SHERPA (Freeman et al., 2001), a general-purpose fitting environment designed for CIAO, the Chandra (X-Ray Observatory) Interactive Analysis of Observations software package (Fruscione et al., 2006). SHERPA can handle multi-component models (Fig. 4.3.3) such as emission lines with broad components (e.g., Seyfert 1 galaxies) or doubled-peaked line profiles resulting from galaxy rotation. One of the most important advantages of SHERPA is its capability of fitting spectra accounting for the flux density uncertainties. We fitted the intensity, full width at half-maximum (FWHM), and central wavelength of each emission line using Gaussian profiles and a constant for the local continuum. The latter is a good approximation given that we are fitting the starlight-subtracted spectra. Uncertainties for the parameters were calculated at the $1\sigma$ confidence intervals. This was done by varying a parameter's value in a grid of values while at the same time the values of the other model parameters were allowed to float to new best-fit values.

We measured the intensities of the forbidden lines [O III] $\lambda$5007, [N II] $\lambda$6583, [S II] $\lambda\lambda$6716, 6731, [O I] $\lambda$6300, and the Balmer H$\beta$ and H$\alpha$ lines. For five galaxies (NGC 3758, UGC 8058, IRAS 13218+0552, MK 268, and UGC 9412) having spectra with extremely broad lines (Fig. 4.3.4) no emission line fitting was performed, since from the profile of the lines they could be clearly classified as AGN. Therefore, they were assigned a Sy-1 classification (see Section 4.4.3). The emission-line intensity ratios with respect

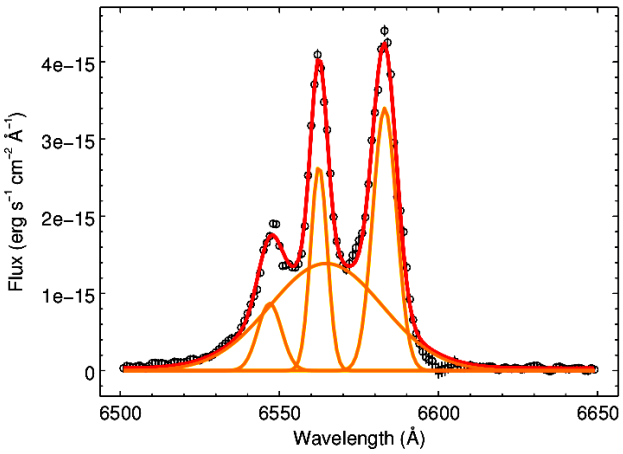


**Figure 4.3.3:** Example of a multi-component emission-line fit with SHERPA of the H$\alpha$ and [N II] $\lambda\lambda$6548,6583 doublet in the nuclear spectrum of Seyfert IC 910. An additional broad component is used in this case. Points show starlight-subtracted data. Orange lines show four individual emission line components, and red line shows the sum which corresponds to the best fit.

to the H$\alpha$ or H$\beta$ lines used in the three activity classification diagnostic diagrams (see Section 4.4.1), along with the intensity of the H$\alpha$ and the STARLIGHT fitted extinction, are presented in Table 4.3.1 along with the corresponding H$\alpha$/H$\beta$ ratio.

### 4.3.5 H$\alpha$ emission line extinction correction

Because the emission-line ratios used in our analysis are very close in wavelength, they are almost completely insensitive to reddening and therefore we do not perform extinction correction to the respective emission lines. However, because we measured nuclear SFR (Section 4.5) based on $L_{H\alpha}$, we did correct the H$\alpha$ flux. The extinction was derived from the relative observed strengths of the H$\alpha$ and H$\beta$ Balmer lines. The intrinsic Balmer decrement remains roughly constant for typical gas conditions, and in our analysis we assumed an intrinsic flux ratio value $(FH\alpha/FH\beta)_0$ of 2.86 for H II regions, corresponding to a temperature $T = 10^4$ K and an electron density $n_e = 10^2$ cm$^{-3}$ for Case B recombination (Osterbrock, 1989). For the narrow line region of AGN a value of 3.1 is generally adopted, where H$\alpha$ emission is slightly enhanced by collisional excitation due to higher density gas and a much higher ionizing continuum.

We adopted the Cardelli et al. (1989) extinction law and calculated the gas extinc-

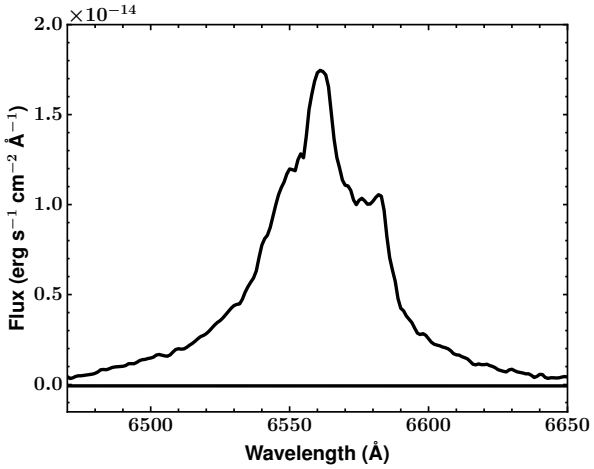


**Figure 4.3.4:** An example of a Type-1 AGN spectrum (NGC 3758) at the H$\alpha$ line wavelength region, where no emission line fitting was performed. For five such galaxies a Sy-1 classification was automatically assigned.

tion $A_V$ based on the following relation:

$$A_V = \frac{\log_{10}[(FH\alpha/FH\beta)/(FH\alpha/FH\beta)_0]}{0.4 \times (A_{H\beta} - A_{H\alpha})}, \tag{4.1}$$

where $A_{H\beta}$ and $A_{H\alpha}$ are the magnitude attenuations at the H$\alpha$ and H$\beta$ wavelengths. The extinction-corrected H$\alpha$ fluxes and the corresponding gas reddening E(B-V) values calculated from Eq. 4.1 and $R_V \equiv A_V/E(B-V) = 3.1$, are given in Table 4.3.1.

**Table 4.3.1:** Nuclear fluxes and flux ratios of optical diagnostic emission lines. Column (1) SFRS ID (Ashby et al. 2011); Column (2) Galaxy name; Column (3) H$\alpha$ emission line flux, normalized to $10^{-14}$ erg cm$^{-2}$ s$^{-1}$; Column (4) Ratio of H$\alpha$ and H$\beta$ Balmer line fluxes. Columns (5) – (8) BPT line ratio measurements and uncertainties; Column (9) Extinction corrected H$\alpha$ emission line flux normalized to $10^{-14}$ erg cm$^{-2}$ s$^{-1}$; Columns (10) and (11) Integrated and nuclear extinction as calculated by STARLIGHT code; Column (12) The nuclear E(B-V) color excess of the gas as calculated from the Balmer decrement; Column (13) Spectral observation method. Emission line fluxes and ratios for the FAST observations come from the nuclear aperture spectrum. F(H$\alpha)_{cor}$ and E(B-V)$_{\rm gas}$ values flagged with a * symbol indicate uncertain measurements due to differences in the flux calibration between the blue and red spectral regions of galaxies observed with the 600 l mm$^{-1}$ grating configuration (Section 4.3.6). The full version of Table 3.2.1 is available online from MNRAS.

| SFRS | Galaxy | F(H$\alpha$) | H$\alpha$/H$\beta$ | [O III]/H$\beta$ | [N II]/H$\alpha$ | [S II]/H$\alpha$ | [O I]/H$\alpha$ | F(H$\alpha)_{cor}$ | $A_V$ | $A_V$ nuc | E(B-V)$_{\rm gas}$ | Observation |
|---|---|---|---|---|---|---|---|---|---|---|---|---|
| (1) | (2) | (3) | (4) | (5) | (6) | (7) | (8) | (9) | (10) | (11) | (12) | (13) |
| 1 | IC 486 | $2.430^{+0.037}_{-0.026}$ | $5.830^{+0.214}_{-0.205}$ | $1.058^{+0.015}_{-0.015}$ | $0.071^{+0.006}_{-0.008}$ | $-0.105^{+0.005}_{-0.007}$ | $-0.727^{+0.019}_{-0.020}$ | $10.788^{+0.164}_{-0.115}$ | ... | 0.68 | 0.64 | SDSS |
| 2 | IC 2217 | $7.660^{+0.045}_{-0.045}$ | $4.935^{+0.085}_{-0.087}$ | $-0.552^{+0.029}_{-0.029}$ | $-0.422^{+0.006}_{-0.006}$ | $-0.474^{+0.003}_{-0.003}$ | $-1.588^{+0.052}_{-0.054}$ | $27.755^{+0.163}_{-0.163}$ | 0.50 | 0.82 | 0.55 | FAST |
| 3 | NGC 2500 | $0.151^{+0.007}_{-0.007}$ | $3.096^{+0.497}_{-0.482}$ | $0.132^{+0.080}_{-0.083}$ | $-0.446^{+0.057}_{-0.058}$ | $-0.268^{+0.022}_{-0.019}$ | $0.127^{+0.031}_{-0.029}$ | $0.182^{+0.008}_{-0.008}$ | 0.81 | 0.68 | 0.08 | FAST |
| 4 | NGC 2512 | $10.800^{+0.008}_{-0.008}$ | $4.713^{+0.017}_{-0.017}$ | $-0.677^{+0.008}_{-0.008}$ | $-0.310^{+0.001}_{-0.001}$ | $-0.564^{+0.002}_{-0.002}$ | $-1.535^{+0.014}_{-0.014}$ | $35.104^{+0.026}_{-0.026}$ | 0.52 | 0.46 | 0.50 | FAST |
| 5 | MCG 6-18-009 | $6.230^{+0.041}_{-0.041}$ | $5.253^{+0.075}_{-0.072}$ | $-0.517^{+0.015}_{-0.014}$ | $-0.289^{+0.004}_{-0.004}$ | $-0.564^{+0.003}_{-0.003}$ | $-1.441^{+0.023}_{-0.024}$ | $26.157^{+0.172}_{-0.172}$ | ... | 0.63 | 0.61 | SDSS |
| 6 | MK 1212 | $0.403^{+0.005}_{-0.004}$ | $6.165^{+0.323}_{-0.318}$ | $-0.316^{+0.054}_{-0.049}$ | $-0.285^{+0.009}_{-0.008}$ | $-0.562^{+0.005}_{-0.005}$ | $-1.441^{+0.053}_{-0.072}$ | $2.469^{+0.031}_{-0.025}$ | ... | 0.94 | 0.78 | SDSS |
| 7 | IRAS 08072+1847 | $1.790^{+0.013}_{-0.013}$ | $8.168^{+0.165}_{-0.160}$ | $-0.239^{+0.020}_{-0.018}$ | $-0.196^{+0.005}_{-0.005}$ | $-0.469^{+0.003}_{-0.003}$ | $-1.187^{+0.023}_{-0.021}$ | $17.611^{+0.128}_{-0.128}$ | ... | 1.51 | 0.98 | SDSS |
| 8 | NGC 2532 | $2.300^{+0.060}_{-0.056}$ | $7.691^{+1.296}_{-1.221}$ | $-0.519^{+0.068}_{-0.072}$ | $-0.415^{+0.028}_{-0.030}$ | $-0.492^{+0.010}_{-0.011}$ | $-1.693^{+0.010}_{-0.011}$ | $23.745^{+0.619}_{-0.578}$ | 0.53 | 0.79 | 1.00 | FAST |
| 9 | UGC 4261 | $8.290^{+0.043}_{-0.043}$ | $4.195^{+0.039}_{-0.040}$ | $0.014^{+0.005}_{-0.005}$ | $-0.597^{+0.004}_{-0.004}$ | $-0.591^{+0.002}_{-0.002}$ | $-1.690^{+0.012}_{-0.012}$ | $20.472^{+0.106}_{-0.106}$ | ... | 0.49 | 0.39 | SDSS |
| 10 | NGC 2535 | $2.310^{+0.013}_{-0.013}$ | $4.137^{+0.089}_{-0.092}$ | $-0.885^{+0.077}_{-0.072}$ | $-0.434^{+0.007}_{-0.007}$ | $-0.614^{+0.002}_{-0.002}$ | $-1.741^{+0.163}_{-0.257}$ | $5.520^{+0.031}_{-0.031}$ | 0.65 | 0.48 | 0.37 | FAST |

### 4.3.6 Fiber and nuclear long-slit spectra emission-line comparison

Fig. 4.3.5 shows a comparison between the nuclear fluxes measured from long-slit spectroscopy and SDSS fibers for the 45 galaxies observed with both methods. The measured scatter between the two methods is 0.45 dex for H$\alpha$ and 0.37 dex for [O III] $\lambda$5007, and the largest deviations appear for galaxies in interacting groups. Depending on distance, the $3.5'' \times 3''$ long-slit aperture and the $3''$-radius circular aperture may encompass different fractions of galaxy light as well as companion galaxy light. Fig. 4.3.6 compares the four line ratios used in the three BPT classification diagrams. There is an overall good agreement between the two observing methods especially in the cases of the most commonly used [O III]/H$\beta$ and [N II]/H$\alpha$ ratios. Part of the observed scatter can be attributed to sensitivity to the exact co-alignment of the fiber and the long slit, which translates to a difference between the areas covered by the two methods. In addition, in the case of the [O I]/H$\alpha$ and [S II]/H$\alpha$ ratios, the scatter is also attributed to the generally weaker [O I] and [S II] emission lines. Indeed, the largest deviations are observed in the few cases of low S/N long-slit spectra, where the fitting of the emission-line profiles is more uncertain. In certain cases, galaxies observed with the 600 l mm$^{-1}$ grating configuration had the blue and red part of their spectrum observed on different nights. As a result, differences in the flux calibration of the two spectral regions are expected depending on the observational conditions and/or the (mis)alignment of the long slit at the exact same location on the galaxy between observing nights. For these cases we used the emission lines measured from the long-slit observations for the nuclear activity classification, because the line ratios used in the optical diagrams are very close in wavelength and in the same spectrum (blue or red). However, for the nuclear SFR measurements (Section 4.5) we used the SDSS spectra, where available, to calculate the Balmer decrement and obtain extinction corrected H$\alpha$ fluxes. 7 star-forming galaxies observed with the 600 l mm$^{-1}$ grating configuration presenting a mismatch between their red and blue spectrum continuum have no available SDSS spectra, and we flag their SFR measurment (Table 4.5.1) as uncertain.

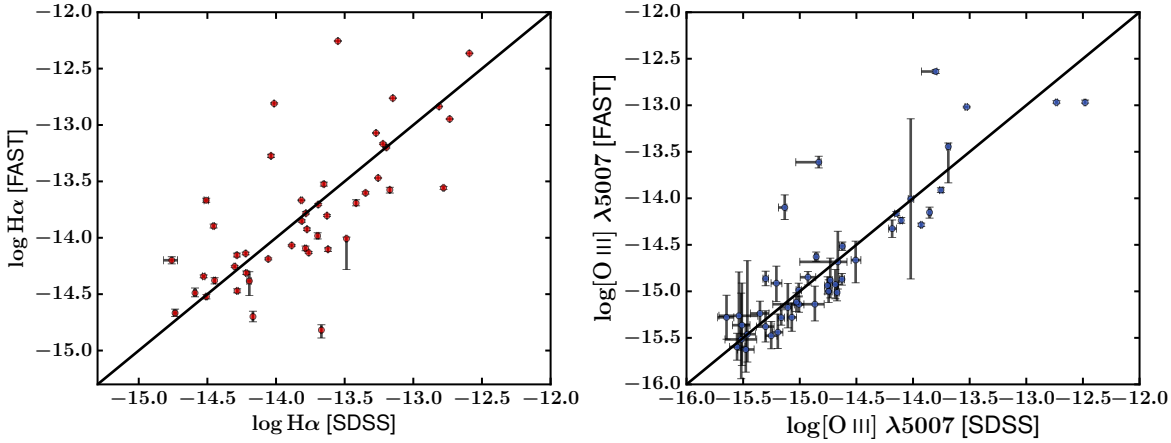


**Figure 4.3.5:** Comparison between the H$\alpha$ and [O III] $\lambda$5007 fluxes measured from the nuclear long-slit and fiber spectroscopy. One-to-one lines are shown. Units are in erg s$^{-1}$ cm$^{-2}$.

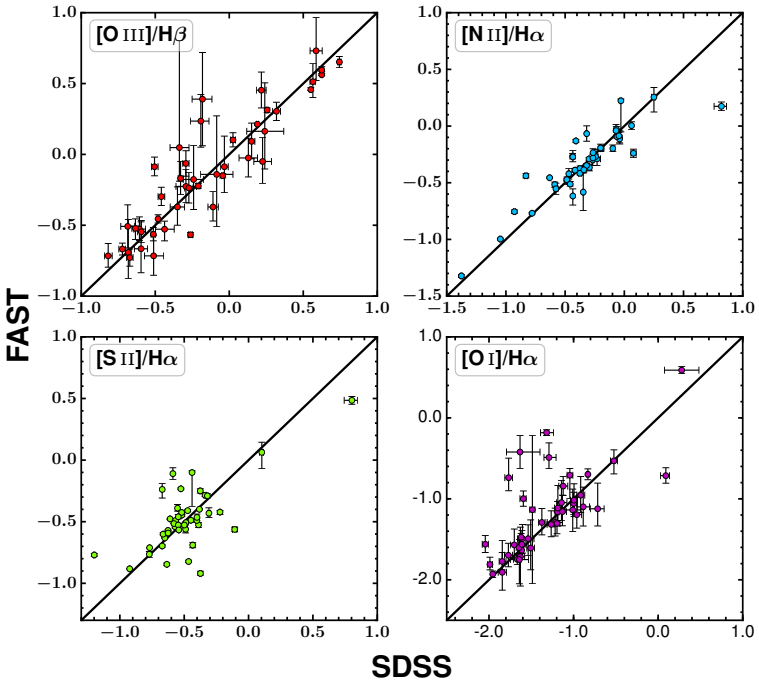


**Figure 4.3.6:** Comparison between the diagnostic line ratios derived from the nuclear long-slit and fiber spectroscopy. FAST measurements are shown on the ordinate and SDSS measurements on the abscissa. All measurements represent the logarithmic values of the line ratios. One-to-one lines are shown.

# 4.4 Activity Classification

## 4.4.1 Optical Diagnostics

The standard optical activity diagnostic diagrams of [O III] $\lambda$5007/H$\beta$ versus [N II] $\lambda$6583/H$\alpha$, [S II] $\lambda\lambda$6716, 6731/H$\alpha$, and [O I] $\lambda$6300/H$\alpha$ (Baldwin, Phillips & Terlevich 1981 (hereafter BPT); Veilleux & Osterbrock 1987) are the primary classifiers for the galactic nuclear activity in our sample (Fig. 4.4.1). The standard BPT diagrams are probably the most widely used and best calibrated activity classification diagnostics for galaxies in the nearby universe ($z < 0.4$). These diagrams are able to distinguish star formation from AGN powered galaxies because the relative intensity of spectral lines with different excitation energies depends on the hardness of the ionizing continuum. The diagrams were refined by Kewley et al. (2001) and Kauffmann et al. (2003), with the former defining a theoretical upper bound to the location of the SFGs using HII region model spectra and the latter empirically separating the pure star forming galaxies in the [O III]/H$\beta$ versus [N II]/H$\alpha$ diagnostic based on a sample of 122,808 galaxies from the SDSS. Objects that host both starburst and AGN activity lie between these lines and are known as composite or transition objects (TO; e.g., Ho et al. 1993). Another refinement on the [S II]/H$\alpha$ and [O I]/H$\alpha$ diagrams was introduced by Kewley et al. (2006), who calculated an empirical separating line in the AGN plane distinguishing the Seyfert populations from the Low-Ionization Nuclear Emission-Line Regions (LINER) (Heckman, 1980). Lastly, Schawinski et al. (2007) defined an empirical line in the [N II]/H$\alpha$ BPT diagnostic separating Seyfert from LINER classes, similarly to the Kewley et al. (2006) empirical lines.

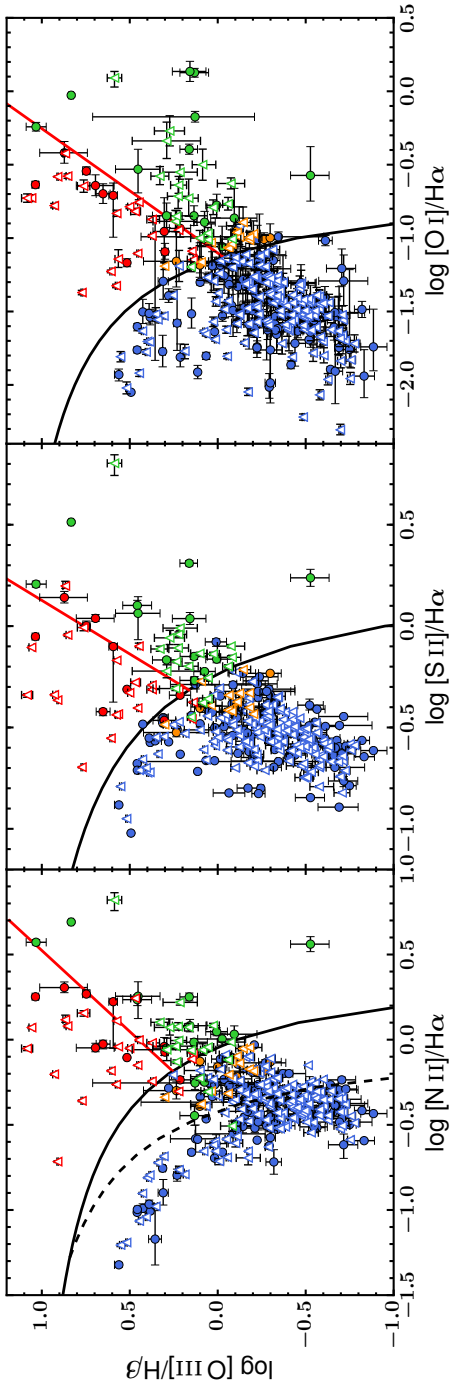


**Figure 4.4.1:** The three BPT diagnostic diagram for the SFRS galaxies. From left to right the [O III]/H$\beta$ versus [N II]/H$\alpha$, [O III]/H$\beta$ versus [S II]/H$\alpha$, and [O III]/H$\beta$ versus [O I]/H$\alpha$ are plotted. The dashed line in the [N II]/H$\alpha$ diagram (left-hand panel) is the empirical star-forming line of Kauffmann et al. (2003), while the solid black line in all three diagrams is the theoretical maximum starburst line from Kewley et al. (2001). The red lines in all diagrams separate Seyfert nuclei from LINERs, and for the [N II]/H$\alpha$ diagram it is defined by Schawinski et al. (2007) while for the [S II]/H$\alpha$ and [O III]/H$\beta$ diagrams they are defined by Kewley et al. (2006). Different color points correspond to the final activity classification obtained using all three diagnostic diagrams. The color code is as follows; Blue: star-forming galaxies, red: Seyfert, orange: TO, green: LINER. Solid circles represent galaxies observed with long-slit spectroscopy and open triangles represent SDSS fiber spectra. Different demarcation lines are described in detail in Section 4.4.1.

**Table 4.4.1:** The activity classification of the SFRS sample. Column (1) SFRS ID (Ashby et al. 2011); Column (2) Galaxy name; Columns (3) - (5) present the nuclear activity classification of the three diagnostic BPT diagrams. Column (6) shows the IRAC color classification based on both the nuclear and integrated colors. Columns (7) and (8) present the MEx and CEx diagrams classification, and Column (9) presents the final adopted classification based on the combination of the three BPT diagnostics and the IRAC color–color diagram. The full Table is presented in Appendix 7, Table 7.A.2.

| SFRS | Galaxy | Nuclear Spectra BPT | | | IRAC Colors | MEx | CEx | Final Classification |
|---|---|---|---|---|---|---|---|---|
| | | [N II]/H$\alpha$ | [S II]/H$\alpha$ | [O I]/H$\alpha$ | | | | |
| (1) | (2) | (3) | (4) | (5) | (6) | (7) | (8) | (9) |
| 1 | IC 486 | Sy | Sy | Sy | Sy | Sy | Sy | Sy |
| 2 | IC 2217 | HII | HII | HII | HII | HII | HII | HII |
| 3 | NGC 2500 | TO | LINER | LINER | HII | HII | ... | LINER |
| 4 | NGC 2512 | HII | HII | HII | HII | HII | ... | HII |
| 5 | MCG 6-18-009 | HII | HII | HII | HII | HII | HII | HII |
| 6 | MK 1212 | TO | HII | HII | HII | HII | HII | HII |
| 7 | IRAS 08072+1847 | TO | HII | HII | Sy | HII | TO | Sy |
| 8 | NGC 2532 | HII | HII | HII | ... | HII | HII | HII |
| 9 | UGC 4261 | HII | HII | HII | HII | TO | HII | HII |
| 10 | NGC 2535 | HII | HII | HII | HII | HII | ... | HII |

### 4.4.2 Infrared Diagnostics

While the BPT method performs well in distinguishing the different type of energy mechanisms in the majority of nearby galaxies, it is insensitive to faint or highly obscured AGN where the characteristic diagnostic lines may be faint or veiled by the gaseous and dusty torus. For these cases, diagnostics employing infrared lines and/or continuum measurements appear more sensitive than optical methods. Stern et al. (2005) used mid-infrared photometry to distinguish AGN dominated from star-forming galaxy SEDs. Galaxies that lie within the following region in the IRAC color–color space are defined as AGN:

$$\begin{aligned} &([5.8]-[8.0]) > 0.6, \\ &([3.6]-[4.5]) > 0.2\cdot([5.8]-[8.0]) + 0.18, \text{ and} \\ &([3.6]-[4.5]) > 2.5\cdot([5.8]-[8.0]) - 3.5 \end{aligned} \tag{4.2}$$

where [3.6], [4.5], [5.8], [8.0] are the IRAC magnitudes at 3.6, 4.5, 5.8, and 8.0 $\mu$m correspondingly in the Vega system.

In an effort to uncover even the most “hidden" cases of galaxies hosting AGN activity, we applied the Stern et al. (2005) criteria to the SFRS galaxies, using both integrated IRAC colors as well as colors from their nuclear region. The use of nuclear colors has the advantage of decreasing host-galaxy light contamination that can potentially mask the presence of AGN. In order to measure nuclear colors in a consistent way avoiding aperture effects due to varying galaxy distances, we performed matched aperture photometry from physical sizes of $1 \times 1$ kpc$^2$ to all galaxies having robust IRAC data in all bands. The apertures were centered on the nucleus, based on the source coordinates (Ashby et al. 2011), and the angular aperture sizes in each galaxy were adjusted according to galaxy distance to ensure consistent sampling of linear scales, following the method described by Maragkoudakis et al. (2017). Fig. 4.4.2 shows the comparison of the nuclear and integrated color–color plots. Galaxies that are BPT-classified as H II, TO, or LINERs and lie within the AGN region defined by Eq 4.2 in both nuclear and total IRAC colors are considered obscured AGN and assigned a Sy classification.

Another criterion to diagnose AGN is based on IR continuum measurements such as the flux-density ratio of the 25 and 60 $\mu$m IRAS bandpasses: “Warm" sources with $F25/F60 > 0.2$ are indicative of AGN signatures (Sanders et al., 1988). Because many SFRS galaxies are not reliably detected by IRAS in the 25 $\mu$m band, we used MIPS 24 $\mu$m flux measurements, which on average closely track the IRAS 25 $\mu$m (Dale et al., 2009). There are 6 galaxies above the $F25/F60 > 0.2$ threshold that are not

recovered by the other diagnostic methods (3 BPT diagrams or the IRAC color-color plot). However, half of them were reported as starbursts by Balzano (1983), and therefore we do not adopt those 6 galaxies as AGN. Ashby et al. (2011) used the Stern et al. (2005) integrated IRAC color diagram, the $F_{24}/F_{60}$ ratio criterion, along with a preliminary application of the BPT method (using the [N II] $\lambda$6583/H$\alpha$ diagram) for the available at the time SDSS spectra to obtain an initial sense of the AGN content for the SFRS sample. Of the 165 SDSS sources, 30 were identified as AGN with the BPT method, while 19 and 22 galaxies from the entire sample where assigned an AGN classification using the Stern et al. (2005) wedge and the $F_{24}/F_{60}$ ratio respectively, giving a total of 52 AGN-powered galaxies when accounting for overlaps among the methods.

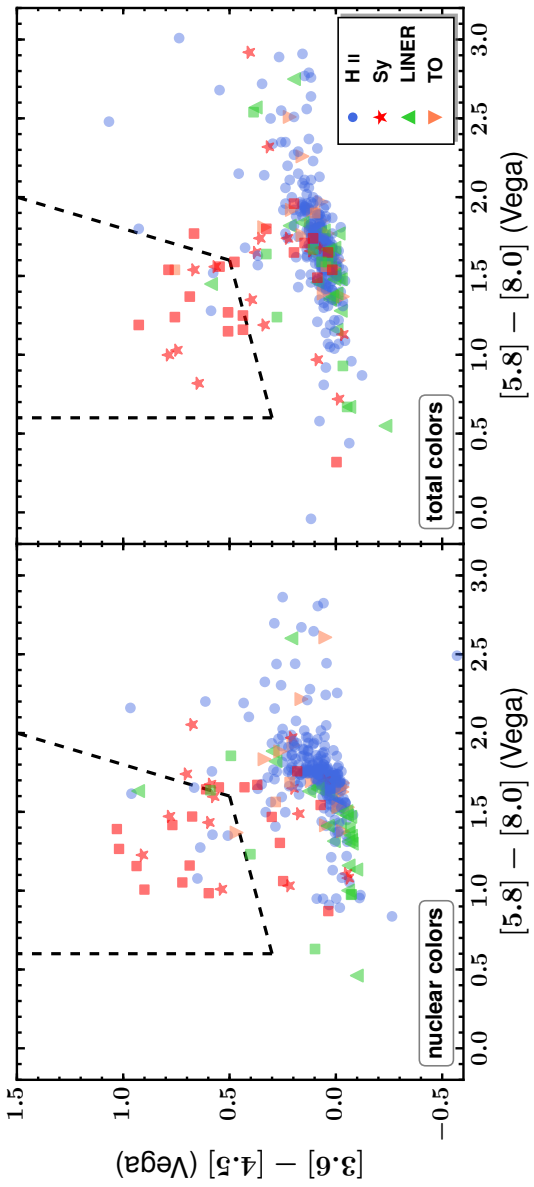


**Figure 4.4.2:** IRAC color–color diagram in the Vega magnitude system using nuclear (left panel) and integrated colors (right panel). The color code is based on the combined BPT classification scheme shown in Fig. 4.4.1. Specifically, blue circles represent H II galaxies, red stars show Sy galaxies, green triangles show LINERs, and upside-down orange triangles show TOs. Squares denote galaxies with broad Hα profiles color-coded based on the combined BPT classification. The dashed lines are the empirically defined lines (Stern et al., 2005) described in Eq 4.2, that separate AGN withing the wedge from SFGs outside of it.

### 4.4.3 Final Activity Classification

The final adopted activity classification for the SFRS galaxies – H II, Sy, LINER, TO – was based on a combination of the three variations of the optical emission-line diagrams (BPT), supplemented by the Stern et al. (2005) IR color–color diagnostics to account for obscured AGN. Specifically, galaxies classified as H II in all three diagrams or classified as TO in the [N II]/H$\alpha$ BPT and H II in the remaining two diagrams where assigned H II class. In general, the TO class is identified explicitly on the [N II]/H$\alpha$ diagram. However, by definition TOs are considered to have a composite contribution from both star forming and AGN activity. Therefore, we assigned TO classification when all of the following three conditions apply: (i) defined as TO in the [N II]/H$\alpha$ diagnostic; (ii) have Sy or LINER classification in one of the other BPTs; and (iii) have H II classification in the remaining diagram. Sy and LINERs were defined when presenting an AGN or TO class in the [N II]/H$\alpha$ BPT and Sy or LINER classification accordingly in both [S II]/H$\alpha$ and [O I]/H$\alpha$ diagrams. Cases of non-unanimous classification were visually inspected in all BPT diagrams (see Appendix 4.C), based on both their positions and their uncertainties in the BPTs, to derive their final classification. To quantify the BPT activity classification uncertainties, especially for the ambiguous cases, we performed Monte Carlo sampling to all 4 diagnostic emission line ratios based on their corresponding ratio uncertainties and derived the probability of a galaxy to belong to a certain class in each BPT diagram (see Appendix 4.A). As mentioned in Section 4.3.4, five galaxies were classified Sy-1 on the basis of extremely broad lines. Finally, 6 H II galaxies, 1 LINER, and 3 TOs that were IR-diagnosed as AGN under the nuclear or total IRAC-color criteria were reassigned a Sy classification. As a result, based on our combined analysis the SFRS sample consists of: 269 (73%) star-forming galaxies, 50 (13%) Seyferts (including 3C 273 and OJ 287), 33 (9%) LINERs, and 17 (5%) TOs.

### 4.4.4 MEx - CEx Diagrams

Recently, several other diagnostics were proposed to distinguish between the different activity types for intermediate or high redshift galaxies. These include the Mass-Excitation (MEx) diagram (Juneau et al., 2011), which substitutes for the standard [N II]/H$\alpha$ ratio of the BPT diagram and plots the [O III] $\lambda$5007/H$\beta$ against stellar mass, and the Color-Excitation (CEx) diagram (Yan et al., 2011) of [O III] $\lambda$5007/H$\beta$ versus the rest-frame $U - B$ color. These can prove beneficial in the case of high-redshift galaxies, as [N II] $\lambda$6583 and H$\alpha$ can only be observed in the optical out to $z \lesssim$

0.45. These methods also avoid blending of lines in low-resolution spectra. In the MEx diagram, two empirically determined dividing lines (Juneau et al., 2014) separate the star-forming, TO, and AGN regions. In the CEx diagram, Yan et al. (2011) provided a demarcation line to distinguish the star-forming and AGN populations, and Juneau et al. (2011) further added a line to mark the region of TO populations.

We used the MEx and CEx diagrams to compare the activity classification derived with the other diagnostics. The SFRS stellar masses were calculated using the asymptotic $K-$band fluxes measured from fitting the galaxy profiles (Bonfini et al. in preparation) and using the $M/L$ calibrations described by Bell et al. (2003):

$$\frac{M_\star}{M_\odot} = 10^{-0.273+(0.091)(u-r)} \times \frac{L_{K_s}}{L_{K_\odot}} \tag{4.3}$$

where $u-r$ are the Petrosian SDSS colors in AB magnitudes. Because the MEx diagram was calibrated based on a Chabrier (2003) initial mass function (IMF) and the Bell et al. (2003) mass-to-light ratio calibration assumes a Salpeter IMF, we converted the stellar masses to the Chabrier IMF following Longhetti & Saracco (2009).

Fig. 4.4.3 and Fig. 4.4.4 show the SFRS galaxies on the MEx and CEx diagram respectively. While the plots visualize the comparison between the BPT and MEx-CEx results, the classification from MEx and CEx methods shown in Table 4.4.1 was obtained using the IDL routines provided by Juneau et al. (2011; 2014). These routines give the probabilities for a given object to belong to each activity class depending on its position on the MEx and CEx diagrams and were calibrated based on the bivariate distribution of a $z \sim 0$ SDSS DR7 sample of galaxies with known activity types.

## 4.5 Gas-Phase Metallicities And Nuclear Star Formation Rates

The most direct way of measuring gas-phase metallicities is based on temperature-sensitive line ratios such as the [O III] $\lambda\lambda$4959,5007/[O III] $\lambda$4363 because the flux ratio of lines originating from different excitation states is temperature-dependent, and metals are the primary coolants of H II regions. Higher metallicity increases the rate of collisional excitation followed by radiative decay resulting in lower nebular temperatures. Unfortunately, this method cannot be used when [O III] $\lambda$4363 is undetectable or extremely weak as it often is. To overcome this difficulty, several empirical or theoretical calibrations involving strong emission lines were developed (e.g. Pagel et al. 1979, Kewley & Dopita 2002). Here we derive metallicities using two different calibrations

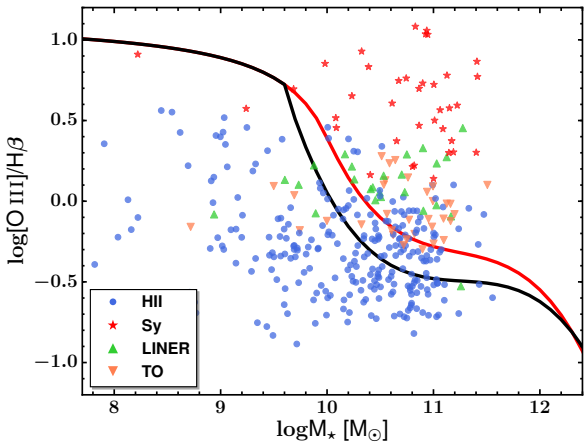


**Figure 4.4.3:** Mass-excitation (Juneau et al., 2011) diagram for the SFRS galaxies. Lines (Juneau et al., 2014) divide the classes with AGN to the upper right, SFGs to the lower left, and TO in the narrow middle region. The point colors are based on the BPT-only classification; blue: star-forming galaxies, red: Seyfert, orange: TO, green: LINER.

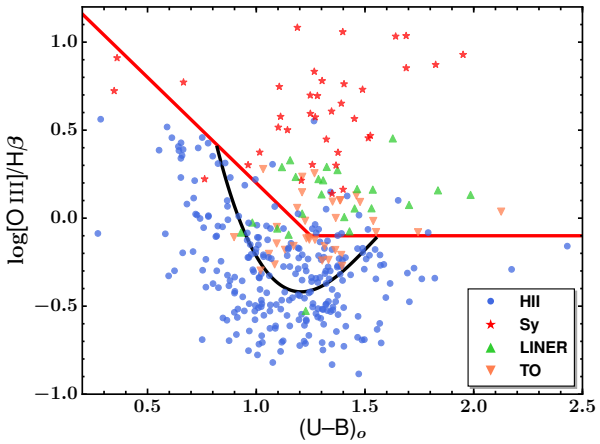


**Figure 4.4.4:** Color-excitation diagram (Yan et al., 2011) for the SFRS galaxies. The red line separates AGN (above the line) from SFGs. The black curve was added by Juneau et al. (2011) and follows the transition where the AGN probability is P(AGN) > 30%. The new region between this curve and the straight lines is analogous to the MEx-intermediate region of the MEx diagram. The point colors are based on the BPT-only classification; blue: star-forming galaxies, red: Seyfert, orange: TO, green: LINER.

as provided by Pettini & Pagel (2004, hereafter PPO4):

$$12 + \log(\mathrm{O/H}) = 8.90 + 0.57 \times \mathrm{N2} \tag{4.4}$$

$$12 + \log(\mathrm{O/H}) = 8.73 - 0.32 \times \mathrm{O3N2} \tag{4.5}$$

where N2 $\equiv \log([\mathrm{N\,II}]\ \lambda6583/\mathrm{H}\alpha)$, and O3N2 $\equiv \log(([\mathrm{O\,III}]\ \lambda5007/\mathrm{H}\beta)/([\mathrm{N\,II}]\ \lambda6583/\mathrm{H}\alpha))$. Equation (4.5) is valid in the range of $-1 <$ O3N2 $< 1.9$. These relations were calibrated using the electron temperature ($\mathrm{T}_e$)-based metallicity for a sample of 137 H II regions. Because the [O III] $\lambda4363$ line was not available in all of our spectra, we used these calibrations to derive the nuclear-region metallicities for the SFGs and the host-galaxy metallicities for all galaxies with available long-slit spectra.

Table 4.5.1 presents the circumnuclear and host-galaxy gas-phase metallicities of the star-forming SFRS galaxies as derived from both N2 and O3N2 calibrations. For galaxies with available long-slit spectra, we also measured host-galaxy elemental abundances, regardless of activity type, by subtracting the nucleus contribution from the integrated spectrum (Table 4.5.2). While in certain cases the long-slit or SDSS fibers don't cover the entire galaxy surface, and the intensity of the individual lines does depend on the area of the galaxy covered by the slit, their ratio on the other hand does not provided the slit or fiber samples a representative section of the galaxy.

Because the emission line spectrum, characterized in the BPT diagrams, is dependent on both the shape of the ionizing radiation as well as on the metallicity, we derived abundance gradients for 12 large, face-on galaxies observed with the FAST spectrograph in order to measure any systematic effects or variations on the average metallicity measured from the integrated long-slit spectra. We extracted spectra from $3.5''$-wide sub-apertures from successive regions of the galactic disks, starting from the nucleus and moving outwards on both sides along the slit. We performed the standard analysis and starlight subtraction procedure on each individual sub-spectrum and measured the [N II] $\lambda6583$, [O III] $\lambda5007$, H$\alpha$, and H$\beta$ emission lines on the corresponding regions. Using the PP04 calibrations, we measured each region's metallicity with respect to the galactocentric radius, normalized to the disk radius ($R_{25}$) at the $B = 25$ mag arcsec$^{-2}$ isophote (Fig. 4.5.1). The abundance gradients were derived using linear regression analysis on the metallicity values calculated with calibrations (4.4) and (4.5). The basic parameters of the 12 galaxies used to derive metallicity gradients are summarized in Table 4.5.3, along with the gradient slopes and the abundances at the central and characteristic radius $r = 0.4R_{25}$.

**Table 4.5.1:** Host galaxy and nuclear metallicities and SFRs for the SFRS SFGs. Host-galaxy metallicities are given only for galaxies observed with long-slit spectroscopy, with their nuclear contribution subtracted. SFR values flagged with a * symbol indicate uncertain measurements due to differences in the flux calibration between the blue and red spectral regions of galaxies observed with the 600 l mm$^{-1}$ grating configuration (Section 4.3.6). The full version of Table 4.5.1 is available online from MNRAS.

| SFRS | Galaxy | Nuclear Metallicity | | Host Galaxy Metallicity | | log SFR |
|---|---|---|---|---|---|---|
| | | O3N2 | N2 | O3N2 | N2 | (Nuclear) |
| 2 | IC 2217 | 8.772 ± 0.009 | 8.659 ± 0.003 | 8.717 ± 0.011 | 8.941 ± 0.004 | 0.014 ± 0.003 |
| 4 | NGC 2512 | 8.847 ± 0.002 | 8.723 ± 0.001 | 8.743 ± 0.013 | 8.909 ± 0.003 | 0.035 ± 0.001 |
| 5 | MCG 6-18-009 | 8.803 ± 0.005 | 8.735 ± 0.002 | ... | ... | 0.657 ± 0.003 |
| 6 | MK 1212 | 8.740 ± 0.017 | 8.738 ± 0.005 | ... | ... | −0.322 ± 0.005 |
| 8 | NGC 2532 | 8.763 ± 0.024 | 8.663 ± 0.017 | 8.722 ± 0.025 | −0.084 ± 0.017 | −0.037 ± 0.011 |
| 9 | UGC 4261 | 8.534 ± 0.002 | 8.560 ± 0.002 | ... | ... | 0.058 ± 0.002 |
| 10 | NGC 2535 | 8.874 ± 0.024 | 8.653 ± 0.004 | 8.656 ± 0.027 | 9.004 ± 0.009 | −0.871 ± 0.002 |
| 11 | NGC 2543 | 8.770 ± 0.006 | 8.701 ± 0.003 | ... | ... | −0.865 ± 0.003 |
| 12 | NGC 2537 | 8.613 ± 0.027 | 8.609 ± 0.023 | 8.714 ± 0.028 | 8.962 ± 0.023 | −3.264 ± 0.012 |
| 13 | IC 2233 | 8.167 ± 0.003 | 8.213 ± 0.005 | ... | ... | −2.397 ± 0.003 |

Nuclear SFRs were calculated for the SFRS SFGs (Table 4.5.1) based on the extinction-corrected H$\alpha$ emission line luminosity. The H$\alpha$ luminosity was measured from the 3.5″-wide spectral apertures in long-slit data or the SDSS 3″-diameter fibers. These correspond to 1.3 and 1.1 kpc respectively at the median distance of the SFRS galaxies. The SFRs were derived based on the Kennicutt & Evans (2012) calibration:

$$\frac{\mathrm{SFR}_{\mathrm{H}\alpha}}{(\mathrm{M}_\odot/\mathrm{yr})} = \frac{L_{\mathrm{H}\alpha}}{(\mathrm{erg/s})} \times 10^{-41.27} \tag{4.6}$$

The nuclear SFRs range between $10^{-5}$ and 6.15 M$_\odot$ yr$^{-1}$ with mean 0.26 M$_\odot$ yr$^{-1}$ and median 0.08 M$_\odot$ yr$^{-1}$.

**Table 4.5.2:** Host galaxy (non-nuclear) metallicities of the non-star-forming SFRS galaxies with available long-slit spectroscopy The nuclear component is subtracted similarly to the SFG host-galaxy metallicities. The full version of Table 4.5.2 is available online from MNRAS.

| SFRS | Galaxy | Host Galaxy Metallicity | | Classification |
|---|---|---|---|---|
| | | O3N2 | N2 | |
| 3 | NGC 2500 | 8.789 ± 0.033 | 8.914 ± 0.033 | LINER |
| 36 | IRAS 08572+3915NW | 8.716 ± 0.025 | 8.905 ± 0.013 | TO |
| 42 | IC 2434 | 8.755 ± 0.024 | 8.891 ± 0.017 | TO |
| 47 | NGC 2824 | 8.689 ± 0.032 | 8.924 ± 0.015 | LINER |
| 51 | IRAS 09197+2210 | 8.719 ± 0.071 | 8.895 ± 0.032 | TO |
| 61 | CGCG 181-068 | 8.676 ± 0.058 | 8.885 ± 0.021 | TO |
| 62 | NGC 2936 | 8.669 ± 0.052 | 8.714 ± 0.033 | LINER |
| 79 | IRAS 10120+1653 | 8.743 ± 0.064 | 8.891 ± 0.029 | LINER |
| 117 | IRAS 11102+3026 | 8.523 ± 0.241 | 8.960 ± 0.044 | Sy |
| 108 | IRAS 10565+2448W | 8.761 ± 0.012 | 9.031 ± 0.003 | Sy |

**Table 4.5.3:** Basic parameters and metallicity gradients for 12 galaxies of the SFRS. Column (1) SFRS Index; Column (2) Galaxy name; Column (3) Morphological types obtained from NED; Column (4) D25 angular diameters taken from Ashby et al.; Column (5) Distances in Mpc taken from Ashby et al.; Column (6) Activity classifications based on the nuclear spectra of galaxies. Columns (7) - (8) Circumnuclear and integrated slit Oxygen abundances, measured from calibration described in equation (4.4); Column (9) Central abundance (at radius r = 0) based on the derived N2 abundance gradient; Column (10) Characteristic abundance at radius r = $0.4R_{25}$ based on the N2 derived abundance gradient; Column (11) Slope of the N2 abundance gradient. Column (12) Central abundance (at radius r = 0) based on the derived O3N2 abundance gradient; Column (13) Characteristic abundance at radius r = $0.4R_{25}$ based on the 03N2 derived abundance gradient; Column (14) Slope of the 03N2 abundance gradient. The full version of Table 4.5.3 is available online from MNRAS.

| SFRS | Galaxy | Morphology | D25 (arcmin) | Distance (Mpc) | Class | 12 + log(O/H) (Nucleus) | 12 + log(O/H) (Integrated) | N2 at r = 0 | N2 at r = $0.4R_{25}$ | N2 Gradient (dex $R_{25}^{-1}$) | O3N2 at r = 0 | O3N2 at r = $0.4R_{25}$ | O3N2 Gradient (dex $R_{25}^{-1}$) |
|---|---|---|---|---|---|---|---|---|---|---|---|---|---|
| (1) | (2) | (3) | (4) | (5) | (6) | (7) | (8) | (9) | (10) | (11) | (12) | (13) | (14) |
| 8 | NGC 2532 | SAB(rs)c | 2.2 | 77.6 | H II | 8.76 (8.66) | 8.72 (8.94) | 8.662 ± 0.003 | 8.608 ± 0.004 | −0.12 ± 0.01 | 8.81 ± 0.01 | 8.66 ± 0.01 | −0.35 ± 0.03 |
| 41 | NGC 2750 | SABc | 2.2 | 37.0 | H II | 8.83 (8.68) | 8.74 (9.04) | 8.663 ± 0.003 | 8.69 ± 0.02 | 0.07 ± 0.04 | 8.81 ± 0.01 | 8.64 ± 0.03 | −0.39 ± 0.07 |
| 55 | NGC 2893 | (R)SB0/a | 1.1 | 24.0 | H II | 8.85 (8.75) | 8.72 (8.95) | 8.783 ± 0.003 | 8.80 ± 0.01 | 0.09 ± 0.04 | 8.89 ± 0.01 | 8.85 ± 0.02 | −0.15 ± 0.08 |
| 129 | NGC 3686 | SB(s)bc | 3.2 | 21.0 | H II | 8.81 (8.62) | 8.75 (9.02) | 8.611 ± 0.002 | 8.69 ± 0.02 | 0.12 ± 0.03 | 8.81 ± 0.01 | 8.52 ± 0.05 | −0.46 ± 0.08 |
| 137 | NGC 3729 | SB(r)apec | 2.8 | 17.1 | H II | 8.63 (8.76) | 8.79 (8.99) | 8.745 ± 0.002 | 8.82 ± 0.02 | 0.14 ± 0.04 | 8.612 ± 0.004 | 8.81 ± 0.06 | 0.36 ± 0.11 |
| 147 | NGC 3811 | SB(r)cd? | 2.2 | 54.2 | H II | 8.74 (8.67) | 8.72 (8.93) | 8.675 ± 0.005 | 8.63 ± 0.01 | −0.11 ± 0.03 | 8.77 ± 0.01 | 8.62 ± 0.03 | −0.33 ± 0.06 |
| 148 | NGC 3822 | S0? | 1.4 | 94.6 | Sy | ... | 8.86 (8.97) | ... | 8.67 ± 0.01 | 0.03 ± 0.02 | ... | 8.69 ± 0.02 | 0.38 ± 0.06 |
| 163 | NGC 4014 | S0/a | 2.2 | 62.6 | H II | 8.67 (8.76) | 8.79 (8.90) | 8.723 ± 0.009 | 8.61 ± 0.03 | −0.25 ± 0.06 | 8.70 ± 0.02 | 8.65 ± 0.07 | −0.11 ± 0.15 |
| 178 | NGC 4162 | (R)SA(rs)bc | 2.3 | 42.5 | H II | 8.67 (8.75) | 8.74 (8.89) | 8.730 ± 0.007 | 8.65 ± 0.01 | −0.17 ± 0.02 | 8.68 ± 0.01 | 8.65 ± 0.02 | −0.07 ± 0.03 |
| 186 | NGC 4234 | (R')SB(s)m | 1.3 | 30.0 | H II | 8.61 (8.56) | 8.86 (9.09) | 8.558 ± 0.002 | 8.585 ± 0.002 | 0.10 ± 0.01 | 8.61 ± 0.002 | 8.649 ± 0.003 | 0.154 ± 0.01 |
| 218 | NGC 4625 | SAB(rs)mpec | 2.2 | 9.2 | H II | 8.69 (8.69) | 8.75 (8.88) | 8.680 ± 0.007 | 8.64 ± 0.02 | −0.08 ± 0.04 | 8.72 ± 0.02 | 8.67 ± 0.05 | −0.10 ± 0.11 |
| 316 | NGC 5660 | SAB(rs)c | 2.8 | 38.9 | H II | 8.75 (8.67) | 8.73 (8.95) | 8.680 ± 0.002 | 8.56 ± 0.01 | −0.21 ± 0.01 | 8.77 ± 0.01 | 8.55 ± 0.01 | −0.39 ± 0.02 |

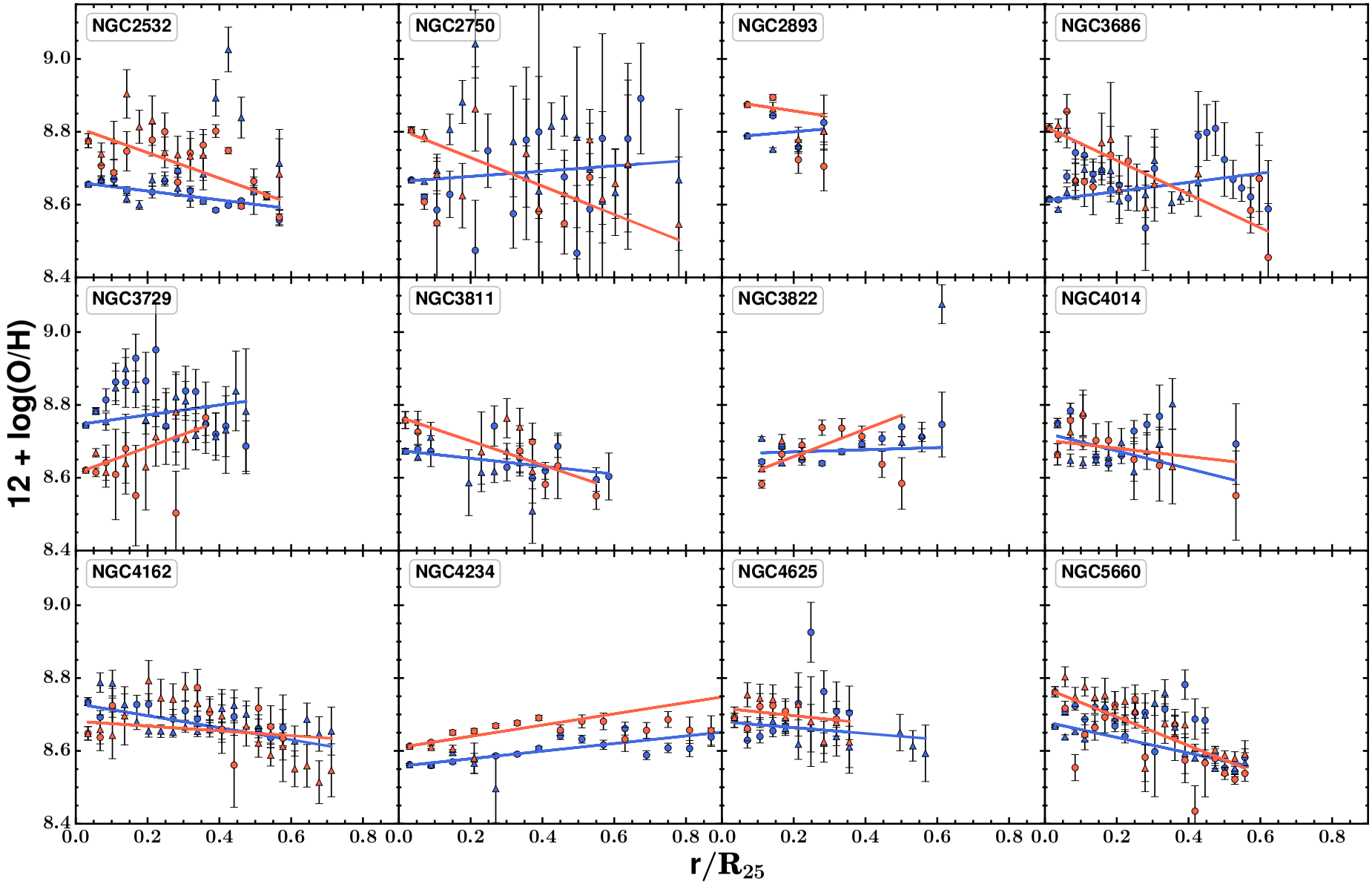


**Figure 4.5.1:** Abundance gradients for the sub-sample of 12 SFRS galaxies. Red points represent metallicities calculated based on the O3N2

# 4.6 Results And Discussion

## 4.6.1 Activity Demographics of IR-selected galaxies

The weights assigned to the SFRS galaxies project the SFRS sample back to the parent PSC$z$ population. Therefore, given the SFRS activity classifications we are able to deliver activity classification fractions for the parent sample (PSC$z$). Specifically, the PSC$z$ comprises 71% H II, 13% Seyferts, 3% TOs, and 13% LINERs. The close similarity between the SFRS demographics and its parent sample demonstrates the representative nature of the SFRS with respect to local IR-selected galaxies.

The fraction of all AGNs (Sy, TO, broad-line LINERs) in the PSC$z$ is 20%. 13% of the PSC$z$ galaxies are Seyferts, of which 39% show broad-line spectral features. The mean FWHM of SFRS galaxies fitted with a broad H$\alpha$ component is $\sim$2923 km s$^{-1}$. The landmark galaxy demographics study of Ho et al. (1997b) (H97), which used the optical magnitude-limited ($B_T \leq 12.5$ mag) sample of the Palomar survey, found 10% Seyfert galaxies of which 20% showed broad lines.The PSC$z$ 39% broad-line fraction is substantially higher than the 20% of H97. The PSC$z$ broad-line LINERs constitute 25%, comparable to the 23% found by H97. In contrast to the PSC$z$, H97 identified a relatively large number of low-luminosity AGNs (LLAGN) with a higher fraction of TOs and LINERs (13% and 19% correspondingly) as opposed to the PSC$z$ (3% and 13% correspondingly). In the case of TOs, this can be attributed to the strict conditions we applied to define them based on all three BPT diagnostics (Section 4.4.3), contrary to the common identification based solely on the [N II] $\lambda$6583/H$\alpha$ BPT. Furthermore, the higher fraction of LLAGN in the H97 sample can be attributed to the larger number of less-active and early-type systems present in the H97 sample.

Star-forming galaxies are the dominant galaxy class in both the SFRS (73%) and PSC$z$ (71%). Despite the broad range in the three-dimensional parameter space covered by the SFRS (Section 4.2), far IR selection is oriented towards selecting star-forming populations, ensuring a small AGN "contamination". This result is of particular importance considering that IR-selection methods are expected to capture both the star-forming phenomenon, as stars are born embedded in dense concentrations of dust and gas, as well as obscured AGN activity. However, the cosmic decrease in the AGN bolometric energy density (e.g., Alexander & Hickox 2012) indicating a downsizing of AGN activity and a subsequent increase of LLAGN in the low-redshift Universe is in agreement with the demographics of H97 but seems at odds with our results. The discrepancy arises because optical selection criteria such as those of H97, are not biased

against passive or elliptical galaxies and are able to capture a fair number of LLAGN systems, while IR-selection criteria show a strong preference for SFGs over LLAGN populations.

### 4.6.2 Classification Comparison

The BPT and MEx diagrams provide consistent classification for 245 out of the 355 galaxies which lie within the predefined bound of the parameter space covered by the SDSS calibration sample (Section 4.4.4) and have available stellar-mass measurements. However, 57 BPT-defined SFGs are classified as TOs by MEx, and likewise 6 BPT-SFGs fall within the Sy region of the MEx diagram. These represent 66% and 15% of the TO and Sy galaxies defined with the MEx method. In reverse 7 and 6 BPT-classified Sy and TOs have an H II classification in the MEx diagram. For BPT-classified LINERs, 12 have a TO classification, 10 have an H II classification, and 5 are classified as Sy in the MEx diagnostic. An important drawback of the MEx diagram is the fact that it is mass dependent and does not rely on direct observable measurements such as flux ratios. This is important because different prescriptions in the $M/L$ calibrations or SED fitting parameters used to determine stellar masses will generally yield different classification results.

The CEx method classifies 300 galaxies that fall within the calibration regions of the CEx diagram. The activity types for 190 of those galaxies are in agreement with the BPT method. Similarly to the MEx classification, the CEx method tends to classify more BPT-SFGs as TO (64 galaxies representing 75% of the CEx TO class). In addition, 10 BPT-Sy and 4 BPT-TOs are classified as LINERs (33% of the CEx LINER class) with the CEx method. The CEx diagram is expected to be biased against broad-line AGNs where the broadband color is not dominated by the host galaxy. Furthermore, as reported by Yan et al. (2011), the emphasis given in the empirical definition of the demarcation line in the CEx diagram was based on limiting contamination of the AGN calibration sample.

The IRAC color classification scheme does not provide detailed demographics on the different activity sub-classes. The separation is done purely on the basis whether a galaxy is classified as an SFG or contains AGN activity and is classified as AGN, regardless its type (Sy, LINER, TO) or intensity. This is evident in Figure 4.4.2, where objects of both Type-1 (broad-line) and Type-2 (narrow-line) classes are found within the AGN "wedge". Specifically, taking into account both the nuclear and integrated color approaches of the IRAC color diagrams (Section 4.4.2), 28 out of the 369 SFRS galaxies are classified as AGN based on the empirical Stern et al. (2005) criteria, 10 of

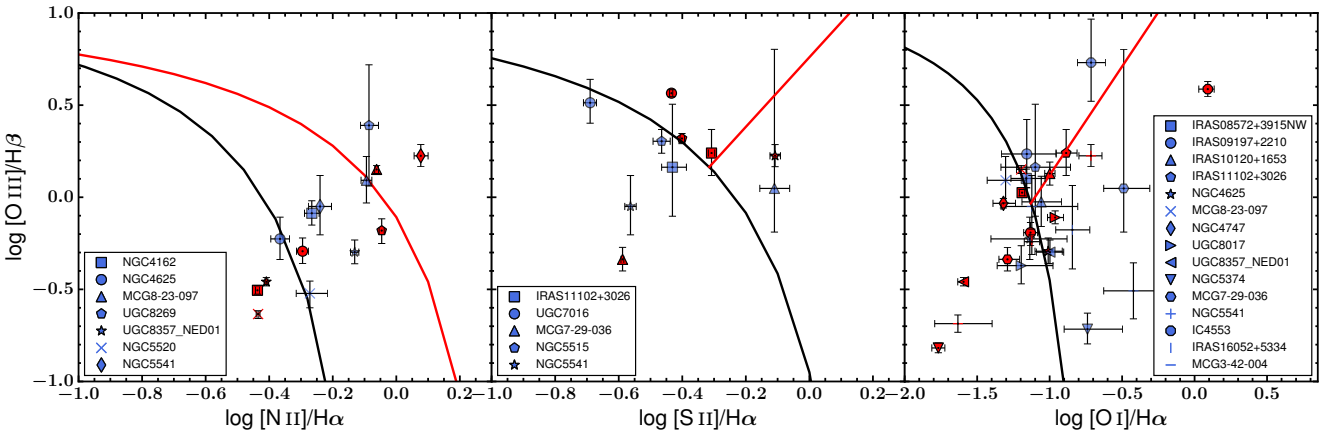


**Figure 4.6.1:** Comparison between the BPT diagrams based on nuclear long-slit and fiber spectroscopy of the SFRS galaxies with inconsistent classifications. Each shape corresponds to a different galaxy; blue shapes show long-slit observation and red shapes SDSS fiber spectra.

which had a non-Sy classification in the BPT diagrams (6 BPT-H II, 3 BPT-TOs, and 1 BPT-LINER). Furthermore, the BPT and IRAC colors diagnostics classify unanimously 72% (265 objects) of the SFRS galaxies as SFGs and 5% (17 objects) as AGN (BPT-Sy).

There are 45 SFRS galaxies which have both nuclear long-slit and SDSS spectra. There is a good agreement between the two observing methods with 38, 39, and 27 galaxies having the same classification in the [N II]/H$\alpha$, [S II]/H$\alpha$, and [O I]/H$\alpha$ BPT diagrams respectively. Fig. 4.6.1 show the galaxies with discrepant classifications in one or more BPT diagrams. Most cases presenting a difference between the two methods agree within $3\sigma$ of the line ratios.

### 4.6.3 Galaxy Properties With Respect To Activity Type

Being an IR-selected sample, the PSC$z$ contains mostly star-forming galaxies. SFGs have a broad range in 60$\mu$m luminosity between $6.53 < \log(L(60_{\mu m})/L_{\odot}) < 11.18$ as seen in Fig. 4.6.2, highlighting the fact that the SFRS selection criteria capture all amplitudes of star-forming activity. AGN hosts (Sy and TO) are preferentially found at $L(60\mu m) > 10^9 L_{\odot}$ while LINERs can be seen at lower $L(60\mu m)$ with a drop at luminosities higher than $\sim 10^9 L_{\odot}$, indicative of hosts without intense star formation. Interestingly, Type-1 and Type-2 Sy and LINERs show similar $L(60\mu m)$ distributions with $p$-values of 0.861 and 0.258 respectively returned from a Kolmogorov-Smirnov

(K-S) test.

The $F60/F100$ flux ratio distribution of SFGs which is a proxy for the dust temperature (Fig. 4.6.2) peaks around 0.45, which is close to the limit ($\sim$0.5) above which starburst galaxies are typically found (Rowan-Robinson & Crawford 1989). Seyfert galaxies have a broad distribution of $F60/F100$ and present a peak around $F60/100 \sim 0.85$ attributed to AGN radiation heating dust to high temperatures. TOs have a dust-temperature distribution with median 0.46, close to the median of SFGs at 0.49, implying that the major contribution to dust heating is from star formation. On the other hand $F60/F100$ in LINERs is confined to lower values, implying both a low radiation density and less dusty environments, the latter typical of early-type galaxies. Again, Type-1 and Type-2 Sy and LINERs have similar $F60/F100$ distributions ($p$-values 0.930 and 0.564 respectively from K-S test application).

The nuclear H$\alpha$ luminosity distribution, serving also as a proxy of SFR for non-AGN hosts, ranges over 7 orders of magnitudes ($10^{36} - 10^{44}$ erg s$^{-1}$) in the case of SFGs. Fig. 4.6.2 shows that Sy show a similar broad range of $L_{\mathrm{H}\alpha}/\mathrm{kpc}^2$ distribution as SFGs ($p$-value = 0.865). In a different manner, TOs and LINERs present lower $L_{\mathrm{H}\alpha}/\mathrm{kpc}^2$ values as opposed to Seyferts, pointing towards gas-deficient hosts. The opposite view is seen in the case of Seyferts, where the AGN enhances gas ionization, and the $L_{\mathrm{H}\alpha}/\mathrm{kpc}^2$ distribution peaks at $10^{40.75}$ erg s$^{-1}$.

The SFGs cover a broad range of stellar masses between $10^{7.64} - 10^{11.56}$ M$_\odot$ as shown in Fig. 4.6.3. The Bell et al. (2003) relations on which mass estimations were based should ideally be applied exclusively to star-forming populations because the presence of non-stellar emission from AGN contaminates the NIR band fluxes, resulting in an overestimation of stellar mass. Therefore, the stellar masses of non-SFG populations should be considered upper limits. Fig. 4.6.3 shows that all galaxy types other than SFGs are preferentially located in massive hosts. With the exception of broad-line LINERs that are clearly related to the AGN phenomenon, LINER emission in local galaxies is now considered to result from photoionisation by hot evolved stars and not AGN (Cid Fernandes et al. 2011; Belfiore et al. 2016a). Therefore, mass estimates of narrow-line LINERs using $M/L$ calibrations should be accurate provided correct stellar populations are assumed. LINER nuclei are predominantly found at higher stellar masses with a median of $10^{10.52}$ M$_\odot$. Mass estimates of TOs where the ionization continuum stems from both star-forming and AGN processes should in most cases be treated as upper limits similarly to Sy mass estimations. The median host-galaxy properties of the SFRS sample and the parent population (an unbiased subset of the PSC$z$) from which SFRS was defined are summarized in Table 4.6.1.

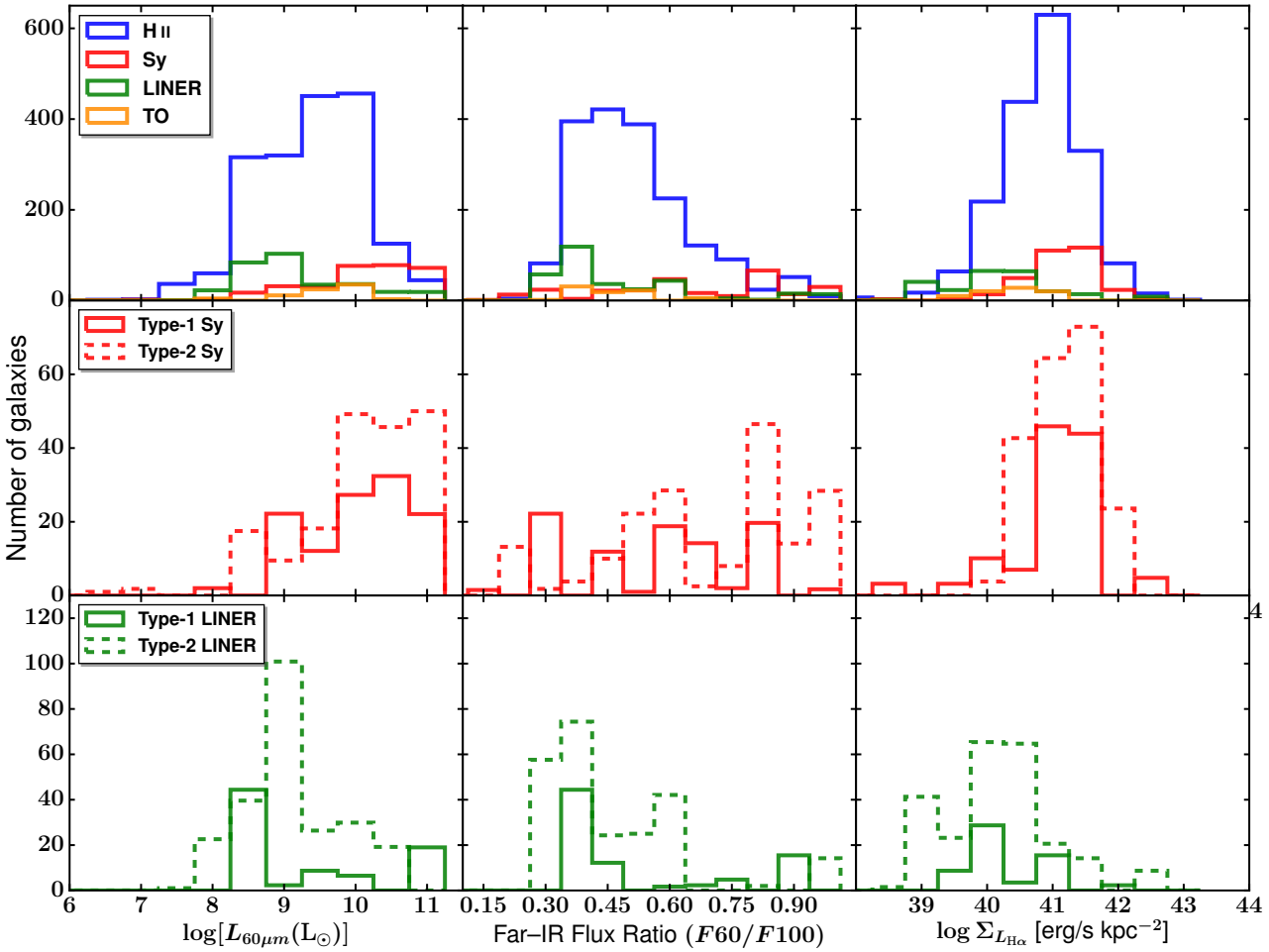


**Figure 4.6.2:** Top panel: Histogram of IRAS 60$\mu$m luminosity (left), $F60/F100$ flux ratio (middle), and circumnuclear $L_{\mathrm{H}\alpha}$ corrected for aperture size (right) for IR-selected galaxies, shown for different activity types. The nuclear area for the $L_{\mathrm{H}\alpha}$ surface density ($\Sigma_{L_{\mathrm{H}\alpha}}$) is calculated based on the $3.5'' \times 3''$ and $3''$-radius apertures of the FAST and SDSS spectra in each case. Blue lines show SFGs (labeled as HII), red lines show Seyfert galaxies, orange lines TOs, and green lines LINERs. Middle panel: The corresponding Type-1 and Type-2 Seyfert class distributions. Bottom panel: The corresponding distributions for Type-1 and Type-2 LINERs. The ordinates are based on using SFRS weights to project back to the parent population.

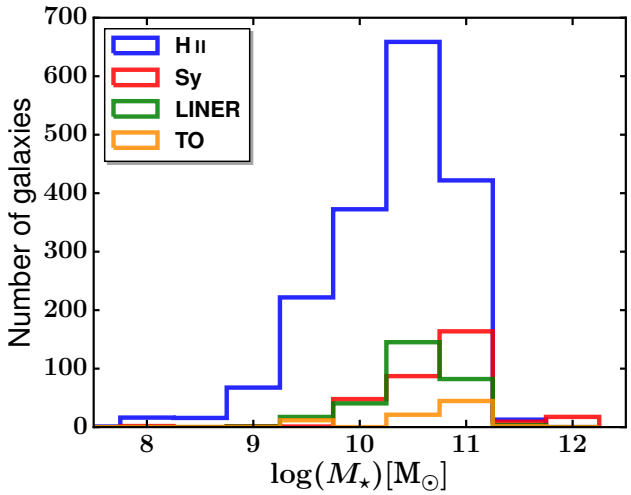


**Figure 4.6.3:** Stellar mass distribution for the different activity types. Blue lines show SFGs (labeled as HII), red lines show Seyfert galaxies, orange lines TO, and green lines LINERs. Masses refer to Chabrier (2003) IMF. Galaxy numbers refer to the SFRS parent sample.

**Table 4.6.1:** Synopsis of the main characteristics of the SFRS and IR-selected galaxies, grouped or in individual activity or luminosity classes. The values in parentheses are calculated based on the weights defined by Ashby et al. (2011) and correspond to the parent population from which SFRS was defined. Column (1): Description of the activity or luminosity class; Column (2): Number of galaxies in each class; Column (3): 60$\mu$m luminosity; Column (4): $F_{60}/F_{100}$ $\mu$m flux density ratio; Column (5): Nuclear $L_{\mathrm{H}\alpha}$ surface density; Column (6): Galaxy mass.

| Activity Class | No. | log $L_{60}$ (L$_\odot$) | $F_{60}/F_{100}$ | log $\Sigma_{L_{\mathrm{H}\alpha}}$ (erg s$^{-1}$kpc$^{-2}$) | log $M_\star$ (M$_\odot$) | Distance (Mpc) |
|---|---|---|---|---|---|---|
| All galaxies | 369 (2560) | 9.55 (9.55) | 0.49 (0.49) | 40.08 (40.10) | 10.49 (10.51) | 77 (71) |
| SFGs | 269 (1815) | 9.41 (9.47) | 0.48 (0.49) | 40.15 (40.17) | 10.35 (10.43) | 69 (69) |
| Seyferts | 50 (345) | 10.07 (10.24) | 0.71 (0.80) | 40.24 (40.26) | 10.87 (10.82) | 117 (105) |
| Transition Objects | 17 (79) | 9.72 (9.71) | 0.41 (0.46) | 39.62 (39.60) | 10.82 (10.80) | 114 (108) |
| LINERs | 33 (321) | 9.26 (9.04) | 0.45 (0.36) | 39.50 (39.53) | 10.55 (10.52) | 54 (34) |
| LIRGs / ULIRGs | 117 / 11 | 10.14 (10.18) | 0.51 (0.55) | 40.08 (40.15) | 11.16 (11.07) | 147 (131) |

### 4.6.4 Dominant Central Ionizing Mechanism in LINERs and TOs

TOs are considered to be galaxies with composite contributions from star-forming and AGN processes in their central energy output. LINERs on the other hand have a much more controversial status in the literature regarding their main ionizing energy source. They are sometimes considered as the low-luminosity, low-accretion-rate branch of Seyfert galaxies (e.g., Ho et al. 1993, Ho et al. 2003), which is still a viable assertion at least for LINERs showing broad H$\alpha$ features. However, this view is disputed in the case of narrow-line LINERs considering that post asymptotic giant branch (post-AGB) stars can produce the required ionizing spectrum necessary to excite LINER emission (e.g., Binette et al. 1994, Stasińska et al. 2008, Belfiore et al. 2016a).

The $L(60\mu\mathrm{m})$ distribution of TOs follows that of SFGs ($p$-value = 0.078) with a median of $\log L(60\mu\mathrm{m}) = 9.7$ $\mathrm{L}_\odot$ and 9.5 $\mathrm{L}_\odot$ respectively, indicative of a similar star-forming activity profile in their host galaxies. Similarly, the median $F60/F100$ ratio of both TOs and SFGs is 0.46 and is distinct from the median of Seyferts at 0.80, suggesting star-forming activity as the main source of dust heating in TOs. The $L_{\mathrm{H}\alpha}$ surface density distribution of TOs has a smaller range than Sy and SFGs, with median $L_{\mathrm{H}\alpha}/\mathrm{kpc}^2 = 10^{40.30}$ erg $\mathrm{s}^{-1}\mathrm{kpc}^{-2}$. While the host-galaxy stellar mass is not a property directly linked to the main source of ionization, it gives a sense of the environment where the TOs reside. TOs are allocated predominately at masses above $10^{10.5}$. However, as discussed in Section 4.6.3, Sy-host masses should be considered only as upper limits, and this would apply to TOs depending on their dominant ionizing mechanism. Nevertheless, given the previously discussed similarities of TOs host-galaxy properties with those of SFGs, star-forming activity should be considered as the main source of ionization in the SFRS (PSC$z$) TOs. Given this assertion, TOs reside in massive hosts.

LINERs in the SFRS sample show a sharp drop in their number densities above $L(60_{\mu\mathrm{m}}) \sim 10^9 L_\odot$, illustrating weak star-forming activity in their hosts. The bulk of LINERs are concentrated mostly at lower values of $F60/F100$ with a median of 0.36, with just 12 LINERs lying above the 0.5 starburst threshold as opposed to 118, 38, and 3 SFGs, Sy, and TOs respectively. Furthermore, the $L_{\mathrm{H}\alpha}$ surface density distribution of LINERs is confined in the narrow range of $10^{38.5} - 10^{40.5}$ erg $\mathrm{s}^{-1}\mathrm{kpc}^{-2}$ and drops significantly above that, as opposed to Sy and SFGs. Lastly, LINERs are found predominantly in high stellar-mass hosts at a median of $10^{10.5}$ $\mathrm{M}_\odot$. Given their generally low H$\alpha$ and 60$\mu$m luminosity it is unlikely that this is the result of bias

due to AGN contamination. The above properties demonstrate that the host-galaxy and nuclear properties of LINER bear close resemblance to those of passive early-type systems, hinting that their ionizing continuum stems mostly from older stellar populations (i.e., post-AGB stars) rather than AGN activity. Nevertheless, if LINERs should be considered as AGN powered systems, given the fact that they reside in more massive hosts they should be associated with more massive central black holes.

### 4.6.5 LIRGs and ULIRGs

The class of LIRGs is characterized by total IR luminosities ($L$(TIR)) between $10^{11} - 10^{12}$ $L_{\odot}$, while galaxies with $L$(TIR) $> 10^{12}$ $L_{\odot}$ are described as ULIRGs. The SFRS sample contains 117 LIRGs and 11 ULIRGs. Previous studies have demonstrated that a varying fraction of local LIRGs and ULIRGs, ranging from 25% (Veilleux et al., 1997) to 70% (Nardini et al., 2010), host an AGN. In the case of SFRS (U)LIRGs, 25% are Sy hosts, while this percentage increases to 43% when including LINERs and TOs. Lee et al. (2011) using a sample of 115 ULIRGs showed that Type-2 AGNs are more frequently encountered (49 galaxies) compared to Type-1 AGNs (8 galaxies), and the percentage of type 2 ULIRGs increases with infrared luminosity. The SFRS LIRGs consist of 45 AGN, considering all non-SFG classes, out of which 13 are Type-1. Similarly 10 out of 11 SFRS ULIRGs are AGN, with 4 being Type-1, showing an agreement with previous studies. The joined properties of SFRS LIRGs and ULIRGs are summarized in Table 4.6.1.

### 4.6.6 Metallicities

The SFG's metallicities derived from the O3N2 and N2 calibrations agree for galaxies with sub-solar metallicities but differ for metallicities larger than solar. However, as discussed by PP04, the O3N2 calibration is particularly useful at solar and super-solar metallicities where [N II] saturates, but the strength of [O III] continues to decrease with increasing metallicity. Furthermore, the abundance gradient slopes derived from the O3N2 calibration are generally comparable to the N2 gradients (Fig. 4.5.1). However, the O3N2 calibration indicates in general higher metallicities for the central galactic regions but shows similar values at the characteristic radii of $r = 0.4R_{25}$ (Table 4.5.3). There is also a good agreement between the nuclear abundances measured directly from the central aperture and the ones calculated from the metallicity gradients at $r = 0$ in both calibrations.

The SFG's abundances have a narrow range close to solar (12 + log(O/H) = 8.66),

with a median value of 8.72 and 8.67 in the O3N2 and N2 calibrations respectively. The sub-sample of 12 galaxies used to derive metallicity gradients show overall flat metallicity profiles as a function of galactocentric radius (Table 4.5.3 and Fig. 4.5.1). The relatively flat profiles derived from our analysis seem to be at odds with similar studies in nearby galaxies (e.g., Pilyugin et al. 2004; Moustakas et al. 2010). However, flat average metallicity profiles were also observed by Moran et al. (2012) (M12) in a sample of 174 local star-forming galaxies using the O3N2 calibration by PP04. As discussed by M12, galaxies from their local sample with $\log(M_\star) > 10.2$ appear to have flatter metallicity profiles and metallicities close to solar. Furthermore, M12 argued that inner metallicity profiles which decline steadily with radius are observed only at the lowest masses. In addition, M12 re-examined the 21 galaxies from the Moustakas et al. (2010) sample and estimated the stellar masses of these galaxies, noting that five out of eight galaxies with gradients have $\log(M_\star) < 10.2$. Nine out of 12 galaxies SFRS galaxies used to derive metallicity gradients in this paper have $\log(M_\star) > 10.2$. Similarly, 178 out of the 261 SFRS SFGs have $\log(M_\star) > 10.2$ and metallicities close to solar, indicating that they are consistent with the metallicity gradients observed in local galaxies. Furthermore, the small abundance gradients with respect to galactocentric radius ensures that on average the emission lines measured from the central extraction aperture are not affected by metallicity, regardless the portion of host-galaxy light encompassed, and therefore the resulting classification is robust, capturing the hardness of the central ionizing radiation spectrum.

# 4.7 Conclusions

Using a fully representative sample of FIR-selected galaxies in the local Universe, we have presented the activity demographics, nuclear metallicities, and host-galaxy properties of the 369 galaxies in the SFRS and derived metallicity gradients for a sub-sample of 12 galaxies. Using the weights assigned to the SFRS galaxies that project the SFRS sample back to the parent PSCz population, we derived the activity demographics and host-galaxy properties for the parent population, summarized as follows.

(i) BPT classification of FIR-selected galaxies gives 71% SFGs, 13% Seyferts, 13% LINERs, and 3% TOs.

(ii) NIR classification (Stern et al., 2005) reveals 6 H II galaxies, 1 LINER, and 3 TOs as defined with the BPT method to be AGN galaxies.

(iii) The MEx method is in agreement with the BPT classification for 69% of galaxies but tends to classify 21% of BPT-SFGs as TO and 2% as Sy.

(iv) The CEx method agrees with BPT classification in 63% of the cases but classifies 24% of BPT-SFGs as TO and 21% as LINER.

(v) The inferred fraction of LLAGN galaxies in the local Universe using IR sample-selection criteria is small compared to SFGs.

(vi) In terms of host-galaxy properties, Sy and TOs are preferentially found at $L(60\mu\mathrm{m}) > 10^{9}\mathrm{L}_{\odot}$ while LINERs have lower $L(60\mu\mathrm{m})$ values with few at luminosities higher than $10^{9.5}\mathrm{L}_{\odot}$, indicative of hosts with no intense star-formation. SFGs cover a broad range in L(60$\mu$m) between $6.5 < \log(L(60_{\mu\mathrm{m}})/\mathrm{L}_{\odot}) < 11.18$.

(vii) Seyfert galaxies have the highest $F60/F100$ ratios. These can be attributed to AGN radiation heating dust to high temperatures. TOs have the same median dust-temperature as SFGs implying star-formation as the dominant ionizing mechanism, while LINERs are confined to lower dust-temperatures indicative of low-ionization mechanisms and dust-deprived environments.

(viii) The stellar mass distribution of SFGs covers a broad range ($10^{7.79} - 10^{12.14}$ $\mathrm{M}_{\odot}$), while TOs and Seyfert are found exclusively in high stellar-mass hosts, albeit their mass estimations are considered mostly as upper limits. LINERs, which are now strongly considered as galaxies powered by non-AGN processes, are found in high stellar masses galaxies with a median of $10^{10.5}\mathrm{M}_{\odot}$.

(ix) SFGs have a wide distribution of nuclear $L_{\mathrm{H}\alpha}$ surface densities, ranging between $10^{36.8} < L_{\mathrm{H}\alpha}/\mathrm{kpc}^2 < 10^{43.0}$ erg $\mathrm{s}^{-1}\mathrm{kpc}^{-2}$, and TOs show a similar distribution. Sy nuclear $L_{\mathrm{H}\alpha}/\mathrm{kpc}^2$ is concentrated above $10^{39.5}$ erg $\mathrm{s}^{-1}\mathrm{kpc}^{-2}$, while LINERs on the other hand are mainly distributed at lower values with median $L_{\mathrm{H}\alpha}/\mathrm{kpc}^2 = 10^{40.18}$ erg $\mathrm{s}^{-1}\mathrm{kpc}^{-2}$.

(x) Based on their host-galaxy and nuclear properties, the dominant ionizing source in the SFRS (PSC$z$) TOs is star-forming activity. Similarly, LINER host-galaxy characteristics resemble those of passive early-type systems, indicating older stellar populations as their main ionizing source, rather than AGN activity.

(xi) The SFRS SFGs have a narrow range of abundances close to solar and have flat metallicity radial profiles, as found from a sub-sample of 12 galaxies. This is evident for galaxies with $\log(M_{\star}) > 10.2$, as discussed by M12, which is the case for 68% of the SFRS SFGs.

We would like to thank the referee for the constructive comments and suggestions that have improved the clarity of this paper. AM and AZ acknowledge funding from the European Research Council under the European Union's Seventh Framework Programme (FP/2007-2013) / ERC Grant Agreement n. 617001. Funding for SDSS-III has been provided by the Alfred P. Sloan Foundation, the Participating Institutions,

the National Science Foundation, and the U.S. Department of Energy Office of Science. The SDSS-III web site is http://www.sdss3.org/. This research has made use of the NASA/IPAC Extragalactic Database (NED) which is operated by the Jet Propulsion Laboratory, California Institute of Technology, under contract with the National Aeronautics and Space Administration. This publication makes use of data products from the Two Micron All Sky Survey, which is a joint project of the University of Massachusetts and the Infrared Processing and Analysis Center/California Institute of Technology, funded by the National Aeronautics and Space Administration and the National Science Foundation. This work is based [in part] on observations made with the Spitzer Space Telescope, which is operated by the Jet Propulsion Laboratory, California Institute of Technology under a contract with NASA. For this research, we have made extensive use of the Tool for Operations on Catalogues And Tables (TOPCAT) software package (Taylor 2005).

# Appendix

## 4.A Probabilistic Activity Classification

Galaxy activity classification based on the BPT diagrams often stumbles upon the complication of deriving an unambiguous or consistent classification from all three diagnostic diagrams, especially in the occasions where galaxies fall near the demarcation lines. Therefore, obtaining a sense of the uncertainty in a galaxy's classification is important, especially for the ambiguous cases. The uncertainties of the intensities of the diagnostic lines can be translated into an uncertainty in a galaxy's activity classification. We quantified this activity classification uncertainty by calculating the probability that a galaxy falls in the locus of a given class. For each galaxy we generated 1000 samples of their line ratios drawn from a Gaussian distribution, based on their line-ratio uncertainties in all three BPT diagrams, and examined their placement and resulting activity classification on each diagnostic. Thus we derived the probability for each galaxy to be classified as H II, TO, or AGN (Seyfert or LINER) in each of the three diagnostic diagrams. The probabilistic activity classifications of the SFRS sample are presented in Table 4.A.1.

## 4.B STARLIGHT Code Simulation Study

### 4.B.1 Modeling the input spectrum

The primary concern when measuring emission lines in galaxy spectra is the efficient subtraction of the underlying stellar continuum and absorption features, especially at the wavelengths where the emission lines of interest reside. While spectral synthesis codes suffer from known degeneracies where different combinations of SSP properties (e.g., ages, metallicities) and galaxy properties (e.g., extinction, AGN component) can

**Table 4.A.1:** Probability classification for the different activity types based on the uncertainties of line measurements and following the methods outlined in Section 4.A.1. The full Table is presented in Appendix 7, Table 7.A.5.

| SFRS | Galaxy | [N II]/H$\alpha$ | | | [S II]/H$\alpha$ | | | [O I]/H$\alpha$ | | |
|---|---|---|---|---|---|---|---|---|---|---|
| | | H II | TO | Sy / LINER | H II | LINER | Sy | H II | LINER | Sy |
| 1 | IC 486 | 0.000 | 0.000 | 1.000 | 0.000 | 0.000 | 1.000 | 0.000 | 0.000 | 1.000 |
| 2 | IC 2217 | 1.000 | 0.000 | 0.000 | 1.000 | 0.000 | 0.000 | 1.000 | 0.000 | 0.000 |
| 3 | NGC 2500 | 0.334 | 0.666 | 0.000 | 0.326 | 0.573 | 0.101 | 0.000 | 1.000 | 0.000 |
| 4 | NGC 2512 | 1.000 | 0.000 | 0.000 | 1.000 | 0.000 | 0.000 | 1.000 | 0.000 | 0.000 |
| 5 | MCG 6-18-009 | 0.729 | 0.271 | 0.000 | 1.000 | 0.000 | 0.000 | 1.000 | 0.000 | 0.000 |
| 6 | MK 1212 | 0.000 | 1.000 | 0.000 | 1.000 | 0.000 | 0.000 | 1.000 | 0.000 | 0.000 |
| 7 | IRAS 08072+1847 | 0.000 | 1.000 | 0.000 | 1.000 | 0.000 | 0.000 | 1.000 | 0.000 | 0.000 |
| 8 | NGC 2532 | 1.000 | 0.000 | 0.000 | 1.000 | 0.000 | 0.000 | 1.000 | 0.000 | 0.000 |
| 9 | UGC 4261 | 1.000 | 0.000 | 0.000 | 1.000 | 0.000 | 0.000 | 1.000 | 0.000 | 0.000 |
| 10 | NGC 2535 | 1.000 | 0.000 | 0.000 | 1.000 | 0.000 | 0.000 | 1.000 | 0.000 | 0.000 |

fairly reproduce the observed spectrum, to a first level, any combination reproducing the input spectrum is considered adequate for starlight subtraction. However, due to STARLIGHT's complicated architecture where the fit is carried out using a mixture of simulated annealing, Metropolis algorithm, and Markov Chain Monte Carlo techniques, intrinsic uncertainties are introduced in the process, and even when making identical-parameter runs the results can slightly vary.

To quantify the above uncertainties in STARLIGHT, we performed 100 identical-parameter runs for two galaxies observed with SDSS (IC 4395) and FAST (NGC 5147), using a two-set grid of base spectra, one with 138 SSPs and one with 45 SSPs. In each run we subtracted the model spectrum from the observed and fitted the H$\beta$ and H$\alpha$ emission lines using SHERPA. The distributions of F(H$\beta$) and F(H$\alpha$) for the two sets of 100 runs (using the 138 and 45 SSP grids respectively) are shown in Figure 4.B.1. While the spread of F(H$\beta$) is somewhat larger compared to F(H$\alpha$), especially when using the 45 SSPs grid, the variance between the values is within the measured line-flux uncertainties. Specifically, in all cases the standard deviation of the F(H$\beta$) and F(H$\alpha$) distributions is smaller by a factor of 10 compared to the uncertainties of the measured fluxes. The previous results are independent from the number of runs performed. We verified this by repeating the tests for 500 identical-parameter runs and recovering a factor of 10 difference between the standard deviation of the fluxes and their measured uncertainties. Therefore, the intrinsic uncertainties introduced by STARLIGHT have no impact on our results.

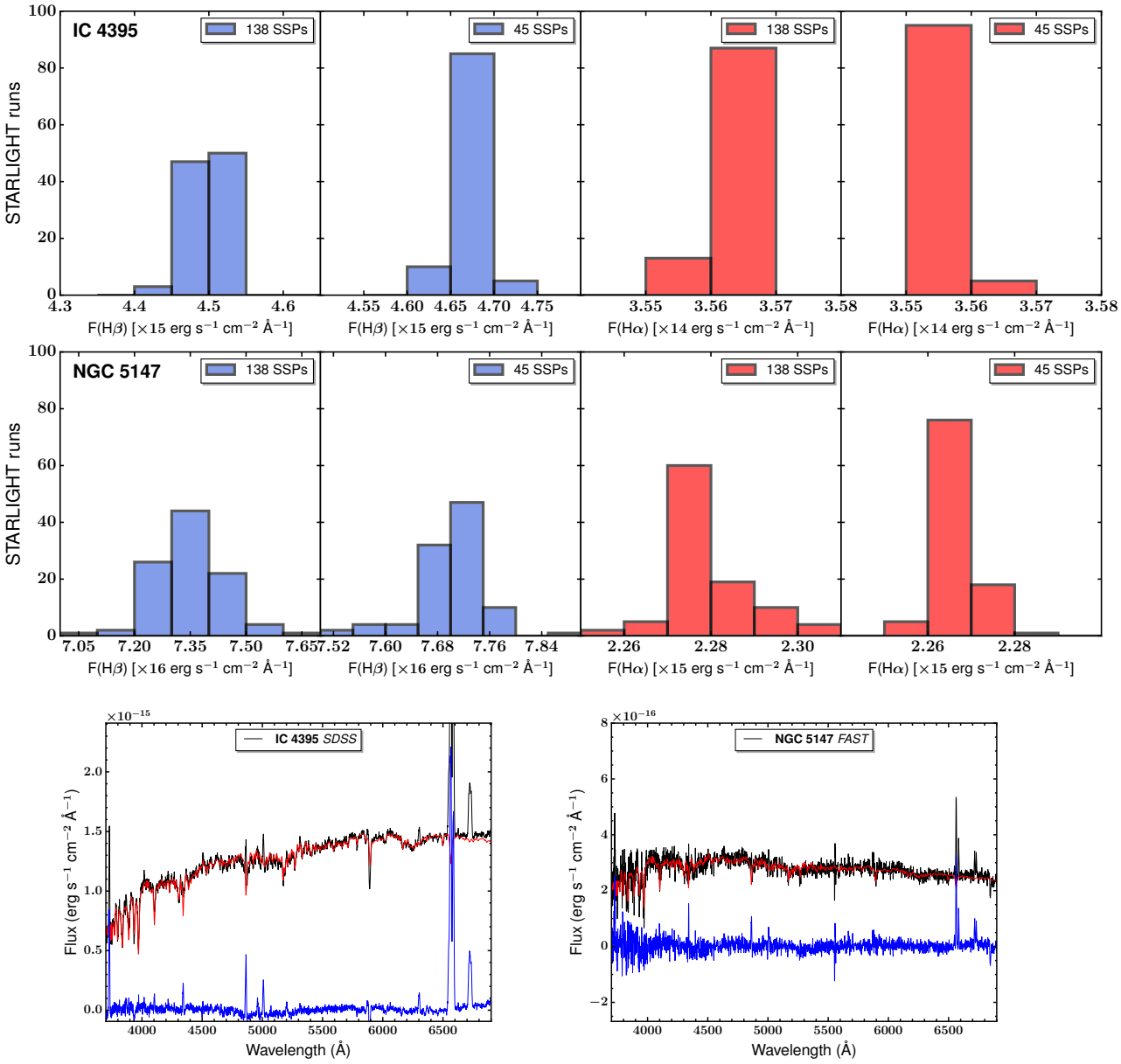


**Figure 4.B.1:** The distribution of F(H$\beta$) and F(H$\alpha$) emission lines for galaxies IC 4395 (top row) and NGC 5147 (middle row) measured after performing 100 STARLIGHT runs and subtracting the model from the observed spectrum. Two sets of identical-parameter STARLIGHT runs were performed using a grid of 138 and 45 SSPs respectively. Their respective nuclear spectra are shown in the bottom row. The observed spectrum is shown with a black line, an example STARLIGHT fit with a red line, and the corresponding starlight subtracted spectrum with a blue line.

### 4.B.2 Global galaxy parameters and AGN component

Cid Fernandes et al. (2014) (F14) made an extensive study of the STARLIGHT code using 1638-zone spectra of the Sb NGC 2916, observed with an Integral Field Unit (IFU). They performed simulations using observed and synthetic spectra (built from STARLIGHT fits to the observed data) to explore uncertainties related to the data and the spectral synthesis method. They added random noise and shape-changing perturbations in both observed and synthetic spectra in order to address noise fluctuations and continuum shape calibrations. These simulations were then used to evaluate uncertainties in the global parameters derived by STARLIGHT such as the mean ages, masses, metallicities, extinction, and star formation histories (SFHs). Despite the fact that STARLIGHT solutions depend on the seed for the random-number generator, given the pseudo-random nature of its Markov chains, variations of this kind have a tiny effect on the derived properties. Furthermore, synthetic unperturbed spectra produce higher dispersions of the $\Delta$ (simulation minus original) value of each derived quantity, compared to the observed unperturbed spectra, attributed to the fact that observed spectra have access to a smaller subspace of acceptable solutions than the synthetic spectra. When introducing random noise F14 found that the mass-weighted ages and metallicities have broader $\Delta$ distributions ($\sim$0.15 sigma variations) than the luminosity-weighted counterparts ($\sim$0.1 sigma variations), while stellar masses are good to $\sim$0.1 dex. Overall, the SFHs appear less constrained than other global galaxy parameters, being a higher-order product of the spectral synthesis. Averaging over spatial regions comprising many zones reduces the uncertainties.

Similar but simpler simulations were also performed by Cid Fernandes et al. (2005) to 65 test galaxies created from the mean derived properties of fits to a sample of SDSS galaxies. The results showed that the population vectors recovered by STARLIGHT are subject to large uncertainties, but mean derived properties such as stellar ages and metallicities were better recovered.

As a supplementary analysis to those studies, we performed a set of simulations using only individual sets of SSPs or, at most, two-component composite stellar populations (CSPs) from the BC03 libraries. We used populations of different ages (5 Myr$-$10 Gyr) at a given metallicity (0.2 $Z_{\odot}$) with a 10% uncertainty on the flux as input in STARLIGHT. The top panels in Figs. 4.B.2, 4.B.4, 4.B.5, and 4.B.7 shows the current mass fraction against age of the input and output spectra that contributes more than 10% to current stellar mass. STARLIGHT is more sensitive in identifying the actual contribution of the younger populations, while it systematically underestimates

the contribution of older populations. In the latter case, while successfully recovering the actual population, it uses supplementary SSPs of similar ages to match the input spectrum. Therefore, in the simplest case of a SSP, STARLIGHT is able to identify both the age and metallicity of the input spectrum but not necessarily its actual contribution (100% in the case of a SSP).

To further assess STARLIGHT's results, we created synthetic spectra, adding noise and extinction separately on the same SSPs used previously, in an effort to simulate an actual spectrum in a fully controlled environment. With the inclusion of Gaussian noise (2% of the input flux, Fig. 4.B.3), there is a deviation from the actual contribution to the current mass for all populations, and in some cases inclusion of extra SSPs, but the dominant component describes the correct age and metallicity (Fig. 4.B.4, second panel).

Adding extinction ($A_V = 0.85$) without noise to the input spectrum will force STARLIGHT in almost every case to split the total contribution using extra SSPs for the fit (Fig. 4.B.5, third panel). While for populations between 100 Myr and 5 Gyr the highest contribution comes from the correct SSP component, in most cases that component is modeled below 50% of the total. However, STARLIGHT will correctly fit the extinction of the input spectrum.

Another test we applied was to limit the spectral area STARLIGHT uses to fit the input spectrum by masking most spectral regions except those containing Lick indices, which are characteristic and representative of the stellar populations. In most cases STARLIGHT was able to attribute more accurately the actual contribution to the input spectrum or even limit the number of extra SSP used in the fit, but the overall improvement was not significant over the default configuration.

Finally, we tested STARLIGHT's sensitivity in uncovering the AGN component of a galaxy spectrum using power-law AGN templates of different indices along with the standard SSPs. We created a synthetic spectrum from an SSP adding an AGN component (Fig. 4.B.6) and provided STARLIGHT with the same AGN template. Although STARLIGHT revealed the correct AGN component, the stellar populations used in the fit varied significantly from the input SSP used to create the synthetic spectrum (Fig. 4.B.7, bottom panel). Furthermore, if more AGN templates of different power-law indices are allowed to be used in the fit, STARLIGHT will use most of them to reproduce the input spectrum. Additionally, by fitting a SSP without AGN component, but allowing STARLIGHT to use AGN templates in the fitting process (which illustrates the case of fitting an actual galaxy spectrum without a prior knowledge for the presence of an AGN or not), STARLIGHT has a tendency to use the AGN templates present.

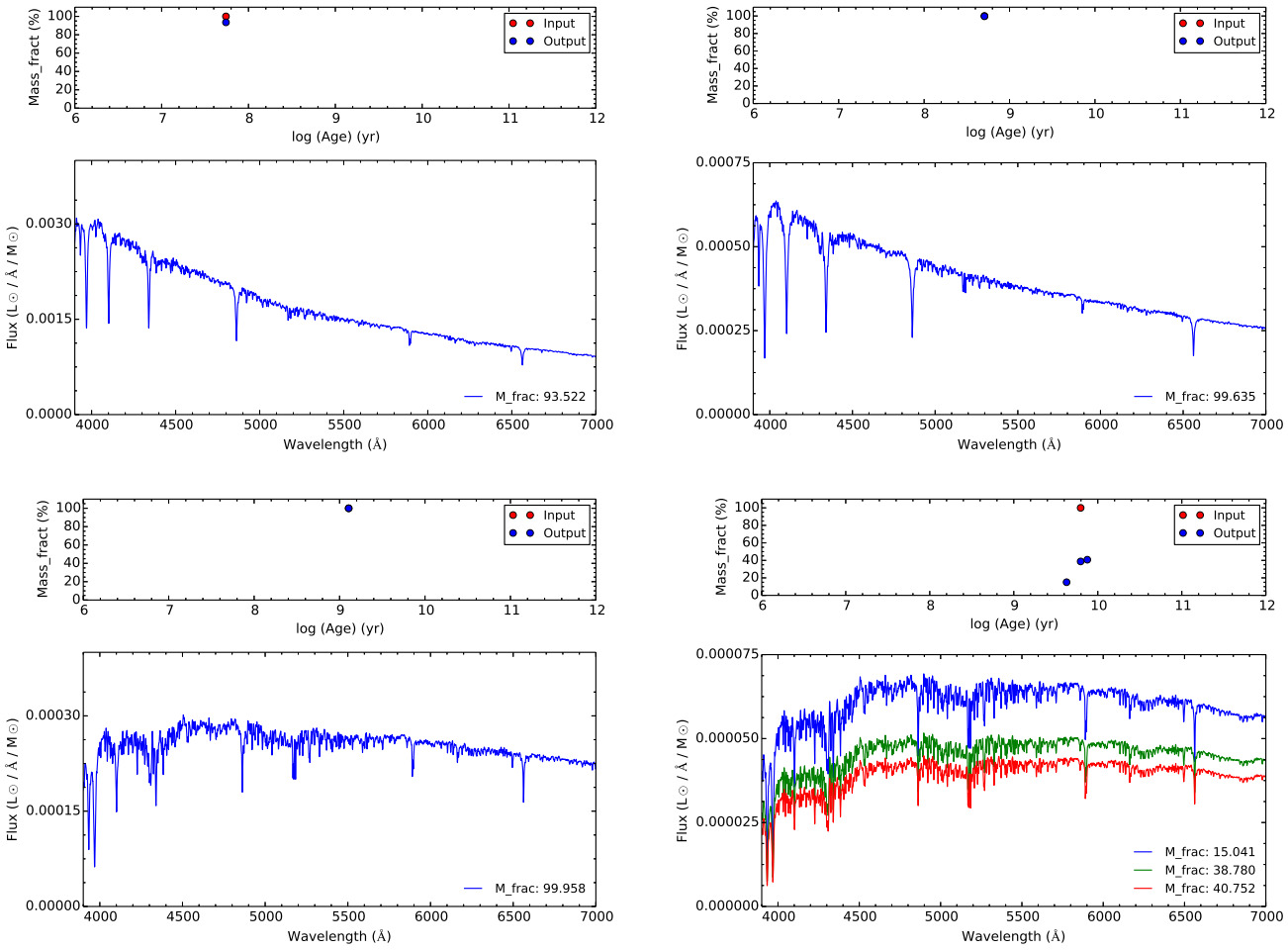


**Figure 4.B.2:** The top panel in all plots shows the SSP of given age and mass fraction used as input in STARLIGHT (red point) and the corresponding output SSP(s) (blue points) from the fit. In cases of exact match, one color is over-plotted on top of the other. The bottom panel in all figures shows the corresponding output spectrum of the SSP(s) used in the fit. The raw input SSPs from the BC03 libraries are presented.

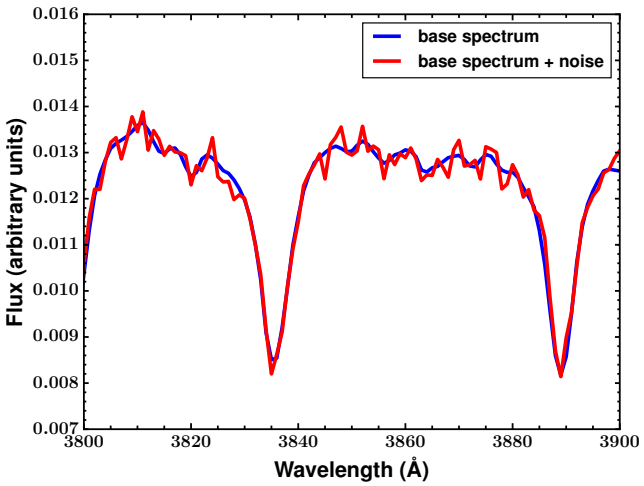


**Figure 4.B.3:** Example of a SSP spectrum (blue line) and the same SSP spectrum perturbed with 2% Gaussian noise (red line)

As a verdict, STARLIGHT heads towards the right direction in uncovering the actual fitted stellar population, but even in ideal environments, absent noise and extinction, older populations are harder to uncover. The presence of an AGN is even trickier to handle, as in the absence of AGN templates the AGN continuum is attributed to and fitted with stellar populations. With the inclusion of AGN templates, STARLIGHT tends to over-assign an AGN contribution to the fitted spectrum even when the galaxy lacks AGN activity. In reality, an actual galactic spectrum has a much higher complexity than independent SSPs, but STARLIGHT remains robust in fitting and allowing the SED of the stellar component to be subtracted.

# 4.C Notes On Individual Galaxies

SFRS 30 ( = *OJ 287*) is a blazar and is assigned a Sy classification to match the terminology adopted for the activity types in this paper.

SFRS 42 ( = *IC 2434*) is an ambiguous case and is assigned a TO classification based on the [N II] BPT diagram. The [S II] $\lambda\lambda 6716, 6731$ and [O I] $\lambda 6300$ detections are considered upper limits.

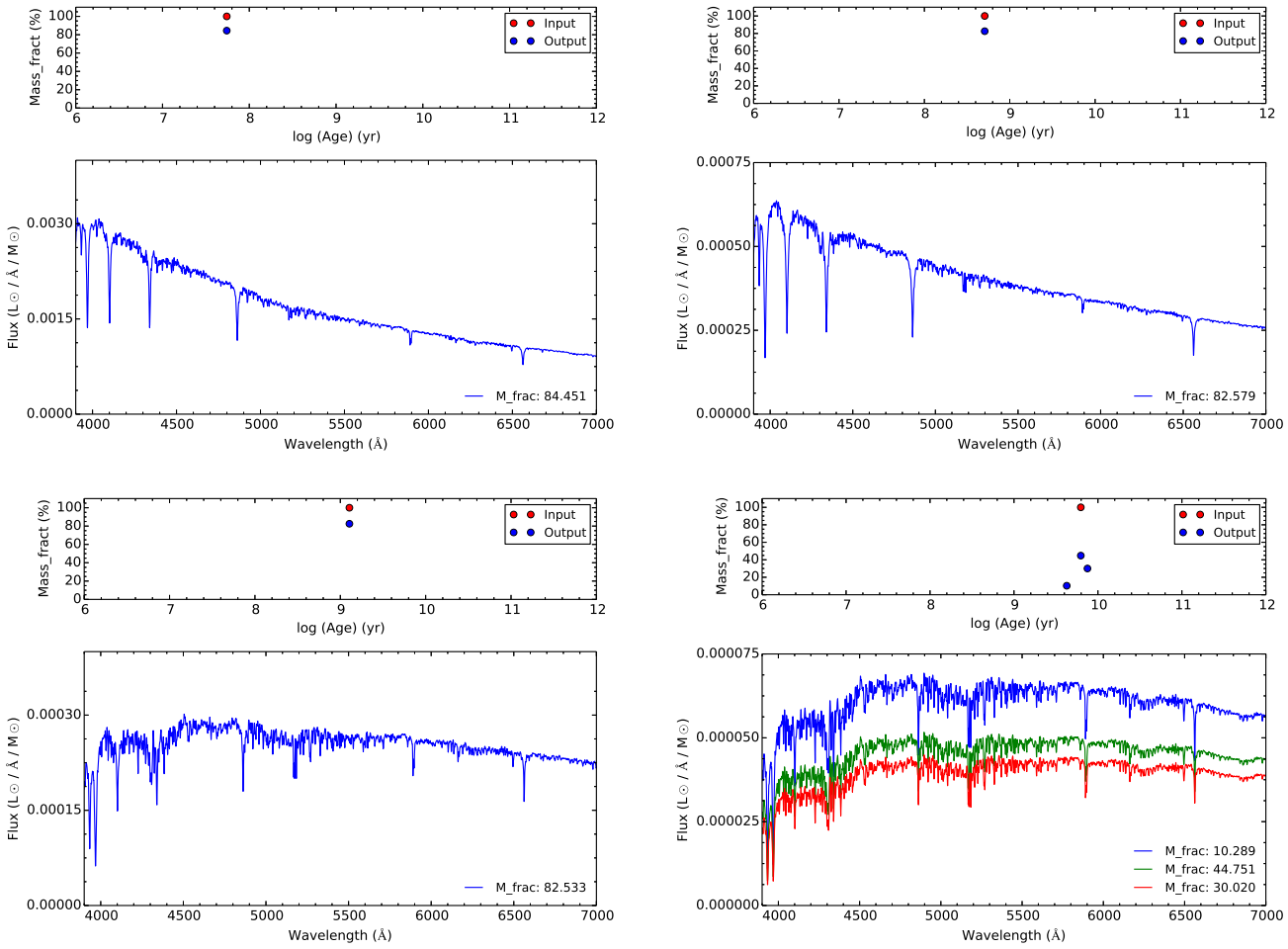


**Figure 4.B.4:** STARLIGHT code simulation study using the same SSPs as in Figure 4.B.2 adding Gaussian noise. The top panel in all plots shows the SSP of given age and mass fraction used as input in STARLIGHT (red point) and the corresponding output SSP(s) (blue points) from the fit. The bottom panel in all figures shows the corresponding output spectrum of the SSP(s) used in the fit.

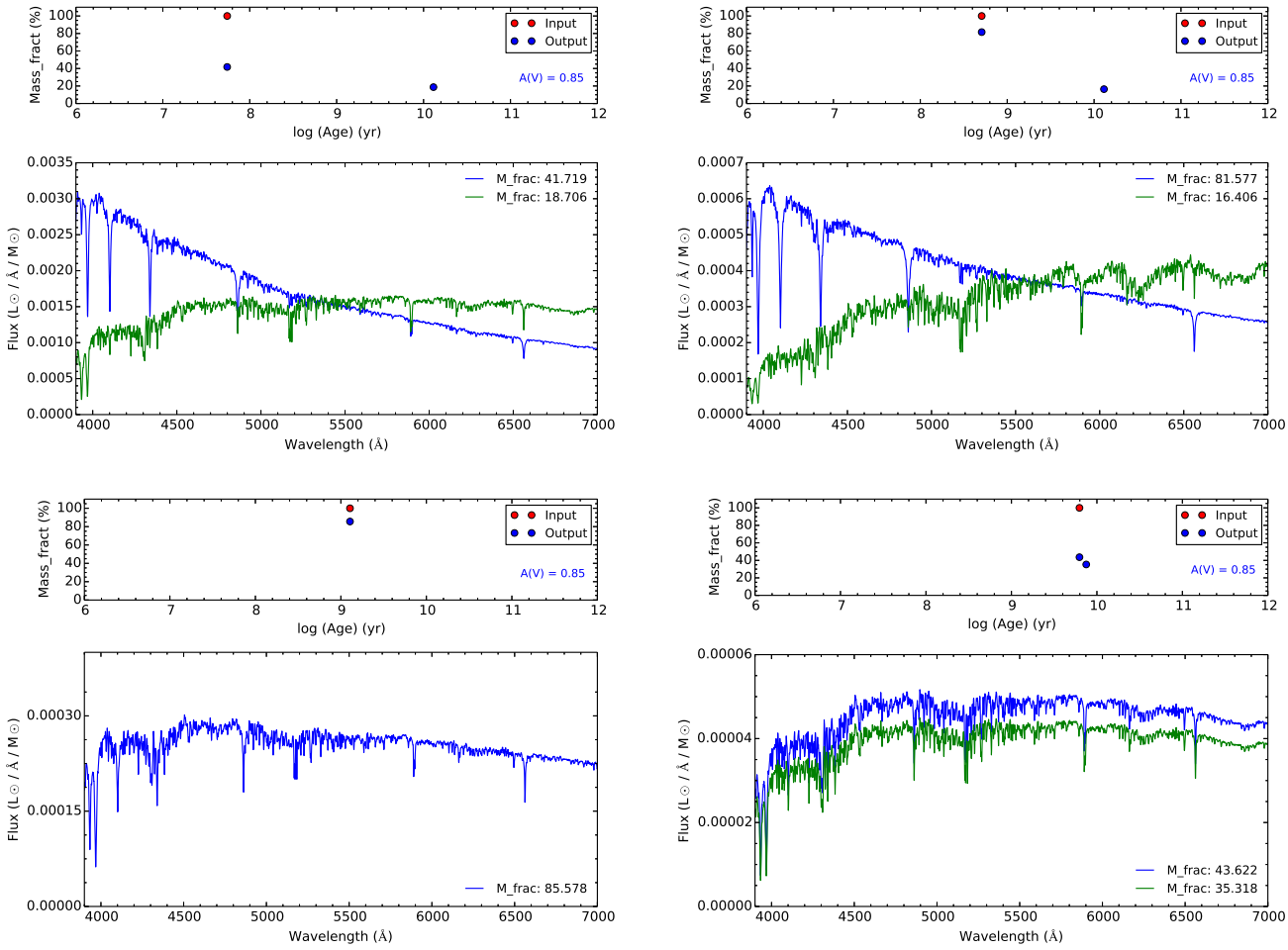


**Figure 4.B.5:** STARLIGHT code simulation study using the same SSPs as in Figure 4.B.2 with added extinction ($A_V = 0.85$), but without Gaussian noise. The top panel in all plots shows the SSP of given age and mass fraction used as input in STARLIGHT (red point) and the corresponding output SSP(s) (blue points) from the fit. The bottom panel in all figures shows the corresponding output spectrum of the SSP(s) used in the fit.

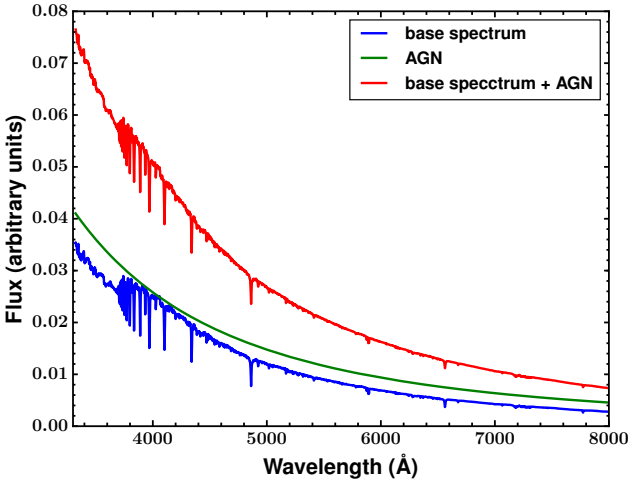


**Figure 4.B.6:** Example of a composite AGN spectrum (red line), composed by a SSP spectrum (green line) and an AGN power-law spectrum (blue line).

SFRS 57 ( = *CGCG 238-066*) is an ambiguous case in the BPT diagrams but is recognized as AGN in the IRAC color-color diagram and is assigned a Sy classification.

SFRS 61 ( = *CGCG 181-068*) is an ambiguous case and is assigned a TO classification based on the [N II] BPT diagnostic. The [S II] $\lambda\lambda 6716, 6731$ and [O I] $\lambda 6300$ measurements are considered upper limits.

SFRS 80 ( = *NGC 3190*) has no detectable H$\beta$ emission in the nuclear spectrum. The integrated spectrum was used to obtain activity classification (LINER).

SFRS 93 ( = *UGC 5720*) H$\alpha$ is absent in the SDSS spectrum. The activity type (H II) was determined solely from the [O III]/H$\beta$ value.

SFRS 139 ( = *NGC 3758*) is a Type-1 AGN with very broad line profiles and is automatically classified as Sy.

SFRS 148 ( = *NGC 3822*) has no [S II] BPT classification because the [S II] $\lambda\lambda 6716, 6731$ doublet falls inside a telluric line region. It is assigned a Sy classification because in the [O I] BPT diagram the galaxy is located inside the Sy region, further away from the Sy/LINER demarcation line compared to the [N II] diagnostic demarcation line.

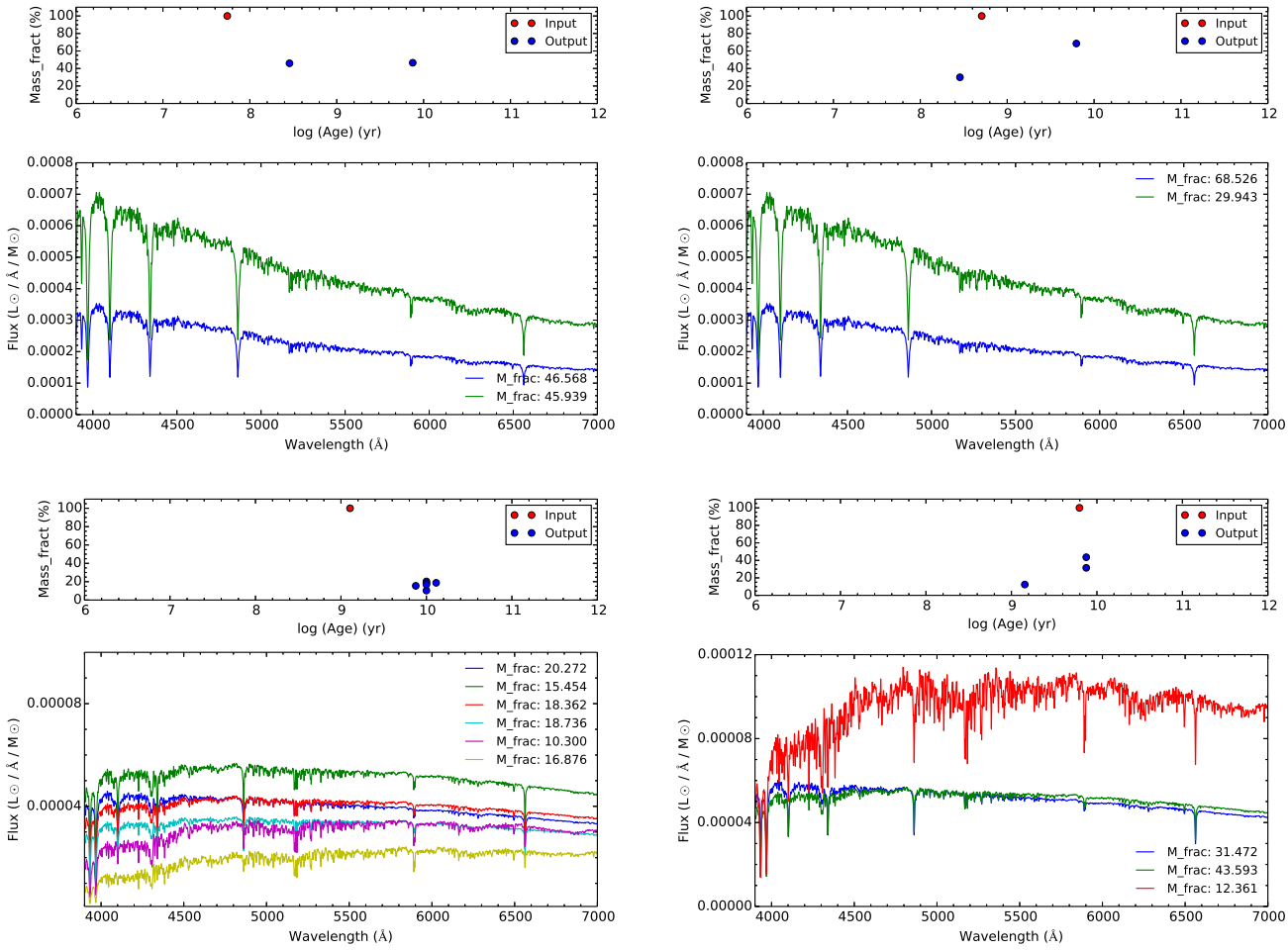


**Figure 4.B.7:** STARLIGHT code simulation study using the same SSPs as in Figure 4.B.2 adding an AGN component. The top panel in all plots shows the SSP of given age and mass fraction used as input in STARLIGHT (red point) and the corresponding output SSP(s) (blue points) from the fit. The bottom panel in all figures shows the corresponding output spectrum of the SSP(s) used in the fit.

SFRS 182 ( = *NGC 4194*) H$\alpha$ is absent in the SDSS spectrum. The activity type (H II) was determined solely from the [O III]/H$\beta$ value.

SFRS 187 ( = *NGC 4237*) is an ambiguous case, classified as TO/H II in the N II/S II-BPT diagnostics. Because the [OI] line is unreliable, this galaxy is assigned an H II classification.

SFRS 201 ( = *NGC 4435*) is an ambiguous case and is assigned a LINER classification because in the [O I] BPT is located in the middle of the LINER region, while there is no [S II] $\lambda\lambda 6716, 6731$ detection.

SFRS 204 ( = *3C 273*) is a quasar and is assigned a Sy classification to match the terminology adopted for the activity types in this paper.

SFRS 227 ( = *NGC 4689*) is assigned an H II classification because in the [S II] BPT diagram the galaxy is located inside the H II region further away from the demarcation line. There is no [O I] $\lambda 6300$ detection.

SFRS 228 ( = *NGC 4688*) is assigned an H II classification because it is located further away from the demarcation line and into the H II region in the [N II] BPT diagram, while it falls right on the line in the [S II] BPT diagnostic. There is no [O I] $\lambda 6300$ detection.

SFRS 233 ( = *MCG 8-23-097*) is an ambiguous case and is assigned a LINER classification.

SFRS 239 ( = *UGC 8058*) is a Type-1 AGN with very broad line profiles and is automatically classified as Sy.

SFRS 259 ( = *NGC 5104*) is an ambiguous case and is assigned a Sy classification.

SFRS 261 ( = *NGC 5112*) is an ambiguous case and is assigned a TO classification because it falls on the [S II] BPT demarcation line, while in the [O I] BPT diagram the emission-line uncertainties can place the galaxy further inside the Sy region.

SFRS 262 ( = *NGC 5123*) is assigned an H II classification. There is no [O I] $\lambda$6300 detection.

SFRS 263 ( = *IRAS 13218+0552*) is a Type-1 AGN with very broad line profiles and is automatically classified as Sy.

SFRS 266 ( = *NGC 5204*) is an ambiguous case, and is assigned an H II classification. There is no [O I] $\lambda$6300 detection. Visual inspection of the SDSS image shows bright blue colors, characteristic of star-forming galaxies.

SFRS 270 ( = *IRAS 13349+2438*) is a literature verified QSO (e.g. Lee et al. 2013) and was assigned a Sy classification.

SFRS 276 ( = *MK 268*) is a Type-1 AGN with very broad line profiles and is automatically classified as Sy.

SFRS 305 ( = *NGC 5515*) is an ambiguous case and is assigned a Sy classification. It is also a literature verified Sy (e.g. Véron-Cetty & Véron 2006)

SFRS 322 ( = *UGC 9412*) is a Type-1 AGN with very broad line profiles and is automatically classified as Sy.

SFRS 331 ( = *UGC 9618_NED02*) has a TO/H II/H II class in the corresponding [N II]/[S II]/[O I] BPT diagnostics. However, because in the O I BPT diagram it falls on top of the demarcation line, it is assigned a TO classification.

SFRS 350 ( = *UGC 10120*) has broad-line profiles and is fitted with an additional broad component along with the narrow ones when measuring its emission lines. However, it is classified as H II in all three BPTs but is recognized as AGN in the IRAC color-color diagram and is reported as Sy in the literature (Contini et al. 1998). Therefore it is assigned a Sy classification.

# 5 The sub-galactic and nuclear main sequences for local star-forming galaxies

This works is published in the Monthly Notices of the Royal Astronomical Society as: A. Maragkoudakis, A. Zezas, M. L. N. Ashby., P. Willner., 2017, MNRAS, Vol 466 1192-1204.

## 5.1 Introduction

The tight relationship between galaxy star-formation rate (SFR) and total stellar mass ($M_\star$), commonly referred to as the star-forming galaxy main sequence (MS), has been extensively investigated over the past decade (e.g., Noeske et al. 2007, Elbaz et al. 2007, Daddi et al. 2007). The MS describes the ratio of current to past star formation and indicates that higher stellar-mass systems undergo more intense star formation activity than lower-mass systems. The low dispersion of the MS suggests that star formation is regulated mostly through secular processes rather than stochastic merger-driven star-forming episodes. A general description of the MS is a power law of the form SFR $\propto M_\star^\alpha$ with typical values of $\alpha$ between 0.6 and 1 (Rodighiero et al. 2011).

The determination of the MS slope depends strongly on the prescriptions used to measure SFR and $M_\star$, luminosity to SFR conversions and stellar population synthesis

(SPS) models. This is true even for samples in narrow redshift ranges, where significant variations (up to ∼0.35 dex) are reported between MS slopes derived from different studies (e.g., Speagle et al. 2014 (S14)). Additional complications arise from the selection criteria for the star-forming galaxy (SFG) samples. For example using the *BzK* two-color selection (Daddi et al. 2007), or selecting blue cloud galaxies by making a cut in the color-magnitude diagram (CMD) (Elbaz et al. 2007), is biased toward more actively star-forming systems missing the non-negligible fraction of galaxies at the lower end of the star-formation range.

More recently, a few studies (e.g., Wuyts et al. 2013 (W13); Hemmati et al. 2014; Magdis et al. 2016 (M16); Cano-Díaz et al. 2016 (C16)) provide evidence that MS-like correlations are also present at sub-galactic scales. These studies compared SFR surface densities with stellar-mass surface densities for individual sub-galactic regions. While at intermediate to higher redshifts ($z > 1$) this correlation has a slope close to unity (W13, M16), at lower redshifts sub-linearity has been reported (C16). González Delgado et al. (2016) (D16) showed that local specific SFR (sSFR) shows radial profiles that increase outwards and scale with Hubble type. Specifically, the sSFR in the inner 1 half light radius is steeper than outwards, suggesting that galaxies are quenched inside-out and that this process is faster in the central part, causing the observed sub-linearity in the MS slope. However, existing studies concentrated mostly on the higher end of the galaxy stellar mass distribution, or they covered a small range in SFR and/or stellar mass. In addition, these studies relied on spectral energy distribution (SED) fitting or stellar population models for the determination of SFR and stellar masses, the results of which depend on parameters such as the choice of star formation history (SFH) priors or the parameters of the stellar templates used (e.g., Conroy 2013). In addition, these methods suffer from degeneracies where several combinations of different models are able to reproduce the observables, and therefore the derived galaxy parameters can be highly uncertain (e.g., Conroy et al. 2010).

This work explores star formation taking place in the sub-galactic regions of a representative sample of 246 SFGs in the local Universe ($z < 0.08$) with respect to their local and total stellar mass content. The sample spans a range of four orders of magnitude in both stellar mass and SFR, greatly expanding the parameter space covered by previous studies. In addition, we explore the MS in the nuclear/circumnuclear region in the context of the general sub-galactic MS (SGMS). Throughout the paper, SGMS will be used to refer to the sequence of local SFR density and local stellar-mass density formed from all sub-galactic regions in galaxies including nuclei, nuclear SGMS to the corresponding sequence formed from nuclear regions only, and nuclear MS (NMS) to

the sequence of nuclear SFR and total stellar mass.

This paper is organized as follows: Section 5.2 describes the sample used in our analysis and the methods used to derive SFRs and stellar masses. Section 5.3 describes the integrated MS of our SFG sample and demonstrates the validity of the SFR and $M_\star$ measures used. Section 5.4 presents the SGMS and its dependence on galaxy morphology (Section 5.4.2) and the nuclear/circumnuclear SGMS (Section 5.4.3). Section 5.5 discusses our results in the context of local and higher-$z$ galaxies. Throughout this paper we adopt a ΛCDM cosmology with $H_0 = 73$ km s$^{-1}$, $\Omega_{\rm M} = 0.3$, $\Omega_\Lambda = 0.7$, and a Salpeter (1955) initial mass function (IMF) for SFRs and stellar mass determination.

# 5.2 Sample Description and Methodology

## 5.2.1 The SFRS sample

The Star Formation Reference Survey (SFRS; Ashby et al. 2011) is representative of the full range of star-formation properties and conditions in the nearby Universe. It consists of 369 galaxies selected from the PSCz catalog (Saunders et al. 2000) in order to sample the entire range of SFR, specific SFR (sSFR), and interstellar dust temperature as represented by the 60 $\mu$m luminosity, the flux ratio of $F_{60}/K_S$, and the far-IR flux density ratio $F_{100}/F_{60}$ respectively.

Owing to the representative nature of the SFRS sample, it includes bona-fide SFGs and AGNs. The latter were retained in order not to bias the sample. Therefore, in order to identify star forming galaxies, Maragkoudakis et al. (in preparation) used a combination of IR diagnostics (Stern et al. 2005) and optical emission-line diagnostics (i.e., BPT diagrams; Baldwin et al. 1981, Kewley et al. 2001, Kauffmann et al. 2003) while accounting for the uncertainties of the prominent emission-lines used in the optical diagnostics. The results of this analysis showed that the SFRS sample consists of 260 SFGs, 49 Seyfert, 34 composite objects, and 26 LINERs. In this work we use 246 SFRS SFGs with $z < 0.08$ and available data to probe the stellar mass and SFR content in global and spatially resolved sub-galactic scales. The remaining 14 galaxies lacked data in one or more IRAC bands, or have unreliable SDSS color information, or are too distant to meet the resolution thresholds (see Section 5.2.2) applied for the sub-galactic analysis. The final sample covers the redshift range of $0.001 < z < 0.08$ with a median redshift of 0.02 and a total stellar mass and SFR range of $7.7 < \log(M_\star/{\rm M}_\odot) < 11.7$ and $-2.2 < \log({\rm SFR}/{\rm M}_\odot{\rm yr}^{-1}) < 2.1$ respectively. These mass and SFR ranges are at

least 1 dex broader than previous studies of the SGMS in local galaxies.

### 5.2.2 IRAC Matched Aperture Photometry

We based our analysis of the total and spatially resolved MS (Sections 5.3 and 5.4) on SFRs and stellar masses estimated with the IRAC 8.0 and 3.6 $\mu$m flux densities tabulated by Ashby et al. (2011). The 8.0 $\mu$m band provides better resolution for measuring SFR compared to MIPS 24 $\mu$m, and it is relatively unaffected by absorption. Numerous studies have shown that in metal-rich SFGs, polycyclic aromatic hydrocarbon (PAH) luminosity scales relatively well with SFR (Calzetti 2011; Kennicutt & Evans 2012 (KE12) and references within). Because the majority of SFRS SFGs have metallicities close to solar (Maragkoudakis et al. in preparation), the 8.0 $\mu$m luminosity should be a good SFR tracer.

The initial reduction of the IRAC data and construction of image mosaics was described by Ashby et al. (2011). To measure the 3.6 and 8.0 $\mu$m flux on sub-galactic scales, we constructed a grid of square apertures centered on the nucleus, based on the source coordinates (Ashby et al. 2011). Each aperture corresponds to a physical size of $1 \times 1$ kpc$^2$. The angular aperture sizes in each galaxy were adjusted according to galaxy distance to ensure consistent sampling of linear scales throughout our study sample. This choice of angular scale was driven by three considerations: (1) 1 kpc is the minimum length scale on which the standard SFR metrics are thought to be reliable (e.g., KE12); (2) we require multiple regions within each galaxy; (3) the IRAC 8.0 $\mu$m angular resolution of $2''$ corresponds to 1kpc at a distance of 100 Mpc and 70% of the SFRS SFGs are closer than this.

We mapped sub-galactic regions within 1.5 times each galaxy's Petrosian radius $R_{P90}$, defined as the radius including 90% of the galaxy light (Figure 5.2.1). Because we are interested in star-forming regions, we rejected regions having surface brightness smaller than 10% of the second highest surface brightness region at 8.0 $\mu$m. The median galaxy had 16 apertures with minimum 1 aperture (11 galaxies) and maximum 452 apertures (1 galaxy). The photometry was performed with CIAO's (Fruscione et al. 2006) "dmstat" and "dmextract" tools. The background contribution was subtracted based on the median value of the background within an elliptical annulus centered on the galaxy and having inner and outer radii of 2 and 2.5 times the galaxy's $R_{p_{90}}$ respectively. The orientation and ellipticity of the background region, in each case, matched that of the galaxy.

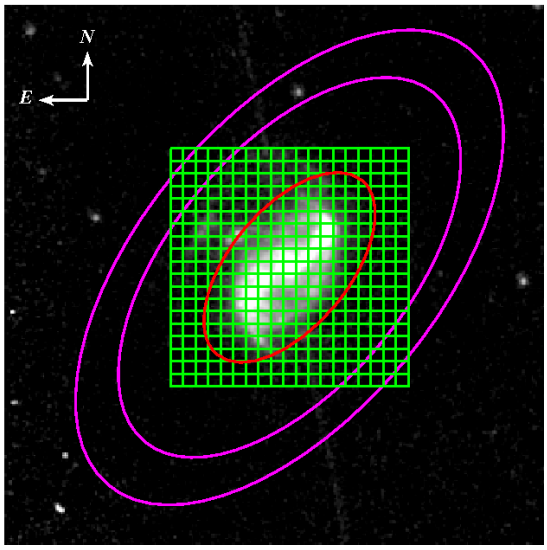


**Figure 5.2.1:** Example of IRAC 8.0 $\mu$m multiple aperture photometry on galaxy NGC 2718. Small green boxes correspond to a physical area of $1 \times 1$ kpc$^2$. Red ellipse corresponds to 1.5 $R_{P90}$ and magenta ellipses to $2R_{P90}$ and $2.5R_{P90}$. The photometry was performed in boxes within the smallest red ellipse. Sky subtraction was performed based on the median background measured between the outer ellipses.

### 5.2.3 Mass and Star-Formation Rate Estimations

Total stellar masses and stellar mass in sub-galactic apertures were calculated using the Zhu et al. (2010) mass-to-light ratio calibration for the IRAC 3.6 $\mu$m band:

$$\frac{M_\star}{M_\odot} = 10^{0.23+(1.14)(g-r)} \times \frac{\nu L_{\nu 3.6\,\mu\mathrm{m}}}{L_\odot} \tag{5.1}$$

where $g$, $r$ are the Petrosian AB magnitudes obtained from the SDSS DR12 (Alam et al. 2015), and galaxy 3.6 $\mu$m magnitudes are from Ashby et al. (2011). Subregion $g-r$ colors were assumed to be the same as the whole galaxy. For the nuclear regions, stellar populations in general consist of a mixture of old stars from the bulge and young stars in circumnuclear star-forming regions. We used the SDSS $g-r$ fiber colors for the nucleus.

We verified the 3.6 $\mu$m derived stellar masses by comparing them with the commonly used and well-calibrated $K$-band relation described by Bell et al. (2003):

$$\frac{M_\star}{M_\odot} = 10^{-0.273+(0.091)(u-r)} \times \frac{L_{K_s}}{L_{K_\odot}} \tag{5.2}$$

where $u-r$ are the Petrosian SDSS colors in AB magnitudes. We calculated $K$-band luminosities using the asymptotic $K$-band magnitudes measured from integrating the 2D model fits to the 2MASS images of the galaxies (Bonfini et al. in preparation). Figure 5.2.2a shows the comparison. The 3.6 $\mu$m tracer shows a systematic underestimation of the stellar-mass compared to the $K$-band calibration. The integrated 3.6 $\mu$m photometry was measured by using SExtractor (Ashby et al. 2011), which is subject to aperture effects depending on the galaxy light traced. The asymptotic $K$-band fluxes measured from fitting the galaxies profiles by Bonfini et al. are generally larger than the ones derived by SExtractor (Ashby et al. 2011). Overall the two stellar-mass tracers differ simply by an offset without showing non-linearity effects, and the offset does not influence the analysis.

We calculated total SFRs and SFRs in sub-galactic apertures from the starlight-subtracted 8.0 $\mu$m images. The starlight subtraction was performed using the scaling of Helou et al. (2004):

$$f_{8\,\mu\mathrm{m,(PAH)}} = f_{8\,\mu\mathrm{m}} - 0.26 f_{3.6\,\mu\mathrm{m}} \tag{5.3}$$

Then the SFR was calculated using the calibration of Pancoast et al. (2010)[1]:

$$\frac{\mathrm{SFR}_{8\,\mu\mathrm{m}}}{[\mathrm{M}_\odot/\mathrm{yr})]} = 6.3 \times 10^{-10} \frac{L_{8\,\mu\mathrm{m}}}{L_\odot} \tag{5.4}$$

[1]In principle the SFR should include ultraviolet emission, but for the SFRS sample, this is typically a 15% effect and never as much as a factor of 2 (Mahajan et al., in preparation).

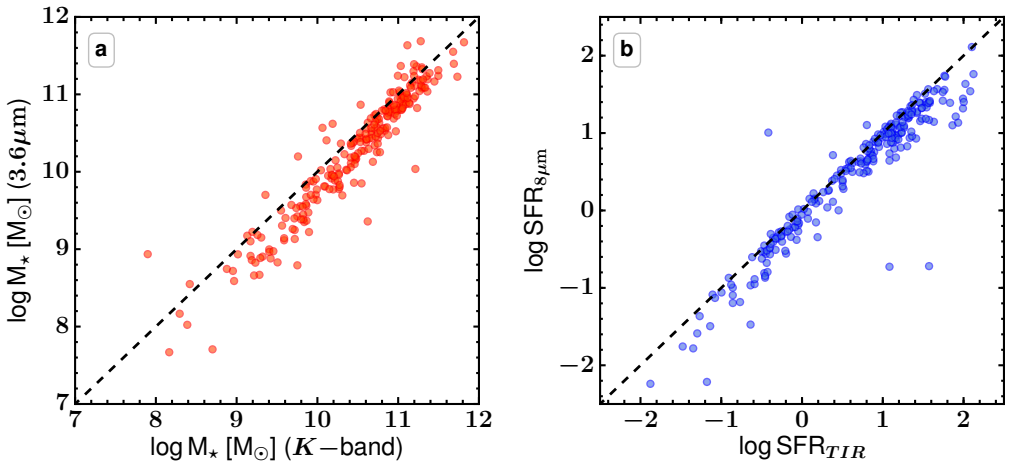


**Figure 5.2.2:** A comparison of the total galaxy SFR and stellar mass estimators. Left panel: Total galaxy stellar mass estimated from the 3.6 $\mu$m calibration (Eq. 5.1) plotted against the $K$-band calibration (Eq. 5.2). Right panel: Total SFR estimated from the 8.0 $\mu$m calibration (Eq. 5.4) plotted against the TIR calibration (Eq. 5.5). Dashed equality lines are drawn in both panels.

For comparison purposes we also measured the total SFR from the TIR luminosity (Ashby et al. 2011) using the Dale & Helou (2002) TIR flux formula $F_{TIR} = 2.403\nu f_{\nu 25\,\mu\mathrm{m}} - 0.245\nu f_{\nu 60\,\mu\mathrm{m}} + 1.347\nu f_{\nu 100\,\mu\mathrm{m}}$ but using the MIPS 24 $\mu$m flux densities where available instead of the less precise IRAS 25 $\mu$m flux densities. We then calculated the SFR using the TIR calibration by KE12:

$$\frac{\mathrm{SFR}}{[\mathrm{M}_\odot/\mathrm{yr})]} = \frac{L_{\mathrm{TIR}}}{[\mathrm{erg/s}]} \times 10^{-43.41} \tag{5.5}$$

Figure 5.2.2b compares the 8.0 $\mu$m and TIR SFR tracers. The two SFR tracers agree apart from an offset, with the 8.0 $\mu$m underestimating the SFR compared to the TIR which is expected because the TIR also traces the contribution from low-mass stars, as well as encompasses the systematic error from the contribution of evolved populations (above ~200 Myr) leading to an overestimate of SFR. As with the different stellar mass estimators, there is only an offset between the two tracers in an otherwise linear conversion.

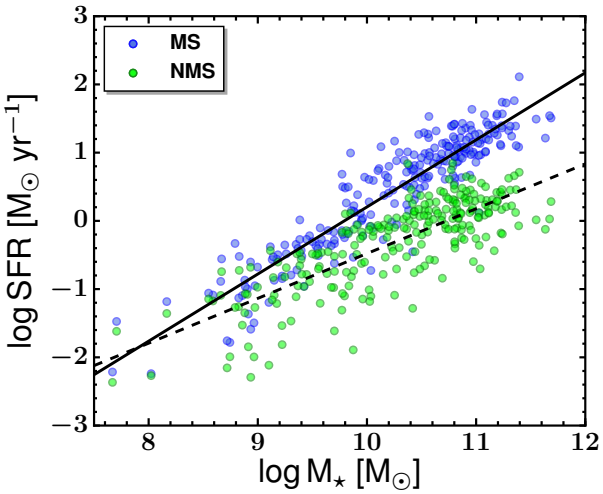


**Figure 5.3.1:** The global MS (blue points) and nuclear region MS (NMS) (green points) of the SFRS SFGs. The SFR is calculated using the 8 $\mu$m calibration, and stellar mass is derived from the 3.6 $\mu$m tracer. Both SFRs are plotted against total stellar mass. The solid line is the fit to the MS (Eq. 5.6), and the dashed line is the fit to the NMS. The properties of the two sequences are given in Table 5.3.1.

## 5.3 The Global Main Sequence of Local Star-Forming Galaxies

With a wide range of galaxy parameters and a fully representative star-forming galaxy sample, the SFRS SFGs provide an ideal set to examine the MS plane in the local Universe, both in integrated and sub-galactic scales. Figure 5.3.1 shows the standard MS fitted with a linear function, in log space, of the form:

$$\log\left(\mathrm{SFR}/\mathrm{M}_{\odot}\mathrm{yr}^{-1}\right) = \alpha \log(M_{\star}/\mathrm{M}_{\odot}) + \beta \tag{5.6}$$

The best-fit parameters (Table 5.3.1) show that the MS of our sample of local galaxies has a slope of $\alpha = 0.98$ and a normalization of $-9.63\log(\mathrm{M}_{\odot}\mathrm{yr}^{-1})$. The dispersion about the best-fit line is 0.32 dex, consistent with the $\sim$0.35 dex MS scatter reported in the literature (S14 and references within).

**Table 5.3.1:** MS, NMS, and SGMS best-fit parameters. Fits of the form $\log SFR = \alpha \log M_\star + \beta$ to the MS in different scales. Column (1): The various sequences examined; Column (2): the number of galaxies in each sequence; Column (3): the median number of apertures per galaxy; Column (4) the best-fit slope ($\alpha$); Column (5): the zero-point ($\beta$) value of the best fit; Column (6) the metric of dispersion ($\sigma$) in dex from the best-fit line.

| Sequence | Num. of galaxies | Apertures | $\alpha$ | $\beta$ | $\sigma$ |
|---|---|---|---|---|---|
| MS | 245[a] | - | 0.98 ± 0.03 | −9.63 ± 0.27 | 0.32 |
| NMS | 246 | - | 0.66 ± 0.03 | −7.05 ± 0.33 | 0.39 |
| SGMS | 246 | 16 | 0.91 ± 0.01 | −9.01 ± 0.05 | 0.31 |
| All morphological types SGMS | 130 | 14 | 0.89 ± 0.01 | −8.97 ± 0.07 | 0.31 |
| (E–S0/a) SGMS | 10 | 11 | 1.09 ± 0.03 | −10.76 ± 0.22 | 0.18 |
| (Sa–Sbc) SGMS | 55 | 17 | 0.81 ± 0.02 | −8.30 ± 0.13 | 0.30 |
| (Sc–Irr) SGMS | 65 | 15 | 0.97 ± 0.01 | −9.52 ± 0.09 | 0.30 |
| Unclassified galaxies SGMS | 116 | 19 | 0.72 ± 0.01 | −7.25 ± 0.08 | 0.26 |

[a] Galaxy IC 3476 has no available total 8.0 $\mu$m photometry.

## 5.4 The sub-galactic Main Sequence of Star-Forming Galaxies

Three variants of the SGMS comprise sequences based on (1) all sub-galactic regions identified in Section 5.2.2; (2) bright regions and random regions, excluding the nuclei; (3) only the nuclear regions.

### 5.4.1 The $\Sigma_{\rm SFR} - \Sigma_\star$ Correlation

In all variants of the SGMS we measured the star formation surface density $\Sigma_{\rm SFR}$ defined as:

$$\Sigma_{\rm SFR} = {\rm SFR/Area} \quad [{\rm M_\odot yr^{-1} kpc^{-2}}] \tag{5.7}$$

and similarly the stellar mass surface density ($\Sigma_\star$). Figure 5.4.1 shows the result, revealing a strong correlation between these two parameters for regions on physical scales of 1 kpc. In all cases we fitted the relation with a linear function in logarithmic space. We performed an additional $M_\star$-dependent fit using the Schreiber et al. (2015) (S15) eq. 9 parametrization, in order to examine whether the flattening towards higher stellar densities reported by Wuyts et al. (2013) is present in our sample. We set all $z$-dependent terms to zero, because all SFRS galaxies allocate a narrow redshift range, but allowed the remaining three parameters to vary. The fit (Figure 5.4.1) is slightly

better in the highest mass bin, but the decrease in overall scatter is only from 0.310 dex to 0.308 dex. The rest of this paper discusses only the linear fit for simplicity and easier comparison to previous results. The mean SFR density in mass bins (Figure 5.4.1) is consistent with the best-fit line within the measured uncertainties. The scatter in the SGMS is 0.31 dex, similar to the 0.32 dex scatter of the global MS and within the range of scatter reported in different MS studies (S14). The best-fit values are shown in Table 5.3.1 along with the dispersion ($\sigma$). The SGMS slope is $\alpha_{\rm SGMS} = 0.91$, slightly less than that of the integrated MS ($\alpha_{\rm MS} = 0.98$).

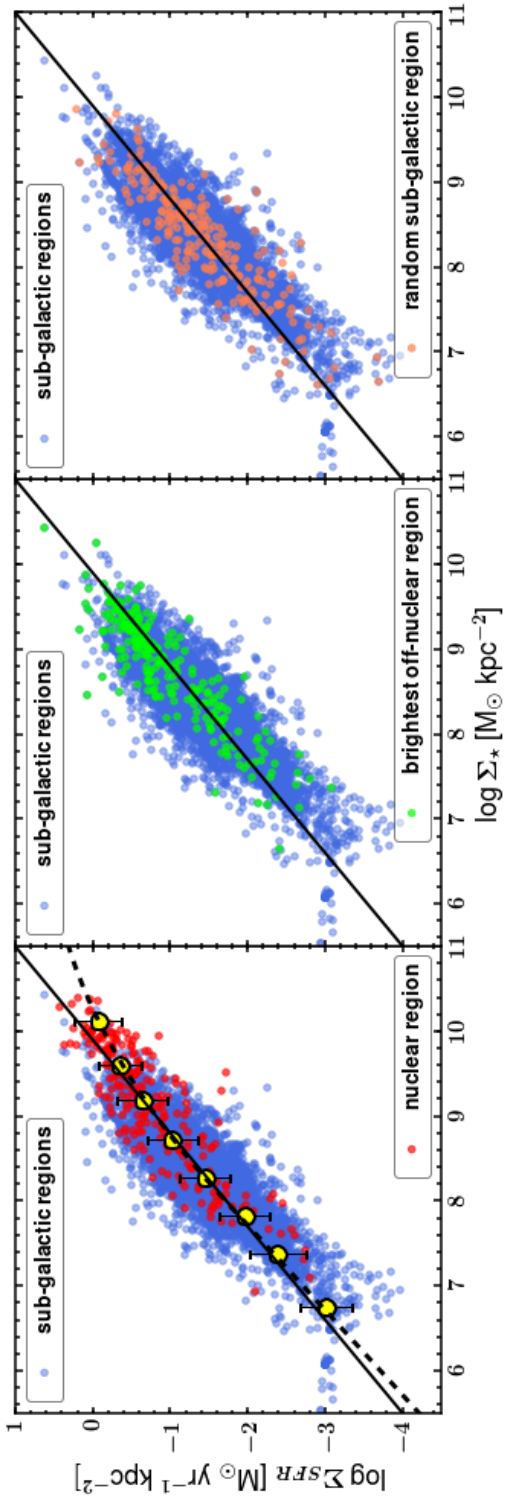


**Figure 5.4.1:** The sub-galactic main sequence between $\Sigma_{\rm SFR}$ and $\Sigma_\star$ for the 246 star-forming galaxies in the SFRS. The blue points in all panels represent the individual sub-galactic regions of all SFGs. The red points in the left panel present the sequence of the nuclear regions, and the yellow points show the mean SFR density in mass bins. The first mass bin is defined between 5.5–7.0 $\log \Sigma_\star[{\rm M}_\odot{\rm kpc}^{-2}]$ and all later at every 0.5 dex mass. The green points in the middle panel show the off-nuclear regions of all galaxies with the highest surface brightness, and the orange points in the right panel correspond to randomly drawn sub-galactic regions. The best-fit line of the SGMS is shown with a solid line in all panels. A $M_\star$-dependent fit for all the regions based on the parametrization of Schreiber et al. (2015) is shown with a dashed line in the left panel.

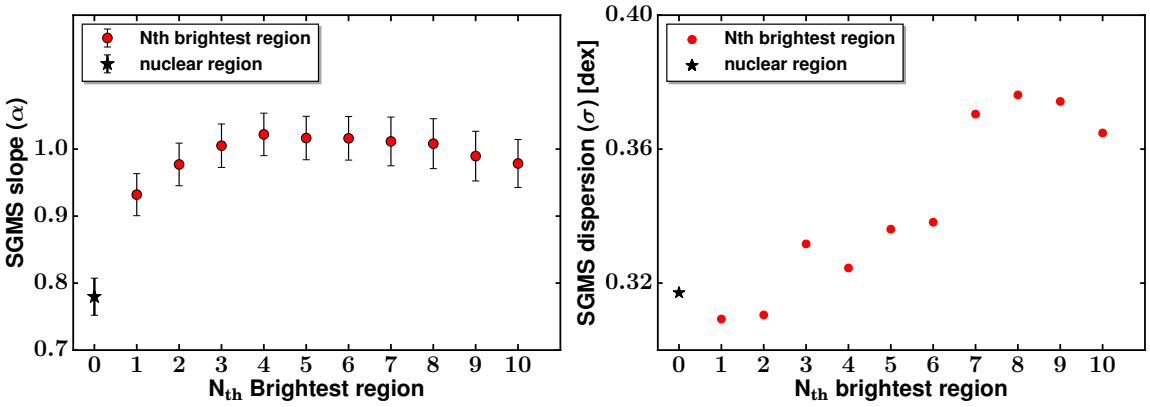


**Figure 5.4.2:** The slope (**left panel**) and dispersion (**right panel**) of the SGMS produced individually from reduced regions of the highest 8$\mu$m surface brightness. Index 0 corresponds to galaxy nuclei, index 1 to the brightest off-nuclear regions, and 10 to the 10th brightest off-nuclear region of each galaxy. The dispersion and slope for the SGMS of the nuclear regions are shown with a star symbol (region number 0).

In order to determine whether the SGMS, and possibly the global MS, are driven by the most active star-forming regions in the galaxy, we measured the SGMS parameters formed from a single region in each galaxy, beginning from the brightest off-nuclear region and progressing to regions of lower surface brightness in the 8 $\mu$m IRAC band. For this analysis we excluded the nuclei (which are discussed in Section 5.4.3) and concentrated explicitly on star formation taking place in the disc. For the 236 galaxies covered by one or more apertures outside the nucleus, we measured $\Sigma_{\rm SFR}$ and $\Sigma_{\star}$ of the brightest off-nuclear region and calculated the slope and dispersion of the produced SGMS. Then, we repeated this analysis for the next brightest region for each galaxy down to the 10th in line. Figure 5.4.2 presents the results. The slope of the SGMS of different (nth) surface brightness regions asymptotically increases towards the slope of the overall SGMS, with regions of higher surface brightness having shallower slopes. Therefore, higher surface brightness regions are not the primary drivers of the correlation. In addition, the right panel of Figure 5.4.2 shows that the measured SGMS scatter for regions of different surface brightness increases progressively from regions of higher to lower surface brightness. This is indicative that the MS and SGMS are not governed by the most active sub-galactic regions in the galaxy.

Furthermore, in order to investigate whether sampling one individual region from different galaxies will give a good representation of the $\Sigma_{\rm SFR}$–$\Sigma_{\star}$ correlation, we measured the SGMS slope and dispersion produced from random sub-galactic regions.

Specifically, we randomly drew a single region from each galaxy and measured the dispersion and slope of the produced SGMS, repeating the process 1000 times. The random-region SGMS from one such draw is shown in Figure 5.4.1. The dispersion in the 1000 trials varied between 0.31 and 0.38 dex with a median of 0.34 dex, and the slope ranged between values of 0.86 and 1.03 with a median of 0.95. This is consistent with our previous result, considering all regions as well as regions of different surface brightness in each galaxy, showing that scatter is driven by the general sub-galactic populations rather than the less active. It also suggests that most sub-galactic star-forming regions can be representative of the star-forming conditions overall.

To trace the behavior of the SGMS in individual galaxies and examine how well it resembles the global SGMS produced from all sub-regions of the entire SFG sample, we measured the SGMS slope, dispersion, and the local sSFR from individual galaxies. In order to obtain meaningful constraints on the SGMS parameters, we examined the 230 galaxies that are resolved in at least 5 apertures. Figure 5.4.3 shows the distribution of individual SGMS slopes.The distribution peaks at a mean value of 0.95 very close to the global SGMS slope ($\alpha_{\rm SGMS} = 0.91$). Within a single galaxy, stars form largely where the stellar mass is already high. Figure 5.4.4 shows the variation of the individual galaxy SGMS slopes with respect to their total SFR, total $M_\star$, and sSFR. The fits reveal a tendency of the individual SGMS slopes to decrease towards higher values of total SFR and total $M_\star$. Most galaxies at $\log(\mathrm{SFR}/\mathrm{M}_\odot\mathrm{yr}^{-1}) < 0$ and $\log(\mathrm{M}_\star/\mathrm{M}_\odot) < 10$ show a super-linear ($\alpha > 1$) correlation between SFR density and stellar-mass density, and the opposite behavior, i.e. a sub-linear correlation, for larger total SFR and $M_\star$ values. Nevertheless, the correlation between local mass and local SFR holds for galaxies with a wide range of properties.

Figure 5.4.5 shows how a local average of the sSFR measured from the sub-galactic regions of a galaxy correlates to the ratio of its total sSFR. The total sSFR is the total SFR divided by total stellar mass. The local average sSFR, plotted on the vertical axis of Figure 5.4.5, was calculated from the fitted slope in the non-logarithmic correlation $\Sigma_{\rm SFR} = \alpha\Sigma_* + \beta$ of the sub-galactic regions in each galaxy. The two measurements agree within 0.3 dex scatter. In other words, galaxies with high sSFR show elevated sSFR on average everywhere (at ∼1 kpc spatial scale), not just in selected regions, and SFR correlates with mass at kpc scales in individual galaxies.

### 5.4.2 Morphology Dependence of the SGMS

While the morphological dependence of the galaxy MS has been examined (Noeske et al. 2007, Wuyts et al. 2011), relatively little is known about the morphological dependence

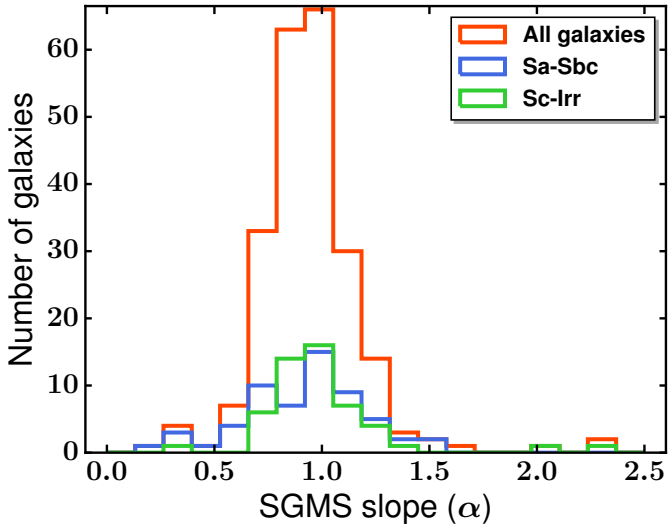


**Figure 5.4.3:** The distribution of SGMS slopes produced by distinct regions within individual galaxies. The histogram for all galaxies is shown in red color, the "early-type spirals" group histogram is shown in blue, and the "late-type" group in green.

of the SGMS. We investigated the SGMS for a subset of 130 SFRS SFGs with available morphological classification (Ashby et al. 2011). We defined three morphological groups. The "lenticulars" group (10 galaxies) contains the single elliptical galaxy in our sample along with S0 to S0/a types. The "early-type spirals" group (55 galaxies) consists of Sa to Sbc types, and lastly all types Sc and later (65 galaxies) are in the "late-type" group. A fourth group containing the galaxies with unknown morphological classes is also defined and studied separately.

The SGMS of all classified morphological types gives the exact same slope and dispersion as the "all-galaxies" SGMS (Figure 5.4.6). The corresponding SGMS of morphologically unclassified galaxies has a sub-linear slope. Figure 5.4.7 shows the sub-galactic $\Sigma_{\rm SFR}$ against $\Sigma_{\star}$ for all regions of the three morphological groups, and the fit parameters are given in Table 5.3.1. The "lenticular" and "late-type" groups have the steepest correlation between $\Sigma_{\rm SFR}$ and $\Sigma_{\star}$. In addition, Figures 5.4.3 and 5.4.4 show the distributions of the individual galaxy SGMS slopes and their variation with total SFR, total $M_{\star}$, and sSFR separated by morphology. Overall there is no substantial variation between the previous properties and the individual SGMS slopes with morphology.

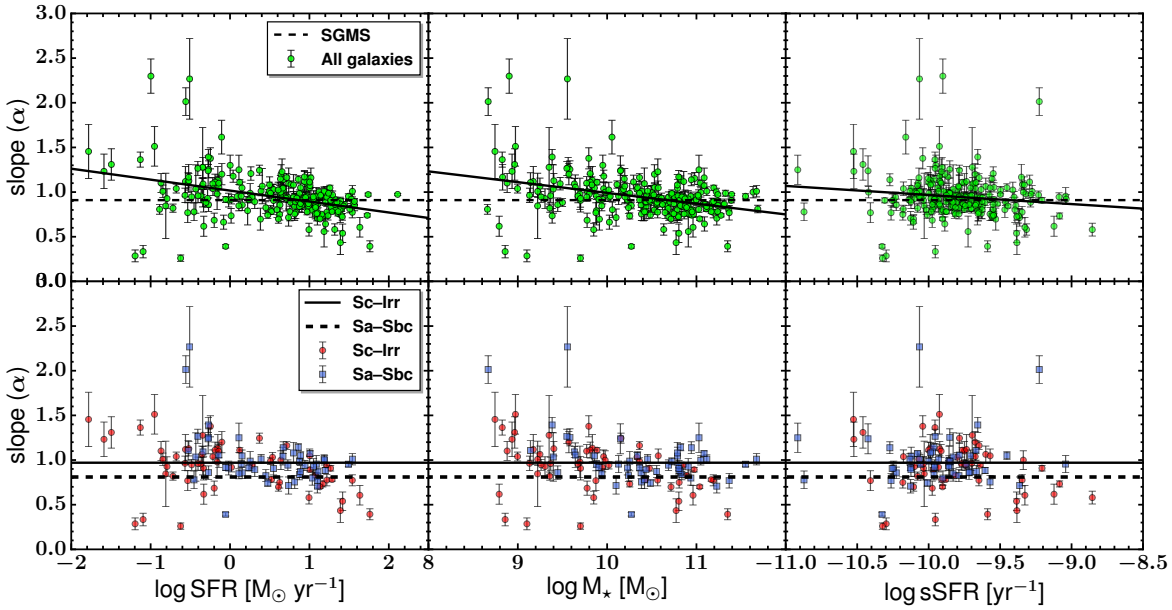


**Figure 5.4.4:** The SGMS slopes within individual galaxies plotted against total SFR (left panels), total $M_\star$ (middle panels), and sSFR (right panels). The top three panels show all the galaxies used (with or without morphological classification), while the bottom three panels show galaxies in the "late-types" group (red circles) and the "early-type spirals" group (blue boxes). In the top panels the SGMS slope of all galaxies is shown with a dashed line, while the best-fit line in each case is shown with a solid line. In the bottom panels the SGMS slope of the "early-type spirals" group is shown with a dashed line and the SGMS slope of the "late-types" group with a solid line.

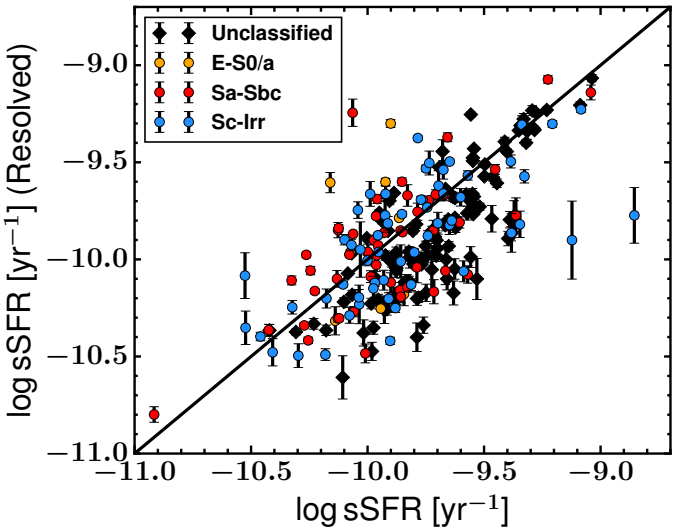


**Figure 5.4.5:** Comparison of sSFRs for individual galaxies. The abscissa shows the global sSFR. The ordinate shows the sSFR measured from the slope derived from a linear fit to each galaxy's SGMS. The solid line indicates equality. Points are color-coded by galaxy type as indicated.

### 5.4.3 The Nuclear Region And Nuclear Main Sequence

Because galaxy nuclei may contain supermassive black holes, these regions can host processes other than star formation (e.g. accretion, outflows, intense UV radiation). The (circum-) nuclear regions hold the most intense activity of star formation in galaxies as well as being the most massive in stellar content for nearly all galaxies in the sample, regardless of Hubble type (Figure 5.4.7). For the 236 galaxies with more than the nuclear aperture covering their surface, the nucleus is the maximum SFR and mass densities for at least 93%[1]. The examples in Figures 5.4.8 and 5.4.9 are typically showing that the nuclear $\Sigma_{\rm SFR}$ and $\Sigma_\star$ are among the highest values in the galaxies and in most cases are the maximum values. Because the average effective bulge radii for all SFRS galaxies is ∼1.4 kpc (Bonfini et al. in preparation) and considering that the aperture size in our analysis is 1 kpc, our nuclear apertures likely include emission from circumnuclear star-forming activity. For the same reason, apertures adjacent to

[1]There are 27 galaxies where the adopted nucleus is not the brightest spot. Of these, 11 have wrong nominal coordinates for the nucleus, which is in fact the brightest spot in the galaxy. The remaining 16 have ambiguous or undefined nuclei because of low surface brightness, multiple nuclei, or possible field stars.

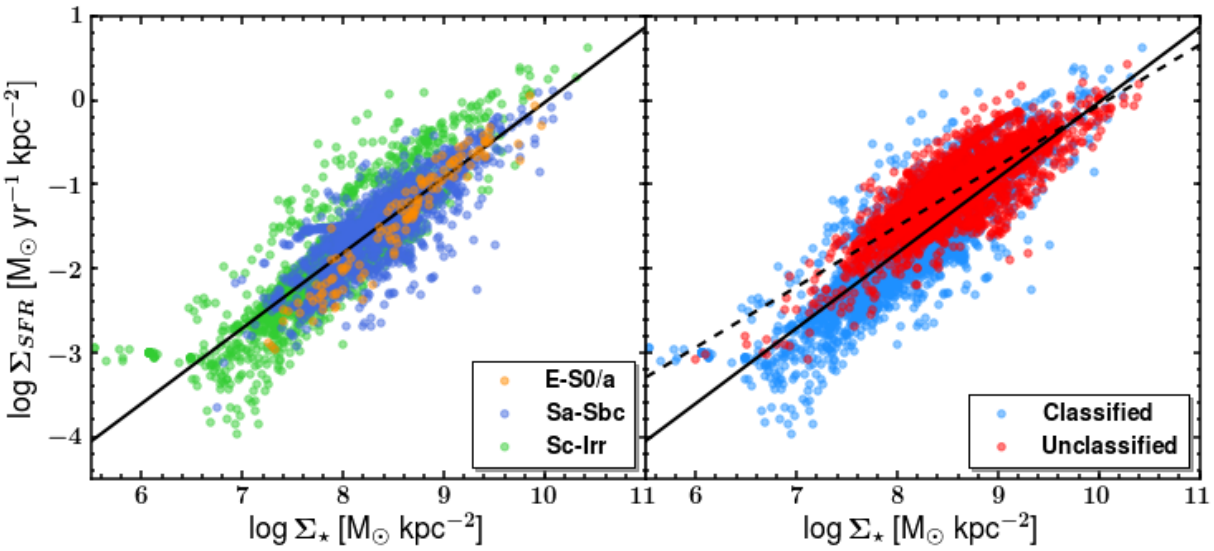


**Figure 5.4.6: Left panel**: The sub-galactic main sequence produced from all morphologically classified galaxies. E to S0/a Hubble types are shown with orange points, Sa–Sbc with blue points, and all types Sc and later with green. **Right panel**: The sub-galactic main sequence of all SFGs with unknown morphological classifications (red points) overplotted on the SGMS of galaxies with known morphological types (blue points). The dotted line is the best fit for galaxies with unknown morphologies, and the solid line in both panels is the best-fit for the combined morphological groups.

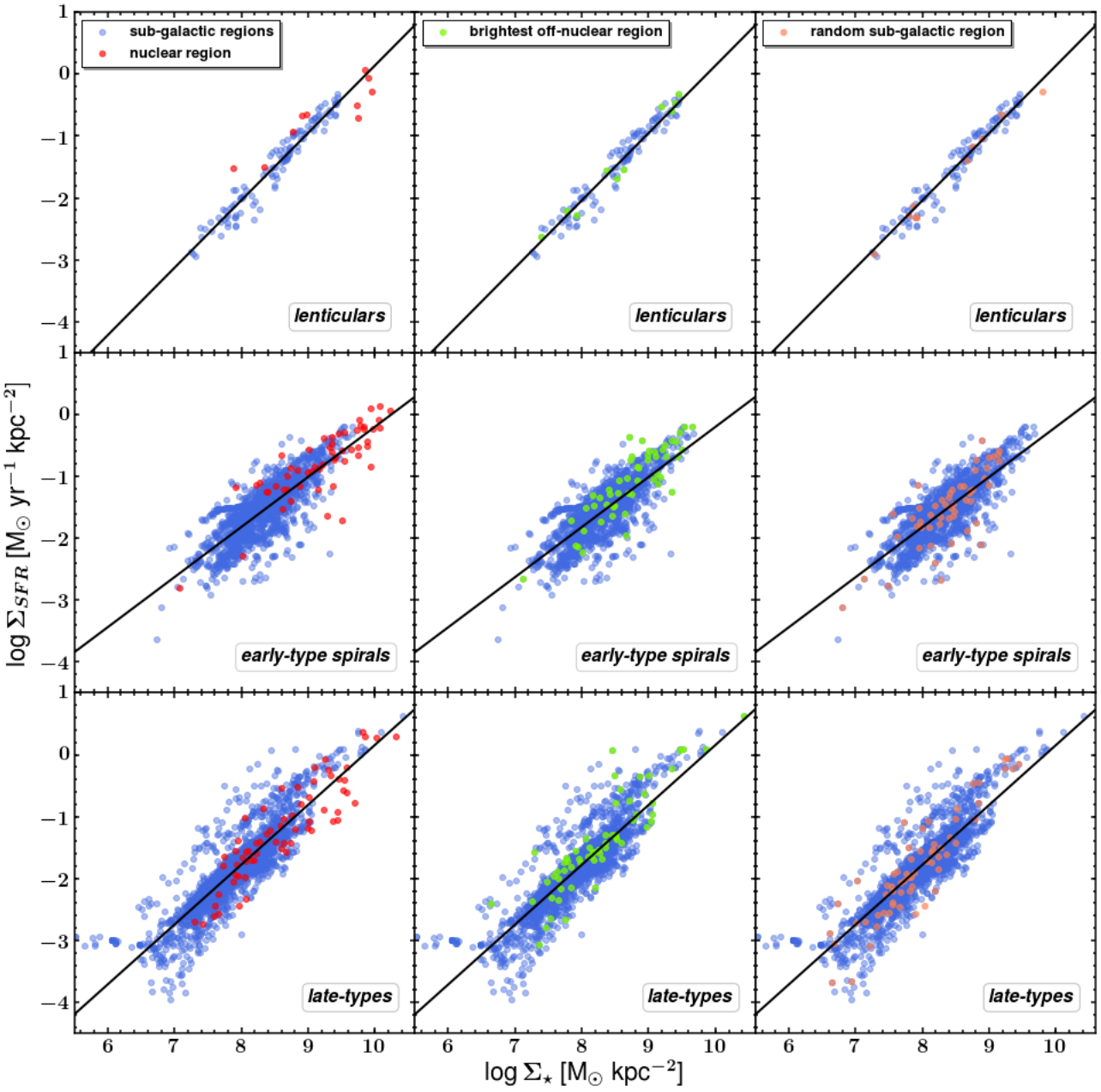


**Figure 5.4.7:** The sub-galactic main sequences calculated for different morphological groups (Top row: E to SO/a, middle row: Sa to Sbc, bottom row: Sc and later). The blue points in all panels represent all the sub-galactic regions from the galaxies in the group shown. The nuclear regions are indicated with red points in the left panels, the brightest off-nuclear regions from each galaxy are shown with green points in the middle panels, and randomly-drawn regions from each galaxy are shown with orange points in the right panels. The best fit to the SGMS (blue points) is shown with black lines.

the nucleus may contain some bulge light which would reduce the inferred sSFR in these regions. Furthermore, in cases of irregular galaxies with no definable nucleus or multiple galaxy systems (e.g., mergers), the coordinates may not target precisely the nucleus. However, 75% of the brightest off-nuclear regions are 1 kpc from the nucleus, 18% lie at distances between 2 and 4 kpc, and only 7% are $> 4$ kpc. This confirms the general trend that the circumnuclear area is where star-formation activity and stellar mass concentration peak.

The (circum-)nuclear regions of galaxies follow the same correlation as the rest of the sub-galactic regions (Figure 5.4.1, left panel) with similar scatter 0.34 dex. Not only do the nuclear regions follow the normal SGMS, they also closely correlate with total galaxy stellar mass (Figure 5.3.1). The scatter is 0.39 dex, moderately larger than for the MS and SGMS. The nuclear MS (NMS) separates from the global MS with increasing stellar mass. To investigate the relation between the total and nuclear SFR at different masses, we measured the ratio of nuclear to total SFR in the entire stellar mass range as well as in mass bins (Figure 5.4.10) and performed linear regression fitting for the binned values to quantify the ratio. The best-fit line is expressed by:

$$\log(\frac{\mathrm{SFR_{nuclear}}}{\mathrm{SFR_{Total}}}) = (-0.37 \pm 0.02)\ \log(\frac{M_\star}{10^{10}\mathrm{M}_\odot}) + (-0.73 \pm 0.02) \tag{5.8}$$

The scatter around the best-fit line is 0.33 dex. Because the bulge component in massive galaxies is larger relative to the disk, the ratio of nuclear to total SFR decreases with stellar mass. This is in agreement with our result (Figure 5.4.10). In contrast, the disk SFR is expected on average to show less variation with increasing stellar mass. To verify this, we measured the ratio of SFR in the 5th brightest off-nuclear region (which is well separated from the nuclear region) to total SFR with respect to total $M_\star$ using the 230 galaxies having at least 5 apertures. Indeed the average $\mathrm{SFR_{Region}/SFR_{Total}}$ (Figure 5.4.10) is nearly independent of galaxy mass, having a slope of $-0.15$ and a scatter of 0.31 dex.

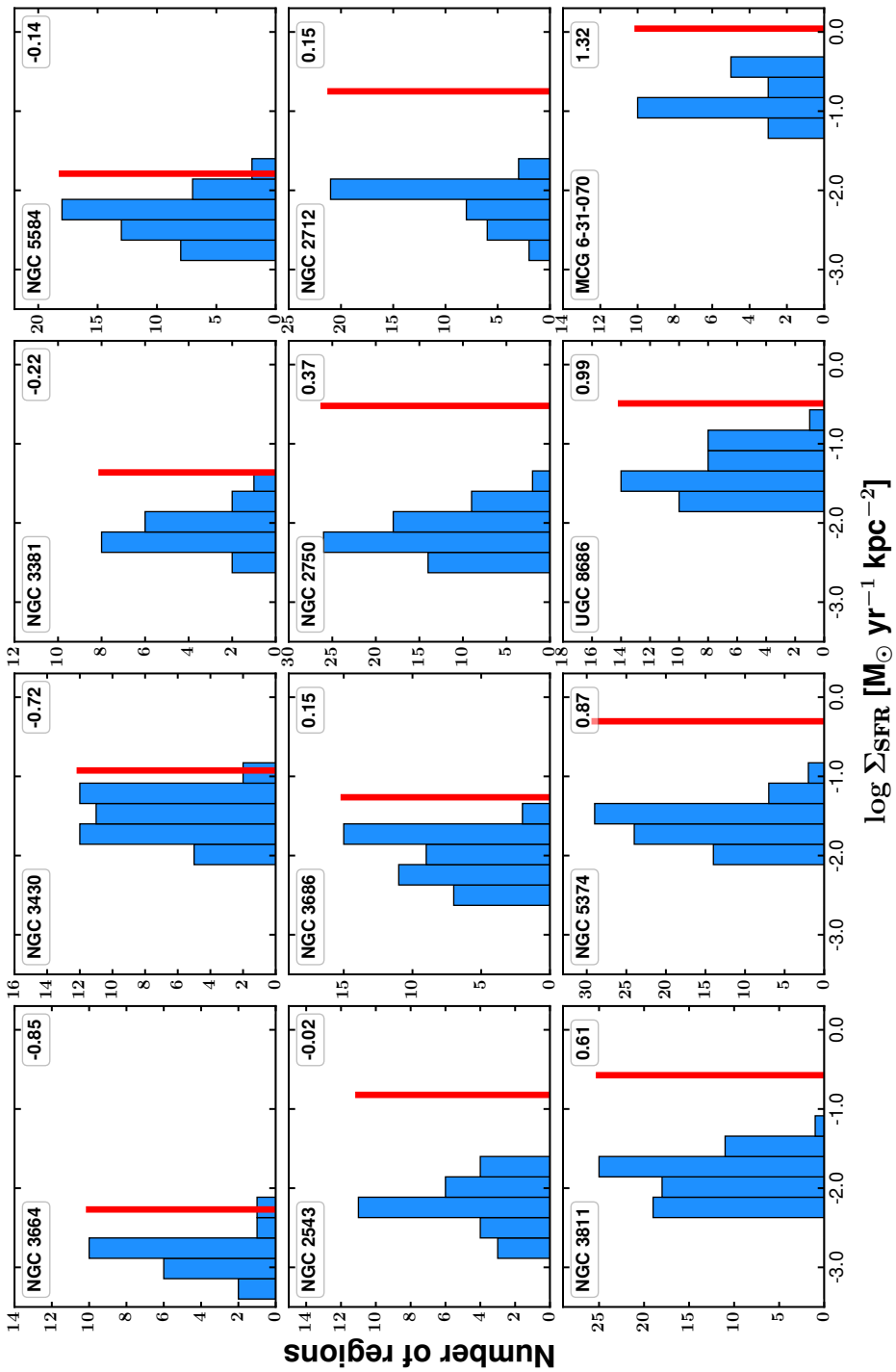


**Figure 5.4.8:** The histograms of off-nucleus $\Sigma_{\rm SFR}$ within 12 galaxies of different SFR (0.14 – 20.9 $M_\odot$/yr) and stellar mass content ($10^{9.05} - 10^{11.17}$ $M_\odot$), chosen to have a large number of apertures ($> 15$). The red bars indicate $\Sigma_{\rm SFR}$ of the nuclear region. The total log SFR of each galaxy is given at the top right corner of each panel in units of log [$M_\odot$ yr$^{-1}$].

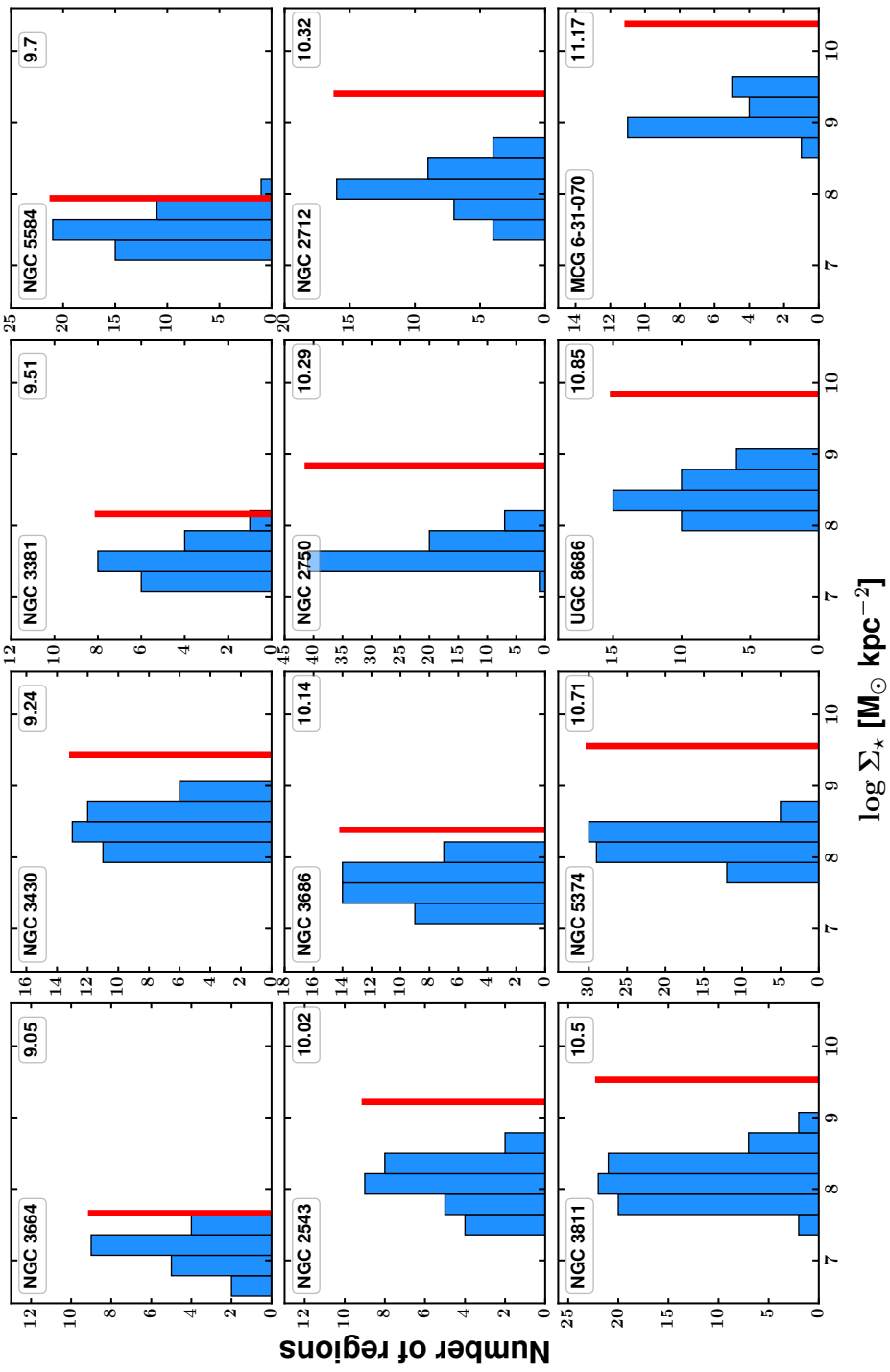


**Figure 5.4.9:** The histograms of $\Sigma_\star$ for off-nucleus regions of the 12 galaxies presented in Figure 5.4.8. The red bars indicate $\Sigma_\star$ of the nuclear region. The total stellar mass of each galaxy is given at the top right corner of each panel in units of $\log(M_\star/M_\odot)$.

## 5.5 Discussion

Although our derived (SG)MS parameters are within the ranges reported in the literature, there are still differences between our results and studies at similar redshifts. These differences reflect the diversity in the definition and selection of SFGs samples as well as the methods used to determine SFR and stellar mass.

### 5.5.1 The global MS of star formation

Previous authors have found that MS slopes range from $\alpha = 0.6$ to 1 (Rodighiero et al. 2011; see also Table 4 of S14). Low-$z$ studies, comparable with the redshift range of our sample, e.g., Whitaker et al. (2012) (W12) or results from the CALIFA (Sánchez et al. 2012) survey (e.g., D16; C16) reported sub-linear slopes, while Elbaz et al. (2011) on the other hand found a MS slope of 1. As discussed in detail by S14, this range of MS slopes is attributed to a number of factors including the methods used to determine SFR and stellar mass. Most of the variation however arises from sample selection. Selecting only actively star-forming galaxies produces MS slopes closer to unity, while a mixture of star forming and passively evolving populations will produce sub-linear slopes (S14). W12 showed that massive quiescent galaxies have lower sSFRs and that the MS slope depends on galaxy colors, with redder dust-attenuated populations having shallower slopes than blue, low-dust galaxies. Furthermore, color-based criteria such as the $BzK$ two-color selection or more generally any technique that selects blue objects will emphasize the most active SFG populations, producing steep MS slopes (Karim et al. 2011).

Our representative sample of nearby IR-selected star-forming galaxies defines a MS with $\alpha_{\rm MS} = 0.98$. This result is in perfect agreement with Elbaz et al. (2011), who also used an IR-selected low-$z$ sample similar to the SFRS. On the other hand, our result differs from the sub-linear MS slopes found in other low-$z$ works, mostly because of sample selection effects. For instance, W12 used a two-color diagram ($U - V$ versus $V - J$) to mostly exclude quiescent galaxies from their analysis and found $\alpha_{\rm W12} = 0.6$. C16 used the CALIFA survey clipping out high-inclination galaxies and therefore not mapping the entire range of conditions in SFG populations and found $\alpha_{\rm C16} = 0.81$.

Unrecognized AGN emission can result in unreliable SFR and stellar-mass determinations, affecting the MS slopes in ways difficult to quantify. W12 used rest-frame colors to distinguish between quiescent and star-forming galaxies, but AGN or composite objects were not necessarily identified or excluded. D16 excluded only type-1

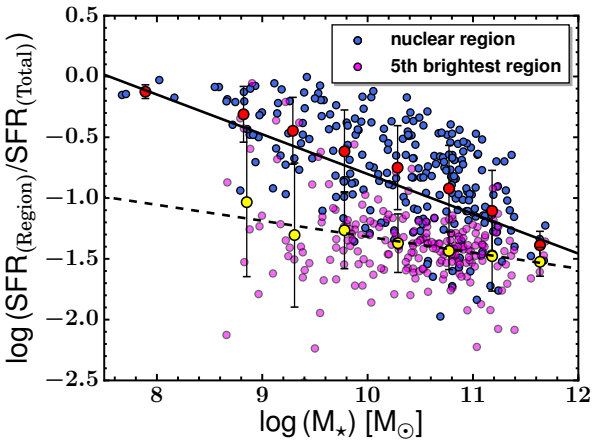


**Figure 5.4.10:** The ratio of nuclear (central 1kpc diameter) to total SFR as a function of total stellar mass (blue points) and the corresponding ratio of the 5th brightest off-nuclear region to total SFR (magenta points). The red points are the nuclear-to-total SFR medians in mass bins and the yellow points are the medians of the 5th brightest region to total SFR, both shown with $1\sigma$ error bars. Due to the small number of galaxies at the low-mass end, we calculated the mean SFR ratio there in a wider bin, from 7.5–8.5 $\log(M_\star/M_\odot)$, but all other medians were calculated in 0.5 dex mass bins.

Seyferts from their sample without accounting for obscured or low-luminosity AGNs. Our approach distinguishes between different activity classes and selects pure SFGs with a combination of IR and optical emission-line diagnostics (Maragkoudakis et al. in preparation). In this way we are able to identify and exclude obscured AGNs and galaxies having contribution from both star-formation and AGN activity (composite objects), providing a clean sample of bona-fide SFGs.

The way stellar masses are determined can lead to additional discrepancies in the MS. Most mass-to-light ($M/L$) ratio conversions assume a galaxy color dependence, the definition of which relies on the assumed model SFH and metallicity. Different combinations of SFH and metallicities will yield different mass-to-light ratio calibrations, resulting in different derived stellar masses between different studies. In addition, for a given color-$M/L$ calibration, dust reddening corrections affect galaxy color determination, introducing additional scatter in the derived stellar masses. The above effects can also be important when considering a mass dependence of the MS slope with a curvature form description (e.g., Whitaker et al. 2014; Lee et al. 2015, Schreiber et al. 2015) rather than a linear form. Differences between stellar mass calibrations cause scatter in the horizontal location of a galaxy in the SFR–$M_\star$ plane, but assuming

a mass-dependent MS slope (i.e., curvature) can also increase the difference between the derived MS slopes reported in the literature. W12 calculated stellar masses using SED modeling, while D16 summed the individual spaxel masses derived from stellar population fits to the optical spectrum. In both cases the results depend on several parameters such as the assumptions of SFHs, the choices of stellar population models, stellar metallicities, dust treatment, or the sampling of these parameter spaces (Conroy 2013). Moreover, for the galaxies hosting AGNs, the SED modeling and stellar population synthesis methods can greatly overestimate stellar mass when the AGN continuum is not properly treated, i.e., when both the AGN and stellar components are modeled only with stellar populations. The SFRS stellar masses in this paper were determined photometrically using IRAC 3.6 $\mu$m measurements in a manner consistent with the well-calibrated $K$-band based determinations (Bonfini et al. in preparation). Because these $M/L$ calibrations are less dependent on stellar population details and dust reddening, they produce robust stellar mass estimations.

Different SFR calibrations can also influence the derived MS properties. Luminosity-to-SFR conversions can vary by up to ∼50% and create large offsets between different studies (e.g., KE12, S14). Davies et al. (2016) showed that even when the most commonly used luminosity to SFR calibrations are re-defined and re-calibrated to each other, there is still a non-linear relation between them, and therefore different SFR indicators will produce different SFR–$M_\star$ slopes. W12 determined SFRs from the combined UV and total IR emission. The total IR luminosity was estimated from a conversion based only on the observed 24 $\mu$m flux density and was derived from a single template that is the log average of the Dale & Helou (2002) templates. The 24 $\mu$m flux however is sensitive to AGN emission, so for AGN hosts some fraction of 24 $\mu$m emission must originate in those AGN. D16 used the stellar population synthesis results of the mass initially turned into stars, with an arbitrary choice of star formation time scale for the determination of SFR. These results are model-dependent and especially unreliable for galaxies hosting AGNs. The use of IRAC 8.0 $\mu$m avoids these difficulties and provides sufficient spatial resolution to isolate distinct regions within galaxies.

### 5.5.2 The Sub-galactic Main Sequence

The SGMS holds at ∼1 kpc scales with a slope of $\alpha_{\rm SGMS} = 0.91$ and dispersion of $\sigma_{\rm SGMS} = 0.31$ dex, similar to the integrated MS. This similarity implies that the ongoing star formation and stellar mass buildup from past star formation trace each other on both global and sub-galactic scales. However, because star formation is a local process, its sub-galactic manifestation and scaling relations are probably more

fundamental compared to their integrated analog. This view is supported by the SGMS from randomly drawn sub-galactic regions (Figure 5.4.7). Random regions produce the same SGMS slope and little more scatter than for all regions combined, implying that any individual region of any galaxy is likely to be representative of the same $\Sigma_{\rm SFR}$–$\Sigma_\star$ correlation as the global SGMS.

Our derived SGMS slope is consistent with W13 and Magdis et al. (2016), who reported $\alpha_{\rm W13} = 0.95$ and $\alpha_{\rm M16} = 0.91$ respectively while sampling similar or larger physical scales. Nevertheless, while C16 have presented sub-galactic MS results in 0.5 – 1.5 kpc scales showing a shallower slope ($\alpha_{\rm C16} = 0.68$), extra caution is needed when the global SFR calibrations are used on scales smaller than 1 kpc. Below 1 kpc several factors introduce stochasticity. Among the most important are incomplete sampling of the IMF, leading to large fluctuations in the luminosity of the SFR tracers, the non-applicability of the continuous star formation assumption embedded in the global SFR recipes, or in cases where the regions are smaller than the Strömgren diameters of HII regions, indirect tracers such as H$\alpha$ can trace diffuse ionized gas located several parsecs away from any young star (see KE12 for details). These effects would introduce scatter to the derived SFR, possibly resulting in the sub-linearity reported by C16 or D16.

The SGMS slope increases from Sa to later types. The “late-type" galaxies (Sc–Irr) show a linear $\Sigma_{\rm SFR} - \Sigma_\star$ relation ($\alpha = 0.97$), compared to the sub-linear slope ($\alpha = 0.81$) of the Sa–Sbc group (Figure 5.4.7), bearing the closest resemblance to the global MS characteristics. The sub-linearity in this group indicates that the sSFR in the most massive regions is not as high as in the disk. In contrast, the unity slope in “late-types" suggests that the sSFR in all sub-galactic regions is similar regardless of local mass, and all regions of the galaxy grow at a similar rate. On the other hand, D16 found that while the global MS slope increases from Sa to Sd Hubble types, the corresponding resolved MS slopes are fairly similar.

The morphology dependence of the SGMS slope can be attributed to the way in which gas is distributed in different galaxy types. Magdis et al. (2012) showed that gas fractions correlate strongly with sSFR, i.e., that $M_{gas}/M_\star$ increases strongly with sSFR at a given redshift. Tacconi et al. (2013) also showed that at constant stellar mass, a galaxy's SFR is mainly driven by the available molecular gas reservoir. Furthermore, the non-linear relationship between the disk-averaged surface densities of star formation and total (atomic and molecular) gas, described by the Kennicutt-Schmidt (KS) law, has a slope of ∼1.4–1.5 (KE12) and states that $\Sigma_{\rm SFR}$ is higher in regions of higher gas density compared to lower gas density regions. Combining the SGMS description ($\Sigma_{\rm SFR} \propto \Sigma_\star^a$) with the KS law ($\Sigma_{\rm SFR} \propto \Sigma_{gas}^{1.4}$), gas mass density scales with stellar

mass density as $\Sigma_{gas} \propto \Sigma_{\star}^{\alpha/1.4}$. This yields that gas concentration, in general, is higher in more massive sub-galactic regions, and this effect is stronger in "late-type" galaxies with an SGMS slope $\alpha = 0.97$ ($\Sigma_{gas} \propto \Sigma_{\star}^{0.69}$) compared to "early-type spirals" with slope $\alpha = 0.81$ ($\Sigma_{gas} \propto \Sigma_{\star}^{0.58}$).

The "lenticulars" (E–S0/a) group has a steep SGMS slope ($\alpha = 1.09$; Figure 5.4.7). This implies that while overall star forming activity in early types is considerably lower due to limited gas, the regions within them that are forming stars have similar properties with later Hubble types. The small number of early-type galaxies (E–S0) in our sample may on one hand not be representative of the general early-type populations, possibly sampling those with highest activity, but nevertheless our current results shows that star formation in bulge-dominated systems follows a similar trend as those in later Hubble types.

The SGMS of all morphologically classified galaxies combined (Figure 5.4.6) has the same properties as the "all-galaxies" SGMS (of known and unknown morphological Hubble types) showing the same slope and dispersion. In contrast, the morphologically unclassified galaxies have a shallower slope of $\alpha = 0.72$ (Figure 5.4.6). The main cause for this difference is that the bulk of unclassified galaxies occupy only the mid to high-stellar mass end with only 8% below $\log(M_{\star}/M_{\odot}) = 9.5$. As shown by Lee et al. (2015), galaxies more massive than $M_{\star} \gtrsim 10^{10}$ have a much lower average sSFR, and additionally the MS appears to flatten at masses above that characteristic mass. Star formation in low-intensity outer disk regions is generally more stochastic and bursty, and the existence of extended UV disks at extreme galactocentric distances (e.g., Thilker et al. 2005; Gil de Paz et al. 2005) supports this view. Thilker et al. (2007) showed that certain extended UV disk galaxies show UV-bright/optically faint emission features beyond the anticipated location of the star formation threshold (e.g., Martin & Kennicutt 2001), which can therefore explain the increasing SGMS slope in regions of lower surface brightness. In addition, the "early-type spirals" and "late-types" groups have a fairly good sampling of the lower-stellar mass end giving a more thorough description of the SGMS. Out of the morphologically classified galaxies, the "late-types" being both the most numerous in our sample and having the largest number of apertures relative to the other morphological groups, appear as the main drivers of both the MS and SGMS. This is further justified from the fact that the "late-types" SGMS has closer characteristics (slope and normalization) to the "all-galaxies" SGMS.

Single-galaxy SGMSs formed from regions within individual galaxies are similar to the SGMS formed from all regions in all galaxies. The average sSFR measured from the local SFR/$M_{\star}$ ratio of all sub-galactic regions within each galaxy is within 0.3 dex

of the total galaxy sSFR (Figure 5.4.5), further supporting the view that kpc-scale star-forming activity is representative of the total. Given the power-law form of the SGMS (SFR $\propto M^{\alpha}$), the sSFR is accordingly described as: SFR/$M_{\star} \propto M^{\alpha-1}$. Therefore, galaxies with steeper individual SGMS slopes lie above the line of equality in Figure 5.4.5 while those with shallower slopes lie below. In addition, bulge-dominated systems are expected to have shallower average sSFR measured from their sub-galactic regions, because the sSFR in the massive bulge regions is generally lower compared to the disk. These systems would lie below the line of equality in Figure 5.4.5. The morphologically unclassified galaxies are predominately located bellow this line, indicating massive bulge-dominated systems. This is in agreement with the fact that the unclassified group, constituting mostly massive galaxies, has a shallower SGMS slope (0.72). The average SGMS slope of individual galaxies ($\alpha = 0.95$) coincides with the "all-galaxies" SGMS slope ($\alpha_{\rm MS} = 0.91$). Galaxies with total $M_{\star} > 10^{10}\,{\rm M}_{\odot}$ or total SFR $> 6\,{\rm M}_{\odot}$/yr have sub-linear ($\alpha < 1$) SGMS slopes, meaning that the sSFR declines with mass. This is expected in earlier Hubble types, and it is evident in the "early-type spirals" morphological group which contains most of the high-$M_{\star}$ and high-SFR end. This result also underlines that incomplete samples or samples selected at mid to high SFR or stellar mass will report a sub-linear SGMS, similar to the results of the morphologically unclassified galaxies in our sample. Our analysis, in a complete sample covering 4 orders of magnitude in both total SFR and $M_{\star}$, shows that the SGMS is not necessarily sub-linear. In contrast the "late-types" group is mostly found at the low-$M_{\star}$ low-SFR end with super-linear slopes. Therefore, a complete framing of the SGMS requires both a wide range in the SFR–$M_{\star}$ space and a mixture of morphological types.

### 5.5.3 The nuclear and circumnuclear regions

Despite the spatially resolved correlation observed for star-forming regions in galaxies, the nuclear regions have not been investigated yet in the literature. Our study shows that the nucleus is among the most active (if not the most active) regions of star formation (Figure 5.4.8), even in the case of the gas-rich late-type galaxies where star formation mainly occurs in the midplane of the thin disks. Similarly, the nucleus has the highest stellar mass concentration (Figure 5.4.9), as expected, because it resides at the center of bulge. The nuclear $\Sigma_{\rm SFR} - \Sigma_{\star}$ correlation, formed exclusively from the nuclear regions of SFGs [1], is almost as tight as the SGMS and MS.

[1] Because the nuclear region potentially encompasses part of the circumnuclear star-forming activity, the nuclear SGMS should be better considered as a "circumnuclear" sequence.

The existence of the NMS suggests a connection between the global and (circum-) nuclear SFR. At the lowest stellar-mass end, the two sequences overlap, which is expected because this end is mostly populated by dwarf galaxies with major axes of ∼4–4.5 kpc, only slightly larger than the aperture used in the analysis. This effect diminishes as we examine more massive and larger galaxies, where the two sequences become distinct. The average logarithmic ratio of nuclear to total SFR (Figure 5.4.10) in the SFRS sample is $\log(\mathrm{SFR}_{(\mathrm{nuclear})}/\mathrm{SFR}_{(\mathrm{total})}) = -0.77$, but the value strongly depends on galaxy mass. The NMS can potentially be a key ingredient in understanding star-forming activity in the nuclear region and its connection to star formation in the main body of the galaxy. For instance, stars that are forming now in the centers of galaxies are the building blocks of bulges. Similarly, past (higher-$z$) star-forming activity in the nuclear regions of galaxies are responsible for the formation and the growth of present day (lower-$z$) bulges. The NMS can therefore provide evolutionary insights on the secular growth of bulges with respect to the total stellar masses of galaxies and their regulation through AGN. Because AGN accretion drives black hole growth, the NMS and its relation to the (SG)MS can be an alternative tool to the average black hole growth and mean stellar mass relation reported by Mullaney et al. (2012) to study growth of black holes and their influence on the nuclear/circumnuclear star formation.

The NMS and its relation to the total SFR may also be an asset in the study of AGN populations and specifically in the still open subject of AGN feedback. For instance, SED modeling codes (e.g., CIGALE; Burgarella et al. 2005, Noll et al. 2009) can simultaneously model and measure the AGN and star-forming luminosity components of galaxies. Comparing the nuclear SFR for a non-AGN host at a given stellar mass via the NMS and the corresponding nuclear SFR of an AGN host at the same stellar mass through SED fitting can provide insights on AGN feedback. Lower SED-derived SFRs compared to NMS-derived SFRs would be indicative of AGN-driven quenching of star formation (negative feedback), while the opposite case would imply AGN-driven boosting of star formation (positive feedback).

# 5.6 Conclusions

Based on a representative sample of local galaxies with a broad range in stellar mass ($7.7 < \log(M_\star/\mathrm{M}_\odot) < 11.7$) and SFR ($-2.2 < \log(\mathrm{SFR}/\mathrm{M}_\odot\mathrm{yr}^{-1}) < 2.1$), we have examined the MS of star formation in global and sub-galactic scales. Our main conclusions are as follows.

(i) The global SFR–$M_\star$ correlation of SFGs at low redshifts has a linear form with a slope of 0.98. The wide range of four orders of magnitude in stellar mass and SFR sets strong constraints on the derived slope and normalization of the MS, and combined with the fact that the SFRS sample is fully representative of the star-forming conditions in the local Universe, this work provides a comprehensive description of the MS of SFGs.

(ii) The correlation between $\Sigma_{\rm SFR}$ and $\Sigma_\star$ at kpc spatial scales within galaxies described by the SGMS has similar characteristics to the global MS. Because star-formation is primarily a small-scale phenomenon, the SGMS can be considered as more fundamental. This assertion is supported by the SGMS produced from random regions within galaxies being on average representative of the global MS characteristics.

(iii) The SGMS produced from sub-galactic regions of individual galaxies has on average the same characteristics as the composite SGMS from all galaxies. Sub- or super-linearity in the SGMS slope may be reported when the observed SFR–$M_\star$ range is limited or samples are not fully representative.

(iv) The slope of the SGMS differs among different Hubble types, increasing from Sa to Irr, explained by the variations of gas content between different morphological types. Furthermore, while bulge-dominated populations are considered quiescent, our S0–S0/a group shows that when star-forming activity is present it has similar characteristics to those in later Hubble types.

(v) The circumnuclear $\Sigma_{\rm SFR}$ has a similarly tight correlation with the $\Sigma_\star$ compared to the rest sub-galactic regions.

(vi) The nuclear SFR correlates with total stellar mass forming a nuclear MS, which can be used to examine the bulge and BH growth of galaxies at different redshifts as well as characterize feedback processes (positive or negative) between AGN and star-forming activity. The ratio of nuclear to total SFR is mass-dependent, consistent with a slope of $-0.36$.

In future work we intend to investigate the dependence of the SGMS parameters on the size of the physical regions examined by sampling varying sized regions and quantifying the impact of aperture effects. Our ongoing H$\alpha$ imaging campaign at the 1.3-m Ritchey-Crétien telescope at the Skinakas Observatory in Crete will allow us to derive H$\alpha$-based SFRs for the same sample of galaxies, addressing the dependence of the SGMS on different SFR calibrations. Lastly, using SED modeling, we will be able to isolate the AGN contribution in AGN hosts and deliver the SGMS of different AGN populations as well as estimate the total and resolved sSFR functions of galaxies along the (SG)MS plane in different activity types.

We would like to thank the referee for the constructive comments and suggestions

which have improved the clarity of this paper. AM and AZ acknowledge funding from the European Research Council under the European Union's Seventh Framework Programme (FP/2007-2013) / ERC Grant Agreement n. 617001. This work is based [in part] on observations made with the Spitzer Space Telescope, which is operated by the Jet Propulsion Laboratory, California Institute of Technology under a contract with NASA. For this research, we have made extensive use of the Tool for Operations on Catalogues And Tables (TOPCAT) software package (Taylor 2005).

# 6 Conclusions & Future Perspectives

## 6.1 Summary of the results

The present thesis work was focused mainly on two major concepts: (a) the determination of the primary source of ionization in a sample of 369 IR-selected nearby galaxies, obtaining detailed activity demographics and host-galaxy properties, and (b) The comprehensive study of the "main sequence" of star-formation in spatially resolved sub-galactic scales.

### 6.1.1 Aperture effects

Using a sample of 14 nearby galaxies, we examined the impact of host-galaxy light contamination in their nuclear activity classification (aperture effects), using both observed long-slit spectra and simulated elliptical-aperture spectra of different sizes.

- We conclude that the degree of change in the activity classification depends on galaxy morphology and nuclear activity type.
- Starlight removal techniques can mitigate but not fully remove the effect of host galaxy contamination in the nuclear aperture.

- Galaxies with extra-nuclear star formation can show higher [O III] $\lambda$5007/H$\beta$ ratios with increasing aperture, in contrast to the naive expectation that integrated light will only dilute the nuclear emission lines.

- We calculated the mean dispersion for the diagnostic line ratios used in the standard BPT diagrams as a function of the central aperture of spectral extraction, in order to obtain an estimate of the uncertainties resulting from aperture effects. We find that the largest scatter is observed in the [O III] $\lambda$5007/H$\beta$ ratio of Seyfert galaxies. This is expected as the intensity of the higher ionization [O III] $\lambda$5007 line drops abruptly as we move farther out from the center of AGN-hosting galaxies.

### 6.1.2 Activity demographics and host-galaxy properties of local IR-selected galaxies

Using a fully representative sample of IR-selected galaxies in the local Universe, we have presented the activity demographics, nuclear metallicities, and distributions of: $L(60\mu\mathrm{m})$, $F60/F100$, $L_{\mathrm{H}\alpha}/\mathrm{kpc}^2$, and total stellar mass of the 369 galaxies in the SFRS, and derived metallicity gradients for a sub-sample of 12 galaxies. Our main conclusions are as follows:

- The activity classification of IR-selected galaxies in the local Universe yields 71% SFGs, 13% Seyferts, 13% LINERs, and 3% TOs.

- Classification using integrated and nuclear IRAC colors based on the Stern et al. (2005) IR color diagnostics identifies 10 AGN missed by the BPT method.

- The MEx and CEx classification methods are in agreement with the BPT classification for 69% and 63% of galaxies respectively.

- The inferred fraction of LLAGN galaxies in the local Universe using IR sample-selection criteria is small compared to SFGs.

- Sy and TO activity classes are preferentially found at relatively high 60$\mu$m luminosities ($L(60\mu\mathrm{m}) > 10^8\mathrm{L}_\odot$) while LINERs have lower $L(60\mu\mathrm{m})$ values with few at luminosities higher than $10^{9.5}\mathrm{L}_\odot$, indicative of hosts with no intense star-formation. SFGs cover a broad range in L(60$\mu$m) between $6.5 < \log(L(60_{\mu\mathrm{m}})/\mathrm{L}_\odot) < 11.18$.

- Seyfert galaxies have the highest $F60/F100$ ratio attributed to AGN radiation heating dust to high temperatures. TOs and SFGs have the same median dust-temperatures implying star-formation as the dominant dust-heating mechanism. LINERs on the other hand are confined to lower dust-temperatures indicative of lower intensity radiation field and dust-deprived environments.

- The stellar mass distribution of SFGs covers a broad range ($10^{7.79} - 10^{12.14}$ $M_\odot$). TOs and Seyferts are found exclusively at high stellar-mass hosts, however we consider their mass estimations mostly as upper limits because the non-stellar emission component dilutes the $M/L$ calibrations overestimating the stellar mass. LINERs, which are now strongly considered as galaxies powered by non-AGN processes (Belfiore et al. 2016b), are found at high stellar-masses (with a median of 10.5 $M_\odot$).

- SFGs have a wide distribution of nuclear $L_{H\alpha}$ surface densities ($L_{H\alpha}/kpc^2$), and TOs show a similar distribution. Sy nuclear $L_{H\alpha}/kpc^2$ is concentrated above $10^{39.5}$ erg $s^{-1}kpc^{-2}$, with a median $L_{H\alpha}/kpc^2 = 10^{41.0}$ erg $s^{-1}kpc^{-2}$, while LINERs on the other hand are mainly distributed at lower values with median $L_{H\alpha}/kpc^2 = 10^{40.2}$ erg $s^{-1}kpc^{-2}$.

- Based on their host-galaxy and nuclear properties we conclude that, the dominant ionizing source in the SFRS (PSC$z$) TOs is star-forming activity. LINER host-galaxy characteristics resemble those of passive early-type systems, indicating older stellar populations as their main ionizing source, rather than AGN activity, in agreement with independent evidence along the same line (Stasińska et al. 2008, Belfiore et al. (2016a)).

- The SFRS SFGs have a narrow range of abundances close to solar and have flat metallicity radial profiles, as found from the analysis of a sub-sample of 12 galaxies.

### 6.1.3 The SGMS and NMS of local star-forming galaxies

We performed a detailed study of the "main sequence" of star forming galaxies in spatially resolved sub-galactic scales, using a representative sample of local galaxies with a broad range in stellar mass ($7.7 < \log(M_\star/M_\odot) < 11.7$) and SFR ($-2.2 < \log(SFR/M_\odot yr^{-1}) < 2.1$). We describe a sub-galactic main sequence (SGMS) relating star formation rate surface density ($\Sigma_{SFR}$) and stellar mass density ($\Sigma_\star$) for distinct

regions within star forming galaxies, including their (non-AGN) nuclei. Our main conclusions are as follows.

- The SGMS holds down to ∼1 kpc scales with a slope of $\alpha = 0.91$ and a dispersion of 0.31 dex, similar to the well-known main sequence (MS) measured for globally integrated star formation rates (SFRs) and stellar masses.
- The SGMS slope depends on galaxy morphology, with late-type galaxies (Sc–Irr) having $\alpha = 0.97$ and early-type spirals (Sa–Sbc) having $\alpha = 0.81$.
- The SGMS constructed from sub-regions of individual galaxies has on average the same characteristics as the composite SGMS from all galaxies.
- The SGMS for galaxy nuclei shows a dispersion similar to that seen for other sub-regions.
- Sampling a limited range of SFR–$M_\star$ space may result in either sub-linearity or super-linearity of the SGMS slope, partially explaining the range of results found in different MS surveys.
- For nearly all galaxies, both SFR and stellar mass peak in the nucleus, indicating that circumnuclear clusters are among the most actively star-forming regions in the galaxy and the most massive.
- The nuclear SFR also correlates with total galaxy mass, forming a distinct sequence from the standard MS of star-formation, with a shallower slope of $\alpha_{\rm NMS} = 0.66$ compared to the near-linear slope ($\alpha_{\rm MS} = 0.98$) of the MS. The nuclear main sequence is useful for studying bulge growth and for characterizing feedback processes connecting AGN and star formation.

## 6.2 Future plans

### 6.2.1 The bivariate sSFR–$M_\star$ function

As part of this thesis work we have extended the work of Bonfini et al. (in preparation) who calculated the univariate and bivariate SFR and stellar mass functions for the overall SFRS sample by decomposing those functions for AGN and non-AGN populations based on our derived activity classification (Chapter 4). We found that

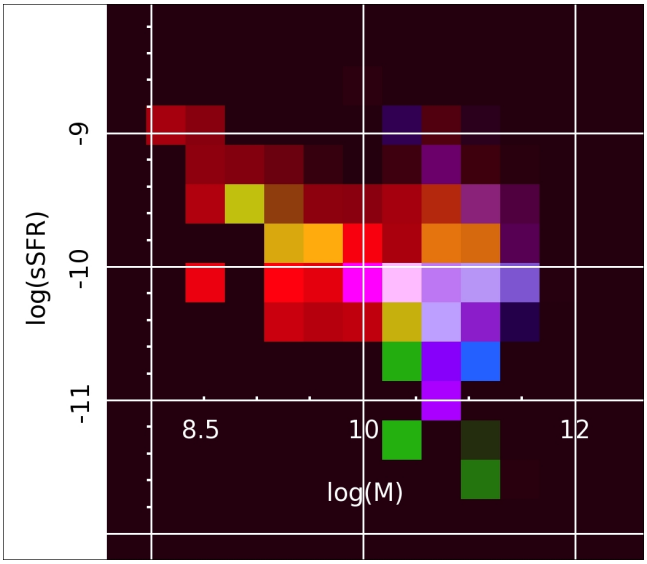


**Figure 6.2.1:** The bivariate sSFR–$M_\star$ function for galaxies of different activity classes, binned in 0.4 x 0.3 dex bins. The abscissa shows the total stellar mass and the ordinate shows the sSFR. Red colors correspond to SFGs, green for Seyferts and TOs, and blue for LINERs.

both star-forming and AGN host galaxies span the same stellar-mass range, with LINERs observed towards intermediate to higher galaxy stellar masses and lower sSFR (in agreement with our findings reported in Chapter 4). This is consistent with previous studies showing that they are preferably found in more massive and passive galaxies.

Furthermore, we have performed an initial assertion of the location of the AGN host galaxies on the "main sequence" plane. Specifically, we find the relative contribution of the different galaxy activity types in the bivariate $M_\odot$ – sSFR function plane (Figure 6.2.1). For the star-forming galaxies we see the signature of the "main sequence", but most importantly we find that Seyfert galaxies and transition objects appear to also form a "main sequence" but at a different slope.

However, the above results are in a preliminary phase, due to the fact that SFR and stellar mass estimation of AGN hosts are based on non-AGN calibrations, and therefore are only considered as upper limits. Using our advanced SP SED method we will be able to precisely decompose the star forming and AGN contribution in AGN hosts and derive accurately stellar mass and SFR measurements, refining the previous results.

### 6.2.2 Spectro-Photometric SED Fitting

Within the context of this thesis we have initiated a major ongoing effort that sets the basis for the "next step" in the SED modeling of galaxies. The current applications of standard photometric SED fitting methods suffer to a great extent from degeneracies, where dramatically different star-formation histories, or mixtures of populations of different ages, metallicities, and dust attenuation can reproduce remarkably similar SEDs. Such degeneracies are affecting to a smaller degree optical population synthesis codes (e.g., Leitherer et al. 1999, Cid Fernandes et al. 2005) which fit the optical spectra of galaxies using combinations of single stellar population (SSP) libraries. Characteristic absorption features in the optical spectra of galaxies are indicative of the ages and metallicities of the stellar populations composing the spectra. Therefore, the key to break such degeneracies is imprinted in the spectra information of galaxies. The identification of the stellar population properties can therefore set better constrains on the derived stellar population and ISM properties obtained from SED fitting.

We have introduced a novel approach in the SED modeling of galaxies, by incorporating spectroscopic information alongside the photometric data. Specifically, we are using the Python[1] version of CIGALE (Burgarella et al. 2005) SED fitting code and included measurements from stellar-population sensitive spectral indices, in order to obtain self-consistent solutions on the stellar populations from SED and the optical spectral data. We achieve this by adding 10 narrow spectral regions (Figure 6.2.2) to our SED analysis. These spectral regions are based on the Lick indices (Worthey & Ottaviani, 1997). They are chosen to be prominent stellar features that are sensitive to the ages and metallicities of the stellar populations. This is of great importance since it limits the degeneracies arising in the standard (photometric-only) SED fitting process alone, and therefore helps us derive more precise measurements for the galactic parameters. Deliberately, Blamer series absorption lines were excluded from the choice of spectral indices to avoid confusion with the corresponding emission components present at the same wavelengths.

Optical spectra acquired from long-slit, fiber, or IFU spectroscopy, often represent only a portion of the galaxy observed. This is evident especially in low-redshift surveys where depending on the galaxy's size and distance aperture effects are introduced as the spectroscopic unit encompasses light from certain portions of the galaxy. The photometric information on the other hand corresponds, for the majority of cases, to the entire galaxy surface. This introduces a complication, as the simultaneous study

[1] http://cigale.lam.fr/

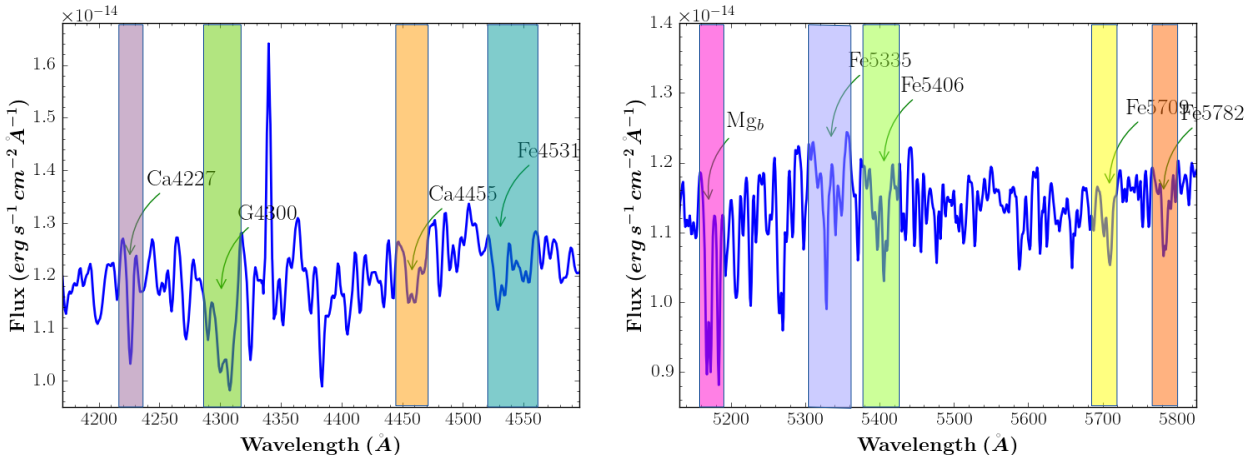


**Figure 6.2.2:** The regions for 9 (out of 10) age-sensitive Lick indices in the optical spectrum of galaxies used in our SP-SED modeling method (the 10th index at 6200 Å lies outside the regions shown). We measured the EW of these indices and used them along with the broadband photometry in the SED fitting process in order to use the joint power of broadband and spectroscopic information for deriving stellar population parameters.

and modeling of the photometric and spectroscopic properties of galaxies requires consistency between the regions where the information is extracted. We have overcome this difficulty using a combination of the standard photometric-only SED method and the equivalent width (EW) of the line indices from a given spectrum, regardless of the physical region they correspond to. Specifically, two steps are performed before the combined spectrophotometric modeling. First, we measure the (EW) of the line indices from the optical spectrum, and second we perform an initial standard SED fitting run, using only photometric data. Subsequently, using the measured EWs and the total galaxy continuum flux at the regions of the line indices, obtained from the best-fit standard SED model, we calculate the total fluxes of the line indices that now correspond to the entire galaxy. Having a consistent spectroscopic and photometric information we are now able to perform simultaneously Spectro-Photometric SED (SP-SED) fitting. Our SP-SED method has the advantage of operating in two modes depending on the galaxy's spectroscopic coverage. In one mode, where the spectrum corresponds to the entire galaxy, no EW measurements are performed, while in the second mode where the spectrum corresponds to a certain portion of the galaxy, the two-step process described previously is performed.

A demonstration of the SP-SED method is shown in Figure for galaxy IC 910. We

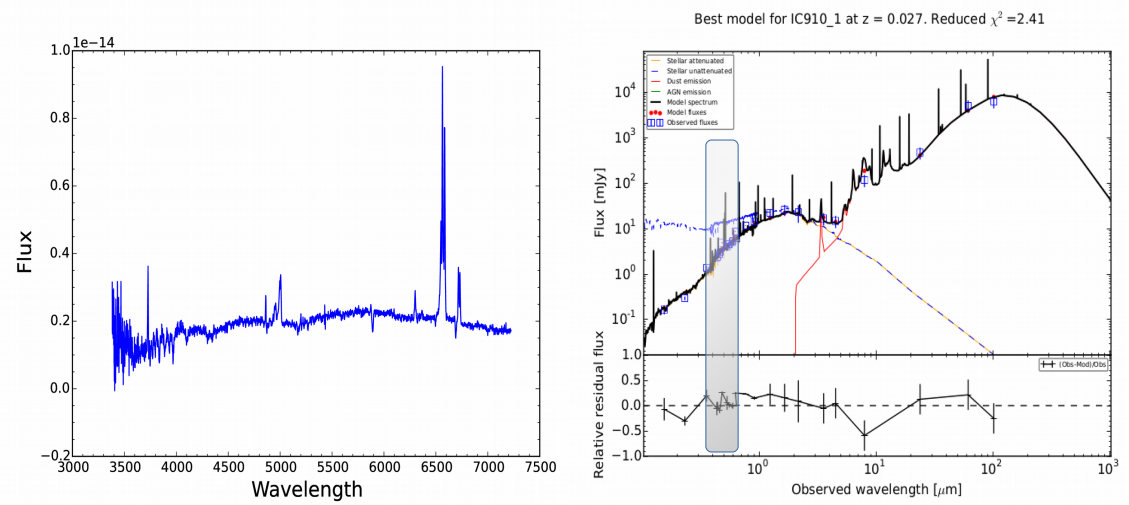


**Figure 6.2.3: Left**: The long-slit optical spectrum of galaxy IC 910 from which the EW of the Lick indices is measured. **Right**: the best-fit model from the SP-SED method along with the residuals (bottom). The shaded area indicates the region of the Lick indices used in the SP-SED method. Small blue boxes indicate the photometric and Lick-indices data, the blue line indicates the intrinsic (unobscured) stellar specrum, the red line indicates the dust emission, and the solid black line is the total SED spectrum fit to the spectro-photometric data.

fit the UV - FIR photometric data along with the spectral flux of the 10 Lick indices measured from a long-slit optical spectrum of galaxy IC 910 (left panel 6.2.3). The best-fit model of the SP-SED method along with the fit residuals is shown in the right panel of Figure 6.2.3. Figure 6.2.4 shows the comparison between the PDFs of different galaxy properties (galaxy mass, stellar mass of young populations, stellar mass of old populations, and SFR averaged over 10 Myrs), derived from the standard SED (blue lines) and SP-SED (red lines) method.

A comparison between the probability density function (PDF) of the derived properties with the standard SED and SP-SED methods, reveals impressive improvement in the determination of the actual galaxy parameters. The multi-modality often encountered in the derived PDFs of the standard SED method is clearly suppressed with the inclusion of spectroscopic data, and the peak of the distribution becomes noticeably prominent (Figure 6.2.4). As a result, the precision in the estimation of the galaxy properties becomes much higher. We clearly see that the SP-SED method suppresses the multiple modes present on the PDFs of the derived galaxy properties if we consider only the photometric data, allowing us to measure with much more precision these parameters. Similar improvement we see in the PDFs of other fitted parameters (e.g.,

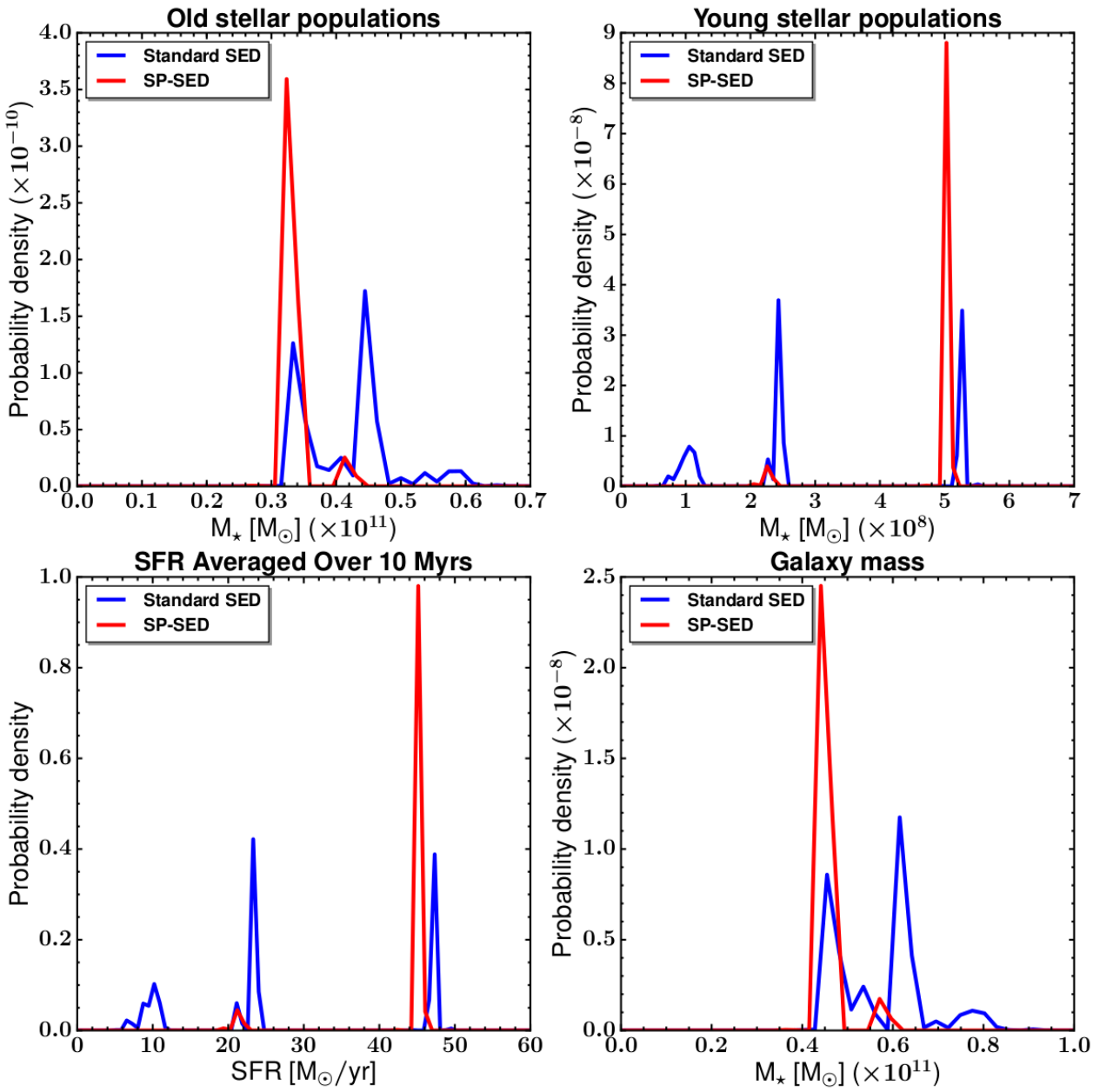


**Figure 6.2.4:** Comparison between the PDFs for the galaxy properties of IC 910, derived from the standard SED (blue lines) and SP-SED (red lines) method. Top-left and top-right panels show the PDFs for the stellar mass of the old and young populations respectively, while bottom-left shows the SFR averaged over 10 Myrs, and bottom-right the total galaxy mass respectively. Our technique yields a single dominant probability peak, instead of the multiple smaller peaks obtained by the standard SED fitting methods (blue lines).

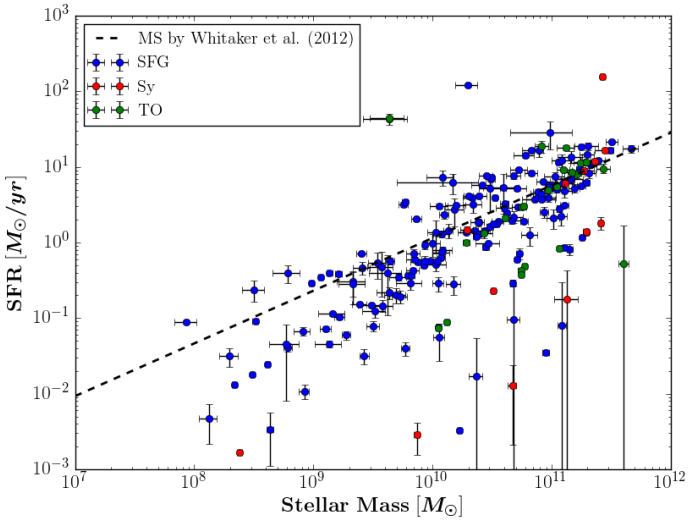


**Figure 6.2.5:** The "main sequence" of star-forming, Sy, and TO galaxies for a sub-sample of the SFRS galaxies. The total SFR and stellar mass where calculated using SP-SED fitting. The redshift-dependent MS line by Whitaker et al. (2012) at the median redshift of the SFRS galaxies ($z = 0.024$) is shown with a dashed line for comparison.

mass of young and old stellar populations, dust luminosity, E(B-V) of young and old populations) for a portion of SFRS galaxies that we have analyzed up to the present point. Therefore, the SP-SED method has the potential to greatly increase the scientific value of the available broadband multi-wavelength photometric data.

Additionally, by comparing the nebular emission lines derived from the SED fit with the ones measured in our spectroscopic analysis, we are able to estimate the relative contribution between AGN and star formation, independently from SED modeling which is mostly based on the shape of the continuum. We apply these methods to the entire SFRS sample which includes high quality multi-wavelength photometric data from the *Spitzer*, the CFHT and PAIRITEL telescopes, as well as from the NVSS, 2MASS, SDSS and GALEX archives. Preliminary results from our SP-SED analysis showing the MS of star-forming and AGN galaxies (Figure 6.2.5) have been presented in international conferences.

Our SP-SED method is particularly useful and applicable to galaxies in the current era of growing IFU spectroscopic surveys, but furthermore it can take full advantage of the James Webb Space Telescope (JWST) Mid-Infrared Instrument (MIRI) spectroscopic capabilities. Specifically, the SP-SED method can be easily generalized to

include NIR and FIR spectra and model IR spectral features of the stellar populations (e.g., CO), dust features (e.g., silicate and PAH), and nebular permitted or fine structure lines. Therefore, the combined optical and IR spectroscopic information will set even stronger constrain to the stellar population and ISM parameters used in the fit. Furthermore, since the JWST will be able to deliver detailed resolved observations of galaxies at higher redshifts where the set of optical region defined in our method will be shifted in the infrared part of the spectrum, the SP-SED fitting technique will be directly applicable to the MIRI data for derivation of robust galaxy parameter information.

# References


Abazajian K. N., et al., 2009, ApJS, 182, 543

Aihara H., et al., 2011, ApJS, 193, 29

Aird J., et al., 2010, MNRAS, 401, 2531

Alam S., et al., 2015, ApJS, 219, 12

Alexander D. M., Hickox R. C., 2012, New Astronomy Review, 56, 93

Antonucci R., 1993, ARAA, 31, 473

Armus L., et al., 2009, PASP, 121, 559

Ashby M. L. N., et al., 2011, PASP, 123, 1011

Baldwin J. A., Phillips M. M., Terlevich R., 1981, PASP, 93, 5

Balzano V. A., 1983, ApJ, 268, 602

Belfiore F., et al., 2016a, preprint, (arXiv:1609.01737)

Belfiore F., et al., 2016b, MNRAS, 461, 3111

Bell E. F., McIntosh D. H., Katz N., Weinberg M. D., 2003, ApJS, 149, 289

Bell E. F., Zheng X. Z., Papovich C., Borch A., Wolf C., Meisenheimer K., 2007, ApJ, 663, 834

Binette L., Magris C. G., Stasińska G., Bruzual A. G., 1994, A&A, 292, 13

Blandford R. D., Netzer H., Woltjer L., Courvoisier T. J.-L., Mayor M., eds, 1990, Active Galactic Nuclei

Blanton M. R., et al., 2001, AJ, 121, 2358

Blum R. D., Conti P. S., Damineli A., 2000, AJ, 119, 1860

Boquien M., Buat V., Perret V., 2014, A&A, 571, A72

Boselli A., et al., 2010, PASP, 122, 261

Brinchmann J., Charlot S., White S. D. M., Tremonti C., Kauffmann G., Heckman T., Brinkmann J., 2004, MNRAS, 351, 1151

Bruzual G., Charlot S., 2003, MNRAS, 344, 1000

Bundy K., et al., 2015, ApJ, 798, 7

Burgarella D., Buat V., Iglesias-Páramo J., 2005, MNRAS, 360, 1413

Buttiglione S., Capetti A., Celotti A., Axon D. J., Chiaberge M., Macchetto F. D., Sparks W. B., 2009, A&A, 495, 1033

Calzetti D., 2011, in Joblin C., Tielens A. G. G. M., eds, EAS Publications Series Vol. 46, EAS Publications Series. pp 133–141 (arXiv:1010.4996), doi:10.1051/eas/1146014

Cano-Díaz M., et al., 2016, ApJ, 821, L26

## References


Cardelli J. A., Clayton G. C., Mathis J. S., 1989, ApJ, 345, 245

Chabrier G., 2003, PASP, 115, 763

Cid Fernandes R., Mateus A., Sodré L., Stasińska G., Gomes J. M., 2005, MNRAS, 358, 363

Cid Fernandes R., Stasińska G., Mateus A., Vale Asari N., 2011, MNRAS, 413, 1687

Cid Fernandes R., et al., 2014, A&A, 561, A130

Conroy C., 2013, ARAA, 51, 393

Conroy C., Gunn J. E., 2010, ApJ, 712, 833

Conroy C., White M., Gunn J. E., 2010, ApJ, 708, 58

Contini T., Considere S., Davoust E., 1998, A&A Supplement, 130, 285

Cowie L. L., Lilly S. J., Gardner J., McLean I. S., 1988, ApJ, 332, L29

Daddi E., et al., 2007, ApJ, 670, 156

Dale D. A., Helou G., 2002, ApJ, 576, 159

Dale D. A., et al., 2009, ApJ, 703, 517

Davies R. I., Müller Sánchez F., Genzel R., Tacconi L. J., Hicks E. K. S., Friedrich S., Sternberg A., 2007, ApJ, 671, 1388

Davies R. L., Kewley L. J., Ho I.-T., Dopita M. A., 2014, MNRAS, 444, 3961

Davies L. J. M., et al., 2016, MNRAS, 461, 458

Dopita M. A., et al., 2015, ApJS, 217, 12

Elbaz D., et al., 2007, A&A, 468, 33

Elbaz D., et al., 2011, A&A, 533, A119

Fabricant D., Cheimets P., Caldwell N., Geary J., 1998, PASP, 110, 79

Ferguson A. M. N., Gallagher J. S., Wyse R. F. G., 1998, AJ, 116, 673

Ferrarese L., Merritt D., 2000, ApJ, 539, L9

Filippenko A. V., Sargent W. L. W., 1985, ApJS, 57, 503

Freeman P., Doe S., Siemiginowska A., 2001, in Starck J.-L., Murtagh F. D., eds, Society of Photo-Optical Instrumentation Engineers (SPIE) Conference Series Vol. 4477, Astronomical Data Analysis. pp 76–87 (arXiv:astro-ph/0108426), doi:10.1117/12.447161

Fruscione A., et al., 2006, in Society of Photo-Optical Instrumentation Engineers (SPIE) Conference Series. p. 1, doi:10.1117/12.671760

García-Burillo S., Combes F., Schinnerer E., Boone F., Hunt L. K., 2005, A&A, 441, 1011

Georgakakis A., et al., 2008, MNRAS, 385, 2049

Gil de Paz A., et al., 2005, ApJ, 627, L29

Goddard D., et al., 2016, MNRAS,

González Delgado R. M., et al., 2016, A&A, 590, A44

Gu Q., Melnick J., Cid Fernandes R., Kunth D., Terlevich E., Terlevich R., 2006, MNRAS, 366, 480

Hao L., et al., 2005, AJ, 129, 1783

Hao C.-N., Kennicutt R. C., Johnson B. D., Calzetti D., Dale D. A., Moustakas J., 2011, ApJ, 741, 124

Hayward C. C., et al., 2014, MNRAS, 445, 1598

Heckman T. M., 1980, A&A, 87, 152

Helou G., et al., 2004, ApJS, 154, 253

Hemmati S., et al., 2014, ApJ, 797, 108

Ho L. C., 2008, ARAA, 46, 475

Ho L. C., Keto E., 2007, ApJ, 658, 314

Ho L. C., Filippenko A. V., Sargent W. L. W., 1993, ApJ, 417, 63

Ho L. C., Filippenko A. V., Sargent W. L., 1995, ApJS, 98, 477

Ho L. C., Filippenko A. V., Sargent W. L. W., 1997a, ApJS, 112, 315

Ho L. C., Filippenko A. V., Sargent W. L. W., 1997b, ApJ, 487, 568

Ho L. C., Filippenko A. V., Sargent W. L. W., 1997c, ApJ, 487, 579

Ho L. C., Filippenko A. V., Sargent W. L. W., 2003, ApJ, 583, 159

Hobbs A., Nayakshin S., Power C., King A., 2011, MNRAS, 413, 2633

Humason M. L., Mayall N. U., Sandage A. R., 1956, AJ, 61, 97

Hyland A. R., McGregor P. J., Robinson G., Thomas J. A., Becklin E. E., Gatley I., Werner M. W., 1980, ApJ, 241, 709

Jarrett T. H., Chester T., Cutri R., Schneider S. E., Huchra J. P., 2003, AJ, 125, 525

Juneau S., Dickinson M., Alexander D. M., Salim S., 2011, ApJ, 736, 104

Juneau S., et al., 2014, ApJ, 788, 88

Karim A., et al., 2011, ApJ, 730, 61

Kauffmann G., et al., 2003, MNRAS, 346, 1055

Kennicutt Jr. R. C., 1998a, ARAA, 36, 189

Kennicutt Jr. R. C., 1998b, ApJ, 498, 541

Kennicutt R. C., Evans N. J., 2012, ARAA, 50, 531

Kennicutt Jr. R. C., Keel W. C., Blaha C. A., 1989, AJ, 97, 1022

Kennicutt Jr. R. C., et al., 2003, PASP, 115, 928

Kennicutt R. C., et al., 2011, PASP, 123, 1347

Kewley L. J., Dopita M. A., 2002, ApJS, 142, 35

Kewley L. J., Dopita M. A., Sutherland R. S., Heisler C. A., Trevena J., 2001, ApJ, 556, 121

Kewley L. J., Groves B., Kauffmann G., Heckman T., 2006, MNRAS, 372, 961

Kewley L. J., Maier C., Yabe K., Ohta K., Akiyama M., Dopita M. A., Yuan T., 2013, ApJ, 774, L10

Kormendy J., Ho L. C., 2013, ARAA, 51, 511

Kormendy J., Richstone D., 1995, ARAA, 33, 581

Lada C. J., Lada E. A., Clemens D. P., Bally J., 1994, ApJ, 429, 694

Lamareille F., 2010, A&A, 509, A53

Le Floc'h E., et al., 2005, ApJ, 632, 169

Lee J. C., Hwang H. S., Lee M. G., Kim M., Kim S. C., 2011, MNRAS, 414, 702

Lee J. C., et al., 2013, MNRAS, 430, 2650

Lee N., et al., 2015, ApJ, 801, 80

Leitherer C., et al., 1999, ApJS, 123, 3

Lilly S. J., Le Fevre O., Hammer F., Crampton D., 1996, ApJ, 460, L1

Longhetti M., Saracco P., 2009, MNRAS, 394, 774

Madau P., Dickinson M., 2014, ARAA, 52, 415

Magdis G. E., et al., 2012, ApJ, 760, 6

Magdis G. E., et al., 2016, MNRAS, 456, 4533

Magorrian J., et al., 1998, AJ, 115, 2285

Maragkoudakis A., Zezas A., Ashby M. L. N., Willner S. P., 2014, MNRAS, 441, 2296

Maragkoudakis A., Zezas A., Ashby M. L. N., Willner S. P., 2017, MNRAS, 466, 1192

Maraston C., 2005, MNRAS, 362, 799

Martin C. L., Kennicutt Jr. R. C., 2001, ApJ, 555, 301

Martin D. C., et al., 2005, ApJ, 619, L1

Martins F., Plez B., 2006, A&A, 457, 637

Massey P., Strobel K., Barnes J. V., Anderson E., 1988, ApJ, 328, 315

Montero-Dorta A. D., et al., 2009, MNRAS, 392, 125

Moran E. C., Filippenko A. V., Chornock R., 2002, ApJ, 579, L71

Moran S. M., et al., 2012, ApJ, 745, 66

Moustakas J., Kennicutt Jr. R. C., Tremonti C. A., Dale D. A., Smith J.-D. T., Calzetti D., 2010, ApJS, 190, 233

Moustakas J., et al., 2013, ApJ, 767, 50

Mullaney J. R., et al., 2012, ApJ, 753, L30

Nandra K., et al., 2007, ApJ, 660, L11

Nardini E., Risaliti G., Watabe Y., Salvati M., Sani E., 2010, MNRAS, 405, 2505

Noeske K. G., et al., 2007, ApJ, 660, L43

Noll S., Burgarella D., Giovannoli E., Buat V., Marcillac D., Muñoz-Mateos J. C., 2009, A&A, 507, 1793

Osterbrock D. E., 1989, Astrophysics of gaseous nebulae and active galactic nuclei

Pagel B. E. J., Edmunds M. G., Blackwell D. E., Chun M. S., Smith G., 1979, MNRAS, 189, 95

Pancoast A., Sajina A., Lacy M., Noriega-Crespo A., Rho J., 2010, ApJ, 723, 530

Peterson B. M., 1997, An Introduction to Active Galactic Nuclei

Pettini M., Pagel B. E. J., 2004, MNRAS, 348, L59

Pilbratt G. L., et al., 2010, A&A, 518, L1

Pilyugin L. S., Vílchez J. M., Contini T., 2004, A&A, 425, 849

Rodighiero G., et al., 2011, ApJ, 739, L40

Rowan-Robinson M., Crawford J., 1989, MNRAS, 238, 523

Salpeter E. E., 1955, ApJ, 121, 161

Sánchez S. F., et al., 2012, A&A, 538, A8

Sanders D. B., Soifer B. T., Elias J. H., Neugebauer G., Matthews K., 1988, ApJ, 328, L35

Sarzi M., Shields J. C., Pogge R. W., Martini P., 2007, in Ho L. C., Wang J.-W., eds, Astronomical Society of the Pacific Conference Series Vol. 373, The Central Engine of Active Galactic Nuclei. p. 643

Saunders W., et al., 2000, MNRAS, 317, 55

Schawinski K., Thomas D., Sarzi M., Maraston C., Kaviraj S., Joo S.-J., Yi S. K., Silk J., 2007, MNRAS, 382, 1415

Schawinski K., Virani S., Simmons B., Urry C. M., Treister E., Kaviraj S., Kushkuley B., 2009, ApJ, 692, L19

Schawinski K., et al., 2010, ApJ, 711, 284

Schiminovich D., et al., 2005, ApJ, 619, L47

Schmidt M., 1959, ApJ, 129, 243

Schreiber C., et al., 2015, A&A, 575, A74

Silverman J. D., et al., 2008, ApJ, 679, 118

Skrutskie M. F., et al., 2006, AJ, 131, 1163

Speagle J. S., Steinhardt C. L., Capak P. L., Silverman J. D., 2014, ApJS, 214, 15

Stasińska G., et al., 2008, MNRAS, 391, L29

Stern D., et al., 2005, ApJ, 631, 163

Tacconi L. J., et al., 2013, ApJ, 768, 74

Taylor M. B., 2005, in Shopbell P., Britton M., Ebert R., eds, Astronomical Society of the Pacific Conference Series Vol. 347, Astronomical Data Analysis Software and Systems XIV. p. 29

Thilker D. A., et al., 2005, ApJ, 619, L79

Thilker D. A., et al., 2007, ApJS, 173, 538

Tody D., 1986, in Crawford D. L., ed., Society of Photo-Optical Instrumentation Engineers (SPIE) Conference Series Vol. 627, Instrumentation in astronomy VI. p. 733

Trouille L., Barger A. J., Tremonti C., 2011, ApJ, 742, 46

Urry C. M., Padovani P., 1995, PASP, 107, 803

Veilleux S., Osterbrock D. E., 1987, ApJS, 63, 295

Veilleux S., Sanders D. B., Kim D.-C., 1997, ApJ, 484, 92

Véron-Cetty M.-P., Véron P., 2006, A&A, 455, 773

Werner M. W., et al., 2004, ApJS, 154, 1

Whitaker K. E., van Dokkum P. G., Brammer G., Franx M., 2012, ApJ, 754, L29

Whitaker K. E., et al., 2014, ApJ, 795, 104

Worthey G., 1994, ApJS, 95, 107

Worthey G., Ottaviani D. L., 1997, ApJS, 111, 377

Wuyts S., et al., 2011, ApJ, 742, 96

Wuyts S., et al., 2013, ApJ, 779, 135

Yan R., et al., 2011, ApJ, 728, 38

York D. G., et al., 2000, AJ, 120, 1579

Zhu Y.-N., Wu H., Li H.-N., Cao C., 2010, Research in Astronomy and Astrophysics, 10, 329

de Vaucouleurs G., 1959, Handbuch der Physik, 53, 275

de Vaucouleurs G., de Vaucouleurs A., Corwin Jr. H. G., Buta R. J., Paturel G., Fouque P., 1991, Sky and Telescope, 82, 621

# Appendix

# 7 Catalogs of the SFRS galaxies properties

## 7.A Summary of catalogs

Catalog 7.A.1 presents the optical diagnostic line ratio fluxes, extinction corrected H$\alpha$ fluxes, STARLIGHT code fitted extinction, nuclear E(B-V) color excess of the gas, and method of observation. Catalog 7.A.2 presents the individual activity classifications for the SFRS sample obtained from different diagnostics, along with the final adopted classification. Catalog 7.A.3 presents the metallicities and SFR for the star-forming galaxies of the SFRS sample. Catalog 7.A.4 presents the host-galaxy metallicities and SFRs for the non-star-forming SFRS galaxies. The probabilistic activity classification is presented in Catalog 7.A.5.

**Table 7.A.1:** Optical Diagnostic Line Ratio Fluxes.

| SFRS | Galaxy | F(H$\alpha$) | H$\alpha$/H$\beta$ | [O III]/H$\beta$ | [N II]/H$\alpha$ | [S II]/H$\alpha$ | [O I]/H$\alpha$ | F(H$\alpha$)$_{cor}$ | A$_V$ | A$_V$nuc | E(B-V)$_{\rm gas}$ | Observation |
|---|---|---|---|---|---|---|---|---|---|---|---|---|
| (1) | (2) | (3) | (4) | (5) | (6) | (7) | (8) | (9) | (10) | (11) | (12) | (13) |
| 1 | IC 486 | $2.430^{+0.037}_{-0.026}$ | $5.830^{+0.214}_{-0.205}$ | $1.058^{+0.015}_{-0.015}$ | $0.071^{+0.006}_{-0.008}$ | $-0.105^{+0.005}_{-0.007}$ | $-0.727^{+0.019}_{-0.020}$ | $10.788^{+0.164}_{-0.115}$ | ... | 0.68 | 0.64 | SDSS |
| 2 | IC 2217 | $7.660^{+0.045}_{-0.045}$ | $4.935^{+0.085}_{-0.087}$ | $-0.552^{+0.029}_{-0.029}$ | $-0.422^{+0.006}_{-0.006}$ | $-0.474^{+0.003}_{-0.003}$ | $-1.588^{+0.052}_{-0.054}$ | $27.755^{+0.163}_{-0.163}$ | 0.50 | 0.82 | 0.55 | FAST |
| 3 | NGC 2500 | $0.151^{+0.007}_{-0.007}$ | $3.096^{+0.497}_{-0.482}$ | $0.132^{+0.080}_{-0.083}$ | $-0.446^{+0.057}_{-0.058}$ | $-0.268^{+0.022}_{-0.019}$ | $0.127^{+0.031}_{-0.029}$ | $0.182^{+0.008}_{-0.008}$ | 0.81 | 0.68 | 0.08 | FAST |
| 4 | NGC 2512 | $10.800^{+0.008}_{-0.008}$ | $4.713^{+0.017}_{-0.017}$ | $-0.677^{+0.008}_{-0.008}$ | $-0.310^{+0.001}_{-0.001}$ | $-0.564^{+0.002}_{-0.002}$ | $-1.535^{+0.014}_{-0.014}$ | $35.104^{+0.026}_{-0.026}$ | 0.52 | 0.46 | 0.50 | FAST |
| 5 | MCG 6-18-009 | $6.230^{+0.041}_{-0.041}$ | $5.253^{+0.075}_{-0.072}$ | $-0.517^{+0.015}_{-0.014}$ | $-0.289^{+0.004}_{-0.004}$ | $-0.564^{+0.003}_{-0.003}$ | $-1.441^{+0.023}_{-0.024}$ | $26.157^{+0.172}_{-0.172}$ | ... | 0.63 | 0.61 | SDSS |
| 6 | MK 1212 | $0.403^{+0.005}_{-0.004}$ | $6.165^{+0.323}_{-0.318}$ | $-0.316^{+0.054}_{-0.049}$ | $-0.285^{+0.009}_{-0.008}$ | $-0.562^{+0.005}_{-0.005}$ | $-1.441^{+0.053}_{-0.072}$ | $2.469^{+0.031}_{-0.025}$ | ... | 0.94 | 0.78 | SDSS |
| 7 | IRAS 08072+1847 | $1.790^{+0.013}_{-0.013}$ | $8.168^{+0.165}_{-0.160}$ | $-0.239^{+0.020}_{-0.018}$ | $-0.196^{+0.005}_{-0.005}$ | $-0.469^{+0.003}_{-0.003}$ | $-1.187^{+0.023}_{-0.021}$ | $17.611^{+0.128}_{-0.128}$ | ... | 1.51 | 0.98 | SDSS |
| 8 | NGC 2532 | $2.300^{+0.060}_{-0.056}$ | $7.691^{+1.296}_{-1.221}$ | $-0.519^{+0.068}_{-0.072}$ | $-0.415^{+0.028}_{-0.030}$ | $-0.492^{+0.010}_{-0.011}$ | $-1.693^{+0.010}_{-0.011}$ | $23.745^{+0.619}_{-0.578}$ | 0.53 | 0.79 | 1.00 | FAST |
| 9 | UGC 4261 | $8.290^{+0.043}_{-0.043}$ | $4.195^{+0.039}_{-0.040}$ | $0.014^{+0.005}_{-0.005}$ | $-0.597^{+0.004}_{-0.004}$ | $-0.591^{+0.002}_{-0.002}$ | $-1.690^{+0.012}_{-0.012}$ | $20.472^{+0.106}_{-0.106}$ | ... | 0.49 | 0.39 | SDSS |
| 10 | NGC 2535 | $2.310^{+0.013}_{-0.013}$ | $4.137^{+0.089}_{-0.092}$ | $-0.885^{+0.077}_{-0.072}$ | $-0.434^{+0.007}_{-0.007}$ | $-0.614^{+0.002}_{-0.002}$ | $-1.741^{+0.163}_{-0.257}$ | $5.520^{+0.031}_{-0.031}$ | 0.65 | 0.48 | 0.37 | FAST |
| 11 | NGC 2543 | $5.190^{+0.036}_{-0.033}$ | $6.076^{+0.094}_{-0.091}$ | $-0.475^{+0.016}_{-0.018}$ | $-0.349^{+0.005}_{-0.005}$ | $-0.580^{+0.003}_{-0.003}$ | $-1.441^{+0.031}_{-0.032}$ | $30.722^{+0.213}_{-0.195}$ | ... | 1.06 | 0.76 | SDSS |
| 12 | NGC 2537 | $0.425^{+0.012}_{-0.012}$ | $2.717^{+0.303}_{-0.288}$ | $-0.143^{+0.072}_{-0.078}$ | $-0.510^{+0.037}_{-0.042}$ | $-0.233^{+0.013}_{-0.013}$ | $-1.283^{+0.170}_{-0.187}$ | $0.377^{+0.011}_{-0.011}$ | 0.73 | 0.67 | -0.05 | FAST |
| 13 | IC 2233 | $1.910^{+0.012}_{-0.011}$ | $3.616^{+0.046}_{-0.049}$ | $0.552^{+0.006}_{-0.006}$ | $-1.206^{+0.009}_{-0.009}$ | $-0.791^{+0.003}_{-0.003}$ | $-1.808^{+0.035}_{-0.035}$ | $3.322^{+0.021}_{-0.019}$ | ... | 0.45 | 0.24 | SDSS |
| 14 | IC 2239 | $2.400^{+0.031}_{-0.019}$ | $6.684^{+0.278}_{-0.267}$ | $-0.115^{+0.033}_{-0.033}$ | $-0.144^{+0.006}_{-0.007}$ | $-0.628^{+0.003}_{-0.006}$ | $-1.331^{+0.163}_{-0.132}$ | $17.792^{+0.230}_{-0.141}$ | 0.57 | 0.61 | 0.86 | FAST |
| 15 | UGC 4286 | $0.404^{+0.008}_{-0.007}$ | $4.598^{+0.322}_{-0.322}$ | $-0.084^{+0.053}_{-0.052}$ | $-0.366^{+0.021}_{-0.021}$ | $-0.473^{+0.008}_{-0.009}$ | $-1.198^{+0.134}_{-0.145}$ | $1.239^{+0.025}_{-0.021}$ | ... | 0.72 | 0.48 | SDSS |
| 16 | UGC 4306 | $0.557^{+0.005}_{-0.005}$ | $5.952^{+0.235}_{-0.244}$ | $-0.296^{+0.037}_{-0.037}$ | $-0.391^{+0.008}_{-0.008}$ | $-0.460^{+0.004}_{-0.004}$ | $-1.370^{+0.074}_{-0.043}$ | $3.141^{+0.028}_{-0.028}$ | ... | 0.99 | 0.74 | SDSS |
| 17 | NGC 2552 | $3.630^{+0.020}_{-0.020}$ | $3.250^{+0.032}_{-0.032}$ | $0.446^{+0.005}_{-0.005}$ | $-1.065^{+0.005}_{-0.005}$ | $-0.711^{+0.002}_{-0.002}$ | $-1.920^{+0.022}_{-0.023}$ | $4.908^{+0.027}_{-0.027}$ | ... | 0.17 | 0.13 | SDSS |
| 18 | UGC 4383 | $11.500^{+0.010}_{-0.010}$ | $4.227^{+0.017}_{-0.017}$ | $0.066^{+0.002}_{-0.002}$ | $-0.465^{+0.001}_{-0.001}$ | $-0.663^{+0.003}_{-0.003}$ | $-1.803^{+0.024}_{-0.025}$ | $28.913^{+0.025}_{-0.025}$ | 0.43 | 0.46 | 0.39 | FAST |
| 19 | IRAS 08234+1054 | $0.582^{+0.005}_{-0.005}$ | $7.313^{+0.276}_{-0.266}$ | $-0.312^{+0.040}_{-0.037}$ | $-0.232^{+0.006}_{-0.006}$ | $-0.388^{+0.004}_{-0.003}$ | $-1.079^{+0.025}_{-0.025}$ | $5.335^{+0.046}_{-0.046}$ | ... | 1.32 | 0.95 | SDSS |
| 20 | IRAS 08269+1514 | $0.823^{+0.006}_{-0.005}$ | $5.773^{+0.165}_{-0.166}$ | $-0.275^{+0.026}_{-0.026}$ | $-0.303^{+0.005}_{-0.005}$ | $-0.449^{+0.003}_{-0.003}$ | $-1.259^{+0.030}_{-0.032}$ | $4.318^{+0.031}_{-0.026}$ | ... | 0.96 | 0.71 | SDSS |
| 21 | NGC 2604 | $7.060^{+0.039}_{-0.039}$ | $3.552^{+0.049}_{-0.049}$ | $-0.173^{+0.007}_{-0.007}$ | $-0.655^{+0.004}_{-0.004}$ | $-0.674^{+0.002}_{-0.002}$ | $-2.048^{+0.024}_{-0.026}$ | $11.773^{+0.065}_{-0.065}$ | ... | 0.35 | 0.22 | SDSS |
| 22 | NGC 2608 | $6.230^{+0.014}_{-0.014}$ | $5.503^{+0.070}_{-0.070}$ | $-0.451^{+0.019}_{-0.019}$ | $-0.314^{+0.003}_{-0.003}$ | $-0.492^{+0.001}_{-0.001}$ | $-1.568^{+0.044}_{-0.046}$ | $29.191^{+0.066}_{-0.066}$ | 0.51 | 0.82 | 0.66 | FAST |
| 23 | MK 92 | $21.800^{+0.098}_{-0.098}$ | $3.786^{+0.052}_{-0.052}$ | $-0.190^{+0.009}_{-0.009}$ | $-0.428^{+0.004}_{-0.004}$ | $-0.545^{+0.002}_{-0.002}$ | $-1.599^{+0.022}_{-0.022}$ | $42.260^{+0.190}_{-0.190}$ | 0.48 | 0.59 | 0.28 | FAST |

**Table 7.A.1:** Continued

| SFRS | Galaxy | F(H$\alpha$) | H$\alpha$/H$\beta$ | [O III]/H$\beta$ | [N II]/H$\alpha$ | [S II]/H$\alpha$ | [O I]/H$\alpha$ | F(H$\alpha$)$_{cor}$ | $A_V$ | $A_V$nuc | E(B-V)$_{\rm gas}$ | Observation |
|---|---|---|---|---|---|---|---|---|---|---|---|---|
| (1) | (2) | (3) | (4) | (5) | (6) | (7) | (8) | (9) | (10) | (11) | (12) | (13) |
| 24 | NGC 2623 | $1.150^{+0.013}_{-0.010}$ | $14.638^{+0.806}_{-1.245}$ | $0.373^{+0.042}_{-0.030}$ | $-0.019^{+0.006}_{-0.007}$ | $-0.313^{+0.004}_{-0.005}$ | $-0.873^{+0.021}_{-0.022}$ | $44.827^{+0.507}_{-0.390}$ | ... | 1.27 | 1.57 | SDSS |
| 25 | CGCG 120-018 | $3.070^{+0.019}_{-0.019}$ | $9.671^{+0.190}_{-0.190}$ | $-0.236^{+0.018}_{-0.018}$ | $-0.163^{+0.004}_{-0.004}$ | $-0.518^{+0.003}_{-0.003}$ | $-1.401^{+0.025}_{-0.024}$ | $54.421^{+0.337}_{-0.337}$ | ... | 1.63 | 1.23 | SDSS |
| 26 | NGC 2644 | $2.170^{+0.014}_{-0.013}$ | $3.709^{+0.094}_{-0.093}$ | $-0.327^{+0.024}_{-0.025}$ | $-0.489^{+0.010}_{-0.011}$ | $-0.381^{+0.003}_{-0.003}$ | $-1.534^{+0.100}_{-0.117}$ | $4.007^{+0.026}_{-0.024}$ | 0.99 | 0.89 | 0.26 | FAST |
| 27 | UGC 4572 | $0.928^{+0.017}_{-0.017}$ | $4.144^{+0.218}_{-0.225}$ | $-0.144^{+0.043}_{-0.042}$ | $-0.052^{+0.013}_{-0.013}$ | $-0.215^{+0.008}_{-0.008}$ | $-0.893^{+0.105}_{-0.105}$ | $2.226^{+0.041}_{-0.041}$ | ... | 0.40 | 0.37 | SDSS |
| 28 | UGC 4653 | $2.100^{+0.007}_{-0.007}$ | $6.498^{+0.138}_{-0.137}$ | $-0.082^{+0.015}_{-0.014}$ | $-0.234^{+0.003}_{-0.003}$ | $-0.383^{+0.002}_{-0.002}$ | $-1.116^{+0.022}_{-0.021}$ | $14.565^{+0.049}_{-0.049}$ | 0.84 | 1.67 | 0.83 | FAST |
| 29 | IRAS 08512+2727 | $1.380^{+0.011}_{-0.010}$ | $5.422^{+0.121}_{-0.119}$ | $-0.509^{+0.037}_{-0.038}$ | $-0.450^{+0.007}_{-0.007}$ | $-0.738^{+0.003}_{-0.003}$ | $-1.529^{+0.056}_{-0.059}$ | $6.244^{+0.050}_{-0.045}$ | ... | 0.49 | 0.65 | SDSS |
| 31 | IRAS 08538+4256 | $2.080^{+0.013}_{-0.013}$ | $7.401^{+0.140}_{-0.139}$ | $-0.342^{+0.022}_{-0.021}$ | $-0.307^{+0.005}_{-0.005}$ | $-0.551^{+0.003}_{-0.003}$ | $-1.428^{+0.031}_{-0.030}$ | $19.612^{+0.123}_{-0.123}$ | ... | 1.18 | 0.96 | SDSS |
| 32 | IRAS 08550+3908 | $0.538^{+0.028}_{-0.015}$ | $3.058^{+0.186}_{-0.131}$ | $0.866^{+0.014}_{-0.014}$ | $0.117^{+0.015}_{-0.027}$ | $0.198^{+0.012}_{-0.023}$ | $-0.424^{+0.018}_{-0.026}$ | $0.521^{+0.027}_{-0.015}$ | ... | 1.01 | -0.01 | SDSS |
| 33 | NGC 2718 | $12.900^{+0.083}_{-0.083}$ | $4.408^{+0.057}_{-0.057}$ | $-0.699^{+0.019}_{-0.018}$ | $-0.327^{+0.004}_{-0.004}$ | $-0.649^{+0.003}_{-0.003}$ | $-1.837^{+0.047}_{-0.049}$ | $35.806^{+0.230}_{-0.230}$ | ... | 0.31 | 0.44 | SDSS |
| 34 | NGC 2712 | $4.410^{+0.045}_{-0.047}$ | $4.203^{+0.120}_{-0.121}$ | $-0.232^{+0.022}_{-0.023}$ | $-0.264^{+0.008}_{-0.008}$ | $-0.428^{+0.005}_{-0.004}$ | $-1.159^{+0.058}_{-0.061}$ | $10.939^{+0.112}_{-0.117}$ | 0.70 | 0.74 | 0.39 | FAST |
| 35 | NGC 2719 | $4.590^{+0.037}_{-0.033}$ | $3.652^{+0.073}_{-0.071}$ | $0.384^{+0.009}_{-0.009}$ | $-1.006^{+0.016}_{-0.015}$ | $-0.574^{+0.003}_{-0.003}$ | $-1.539^{+0.052}_{-0.054}$ | $8.172^{+0.066}_{-0.059}$ | 0.73 | 0.66 | 0.25 | FAST |
| 36 | IRAS 08572+3915NW | $15.500^{+0.265}_{-0.169}$ | $8.024^{+0.700}_{-0.675}$ | $0.102^{+0.049}_{-0.051}$ | $-0.391^{+0.015}_{-0.017}$ | $-0.399^{+0.005}_{-0.007}$ | $-1.161^{+0.106}_{-0.129}$ | $146.229^{+2.500}_{-1.594}$ | 0.70 | 1.05 | 0.96 | FAST |
| 36 | IRAS 08572+3915NW | $0.969^{+0.008}_{-0.008}$ | $6.982^{+0.196}_{-0.195}$ | $0.025^{+0.017}_{-0.017}$ | $-0.417^{+0.006}_{-0.006}$ | $-0.382^{+0.003}_{-0.003}$ | $-1.190^{+0.019}_{-0.018}$ | $6.584^{+0.051}_{-0.051}$ | ... | 1.05 | 0.82 | SDSS |
| 37 | IRAS 08579+3447 | $0.556^{+0.010}_{-0.012}$ | $4.234^{+0.358}_{-0.355}$ | $-0.716^{+0.137}_{-0.142}$ | $-0.375^{+0.024}_{-0.022}$ | $-0.446^{+0.010}_{-0.007}$ | $-1.292^{+0.167}_{-0.177}$ | $1.403^{+0.025}_{-0.030}$ | 0.86 | 1.10 | 0.40 | FAST |
| 37 | IRAS 08579+3447 | $0.500^{+0.006}_{-0.006}$ | $5.515^{+0.253}_{-0.238}$ | $-0.511^{+0.062}_{-0.068}$ | $-0.374^{+0.011}_{-0.011}$ | $-0.518^{+0.005}_{-0.005}$ | $-1.218^{+0.094}_{-0.087}$ | $2.355^{+0.026}_{-0.027}$ | ... | 1.21 | 0.66 | SDSS |
| 38 | NGC 2731 | $12.400^{+0.015}_{-0.015}$ | $4.191^{+0.021}_{-0.021}$ | $-0.416^{+0.006}_{-0.006}$ | $-0.460^{+0.001}_{-0.001}$ | $-0.616^{+0.001}_{-0.001}$ | $-1.863^{+0.027}_{-0.027}$ | $30.553^{+0.037}_{-0.037}$ | 0.52 | 0.29 | 0.39 | FAST |
| 39 | NGC 2730 | $0.458^{+0.004}_{-0.004}$ | $4.254^{+0.119}_{-0.113}$ | $-0.441^{+0.030}_{-0.039}$ | $-0.412^{+0.007}_{-0.008}$ | $-0.484^{+0.003}_{-0.004}$ | $-0.978^{+0.122}_{-0.207}$ | $1.169^{+0.010}_{-0.010}$ | ... | 0.41 | 0.40 | SDSS |
| 40 | IC 2431 | $4.510^{+0.024}_{-0.024}$ | $4.282^{+0.044}_{-0.044}$ | $-0.234^{+0.006}_{-0.006}$ | $-0.441^{+0.004}_{-0.004}$ | $-0.529^{+0.002}_{-0.002}$ | $-1.518^{+0.013}_{-0.013}$ | $11.690^{+0.062}_{-0.062}$ | ... | 0.47 | 0.41 | SDSS |
| 41 | NGC 2750 | $9.900^{+0.056}_{-0.051}$ | $5.019^{+0.091}_{-0.086}$ | $-0.690^{+0.026}_{-0.026}$ | $-0.391^{+0.005}_{-0.005}$ | $-0.595^{+0.002}_{-0.002}$ | $-1.746^{+0.055}_{-0.048}$ | $37.328^{+0.211}_{-0.192}$ | 0.69 | 0.66 | 0.57 | FAST |
| 42 | IC 2434 | $0.570^{+0.013}_{-0.033}$ | $4.807^{+0.477}_{-0.525}$ | $0.001^{+0.053}_{-0.054}$ | $-0.160^{+0.029}_{-0.023}$ | $-0.817^{+0.025}_{-0.010}$ | $-0.951^{+0.115}_{-0.130}$ | $1.941^{+0.044}_{-0.112}$ | 0.73 | 0.98 | 0.52 | FAST |
| 43 | NGC 2761 | $2.200^{+0.013}_{-0.015}$ | $11.056^{+0.326}_{-0.326}$ | $-0.371^{+0.032}_{-0.032}$ | $-0.290^{+0.005}_{-0.004}$ | $-0.569^{+0.003}_{-0.003}$ | $-1.435^{+0.029}_{-0.029}$ | $53.484^{+0.316}_{-0.365}$ | ... | 1.97 | 1.37 | SDSS |
| 44 | NGC 2773 | $3.760^{+0.027}_{-0.027}$ | $5.881^{+0.100}_{-0.102}$ | $-0.712^{+0.027}_{-0.025}$ | $-0.425^{+0.006}_{-0.005}$ | $-0.665^{+0.003}_{-0.003}$ | $-1.558^{+0.037}_{-0.038}$ | $20.608^{+0.148}_{-0.148}$ | ... | 1.31 | 0.73 | SDSS |
| 45 | NGC 2776 | $0.971^{+0.017}_{-0.016}$ | $3.995^{+0.166}_{-0.158}$ | $-0.224^{+0.029}_{-0.033}$ | $-0.341^{+0.014}_{-0.014}$ | $-0.662^{+0.007}_{-0.008}$ | $-1.572^{+0.210}_{-0.210}$ | $2.137^{+0.037}_{-0.035}$ | ... | 0.32 | 0.34 | SDSS |

**Table 7.A.1:** Continued

| SFRS | Galaxy | F(H$\alpha$) | H$\alpha$/H$\beta$ | [O III]/H$\beta$ | [N II]/H$\alpha$ | [S II]/H$\alpha$ | [O I]/H$\alpha$ | F(H$\alpha$)$_{cor}$ | A$_V$ | A$_V$nuc | E(B-V)$_{\rm gas}$ | Observation |
|---|---|---|---|---|---|---|---|---|---|---|---|---|
| (1) | (2) | (3) | (4) | (5) | (6) | (7) | (8) | (9) | (10) | (11) | (12) | (13) |
| 46 | NGC 2789 | $4.340^{+0.042}_{-0.048}$ | $7.210^{+0.250}_{-0.310}$ | $-0.222^{+0.039}_{-0.038}$ | $-0.191^{+0.008}_{-0.007}$ | $-0.633^{+0.005}_{-0.004}$ | $-1.275^{+0.056}_{-0.058}$ | $38.472^{+0.372}_{-0.425}$ | ... | 0.56 | 0.93 | SDSS |
| 47 | NGC 2824 | $1.140^{+0.038}_{-0.041}$ | $6.729^{+0.949}_{-0.921}$ | $0.135^{+0.076}_{-0.079}$ | $-0.015^{+0.022}_{-0.021}$ | $-0.150^{+0.015}_{-0.014}$ | $-0.848^{+0.066}_{-0.068}$ | $8.586^{+0.286}_{-0.309}$ | 0.86 | 0.91 | 0.86 | FAST |
| 48 | IRAS 09121+3908 | $0.934^{+0.014}_{-0.008}$ | $7.912^{+0.335}_{-0.309}$ | $-0.277^{+0.039}_{-0.039}$ | $-0.249^{+0.006}_{-0.008}$ | $-0.533^{+0.004}_{-0.006}$ | $-1.304^{+0.140}_{-0.152}$ | $10.309^{+0.155}_{-0.088}$ | ... | 1.63 | 1.03 | SDSS |
| 49 | IRAS 09184+4356 | $1.240^{+0.007}_{-0.008}$ | $7.923^{+0.335}_{-0.330}$ | $-0.525^{+0.058}_{-0.057}$ | $-0.304^{+0.007}_{-0.006}$ | $-0.593^{+0.003}_{-0.003}$ | $-1.568^{+0.113}_{-0.120}$ | $13.732^{+0.078}_{-0.089}$ | 1.19 | 1.52 | 1.03 | FAST |
| 50 | CGCG 238-041 | $6.570^{+0.031}_{-0.031}$ | $4.388^{+0.039}_{-0.040}$ | $0.080^{+0.005}_{-0.005}$ | $-0.655^{+0.004}_{-0.004}$ | $-0.609^{+0.002}_{-0.002}$ | $-1.637^{+0.011}_{-0.010}$ | $18.041^{+0.085}_{-0.085}$ | ... | 0.34 | 0.43 | SDSS |
| 51 | IRAS 09197+2210 | $0.301^{+0.014}_{-0.014}$ | $9.836^{+3.277}_{-3.291}$ | $0.235^{+0.184}_{-0.187}$ | $-0.299^{+0.049}_{-0.051}$ | $-0.525^{+0.021}_{-0.020}$ | $-1.158^{+0.175}_{-0.203}$ | $5.553^{+0.258}_{-0.258}$ | 1.05 | 1.28 | 1.25 | FAST |
| 51 | IRAS 09197+2210 | $0.311^{+0.004}_{-0.003}$ | $8.861^{+0.773}_{-0.667}$ | $-0.192^{+0.069}_{-0.055}$ | $-0.267^{+0.009}_{-0.009}$ | $-0.389^{+0.005}_{-0.005}$ | $-1.132^{+0.047}_{-0.049}$ | $4.485^{+0.050}_{-0.048}$ | ... | 1.48 | 1.14 | SDSS |
| 52 | NGC 2854 | $0.366^{+0.005}_{-0.005}$ | $6.704^{+0.461}_{-0.467}$ | $-0.180^{+0.060}_{-0.057}$ | $-0.173^{+0.011}_{-0.010}$ | $-0.330^{+0.005}_{-0.006}$ | $-1.014^{+0.053}_{-0.053}$ | $2.733^{+0.037}_{-0.037}$ | ... | 1.53 | 0.86 | SDSS |
| 53 | UGC 5046 | $7.520^{+0.047}_{-0.044}$ | $4.210^{+0.051}_{-0.051}$ | $-0.626^{+0.011}_{-0.012}$ | $-0.473^{+0.005}_{-0.005}$ | $-0.610^{+0.003}_{-0.003}$ | $-1.963^{+0.037}_{-0.040}$ | $18.728^{+0.117}_{-0.110}$ | ... | 0.66 | 0.39 | SDSS |
| 54 | UGC 5055 | $4.350^{+0.025}_{-0.025}$ | $5.321^{+0.077}_{-0.076}$ | $-0.577^{+0.020}_{-0.023}$ | $-0.319^{+0.004}_{-0.004}$ | $-0.656^{+0.002}_{-0.002}$ | $-1.397^{+0.038}_{-0.041}$ | $18.827^{+0.108}_{-0.108}$ | ... | 0.63 | 0.63 | SDSS |
| 55 | NGC 2893 | $24.600^{+0.019}_{-0.019}$ | $4.003^{+0.009}_{-0.009}$ | $-0.641^{+0.004}_{-0.004}$ | $-0.265^{+0.001}_{-0.001}$ | $-0.636^{+0.002}_{-0.002}$ | $-1.894^{+0.018}_{-0.018}$ | $54.391^{+0.042}_{-0.042}$ | 0.55 | 0.40 | 0.34 | FAST |
| 56 | MCG 3-24-062 | $0.645^{+0.009}_{-0.010}$ | $6.345^{+0.427}_{-0.432}$ | $-0.213^{+0.074}_{-0.069}$ | $-0.386^{+0.014}_{-0.014}$ | $-0.270^{+0.007}_{-0.006}$ | $-1.456^{+0.120}_{-0.141}$ | $4.229^{+0.059}_{-0.066}$ | 1.00 | 1.11 | 0.81 | FAST |
| 57 | CGCG 238-066 | $2.300^{+0.014}_{-0.014}$ | $5.369^{+0.094}_{-0.107}$ | $0.147^{+0.011}_{-0.010}$ | $-0.114^{+0.004}_{-0.004}$ | $-0.459^{+0.003}_{-0.003}$ | $-1.089^{+0.019}_{-0.019}$ | $8.407^{+0.051}_{-0.051}$ | ... | 0.24 | 0.56 | SDSS |
| 58 | UGC 5097 | $10.100^{+0.065}_{-0.066}$ | $3.846^{+0.042}_{-0.042}$ | $-0.054^{+0.006}_{-0.006}$ | $-0.691^{+0.004}_{-0.004}$ | $-0.612^{+0.003}_{-0.003}$ | $-1.805^{+0.017}_{-0.018}$ | $20.319^{+0.131}_{-0.133}$ | ... | 0.45 | 0.30 | SDSS |
| 59 | CGCG 289-012 | $1.680^{+0.010}_{-0.010}$ | $4.693^{+0.141}_{-0.136}$ | $-0.661^{+0.056}_{-0.053}$ | $-0.422^{+0.007}_{-0.007}$ | $-0.639^{+0.003}_{-0.003}$ | $-1.607^{+0.088}_{-0.095}$ | $5.406^{+0.032}_{-0.032}$ | 0.57 | 0.62 | 0.50 | FAST |
| 60 | MCG 8-18-013 | $2.590^{+0.024}_{-0.010}$ | $7.904^{+0.218}_{-0.206}$ | $-0.159^{+0.020}_{-0.020}$ | $-0.275^{+0.005}_{-0.007}$ | $-0.557^{+0.002}_{-0.004}$ | $-1.329^{+0.110}_{-0.119}$ | $28.520^{+0.264}_{-0.110}$ | 0.85 | 1.25 | 1.03 | FAST |
| 61 | CGCG 181-068 | $0.256^{+0.010}_{-0.010}$ | $5.133^{+0.956}_{-0.916}$ | $-0.209^{+0.135}_{-0.145}$ | $-0.185^{+0.031}_{-0.032}$ | $-0.787^{+0.016}_{-0.017}$ | $-1.053^{+0.168}_{-0.214}$ | $1.018^{+0.040}_{-0.040}$ | 1.03 | 1.18 | 0.59 | FAST |
| 62 | NGC 2936 | $0.241^{+0.018}_{-0.017}$ | $4.197^{+0.871}_{-0.856}$ | $-0.094^{+0.129}_{-0.134}$ | $0.032^{+0.047}_{-0.049}$ | ... | $-0.864^{+0.203}_{-0.203}$ | $0.493^{+0.037}_{-0.035}$ | 0.34 | 0.37 | 0.31 | FAST |
| 63 | NGC 2955 | $1.430^{+0.028}_{-0.028}$ | $6.420^{+0.611}_{-0.597}$ | $-0.300^{+0.086}_{-0.092}$ | $-0.359^{+0.020}_{-0.018}$ | ... | $-1.435^{+0.150}_{-0.219}$ | $9.640^{+0.189}_{-0.189}$ | 0.43 | 0.50 | 0.82 | FAST |
| 64 | CGCG 182-010 | $3.330^{+0.021}_{-0.020}$ | $6.764^{+0.115}_{-0.117}$ | $-0.548^{+0.023}_{-0.022}$ | $-0.331^{+0.004}_{-0.005}$ | $-0.614^{+0.003}_{-0.003}$ | $-1.528^{+0.033}_{-0.031}$ | $25.390^{+0.160}_{-0.152}$ | ... | 1.22 | 0.87 | SDSS |
| 65 | UGC 5228 | $2.980^{+0.026}_{-0.022}$ | $5.494^{+0.156}_{-0.154}$ | $-0.284^{+0.024}_{-0.024}$ | $-0.482^{+0.007}_{-0.008}$ | $-0.382^{+0.003}_{-0.004}$ | $-1.627^{+0.064}_{-0.068}$ | $13.909^{+0.121}_{-0.103}$ | 1.16 | 1.41 | 0.66 | FAST |
| 66 | IRAS 09438+1141 | $1.400^{+0.011}_{-0.011}$ | $5.477^{+0.130}_{-0.137}$ | $-0.577^{+0.039}_{-0.046}$ | $-0.438^{+0.007}_{-0.007}$ | $-0.697^{+0.004}_{-0.004}$ | $-1.481^{+0.052}_{-0.052}$ | $6.487^{+0.051}_{-0.051}$ | ... | 0.67 | 0.66 | SDSS |
| 67 | NGC 3015 | $1.670^{+0.021}_{-0.021}$ | $5.851^{+0.243}_{-0.248}$ | $-0.203^{+0.038}_{-0.038}$ | $-0.184^{+0.010}_{-0.010}$ | $-0.434^{+0.006}_{-0.005}$ | $-0.971^{+0.069}_{-0.088}$ | $9.043^{+0.114}_{-0.114}$ | ... | 0.65 | 0.72 | SDSS |

**Table 7.A.1:** Continued

| SFRS | Galaxy | F(H$\alpha$) | H$\alpha$/H$\beta$ | [O III]/H$\beta$ | [N II]/H$\alpha$ | [S II]/H$\alpha$ | [O I]/H$\alpha$ | F(H$\alpha$)$_{cor}$ | $A_V$ | $A_V$nuc | E(B-V)$_{\rm gas}$ | Observation |
|---|---|---|---|---|---|---|---|---|---|---|---|---|
| (1) | (2) | (3) | (4) | (5) | (6) | (7) | (8) | (9) | (10) | (11) | (12) | (13) |
| 68 | MCG 2-25-039 | $2.340^{+0.022}_{-0.022}$ | $5.393^{+0.114}_{-0.118}$ | $-0.466^{+0.024}_{-0.023}$ | $-0.421^{+0.007}_{-0.007}$ | $-0.515^{+0.004}_{-0.004}$ | $-1.527^{+0.044}_{-0.046}$ | $10.454^{+0.098}_{-0.098}$ | ... | 0.67 | 0.64 | SDSS |
| 69 | NGC 3020 | $0.585^{+0.007}_{-0.006}$ | $3.475^{+0.116}_{-0.133}$ | $0.023^{+0.021}_{-0.020}$ | $-0.618^{+0.014}_{-0.013}$ | $-0.340^{+0.005}_{-0.005}$ | $-1.293^{+0.062}_{-0.051}$ | $0.926^{+0.011}_{-0.010}$ | ... | 0.22 | 0.20 | SDSS |
| 70 | NGC 3049 | $30.300^{+0.189}_{-0.189}$ | $3.873^{+0.038}_{-0.037}$ | $-0.486^{+0.006}_{-0.006}$ | $-0.421^{+0.004}_{-0.004}$ | $-0.692^{+0.003}_{-0.003}$ | $-2.219^{+0.021}_{-0.021}$ | $61.972^{+0.387}_{-0.387}$ | ... | 0.20 | 0.31 | SDSS |
| 71 | NGC 3055 | $19.900^{+0.113}_{-0.113}$ | $4.244^{+0.036}_{-0.036}$ | $-0.151^{+0.004}_{-0.004}$ | $-0.309^{+0.003}_{-0.003}$ | $-0.585^{+0.002}_{-0.002}$ | $-1.713^{+0.010}_{-0.010}$ | $50.508^{+0.287}_{-0.287}$ | ... | 0.75 | 0.40 | SDSS |
| 72 | IC 2520 | $1.530^{+0.017}_{-0.014}$ | $5.308^{+0.136}_{-0.146}$ | $-0.040^{+0.016}_{-0.016}$ | $-0.430^{+0.008}_{-0.009}$ | $-0.461^{+0.004}_{-0.005}$ | $-1.485^{+0.058}_{-0.046}$ | $6.584^{+0.073}_{-0.060}$ | ... | 1.57 | 0.63 | SDSS |
| 73 | UGC 5403 | $8.180^{+0.056}_{-0.050}$ | $7.542^{+0.106}_{-0.106}$ | $-0.569^{+0.014}_{-0.015}$ | $-0.308^{+0.004}_{-0.005}$ | $-0.531^{+0.003}_{-0.003}$ | ... | $80.640^{+0.552}_{-0.493}$ | ... | 1.59 | 0.98 | SDSS |
| 74 | UGC 5459 | $0.386^{+0.007}_{-0.007}$ | $4.503^{+0.357}_{-0.353}$ | $-0.211^{+0.081}_{-0.092}$ | $-0.519^{+0.025}_{-0.024}$ | $-0.338^{+0.008}_{-0.008}$ | $-1.377^{+0.167}_{-0.173}$ | $1.127^{+0.020}_{-0.020}$ | 0.37 | 0.79 | 0.46 | FAST |
| 75 | MCG 5-24-022 | $1.850^{+0.017}_{-0.017}$ | $5.597^{+0.172}_{-0.172}$ | $-0.405^{+0.032}_{-0.033}$ | $-0.372^{+0.008}_{-0.008}$ | $-0.665^{+0.004}_{-0.004}$ | $-1.630^{+0.138}_{-0.239}$ | $9.022^{+0.083}_{-0.083}$ | ... | 0.80 | 0.68 | SDSS |
| 76 | IC 2551 | $30.400^{+0.147}_{-0.147}$ | $5.325^{+0.047}_{-0.045}$ | $-0.206^{+0.005}_{-0.005}$ | $-0.329^{+0.003}_{-0.003}$ | $-0.608^{+0.002}_{-0.002}$ | $-1.646^{+0.013}_{-0.013}$ | $131.805^{+0.637}_{-0.637}$ | ... | 0.72 | 0.63 | SDSS |
| 77 | IRAS 10106+2745 | $0.590^{+0.005}_{-0.006}$ | $5.713^{+0.165}_{-0.186}$ | $-0.365^{+0.035}_{-0.027}$ | $-0.432^{+0.008}_{-0.008}$ | $-0.520^{+0.004}_{-0.004}$ | $-1.718^{+0.072}_{-0.079}$ | $3.020^{+0.026}_{-0.031}$ | ... | 0.89 | 0.70 | SDSS |
| 78 | NGC 3162 | $3.500^{+0.036}_{-0.036}$ | $3.735^{+0.139}_{-0.143}$ | $-0.706^{+0.072}_{-0.083}$ | $-0.464^{+0.032}_{-0.019}$ | $-0.625^{+0.004}_{-0.004}$ | ... | $6.571^{+0.068}_{-0.068}$ | 0.16 | 0.33 | 0.27 | FAST |
| 79 | IRAS 10120+1653 | $0.418^{+0.024}_{-0.029}$ | $9.443^{+2.062}_{-2.001}$ | $-0.025^{+0.134}_{-0.139}$ | $0.004^{+0.036}_{-0.034}$ | ... | $-1.058^{+0.133}_{-0.139}$ | $5.791^{+0.333}_{-0.402}$ | 1.67 | 1.72 | 1.13 | FAST |
| 79 | IRAS 10120+1653 | $0.357^{+0.005}_{-0.005}$ | $9.631^{+0.951}_{-0.938}$ | $0.129^{+0.063}_{-0.062}$ | $0.061^{+0.009}_{-0.009}$ | $-0.370^{+0.006}_{-0.006}$ | $-0.999^{+0.035}_{-0.036}$ | $6.267^{+0.094}_{-0.094}$ | ... | 1.45 | 1.23 | SDSS |
| 81 | IC 602 | $1.170^{+0.012}_{-0.011}$ | $4.268^{+0.143}_{-0.110}$ | $-0.372^{+0.029}_{-0.033}$ | $-0.430^{+0.009}_{-0.009}$ | $-0.461^{+0.004}_{-0.005}$ | $-1.303^{+0.065}_{-0.063}$ | $3.009^{+0.031}_{-0.028}$ | ... | 0.51 | 0.40 | SDSS |
| 82 | NGC 3191 | $0.913^{+0.023}_{-0.023}$ | $4.731^{+0.578}_{-0.559}$ | $-0.535^{+0.183}_{-0.213}$ | $-0.453^{+0.032}_{-0.033}$ | $-0.582^{+0.011}_{-0.011}$ | ... | $2.994^{+0.075}_{-0.075}$ | 0.17 | 0.31 | 0.51 | FAST |
| 83 | NGC 3206 | $1.740^{+0.013}_{-0.013}$ | $3.522^{+0.060}_{-0.058}$ | $0.187^{+0.008}_{-0.009}$ | $-0.791^{+0.007}_{-0.009}$ | $-0.530^{+0.003}_{-0.003}$ | $-1.770^{+0.052}_{-0.046}$ | $2.844^{+0.021}_{-0.021}$ | ... | 0.05 | 0.21 | SDSS |
| 84 | UGC 5613 | $2.970^{+0.022}_{-0.021}$ | $6.604^{+0.140}_{-0.139}$ | $0.058^{+0.013}_{-0.013}$ | $-0.223^{+0.005}_{-0.005}$ | $-0.443^{+0.003}_{-0.003}$ | $-1.268^{+0.024}_{-0.024}$ | $21.401^{+0.159}_{-0.151}$ | ... | 1.32 | 0.85 | SDSS |
| 85 | UGC 5644 | $0.133^{+0.011}_{-0.010}$ | $2.860^{+0.550}_{-0.523}$ | $0.273^{+0.084}_{-0.087}$ | $0.072^{+0.045}_{-0.049}$ | $-0.058^{+0.033}_{-0.037}$ | $-0.270^{+0.102}_{-0.103}$ | $0.133^{+0.011}_{-0.010}$ | ... | -0.02 | 0.00 | SDSS |
| 86 | NGC 3245 | $5.960^{+0.135}_{-0.135}$ | $5.877^{+0.439}_{-0.426}$ | $-0.079^{+0.047}_{-0.049}$ | $-0.104^{+0.015}_{-0.015}$ | $-0.431^{+0.010}_{-0.010}$ | $-1.459^{+0.076}_{-0.076}$ | $32.613^{+0.739}_{-0.739}$ | 0.15 | 0.15 | 0.73 | FAST |
| 87 | IRAS 10246+2042 | $2.740^{+0.022}_{-0.022}$ | $6.935^{+0.152}_{-0.151}$ | $-0.528^{+0.029}_{-0.028}$ | $-0.246^{+0.006}_{-0.005}$ | $-0.552^{+0.003}_{-0.003}$ | $-1.432^{+0.038}_{-0.038}$ | $22.159^{+0.178}_{-0.178}$ | ... | 1.15 | 0.90 | SDSS |
| 88 | MCG 7-22-012 | $0.791^{+0.011}_{-0.009}$ | $5.971^{+0.374}_{-0.370}$ | $-0.322^{+0.056}_{-0.057}$ | $-0.446^{+0.013}_{-0.012}$ | $-0.408^{+0.005}_{-0.006}$ | $-1.365^{+0.106}_{-0.144}$ | $4.494^{+0.062}_{-0.051}$ | 0.53 | 0.67 | 0.74 | FAST |
| 89 | IRAS 10276+1119 | $3.420^{+0.025}_{-0.025}$ | $4.532^{+0.073}_{-0.073}$ | $-0.447^{+0.022}_{-0.022}$ | $-0.284^{+0.005}_{-0.005}$ | $-0.587^{+0.003}_{-0.003}$ | $-1.487^{+0.032}_{-0.033}$ | $10.135^{+0.074}_{-0.074}$ | ... | 0.40 | 0.47 | SDSS |
| 90 | NGC 3265 | $16.300^{+0.110}_{-0.111}$ | $4.294^{+0.053}_{-0.052}$ | $-0.424^{+0.009}_{-0.008}$ | $-0.396^{+0.004}_{-0.004}$ | $-0.535^{+0.003}_{-0.003}$ | $-1.810^{+0.027}_{-0.028}$ | $42.530^{+0.287}_{-0.290}$ | ... | 0.47 | 0.41 | SDSS |

**Table 7.A.1:** Continued

| SFRS | Galaxy | F(H$\alpha$) | H$\alpha$/H$\beta$ | [O III]/H$\beta$ | [N II]/H$\alpha$ | [S II]/H$\alpha$ | [O I]/H$\alpha$ | F(H$\alpha$)$_{cor}$ | A$_V$ | A$_V$nuc | E(B-V)$_{\rm gas}$ | Observation |
|---|---|---|---|---|---|---|---|---|---|---|---|---|
| (1) | (2) | (3) | (4) | (5) | (6) | (7) | (8) | (9) | (10) | (11) | (12) | (13) |
| 91 | UGC 5713 | $0.764^{+0.019}_{-0.029}$ | $5.641^{+0.475}_{-0.487}$ | $0.762^{+0.035}_{-0.036}$ | $0.156^{+0.018}_{-0.014}$ | $-0.007^{+0.016}_{-0.011}$ | $-0.646^{+0.042}_{-0.042}$ | $3.138^{+0.078}_{-0.119}$ | ... | 1.12 | 0.61 | SDSS |
| 92 | NGC 3274 | $3.860^{+0.026}_{-0.022}$ | $2.977^{+0.064}_{-0.063}$ | $0.426^{+0.009}_{-0.009}$ | $-0.991^{+0.022}_{-0.027}$ | $-0.484^{+0.003}_{-0.003}$ | $-1.503^{+0.079}_{-0.086}$ | $4.243^{+0.029}_{-0.024}$ | 0.27 | 0.24 | 0.04 | FAST |
| 93 | UGC 5720 | $2.080^{+0.033}_{-0.058}$ | $0.127^{+0.002}_{-0.004}$ | $0.231^{+0.004}_{-0.005}$ | $0.718^{+0.012}_{-0.008}$ | $0.724^{+0.012}_{-0.007}$ | $-0.448^{+0.018}_{-0.015}$ | $0.001^{+0.001}_{-0.001}$ | ... | 0.50 | -3.15 | SDSS |
| 94 | KUG 1031+351 | $5.100^{+0.034}_{-0.034}$ | $5.112^{+0.072}_{-0.072}$ | $-0.516^{+0.016}_{-0.014}$ | $-0.384^{+0.005}_{-0.005}$ | $-0.571^{+0.003}_{-0.003}$ | $-1.414^{+0.017}_{-0.018}$ | $20.081^{+0.134}_{-0.134}$ | ... | 0.52 | 0.59 | SDSS |
| 95 | NGC 3306 | $3.110^{+0.028}_{-0.025}$ | $4.912^{+0.216}_{-0.214}$ | $-0.612^{+0.079}_{-0.087}$ | $-0.390^{+0.009}_{-0.009}$ | $-0.495^{+0.004}_{-0.004}$ | $-1.532^{+0.121}_{-0.137}$ | $11.145^{+0.100}_{-0.090}$ | 1.14 | 1.45 | 0.55 | FAST |
| 96 | NGC 3323 | $1.480^{+0.012}_{-0.012}$ | $3.903^{+0.082}_{-0.073}$ | $-0.395^{+0.020}_{-0.018}$ | $-0.496^{+0.007}_{-0.007}$ | $-0.480^{+0.004}_{-0.004}$ | $-1.614^{+0.055}_{-0.054}$ | $3.083^{+0.025}_{-0.025}$ | ... | 0.39 | 0.31 | SDSS |
| 97 | IC 2598 | $3.310^{+0.021}_{-0.020}$ | $4.810^{+0.064}_{-0.065}$ | $-0.493^{+0.013}_{-0.012}$ | $-0.428^{+0.005}_{-0.005}$ | $-0.556^{+0.003}_{-0.003}$ | $-1.623^{+0.021}_{-0.022}$ | $11.289^{+0.072}_{-0.068}$ | ... | 0.84 | 0.53 | SDSS |
| 98 | NGC 3338 | $0.155^{+0.008}_{-0.007}$ | $2.826^{+0.346}_{-0.368}$ | $0.086^{+0.075}_{-0.059}$ | $-0.060^{+0.032}_{-0.036}$ | $-0.378^{+0.020}_{-0.023}$ | $-0.500^{+0.106}_{-0.106}$ | $0.151^{+0.008}_{-0.007}$ | ... | 0.46 | -0.01 | SDSS |
| 99 | NGC 3353 | $12.700^{+0.088}_{-0.083}$ | $2.994^{+0.033}_{-0.032}$ | $0.428^{+0.005}_{-0.006}$ | $-0.903^{+0.005}_{-0.006}$ | $-0.657^{+0.003}_{-0.003}$ | $-1.633^{+0.014}_{-0.015}$ | $14.149^{+0.098}_{-0.092}$ | ... | 0.32 | 0.05 | SDSS |
| 100 | UGC 5881 | $6.910^{+0.041}_{-0.041}$ | $5.363^{+0.076}_{-0.076}$ | $0.255^{+0.007}_{-0.007}$ | $-0.207^{+0.004}_{-0.004}$ | $-0.487^{+0.003}_{-0.003}$ | $-1.389^{+0.026}_{-0.027}$ | $30.467^{+0.181}_{-0.181}$ | ... | 0.86 | 0.64 | SDSS |
| 101 | NGC 3370 | $2.110^{+0.006}_{-0.006}$ | $4.667^{+0.084}_{-0.084}$ | $-0.612^{+0.039}_{-0.039}$ | $-0.432^{+0.003}_{-0.003}$ | $-0.593^{+0.001}_{-0.001}$ | $-1.017^{+0.035}_{-0.035}$ | $6.701^{+0.019}_{-0.019}$ | 0.83 | 0.85 | 0.49 | FAST |
| 102 | NGC 3381 | $10.900^{+0.073}_{-0.073}$ | $3.591^{+0.039}_{-0.039}$ | $-0.697^{+0.009}_{-0.008}$ | $-0.524^{+0.004}_{-0.004}$ | $-0.740^{+0.003}_{-0.003}$ | $-2.306^{+0.034}_{-0.038}$ | $18.651^{+0.125}_{-0.125}$ | ... | -0.00 | 0.23 | SDSS |
| 103 | UGC 5941_NED02 | $6.920^{+0.046}_{-0.047}$ | $6.384^{+0.110}_{-0.111}$ | $-0.644^{+0.028}_{-0.029}$ | $-0.301^{+0.005}_{-0.005}$ | $-0.669^{+0.003}_{-0.003}$ | $-1.624^{+0.046}_{-0.048}$ | $46.032^{+0.306}_{-0.313}$ | ... | 0.86 | 0.81 | SDSS |
| 104 | NGC 3413 | $2.020^{+0.017}_{-0.015}$ | $3.896^{+0.081}_{-0.068}$ | $0.352^{+0.009}_{-0.010}$ | $-0.979^{+0.013}_{-0.014}$ | $-0.548^{+0.003}_{-0.004}$ | $-1.518^{+0.048}_{-0.044}$ | $4.190^{+0.035}_{-0.031}$ | ... | 0.35 | 0.31 | SDSS |
| 105 | NGC 3408 | $1.230^{+0.011}_{-0.012}$ | $5.174^{+0.206}_{-0.154}$ | $-0.577^{+0.082}_{-0.053}$ | $-0.445^{+0.009}_{-0.009}$ | $-0.792^{+0.004}_{-0.004}$ | $-1.449^{+0.093}_{-0.098}$ | $4.983^{+0.045}_{-0.049}$ | ... | 0.53 | 0.60 | SDSS |
| 106 | NGC 3430 | $2.910^{+0.026}_{-0.027}$ | $6.488^{+0.384}_{-0.382}$ | $-0.609^{+0.086}_{-0.087}$ | $-0.421^{+0.011}_{-0.010}$ | $-0.553^{+0.004}_{-0.004}$ | $-1.402^{+0.072}_{-0.072}$ | $20.110^{+0.180}_{-0.187}$ | 1.36 | 0.92 | 0.83 | FAST |
| 107 | CGCG 95-055 | $1.250^{+0.022}_{-0.013}$ | $6.441^{+0.259}_{-0.241}$ | $0.574^{+0.017}_{-0.017}$ | $0.110^{+0.006}_{-0.009}$ | $-0.169^{+0.005}_{-0.008}$ | $-0.832^{+0.020}_{-0.022}$ | $7.021^{+0.124}_{-0.073}$ | ... | 0.88 | 0.74 | SDSS |
| 108 | IRAS 10565+2448W | $5.120^{+0.013}_{-0.013}$ | $10.717^{+0.247}_{-0.243}$ | $-0.360^{+0.027}_{-0.027}$ | $-0.294^{+0.003}_{-0.003}$ | $-0.576^{+0.001}_{-0.001}$ | $-1.378^{+0.032}_{-0.032}$ | $95.624^{+0.243}_{-0.243}$ | 1.36 | 1.85 | 1.25 | FAST |
| 109 | UGC 6074 | $8.230^{+0.051}_{-0.051}$ | $8.259^{+0.114}_{-0.115}$ | $-0.599^{+0.015}_{-0.015}$ | $-0.233^{+0.004}_{-0.004}$ | $-0.565^{+0.003}_{-0.003}$ | $-1.705^{+0.023}_{-0.024}$ | $100.525^{+0.623}_{-0.623}$ | ... | 1.57 | 1.07 | SDSS |
| 110 | NGC 3495 | $0.246^{+0.010}_{-0.009}$ | $3.788^{+0.557}_{-0.528}$ | $-0.291^{+0.147}_{-0.155}$ | $-0.368^{+0.080}_{-0.071}$ | $-0.311^{+0.017}_{-0.017}$ | $-0.244^{+0.085}_{-0.108}$ | $0.477^{+0.019}_{-0.017}$ | 0.45 | 0.56 | 0.28 | FAST |
| 111 | UGC 6103 | $7.540^{+0.054}_{-0.054}$ | $4.594^{+0.070}_{-0.070}$ | $-0.125^{+0.010}_{-0.010}$ | $-0.240^{+0.005}_{-0.005}$ | $-0.530^{+0.003}_{-0.003}$ | $-1.514^{+0.028}_{-0.028}$ | $23.073^{+0.165}_{-0.165}$ | ... | 0.37 | 0.48 | SDSS |
| 112 | MCG 7-23-019 | $2.050^{+0.024}_{-0.024}$ | $7.338^{+0.696}_{-0.680}$ | $-0.084^{+0.058}_{-0.059}$ | $-0.350^{+0.013}_{-0.013}$ | $-0.540^{+0.005}_{-0.005}$ | $-1.198^{+0.088}_{-0.096}$ | $18.943^{+0.222}_{-0.222}$ | 0.23 | 0.02 | 0.95 | FAST |
| 113 | UGC 6135 | $0.548^{+0.018}_{-0.014}$ | $5.054^{+0.505}_{-0.482}$ | $0.329^{+0.051}_{-0.051}$ | $0.102^{+0.016}_{-0.018}$ | $-0.113^{+0.011}_{-0.014}$ | $-0.578^{+0.058}_{-0.065}$ | $2.100^{+0.069}_{-0.054}$ | ... | 0.39 | 0.58 | SDSS |

**Table 7.A.1:** Continued

| SFRS | Galaxy | F(H$\alpha$) | H$\alpha$/H$\beta$ | [O III]/H$\beta$ | [N II]/H$\alpha$ | [S II]/H$\alpha$ | [O I]/H$\alpha$ | F(H$\alpha$)$_{cor}$ | $A_V$ | $A_V$nuc | E(B-V)$_{\rm gas}$ | Observation |
|---|---|---|---|---|---|---|---|---|---|---|---|---|
| (1) | (2) | (3) | (4) | (5) | (6) | (7) | (8) | (9) | (10) | (11) | (12) | (13) |
| 114 | CGCG 241-078 | $1.730^{+0.015}_{-0.014}$ | $10.890^{+0.448}_{-0.435}$ | $-0.213^{+0.035}_{-0.036}$ | $-0.184^{+0.006}_{-0.006}$ | $-0.453^{+0.003}_{-0.004}$ | $-1.258^{+0.034}_{-0.036}$ | $40.583^{+0.352}_{-0.328}$ | ... | 1.53 | 1.35 | SDSS |
| 115 | IRAS 11069+2711 | $0.507^{+0.005}_{-0.004}$ | $4.080^{+0.107}_{-0.095}$ | $0.011^{+0.015}_{-0.014}$ | $-0.655^{+0.008}_{-0.008}$ | $-0.521^{+0.004}_{-0.004}$ | $-1.432^{+0.032}_{-0.033}$ | $1.173^{+0.012}_{-0.009}$ | ... | 0.29 | 0.36 | SDSS |
| 116 | IC 676 | $5.080^{+0.037}_{-0.038}$ | $5.527^{+0.092}_{-0.091}$ | $-0.558^{+0.022}_{-0.022}$ | $-0.345^{+0.005}_{-0.005}$ | $-0.478^{+0.003}_{-0.003}$ | $-1.608^{+0.041}_{-0.042}$ | $24.048^{+0.175}_{-0.180}$ | ... | 0.73 | 0.67 | SDSS |
| 117 | IRAS 11102+3026 | $0.324^{+0.033}_{-0.025}$ | $8.634^{+6.381}_{-4.190}$ | $0.163^{+0.266}_{-0.342}$ | $-0.105^{+0.053}_{-0.063}$ | $-0.431^{+0.034}_{-0.044}$ | $-1.099^{+0.237}_{-0.243}$ | $4.395^{+0.448}_{-0.339}$ | 0.38 | 0.68 | 1.12 | FAST |
| 117 | IRAS 11102+3026 | $0.257^{+0.006}_{-0.006}$ | $15.387^{+3.575}_{-3.773}$ | $0.240^{+0.122}_{-0.128}$ | $-0.038^{+0.014}_{-0.015}$ | $-0.308^{+0.010}_{-0.010}$ | $-0.886^{+0.070}_{-0.075}$ | $13.630^{+0.318}_{-0.299}$ | ... | 0.95 | 1.70 | SDSS |
| 118 | IC 2637 | $4.700^{+0.041}_{-0.041}$ | $5.431^{+0.136}_{-0.135}$ | $0.501^{+0.011}_{-0.011}$ | $-0.050^{+0.006}_{-0.006}$ | $-0.329^{+0.004}_{-0.004}$ | $-0.787^{+0.013}_{-0.013}$ | $17.651^{+0.154}_{-0.154}$ | ... | 0.21 | 0.57 | SDSS |
| 119 | MCG 9-19-013 | $0.408^{+0.005}_{-0.005}$ | $6.512^{+0.461}_{-0.374}$ | $-0.059^{+0.048}_{-0.049}$ | $-0.316^{+0.011}_{-0.011}$ | $-0.415^{+0.006}_{-0.005}$ | $-1.064^{+0.073}_{-0.067}$ | $2.844^{+0.035}_{-0.035}$ | ... | 0.98 | 0.83 | SDSS |
| 120 | 7ZW384 | $2.690^{+0.010}_{-0.010}$ | $4.254^{+0.076}_{-0.075}$ | $-0.108^{+0.012}_{-0.012}$ | $-0.216^{+0.003}_{-0.003}$ | $-0.388^{+0.002}_{-0.002}$ | $-0.951^{+0.016}_{-0.016}$ | $6.865^{+0.026}_{-0.026}$ | 0.32 | 0.29 | 0.40 | FAST |
| 121 | 2MASX J11193404+5335181 | $2.750^{+0.041}_{-0.078}$ | $5.030^{+0.110}_{-0.163}$ | $0.302^{+0.008}_{-0.008}$ | $-0.338^{+0.014}_{-0.022}$ | $-0.499^{+0.012}_{-0.006}$ | $-1.204^{+0.024}_{-0.022}$ | $8.618^{+0.128}_{-0.244}$ | ... | 1.21 | 0.49 | SDSS |
| 122 | NGC 3633 | $3.400^{+0.026}_{-0.026}$ | $7.274^{+0.175}_{-0.184}$ | $-0.584^{+0.036}_{-0.036}$ | $-0.306^{+0.006}_{-0.006}$ | $-0.638^{+0.003}_{-0.003}$ | $-1.673^{+0.065}_{-0.068}$ | $30.775^{+0.235}_{-0.235}$ | ... | 1.64 | 0.94 | SDSS |
| 123 | NGC 3652 | $1.610^{+0.012}_{-0.012}$ | $3.760^{+0.063}_{-0.066}$ | $-0.384^{+0.015}_{-0.015}$ | $-0.512^{+0.006}_{-0.007}$ | $-0.424^{+0.003}_{-0.003}$ | $-1.590^{+0.043}_{-0.041}$ | $3.071^{+0.023}_{-0.023}$ | ... | 0.39 | 0.28 | SDSS |
| 124 | NGC 3656 | $1.030^{+0.011}_{-0.011}$ | $5.699^{+0.210}_{-0.208}$ | $0.055^{+0.022}_{-0.022}$ | $-0.306^{+0.009}_{-0.010}$ | $-0.255^{+0.005}_{-0.005}$ | $-1.011^{+0.036}_{-0.038}$ | $5.242^{+0.056}_{-0.056}$ | ... | 1.15 | 0.70 | SDSS |
| 125 | NGC 3659 | $1.800^{+0.020}_{-0.026}$ | $3.767^{+0.121}_{-0.128}$ | $-0.335^{+0.030}_{-0.030}$ | $-0.527^{+0.015}_{-0.014}$ | $-0.525^{+0.006}_{-0.005}$ | $-1.656^{+0.130}_{-0.110}$ | $3.448^{+0.038}_{-0.050}$ | -0.02 | -0.06 | 0.28 | FAST |
| 126 | NGC 3664 | $0.773^{+0.010}_{-0.009}$ | $2.695^{+0.070}_{-0.068}$ | $0.149^{+0.012}_{-0.012}$ | $-0.661^{+0.014}_{-0.014}$ | $-0.441^{+0.005}_{-0.006}$ | $-1.516^{+0.097}_{-0.108}$ | $0.672^{+0.009}_{-0.008}$ | 0.14 | -0.13 | -0.06 | FAST |
| 127 | NGC 3666 | $0.602^{+0.009}_{-0.008}$ | $5.509^{+0.289}_{-0.273}$ | $-0.290^{+0.051}_{-0.056}$ | $-0.373^{+0.015}_{-0.013}$ | $-0.400^{+0.006}_{-0.006}$ | $-1.311^{+0.103}_{-0.097}$ | $2.828^{+0.042}_{-0.038}$ | ... | 0.85 | 0.66 | SDSS |
| 128 | IC 691 | $22.400^{+0.116}_{-0.116}$ | $5.174^{+0.049}_{-0.049}$ | $0.399^{+0.004}_{-0.005}$ | $-0.811^{+0.004}_{-0.004}$ | $-0.723^{+0.002}_{-0.002}$ | $-1.704^{+0.012}_{-0.012}$ | $90.745^{+0.470}_{-0.470}$ | ... | 0.93 | 0.60 | SDSS |
| 129 | NGC 3686 | $12.100^{+0.075}_{-0.068}$ | $4.077^{+0.060}_{-0.071}$ | $-0.749^{+0.038}_{-0.037}$ | $-0.499^{+0.006}_{-0.006}$ | $-0.787^{+0.002}_{-0.003}$ | $-1.759^{+0.119}_{-0.544}$ | $27.935^{+0.173}_{-0.157}$ | 0.63 | 0.22 | 0.36 | FAST |
| 130 | UGC 6469 | $2.460^{+0.048}_{-0.016}$ | $4.066^{+0.130}_{-0.085}$ | $-0.245^{+0.016}_{-0.018}$ | $-0.469^{+0.007}_{-0.012}$ | $-0.800^{+0.003}_{-0.009}$ | $-1.541^{+0.071}_{-0.077}$ | $5.643^{+0.110}_{-0.037}$ | 0.06 | 0.06 | 0.36 | FAST |
| 131 | NGC 3690 | $12.000^{+0.057}_{-0.057}$ | $3.706^{+0.043}_{-0.041}$ | $0.100^{+0.006}_{-0.006}$ | $-0.336^{+0.004}_{-0.004}$ | $-0.482^{+0.002}_{-0.002}$ | $-1.301^{+0.019}_{-0.019}$ | $18.288^{+0.087}_{-0.087}$ | 0.40 | 0.42 | 0.18 | FAST |
| 132 | IC 698 | $1.670^{+0.018}_{-0.018}$ | $7.780^{+0.330}_{-0.324}$ | $-0.352^{+0.049}_{-0.048}$ | $-0.355^{+0.009}_{-0.010}$ | $-0.612^{+0.005}_{-0.005}$ | $-1.409^{+0.076}_{-0.081}$ | $17.716^{+0.191}_{-0.191}$ | ... | 1.07 | 1.01 | SDSS |
| 133 | IRAS 11267+1558 | $1.120^{+0.028}_{-0.014}$ | $9.113^{+0.682}_{-0.653}$ | $-0.197^{+0.062}_{-0.064}$ | $-0.280^{+0.015}_{-0.019}$ | $-0.648^{+0.006}_{-0.011}$ | $-1.495^{+0.154}_{-0.160}$ | $17.256^{+0.431}_{-0.216}$ | 1.38 | 2.20 | 1.17 | FAST |
| 134 | NGC 3705 | $2.580^{+0.060}_{-0.060}$ | $8.431^{+1.257}_{-1.274}$ | $0.291^{+0.079}_{-0.080}$ | $-0.050^{+0.016}_{-0.016}$ | $-0.167^{+0.010}_{-0.010}$ | $-0.848^{+0.080}_{-0.087}$ | $33.084^{+0.769}_{-0.769}$ | 0.59 | 1.07 | 1.09 | FAST |
| 135 | MCG 3-29-061 | $2.250^{+0.016}_{-0.016}$ | $8.469^{+0.233}_{-0.147}$ | $-0.425^{+0.021}_{-0.024}$ | $-0.263^{+0.005}_{-0.005}$ | $-0.460^{+0.003}_{-0.003}$ | $-1.388^{+0.024}_{-0.025}$ | $29.160^{+0.207}_{-0.207}$ | ... | 1.45 | 1.10 | SDSS |

**Table 7.A.1:** Continued

| SFRS | Galaxy | F(H$\alpha$) | H$\alpha$/H$\beta$ | [O III]/H$\beta$ | [N II]/H$\alpha$ | [S II]/H$\alpha$ | [O I]/H$\alpha$ | F(H$\alpha$)$_{cor}$ | A$_V$ | A$_V$nuc | E(B-V)$_{\rm gas}$ | Observation |
|---|---|---|---|---|---|---|---|---|---|---|---|---|
| (1) | (2) | (3) | (4) | (5) | (6) | (7) | (8) | (9) | (10) | (11) | (12) | (13) |
| 136 | NGC 3720 | $1.070^{+0.010}_{-0.008}$ | $4.850^{+0.124}_{-0.118}$ | $-0.707^{+0.044}_{-0.046}$ | $-0.505^{+0.007}_{-0.008}$ | $-0.822^{+0.003}_{-0.004}$ | $-1.523^{+0.065}_{-0.060}$ | $3.721^{+0.035}_{-0.028}$ | ... | 0.33 | 0.53 | SDSS |
| 137 | NGC 3729 | $7.150^{+0.046}_{-0.047}$ | $4.884^{+0.101}_{-0.103}$ | $0.051^{+0.012}_{-0.012}$ | $-0.253^{+0.005}_{-0.005}$ | $-0.422^{+0.003}_{-0.003}$ | $-1.269^{+0.036}_{-0.037}$ | $25.279^{+0.163}_{-0.166}$ | 0.63 | 0.94 | 0.54 | FAST |
| 138 | MCG 10-17-019 | $1.450^{+0.014}_{-0.013}$ | $6.900^{+0.225}_{-0.233}$ | $-0.491^{+0.050}_{-0.052}$ | $-0.435^{+0.009}_{-0.009}$ | $-0.747^{+0.004}_{-0.004}$ | $-1.516^{+0.079}_{-0.074}$ | $11.587^{+0.112}_{-0.104}$ | ... | 0.88 | 0.89 | SDSS |
| 139 | NGC 3758 | $15.000^{+0.375}_{-0.375}$ | $14.348^{+1.226}_{-1.226}$ | $0.698^{+0.036}_{-0.036}$ | $-0.123^{+0.015}_{-0.015}$ | $-0.969^{+0.011}_{-0.011}$ | $-1.700^{+0.074}_{-0.079}$ | $557.737^{+13.943}_{-13.943}$ | 0.39 | 0.59 | 1.55 | FAST |
| 140 | UGC 6583 | $12.500^{+0.015}_{-0.015}$ | $4.315^{+0.019}_{-0.019}$ | $-0.324^{+0.005}_{-0.005}$ | $-0.438^{+0.001}_{-0.001}$ | $-0.609^{+0.001}_{-0.001}$ | $-1.586^{+0.017}_{-0.018}$ | $32.993^{+0.040}_{-0.040}$ | 0.38 | 0.48 | 0.42 | FAST |
| 141 | MCG 1-30-003 | $2.620^{+0.012}_{-0.012}$ | $7.292^{+0.089}_{-0.101}$ | $-0.420^{+0.012}_{-0.012}$ | $-0.361^{+0.003}_{-0.003}$ | $-0.500^{+0.002}_{-0.002}$ | $-1.523^{+0.018}_{-0.019}$ | $23.853^{+0.109}_{-0.109}$ | ... | 1.58 | 0.95 | SDSS |
| 142 | NGC 3769 | $0.895^{+0.012}_{-0.011}$ | $3.911^{+0.154}_{-0.150}$ | $-0.197^{+0.035}_{-0.036}$ | $-0.405^{+0.012}_{-0.013}$ | $-0.274^{+0.005}_{-0.006}$ | $-1.349^{+0.086}_{-0.092}$ | $1.873^{+0.025}_{-0.023}$ | ... | 0.43 | 0.32 | SDSS |
| 143 | NGC 3773 | $17.300^{+0.096}_{-0.096}$ | $2.946^{+0.035}_{-0.042}$ | $0.213^{+0.007}_{-0.005}$ | $-0.769^{+0.007}_{-0.007}$ | $-0.632^{+0.002}_{-0.002}$ | $-1.811^{+0.066}_{-0.090}$ | $18.553^{+0.103}_{-0.103}$ | 0.35 | 0.13 | 0.03 | FAST |
| 143 | NGC 3773 | $7.090^{+0.046}_{-0.041}$ | $3.688^{+0.041}_{-0.043}$ | $0.190^{+0.006}_{-0.006}$ | $-0.779^{+0.005}_{-0.005}$ | $-0.651^{+0.003}_{-0.003}$ | $-1.989^{+0.031}_{-0.031}$ | $12.919^{+0.084}_{-0.075}$ | ... | 0.42 | 0.26 | SDSS |
| 144 | NGC 3781 | $2.600^{+0.032}_{-0.032}$ | $13.022^{+0.703}_{-0.796}$ | $0.469^{+0.030}_{-0.026}$ | $0.243^{+0.006}_{-0.006}$ | $-0.278^{+0.005}_{-0.005}$ | $-0.818^{+0.021}_{-0.021}$ | $76.900^{+0.946}_{-0.946}$ | ... | 1.32 | 1.45 | SDSS |
| 145 | UGC 6625 | $1.440^{+0.011}_{-0.011}$ | $4.480^{+0.127}_{-0.127}$ | $-0.263^{+0.024}_{-0.024}$ | $-0.185^{+0.006}_{-0.006}$ | $-0.485^{+0.003}_{-0.003}$ | $-1.009^{+0.045}_{-0.045}$ | $4.153^{+0.032}_{-0.032}$ | 0.02 | 0.08 | 0.45 | FAST |
| 146 | NGC 3808_NED02 | $2.210^{+0.018}_{-0.017}$ | $4.548^{+0.093}_{-0.083}$ | $-0.466^{+0.020}_{-0.023}$ | $-0.368^{+0.006}_{-0.006}$ | $-0.454^{+0.003}_{-0.004}$ | $-1.344^{+0.032}_{-0.032}$ | $6.604^{+0.054}_{-0.051}$ | ... | 0.60 | 0.47 | SDSS |
| 147 | NGC 3811 | $2.220^{+0.030}_{-0.029}$ | $5.567^{+0.279}_{-0.276}$ | $-0.439^{+0.060}_{-0.061}$ | $-0.397^{+0.013}_{-0.013}$ | $-0.636^{+0.006}_{-0.006}$ | $-1.717^{+0.155}_{-0.167}$ | $10.690^{+0.144}_{-0.140}$ | 0.01 | 0.29 | 0.67 | FAST |
| 148 | NGC 3822 | $3.070^{+0.034}_{-0.034}$ | $6.101^{+0.250}_{-0.248}$ | $0.300^{+0.019}_{-0.019}$ | $-0.073^{+0.007}_{-0.007}$ | ... | $-1.093^{+0.051}_{-0.057}$ | $15.172^{+0.168}_{-0.168}$ | 0.47 | 0.33 | 0.68 | FAST |
| 149 | UGC 6665 | $24.100^{+0.217}_{-0.217}$ | $3.481^{+0.042}_{-0.042}$ | $0.386^{+0.005}_{-0.005}$ | $-0.795^{+0.005}_{-0.005}$ | $-0.721^{+0.004}_{-0.004}$ | $-1.707^{+0.010}_{-0.010}$ | $38.318^{+0.345}_{-0.345}$ | ... | 0.08 | 0.20 | SDSS |
| 150 | MCG 3-30-051 | $1.500^{+0.013}_{-0.013}$ | $5.980^{+0.163}_{-0.159}$ | $-0.531^{+0.041}_{-0.042}$ | $-0.546^{+0.009}_{-0.009}$ | $-0.720^{+0.004}_{-0.004}$ | $-1.628^{+0.071}_{-0.077}$ | $8.552^{+0.074}_{-0.074}$ | ... | 0.99 | 0.75 | SDSS |
| 151 | NGC 3839 | $3.160^{+0.024}_{-0.022}$ | $6.085^{+0.115}_{-0.112}$ | $-0.486^{+0.021}_{-0.022}$ | $-0.454^{+0.006}_{-0.006}$ | $-0.548^{+0.003}_{-0.003}$ | $-1.595^{+0.038}_{-0.039}$ | $18.771^{+0.143}_{-0.131}$ | ... | 1.25 | 0.76 | SDSS |
| 152 | UGC 6732 | $3.860^{+0.022}_{-0.022}$ | $14.725^{+0.418}_{-0.418}$ | $0.833^{+0.013}_{-0.013}$ | $0.142^{+0.003}_{-0.003}$ | $-0.160^{+0.002}_{-0.002}$ | $-0.700^{+0.009}_{-0.009}$ | $152.583^{+0.870}_{-0.870}$ | 0.73 | 0.79 | 1.57 | FAST |
| 153 | IC 730 | $3.740^{+0.029}_{-0.032}$ | $8.058^{+0.203}_{-0.199}$ | $-0.505^{+0.036}_{-0.037}$ | $-0.343^{+0.007}_{-0.006}$ | $-0.747^{+0.004}_{-0.003}$ | $-1.538^{+0.058}_{-0.060}$ | $43.102^{+0.334}_{-0.369}$ | ... | 1.48 | 1.05 | SDSS |
| 154 | IC 732_NED01 | $0.849^{+0.007}_{-0.013}$ | $9.834^{+0.751}_{-0.745}$ | $-0.172^{+0.060}_{-0.062}$ | $-0.345^{+0.012}_{-0.008}$ | $-0.799^{+0.007}_{-0.004}$ | $-1.302^{+0.073}_{-0.078}$ | $15.655^{+0.129}_{-0.240}$ | 0.47 | 0.60 | 1.25 | FAST |
| 155 | NGC 3912 | $2.670^{+0.021}_{-0.020}$ | $4.882^{+0.095}_{-0.096}$ | $-0.274^{+0.015}_{-0.015}$ | $-0.471^{+0.006}_{-0.006}$ | $-0.429^{+0.003}_{-0.003}$ | $-1.565^{+0.038}_{-0.038}$ | $9.431^{+0.074}_{-0.071}$ | ... | 0.81 | 0.54 | SDSS |
| 156 | NGC 3928 | $8.790^{+0.068}_{-0.068}$ | $3.298^{+0.048}_{-0.046}$ | $-0.219^{+0.009}_{-0.009}$ | $-0.315^{+0.006}_{-0.006}$ | $-0.507^{+0.003}_{-0.003}$ | $-1.457^{+0.032}_{-0.033}$ | $12.304^{+0.095}_{-0.095}$ | ... | 0.51 | 0.14 | SDSS |
| 157 | NGC 3934 | $0.467^{+0.009}_{-0.009}$ | $9.124^{+0.965}_{-0.970}$ | $0.075^{+0.061}_{-0.061}$ | $-0.249^{+0.015}_{-0.015}$ | $-0.224^{+0.008}_{-0.008}$ | $-0.892^{+0.069}_{-0.074}$ | $7.216^{+0.139}_{-0.139}$ | 1.14 | 1.66 | 1.17 | FAST |

**Table 7.A.1:** Continued

| SFRS | Galaxy | F(H$\alpha$) | H$\alpha$/H$\beta$ | [O III]/H$\beta$ | [N II]/H$\alpha$ | [S II]/H$\alpha$ | [O I]/H$\alpha$ | F(H$\alpha$)$_{cor}$ | $A_V$ | $A_V$nuc | E(B-V)$_{\rm gas}$ | Observation |
|---|---|---|---|---|---|---|---|---|---|---|---|---|
| (1) | (2) | (3) | (4) | (5) | (6) | (7) | (8) | (9) | (10) | (11) | (12) | (13) |
| 158 | UGC 6865 | $0.926^{+0.012}_{-0.012}$ | $7.113^{+0.418}_{-0.413}$ | $-0.474^{+0.080}_{-0.084}$ | $-0.437^{+0.014}_{-0.013}$ | $-0.689^{+0.006}_{-0.006}$ | $-1.308^{+0.084}_{-0.089}$ | $7.950^{+0.103}_{-0.103}$ | ... | 1.35 | 0.92 | SDSS |
| 159 | UGC 6901 | $1.710^{+0.015}_{-0.015}$ | $8.718^{+0.330}_{-0.323}$ | $-0.488^{+0.051}_{-0.058}$ | $-0.430^{+0.008}_{-0.008}$ | $-0.678^{+0.004}_{-0.004}$ | $-1.420^{+0.065}_{-0.065}$ | $23.730^{+0.208}_{-0.208}$ | ... | 1.04 | 1.13 | SDSS |
| 160 | CGCG 013-010 | $1.480^{+0.015}_{-0.011}$ | $8.344^{+0.276}_{-0.296}$ | $-0.016^{+0.027}_{-0.025}$ | $-0.173^{+0.006}_{-0.006}$ | $-0.452^{+0.003}_{-0.004}$ | $-1.154^{+0.124}_{-0.114}$ | $18.519^{+0.188}_{-0.138}$ | ... | 1.47 | 1.08 | SDSS |
| 161 | NGC 3991 | $10.300^{+0.014}_{-0.014}$ | $2.136^{+0.005}_{-0.005}$ | $0.458^{+0.001}_{-0.001}$ | $-1.014^{+0.003}_{-0.003}$ | $-0.678^{+0.001}_{-0.001}$ | $-1.762^{+0.020}_{-0.020}$ | $5.172^{+0.007}_{-0.007}$ | 0.18 | -0.36 | -0.30 | FAST |
| 162 | NGC 4004 | $1.960^{+0.014}_{-0.015}$ | $6.010^{+0.113}_{-0.112}$ | $-0.356^{+0.015}_{-0.017}$ | $-0.464^{+0.006}_{-0.005}$ | $-0.498^{+0.003}_{-0.003}$ | $-1.523^{+0.034}_{-0.031}$ | $11.307^{+0.081}_{-0.087}$ | ... | 1.17 | 0.75 | SDSS |
| 163 | NGC 4014 | $1.070^{+0.042}_{-0.032}$ | $5.083^{+0.740}_{-0.714}$ | $-0.060^{+0.093}_{-0.098}$ | $-0.244^{+0.027}_{-0.032}$ | $-0.422^{+0.013}_{-0.017}$ | $-1.285^{+0.163}_{-0.204}$ | $4.157^{+0.163}_{-0.124}$ | 0.76 | 0.84 | 0.58 | FAST |
| 164 | NGC 4010 | $0.370^{+0.004}_{-0.004}$ | $4.656^{+0.181}_{-0.209}$ | $-0.345^{+0.039}_{-0.040}$ | $-0.518^{+0.012}_{-0.013}$ | $-0.346^{+0.005}_{-0.005}$ | $-1.348^{+0.074}_{-0.068}$ | $1.169^{+0.013}_{-0.013}$ | ... | 1.11 | 0.49 | SDSS |
| 165 | NGC 4018 | $0.501^{+0.006}_{-0.005}$ | $6.511^{+0.294}_{-0.336}$ | $-0.135^{+0.037}_{-0.033}$ | $-0.408^{+0.011}_{-0.010}$ | $-0.335^{+0.005}_{-0.005}$ | $-1.159^{+0.044}_{-0.041}$ | $3.491^{+0.042}_{-0.035}$ | ... | 1.51 | 0.83 | SDSS |
| 166 | NGC 4020 | $0.133^{+0.003}_{-0.003}$ | $4.253^{+0.411}_{-0.282}$ | $-0.082^{+0.049}_{-0.066}$ | $-0.507^{+0.031}_{-0.029}$ | $-0.154^{+0.009}_{-0.010}$ | $-1.007^{+0.093}_{-0.089}$ | $0.339^{+0.008}_{-0.008}$ | ... | 0.47 | 0.40 | SDSS |
| 167 | IRAS 11571+3003 | $0.908^{+0.007}_{-0.007}$ | $8.107^{+0.276}_{-0.318}$ | $-0.562^{+0.057}_{-0.058}$ | $-0.304^{+0.007}_{-0.006}$ | $-0.525^{+0.004}_{-0.004}$ | $-1.389^{+0.050}_{-0.053}$ | $10.615^{+0.082}_{-0.082}$ | ... | 1.37 | 1.05 | SDSS |
| 168 | UGC 7017 | $2.790^{+0.021}_{-0.021}$ | $6.423^{+0.117}_{-0.119}$ | $-0.503^{+0.018}_{-0.021}$ | $-0.413^{+0.006}_{-0.006}$ | $-0.527^{+0.003}_{-0.003}$ | $-1.510^{+0.031}_{-0.032}$ | $18.828^{+0.142}_{-0.142}$ | ... | 1.43 | 0.82 | SDSS |
| 169 | UGC 7016 | $1.640^{+0.017}_{-0.024}$ | $6.313^{+0.262}_{-0.270}$ | $0.565^{+0.019}_{-0.019}$ | $-0.041^{+0.008}_{-0.007}$ | $-0.434^{+0.006}_{-0.004}$ | $-1.143^{+0.057}_{-0.064}$ | $8.785^{+0.091}_{-0.129}$ | ... | 0.85 | 0.72 | SDSS |
| 170 | MCG 3-31-030 | $0.738^{+0.015}_{-0.015}$ | $0.857^{+0.033}_{-0.031}$ | $-0.564^{+0.046}_{-0.048}$ | $-0.516^{+0.024}_{-0.022}$ | $-0.410^{+0.009}_{-0.009}$ | $-1.569^{+0.179}_{-0.196}$ | $0.043^{*+0.001}_{-0.001}$ | 0.50 | 0.52 | -1.22* | FAST |
| 170 | MCG 3-31-030 | $1.730^{+0.014}_{-0.012}$ | $3.800^{+0.059}_{-0.064}$ | $-0.513^{+0.015}_{-0.015}$ | $-0.588^{+0.006}_{-0.007}$ | $-0.473^{+0.003}_{-0.003}$ | $-1.701^{+0.043}_{-0.045}$ | $3.383^{+0.027}_{-0.023}$ | ... | 0.34 | 0.29 | SDSS |
| 171 | NGC 4062 | $0.325^{+0.009}_{-0.005}$ | $5.985^{+0.587}_{-0.581}$ | $-0.263^{+0.172}_{-0.127}$ | $-0.354^{+0.016}_{-0.024}$ | $-0.513^{+0.006}_{-0.012}$ | $-0.399^{+0.191}_{-0.642}$ | $1.856^{+0.051}_{-0.029}$ | ... | 0.62 | 0.75 | SDSS |
| 172 | NGC 4064 | $3.620^{+0.025}_{-0.020}$ | $5.002^{+0.116}_{-0.119}$ | $-0.832^{+0.059}_{-0.057}$ | $-0.593^{+0.006}_{-0.007}$ | $-0.644^{+0.002}_{-0.003}$ | $-1.940^{+0.147}_{-0.180}$ | $13.541^{+0.094}_{-0.075}$ | 0.34 | 0.69 | 0.57 | FAST |
| 173 | CGCG 098-059 | $7.700^{+0.050}_{-0.047}$ | $6.850^{+0.106}_{-0.110}$ | $-0.724^{+0.028}_{-0.029}$ | $-0.378^{+0.005}_{-0.005}$ | $-0.713^{+0.003}_{-0.003}$ | $-1.699^{+0.038}_{-0.037}$ | $60.486^{+0.393}_{-0.369}$ | ... | 1.10 | 0.88 | SDSS |
| 174 | NGC 4116 | $2.990^{+0.012}_{-0.012}$ | $3.508^{+0.041}_{-0.041}$ | $-0.293^{+0.009}_{-0.009}$ | $-0.623^{+0.005}_{-0.005}$ | $-0.564^{+0.002}_{-0.002}$ | $-2.015^{+0.076}_{-0.092}$ | $4.841^{+0.019}_{-0.019}$ | 0.02 | -0.24 | 0.21 | FAST |
| 175 | NGC 4136 | $0.827^{+0.029}_{-0.037}$ | $3.196^{+0.270}_{-0.279}$ | $-0.299^{+0.069}_{-0.072}$ | $-0.454^{+0.048}_{-0.037}$ | $-0.340^{+0.019}_{-0.015}$ | $-1.762^{+0.255}_{-0.359}$ | $1.075^{+0.038}_{-0.048}$ | 0.39 | 0.42 | 0.11 | FAST |
| 176 | NGC 4150 | $0.857^{+0.037}_{-0.030}$ | $8.572^{+2.060}_{-1.990}$ | $0.695^{+0.106}_{-0.109}$ | $-0.048^{+0.023}_{-0.027}$ | $0.038^{+0.015}_{-0.019}$ | $-0.642^{+0.069}_{-0.073}$ | $9.449^{+0.408}_{-0.331}$ | 0.28 | 0.39 | 1.03 | FAST |
| 177 | IRAS 12086+1441 | $2.300^{+0.015}_{-0.015}$ | $5.994^{+0.089}_{-0.092}$ | $-0.223^{+0.010}_{-0.010}$ | $-0.439^{+0.005}_{-0.005}$ | $-0.524^{+0.003}_{-0.003}$ | $-1.471^{+0.020}_{-0.017}$ | $13.185^{+0.086}_{-0.086}$ | ... | 1.17 | 0.75 | SDSS |
| 178 | NGC 4162 | $0.726^{+0.019}_{-0.019}$ | $4.342^{+0.411}_{-0.387}$ | $-0.087^{+0.064}_{-0.068}$ | $-0.266^{+0.023}_{-0.023}$ | $-0.425^{+0.011}_{-0.011}$ | $-1.493^{+0.177}_{-0.177}$ | $1.945^{+0.051}_{-0.051}$ | 0.36 | 0.59 | 0.42 | FAST |
| 178 | NGC 4162 | $0.601^{+0.005}_{-0.004}$ | $3.759^{+0.071}_{-0.085}$ | $-0.505^{+0.021}_{-0.024}$ | $-0.437^{+0.006}_{-0.007}$ | $-0.520^{+0.003}_{-0.003}$ | $-1.604^{+0.060}_{-0.058}$ | $1.146^{+0.009}_{-0.008}$ | ... | 0.18 | 0.28 | SDSS |

**Table 7.A.1:** Continued

| SFRS | Galaxy | F(H$\alpha$) | H$\alpha$/H$\beta$ | [O III]/H$\beta$ | [N II]/H$\alpha$ | [S II]/H$\alpha$ | [O I]/H$\alpha$ | F(H$\alpha$)$_{cor}$ | A$_V$ | A$_V$nuc | E(B-V)$_{\rm gas}$ | Observation |
|---|---|---|---|---|---|---|---|---|---|---|---|---|
| (1) | (2) | (3) | (4) | (5) | (6) | (7) | (8) | (9) | (10) | (11) | (12) | (13) |
| 179 | NGC 4178 | $0.539^{+0.013}_{-0.011}$ | $4.189^{+0.809}_{-0.652}$ | $-0.278^{+0.161}_{-0.200}$ | $-0.505^{+0.024}_{-0.029}$ | $-0.322^{+0.009}_{-0.010}$ | $-1.576^{+0.254}_{-0.359}$ | $1.327^{+0.032}_{-0.027}$ | 1.27 | 0.87 | 0.39 | FAST |
| 180 | IRAS 12112+0305 | $1.230^{+0.008}_{-0.008}$ | $7.116^{+0.179}_{-0.175}$ | $0.222^{+0.012}_{-0.012}$ | $-0.304^{+0.005}_{-0.005}$ | $-0.312^{+0.003}_{-0.003}$ | $-0.946^{+0.012}_{-0.012}$ | $8.740^{+0.057}_{-0.057}$ | ... | 0.82 | 0.84 | SDSS |
| 181 | NGC 4189 | $3.640^{+0.027}_{-0.028}$ | $5.178^{+0.086}_{-0.086}$ | $-0.757^{+0.026}_{-0.029}$ | $-0.449^{+0.006}_{-0.006}$ | $-0.612^{+0.003}_{-0.003}$ | $-1.830^{+0.054}_{-0.059}$ | $14.773^{+0.110}_{-0.114}$ | ... | 0.62 | 0.60 | SDSS |
| 182 | NGC 4194 | $7.040^{+0.056}_{-0.056}$ | $0.807^{+0.010}_{-0.010}$ | $-0.045^{+0.006}_{-0.006}$ | $0.414^{+0.004}_{-0.004}$ | $0.163^{+0.003}_{-0.003}$ | $-0.893^{+0.015}_{-0.015}$ | $0.355^{+0.003}_{-0.003}$ | ... | 0.36 | -1.28 | SDSS |
| 183 | NGC 4204 | $0.163^{+0.003}_{-0.003}$ | $3.090^{+0.194}_{-0.181}$ | $-0.101^{+0.041}_{-0.042}$ | $-0.608^{+0.022}_{-0.037}$ | $-0.228^{+0.008}_{-0.008}$ | $-1.158^{+0.101}_{-0.112}$ | $0.196^{+0.004}_{-0.004}$ | ... | 0.33 | 0.08 | SDSS |
| 184 | NGC 4207 | $1.190^{+0.013}_{-0.012}$ | $6.139^{+0.206}_{-0.181}$ | $-0.354^{+0.028}_{-0.032}$ | $-0.460^{+0.010}_{-0.009}$ | $-0.418^{+0.004}_{-0.005}$ | $-1.358^{+0.055}_{-0.057}$ | $7.218^{+0.079}_{-0.073}$ | ... | 1.45 | 0.77 | SDSS |
| 185 | UGC 7286 | $0.865^{+0.055}_{-0.052}$ | $7.149^{+1.276}_{-1.218}$ | $-0.209^{+0.124}_{-0.133}$ | $-0.301^{+0.034}_{-0.034}$ | $-0.666^{+0.026}_{-0.027}$ | $-1.307^{+0.156}_{-0.180}$ | $7.516^{+0.478}_{-0.452}$ | 0.73 | 1.05 | 0.93 | FAST |
| 186 | NGC 4234 | $3.310^{+0.014}_{-0.026}$ | $3.403^{+0.037}_{-0.044}$ | $-0.224^{+0.008}_{-0.008}$ | $-0.590^{+0.006}_{-0.004}$ | $-0.488^{+0.003}_{-0.002}$ | $-1.741^{+0.040}_{-0.041}$ | $4.989^{+0.021}_{-0.039}$ | -0.09 | -0.03 | 0.18 | FAST |
| 187 | NGC 4237 | $0.374^{+0.009}_{-0.009}$ | $4.619^{+0.424}_{-0.431}$ | $-0.122^{+0.070}_{-0.072}$ | $-0.295^{+0.021}_{-0.026}$ | $-0.596^{+0.010}_{-0.011}$ | $-0.916^{+0.129}_{-0.129}$ | $1.159^{+0.028}_{-0.028}$ | ... | 0.37 | 0.48 | SDSS |
| 188 | NGC 4244 | $0.406^{+0.009}_{-0.009}$ | $4.742^{+0.390}_{-0.415}$ | $-0.173^{+0.069}_{-0.068}$ | $-0.694^{+0.041}_{-0.043}$ | $-0.431^{+0.009}_{-0.010}$ | $-1.305^{+0.196}_{-0.315}$ | $1.339^{+0.030}_{-0.030}$ | ... | 0.58 | 0.51 | SDSS |
| 189 | NGC 4253 | $1.780^{+0.013}_{-0.013}$ | $3.693^{+0.068}_{-0.070}$ | $-0.169^{+0.014}_{-0.013}$ | $-0.367^{+0.006}_{-0.006}$ | $-0.590^{+0.003}_{-0.003}$ | $-1.478^{+0.187}_{-0.126}$ | $2.690^{+0.020}_{-0.020}$ | ... | 0.26 | 0.18 | SDSS |
| 190 | MCG 3-32-005 | $2.690^{+0.019}_{-0.018}$ | $6.285^{+0.125}_{-0.089}$ | $-0.626^{+0.021}_{-0.025}$ | $-0.445^{+0.005}_{-0.006}$ | $-0.576^{+0.003}_{-0.003}$ | $-1.530^{+0.030}_{-0.030}$ | $17.246^{+0.122}_{-0.115}$ | ... | 1.18 | 0.80 | SDSS |
| 191 | NGC 4290 | $8.190^{+0.057}_{-0.057}$ | $5.997^{+0.101}_{-0.100}$ | $-0.709^{+0.029}_{-0.029}$ | $-0.344^{+0.005}_{-0.005}$ | $-0.641^{+0.003}_{-0.003}$ | $-1.662^{+0.048}_{-0.048}$ | $47.005^{+0.327}_{-0.327}$ | ... | 0.91 | 0.75 | SDSS |
| 192 | NGC 4294 | $55.500^{+0.562}_{-0.596}$ | $4.949^{+0.156}_{-0.158}$ | $0.313^{+0.016}_{-0.015}$ | $-0.755^{+0.015}_{-0.015}$ | $-0.477^{+0.005}_{-0.004}$ | $-1.773^{+0.104}_{-0.111}$ | $202.443^{+2.050}_{-2.174}$ | 0.53 | 0.55 | 0.55 | FAST |
| 192 | NGC 4294 | $2.820^{+0.024}_{-0.017}$ | $3.204^{+0.043}_{-0.046}$ | $0.256^{+0.007}_{-0.007}$ | $-0.928^{+0.007}_{-0.008}$ | $-0.610^{+0.003}_{-0.004}$ | $-1.844^{+0.036}_{-0.045}$ | $3.687^{+0.031}_{-0.022}$ | ... | 0.40 | 0.12 | SDSS |
| 193 | NGC 4314 | $1.160^{+0.045}_{-0.048}$ | $3.668^{+0.385}_{-0.383}$ | $0.006^{+0.061}_{-0.062}$ | $0.047^{+0.024}_{-0.023}$ | $-0.163^{+0.018}_{-0.017}$ | $-0.776^{+0.086}_{-0.075}$ | $2.087^{+0.081}_{-0.086}$ | 0.33 | 0.37 | 0.25 | FAST |
| 194 | NGC 4385 | $3.500^{+0.048}_{-0.048}$ | $0.368^{+0.006}_{-0.006}$ | $-0.208^{+0.007}_{-0.007}$ | $-0.031^{+0.007}_{-0.007}$ | $-0.464^{+0.006}_{-0.006}$ | $-1.613^{+0.063}_{-0.069}$ | $0.028^{*+0.001}_{-0.001}$ | -0.18 | -0.31 | -2.07* | FAST |
| 195 | NGC 4395 | $12.400^{+0.082}_{-0.082}$ | $3.311^{+0.033}_{-0.033}$ | $0.910^{+0.004}_{-0.004}$ | $-0.716^{+0.005}_{-0.005}$ | $-0.365^{+0.003}_{-0.003}$ | $-0.582^{+0.004}_{-0.004}$ | $14.485^{+0.096}_{-0.096}$ | ... | 0.55 | 0.07 | SDSS |
| 196 | NGC 4396 | $0.742^{+0.008}_{-0.007}$ | $3.586^{+0.085}_{-0.082}$ | $-0.288^{+0.017}_{-0.018}$ | $-0.630^{+0.010}_{-0.009}$ | $-0.443^{+0.004}_{-0.004}$ | $-1.577^{+0.056}_{-0.076}$ | $1.265^{+0.014}_{-0.012}$ | ... | 0.59 | 0.23 | SDSS |
| 197 | NGC 4412 | $2.080^{+0.009}_{-0.009}$ | $5.249^{+0.120}_{-0.119}$ | $0.516^{+0.010}_{-0.010}$ | $-0.105^{+0.003}_{-0.003}$ | $-0.312^{+0.002}_{-0.002}$ | $-1.168^{+0.027}_{-0.027}$ | $7.208^{+0.031}_{-0.031}$ | 0.67 | 1.24 | 0.53 | FAST |
| 198 | NGC 4418 | $0.590^{+0.011}_{-0.011}$ | $8.417^{+0.849}_{-0.789}$ | $-0.075^{+0.078}_{-0.077}$ | $-0.014^{+0.012}_{-0.012}$ | $-0.099^{+0.008}_{-0.008}$ | $-0.628^{+0.037}_{-0.038}$ | $6.231^{+0.116}_{-0.116}$ | ... | 1.28 | 1.01 | SDSS |
| 199 | NGC 4420 | $0.510^{+0.006}_{-0.006}$ | $3.632^{+0.122}_{-0.112}$ | $-0.340^{+0.027}_{-0.029}$ | $-0.429^{+0.011}_{-0.010}$ | $-0.352^{+0.005}_{-0.005}$ | $-1.258^{+0.063}_{-0.062}$ | $0.896^{+0.011}_{-0.011}$ | ... | 0.58 | 0.24 | SDSS |
| 200 | NGC 4424 | $2.500^{+0.062}_{-0.059}$ | $3.859^{+0.389}_{-0.376}$ | $-0.692^{+0.185}_{-0.233}$ | $-0.484^{+0.033}_{-0.035}$ | $-0.490^{+0.010}_{-0.011}$ | ... | $5.070^{+0.126}_{-0.120}$ | 0.92 | 0.79 | 0.30 | FAST |

**Table 7.A.1:** Continued

| SFRS | Galaxy | F(H$\alpha$) | H$\alpha$/H$\beta$ | [O III]/H$\beta$ | [N II]/H$\alpha$ | [S II]/H$\alpha$ | [O I]/H$\alpha$ | F(H$\alpha$)$_{cor}$ | $A_V$ | $A_V$nuc | E(B-V)$_{\rm gas}$ | Observation |
|---|---|---|---|---|---|---|---|---|---|---|---|---|
| (1) | (2) | (3) | (4) | (5) | (6) | (7) | (8) | (9) | (10) | (11) | (12) | (13) |
| 200 | NGC 4424 | $4.490^{+0.034}_{-0.033}$ | $5.023^{+0.076}_{-0.079}$ | $-0.682^{+0.020}_{-0.019}$ | $-0.484^{+0.005}_{-0.005}$ | $-0.567^{+0.003}_{-0.003}$ | $-2.010^{+0.059}_{-0.059}$ | $16.962^{+0.130}_{-0.125}$ | ... | 0.57 | 0.57 | SDSS |
| 201 | NGC 4435 | $1.250^{+0.054}_{-0.052}$ | $3.643^{+2.903}_{-2.113}$ | $0.129^{+0.338}_{-0.582}$ | $-0.254^{+0.038}_{-0.038}$ | $-0.794^{+0.018}_{-0.019}$ | $-0.174^{+0.036}_{-0.037}$ | $2.213^{*+0.096}_{-0.092}$ | 0.37 | 0.51 | 0.24* | FAST |
| 202 | NGC 4438 | $2.070^{+0.063}_{-0.063}$ | $3.757^{+0.394}_{-0.358}$ | $0.162^{+0.047}_{-0.053}$ | $0.251^{+0.023}_{-0.023}$ | $0.310^{+0.013}_{-0.013}$ | $-0.395^{+0.034}_{-0.035}$ | $3.258^{+0.099}_{-0.099}$ | 1.27 | 1.49 | 0.19 | FAST |
| 203 | NGC 4448 | $8.190^{+0.132}_{-0.164}$ | $18.297^{+5.344}_{-4.473}$ | $-0.345^{+0.258}_{-0.781}$ | $-0.367^{+0.018}_{-0.018}$ | $-0.668^{+0.009}_{-0.007}$ | $-0.991^{+0.032}_{-0.033}$ | $653.709^{*+10.536}_{-13.090}$ | 0.62 | 0.75 | 1.88* | FAST |
| 205 | NGC 4470 | $1.100^{+0.011}_{-0.009}$ | $3.224^{+0.066}_{-0.066}$ | $-0.355^{+0.018}_{-0.016}$ | $-0.523^{+0.008}_{-0.009}$ | $-0.407^{+0.004}_{-0.005}$ | $-1.494^{+0.061}_{-0.048}$ | $1.459^{+0.015}_{-0.012}$ | ... | 0.35 | 0.12 | SDSS |
| 206 | IRAS 12274+0018 | $2.050^{+0.013}_{-0.013}$ | $6.899^{+0.134}_{-0.134}$ | $-0.435^{+0.019}_{-0.020}$ | $-0.467^{+0.005}_{-0.005}$ | $-0.496^{+0.003}_{-0.003}$ | $-1.555^{+0.030}_{-0.031}$ | $16.377^{+0.104}_{-0.104}$ | ... | 1.53 | 0.89 | SDSS |
| 207 | NGC 4491 | $2.020^{+0.061}_{-0.058}$ | $3.167^{+0.340}_{-0.326}$ | $-0.319^{+0.043}_{-0.045}$ | $-0.718^{+0.072}_{-0.072}$ | $-0.696^{+0.012}_{-0.013}$ | ... | $2.570^{+0.078}_{-0.074}$ | -0.08 | -0.02 | 0.10 | FAST |
| 208 | NGC 4500 | $11.600^{+0.064}_{-0.052}$ | $4.049^{+0.075}_{-0.074}$ | $0.279^{+0.008}_{-0.009}$ | $-0.285^{+0.005}_{-0.006}$ | $-0.571^{+0.002}_{-0.002}$ | $-1.393^{+0.045}_{-0.048}$ | $26.349^{+0.145}_{-0.118}$ | 0.51 | 0.43 | 0.35 | FAST |
| 209 | NGC 4495 | $1.790^{+0.017}_{-0.018}$ | $8.150^{+0.290}_{-0.284}$ | $-0.275^{+0.034}_{-0.034}$ | $-0.251^{+0.007}_{-0.007}$ | $-0.486^{+0.004}_{-0.004}$ | $-1.305^{+0.047}_{-0.049}$ | $21.189^{+0.201}_{-0.213}$ | ... | 1.28 | 1.06 | SDSS |
| 210 | IC 3476 | $0.428^{+0.005}_{-0.006}$ | $3.263^{+0.116}_{-0.122}$ | $-0.299^{+0.029}_{-0.030}$ | $-0.575^{+0.014}_{-0.014}$ | $-0.414^{+0.006}_{-0.005}$ | $-1.986^{+0.137}_{-0.319}$ | $0.584^{+0.007}_{-0.008}$ | -0.04 | -0.09 | 0.13 | FAST |
| 211 | NGC 4509 | $2.020^{+0.051}_{-0.051}$ | $2.568^{+0.213}_{-0.208}$ | $0.356^{+0.036}_{-0.037}$ | $-1.171^{+0.152}_{-0.167}$ | $-0.566^{+0.011}_{-0.011}$ | $-1.526^{+0.307}_{-0.672}$ | $1.567^{+0.040}_{-0.040}$ | -0.15 | -0.09 | -0.11 | FAST |
| 212 | NGC 4519 | $2.770^{+0.017}_{-0.017}$ | $3.666^{+0.049}_{-0.049}$ | $-0.542^{+0.012}_{-0.012}$ | $-0.486^{+0.005}_{-0.005}$ | $-0.599^{+0.003}_{-0.003}$ | $-1.783^{+0.057}_{-0.056}$ | $4.977^{+0.031}_{-0.031}$ | ... | 0.38 | 0.25 | SDSS |
| 213 | NGC 4548 | $0.813^{+0.056}_{-0.050}$ | $8.302^{+2.680}_{-2.490}$ | $0.872^{+0.131}_{-0.140}$ | $0.306^{+0.030}_{-0.033}$ | $0.141^{+0.027}_{-0.030}$ | $-0.419^{+0.071}_{-0.077}$ | $8.312^{+0.573}_{-0.511}$ | 0.07 | 0.42 | 1.00 | FAST |
| 214 | IRAS 12337+5044 | $1.940^{+0.013}_{-0.015}$ | $6.599^{+0.124}_{-0.131}$ | $-0.123^{+0.013}_{-0.012}$ | $-0.468^{+0.006}_{-0.005}$ | $-0.540^{+0.003}_{-0.003}$ | $-1.522^{+0.030}_{-0.027}$ | $13.954^{+0.094}_{-0.108}$ | ... | 1.34 | 0.85 | SDSS |
| 215 | IC 3581 | $1.580^{+0.016}_{-0.013}$ | $6.010^{+0.180}_{-0.162}$ | $-0.275^{+0.027}_{-0.028}$ | $-0.276^{+0.006}_{-0.008}$ | $-0.482^{+0.003}_{-0.004}$ | $-1.259^{+0.045}_{-0.043}$ | $9.115^{+0.092}_{-0.075}$ | ... | 0.84 | 0.75 | SDSS |
| 216 | NGC 4592 | $0.360^{+0.004}_{-0.004}$ | $3.790^{+0.161}_{-0.151}$ | $-0.009^{+0.024}_{-0.025}$ | $-0.714^{+0.020}_{-0.016}$ | $-0.306^{+0.005}_{-0.005}$ | $-1.241^{+0.055}_{-0.059}$ | $0.700^{+0.008}_{-0.008}$ | ... | 0.43 | 0.28 | SDSS |
| 217 | NGC 4607 | $0.271^{+0.004}_{-0.004}$ | $6.235^{+0.531}_{-0.467}$ | $0.102^{+0.041}_{-0.052}$ | $-0.227^{+0.011}_{-0.012}$ | $-0.135^{+0.007}_{-0.006}$ | $-1.000^{+0.051}_{-0.052}$ | $1.705^{+0.025}_{-0.025}$ | ... | 1.55 | 0.79 | SDSS |
| 218 | NGC 4625 | $0.455^{+0.013}_{-0.013}$ | $4.674^{+0.614}_{-0.594}$ | $-0.226^{+0.112}_{-0.118}$ | $-0.366^{+0.029}_{-0.030}$ | $-0.285^{+0.012}_{-0.012}$ | $-1.010^{+0.091}_{-0.097}$ | $1.450^{+0.041}_{-0.041}$ | 0.47 | 0.61 | 0.50 | FAST |
| 218 | NGC 4625 | $0.297^{+0.006}_{-0.006}$ | $3.397^{+0.254}_{-0.251}$ | $-0.293^{+0.067}_{-0.072}$ | $-0.295^{+0.019}_{-0.019}$ | $-0.338^{+0.009}_{-0.009}$ | $-1.010^{+0.091}_{-0.097}$ | $0.446^{+0.009}_{-0.009}$ | ... | 0.28 | 0.17 | SDSS |
| 219 | NGC 4630 | $4.790^{+0.035}_{-0.028}$ | $4.155^{+0.056}_{-0.053}$ | $-0.753^{+0.016}_{-0.015}$ | $-0.588^{+0.005}_{-0.005}$ | $-0.581^{+0.003}_{-0.003}$ | $-1.957^{+0.040}_{-0.042}$ | $11.564^{+0.084}_{-0.068}$ | ... | 0.20 | 0.38 | SDSS |
| 220 | IC 3690 | $0.711^{+0.008}_{-0.007}$ | $9.790^{+0.636}_{-0.628}$ | $-0.159^{+0.050}_{-0.050}$ | $-0.104^{+0.007}_{-0.007}$ | $-0.419^{+0.004}_{-0.005}$ | $-1.112^{+0.039}_{-0.041}$ | $12.973^{+0.146}_{-0.128}$ | ... | 1.50 | 1.24 | SDSS |
| 221 | UGC 7905_NED01 | $1.790^{+0.019}_{-0.018}$ | $4.074^{+0.111}_{-0.111}$ | $0.390^{+0.012}_{-0.013}$ | $-0.966^{+0.024}_{-0.024}$ | $-0.552^{+0.004}_{-0.005}$ | $-1.513^{+0.066}_{-0.067}$ | $4.125^{+0.044}_{-0.041}$ | 0.25 | -0.07 | 0.36 | FAST |
| 222 | MCG 5-30-069 | $3.350^{+0.018}_{-0.018}$ | $10.514^{+0.176}_{-0.175}$ | $-0.491^{+0.022}_{-0.021}$ | $-0.328^{+0.003}_{-0.003}$ | $-0.509^{+0.002}_{-0.002}$ | $-1.538^{+0.021}_{-0.020}$ | $72.332^{+0.389}_{-0.389}$ | ... | 1.68 | 1.32 | SDSS |

**Table 7.A.1:** Continued

| SFRS | Galaxy | F(H$\alpha$) | H$\alpha$/H$\beta$ | [O III]/H$\beta$ | [N II]/H$\alpha$ | [S II]/H$\alpha$ | [O I]/H$\alpha$ | F(H$\alpha$)$_{cor}$ | A$_V$ | A$_V$nuc | E(B-V)$_{\rm gas}$ | Observation |
|---|---|---|---|---|---|---|---|---|---|---|---|---|
| (1) | (2) | (3) | (4) | (5) | (6) | (7) | (8) | (9) | (10) | (11) | (12) | (13) |
| 223 | IC 3721 | $1.430^{+0.027}_{-0.032}$ | $4.615^{+0.391}_{-0.387}$ | $-0.178^{+0.060}_{-0.060}$ | $-0.353^{+0.027}_{-0.020}$ | $-0.619^{+0.010}_{-0.008}$ | $-1.589^{+0.167}_{-0.167}$ | $4.423^{+0.084}_{-0.099}$ | 0.25 | 0.38 | 0.48 | FAST |
| 224 | NGC 4670 | $14.600^{+0.071}_{-0.071}$ | $2.977^{+0.030}_{-0.027}$ | $0.518^{+0.004}_{-0.005}$ | $-1.191^{+0.007}_{-0.007}$ | $-0.950^{+0.002}_{-0.002}$ | $-2.021^{+0.040}_{-0.041}$ | $16.049^{+0.078}_{-0.078}$ | ... | 0.42 | 0.04 | SDSS |
| 225 | NGC 4675 | $2.290^{+0.018}_{-0.019}$ | $9.119^{+0.277}_{-0.300}$ | $-0.337^{+0.032}_{-0.031}$ | $-0.225^{+0.006}_{-0.006}$ | $-0.528^{+0.004}_{-0.003}$ | $-1.308^{+0.035}_{-0.036}$ | $35.337^{+0.278}_{-0.293}$ | ... | 1.54 | 1.17 | SDSS |
| 226 | MCG 7-26-051 | $0.862^{+0.007}_{-0.006}$ | $8.984^{+0.511}_{-0.511}$ | $0.017^{+0.035}_{-0.035}$ | $-0.264^{+0.007}_{-0.008}$ | $-0.501^{+0.003}_{-0.004}$ | $-1.189^{+0.057}_{-0.059}$ | $12.841^{+0.104}_{-0.089}$ | 0.64 | 1.23 | 1.16 | FAST |
| 227 | NGC 4689 | $0.184^{+0.006}_{-0.006}$ | $4.974^{+0.915}_{-0.911}$ | $-0.085^{+0.108}_{-0.110}$ | $-0.230^{+0.027}_{-0.029}$ | $-0.489^{+0.013}_{-0.014}$ | ... | $0.679^{+0.022}_{-0.022}$ | ... | 0.32 | 0.56 | SDSS |
| 228 | NGC 4688 | $0.248^{+0.013}_{-0.012}$ | $4.128^{+1.119}_{-1.055}$ | $0.126^{+0.135}_{-0.143}$ | $-0.582^{+0.078}_{-0.081}$ | $-0.288^{+0.022}_{-0.022}$ | ... | $0.590^{+0.031}_{-0.029}$ | -0.68 | -0.11 | 0.37 | FAST |
| 229 | NGC 4704 | $0.625^{+0.022}_{-0.022}$ | $4.305^{+0.567}_{-0.586}$ | $1.033^{+0.058}_{-0.056}$ | $0.572^{+0.016}_{-0.016}$ | $0.207^{+0.015}_{-0.015}$ | $-0.242^{+0.029}_{-0.030}$ | $1.357^{+0.048}_{-0.048}$ | 0.36 | 0.53 | 0.33 | FAST |
| 230 | NGC 4701 | $1.790^{+0.013}_{-0.013}$ | $3.963^{+0.073}_{-0.073}$ | $-0.777^{+0.031}_{-0.032}$ | $-0.489^{+0.007}_{-0.007}$ | $-0.588^{+0.003}_{-0.003}$ | $-1.719^{+0.057}_{-0.060}$ | $3.865^{+0.028}_{-0.028}$ | ... | 0.40 | 0.33 | SDSS |
| 231 | IRAS 12468+3436 | $0.884^{+0.019}_{-0.022}$ | $11.298^{+1.282}_{-1.274}$ | $0.214^{+0.060}_{-0.061}$ | $-0.236^{+0.019}_{-0.020}$ | $-0.341^{+0.011}_{-0.009}$ | $-0.934^{+0.061}_{-0.062}$ | $18.701^{+0.402}_{-0.465}$ | 1.23 | 1.26 | 1.31 | FAST |
| 232 | IRAS 12470+1404 | $1.990^{+0.015}_{-0.015}$ | $3.489^{+0.054}_{-0.054}$ | $-0.392^{+0.013}_{-0.012}$ | $-0.285^{+0.005}_{-0.005}$ | $-0.515^{+0.003}_{-0.003}$ | $-1.459^{+0.024}_{-0.024}$ | $3.181^{+0.024}_{-0.024}$ | ... | 0.46 | 0.20 | SDSS |
| 233 | MCG 8-23-097 | $1.410^{+0.032}_{-0.038}$ | $14.704^{+3.208}_{-3.090}$ | $0.092^{+0.123}_{-0.129}$ | $-0.094^{+0.017}_{-0.017}$ | $-0.488^{+0.012}_{-0.010}$ | $-1.304^{+0.127}_{-0.142}$ | $67.183^{+1.525}_{-1.811}$ | 1.59 | 1.93 | 1.65 | FAST |
| 233 | MCG 8-23-097 | $1.540^{+0.015}_{-0.013}$ | $10.566^{+0.422}_{-0.418}$ | $0.151^{+0.022}_{-0.022}$ | $-0.062^{+0.006}_{-0.006}$ | $-0.448^{+0.004}_{-0.004}$ | $-1.196^{+0.033}_{-0.034}$ | $33.640^{+0.336}_{-0.284}$ | ... | 1.78 | 1.32 | SDSS |
| 234 | NGC 4747 | $1.270^{+0.051}_{-0.049}$ | $15.486^{+5.050}_{-4.264}$ | $-0.087^{+0.183}_{-0.216}$ | $-0.553^{+0.049}_{-0.049}$ | $-0.290^{+0.017}_{-0.017}$ | $-0.183^{+0.035}_{-0.036}$ | $68.384^{*+2.746}_{-2.638}$ | 1.22 | 0.95 | 1.71* | FAST |
| 234 | NGC 4747 | $0.351^{+0.005}_{-0.004}$ | $4.146^{+0.144}_{-0.189}$ | $-0.033^{+0.025}_{-0.026}$ | $-0.578^{+0.015}_{-0.018}$ | $-0.320^{+0.005}_{-0.006}$ | $-1.319^{+0.072}_{-0.083}$ | $0.843^{+0.011}_{-0.010}$ | ... | 0.66 | 0.38 | SDSS |
| 235 | UGC 8017 | $0.607^{+0.008}_{-0.008}$ | $5.539^{+0.259}_{-0.231}$ | $-0.110^{+0.034}_{-0.036}$ | $-0.097^{+0.009}_{-0.010}$ | $-0.374^{+0.006}_{-0.006}$ | $-0.962^{+0.053}_{-0.057}$ | $2.888^{+0.038}_{-0.038}$ | ... | 0.97 | 0.67 | SDSS |
| 236 | NGC 4765 | $14.600^{+0.090}_{-0.090}$ | $3.499^{+0.036}_{-0.038}$ | $0.407^{+0.005}_{-0.005}$ | $-1.041^{+0.005}_{-0.005}$ | $-0.699^{+0.003}_{-0.003}$ | $-1.776^{+0.015}_{-0.016}$ | $23.498^{+0.145}_{-0.145}$ | ... | 0.02 | 0.20 | SDSS |
| 237 | VCC 2096 | $1.860^{+0.014}_{-0.014}$ | $5.053^{+0.108}_{-0.100}$ | $-0.176^{+0.015}_{-0.015}$ | $-0.349^{+0.006}_{-0.006}$ | $-0.388^{+0.003}_{-0.003}$ | $-1.174^{+0.020}_{-0.020}$ | $7.126^{+0.054}_{-0.054}$ | ... | 0.79 | 0.58 | SDSS |
| 238 | UGC 8041 | $0.516^{+0.006}_{-0.005}$ | $4.044^{+0.140}_{-0.151}$ | $-0.177^{+0.025}_{-0.028}$ | $-0.479^{+0.010}_{-0.012}$ | $-0.355^{+0.004}_{-0.005}$ | $-1.584^{+0.080}_{-0.091}$ | $1.169^{+0.014}_{-0.011}$ | ... | 0.38 | 0.35 | SDSS |
| 240 | NGC 4837_NED01 | $1.790^{+0.021}_{-0.023}$ | $3.587^{+0.147}_{-0.153}$ | $-0.316^{+0.038}_{-0.038}$ | $-0.255^{+0.014}_{-0.013}$ | $-0.385^{+0.006}_{-0.005}$ | $-1.152^{+0.075}_{-0.080}$ | $3.055^{+0.036}_{-0.039}$ | 0.05 | 0.19 | 0.23 | FAST |
| 241 | UM 530 | $5.620^{+0.035}_{-0.030}$ | $3.806^{+0.044}_{-0.042}$ | $0.340^{+0.005}_{-0.005}$ | $-0.722^{+0.005}_{-0.005}$ | $-0.631^{+0.002}_{-0.003}$ | $-1.556^{+0.013}_{-0.013}$ | $11.031^{+0.069}_{-0.059}$ | ... | 0.41 | 0.29 | SDSS |
| 242 | NGC 4861 | $56.800^{+0.061}_{-0.061}$ | $2.149^{+0.004}_{-0.004}$ | $0.493^{+0.001}_{-0.001}$ | $-1.533^{+0.003}_{-0.003}$ | $-1.021^{+0.001}_{-0.001}$ | $-2.050^{+0.007}_{-0.007}$ | $28.934^{+0.031}_{-0.031}$ | 0.45 | 0.11 | -0.29 | FAST |
| 243 | NGC 4868 | $3.350^{+0.013}_{-0.013}$ | $4.143^{+0.059}_{-0.059}$ | $-0.820^{+0.043}_{-0.043}$ | $-0.416^{+0.005}_{-0.005}$ | $-0.564^{+0.002}_{-0.002}$ | $-1.486^{+0.055}_{-0.055}$ | $8.033^{+0.031}_{-0.031}$ | 0.46 | 0.53 | 0.37 | FAST |
| 244 | NGC 4922_NED02 | $7.900^{+0.043}_{-0.043}$ | $6.885^{+0.078}_{-0.078}$ | $0.455^{+0.005}_{-0.005}$ | $-0.150^{+0.003}_{-0.003}$ | $-0.404^{+0.002}_{-0.002}$ | $-1.105^{+0.007}_{-0.007}$ | $51.931^{+0.283}_{-0.283}$ | ... | 1.28 | 0.81 | SDSS |

**Table 7.A.1:** Continued

| SFRS | Galaxy | F(H$\alpha$) | H$\alpha$/H$\beta$ | [O III]/H$\beta$ | [N II]/H$\alpha$ | [S II]/H$\alpha$ | [O I]/H$\alpha$ | F(H$\alpha$)$_{cor}$ | $A_V$ | $A_V$nuc | E(B-V)$_{\rm gas}$ | Observation |
|---|---|---|---|---|---|---|---|---|---|---|---|---|
| (1) | (2) | (3) | (4) | (5) | (6) | (7) | (8) | (9) | (10) | (11) | (12) | (13) |
| 245 | UGC 8179 | $0.924^{+0.011}_{-0.012}$ | $6.216^{+0.299}_{-0.273}$ | $-0.268^{+0.048}_{-0.045}$ | $-0.342^{+0.012}_{-0.012}$ | $-0.711^{+0.006}_{-0.005}$ | $-1.101^{+0.111}_{-0.120}$ | $5.772^{+0.069}_{-0.075}$ | ... | 0.72 | 0.78 | SDSS |
| 246 | NGC 5001 | $0.977^{+0.013}_{-0.018}$ | $8.458^{+0.859}_{-0.829}$ | $-0.036^{+0.065}_{-0.067}$ | $-0.233^{+0.014}_{-0.013}$ | $-0.496^{+0.008}_{-0.006}$ | $-1.256^{+0.120}_{-0.155}$ | $12.623^{+0.168}_{-0.233}$ | 0.73 | 0.91 | 1.10 | FAST |
| 247 | IC 856 | $2.450^{+0.015}_{-0.014}$ | $5.172^{+0.073}_{-0.070}$ | $-0.110^{+0.008}_{-0.008}$ | $-0.568^{+0.005}_{-0.005}$ | $-0.512^{+0.002}_{-0.003}$ | $-1.582^{+0.022}_{-0.021}$ | $9.916^{+0.061}_{-0.057}$ | ... | 0.79 | 0.60 | SDSS |
| 248 | UGC 8269 | $0.519^{+0.006}_{-0.006}$ | $11.109^{+0.837}_{-0.844}$ | $-0.181^{+0.070}_{-0.064}$ | $-0.046^{+0.008}_{-0.008}$ | $-0.402^{+0.005}_{-0.005}$ | $-0.995^{+0.041}_{-0.042}$ | $12.761^{+0.148}_{-0.148}$ | ... | 1.70 | 1.37 | SDSS |
| 249 | NGC 5014 | $8.490^{+0.103}_{-0.060}$ | $7.422^{+0.207}_{-0.149}$ | $-0.223^{+0.016}_{-0.018}$ | $-0.473^{+0.010}_{-0.008}$ | $-0.507^{+0.003}_{-0.005}$ | $-1.747^{+0.066}_{-0.070}$ | $80.587^{+0.978}_{-0.570}$ | 0.99 | 0.85 | 0.96 | FAST |
| 249 | NGC 5014 | $5.350^{+0.037}_{-0.038}$ | $4.646^{+0.074}_{-0.071}$ | $-0.209^{+0.012}_{-0.011}$ | $-0.486^{+0.006}_{-0.006}$ | $-0.487^{+0.003}_{-0.003}$ | $-1.666^{+0.043}_{-0.045}$ | $16.812^{+0.116}_{-0.119}$ | ... | 0.53 | 0.49 | SDSS |
| 250 | NGC 5012 | $0.479^{+0.018}_{-0.016}$ | $4.262^{+0.459}_{-0.448}$ | $0.165^{+0.054}_{-0.056}$ | $0.073^{+0.022}_{-0.022}$ | $-0.198^{+0.015}_{-0.016}$ | $-0.728^{+0.123}_{-0.130}$ | $1.228^{+0.046}_{-0.041}$ | ... | 0.59 | 0.40 | SDSS |
| 251 | IRAS 13116+4508 | $0.873^{+0.008}_{-0.008}$ | $6.682^{+0.240}_{-0.242}$ | $-0.452^{+0.056}_{-0.062}$ | $-0.399^{+0.008}_{-0.008}$ | $-0.627^{+0.004}_{-0.004}$ | $-1.409^{+0.060}_{-0.065}$ | $6.467^{+0.059}_{-0.059}$ | ... | 1.20 | 0.86 | SDSS |
| 252 | IC 860 | $0.280^{+0.009}_{-0.008}$ | $7.700^{+1.440}_{-1.350}$ | $0.215^{+0.099}_{-0.096}$ | $0.219^{+0.016}_{-0.017}$ | $-0.010^{+0.013}_{-0.013}$ | $-0.551^{+0.048}_{-0.050}$ | $2.899^{+0.093}_{-0.083}$ | ... | 1.21 | 1.00 | SDSS |
| 253 | IRAS 13144+4508 | $4.850^{+0.034}_{-0.034}$ | $4.392^{+0.058}_{-0.058}$ | $0.772^{+0.005}_{-0.005}$ | $-0.359^{+0.005}_{-0.005}$ | $-0.696^{+0.003}_{-0.003}$ | $-1.371^{+0.015}_{-0.015}$ | $11.036^{+0.077}_{-0.077}$ | ... | 0.27 | 0.35 | SDSS |
| 254 | NGC 5060 | $1.500^{+0.024}_{-0.025}$ | $4.053^{+0.210}_{-0.208}$ | $-0.690^{+0.108}_{-0.120}$ | $-0.295^{+0.014}_{-0.014}$ | $-0.893^{+0.007}_{-0.007}$ | $-1.511^{+0.149}_{-0.180}$ | $3.415^{*+0.055}_{-0.057}$ | 0.91 | 1.02 | 0.35* | FAST |
| 255 | UGC 8357_NED01 | $0.855^{+0.013}_{-0.013}$ | $4.182^{+0.338}_{-0.339}$ | $-0.298^{+0.063}_{-0.066}$ | $-0.131^{+0.013}_{-0.013}$ | $-0.233^{+0.007}_{-0.007}$ | $-0.998^{+0.094}_{-0.095}$ | $2.096^{+0.032}_{-0.032}$ | 0.71 | 1.13 | 0.38 | FAST |
| 255 | UGC 8357_NED01 | $1.300^{+0.009}_{-0.008}$ | $4.616^{+0.093}_{-0.094}$ | $-0.459^{+0.022}_{-0.023}$ | $-0.409^{+0.005}_{-0.005}$ | $-0.526^{+0.003}_{-0.003}$ | $-1.594^{+0.040}_{-0.033}$ | $4.023^{+0.027}_{-0.025}$ | ... | 0.33 | 0.48 | SDSS |
| 256 | UGC 8361 | $1.950^{+0.021}_{-0.021}$ | $7.259^{+0.331}_{-0.332}$ | $-0.232^{+0.037}_{-0.038}$ | $-0.263^{+0.008}_{-0.008}$ | $-0.826^{+0.005}_{-0.005}$ | $-1.279^{+0.054}_{-0.056}$ | $17.564^{+0.189}_{-0.189}$ | 0.19 | 0.20 | 0.94 | FAST |
| 257 | IC 883 | $2.760^{+0.018}_{-0.018}$ | $11.586^{+0.315}_{-0.355}$ | $-0.063^{+0.022}_{-0.019}$ | $-0.206^{+0.005}_{-0.005}$ | $-0.341^{+0.003}_{-0.003}$ | $-1.070^{+0.012}_{-0.012}$ | $61.960^{+0.404}_{-0.404}$ | ... | 1.12 | 1.33 | SDSS |
| 258 | NGC 5100_NED02 | $3.150^{+0.039}_{-0.058}$ | $6.932^{+0.494}_{-0.493}$ | $-0.015^{+0.049}_{-0.050}$ | $-0.114^{+0.014}_{-0.012}$ | $-0.345^{+0.008}_{-0.005}$ | $-1.185^{+0.097}_{-0.031}$ | $21.042^{+0.261}_{-0.387}$ | 0.64 | 0.80 | 0.81 | FAST |
| 259 | NGC 5104 | $1.650^{+0.018}_{-0.018}$ | $14.291^{+0.859}_{-0.841}$ | $0.140^{+0.033}_{-0.033}$ | $-0.077^{+0.007}_{-0.006}$ | $-0.376^{+0.005}_{-0.005}$ | $-1.147^{+0.035}_{-0.036}$ | $60.777^{+0.663}_{-0.663}$ | ... | 1.97 | 1.54 | SDSS |
| 260 | NGC 5107 | $0.417^{+0.010}_{-0.011}$ | $1.793^{+0.112}_{-0.114}$ | $0.310^{+0.029}_{-0.029}$ | $-0.899^{+0.072}_{-0.078}$ | $-0.451^{+0.012}_{-0.010}$ | $-1.294^{+0.123}_{-0.209}$ | $0.139^{*+0.003}_{-0.004}$ | 0.16 | 0.09 | -0.47* | FAST |
| 261 | NGC 5112 | $0.134^{+0.003}_{-0.003}$ | $4.815^{+0.472}_{-0.492}$ | $0.094^{+0.061}_{-0.060}$ | $-0.379^{+0.022}_{-0.024}$ | $-0.272^{+0.009}_{-0.010}$ | $-1.163^{+0.125}_{-0.135}$ | $0.458^{+0.010}_{-0.010}$ | ... | 0.40 | 0.53 | SDSS |
| 262 | NGC 5123 | $0.294^{+0.010}_{-0.009}$ | $5.745^{+0.823}_{-0.806}$ | $0.101^{+0.090}_{-0.089}$ | $-0.181^{+0.026}_{-0.028}$ | $-0.512^{+0.014}_{-0.015}$ | $-0.327^{+0.121}_{-0.180}$ | $1.525^{+0.052}_{-0.047}$ | ... | 0.43 | 0.70 | SDSS |
| 264 | IRAS 13232+1731 | $1.950^{+0.014}_{-0.014}$ | $5.176^{+0.095}_{-0.096}$ | $-0.696^{+0.034}_{-0.033}$ | $-0.424^{+0.006}_{-0.006}$ | $-0.743^{+0.003}_{-0.003}$ | $-1.684^{+0.055}_{-0.054}$ | $7.907^{+0.057}_{-0.057}$ | ... | 0.57 | 0.60 | SDSS |
| 265 | NGC 5147 | $0.228^{+0.009}_{-0.009}$ | $3.105^{+0.466}_{-0.456}$ | $-0.230^{+0.126}_{-0.127}$ | $-0.483^{+0.047}_{-0.048}$ | $-0.353^{+0.017}_{-0.017}$ | ... | $0.277^{+0.011}_{-0.011}$ | 0.14 | 0.12 | 0.08 | FAST |
| 266 | NGC 5204 | $0.181^{+0.006}_{-0.009}$ | $3.334^{+0.371}_{-0.387}$ | $0.009^{+0.059}_{-0.062}$ | $-0.610^{+0.052}_{-0.052}$ | $-0.078^{+0.022}_{-0.016}$ | ... | $0.260^{+0.009}_{-0.013}$ | 0.46 | 0.55 | 0.15 | FAST |

**Table 7.A.1:** Continued

| SFRS | Galaxy | F(H$\alpha$) | H$\alpha$/H$\beta$ | [O III]/H$\beta$ | [N II]/H$\alpha$ | [S II]/H$\alpha$ | [O I]/H$\alpha$ | F(H$\alpha$)$_{cor}$ | A$_V$ | A$_V$nuc | E(B-V)$_{\rm gas}$ | Observation |
|---|---|---|---|---|---|---|---|---|---|---|---|---|
| (1) | (2) | (3) | (4) | (5) | (6) | (7) | (8) | (9) | (10) | (11) | (12) | (13) |
| 267 | UGC 8502_NED02 | $7.430^{+0.121}_{-0.124}$ | $2.257^{+0.042}_{-0.041}$ | $0.114^{+0.004}_{-0.009}$ | $-0.585^{+0.008}_{-0.010}$ | $-0.717^{+0.007}_{-0.007}$ | $-1.913^{+0.045}_{-0.046}$ | $4.249^{+0.069}_{-0.071}$ | 0.12 | 0.01 | -0.24 | FAST |
| 268 | UGC 8561 | $1.570^{+0.035}_{-0.031}$ | $6.444^{+0.395}_{-0.395}$ | $-0.527^{+0.080}_{-0.086}$ | $-0.348^{+0.019}_{-0.019}$ | $-0.846^{+0.009}_{-0.010}$ | $-1.493^{+0.209}_{-0.172}$ | $10.677^{+0.238}_{-0.211}$ | 0.67 | 0.74 | 0.82 | FAST |
| 268 | UGC 8561 | $2.350^{+0.019}_{-0.019}$ | $5.902^{+0.140}_{-0.141}$ | $-0.607^{+0.038}_{-0.042}$ | $-0.319^{+0.006}_{-0.007}$ | $-0.635^{+0.003}_{-0.004}$ | $-1.537^{+0.065}_{-0.069}$ | $12.989^{+0.107}_{-0.103}$ | ... | 0.79 | 0.73 | SDSS |
| 269 | NGC 5230 | $3.530^{+0.109}_{-0.098}$ | $20.356^{+2.167}_{-2.115}$ | $-0.614^{+0.201}_{-0.237}$ | $-0.350^{+0.028}_{-0.030}$ | ... | ... | $362.383^{*+11.190}_{-10.060}$ | 0.24 | 0.30 | 1.98* | FAST |
| 271 | NGC 5256 | $8.840^{+0.048}_{-0.048}$ | $5.332^{+0.063}_{-0.063}$ | $0.577^{+0.005}_{-0.005}$ | $-0.263^{+0.004}_{-0.004}$ | $-0.438^{+0.002}_{-0.002}$ | $-1.325^{+0.013}_{-0.011}$ | $31.789^{+0.173}_{-0.173}$ | ... | 1.11 | 0.55 | SDSS |
| 272 | UGC 8626 | $3.520^{+0.020}_{-0.019}$ | $6.863^{+0.110}_{-0.110}$ | $-0.418^{+0.019}_{-0.020}$ | $-0.322^{+0.004}_{-0.004}$ | $-0.615^{+0.002}_{-0.002}$ | $-1.569^{+0.038}_{-0.037}$ | $27.775^{+0.158}_{-0.150}$ | ... | 1.08 | 0.88 | SDSS |
| 273 | NGC 5263 | $1.740^{+0.012}_{-0.011}$ | $11.236^{+0.861}_{-0.869}$ | $-0.315^{+0.076}_{-0.081}$ | $-0.323^{+0.006}_{-0.007}$ | $-0.399^{+0.003}_{-0.003}$ | $-1.318^{+0.063}_{-0.067}$ | $43.944^{+0.303}_{-0.278}$ | 1.21 | 1.48 | 1.38 | FAST |
| 274 | MCG 1-35-028 | $5.650^{+0.032}_{-0.032}$ | $6.602^{+0.083}_{-0.094}$ | $-0.300^{+0.011}_{-0.011}$ | $-0.191^{+0.004}_{-0.004}$ | $-0.571^{+0.002}_{-0.002}$ | $-1.386^{+0.022}_{-0.023}$ | $40.683^{+0.230}_{-0.230}$ | ... | 1.35 | 0.85 | SDSS |
| 275 | IC 910 | $3.630^{+0.040}_{-0.040}$ | $9.765^{+0.459}_{-0.463}$ | $0.747^{+0.021}_{-0.021}$ | $0.159^{+0.006}_{-0.006}$ | $-0.322^{+0.005}_{-0.005}$ | $-0.868^{+0.020}_{-0.021}$ | $54.433^{+0.600}_{-0.600}$ | 0.62 | 1.13 | 1.16 | FAST |
| 276 | MK 268 | $4.390^{+0.329}_{-0.329}$ | $3.872^{+0.300}_{-0.300}$ | $0.780^{+0.009}_{-0.009}$ | $0.425^{+0.033}_{-0.033}$ | $0.135^{+0.033}_{-0.033}$ | $-0.479^{+0.034}_{-0.034}$ | $7.419^{+0.556}_{-0.556}$ | ... | 0.54 | 0.22 | SDSS |
| 277 | NGC 5278 | $0.451^{+0.007}_{-0.006}$ | $4.703^{+0.295}_{-0.290}$ | $0.234^{+0.031}_{-0.032}$ | $-0.130^{+0.010}_{-0.011}$ | $-0.175^{+0.006}_{-0.007}$ | $-0.851^{+0.038}_{-0.038}$ | $1.459^{+0.023}_{-0.019}$ | ... | 0.91 | 0.50 | SDSS |
| 278 | NGC 5273 | $3.030^{+0.048}_{-0.052}$ | $2.425^{+0.062}_{-0.064}$ | $0.853^{+0.009}_{-0.009}$ | $0.080^{+0.010}_{-0.009}$ | $-0.044^{+0.007}_{-0.007}$ | $-0.578^{+0.015}_{-0.015}$ | $1.697^{+0.027}_{-0.029}$ | ... | 0.27 | -0.25 | SDSS |
| 279 | UGC 8685 | $2.920^{+0.021}_{-0.021}$ | $7.776^{+0.185}_{-0.185}$ | $-0.485^{+0.031}_{-0.032}$ | $-0.276^{+0.005}_{-0.005}$ | $-0.605^{+0.003}_{-0.003}$ | $-1.520^{+0.050}_{-0.047}$ | $30.938^{+0.223}_{-0.223}$ | ... | 1.05 | 1.01 | SDSS |
| 280 | UGC 8686 | $0.649^{+0.014}_{-0.012}$ | $7.319^{+0.746}_{-0.723}$ | $-0.064^{+0.090}_{-0.090}$ | $-0.269^{+0.021}_{-0.021}$ | $-0.823^{+0.008}_{-0.010}$ | $-1.316^{+0.152}_{-0.168}$ | $5.960^{+0.129}_{-0.110}$ | 0.52 | 1.22 | 0.95 | FAST |
| 280 | UGC 8686 | $0.878^{+0.007}_{-0.007}$ | $4.786^{+0.115}_{-0.112}$ | $-0.293^{+0.021}_{-0.021}$ | $-0.243^{+0.006}_{-0.006}$ | $-0.466^{+0.003}_{-0.003}$ | $-1.265^{+0.048}_{-0.035}$ | $2.959^{+0.022}_{-0.022}$ | ... | 1.29 | 0.52 | SDSS |
| 281 | UGC 8696 | $7.900^{+0.065}_{-0.065}$ | $7.981^{+0.135}_{-0.135}$ | $0.448^{+0.007}_{-0.007}$ | $0.010^{+0.004}_{-0.004}$ | $-0.241^{+0.004}_{-0.004}$ | $-0.898^{+0.008}_{-0.008}$ | $73.591^{+0.605}_{-0.605}$ | ... | 1.06 | 0.96 | SDSS |
| 282 | NGC 5297 | $0.201^{+0.014}_{-0.014}$ | $2.706^{+0.564}_{-0.514}$ | $0.158^{+0.091}_{-0.100}$ | $0.082^{+0.036}_{-0.037}$ | $0.037^{+0.029}_{-0.030}$ | $0.135^{+0.068}_{-0.069}$ | $0.176^{+0.012}_{-0.012}$ | 0.61 | 0.58 | -0.06 | FAST |
| 283 | MK 796 | $19.200^{+0.096}_{-0.096}$ | $4.514^{+0.040}_{-0.040}$ | $0.067^{+0.004}_{-0.004}$ | $-0.392^{+0.003}_{-0.003}$ | $-0.660^{+0.002}_{-0.002}$ | $-1.653^{+0.014}_{-0.014}$ | $46.605^{+0.233}_{-0.233}$ | ... | 0.43 | 0.38 | SDSS |
| 284 | IRAS 13446+1121 | $12.900^{+0.073}_{-0.073}$ | $8.276^{+0.105}_{-0.105}$ | $0.607^{+0.006}_{-0.006}$ | $-0.183^{+0.004}_{-0.004}$ | $-0.553^{+0.002}_{-0.002}$ | $-1.227^{+0.009}_{-0.009}$ | $130.913^{+0.741}_{-0.741}$ | ... | 1.50 | 0.99 | SDSS |
| 285 | NGC 5303 | $1.440^{+0.021}_{-0.024}$ | $3.445^{+0.143}_{-0.148}$ | $-0.105^{+0.029}_{-0.028}$ | $-0.492^{+0.019}_{-0.019}$ | $-0.432^{+0.007}_{-0.006}$ | $-1.191^{+0.108}_{-0.117}$ | $2.234^{+0.033}_{-0.037}$ | 0.22 | 0.33 | 0.19 | FAST |
| 286 | NGC 5313 | $1.540^{+0.033}_{-0.026}$ | $4.849^{+0.283}_{-0.272}$ | $0.026^{+0.035}_{-0.036}$ | $0.083^{+0.011}_{-0.013}$ | $-0.138^{+0.007}_{-0.009}$ | $-0.791^{+0.049}_{-0.051}$ | $5.353^{+0.115}_{-0.090}$ | ... | 0.81 | 0.53 | SDSS |
| 287 | MCG 3-35-034_NED01 | $2.000^{+0.020}_{-0.027}$ | $5.631^{+0.173}_{-0.180}$ | $-0.123^{+0.023}_{-0.023}$ | $-0.138^{+0.008}_{-0.007}$ | $-0.331^{+0.006}_{-0.004}$ | $-0.993^{+0.029}_{-0.029}$ | $9.894^{+0.099}_{-0.134}$ | ... | 0.72 | 0.68 | SDSS |
| 288 | NGC 5347 | $3.360^{+0.030}_{-0.030}$ | $5.143^{+0.115}_{-0.127}$ | $0.929^{+0.010}_{-0.009}$ | $-0.203^{+0.006}_{-0.006}$ | $-0.339^{+0.004}_{-0.004}$ | $-0.779^{+0.015}_{-0.015}$ | $11.096^{+0.099}_{-0.099}$ | ... | 0.79 | 0.51 | SDSS |

**Table 7.A.1:** Continued

| SFRS | Galaxy | F(H$\alpha$) | H$\alpha$/H$\beta$ | [O III]/H$\beta$ | [N II]/H$\alpha$ | [S II]/H$\alpha$ | [O I]/H$\alpha$ | F(H$\alpha$)$_{cor}$ | $A_V$ | $A_V$nuc | E(B-V)$_{\rm gas}$ | Observation |
|---|---|---|---|---|---|---|---|---|---|---|---|---|
| (1) | (2) | (3) | (4) | (5) | (6) | (7) | (8) | (9) | (10) | (11) | (12) | (13) |
| 289 | NGC 5350 | $4.210^{+0.028}_{-0.028}$ | $4.233^{+0.071}_{-0.071}$ | $-0.178^{+0.013}_{-0.013}$ | $-0.099^{+0.004}_{-0.004}$ | $-0.580^{+0.003}_{-0.003}$ | $-1.319^{+0.032}_{-0.033}$ | $10.620^{+0.071}_{-0.071}$ | ... | 0.36 | 0.40 | SDSS |
| 290 | NGC 5368 | $2.630^{+0.030}_{-0.029}$ | $5.696^{+0.205}_{-0.207}$ | $-0.270^{+0.034}_{-0.035}$ | $-0.156^{+0.008}_{-0.008}$ | $-0.388^{+0.005}_{-0.005}$ | $-1.194^{+0.056}_{-0.058}$ | $13.367^{+0.152}_{-0.147}$ | ... | 0.69 | 0.70 | SDSS |
| 291 | UGC 8827 | $14.400^{+0.109}_{-0.093}$ | $4.825^{+0.068}_{-0.063}$ | $0.025^{+0.007}_{-0.008}$ | $-0.234^{+0.004}_{-0.005}$ | $-0.569^{+0.003}_{-0.003}$ | $-1.570^{+0.033}_{-0.032}$ | $49.473^{+0.374}_{-0.320}$ | ... | 0.77 | 0.53 | SDSS |
| 292 | UGC 8850 | $3.530^{+0.021}_{-0.021}$ | $4.365^{+0.060}_{-0.060}$ | $0.374^{+0.007}_{-0.007}$ | $-0.244^{+0.004}_{-0.004}$ | $-0.291^{+0.003}_{-0.003}$ | $-0.985^{+0.010}_{-0.010}$ | $7.916^{+0.047}_{-0.047}$ | ... | 0.69 | 0.35 | SDSS |
| 293 | UGC 8856_NED01 | $1.800^{+0.011}_{-0.011}$ | $7.832^{+0.176}_{-0.172}$ | $-0.287^{+0.018}_{-0.019}$ | $-0.302^{+0.005}_{-0.004}$ | $-0.420^{+0.003}_{-0.003}$ | $-1.264^{+0.020}_{-0.020}$ | $19.397^{+0.119}_{-0.119}$ | ... | 1.60 | 1.02 | SDSS |
| 294 | NGC 5374 | $2.660^{+0.138}_{-0.173}$ | $4.430^{+0.277}_{-0.328}$ | $-0.716^{+0.080}_{-0.087}$ | $-0.617^{+0.080}_{-0.063}$ | $-0.764^{+0.028}_{-0.022}$ | $-0.739^{+0.161}_{-0.241}$ | $7.470^{*+0.388}_{-0.486}$ | 0.26 | 0.61 | 0.44* | FAST |
| 294 | NGC 5374 | $6.740^{+0.038}_{-0.039}$ | $5.821^{+0.078}_{-0.078}$ | $-0.818^{+0.026}_{-0.027}$ | $-0.435^{+0.004}_{-0.004}$ | $-0.771^{+0.002}_{-0.002}$ | $-1.768^{+0.045}_{-0.045}$ | $36.057^{+0.203}_{-0.207}$ | ... | 0.77 | 0.72 | SDSS |
| 295 | UGC 8902 | $0.918^{+0.021}_{-0.018}$ | $6.557^{+0.501}_{-0.544}$ | $-0.080^{+0.057}_{-0.055}$ | $-0.131^{+0.014}_{-0.016}$ | $-0.420^{+0.008}_{-0.010}$ | $-1.041^{+0.134}_{-0.097}$ | $6.504^{+0.149}_{-0.128}$ | ... | 0.66 | 0.84 | SDSS |
| 296 | NGC 5403 | $0.210^{+0.005}_{-0.004}$ | $6.343^{+0.675}_{-0.634}$ | $0.037^{+0.062}_{-0.059}$ | $-0.302^{+0.018}_{-0.020}$ | $-0.392^{+0.009}_{-0.009}$ | $-1.031^{+0.339}_{-0.128}$ | $1.376^{+0.033}_{-0.026}$ | ... | 1.62 | 0.81 | SDSS |
| 297 | MCG 7-29-036 | $0.679^{+0.007}_{-0.007}$ | $9.069^{+0.579}_{-0.605}$ | $-0.337^{+0.063}_{-0.065}$ | $-0.318^{+0.009}_{-0.008}$ | $-0.588^{+0.005}_{-0.004}$ | $-1.291^{+0.059}_{-0.084}$ | $10.343^{+0.107}_{-0.107}$ | ... | 1.78 | 1.17 | SDSS |
| 298 | NGC 5414 | $6.180^{+0.052}_{-0.046}$ | $4.167^{+0.057}_{-0.055}$ | $-0.049^{+0.007}_{-0.007}$ | $-0.584^{+0.005}_{-0.006}$ | $-0.553^{+0.003}_{-0.004}$ | $-1.624^{+0.024}_{-0.024}$ | $15.022^{+0.126}_{-0.112}$ | ... | 0.24 | 0.38 | SDSS |
| 299 | MCG 5-33-046 | $2.040^{+0.015}_{-0.016}$ | $11.884^{+0.397}_{-0.408}$ | $-0.195^{+0.026}_{-0.027}$ | $-0.177^{+0.005}_{-0.005}$ | $-0.484^{+0.003}_{-0.003}$ | $-1.350^{+0.031}_{-0.031}$ | $58.809^{+0.432}_{-0.461}$ | ... | 1.87 | 1.44 | SDSS |
| 300 | NGC 5474 | $0.721^{+0.012}_{-0.012}$ | $3.481^{+0.140}_{-0.145}$ | $0.231^{+0.020}_{-0.020}$ | $-0.796^{+0.035}_{-0.036}$ | $-0.511^{+0.007}_{-0.007}$ | $-1.579^{+0.186}_{-0.230}$ | $1.146^{+0.019}_{-0.019}$ | 0.39 | 0.29 | 0.20 | FAST |
| 301 | NGC 5480 | $6.330^{+0.177}_{-0.080}$ | $4.460^{+0.158}_{-0.121}$ | $-0.668^{+0.042}_{-0.042}$ | $-0.389^{+0.013}_{-0.016}$ | $-0.601^{+0.005}_{-0.012}$ | $-1.907^{+0.221}_{-0.391}$ | $18.063^{+0.505}_{-0.228}$ | 0.62 | 0.42 | 0.45 | FAST |
| 301 | NGC 5480 | $6.370^{+0.048}_{-0.040}$ | $5.087^{+0.076}_{-0.079}$ | $-0.722^{+0.024}_{-0.020}$ | $-0.417^{+0.005}_{-0.005}$ | $-0.664^{+0.003}_{-0.003}$ | $-1.843^{+0.048}_{-0.049}$ | $24.793^{+0.188}_{-0.156}$ | ... | 0.46 | 0.58 | SDSS |
| 302 | MCG 6-31-070 | $1.190^{+0.032}_{-0.031}$ | $15.179^{+1.946}_{-1.880}$ | $-0.371^{+0.129}_{-0.142}$ | $-0.199^{+0.021}_{-0.021}$ | $-0.541^{+0.011}_{-0.012}$ | $-1.292^{+0.153}_{-0.172}$ | $61.119^{+1.644}_{-1.592}$ | 1.32 | 1.79 | 1.69 | FAST |
| 302 | MCG 6-31-070 | $1.680^{+0.014}_{-0.013}$ | $13.406^{+0.589}_{-0.596}$ | $-0.350^{+0.049}_{-0.048}$ | $-0.195^{+0.006}_{-0.006}$ | $-0.571^{+0.003}_{-0.004}$ | $-1.375^{+0.038}_{-0.038}$ | $64.363^{+0.529}_{-0.510}$ | ... | 2.11 | 1.56 | SDSS |
| 303 | CGCG 74-129 | $0.791^{+0.023}_{-0.037}$ | $5.029^{+0.449}_{-0.494}$ | $0.652^{+0.040}_{-0.039}$ | $-0.026^{+0.028}_{-0.023}$ | $-0.422^{+0.020}_{-0.013}$ | $-0.698^{+0.066}_{-0.068}$ | $2.478^{+0.072}_{-0.116}$ | 1.42 | 1.50 | 0.49 | FAST |
| 303 | CGCG 74-129 | $2.390^{+0.018}_{-0.018}$ | $9.471^{+0.245}_{-0.227}$ | $0.744^{+0.011}_{-0.011}$ | $-0.067^{+0.005}_{-0.005}$ | $-0.222^{+0.003}_{-0.003}$ | $-0.831^{+0.012}_{-0.012}$ | $33.344^{+0.257}_{-0.257}$ | ... | 1.75 | 1.13 | SDSS |
| 304 | NGC 5520 | $2.030^{+0.140}_{-0.112}$ | $6.275^{+0.611}_{-0.546}$ | $-0.522^{+0.078}_{-0.067}$ | $-0.272^{+0.043}_{-0.055}$ | $-0.390^{+0.024}_{-0.030}$ | $-1.629^{+0.045}_{-0.047}$ | $12.966^{*+0.894}_{-0.715}$ | 0.51 | 0.37 | 0.79* | FAST |
| 304 | NGC 5520 | $3.830^{+0.027}_{-0.027}$ | $4.170^{+0.070}_{-0.067}$ | $-0.634^{+0.024}_{-0.018}$ | $-0.435^{+0.006}_{-0.006}$ | $-0.552^{+0.003}_{-0.003}$ | $-1.629^{+0.045}_{-0.047}$ | $9.326^{+0.065}_{-0.066}$ | ... | 0.33 | 0.38 | SDSS |
| 305 | NGC 5515 | $1.040^{+0.066}_{-0.066}$ | $4.435^{+0.630}_{-0.638}$ | $0.304^{+0.065}_{-0.064}$ | $-0.040^{+0.052}_{-0.053}$ | $-0.465^{+0.027}_{-0.027}$ | $-0.955^{+0.213}_{-0.230}$ | $2.421^{*+0.154}_{-0.154}$ | 0.49 | 0.64 | 0.36* | FAST |
| 305 | NGC 5515 | $2.010^{+0.039}_{-0.026}$ | $6.405^{+0.361}_{-0.370}$ | $0.319^{+0.028}_{-0.027}$ | $-0.070^{+0.009}_{-0.011}$ | $-0.401^{+0.006}_{-0.008}$ | $-0.916^{+0.046}_{-0.048}$ | $11.141^{+0.218}_{-0.146}$ | ... | 0.57 | 0.73 | SDSS |

**Table 7.A.1:** Continued

| SFRS | Galaxy | F(H$\alpha$) | H$\alpha$/H$\beta$ | [O III]/H$\beta$ | [N II]/H$\alpha$ | [S II]/H$\alpha$ | [O I]/H$\alpha$ | F(H$\alpha$)$_{cor}$ | A$_V$ | A$_V$nuc | E(B-V)$_{\rm gas}$ | Observation |
|---|---|---|---|---|---|---|---|---|---|---|---|---|
| (1) | (2) | (3) | (4) | (5) | (6) | (7) | (8) | (9) | (10) | (11) | (12) | (13) |
| 306 | NGC 5526_NED02 | $1.750^{+0.013}_{-0.028}$ | $5.316^{+0.136}_{-0.157}$ | $-0.304^{+0.024}_{-0.024}$ | $-0.521^{+0.011}_{-0.008}$ | $-0.426^{+0.007}_{-0.003}$ | $-1.423^{+0.116}_{-0.124}$ | $7.557^{+0.056}_{-0.121}$ | 0.85 | 1.11 | 0.63 | FAST |
| 307 | NGC 5522 | $2.990^{+0.120}_{-0.121}$ | $17.320^{+2.338}_{-2.271}$ | $-0.237^{+0.106}_{-0.108}$ | $-0.193^{+0.033}_{-0.033}$ | $-0.250^{+0.018}_{-0.017}$ | $-1.114^{+0.219}_{-0.278}$ | $209.667^{*+8.415}_{-8.485}$ | 1.19 | 1.28 | 1.82* | FAST |
| 307 | NGC5522 | $2.230^{+0.020}_{-0.024}$ | $6.612^{+0.207}_{-0.204}$ | $-0.273^{+0.028}_{-0.028}$ | $-0.201^{+0.008}_{-0.007}$ | $-0.375^{+0.005}_{-0.004}$ | $-1.186^{+0.041}_{-0.043}$ | $16.115^{+0.148}_{-0.172}$ | ... | 1.22 | 0.85 | SDSS |
| 308 | NGC 5541 | $2.150^{+0.090}_{-0.089}$ | $26.360^{+5.787}_{-5.476}$ | $-0.050^{+0.154}_{-0.168}$ | $-0.240^{+0.036}_{-0.036}$ | $-0.563^{+0.018}_{-0.018}$ | $-1.123^{+0.212}_{-0.317}$ | $406.196^{*+17.004}_{-16.815}$ | 1.06 | 0.72 | 2.24* | FAST |
| 308 | NGC 5541 | $0.310^{+0.012}_{-0.011}$ | $3.830^{+0.446}_{-0.464}$ | $0.225^{+0.059}_{-0.061}$ | $0.077^{+0.021}_{-0.023}$ | $-0.108^{+0.016}_{-0.017}$ | $-0.715^{+0.083}_{-0.076}$ | $0.618^{+0.025}_{-0.022}$ | ... | 0.37 | 0.30 | SDSS |
| 309 | IC 4395 | $3.560^{+0.036}_{-0.058}$ | $7.943^{+0.245}_{-0.280}$ | $-0.171^{+0.026}_{-0.025}$ | $-0.181^{+0.009}_{-0.007}$ | $-0.468^{+0.007}_{-0.004}$ | $-1.295^{+0.040}_{-0.039}$ | $39.659^{+0.401}_{-0.646}$ | ... | 0.97 | 1.03 | SDSS |
| 310 | UGC 9165 | $0.345^{+0.009}_{-0.009}$ | $12.376^{+2.547}_{-2.431}$ | $-0.230^{+0.185}_{-0.208}$ | $-0.340^{+0.026}_{-0.026}$ | $-0.322^{+0.011}_{-0.011}$ | $-1.209^{+0.159}_{-0.164}$ | $10.945^{+0.286}_{-0.286}$ | 1.62 | 2.05 | 1.48 | FAST |
| 311 | MK 1490 | $6.630^{+0.038}_{-0.038}$ | $9.468^{+0.170}_{-0.120}$ | $-0.514^{+0.019}_{-0.019}$ | $-0.150^{+0.004}_{-0.004}$ | $-0.614^{+0.002}_{-0.002}$ | $-1.513^{+0.026}_{-0.025}$ | $111.789^{+0.641}_{-0.641}$ | ... | 1.54 | 1.21 | SDSS |
| 312 | NGC 5585 | $0.410^{+0.005}_{-0.005}$ | $2.916^{+0.100}_{-0.095}$ | $0.220^{+0.016}_{-0.018}$ | $-0.764^{+0.021}_{-0.021}$ | $-0.472^{+0.005}_{-0.005}$ | $-1.190^{+0.106}_{-0.106}$ | $0.429^{+0.005}_{-0.005}$ | ... | 0.08 | 0.02 | SDSS |
| 313 | IC 4408 | $2.080^{+0.017}_{-0.019}$ | $6.956^{+0.202}_{-0.205}$ | $-0.208^{+0.022}_{-0.024}$ | $-0.320^{+0.007}_{-0.007}$ | $-0.691^{+0.004}_{-0.004}$ | $-1.263^{+0.046}_{-0.048}$ | $16.942^{+0.138}_{-0.155}$ | ... | 1.18 | 0.90 | SDSS |
| 314 | NGC 5584 | $0.732^{+0.007}_{-0.006}$ | $3.606^{+0.098}_{-0.098}$ | $-0.505^{+0.028}_{-0.039}$ | $-0.484^{+0.008}_{-0.008}$ | $-0.506^{+0.004}_{-0.004}$ | ... | $1.265^{+0.012}_{-0.010}$ | ... | 0.18 | 0.23 | SDSS |
| 315 | NGC 5633 | $1.600^{+0.016}_{-0.016}$ | $4.348^{+0.124}_{-0.126}$ | $-0.496^{+0.034}_{-0.034}$ | $-0.417^{+0.008}_{-0.009}$ | $-0.593^{+0.004}_{-0.004}$ | $-1.493^{+0.098}_{-0.097}$ | $4.300^{+0.043}_{-0.043}$ | ... | 0.54 | 0.42 | SDSS |
| 316 | NGC 5660 | $1.900^{+0.018}_{-0.018}$ | $4.642^{+0.289}_{-0.286}$ | $-0.473^{+0.087}_{-0.089}$ | $-0.405^{+0.010}_{-0.010}$ | $-0.548^{+0.004}_{-0.004}$ | $-1.303^{+0.110}_{-0.122}$ | $5.958^{+0.056}_{-0.056}$ | 0.32 | 0.30 | 0.49 | FAST |
| 317 | NGC 5656 | $0.162^{+0.012}_{-0.013}$ | $4.357^{+1.737}_{-1.603}$ | $0.290^{+0.192}_{-0.196}$ | $-0.059^{+0.064}_{-0.068}$ | $-0.222^{+0.033}_{-0.031}$ | $-0.338^{+0.120}_{-0.128}$ | $0.437^{+0.032}_{-0.035}$ | ... | 0.25 | 0.43 | SDSS |
| 318 | NGC 5657 | $4.390^{+0.029}_{-0.029}$ | $5.896^{+0.095}_{-0.096}$ | $-0.603^{+0.021}_{-0.020}$ | $-0.390^{+0.005}_{-0.005}$ | $-0.580^{+0.003}_{-0.003}$ | $-1.800^{+0.050}_{-0.053}$ | $24.206^{+0.160}_{-0.160}$ | ... | 0.92 | 0.73 | SDSS |
| 319 | CGCG 133-083 | $3.840^{+0.024}_{-0.024}$ | $8.488^{+0.142}_{-0.113}$ | $-0.553^{+0.018}_{-0.018}$ | $-0.257^{+0.004}_{-0.004}$ | $-0.633^{+0.003}_{-0.003}$ | $-1.495^{+0.025}_{-0.025}$ | $50.030^{+0.313}_{-0.313}$ | ... | 1.68 | 1.10 | SDSS |
| 320 | MCG 7-30-028 | $4.220^{+0.033}_{-0.033}$ | $5.761^{+0.125}_{-0.127}$ | $-0.632^{+0.032}_{-0.035}$ | $-0.352^{+0.006}_{-0.006}$ | $-0.594^{+0.003}_{-0.003}$ | $-1.439^{+0.063}_{-0.056}$ | $22.031^{+0.172}_{-0.172}$ | ... | 0.86 | 0.71 | SDSS |
| 321 | MCG 6-32-070 | $2.150^{+0.019}_{-0.019}$ | $4.494^{+0.206}_{-0.159}$ | $-0.528^{+0.082}_{-0.057}$ | $-0.417^{+0.014}_{-0.020}$ | $-0.571^{+0.004}_{-0.004}$ | $-1.641^{+0.103}_{-0.109}$ | $6.246^{+0.055}_{-0.055}$ | 0.69 | 0.36 | 0.46 | FAST |
| 321 | MCG 6-32-070 | $1.530^{+0.022}_{-0.020}$ | $4.740^{+0.220}_{-0.226}$ | $-0.437^{+0.061}_{-0.065}$ | $-0.375^{+0.012}_{-0.012}$ | $-0.626^{+0.006}_{-0.006}$ | $-1.641^{+0.103}_{-0.109}$ | $5.041^{+0.072}_{-0.065}$ | ... | 0.58 | 0.51 | SDSS |
| 322 | UGC 9412 | $3.710^{+0.023}_{-0.023}$ | $1.722^{+0.026}_{-0.026}$ | $0.723^{+0.006}_{-0.006}$ | $-0.051^{+0.007}_{-0.007}$ | $-0.422^{+0.003}_{-0.003}$ | $-1.078^{+0.014}_{-0.014}$ | $0.926^{+0.006}_{-0.006}$ | 0.08 | 0.02 | -0.59 | FAST |
| 323 | NGC 5698 | $6.800^{+0.141}_{-0.090}$ | $9.437^{+0.329}_{-0.297}$ | $-0.728^{+0.061}_{-0.060}$ | $-0.290^{+0.012}_{-0.014}$ | $-0.592^{+0.006}_{-0.009}$ | $-1.697^{+0.142}_{-0.148}$ | $113.772^{+2.359}_{-1.506}$ | 1.06 | 0.92 | 1.21 | FAST |
| 323 | NGC 5698 | $6.010^{+0.039}_{-0.039}$ | $5.433^{+0.078}_{-0.080}$ | $-0.672^{+0.021}_{-0.022}$ | $-0.298^{+0.005}_{-0.005}$ | $-0.625^{+0.003}_{-0.003}$ | $-1.771^{+0.046}_{-0.048}$ | $27.322^{+0.177}_{-0.177}$ | ... | 0.83 | 0.65 | SDSS |
| 324 | NGC 5691 | $3.350^{+0.021}_{-0.026}$ | $3.241^{+0.063}_{-0.067}$ | $-0.109^{+0.013}_{-0.013}$ | $-0.532^{+0.007}_{-0.007}$ | $-0.452^{+0.003}_{-0.003}$ | $-1.576^{+0.068}_{-0.069}$ | $4.500^{+0.028}_{-0.035}$ | 0.07 | -0.23 | 0.13 | FAST |

**Table 7.A.1:** Continued

| SFRS | Galaxy | F(H$\alpha$) | H$\alpha$/H$\beta$ | [O III]/H$\beta$ | [N II]/H$\alpha$ | [S II]/H$\alpha$ | [O I]/H$\alpha$ | F(H$\alpha$)$_{cor}$ | A$_V$ | A$_V$nuc | E(B-V)$_{\rm gas}$ | Observation |
|---|---|---|---|---|---|---|---|---|---|---|---|---|
| (1) | (2) | (3) | (4) | (5) | (6) | (7) | (8) | (9) | (10) | (11) | (12) | (13) |
| 325 | MCG 9-24-035 | $4.320^{+0.035}_{-0.035}$ | $7.851^{+0.224}_{-0.192}$ | $-0.300^{+0.027}_{-0.026}$ | $-0.111^{+0.005}_{-0.005}$ | $-0.488^{+0.003}_{-0.003}$ | $-1.275^{+0.036}_{-0.038}$ | $46.820^{+0.379}_{-0.379}$ | ... | 1.04 | 1.02 | SDSS |
| 326 | MCG 9-24-038 | $0.784^{+0.009}_{-0.008}$ | $10.573^{+0.649}_{-0.649}$ | $-0.158^{+0.051}_{-0.055}$ | $-0.316^{+0.009}_{-0.009}$ | $-0.568^{+0.005}_{-0.005}$ | $-1.312^{+0.065}_{-0.066}$ | $17.153^{+0.197}_{-0.175}$ | ... | 1.77 | 1.32 | SDSS |
| 327 | UGC 9560 | $43.200^{+0.295}_{-0.295}$ | $14.702^{+0.197}_{-0.162}$ | $0.562^{+0.005}_{-0.025}$ | $-1.322^{+0.014}_{-0.014}$ | $-0.882^{+0.003}_{-0.003}$ | $-1.930^{+0.043}_{-0.038}$ | $2057.723^{+14.052}_{-14.052}$ | 0.66 | 0.69 | 1.65 | FAST |
| 327 | UGC 9560 | $25.600^{+0.148}_{-0.148}$ | $3.265^{+0.030}_{-0.030}$ | $0.625^{+0.004}_{-0.004}$ | $-1.376^{+0.005}_{-0.005}$ | $-0.924^{+0.003}_{-0.003}$ | $-1.956^{+0.010}_{-0.010}$ | $34.992^{+0.202}_{-0.202}$ | ... | -0.07 | 0.13 | SDSS |
| 328 | IC 1076 | $1.480^{+0.013}_{-0.013}$ | $4.388^{+0.096}_{-0.094}$ | $-0.426^{+0.021}_{-0.024}$ | $-0.459^{+0.007}_{-0.008}$ | $-0.422^{+0.004}_{-0.004}$ | $-1.441^{+0.048}_{-0.046}$ | $4.064^{+0.036}_{-0.036}$ | ... | 0.72 | 0.43 | SDSS |
| 329 | IRAS 14538+1730 | $0.775^{+0.006}_{-0.008}$ | $11.302^{+0.605}_{-0.520}$ | $-0.044^{+0.035}_{-0.035}$ | $-0.088^{+0.006}_{-0.006}$ | $-0.437^{+0.004}_{-0.003}$ | $-1.140^{+0.032}_{-0.032}$ | $19.845^{+0.154}_{-0.205}$ | ... | 1.93 | 1.39 | SDSS |
| 330 | NGC 5795 | $0.731^{+0.007}_{-0.008}$ | $4.640^{+0.201}_{-0.210}$ | $-0.345^{+0.046}_{-0.047}$ | $-0.440^{+0.011}_{-0.011}$ | $-0.414^{+0.005}_{-0.004}$ | $-1.449^{+0.101}_{-0.101}$ | $2.290^{+0.022}_{-0.025}$ | 0.68 | -0.13 | 0.49 | FAST |
| 331 | UGC 9618_NED02 | $1.060^{+0.009}_{-0.009}$ | $7.364^{+0.366}_{-0.360}$ | $0.101^{+0.031}_{-0.031}$ | $-0.127^{+0.007}_{-0.007}$ | $-0.405^{+0.003}_{-0.003}$ | $-1.184^{+0.053}_{-0.059}$ | $9.877^{+0.084}_{-0.084}$ | 1.38 | 1.77 | 0.96 | FAST |
| 332 | UGC 9639 | $0.982^{+0.031}_{-0.621}$ | $1.073^{+0.066}_{-0.680}$ | $0.594^{+0.024}_{-0.025}$ | $0.223^{+0.274}_{-0.016}$ | $-0.101^{+0.274}_{-0.014}$ | $-0.709^{+0.285}_{-0.084}$ | $0.080^{*+0.003}_{-0.051}$ | 0.62 | 0.62 | -1.07* | FAST |
| 332 | UGC 9639 | $3.260^{+0.028}_{-0.042}$ | $6.709^{+0.215}_{-0.207}$ | $0.625^{+0.014}_{-0.014}$ | $-0.029^{+0.007}_{-0.006}$ | $-0.439^{+0.006}_{-0.004}$ | $-1.044^{+0.033}_{-0.035}$ | $20.159^{+0.171}_{-0.260}$ | ... | 0.73 | 0.78 | SDSS |
| 333 | MCG 6-33-022 | $25.300^{+0.301}_{-0.382}$ | $14.297^{+1.617}_{-1.562}$ | $0.031^{+0.071}_{-0.068}$ | $-0.334^{+0.012}_{-0.014}$ | $-0.425^{+0.005}_{-0.007}$ | $-1.189^{+0.096}_{-0.087}$ | $1128.223^{+13.423}_{-17.035}$ | 1.13 | 1.37 | 1.63 | FAST |
| 334 | NGC 5879 | $0.650^{+0.019}_{-0.018}$ | $4.754^{+0.425}_{-0.394}$ | $0.222^{+0.045}_{-0.046}$ | $-0.005^{+0.019}_{-0.019}$ | $-0.041^{+0.012}_{-0.012}$ | $-0.639^{+0.056}_{-0.059}$ | $2.156^{+0.063}_{-0.060}$ | ... | 0.56 | 0.51 | SDSS |
| 335 | MCG 9-25-036 | $0.817^{+0.008}_{-0.008}$ | $5.310^{+0.192}_{-0.194}$ | $-0.466^{+0.048}_{-0.050}$ | $-0.352^{+0.009}_{-0.008}$ | $-0.598^{+0.004}_{-0.004}$ | $-1.318^{+0.057}_{-0.060}$ | $3.519^{+0.034}_{-0.034}$ | ... | 0.73 | 0.63 | SDSS |
| 336 | NGC 5899 | $4.170^{+0.054}_{-0.107}$ | $5.569^{+0.250}_{-0.275}$ | $1.036^{+0.018}_{-0.019}$ | $0.252^{+0.012}_{-0.007}$ | $-0.052^{+0.011}_{-0.006}$ | $-0.636^{+0.022}_{-0.020}$ | $16.616^{+0.215}_{-0.426}$ | 0.34 | 0.56 | 0.59 | FAST |
| 337 | NGC 5905 | $9.300^{+0.026}_{-0.026}$ | $5.540^{+0.078}_{-0.078}$ | $-0.341^{+0.014}_{-0.014}$ | $-0.419^{+0.004}_{-0.004}$ | $-0.554^{+0.001}_{-0.001}$ | $-1.617^{+0.034}_{-0.034}$ | $44.270^{+0.124}_{-0.124}$ | 1.09 | 0.70 | 0.67 | FAST |
| 338 | MK 848 | $9.740^{+0.052}_{-0.052}$ | $7.049^{+0.071}_{-0.071}$ | $-0.059^{+0.006}_{-0.006}$ | $-0.311^{+0.003}_{-0.003}$ | $-0.562^{+0.002}_{-0.002}$ | $-1.428^{+0.010}_{-0.009}$ | $81.860^{+0.437}_{-0.437}$ | ... | 1.11 | 0.91 | SDSS |
| 339 | IC 4553 | $0.632^{+0.046}_{-0.046}$ | $16.402^{+8.553}_{-7.568}$ | $0.731^{+0.210}_{-0.236}$ | $0.174^{+0.038}_{-0.038}$ | $0.485^{+0.032}_{-0.031}$ | $-0.714^{+0.093}_{-0.098}$ | $32.224^{*+2.345}_{-2.345}$ | 1.02 | 1.87 | 1.68* | FAST |
| 339 | IC 4553 | $0.174^{+0.017}_{-0.024}$ | $3.101^{+0.500}_{-0.399}$ | $0.587^{+0.041}_{-0.041}$ | $0.820^{+0.062}_{-0.043}$ | $0.803^{+0.060}_{-0.042}$ | $0.091^{+0.062}_{-0.044}$ | $0.174^{+0.017}_{-0.024}$ | ... | 1.98 | 0.01 | SDSS |
| 340 | UGC 9922_NED02 | $3.840^{+0.226}_{-0.286}$ | $4.097^{+0.051}_{-0.062}$ | $-0.291^{+0.009}_{-0.010}$ | $-0.518^{+0.005}_{-0.005}$ | $-0.489^{+0.003}_{-0.003}$ | $-1.595^{+0.023}_{-0.025}$ | $8.968^{+0.528}_{-0.668}$ | ... | 0.31 | 0.36 | SDSS |
| 341 | IC 4567 | $1.210^{+0.013}_{-0.013}$ | $5.029^{+0.192}_{-0.186}$ | $-0.099^{+0.025}_{-0.025}$ | $-0.351^{+0.011}_{-0.010}$ | $-0.699^{+0.005}_{-0.005}$ | $-1.133^{+0.069}_{-0.075}$ | $4.584^{+0.049}_{-0.049}$ | ... | 0.60 | 0.57 | SDSS |
| 342 | MCG 4-37-016 | $4.110^{+0.038}_{-0.042}$ | $1.568^{+0.035}_{-0.041}$ | $-0.405^{+0.022}_{-0.020}$ | $-0.199^{+0.008}_{-0.007}$ | $-0.647^{+0.004}_{-0.004}$ | $-1.523^{+0.062}_{-0.065}$ | $0.995^{*+0.009}_{-0.010}$ | 0.44 | 0.48 | -0.61* | FAST |
| 343 | NGC 5975 | $0.900^{+0.011}_{-0.011}$ | $9.656^{+0.497}_{-0.489}$ | $0.056^{+0.033}_{-0.030}$ | $-0.044^{+0.008}_{-0.008}$ | $-0.359^{+0.005}_{-0.005}$ | $-0.967^{+0.038}_{-0.039}$ | $15.896^{+0.194}_{-0.194}$ | ... | 1.63 | 1.23 | SDSS |
| 344 | NGC 5980 | $1.170^{+0.039}_{-0.042}$ | $6.908^{+1.347}_{-1.270}$ | $-0.129^{+0.143}_{-0.153}$ | $-0.252^{+0.029}_{-0.031}$ | $-0.395^{+0.015}_{-0.014}$ | $-1.180^{+0.200}_{-0.256}$ | $9.375^{+0.313}_{-0.337}$ | 0.53 | 0.63 | 0.89 | FAST |

**Table 7.A.1:** Continued

| SFRS | Galaxy | F(H$\alpha$) | H$\alpha$/H$\beta$ | [O III]/H$\beta$ | [N II]/H$\alpha$ | [S II]/H$\alpha$ | [O I]/H$\alpha$ | F(H$\alpha$)$_{cor}$ | A$_V$ | A$_V$nuc | E(B-V)$_{\rm gas}$ | Observation |
|---|---|---|---|---|---|---|---|---|---|---|---|---|
| (1) | (2) | (3) | (4) | (5) | (6) | (7) | (8) | (9) | (10) | (11) | (12) | (13) |
| 345 | NGC 5992 | $3.390^{+0.014}_{-0.015}$ | $4.631^{+0.105}_{-0.104}$ | $-0.150^{+0.016}_{-0.016}$ | $-0.456^{+0.006}_{-0.006}$ | $-0.515^{+0.002}_{-0.002}$ | $-1.474^{+0.041}_{-0.045}$ | $10.572^{+0.044}_{-0.047}$ | 0.37 | 0.01 | 0.49 | FAST |
| 345 | NGC 5992 | $5.540^{+0.032}_{-0.032}$ | $4.239^{+0.047}_{-0.047}$ | $-0.044^{+0.006}_{-0.006}$ | $-0.631^{+0.004}_{-0.004}$ | $-0.580^{+0.003}_{-0.003}$ | $-1.620^{+0.013}_{-0.013}$ | $14.022^{+0.081}_{-0.081}$ | ... | -0.22 | 0.40 | SDSS |
| 346 | NGC 5996 | $23.100^{+0.145}_{-0.145}$ | $3.971^{+0.044}_{-0.044}$ | $-0.580^{+0.009}_{-0.009}$ | $-0.410^{+0.004}_{-0.004}$ | $-0.688^{+0.003}_{-0.003}$ | $-2.068^{+0.034}_{-0.035}$ | $50.116^{+0.315}_{-0.315}$ | ... | 0.14 | 0.33 | SDSS |
| 347 | IRAS 15519+3537 | $5.320^{+0.174}_{-0.180}$ | $4.526^{+0.678}_{-0.629}$ | $-0.169^{+0.113}_{-0.118}$ | $-0.421^{+0.046}_{-0.048}$ | $-0.527^{+0.015}_{-0.014}$ | $-1.487^{+0.030}_{-0.030}$ | $15.716^{+0.514}_{-0.532}$ | 1.41 | 1.06 | 0.46 | FAST |
| 347 | IRAS 15519+3537 | $0.919^{+0.008}_{-0.008}$ | $5.851^{+0.110}_{-0.109}$ | $-0.329^{+0.016}_{-0.016}$ | $-0.469^{+0.006}_{-0.006}$ | $-0.546^{+0.004}_{-0.004}$ | $-1.487^{+0.030}_{-0.030}$ | $4.976^{+0.046}_{-0.046}$ | ... | 1.12 | 0.72 | SDSS |
| 348 | UGC 10099 | $7.680^{+0.052}_{-0.052}$ | $4.018^{+0.060}_{-0.060}$ | $-0.002^{+0.009}_{-0.009}$ | $-0.333^{+0.005}_{-0.005}$ | $-0.549^{+0.003}_{-0.003}$ | $-1.375^{+0.029}_{-0.029}$ | $17.131^{+0.116}_{-0.116}$ | ... | 0.15 | 0.34 | SDSS |
| 349 | MCG 5-38-006 | $14.600^{+0.087}_{-0.087}$ | $8.850^{+0.224}_{-0.213}$ | $-0.455^{+0.029}_{-0.029}$ | $-0.281^{+0.004}_{-0.004}$ | $-0.527^{+0.003}_{-0.003}$ | $-1.635^{+0.044}_{-0.046}$ | $209.923^{+1.251}_{-1.251}$ | 0.52 | 0.53 | 1.14 | FAST |
| 349 | MCG 5-38-006 | $15.400^{+0.079}_{-0.080}$ | $6.467^{+0.069}_{-0.069}$ | $-0.481^{+0.010}_{-0.010}$ | $-0.265^{+0.003}_{-0.003}$ | $-0.499^{+0.002}_{-0.002}$ | $-1.614^{+0.019}_{-0.019}$ | $105.612^{+0.544}_{-0.547}$ | ... | 1.02 | 0.83 | SDSS |
| 350 | UGC 10120 | $2.770^{+0.083}_{-0.083}$ | $0.613^{+0.021}_{-0.021}$ | $-0.567^{+0.016}_{-0.016}$ | $-0.439^{+0.019}_{-0.019}$ | $-0.770^{+0.013}_{-0.013}$ | $-1.561^{+0.102}_{-0.109}$ | $0.060^{*+0.002}_{-0.002}$ | 0.40 | 0.88 | -1.64* | FAST |
| 350 | UGC 10120 | $16.600^{+0.178}_{-0.178}$ | $5.156^{+0.148}_{-0.148}$ | $-0.262^{+0.013}_{-0.013}$ | $-0.831^{+0.010}_{-0.010}$ | $-1.199^{+0.005}_{-0.005}$ | $-2.044^{+0.036}_{-0.036}$ | $55.148^{+0.591}_{-0.591}$ | ... | 0.62 | 0.51 | SDSS |
| 351 | NGC 6027A | $1.240^{+0.021}_{-0.021}$ | $4.648^{+0.224}_{-0.220}$ | $-0.235^{+0.041}_{-0.043}$ | $-0.329^{+0.015}_{-0.015}$ | $-0.478^{+0.008}_{-0.008}$ | $-1.193^{+0.065}_{-0.051}$ | $3.901^{+0.066}_{-0.066}$ | -0.21 | 0.58 | 0.49 | FAST |
| 352 | NGC 6040B | $0.414^{+0.078}_{-0.124}$ | $5.422^{+1.687}_{-2.050}$ | $0.453^{+0.125}_{-0.128}$ | $0.255^{+0.131}_{-0.085}$ | $0.063^{+0.130}_{-0.082}$ | $-0.531^{+0.161}_{-0.136}$ | $1.549^{+0.292}_{-0.464}$ | 0.39 | 0.58 | 0.57 | FAST |
| 352 | NGC 6040B | $0.639^{+0.020}_{-0.026}$ | $3.382^{+0.249}_{-0.235}$ | $0.217^{+0.032}_{-0.032}$ | $0.250^{+0.019}_{-0.015}$ | $0.103^{+0.017}_{-0.013}$ | $-0.523^{+0.040}_{-0.041}$ | $0.949^{+0.029}_{-0.038}$ | ... | 0.21 | 0.17 | SDSS |
| 353 | UGC 10200 | $11.300^{+0.086}_{-0.086}$ | $3.012^{+0.075}_{-0.041}$ | $0.457^{+0.006}_{-0.014}$ | $-0.997^{+0.008}_{-0.008}$ | $-0.711^{+0.003}_{-0.003}$ | $-1.603^{+0.029}_{-0.020}$ | $12.769^{+0.097}_{-0.097}$ | 0.07 | 0.05 | 0.05 | FAST |
| 353 | UGC 10200 | $18.400^{+0.131}_{-0.126}$ | $3.543^{+0.039}_{-0.040}$ | $0.551^{+0.005}_{-0.005}$ | $-1.047^{+0.006}_{-0.006}$ | $-0.769^{+0.003}_{-0.003}$ | $-1.646^{+0.012}_{-0.013}$ | $30.500^{+0.217}_{-0.209}$ | ... | 0.28 | 0.22 | SDSS |
| 354 | IRAS 16052+5334 | $0.521^{+0.009}_{-0.005}$ | $9.481^{+2.795}_{-2.598}$ | $-0.241^{+0.070}_{-0.068}$ | $-0.264^{+0.008}_{-0.011}$ | $-0.546^{+0.004}_{-0.007}$ | $-1.123^{+0.052}_{-0.054}$ | $8.813^{+0.152}_{-0.085}$ | ... | 1.79 | 1.21 | SDSS |
| 355 | IRAS 16053+1836 | $3.460^{+0.026}_{-0.026}$ | $8.782^{+0.200}_{-0.209}$ | $-0.337^{+0.025}_{-0.025}$ | $-0.224^{+0.005}_{-0.005}$ | $-0.509^{+0.003}_{-0.003}$ | $-1.393^{+0.074}_{-0.083}$ | $48.851^{+0.367}_{-0.367}$ | ... | 1.47 | 1.13 | SDSS |
| 356 | NGC 6090_NED01 | $15.200^{+0.107}_{-0.107}$ | $2.181^{+0.028}_{-0.025}$ | $-0.328^{+0.007}_{-0.009}$ | $-0.302^{+0.005}_{-0.005}$ | $-0.523^{+0.003}_{-0.003}$ | $-1.627^{+0.034}_{-0.035}$ | $8.018^{+0.056}_{-0.056}$ | 1.48 | 1.48 | -0.27 | FAST |
| 357 | UGC 10273_NED01 | $2.130^{+0.009}_{-0.009}$ | $5.305^{+0.076}_{-0.082}$ | $-0.027^{+0.009}_{-0.008}$ | $-0.661^{+0.006}_{-0.006}$ | $-0.543^{+0.002}_{-0.002}$ | $-1.530^{+0.037}_{-0.037}$ | $9.153^{+0.039}_{-0.039}$ | 0.68 | 0.77 | 0.62 | FAST |
| 358 | P 16150+2233 | $0.373^{+0.006}_{-0.009}$ | $7.176^{+0.527}_{-0.533}$ | $1.083^{+0.031}_{-0.032}$ | $-0.052^{+0.012}_{-0.011}$ | $-0.340^{+0.011}_{-0.006}$ | $-0.728^{+0.028}_{-0.029}$ | $2.704^{+0.043}_{-0.065}$ | ... | 1.00 | 0.85 | SDSS |
| 359 | UGC 10322 | $1.650^{+0.053}_{-0.028}$ | $9.002^{+0.585}_{-0.473}$ | $-0.546^{+0.077}_{-0.079}$ | $-0.512^{+0.017}_{-0.023}$ | $-0.567^{+0.007}_{-0.014}$ | $-1.562^{+0.154}_{-0.169}$ | $24.697^{+0.793}_{-0.419}$ | 1.05 | 1.16 | 1.16 | FAST |
| 359 | UGC 10322 | $1.650^{+0.012}_{-0.012}$ | $6.125^{+0.134}_{-0.117}$ | $-0.594^{+0.027}_{-0.027}$ | $-0.457^{+0.006}_{-0.006}$ | $-0.542^{+0.003}_{-0.003}$ | $-1.611^{+0.046}_{-0.047}$ | $9.954^{+0.071}_{-0.074}$ | ... | 1.46 | 0.77 | SDSS |
| 360 | NGC 6120 | $1.470^{+0.028}_{-0.028}$ | $1.454^{+0.055}_{-0.053}$ | $-0.705^{+0.079}_{-0.087}$ | $-0.236^{+0.016}_{-0.016}$ | $-0.630^{+0.008}_{-0.008}$ | $-1.207^{+0.119}_{-0.133}$ | $0.298^{*+0.006}_{-0.006}$ | 1.02 | 1.22 | -0.68* | FAST |

**Table 7.A.1:** Continued

| SFRS | Galaxy | F(H$\alpha$) | H$\alpha$/H$\beta$ | [O III]/H$\beta$ | [N II]/H$\alpha$ | [S II]/H$\alpha$ | [O I]/H$\alpha$ | F(H$\alpha$)$_{cor}$ | $A_V$ | $A_V$nuc | E(B-V)$_{\rm gas}$ | Observation |
|---|---|---|---|---|---|---|---|---|---|---|---|---|
| (1) | (2) | (3) | (4) | (5) | (6) | (7) | (8) | (9) | (10) | (11) | (12) | (13) |
| 361 | MCG 3-42-004 | $0.152^{+0.017}_{-0.025}$ | $0.386^{+0.081}_{-0.094}$ | $-0.508^{+0.152}_{-0.152}$ | $-0.583^{+0.161}_{-0.168}$ | $-0.238^{+0.070}_{-0.047}$ | $-0.422^{+0.205}_{-0.203}$ | $0.001^{+0.001}_{-0.001}$ | 1.08 | 0.70 | -2.02 | FAST |
| 361 | MCG 3-42-004 | $2.140^{+0.016}_{-0.016}$ | $7.093^{+0.189}_{-0.181}$ | $-0.686^{+0.047}_{-0.047}$ | $-0.347^{+0.006}_{-0.006}$ | $-0.671^{+0.003}_{-0.003}$ | $-1.633^{+0.160}_{-0.236}$ | $18.252^{+0.133}_{-0.139}$ | ... | 1.12 | 0.92 | SDSS |
| 362 | UGC 10407 | $4.910^{+0.011}_{-0.009}$ | $3.379^{+0.027}_{-0.027}$ | $0.018^{+0.005}_{-0.005}$ | $-0.695^{+0.004}_{-0.005}$ | $-0.664^{+0.001}_{-0.001}$ | $-1.638^{+0.044}_{-0.046}$ | $7.278^{+0.016}_{-0.013}$ | -0.00 | -0.14 | 0.17 | FAST |
| 363 | IRAS 16320+3922 | $0.686^{+0.013}_{-0.012}$ | $3.644^{+0.168}_{-0.164}$ | $-0.059^{+0.031}_{-0.031}$ | $-0.118^{+0.012}_{-0.012}$ | $-0.199^{+0.007}_{-0.008}$ | $-0.767^{+0.042}_{-0.044}$ | $1.215^{+0.023}_{-0.021}$ | ... | 0.50 | 0.24 | SDSS |
| 364 | NGC 6186 | $2.710^{+0.026}_{-0.024}$ | $5.700^{+0.132}_{-0.128}$ | $-0.598^{+0.033}_{-0.030}$ | $-0.353^{+0.007}_{-0.008}$ | $-0.644^{+0.004}_{-0.004}$ | $-1.445^{+0.061}_{-0.058}$ | $13.797^{+0.132}_{-0.122}$ | ... | 0.95 | 0.70 | SDSS |
| 365 | MCG 9-27-053 | $0.366^{+0.009}_{-0.009}$ | $5.718^{+0.756}_{-0.734}$ | $-0.271^{+0.116}_{-0.128}$ | $-0.136^{+0.019}_{-0.019}$ | $-0.425^{+0.010}_{-0.010}$ | $-1.114^{+0.131}_{-0.138}$ | $1.877^{+0.046}_{-0.046}$ | 0.03 | 0.45 | 0.70 | FAST |
| 366 | UGC 10514 | $3.420^{+0.021}_{-0.022}$ | $4.632^{+0.060}_{-0.063}$ | $0.306^{+0.007}_{-0.006}$ | $-0.685^{+0.005}_{-0.005}$ | $-0.545^{+0.003}_{-0.003}$ | $-1.530^{+0.015}_{-0.015}$ | $10.671^{+0.066}_{-0.069}$ | ... | 0.88 | 0.49 | SDSS |
| 367 | IRAS 16435+2154 | $2.350^{+0.016}_{-0.016}$ | $7.582^{+0.154}_{-0.157}$ | $-0.517^{+0.021}_{-0.026}$ | $-0.376^{+0.005}_{-0.005}$ | $-0.559^{+0.003}_{-0.003}$ | $-1.531^{+0.032}_{-0.031}$ | $23.458^{+0.160}_{-0.160}$ | ... | 1.34 | 0.99 | SDSS |
| 368 | IC 4623 | $1.970^{+0.044}_{-0.043}$ | $11.694^{+1.193}_{-1.155}$ | $-0.666^{+0.169}_{-0.190}$ | $-0.386^{+0.021}_{-0.021}$ | $-0.697^{+0.009}_{-0.010}$ | $-1.507^{+0.046}_{-0.044}$ | $54.672^{+1.221}_{-1.193}$ | 1.41 | 1.45 | 1.42 | FAST |
| 368 | IC 4623 | $2.030^{+0.015}_{-0.014}$ | $8.041^{+0.213}_{-0.214}$ | $-0.596^{+0.045}_{-0.043}$ | $-0.342^{+0.005}_{-0.006}$ | $-0.671^{+0.003}_{-0.003}$ | $-1.507^{+0.046}_{-0.044}$ | $23.278^{+0.175}_{-0.166}$ | ... | 1.40 | 1.05 | SDSS |
| 369 | IRAS 16516+3030 | $0.366^{+0.036}_{-0.036}$ | $1.307^{+0.163}_{-0.162}$ | $-0.527^{+0.106}_{-0.113}$ | $0.561^{+0.044}_{-0.044}$ | $0.238^{+0.042}_{-0.042}$ | $-0.573^{+0.175}_{-0.196}$ | $0.058^{+0.006}_{-0.006}$ | 1.91 | 1.94 | -0.79 | FAST |

**Table 7.A.1:** Nuclear fluxes and flux ratios of optical diagnostic emission lines. Column (1) SFRS ID (Ashby et al. 2011); Column (2) Galaxy name; Column (3) H$\alpha$ emission line flux, normalized to $10^{-14}$ erg cm$^{-2}$ s$^{-1}$; Column (4) Ratio of H$\alpha$ and H$\beta$ Balmer line fluxes. Columns (5) – (8) BPT line ratio measurements and uncertainties; Column (9) Extinction corrected H$\alpha$ emission line flux normalized to $10^{-14}$ erg cm$^{-2}$ s$^{-1}$; Columns (10) and (11) Integrated and nuclear extinction as calculated by STARLIGHT code; Column (12) The nuclear E(B-V) color excess of the gas as calculated from the Balmer decrement; Column (13) Spectral observation method. Emission line fluxes and ratios for the FAST observations come from the nuclear aperture spectrum. F(H$\alpha$)$_{cor}$ and E(B-V)$_{\rm gas}$ values flagged with a * symbol indicate uncertain measurements due to differences in the flux calibration between the blue and red spectral regions of galaxies observed with the 600 l mm$^{-1}$ grating configuration (Section 4.3.6).

**Table 7.A.2:** Activity Classification Based On Various Diagnostics.

| SFRS | Galaxy | Nuclear Spectra BPT | | | IRAC Colors | MEx | CEx | Final Classification |
|---|---|---|---|---|---|---|---|---|
| | | [N II]/H$\alpha$ | [S II]/H$\alpha$ | [O I]/H$\alpha$ | | | | |
| (1) | (2) | (3) | (4) | (5) | (6) | (7) | (8) | (9) |
| 1 | IC 486 | Sy | Sy | Sy | Sy | Sy | Sy | Sy |
| 2 | IC 2217 | HII | HII | HII | HII | HII | HII | HII |
| 3 | NGC 2500 | TO | LINER | LINER | HII | HII | ... | LINER |
| 4 | NGC 2512 | HII | HII | HII | HII | HII | ... | HII |
| 5 | MCG 6-18-009 | HII | HII | HII | HII | HII | HII | HII |
| 6 | MK 1212 | TO | HII | HII | HII | HII | HII | HII |
| 7 | IRAS 08072+1847 | TO | HII | HII | Sy | HII | TO | Sy |
| 8 | NGC 2532 | HII | HII | HII | ... | HII | HII | HII |
| 9 | UGC 4261 | HII | HII | HII | HII | TO | HII | HII |
| 10 | NGC 2535 | HII | HII | HII | HII | HII | ... | HII |
| 11 | NGC 2543 | HII | HII | HII | HII | HII | HII | HII |
| 12 | NGC 2537 | HII | HII | HII | HII | TO | TO | HII |
| 13 | IC 2233 | HII | HII | HII | HII | HII | ... | HII |
| 14 | IC 2239 | TO | HII | HII | HII | TO | TO | HII |
| 15 | UGC 4286 | TO | HII | HII | HII | TO | TO | HII |
| 16 | UGC 4306 | HII | HII | HII | HII | HII | HII | HII |
| 17 | NGC 2552 | HII | HII | HII | HII | HII | ... | HII |
| 18 | UGC 4383 | HII | HII | HII | HII | TO | ... | HII |
| 19 | IRAS 08234+1054 | TO | HII | HII | HII | HII | HII | HII |
| 20 | IRAS 08269+1514 | TO | HII | HII | HII | HII | TO | HII |
| 21 | NGC 2604 | HII | HII | HII | HII | TO | ... | HII |
| 22 | NGC 2608 | HII | HII | HII | HII | HII | HII | HII |
| 23 | MK 92 | HII | HII | HII | HII | TO | HII | HII |

**Table 7.A.2:** Continued

| SFRS | Galaxy | Nuclear Classification | | | IR | MEx | CEx | Final Classification |
|---|---|---|---|---|---|---|---|---|
| | | [N II]/H$\alpha$ | [S II]/H$\alpha$ | [O I]/H$\alpha$ | | | | |
| (1) | (2) | (3) | (4) | (5) | (6) | (7) | (8) | (9) |
| 24 | NGC 2623 | LINER | Sy | Sy | HII | Sy | LINER | Sy |
| 25 | CGCG 120-018 | TO | HII | HII | HII | HII | TO | HII |
| 26 | NGC 2644 | HII | HII | HII | HII | HII | HII | HII |
| 27 | UGC 4572 | TO | HII | LINER | HII | TO | TO | TO |
| 28 | UGC 4653 | TO | HII | HII | HII | TO | TO | HII |
| 29 | IRAS 08512+2727 | HII | HII | HII | HII | HII | HII | HII |
| 30 | OJ 287 | ... | ... | ... | Sy | ... | ... | Sy |
| 31 | IRAS 08538+4256 | TO | HII | HII | HII | HII | TO | HII |
| 32 | IRAS 08550+3908 | Sy | LINER | Sy | Sy | Sy | ... | Sy |
| 33 | NGC 2718 | HII | HII | HII | HII | HII | HII | HII |
| 34 | NGC 2712 | TO | HII | HII | HII | HII | TO | HII |
| 35 | NGC 2719 | HII | HII | HII | HII | Sy | HII | HII |
| 36 | IRAS 08572+3915NW | TO | HII | Sy | Sy | HII | LINER | Sy |
| 37 | IRAS 08579+3447 | HII | HII | HII | HII | HII | HII | HII |
| 38 | NGC 2731 | HII | HII | HII | HII | HII | HII | HII |
| 39 | NGC 2730 | HII | HII | ... | HII | HII | HII | HII |
| 40 | IC 2431 | HII | HII | HII | HII | HII | HII | HII |
| 41 | NGC 2750 | HII | HII | HII | HII | HII | HII | HII |
| 42 | IC 2434 | TO | HII | LINER | HII | TO | LINER | TO |
| 43 | NGC 2761 | TO | HII | HII | HII | HII | HII | HII |
| 44 | NGC 2773 | HII | HII | HII | HII | HII | HII | HII |
| 45 | NGC 2776 | TO | HII | HII | HII | HII | TO | HII |
| 46 | NGC 2789 | TO | HII | HII | HII | HII | TO | HII |
| 47 | NGC 2824 | LINER | LINER | LINER | HII | HII | LINER | LINER |

**Table 7.A.2:** Continued

| SFRS | Galaxy | Nuclear Classification | | | IR | MEx | CEx | Final Classification |
|---|---|---|---|---|---|---|---|---|
| | | [N II]/H$\alpha$ | [S II]/H$\alpha$ | [O I]/H$\alpha$ | | | | |
| (1) | (2) | (3) | (4) | (5) | (6) | (7) | (8) | (9) |
| 48 | IRAS 09121+3908 | TO | HII | HII | HII | HII | TO | HII |
| 49 | IRAS 09184+4356 | HII | HII | HII | HII | HII | HII | HII |
| 50 | CGCG 238-041 | HII | HII | HII | HII | TO | ... | HII |
| 51 | IRAS 09197+2210 | TO | HII | Sy | HII | HII | LINER | TO |
| 52 | NGC 2854 | TO | HII | LINER | HII | TO | TO | TO |
| 53 | UGC 5046 | HII | HII | HII | HII | HII | HII | HII |
| 54 | UGC 5055 | HII | HII | HII | HII | HII | HII | HII |
| 55 | NGC 2893 | HII | HII | HII | HII | HII | HII | HII |
| 56 | MCG 3-24-062 | HII | HII | HII | HII | HII | TO | HII |
| 57 | CGCG 238-066 | LINER | HII | Sy | Sy | HII | LINER | Sy |
| 58 | UGC 5097 | HII | HII | HII | HII | TO | ... | HII |
| 59 | CGCG 289-012 | HII | HII | HII | HII | HII | HII | HII |
| 60 | MCG 8-18-013 | TO | HII | HII | HII | TO | TO | HII |
| 61 | CGCG 181-068 | TO | HII | LINER | HII | HII | TO | TO |
| 62 | NGC 2936 | LINER | ... | LINER | HII | TO | TO | LINER |
| 63 | NGC 2955 | HII | ... | HII | HII | HII | TO | HII |
| 64 | CGCG 182-010 | HII | HII | HII | HII | HII | HII | HII |
| 65 | UGC 5228 | HII | HII | HII | HII | HII | TO | HII |
| 66 | IRAS 09438+1141 | HII | HII | HII | HII | HII | HII | HII |
| 67 | NGC 3015 | TO | HII | LINER | HII | HII | TO | TO |
| 68 | MCG 2-25-039 | HII | HII | HII | HII | HII | HII | HII |
| 69 | NGC 3020 | HII | HII | HII | HII | HII | HII | HII |
| 70 | NGC 3049 | HII | HII | HII | HII | HII | HII | HII |
| 71 | NGC 3055 | TO | HII | HII | HII | TO | ... | HII |

**Table 7.A.2:** Continued

| SFRS | Galaxy | Nuclear Classification | | | IR | MEx | CEx | Final Classification |
|---|---|---|---|---|---|---|---|---|
| | | [N II]/H$\alpha$ | [S II]/H$\alpha$ | [O I]/H$\alpha$ | | | | |
| (1) | (2) | (3) | (4) | (5) | (6) | (7) | (8) | (9) |
| 72 | IC 2520 | HII | HII | HII | HII | TO | HII | HII |
| 73 | UGC 5403 | HII | HII | ... | HII | HII | HII | HII |
| 74 | UGC 5459 | HII | HII | HII | HII | HII | HII | HII |
| 75 | MCG 5-24-022 | HII | HII | HII | HII | HII | HII | HII |
| 76 | IC 2551 | TO | HII | HII | HII | TO | ... | HII |
| 77 | IRAS 10106+2745 | HII | HII | HII | HII | HII | HII | HII |
| 78 | NGC 3162 | HII | HII | ... | HII | HII | HII | HII |
| 79 | IRAS 10120+1653 | LINER | ... | LINER | HII | TO | HII | LINER |
| 80 | NGC 3190 | LINER | LINER | ... | HII | ... | ... | LINER |
| 81 | IC 602 | HII | HII | HII | HII | HII | HII | HII |
| 82 | NGC 3191 | HII | HII | ... | HII | HII | HII | HII |
| 83 | NGC 3206 | HII | HII | HII | HII | HII | TO | HII |
| 84 | UGC 5613 | TO | HII | HII | HII | TO | LINER | HII |
| 85 | UGC 5644 | LINER | LINER | LINER | HII | LINER | LINER | LINER |
| 86 | NGC 3245 | TO | HII | HII | HII | TO | LINER | HII |
| 87 | IRAS 10246+2042 | TO | HII | HII | HII | HII | HII | HII |
| 88 | MCG 7-22-012 | HII | HII | HII | HII | HII | HII | HII |
| 89 | IRAS 10276+1119 | TO | HII | HII | HII | HII | HII | HII |
| 90 | NGC 3265 | HII | HII | HII | HII | HII | ... | HII |
| 91 | UGC 5713 | Sy | Sy | Sy | Sy | Sy | Sy | Sy |
| 92 | NGC 3274 | HII | Sy | HII | HII | HII | ... | HII |
| 93 | UGC 5720 | LINER | LINER | LINER | HII | HII | ... | HII |
| 94 | KUG 1031+351 | HII | HII | HII | HII | HII | HII | HII |
| 95 | NGC 3306 | HII | HII | HII | HII | HII | HII | HII |

**Table 7.A.2:** Continued

| SFRS | Galaxy | Nuclear Classification | | | IR | MEx | CEx | Final Classification |
|---|---|---|---|---|---|---|---|---|
| | | [N II]/H$\alpha$ | [S II]/H$\alpha$ | [O I]/H$\alpha$ | | | | |
| (1) | (2) | (3) | (4) | (5) | (6) | (7) | (8) | (9) |
| 96 | NGC 3323 | HII | HII | HII | HII | HII | HII | HII |
| 97 | IC 2598 | HII | HII | HII | HII | HII | HII | HII |
| 98 | NGC 3338 | LINER | HII | LINER | HII | TO | ... | LINER |
| 99 | NGC 3353 | HII | HII | HII | HII | HII | ... | HII |
| 100 | UGC 5881 | TO | HII | HII | HII | HII | ... | HII |
| 101 | NGC 3370 | HII | HII | HII | HII | HII | HII | HII |
| 102 | NGC 3381 | HII | HII | HII | HII | HII | ... | HII |
| 103 | UGC 5941_NED02 | HII | HII | HII | HII | HII | HII | HII |
| 104 | NGC 3413 | HII | HII | HII | HII | HII | ... | HII |
| 105 | NGC 3408 | HII | HII | HII | HII | HII | HII | HII |
| 106 | NGC 3430 | HII | HII | HII | HII | HII | HII | HII |
| 107 | CGCG 95-055 | Sy | Sy | Sy | HII | Sy | Sy | Sy |
| 108 | IRAS 10565+2448W | TO | HII | HII | Sy | HII | TO | Sy |
| 109 | UGC 6074 | TO | HII | HII | HII | HII | HII | HII |
| 110 | NGC 3495 | HII | HII | ... | HII | HII | ... | HII |
| 111 | UGC 6103 | TO | HII | HII | HII | TO | ... | HII |
| 112 | MCG 7-23-019 | TO | HII | HII | HII | TO | HII | HII |
| 113 | UGC 6135 | LINER | LINER | LINER | HII | Sy | Sy | LINER |
| 114 | CGCG 241-078 | TO | HII | HII | HII | HII | TO | HII |
| 115 | IRAS 11069+2711 | HII | HII | HII | HII | TO | HII | HII |
| 116 | IC 676 | HII | HII | HII | HII | HII | HII | HII |
| 117 | IRAS 11102+3026 | LINER | Sy | LINER | HII | TO | LINER | LINER |
| 118 | IC 2637 | Sy | Sy | Sy | HII | Sy | ... | Sy |
| 119 | MCG 9-19-013 | TO | HII | LINER | HII | TO | TO | TO |

**Table 7.A.2:** Continued

| SFRS | Galaxy | Nuclear Classification | | | IR | MEx | CEx | Final Classification |
|---|---|---|---|---|---|---|---|---|
| | | [N II]/H$\alpha$ | [S II]/H$\alpha$ | [O I]/H$\alpha$ | | | | |
| (1) | (2) | (3) | (4) | (5) | (6) | (7) | (8) | (9) |
| 120 | 7ZW 384 | TO | HII | LINER | HII | TO | HII | TO |
| 121 | 2MASXJ 11193404+5335181 | TO | HII | Sy | Sy | Sy | ... | Sy |
| 122 | NGC 3633 | HII | HII | HII | HII | HII | HII | HII |
| 123 | NGC 3652 | HII | HII | HII | HII | HII | HII | HII |
| 124 | NGC 3656 | TO | LINER | LINER | HII | TO | LINER | LINER |
| 125 | NGC 3659 | HII | HII | HII | HII | HII | HII | HII |
| 126 | NGC 3664 | HII | HII | HII | HII | HII | LINER | HII |
| 127 | NGC 3666 | HII | HII | HII | HII | HII | TO | HII |
| 128 | IC 691 | HII | HII | HII | HII | HII | ... | HII |
| 129 | NGC 3686 | HII | HII | HII | HII | HII | HII | HII |
| 130 | UGC 6469 | HII | HII | HII | HII | HII | HII | HII |
| 131 | NGC 3690 | TO | HII | HII | Sy | TO | ... | Sy |
| 132 | IC 698 | HII | HII | HII | HII | HII | HII | HII |
| 133 | IRAS 11267+1558 | TO | HII | HII | HII | TO | HII | HII |
| 134 | NGC 3705 | LINER | LINER | LINER | HII | HII | LINER | LINER |
| 135 | MCG 3-29-061 | TO | HII | HII | HII | HII | HII | HII |
| 136 | NGC 3720 | HII | HII | HII | HII | HII | HII | HII |
| 137 | NGC 3729 | TO | HII | HII | HII | TO | LINER | HII |
| 138 | MCG 10-17-019 | HII | HII | HII | HII | HII | HII | HII |
| 139 | NGC 3758 | ... | ... | ... | HII | Sy | Sy | Sy |
| 140 | UGC 6583 | HII | HII | HII | HII | HII | ... | HII |
| 141 | MCG 1-30-003 | HII | HII | HII | HII | HII | HII | HII |
| 142 | NGC 3769 | HII | HII | HII | HII | TO | HII | HII |
| 143 | NGC 3773 | HII | HII | HII | HII | HII | HII | HII |

**Table 7.A.2:** Continued

| SFRS | Galaxy | Nuclear Classification | | | IR | MEx | CEx | Final Classification |
|---|---|---|---|---|---|---|---|---|
| | | [N II]/H$\alpha$ | [S II]/H$\alpha$ | [O I]/H$\alpha$ | | | | |
| (1) | (2) | (3) | (4) | (5) | (6) | (7) | (8) | (9) |
| 144 | NGC 3781 | LINER | Sy | Sy | HII | Sy | LINER | Sy |
| 145 | UGC 6625 | TO | HII | LINER | HII | HII | TO | TO |
| 146 | NGC 3808_NED02 | HII | HII | HII | HII | HII | HII | HII |
| 147 | NGC 3811 | HII | HII | HII | HII | HII | HII | HII |
| 148 | NGC 3822 | LINER | ... | Sy | HII | Sy | LINER | Sy |
| 149 | UGC 6665 | HII | HII | HII | HII | Sy | HII | HII |
| 150 | MCG 3-30-051 | HII | HII | HII | HII | HII | HII | HII |
| 151 | NGC 3839 | HII | HII | HII | HII | HII | HII | HII |
| 152 | UGC 6732 | LINER | LINER | LINER | HII | Sy | Sy | LINER |
| 153 | IC 730 | HII | HII | HII | HII | HII | HII | HII |
| 154 | IC 732_NED01 | TO | HII | HII | HII | TO | TO | HII |
| 155 | NGC 3912 | HII | HII | HII | HII | HII | TO | HII |
| 156 | NGC 3928 | TO | HII | HII | HII | HII | TO | HII |
| 157 | NGC 3934 | TO | LINER | LINER | HII | TO | TO | LINER |
| 158 | UGC 6865 | HII | HII | HII | HII | HII | HII | HII |
| 159 | UGC 6901 | HII | HII | HII | HII | HII | HII | HII |
| 160 | CGCG 013-010 | TO | HII | HII | HII | TO | LINER | HII |
| 161 | NGC 3991 | HII | HII | HII | HII | Sy | ... | HII |
| 162 | NGC 4004 | HII | HII | HII | HII | HII | HII | HII |
| 163 | NGC 4014 | TO | HII | HII | HII | TO | TO | HII |
| 164 | NGC 4010 | HII | HII | HII | HII | HII | TO | HII |
| 165 | NGC 4018 | HII | HII | HII | HII | TO | TO | HII |
| 166 | NGC 4020 | HII | LINER | LINER | HII | HII | HII | LINER |
| 167 | IRAS 11571+3003 | HII | HII | HII | HII | HII | HII | HII |

**Table 7.A.2:** Continued

| SFRS | Galaxy | Nuclear Classification | | | IR | MEx | CEx | Final Classification |
|---|---|---|---|---|---|---|---|---|
| | | [N II]/H$\alpha$ | [S II]/H$\alpha$ | [O I]/H$\alpha$ | | | | |
| (1) | (2) | (3) | (4) | (5) | (6) | (7) | (8) | (9) |
| 168 | UGC 7017 | HII | HII | HII | HII | HII | HII | HII |
| 169 | UGC 7016 | Sy | Sy | Sy | HII | Sy | LINER | Sy |
| 170 | MCG 3-31-030 | HII | HII | HII | HII | HII | HII | HII |
| 171 | NGC 4062 | HII | HII | ... | HII | HII | HII | HII |
| 172 | NGC 4064 | HII | HII | HII | HII | HII | HII | HII |
| 173 | CGCG 098-059 | HII | HII | HII | HII | HII | HII | HII |
| 174 | NGC 4116 | HII | HII | HII | HII | HII | HII | HII |
| 175 | NGC 4136 | HII | HII | HII | HII | HII | HII | HII |
| 176 | NGC 4150 | Sy | LINER | Sy | HII | Sy | ... | Sy |
| 177 | IRAS 12086+1441 | HII | HII | HII | HII | HII | ... | HII |
| 178 | NGC 4162 | TO | HII | HII | HII | TO | HII | HII |
| 179 | NGC 4178 | HII | HII | HII | HII | HII | TO | HII |
| 180 | IRAS 12112+0305 | TO | Sy | Sy | HII | HII | HII | Sy |
| 181 | NGC 4189 | HII | HII | HII | HII | HII | HII | HII |
| 182 | NGC 4194 | LINER | LINER | LINER | HII | TO | ... | HII |
| 183 | NGC 4204 | HII | HII | HII | HII | HII | HII | HII |
| 184 | NGC 4207 | HII | HII | HII | HII | HII | HII | HII |
| 185 | UGC 7286 | TO | HII | HII | HII | HII | TO | HII |
| 186 | NGC 4234 | HII | HII | HII | HII | HII | ... | HII |
| 187 | NGC 4237 | TO | HII | ... | HII | TO | TO | HII |
| 188 | NGC 4244 | HII | HII | ... | HII | HII | TO | HII |
| 189 | NGC 4253 | HII | HII | HII | Sy | TO | TO | Sy |
| 190 | MCG 3-32-005 | HII | HII | HII | HII | HII | HII | HII |
| 191 | NGC 4290 | HII | HII | HII | HII | HII | ... | HII |

**Table 7.A.2:** Continued

| SFRS | Galaxy | Nuclear Classification | | | IR | MEx | CEx | Final Classification |
|---|---|---|---|---|---|---|---|---|
| | | [N II]/H$\alpha$ | [S II]/H$\alpha$ | [O I]/H$\alpha$ | | | | |
| (1) | (2) | (3) | (4) | (5) | (6) | (7) | (8) | (9) |
| 192 | NGC 4294 | HII | HII | HII | HII | HII | HII | HII |
| 193 | NGC 4314 | LINER | LINER | LINER | HII | TO | LINER | LINER |
| 194 | NGC 4385 | TO | HII | HII | HII | TO | TO | HII |
| 195 | NGC 4395 | Sy | Sy | Sy | HII | Sy | Sy | Sy |
| 196 | NGC 4396 | HII | HII | HII | HII | ... | HII | HII |
| 197 | NGC 4412 | Sy | Sy | Sy | HII | Sy | Sy | Sy |
| 198 | NGC 4418 | TO | LINER | LINER | Sy | TO | TO | Sy |
| 199 | NGC 4420 | HII | HII | HII | HII | HII | HII | HII |
| 200 | NGC 4424 | HII | HII | ... | HII | HII | HII | HII |
| 201 | NGC 4435 | TO | HII | LINER | HII | TO | ... | LINER |
| 202 | NGC 4438 | LINER | LINER | LINER | LINER | ... | LINER | LINER |
| 203 | NGC 4448 | HII | HII | LINER | HII | HII | HII | HII |
| 204 | 3C 273 | ... | ... | ... | Sy | ... | ... | Sy |
| 205 | NGC 4470 | HII | HII | HII | HII | HII | ... | HII |
| 206 | IRAS 12274+0018 | HII | HII | HII | HII | HII | HII | HII |
| 207 | NGC 4491 | HII | HII | ... | ... | HII | HII | HII |
| 208 | NGC 4500 | TO | HII | HII | HII | HII | Sy | HII |
| 209 | NGC 4495 | TO | HII | HII | HII | HII | TO | HII |
| 210 | IC 3476 | HII | HII | HII | HII | HII | HII | HII |
| 211 | NGC 4509 | HII | HII | HII | HII | HII | HII | HII |
| 212 | NGC 4519 | HII | HII | HII | HII | HII | HII | HII |
| 213 | NGC 4548 | Sy | LINER | Sy | HII | ... | ... | Sy |
| 214 | IRAS 12337+5044 | HII | HII | HII | HII | TO | TO | HII |
| 215 | IC 3581 | TO | HII | HII | HII | HII | TO | HII |

**Table 7.A.2:** Continued

| SFRS | Galaxy | Nuclear Classification | | | IR | MEx | CEx | Final Classification |
|---|---|---|---|---|---|---|---|---|
| | | [N II]/H$\alpha$ | [S II]/H$\alpha$ | [O I]/H$\alpha$ | | | | |
| (1) | (2) | (3) | (4) | (5) | (6) | (7) | (8) | (9) |
| 216 | NGC 4592 | HII | HII | HII | HII | HII | HII | HII |
| 217 | NGC 4607 | TO | LINER | LINER | HII | HII | LINER | LINER |
| 218 | NGC 4625 | HII | HII | LINER | HII | HII | TO | HII |
| 219 | NGC 4630 | HII | HII | HII | HII | HII | HII | HII |
| 220 | IC 3690 | TO | HII | HII | HII | HII | TO | HII |
| 221 | UGC 7905_NED01 | HII | HII | HII | HII | Sy | HII | HII |
| 222 | MCG 5-30-069 | HII | HII | HII | HII | HII | HII | HII |
| 223 | IC 3721 | TO | HII | HII | HII | TO | TO | HII |
| 224 | NGC 4670 | HII | HII | HII | HII | Sy | ... | HII |
| 225 | NGC 4675 | TO | HII | HII | HII | HII | TO | HII |
| 226 | MCG 7-26-051 | TO | HII | HII | HII | TO | LINER | HII |
| 227 | NGC 4689 | TO | HII | ... | HII | TO | HII | HII |
| 228 | NGC 4688 | HII | LINER | ... | HII | HII | LINER | HII |
| 229 | NGC 4704 | LINER | LINER | Sy | HII | Sy | Sy | LINER |
| 230 | NGC 4701 | HII | HII | HII | HII | HII | HII | HII |
| 231 | IRAS 12468+3436 | TO | Sy | Sy | HII | HII | LINER | Sy |
| 232 | IRAS 12470+1404 | TO | HII | HII | ... | HII | HII | HII |
| 233 | MCG 8-23-097 | LINER | HII | Sy | HII | TO | LINER | LINER |
| 234 | NGC 4747 | HII | HII | ... | HII | HII | LINER | HII |
| 235 | UGC 8017 | TO | HII | LINER | HII | TO | TO | TO |
| 236 | NGC 4765 | HII | HII | HII | HII | HII | ... | HII |
| 237 | VCC2096 | TO | HII | HII | HII | HII | HII | HII |
| 239 | UGC 8058 | ... | ... | ... | ... | ... | ... | Sy |
| 238 | UGC 8041 | HII | HII | HII | HII | TO | TO | HII |

**Table 7.A.2:** Continued

| SFRS | Galaxy | Nuclear Classification | | | IR | MEx | CEx | Final Classification |
|---|---|---|---|---|---|---|---|---|
| | | [N II]/H$\alpha$ | [S II]/H$\alpha$ | [O I]/H$\alpha$ | | | | |
| (1) | (2) | (3) | (4) | (5) | (6) | (7) | (8) | (9) |
| 240 | NGC 4837_NED01 | TO | HII | HII | HII | HII | TO | HII |
| 241 | UM530 | HII | HII | HII | HII | HII | HII | HII |
| 242 | NGC 4861 | HII | HII | HII | HII | ... | ... | HII |
| 243 | NGC 4868 | HII | HII | HII | HII | HII | HII | HII |
| 244 | NGC 4922_NED02 | Sy | Sy | Sy | Sy | Sy | ... | Sy |
| 245 | UGC 8179 | HII | HII | HII | HII | HII | HII | HII |
| 246 | NGC 5001 | TO | HII | HII | HII | TO | TO | HII |
| 247 | IC 856 | HII | HII | HII | HII | TO | TO | HII |
| 248 | UGC 8269 | TO | HII | LINER | HII | TO | TO | TO |
| 249 | NGC 5014 | HII | HII | HII | HII | HII | TO | HII |
| 250 | NGC 5012 | LINER | LINER | LINER | HII | LINER | LINER | LINER |
| 251 | IRAS 13116+4508 | HII | HII | HII | HII | HII | HII | HII |
| 252 | IC 860 | LINER | LINER | LINER | HII | HII | LINER | LINER |
| 253 | IRAS 13144+4508 | Sy | Sy | Sy | HII | Sy | ... | Sy |
| 254 | NGC 5060 | HII | HII | HII | HII | HII | HII | HII |
| 255 | UGC 8357_NED01 | TO | HII | LINER | HII | HII | HII | TO |
| 256 | UGC 8361 | TO | HII | HII | HII | HII | TO | HII |
| 257 | IC 883 | TO | HII | LINER | Sy | TO | TO | Sy |
| 258 | NGC 5100_NED02 | TO | HII | HII | Sy | TO | TO | Sy |
| 259 | NGC 5104 | LINER | HII | Sy | HII | LINER | LINER | Sy |
| 260 | NGC 5107 | HII | HII | Sy | HII | HII | HII | HII |
| 261 | NGC 5112 | TO | LINER | Sy | HII | HII | LINER | TO |
| 262 | NGC 5123 | TO | HII | ... | HII | TO | LINER | HII |
| 263 | IRAS 13218+0552 | ... | ... | ... | Sy | ... | ... | Sy |

**Table 7.A.2:** Continued

| SFRS | Galaxy | Nuclear Classification | | | IR | MEx | CEx | Final Classification |
|---|---|---|---|---|---|---|---|---|
| | | [N II]/H$\alpha$ | [S II]/H$\alpha$ | [O I]/H$\alpha$ | | | | |
| (1) | (2) | (3) | (4) | (5) | (6) | (7) | (8) | (9) |
| 264 | IRAS 13232+1731 | HII | HII | HII | HII | HII | HII | HII |
| 265 | NGC 5147 | HII | HII | ... | HII | HII | HII | HII |
| 266 | NGC 5204 | HII | LINER | ... | HII | HII | HII | HII |
| 267 | UGC 8502_NED02 | HII | HII | HII | HII | HII | HII | HII |
| 268 | UGC 8561 | HII | HII | HII | HII | HII | HII | HII |
| 269 | NGC 5230 | HII | ... | ... | HII | HII | HII | HII |
| 270 | IRAS 13349+2438 | ... | ... | ... | ... | ... | ... | Sy |
| 271 | NGC 5256 | Sy | Sy | Sy | HII | Sy | ... | Sy |
| 272 | UGC 8626 | HII | HII | HII | HII | HII | HII | HII |
| 273 | NGC 5263 | TO | HII | HII | HII | HII | TO | HII |
| 274 | MCG 1-35-028 | TO | HII | HII | HII | HII | ... | HII |
| 275 | IC 910 | Sy | LINER | Sy | Sy | Sy | Sy | Sy |
| 276 | MK 268 | ... | ... | ... | Sy | Sy | Sy | Sy |
| 277 | NGC 5278 | LINER | LINER | LINER | HII | LINER | LINER | LINER |
| 278 | NGC 5273 | Sy | Sy | Sy | HII | Sy | ... | Sy |
| 279 | UGC 8685 | TO | HII | HII | HII | HII | HII | HII |
| 280 | UGC 8686 | TO | HII | HII | HII | TO | LINER | HII |
| 281 | UGC 8696 | Sy | LINER | Sy | Sy | Sy | ... | Sy |
| 282 | NGC 5297 | LINER | LINER | LINER | HII | HII | LINER | LINER |
| 283 | MK 796 | TO | HII | HII | Sy | TO | ... | Sy |
| 284 | IRAS 13446+1121 | Sy | Sy | Sy | Sy | Sy | LINER | Sy |
| 285 | NGC 5303 | HII | HII | HII | HII | TO | HII | HII |
| 286 | NGC 5313 | LINER | LINER | LINER | HII | TO | TO | LINER |
| 287 | MCG 3-35-034_NED01 | TO | HII | LINER | HII | TO | TO | TO |

**Table 7.A.2:** Continued

| SFRS | Galaxy | Nuclear Classification | | | IR | MEx | CEx | Final Classification |
|---|---|---|---|---|---|---|---|---|
| | | [N II]/H$\alpha$ | [S II]/H$\alpha$ | [O I]/H$\alpha$ | | | | |
| (1) | (2) | (3) | (4) | (5) | (6) | (7) | (8) | (9) |
| 288 | NGC 5347 | Sy | Sy | Sy | Sy | Sy | ... | Sy |
| 289 | NGC 5350 | TO | HII | HII | HII | ... | TO | HII |
| 290 | NGC 5368 | TO | HII | HII | HII | HII | TO | HII |
| 291 | UGC 8827 | TO | HII | HII | HII | TO | ... | HII |
| 292 | UGC 8850 | Sy | Sy | Sy | HII | Sy | ... | Sy |
| 293 | UGC 8856_NED01 | TO | HII | HII | HII | HII | TO | HII |
| 294 | NGC 5374 | HII | HII | ... | HII | HII | HII | HII |
| 295 | UGC 8902 | TO | HII | LINER | HII | TO | TO | TO |
| 296 | NGC 5403 | TO | HII | LINER | HII | TO | ... | TO |
| 297 | MCG 7-29-036 | TO | HII | HII | HII | HII | TO | HII |
| 298 | NGC 5414 | HII | HII | HII | HII | TO | ... | HII |
| 299 | MCG 5-33-046 | TO | HII | HII | HII | TO | TO | HII |
| 300 | NGC 5474 | HII | HII | HII | HII | ... | HII | HII |
| 301 | NGC 5480 | HII | HII | HII | HII | HII | HII | HII |
| 302 | MCG 6-31-070 | TO | HII | HII | HII | HII | TO | HII |
| 303 | CGCG 74-129 | Sy | Sy | Sy | Sy | Sy | Sy | Sy |
| 304 | NGC 5520 | TO | HII | HII | HII | HII | HII | HII |
| 305 | NGC 5515 | LINER | HII | Sy | HII | Sy | LINER | Sy |
| 306 | NGC 5526_NED02 | HII | HII | HII | HII | HII | HII | HII |
| 307 | NGC 5522 | TO | HII | HII | HII | HII | TO | HII |
| 308 | NGC 5541 | LINER | LINER | LINER | HII | ... | TO | LINER |
| 309 | IC 4395 | TO | HII | HII | HII | TO | TO | HII |
| 310 | UGC 9165 | TO | HII | HII | HII | HII | TO | HII |
| 311 | MK 1490 | TO | HII | HII | HII | HII | HII | HII |

**Table 7.A.2:** Continued

| SFRS | Galaxy | Nuclear Classification | | | IR | MEx | CEx | Final Classification |
|---|---|---|---|---|---|---|---|---|
| | | [N II]/H$\alpha$ | [S II]/H$\alpha$ | [O I]/H$\alpha$ | | | | |
| (1) | (2) | (3) | (4) | (5) | (6) | (7) | (8) | (9) |
| 312 | NGC 5585 | HII | HII | Sy | HII | HII | TO | HII |
| 313 | IC 4408 | TO | HII | HII | HII | TO | TO | HII |
| 314 | NGC 5584 | HII | HII | ... | HII | HII | HII | HII |
| 315 | NGC 5633 | HII | HII | HII | HII | HII | HII | HII |
| 316 | NGC 5660 | HII | HII | HII | HII | HII | HII | HII |
| 317 | NGC 5656 | LINER | LINER | LINER | HII | HII | LINER | LINER |
| 318 | NGC 5657 | HII | HII | HII | ... | HII | HII | HII |
| 319 | CGCG 133-083 | TO | HII | HII | HII | HII | HII | HII |
| 320 | MCG 7-30-028 | HII | HII | HII | HII | HII | ... | HII |
| 321 | MCG 6-32-070 | HII | HII | HII | HII | HII | HII | HII |
| 322 | UGC 9412 | ... | ... | ... | Sy | Sy | ... | Sy |
| 323 | NGC 5698 | HII | HII | HII | HII | HII | HII | HII |
| 324 | NGC 5691 | HII | HII | HII | HII | TO | TO | HII |
| 325 | MCG 9-24-035 | TO | HII | HII | HII | HII | TO | HII |
| 326 | MCG 9-24-038 | TO | HII | HII | HII | TO | TO | HII |
| 327 | UGC 9560 | HII | HII | HII | HII | HII | ... | HII |
| 328 | IC 1076 | HII | HII | HII | HII | HII | HII | HII |
| 329 | IRAS 14538+1730 | TO | HII | HII | HII | TO | TO | HII |
| 330 | NGC 5795 | HII | HII | HII | HII | HII | HII | HII |
| 331 | UGC 9618_NED02 | TO | HII | HII | HII | TO | LINER | TO |
| 332 | UGC 9639 | LINER | Sy | Sy | HII | Sy | Sy | Sy |
| 333 | MCG 6-33-022 | TO | HII | HII | HII | TO | HII | HII |
| 334 | NGC 5879 | LINER | LINER | LINER | HII | HII | LINER | LINER |
| 335 | MCG 9-25-036 | HII | HII | HII | HII | HII | HII | HII |

**Table 7.A.2:** Continued

| SFRS | Galaxy | Nuclear Classification | | | IR | MEx | CEx | Final Classification |
|---|---|---|---|---|---|---|---|---|
| | | [N II]/H$\alpha$ | [S II]/H$\alpha$ | [O I]/H$\alpha$ | | | | |
| (1) | (2) | (3) | (4) | (5) | (6) | (7) | (8) | (9) |
| 336 | NGC 5899 | Sy | Sy | Sy | HII | Sy | ... | Sy |
| 337 | NGC 5905 | HII | HII | HII | HII | HII | HII | HII |
| 338 | MK 848 | TO | HII | HII | HII | TO | TO | HII |
| 339 | IC 4553 | LINER | LINER | LINER | HII | Sy | LINER | LINER |
| 340 | UGC 9922_NED02 | HII | HII | HII | HII | ... | ... | HII |
| 341 | IC 4567 | TO | HII | HII | HII | TO | TO | HII |
| 342 | MCG 4-37-016 | TO | HII | HII | HII | HII | HII | HII |
| 343 | NGC 5975 | LINER | HII | LINER | HII | TO | LINER | LINER |
| 344 | NGC 5980 | TO | HII | HII | HII | TO | TO | HII |
| 345 | NGC 5992 | HII | HII | HII | HII | TO | HII | HII |
| 346 | NGC 5996 | HII | HII | HII | HII | HII | HII | HII |
| 347 | IRAS 15519+3537 | HII | HII | HII | HII | TO | TO | HII |
| 348 | UGC 10099 | TO | HII | HII | HII | TO | ... | HII |
| 349 | MCG 5-38-006 | TO | HII | HII | HII | HII | HII | HII |
| 350 | UGC 10120 | HII | HII | HII | Sy | HII | HII | Sy |
| 351 | NGC 6027A | TO | HII | HII | HII | HII | HII | HII |
| 352 | NGC 6040B | LINER | LINER | LINER | HII | Sy | LINER | LINER |
| 353 | UGC 10200 | HII | HII | HII | HII | Sy | ... | HII |
| 354 | IRAS 16052+5334 | TO | HII | HII | HII | HII | TO | HII |
| 355 | IRAS 16053+1836 | TO | HII | HII | HII | HII | HII | HII |
| 356 | NGC 6090_NED01 | TO | HII | HII | HII | HII | ... | HII |
| 357 | UGC 10273_NED01 | HII | HII | HII | HII | TO | ... | HII |
| 358 | P 16150+2233 | Sy | Sy | Sy | Sy | Sy | Sy | Sy |
| 359 | UGC 10322 | HII | HII | HII | HII | HII | HII | HII |

**Table 7.A.2:** Continued

| SFRS | Galaxy | Nuclear Classification | | | IR | MEx | CEx | Final Classification |
|---|---|---|---|---|---|---|---|---|
| | | [N II]/H$\alpha$ | [S II]/H$\alpha$ | [O I]/H$\alpha$ | | | | |
| (1) | (2) | (3) | (4) | (5) | (6) | (7) | (8) | (9) |
| 360 | NGC 6120 | TO | HII | HII | HII | HII | HII | HII |
| 361 | MCG 3-42-004 | HII | HII | LINER | HII | HII | HII | HII |
| 362 | UGC 10407 | HII | HII | HII | HII | TO | ... | HII |
| 363 | IRAS 16320+3922 | TO | LINER | LINER | HII | TO | TO | LINER |
| 364 | NGC 6186 | HII | HII | HII | HII | HII | ... | HII |
| 365 | MCG 9-27-053 | TO | HII | HII | HII | HII | TO | HII |
| 366 | UGC 10514 | HII | HII | HII | HII | HII | ... | HII |
| 367 | IRAS 16435+2154 | HII | HII | HII | HII | HII | HII | HII |
| 368 | IC 4623 | HII | HII | HII | HII | HII | HII | HII |
| 369 | IRAS 16516+3030 | LINER | LINER | LINER | HII | HII | HII | LINER |

**Table 7.A.2:** The activity classification of the SFRS sample. Column (1) SFRS ID (Ashby et al. 2011); Column (2) Galaxy name; Columns (3) - (5) present the nuclear activity classification of the three diagnostic BPT diagrams. Column (6) shows the IRAC color classification based on both the nuclear and integrated colors. Columns (7) and (8) present the MEx and CEx diagrams classification, and Column (9) presents the final adopted classification based on the combination of the three BPT diagnostics and the IRAC color–color diagram.

**Table 7.A.3:** Host galaxy and nuclear metallicities and SFRs for the SFRS SFGs.

| SFRS | Galaxy | Nuclear Metallicity | | Host Galaxy Metallicity | | log SFR |
|---|---|---|---|---|---|---|
| | | O3N2 | N2 | O3N2 | N2 | (Nuclear) |
| 2 | IC 2217 | 8.772 ± 0.009 | 8.659 ± 0.003 | 8.717 ± 0.011 | 8.941 ± 0.004 | 0.014 ± 0.003 |
| 4 | NGC 2512 | 8.847 ± 0.002 | 8.723 ± 0.001 | 8.743 ± 0.013 | 8.909 ± 0.003 | 0.035 ± 0.001 |
| 5 | MCG 6-18-009 | 8.803 ± 0.005 | 8.735 ± 0.002 | ... | ... | 0.657 ± 0.003 |
| 6 | MK 1212 | 8.740 ± 0.017 | 8.738 ± 0.005 | ... | ... | -0.322 ± 0.005 |
| 8 | NGC 2532 | 8.763 ± 0.024 | 8.663 ± 0.017 | 8.722 ± 0.025 | 8.936 ± 0.017 | -0.037 ± 0.011 |
| 9 | UGC 4261 | 8.534 ± 0.002 | 8.560 ± 0.002 | ... | ... | 0.058 ± 0.002 |
| 10 | NGC 2535 | 8.874 ± 0.024 | 8.653 ± 0.004 | 8.656 ± 0.027 | 9.004 ± 0.009 | -0.871 ± 0.002 |
| 11 | NGC 2543 | 8.770 ± 0.006 | 8.701 ± 0.003 | ... | ... | -0.865 ± 0.003 |
| 12 | NGC 2537 | 8.613 ± 0.027 | 8.609 ± 0.023 | 8.714 ± 0.028 | 8.962 ± 0.023 | -3.264 ± 0.012 |
| 13 | IC 2233 | 8.167 ± 0.003 | 8.213 ± 0.005 | ... | ... | -2.397 ± 0.003 |
| 14 | IC 2239 | 8.721 ± 0.011 | 8.818 ± 0.004 | 8.743 ± 0.014 | 8.897 ± 0.005 | -0.048 ± 0.005 |
| 15 | UGC 4286 | 8.640 ± 0.018 | 8.691 ± 0.012 | ... | ... | -1.367 ± 0.008 |
| 16 | UGC 4306 | 8.700 ± 0.012 | 8.677 ± 0.005 | ... | ... | -1.582 ± 0.004 |
| 17 | NGC 2552 | 8.246 ± 0.002 | 8.293 ± 0.003 | ... | ... | -2.387 ± 0.002 |
| 18 | UGC 4383 | 8.560 ± 0.001 | 8.635 ± 0.001 | ... | 9.640 ± 0.060 | 0.068 ± 0.001 |
| 19 | IRAS 08234+1054 | 8.756 ± 0.012 | 8.768 ± 0.003 | ... | ... | 0.406 ± 0.004 |
| 20 | IRAS 08269+1514 | 8.721 ± 0.008 | 8.727 ± 0.003 | ... | ... | -0.299 ± 0.003 |
| 21 | NGC 2604 | 8.576 ± 0.003 | 8.527 ± 0.002 | ... | ... | -1.001 ± 0.002 |
| 22 | NGC 2608 | 8.774 ± 0.006 | 8.721 ± 0.002 | 8.793 ± 0.008 | 9.050 ± 0.004 | -0.607 ± 0.001 |
| 23 | MK 92 | 8.654 ± 0.003 | 8.656 ± 0.002 | 8.731 ± 0.004 | 8.931 ± 0.003 | 0.109 ± 0.002 |
| 25 | CGCG 120-018 | 8.753 ± 0.006 | 8.807 ± 0.002 | ... | ... | 0.610 ± 0.003 |

**Table 7.A.3:** Continued

| SFRS | Galaxy | Nuclear Metallicity | | Host Galaxy Metallicity | | log SFR |
|---|---|---|---|---|---|---|
| | | O3N2 | N2 | O3N2 | N2 | (Nuclear) |
| 26 | NGC 2644 | 8.678 ± 0.009 | 8.621 ± 0.006 | 8.756 ± 0.010 | 8.994 ± 0.007 | -1.793 ± 0.003 |
| 28 | UGC 4653 | 8.681 ± 0.005 | 8.767 ± 0.002 | 8.966 ± 0.022 | 9.305 ± 0.038 | 0.710 ± 0.001 |
| 29 | IRAS 08512+2727 | 8.749 ± 0.012 | 8.643 ± 0.004 | ... | ... | 0.451 ± 0.003 |
| 31 | IRAS 08538+4256 | 8.741 ± 0.007 | 8.725 ± 0.003 | ... | ... | 0.267 ± 0.003 |
| 33 | NGC 2718 | 8.849 ± 0.006 | 8.714 ± 0.002 | ... | ... | -0.120 ± 0.003 |
| 34 | NGC 2712 | 8.720 ± 0.008 | 8.75 ± 0.005 | 8.801 ± 0.011 | 8.967 ± 0.006 | -1.173 ± 0.005 |
| 35 | NGC 2719 | 8.285 ± 0.006 | 8.327 ± 0.009 | 8.744 ± 0.007 | 8.917 ± 0.011 | -0.863 ± 0.003 |
| 37 | IRAS 08579+3447 | 8.839 ± 0.045 | 8.686 ± 0.013 | 8.672 ± 0.052 | 8.882 ± 0.016 | -0.171 ± 0.009 |
| 38 | NGC 2731 | 8.716 ± 0.002 | 8.638 ± 0.001 | 8.975 ± 0.008 | 9.359 ± 0.011 | -0.619 ± 0.001 |
| 39 | NGC 2730 | 8.739 ± 0.011 | 8.665 ± 0.004 | ... | ... | -1.584 ± 0.004 |
| 40 | IC 2431 | 8.664 ± 0.002 | 8.649 ± 0.002 | ... | ... | 0.516 ± 0.002 |
| 41 | NGC 2750 | 8.826 ± 0.008 | 8.677 ± 0.003 | 8.745 ± 0.012 | 9.040 ± 0.005 | -0.484 ± 0.002 |
| 43 | NGC 2761 | 8.756 ± 0.010 | 8.735 ± 0.003 | ... | ... | 0.730 ± 0.003 |
| 44 | NGC 2773 | 8.822 ± 0.009 | 8.658 ± 0.003 | ... | ... | -0.068 ± 0.003 |
| 45 | NGC 2776 | 8.693 ± 0.011 | 8.706 ± 0.008 | ... | ... | -1.750 ± 0.007 |
| 46 | NGC 2789 | 8.740 ± 0.013 | 8.791 ± 0.004 | ... | ... | 0.336 ± 0.004 |
| 48 | IRAS 09121+3908 | 8.739 ± 0.013 | 8.758 ± 0.004 | ... | ... | -1.042 ± 0.005 |
| 49 | IRAS 09184+4356 | 8.801 ± 0.019 | 8.727 ± 0.004 | 8.810 ± 0.023 | 9.085 ± 0.006 | 0.407 ± 0.003 |
| 50 | CGCG 238-041 | 8.495 ± 0.002 | 8.527 ± 0.002 | ... | ... | 0.302 ± 0.002 |
| 53 | UGC 5046 | 8.779 ± 0.004 | 8.630 ± 0.003 | ... | ... | -0.295 ± 0.003 |
| 54 | UGC 5055 | 8.813 ± 0.007 | 8.718 ± 0.002 | ... | ... | 0.170 ± 0.002 |
| 55 | NGC 2893 | 8.850 ± 0.001 | 8.749 ± 0.001 | 8.716 ± 0.008 | 8.948 ± 0.013 | -0.696 ± 0.001 |

**Table 7.A.3:** Continued

| SFRS | Galaxy | Nuclear Metallicity | | Host Galaxy Metallicity | | log SFR |
|---|---|---|---|---|---|---|
| | | O3N2 | N2 | O3N2 | N2 | (Nuclear) |
| 56 | MCG 3-24-062 | 8.675 ± 0.023 | 8.680 ± 0.008 | 8.803 ± 0.025 | 9.005 ± 0.01 | -0.924 ± 0.006 |
| 58 | UGC 5097 | 8.526 ± 0.002 | 8.506 ± 0.002 | ... | ... | -0.164 ± 0.003 |
| 59 | CGCG 289-012 | 8.806 ± 0.018 | 8.659 ± 0.004 | 8.690 ± 0.019 | 8.918 ± 0.005 | 0.014 ± 0.003 |
| 60 | MCG 8-18-013 | 8.693 ± 0.007 | 8.743 ± 0.003 | 8.754 ± 0.007 | 8.978 ± 0.004 | 0.353 ± 0.003 |
| 63 | NGC 2955 | 8.711 ± 0.029 | 8.695 ± 0.011 | 8.823 ± 0.033 | 8.995 ± 0.013 | -0.178 ± 0.008 |
| 64 | CGCG 182-010 | 8.799 ± 0.007 | 8.711 ± 0.003 | ... | ... | 0.699 ± 0.003 |
| 65 | UGC 5228 | 8.667 ± 0.008 | 8.625 ± 0.004 | 8.726 ± 0.009 | 8.99 ± 0.005 | -1.148 ± 0.003 |
| 66 | IRAS 09438+1141 | 8.774 ± 0.014 | 8.650 ± 0.004 | ... | ... | 0.235 ± 0.003 |
| 68 | MCG 2-25-039 | 8.744 ± 0.008 | 8.660 ± 0.004 | ... | ... | -0.393 ± 0.004 |
| 69 | NGC 3020 | 8.525 ± 0.008 | 8.548 ± 0.008 | ... | ... | -2.700 ± 0.005 |
| 70 | NGC 3049 | 8.751 ± 0.002 | 8.660 ± 0.002 | ... | ... | -0.875 ± 0.003 |
| 71 | NGC 3055 | 8.679 ± 0.002 | 8.724 ± 0.002 | ... | ... | -0.693 ± 0.002 |
| 72 | IC 2520 | 8.605 ± 0.006 | 8.655 ± 0.005 | ... | ... | -1.530 ± 0.004 |
| 73 | UGC 5403 | 8.814 ± 0.005 | 8.724 ± 0.003 | ... | ... | -0.249 ± 0.003 |
| 74 | UGC 5459 | 8.631 ± 0.029 | 8.604 ± 0.014 | 8.621 ± 0.029 | 8.866 ± 0.014 | -2.317 ± 0.008 |
| 75 | MCG 5-24-022 | 8.741 ± 0.011 | 8.688 ± 0.005 | ... | ... | -0.308 ± 0.004 |
| 76 | IC 2551 | 8.691 ± 0.002 | 8.712 ± 0.002 | ... | ... | 0.882 ± 0.002 |
| 77 | IRAS 10106+2745 | 8.709 ± 0.010 | 8.654 ± 0.005 | ... | ... | -0.045 ± 0.004 |
| 78 | NGC 3162 | 8.807 ± 0.026 | 8.636 ± 0.015 | 8.698 ± 0.028 | 9.035 ± 0.017 | -1.531 ± 0.004 |
| 81 | IC 602 | 8.711 ± 0.010 | 8.655 ± 0.005 | ... | ... | -1.193 ± 0.004 |
| 82 | NGC 3191 | 8.756 ± 0.064 | 8.642 ± 0.019 | 8.713 ± 0.065 | 8.962 ± 0.019 | -0.462 ± 0.011 |
| 83 | NGC 3206 | 8.417 ± 0.004 | 8.449 ± 0.005 | ... | ... | -1.915 ± 0.003 |

**Table 7.A.3:** Continued

| SFRS | Galaxy | Nuclear Metallicity | | Host Galaxy Metallicity | | log SFR |
|---|---|---|---|---|---|---|
| | | O3N2 | N2 | O3N2 | N2 | (Nuclear) |
| 84 | UGC 5613 | 8.640 ± 0.004 | 8.773 ± 0.003 | ... | ... | 0.429 ± 0.003 |
| 86 | NGC 3245 | 8.722 ± 0.016 | 8.841 ± 0.009 | 8.737 ± 0.023 | 8.953 ± 0.015 | -1.038 ± 0.010 |
| 87 | IRAS 10246+2042 | 8.820 ± 0.009 | 8.760 ± 0.003 | ... | ... | 0.004 ± 0.003 |
| 88 | MCG 7-22-012 | 8.690 ± 0.019 | 8.646 ± 0.007 | 8.723 ± 0.021 | 8.975 ± 0.008 | -0.900 ± 0.005 |
| 89 | IRAS 10276+1119 | 8.782 ± 0.007 | 8.738 ± 0.003 | ... | ... | 0.681 ± 0.003 |
| 90 | NGC 3265 | 8.739 ± 0.003 | 8.674 ± 0.002 | ... | ... | -0.886 ± 0.003 |
| 92 | NGC 3274 | 8.277 ± 0.008 | 8.335 ± 0.014 | 8.799 ± 0.01 | 8.944 ± 0.017 | -2.564 ± 0.003 |
| 93 | UGC 5720 | 8.886 ± 0.004 | 9.309 ± 0.006 | ... | ... | -5.464 ± 0.009 |
| 94 | KUG 1031+351 | 8.772 ± 0.005 | 8.681 ± 0.003 | ... | ... | 1.060 ± 0.003 |
| 95 | NGC 3306 | 8.801 ± 0.027 | 8.678 ± 0.005 | 8.777 ± 0.027 | 9.088 ± 0.006 | -0.808 ± 0.004 |
| 96 | NGC 3323 | 8.698 ± 0.006 | 8.617 ± 0.004 | ... | ... | -0.902 ± 0.004 |
| 97 | IC 2598 | 8.751 ± 0.004 | 8.656 ± 0.003 | ... | ... | -0.240 ± 0.003 |
| 99 | NGC 3353 | 8.304 ± 0.002 | 8.385 ± 0.003 | ... | ... | -1.633 ± 0.003 |
| 100 | UGC 5881 | 8.582 ± 0.003 | 8.782 ± 0.002 | ... | ... | 0.229 ± 0.003 |
| 101 | NGC 3370 | 8.788 ± 0.013 | 8.654 ± 0.002 | 8.622 ± 0.016 | 8.916 ± 0.006 | -1.726 ± 0.001 |
| 102 | NGC 3381 | 8.785 ± 0.003 | 8.601 ± 0.002 | ... | ... | -1.102 ± 0.003 |
| 103 | UGC 5941_NED02 | 8.840 ± 0.009 | 8.728 ± 0.003 | ... | ... | 0.530 ± 0.003 |
| 104 | NGC 3413 | 8.304 ± 0.005 | 8.342 ± 0.008 | ... | ... | -2.151 ± 0.003 |
| 105 | NGC 3408 | 8.772 ± 0.022 | 8.646 ± 0.005 | ... | ... | -0.215 ± 0.004 |
| 106 | NGC 3430 | 8.790 ± 0.028 | 8.660 ± 0.006 | 8.661 ± 0.033 | 8.992 ± 0.010 | -0.982 ± 0.004 |
| 109 | UGC 6074 | 8.847 ± 0.005 | 8.767 ± 0.002 | ... | ... | -0.030 ± 0.003 |
| 110 | NGC 3495 | 8.705 ± 0.054 | 8.690 ± 0.043 | 8.684 ± 0.054 | 8.905 ± 0.043 | -3.027 ± 0.017 |

**Table 7.A.3:** Continued

| SFRS | Galaxy | Nuclear Metallicity | | Host Galaxy Metallicity | | log SFR |
|---|---|---|---|---|---|---|
| | | O3N2 | N2 | O3N2 | N2 | (Nuclear) |
| 111 | UGC 6103 | 8.693 ± 0.004 | 8.763 ± 0.003 | ... | ... | 0.096 ± 0.003 |
| 112 | MCG 7-23-019 | 8.645 ± 0.019 | 8.700 ± 0.007 | 8.774 ± 0.020 | 8.89 ± 0.008 | 0.441 ± 0.005 |
| 114 | CGCG 241-078 | 8.739 ± 0.012 | 8.795 ± 0.003 | ... | ... | 0.506 ± 0.004 |
| 115 | IRAS 11069+2711 | 8.517 ± 0.005 | 8.527 ± 0.005 | ... | ... | -0.179 ± 0.004 |
| 116 | IC 676 | 8.798 ± 0.007 | 8.703 ± 0.003 | ... | ... | -0.952 ± 0.003 |
| 122 | NGC 3633 | 8.819 ± 0.012 | 8.726 ± 0.003 | ... | ... | -0.750 ± 0.003 |
| 123 | NGC 3652 | 8.689 ± 0.005 | 8.608 ± 0.004 | ... | ... | -2.324 ± 0.003 |
| 125 | NGC 3659 | 8.669 ± 0.011 | 8.600 ± 0.008 | 8.699 ± 0.012 | 8.894 ± 0.009 | -2.010 ± 0.006 |
| 126 | NGC 3664 | 8.471 ± 0.006 | 8.523 ± 0.008 | 8.747 ± 0.006 | 8.922 ± 0.009 | -2.505 ± 0.005 |
| 127 | NGC 3666 | 8.703 ± 0.018 | 8.687 ± 0.008 | ... | ... | -2.316 ± 0.006 |
| 128 | IC 691 | 8.343 ± 0.002 | 8.438 ± 0.002 | ... | ... | -0.826 ± 0.002 |
| 129 | NGC 3686 | 8.810 ± 0.012 | 8.616 ± 0.003 | 8.750 ± 0.016 | 9.025 ± 0.006 | -1.102 ± 0.003 |
| 130 | UGC 6469 | 8.658 ± 0.006 | 8.633 ± 0.005 | 8.735 ± 0.007 | 9.003 ± 0.007 | -0.418 ± 0.006 |
| 132 | IC 698 | 8.729 ± 0.016 | 8.698 ± 0.005 | ... | ... | 0.028 ± 0.005 |
| 133 | IRAS 11267+1558 | 8.703 ± 0.021 | 8.740 ± 0.010 | 8.758 ± 0.028 | 8.899 ± 0.013 | 1.779 ± 0.008 |
| 135 | MCG 3-29-061 | 8.782 ± 0.007 | 8.750 ± 0.003 | ... | ... | -0.069 ± 0.003 |
| 136 | NGC 3720 | 8.795 ± 0.015 | 8.612 ± 0.004 | ... | ... | -0.715 ± 0.004 |
| 137 | NGC 3729 | 8.633 ± 0.004 | 8.756 ± 0.003 | 8.785 ± 0.009 | 8.993 ± 0.008 | -1.323 ± 0.003 |
| 138 | MCG 10-17-019 | 8.748 ± 0.017 | 8.652 ± 0.005 | ... | ... | 0.083 ± 0.004 |
| 140 | UGC 6583 | 8.694 ± 0.002 | 8.650 ± 0.001 | 8.688 ± 0.004 | 8.897 ± 0.003 | 0.265 ± 0.001 |
| 141 | MCG 1-30-003 | 8.749 ± 0.004 | 8.694 ± 0.002 | ... | ... | 0.406 ± 0.002 |
| 142 | NGC 3769 | 8.663 ± 0.012 | 8.669 ± 0.007 | ... | ... | -2.454 ± 0.006 |

**Table 7.A.3:** Continued

| SFRS | Galaxy | Nuclear Metallicity | | Host Galaxy Metallicity | | log SFR |
|---|---|---|---|---|---|---|
| | | O3N2 | N2 | O3N2 | N2 | (Nuclear) |
| 143 | NGC 3773 | 8.416 ± 0.003 | 8.462 ± 0.004 | 8.875 ± 0.004 | 9.064 ± 0.005 | -1.499 ± 0.002 |
| 146 | NGC 3808_NED02 | 8.761 ± 0.007 | 8.690 ± 0.003 | ... | ... | -0.312 ± 0.003 |
| 147 | NGC 3811 | 8.743 ± 0.020 | 8.674 ± 0.007 | 8.727 ± 0.025 | 8.926 ± 0.010 | -0.695 ± 0.006 |
| 149 | UGC 6665 | 8.352 ± 0.002 | 8.447 ± 0.003 | ... | ... | 0.250 ± 0.004 |
| 150 | MCG 3-30-051 | 8.725 ± 0.014 | 8.589 ± 0.005 | ... | ... | -0.348 ± 0.004 |
| 151 | NGC 3839 | 8.740 ± 0.007 | 8.641 ± 0.003 | ... | ... | 0.002 ± 0.003 |
| 153 | IC 730 | 8.782 ± 0.012 | 8.704 ± 0.004 | ... | ... | 0.380 ± 0.004 |
| 154 | IC 732_NED01 | 8.675 ± 0.020 | 8.703 ± 0.006 | 8.723 ± 0.026 | 8.936 ± 0.008 | 0.085 ± 0.005 |
| 155 | NGC 3912 | 8.667 ± 0.005 | 8.632 ± 0.003 | ... | ... | -1.513 ± 0.003 |
| 156 | NGC 3928 | 8.699 ± 0.003 | 8.720 ± 0.003 | ... | ... | -1.646 ± 0.003 |
| 158 | UGC 6865 | 8.742 ± 0.027 | 8.651 ± 0.008 | ... | ... | -0.372 ± 0.006 |
| 159 | UGC 6901 | 8.749 ± 0.018 | 8.655 ± 0.005 | ... | ... | 0.247 ± 0.004 |
| 160 | CGCG 013-010 | 8.680 ± 0.009 | 8.801 ± 0.003 | ... | ... | 0.548 ± 0.004 |
| 161 | NGC 3991 | 8.259 ± 0.001 | 8.322 ± 0.002 | 8.954 ± 0.002 | 9.127 ± 0.003 | -0.988 ± 0.001 |
| 162 | NGC 4004 | 8.695 ± 0.005 | 8.636 ± 0.003 | ... | ... | -0.613 ± 0.003 |
| 163 | NGC 4014 | 8.671 ± 0.032 | 8.761 ± 0.017 | 8.793 ± 0.038 | 8.901 ± 0.019 | -0.980 ± 0.015 |
| 164 | NGC 4010 | 8.675 ± 0.013 | 8.605 ± 0.007 | ... | ... | -2.658 ± 0.005 |
| 165 | NGC 4018 | 8.643 ± 0.012 | 8.667 ± 0.006 | ... | ... | -0.927 ± 0.005 |
| 167 | IRAS 11571+3003 | 8.813 ± 0.019 | 8.727 ± 0.004 | ... | ... | 0.513 ± 0.003 |
| 168 | UGC 7017 | 8.759 ± 0.007 | 8.665 ± 0.003 | ... | ... | -0.433 ± 0.003 |
| 170 | MCG 3-31-030 | 8.745 ± 0.017 | 8.606 ± 0.013 | 8.776 ± 0.019 | 9.015 ± 0.016 | -2.428 ± 0.003 |
| 171 | NGC 4062 | 8.701 ± 0.048 | 8.698 ± 0.011 | ... | ... | -2.499 ± 0.009 |

**Table 7.A.3:** Continued

| SFRS | Galaxy | Nuclear Metallicity | | Host Galaxy Metallicity | | log SFR |
|---|---|---|---|---|---|---|
| | | O3N2 | N2 | O3N2 | N2 | (Nuclear) |
| 172 | NGC 4064 | 8.806 ± 0.019 | 8.562 ± 0.004 | 8.859 ± 0.025 | 9.310 ± 0.025 | -2.202 ± 0.003 |
| 173 | CGCG 098-059 | 8.841 ± 0.009 | 8.685 ± 0.003 | ... | ... | 0.609 ± 0.003 |
| 174 | NGC 4116 | 8.624 ± 0.003 | 8.545 ± 0.003 | 8.739 ± 0.004 | 9.031 ± 0.004 | -2.099 ± 0.002 |
| 175 | NGC 4136 | 8.680 ± 0.026 | 8.641 ± 0.024 | 8.714 ± 0.037 | 8.935 ± 0.039 | -2.736 ± 0.017 |
| 177 | IRAS 12086+1441 | 8.661 ± 0.004 | 8.650 ± 0.003 | ... | ... | -1.837 ± 0.003 |
| 178 | NGC 4162 | 8.673 ± 0.022 | 8.748 ± 0.013 | 8.743 ± 0.025 | 8.885 ± 0.015 | -1.646 ± 0.011 |
| 179 | NGC 4178 | 8.657 ± 0.058 | 8.612 ± 0.015 | 8.763 ± 0.060 | 8.968 ± 0.016 | -2.619 ± 0.010 |
| 181 | NGC 4189 | 8.829 ± 0.009 | 8.644 ± 0.003 | ... | ... | -1.572 ± 0.003 |
| 182 | NGC 4194 | 8.877 ± 0.002 | 9.136 ± 0.002 | ... | ... | -2.529 ± 0.003 |
| 183 | NGC 4204 | 8.568 ± 0.016 | 8.553 ± 0.017 | ... | ... | -3.901 ± 0.008 |
| 184 | NGC 4207 | 8.696 ± 0.010 | 8.638 ± 0.005 | ... | ... | -1.883 ± 0.005 |
| 185 | UGC 7286 | 8.701 ± 0.043 | 8.728 ± 0.019 | 8.732 ± 0.059 | 8.939 ± 0.030 | -0.192 ± 0.027 |
| 186 | NGC 4234 | 8.613 ± 0.003 | 8.564 ± 0.003 | 8.855 ± 0.004 | 9.089 ± 0.004 | -1.540 ± 0.003 |
| 187 | NGC 4237 | 8.675 ± 0.024 | 8.732 ± 0.013 | ... | ... | -2.677 ± 0.010 |
| 188 | NGC 4244 | 8.563 ± 0.026 | 8.504 ± 0.024 | ... | ... | -3.798 ± 0.010 |
| 190 | MCG 3-32-005 | 8.788 ± 0.008 | 8.646 ± 0.003 | ... | ... | -1.721 ± 0.003 |
| 191 | NGC 4290 | 8.847 ± 0.009 | 8.704 ± 0.003 | ... | ... | -0.384 ± 0.003 |
| 192 | NGC 4294 | 8.388 ± 0.007 | 8.470 ± 0.009 | 8.796 ± 0.008 | 8.928 ± 0.010 | -0.435 ± 0.005 |
| 194 | NGC 4385 | 8.787 ± 0.003 | 8.882 ± 0.004 | 8.897 ± 0.013 | 9.227 ± 0.022 | -3.825* ± 0.006 |
| 196 | NGC 4396 | 8.621 ± 0.006 | 8.541 ± 0.005 | ... | ... | -2.639 ± 0.004 |
| 199 | NGC 4420 | 8.702 ± 0.010 | 8.655 ± 0.006 | ... | ... | -2.749 ± 0.005 |
| 200 | NGC 4424 | 8.797 ± 0.068 | 8.624 ± 0.019 | 8.804 ± 0.068 | 9.180 ± 0.021 | -2.931 ± 0.011 |

**Table 7.A.3:** Continued

| SFRS | Galaxy | Nuclear Metallicity | | Host Galaxy Metallicity | | log SFR |
|---|---|---|---|---|---|---|
| | | O3N2 | N2 | O3N2 | N2 | (Nuclear) |
| 203 | NGC 4448 | 8.723 ± 0.166 | 8.691 ± 0.010 | 8.720 ± 0.169 | 9.035 ± 0.019 | 0.048* ± 0.008 |
| 205 | NGC 4470 | 8.676 ± 0.006 | 8.602 ± 0.005 | ... | ... | -2.577 ± 0.004 |
| 206 | IRAS 12274+0018 | 8.720 ± 0.006 | 8.634 ± 0.003 | ... | ... | -0.816 ± 0.003 |
| 207 | NGC 4491 | 8.602 ± 0.027 | 8.491 ± 0.041 | 9.002 ± 0.041 | 9.202 ± 0.045 | -2.332 ± 0.013 |
| 208 | NGC 4500 | 8.550 ± 0.003 | 8.738 ± 0.003 | 8.866 ± 0.006 | 8.954 ± 0.010 | -0.339 ± 0.002 |
| 209 | NGC 4495 | 8.738 ± 0.011 | 8.757 ± 0.004 | ... | ... | -0.125 ± 0.004 |
| 210 | IC 3476 | 8.642 ± 0.010 | 8.572 ± 0.008 | 8.768 ± 0.012 | 8.980 ± 0.009 | -2.975 ± 0.006 |
| 211 | NGC 4509 | 8.241 ± 0.052 | 8.233 ± 0.091 | 8.817 ± 0.053 | 8.995 ± 0.091 | -2.906 ± 0.011 |
| 212 | NGC 4519 | 8.748 ± 0.004 | 8.623 ± 0.003 | ... | ... | -2.045 ± 0.003 |
| 214 | IRAS 12337+5044 | 8.620 ± 0.004 | 8.633 ± 0.003 | ... | ... | 0.426 ± 0.003 |
| 215 | IC 3581 | 8.730 ± 0.009 | 8.743 ± 0.004 | ... | ... | -0.181 ± 0.004 |
| 216 | NGC 4592 | 8.504 ± 0.010 | 8.493 ± 0.010 | ... | ... | -3.257 ± 0.005 |
| 218 | NGC 4625 | 8.685 ± 0.038 | 8.691 ± 0.017 | 8.753 ± 0.040 | 8.877 ± 0.018 | -3.103 ± 0.012 |
| 219 | NGC 4630 | 8.783 ± 0.005 | 8.565 ± 0.003 | ... | ... | -1.743 ± 0.003 |
| 220 | IC 3690 | 8.748 ± 0.016 | 8.841 ± 0.004 | ... | ... | -1.845 ± 0.005 |
| 221 | UGC 7905_NED01 | 8.296 ± 0.009 | 8.349 ± 0.014 | 8.872 ± 0.012 | 9.043 ± 0.018 | -0.785 ± 0.004 |
| 222 | MCG 5-30-069 | 8.782 ± 0.007 | 8.713 ± 0.002 | ... | ... | 0.406 ± 0.002 |
| 223 | IC 3721 | 8.674 ± 0.021 | 8.699 ± 0.013 | 8.755 ± 0.025 | 8.952 ± 0.017 | -0.559 ± 0.009 |
| 224 | NGC 4670 | 8.183 ± 0.003 | 8.221 ± 0.004 | ... | ... | -1.676 ± 0.002 |
| 225 | NGC 4675 | 8.766 ± 0.010 | 8.772 ± 0.003 | ... | ... | 0.128 ± 0.004 |
| 226 | MCG 7-26-051 | 8.640 ± 0.011 | 8.750 ± 0.004 | 8.846 ± 0.014 | 9.053 ± 0.006 | 0.251 ± 0.003 |
| 227 | NGC 4689 | 8.684 ± 0.036 | 8.769 ± 0.016 | 8.801 ± 0.131 | 8.826 ± 0.042 | -2.909 ± 0.014 |

**Table 7.A.3:** Continued

| SFRS | Galaxy | Nuclear Metallicity | | Host Galaxy Metallicity | | log SFR |
|---|---|---|---|---|---|---|
| | | O3N2 | N2 | O3N2 | N2 | (Nuclear) |
| 228 | NGC 4688 | 8.503 ± 0.051 | 8.568 ± 0.045 | 8.678 ± 0.052 | 8.844 ± 0.046 | -3.035 ± 0.022 |
| 230 | NGC 4701 | 8.822 ± 0.010 | 8.621 ± 0.004 | ... | ... | -2.219 ± 0.003 |
| 232 | IRAS 12470+1404 | 8.764 ± 0.004 | 8.738 ± 0.003 | ... | ... | -2.455 ± 0.003 |
| 234 | NGC 4747 | 8.581 ± 0.066 | 8.585 ± 0.028 | 8.766 ± 0.067 | 9.019 ± 0.029 | -2.956 ± 0.005 |
| 236 | NGC 4765 | 8.267 ± 0.002 | 8.307 ± 0.003 | ... | ... | -1.435 ± 0.003 |
| 237 | VCC 2096 | 8.675 ± 0.005 | 8.701 ± 0.003 | ... | ... | -2.105 ± 0.003 |
| 238 | UGC 8041 | 8.633 ± 0.009 | 8.627 ± 0.006 | ... | ... | -2.401 ± 0.005 |
| 240 | NGC 4837_NED01 | 8.750 ± 0.013 | 8.755 ± 0.008 | 8.854 ± 0.014 | 9.143 ± 0.010 | -0.463 ± 0.005 |
| 241 | UM 530 | 8.390 ± 0.002 | 8.488 ± 0.003 | ... | ... | 0.753 ± 0.003 |
| 242 | NGC 4861 | ... | 8.028 ± 0.002 | ... | 9.664 ± 0.003 | -1.196 ± 0.001 |
| 243 | NGC 4868 | 8.859 ± 0.014 | 8.663 ± 0.003 | 8.664 ± 0.023 | 8.952 ± 0.006 | -0.549 ± 0.002 |
| 245 | UGC 8179 | 8.706 ± 0.015 | 8.705 ± 0.007 | ... | ... | 0.262 ± 0.005 |
| 246 | NGC 5001 | 8.667 ± 0.022 | 8.767 ± 0.008 | 8.831 ± 0.025 | 8.981 ± 0.010 | 0.168 ± 0.007 |
| 247 | IC 856 | 8.583 ± 0.003 | 8.576 ± 0.003 | ... | ... | -0.579 ± 0.003 |
| 249 | NGC 5014 | 8.650 ± 0.006 | 8.630 ± 0.005 | 8.815 ± 0.009 | 9.102 ± 0.011 | -1.432 ± 0.003 |
| 251 | IRAS 13116+4508 | 8.747 ± 0.019 | 8.673 ± 0.005 | ... | ... | 0.443 ± 0.004 |
| 254 | NGC 5060 | 8.856 ± 0.037 | 8.732 ± 0.008 | 8.766 ± 0.041 | 8.976 ± 0.01 | -0.682* ± 0.007 |
| 256 | UGC 8361 | 8.720 ± 0.012 | 8.750 ± 0.005 | 8.770 ± 0.016 | 8.972 ± 0.007 | 0.106 ± 0.005 |
| 260 | NGC 5107 | 8.343 ± 0.026 | 8.388 ± 0.043 | 8.774 ± 0.027 | 8.929 ± 0.044 | -3.516* ± 0.011 |
| 262 | NGC 5123 | 8.640 ± 0.030 | 8.797 ± 0.015 | 8.868 ± 0.045 | 8.763 ± 0.019 | -0.826 ± 0.014 |
| 264 | IRAS 13232+1731 | 8.817 ± 0.011 | 8.658 ± 0.003 | ... | ... | 0.748 ± 0.003 |
| 265 | NGC 5147 | 8.649 ± 0.043 | 8.625 ± 0.027 | 8.725 ± 0.044 | 8.958 ± 0.028 | -3.239 ± 0.017 |

**Table 7.A.3:** Continued

| SFRS | Galaxy | Nuclear Metallicity | | Host Galaxy Metallicity | | log SFR |
|---|---|---|---|---|---|---|
| | | O3N2 | N2 | O3N2 | N2 | (Nuclear) |
| 266 | NGC 5204 | 8.532 ± 0.026 | 8.552 ± 0.030 | 8.696 ± 0.028 | 8.856 ± 0.035 | -4.767 ± 0.018 |
| 267 | UGC 8502_NED02 | 8.506 ± 0.004 | 8.567 ± 0.005 | 9.046 ± 0.005 | 9.215 ± 0.007 | -0.212 ± 0.007 |
| 268 | UGC 8561 | 8.787 ± 0.027 | 8.702 ± 0.011 | 8.721 ± 0.030 | 8.917 ± 0.013 | -0.016 ± 0.004 |
| 269 | NGC 5230 | 8.814 ± 0.071 | 8.700 ± 0.017 | 8.756 ± 0.109 | 8.907 ± 0.022 | 1.414* ± 0.013 |
| 272 | UGC 8626 | 8.761 ± 0.006 | 8.716 ± 0.002 | ... | ... | 0.325 ± 0.002 |
| 273 | NGC 5263 | 8.727 ± 0.025 | 8.716 ± 0.004 | 8.706 ± 0.028 | 8.92 ± 0.006 | 0.229 ± 0.003 |
| 274 | MCG 1-35-028 | 8.765 ± 0.004 | 8.791 ± 0.002 | ... | ... | 0.461 ± 0.002 |
| 279 | UGC 8685 | 8.797 ± 0.010 | 8.743 ± 0.003 | ... | ... | 0.666 ± 0.003 |
| 280 | UGC 8686 | 8.664 ± 0.030 | 8.747 ± 0.012 | 8.692 ± 0.032 | 8.828 ± 0.014 | -0.371 ± 0.009 |
| 285 | NGC 5303 | 8.606 ± 0.011 | 8.620 ± 0.011 | 8.741 ± 0.011 | 8.946 ± 0.011 | -2.120 ± 0.007 |
| 289 | NGC 5350 | 8.755 ± 0.004 | 8.844 ± 0.002 | ... | ... | -1.186 ± 0.003 |
| 290 | NGC 5368 | 8.766 ± 0.011 | 8.811 ± 0.005 | ... | ... | -0.321 ± 0.005 |
| 291 | UGC 8827 | 8.647 ± 0.003 | 8.767 ± 0.003 | ... | ... | 0.365 ± 0.003 |
| 293 | UGC 8856_NED01 | 8.725 ± 0.006 | 8.728 ± 0.003 | ... | ... | 0.375 ± 0.003 |
| 294 | NGC 5374 | 8.762 ± 0.035 | 8.548 ± 0.041 | 8.782 ± 0.042 | 9.015 ± 0.045 | 0.041 ± 0.002 |
| 297 | MCG 7-29-036 | 8.736 ± 0.021 | 8.719 ± 0.005 | 8.688 ± 0.185 | 8.791 ± 0.046 | 0.143 ± 0.004 |
| 298 | NGC 5414 | 8.559 ± 0.003 | 8.567 ± 0.003 | ... | ... | -0.347 ± 0.003 |
| 299 | MCG 5-33-046 | 8.736 ± 0.009 | 8.799 ± 0.003 | ... | ... | 0.709 ± 0.003 |
| 300 | NGC 5474 | 8.401 ± 0.013 | 8.446 ± 0.020 | 8.804 ± 0.014 | 9.020 ± 0.021 | -3.636 ± 0.007 |
| 301 | NGC 5480 | 8.819 ± 0.014 | 8.678 ± 0.008 | 8.718 ± 0.018 | 8.883 ± 0.010 | -0.829 ± 0.003 |
| 302 | MCG 6-31-070 | 8.785 ± 0.044 | 8.787 ± 0.012 | 8.716 ± 0.050 | 8.882 ± 0.015 | 1.002 ± 0.004 |
| 304 | NGC 5520 | 8.810 ± 0.028 | 8.745 ± 0.028 | 8.737 ± 0.035 | 8.876 ± 0.029 | -1.254 ± 0.003 |

**Table 7.A.3:** Continued

| SFRS | Galaxy | Nuclear Metallicity | | Host Galaxy Metallicity | | log SFR |
|---|---|---|---|---|---|---|
| | | O3N2 | N2 | O3N2 | N2 | (Nuclear) |
| 306 | NGC 5526_NED02 | 8.661 ± 0.008 | 8.603 ± 0.005 | 8.818 ± 0.009 | 9.093 ± 0.006 | -1.423 ± 0.005 |
| 307 | NGC 5522 | 8.744 ± 0.036 | 8.790 ± 0.019 | 8.737 ± 0.047 | 8.888 ± 0.023 | -0.269 ± 0.004 |
| 309 | IC 4395 | 8.727 ± 0.009 | 8.797 ± 0.005 | ... | ... | 0.817 ± 0.006 |
| 310 | UGC 9165 | 8.695 ± 0.063 | 8.706 ± 0.015 | 8.869 ± 0.069 | 9.011 ± 0.017 | -0.333 ± 0.011 |
| 311 | MK 1490 | 8.846 ± 0.006 | 8.815 ± 0.002 | ... | ... | 0.987 ± 0.002 |
| 312 | NGC 5585 | 8.415 ± 0.009 | 8.465 ± 0.012 | ... | ... | -4.063 ± 0.005 |
| 313 | IC 4408 | 8.694 ± 0.008 | 8.718 ± 0.004 | ... | ... | 0.297 ± 0.004 |
| 314 | NGC 5584 | 8.737 ± 0.011 | 8.624 ± 0.005 | ... | ... | -2.363 ± 0.004 |
| 315 | NGC 5633 | 8.755 ± 0.011 | 8.662 ± 0.005 | ... | ... | -1.434 ± 0.004 |
| 316 | NGC 5660 | 8.752 ± 0.028 | 8.669 ± 0.006 | 8.734 ± 0.029 | 8.952 ± 0.006 | -1.237 ± 0.004 |
| 318 | NGC 5657 | 8.798 ± 0.007 | 8.678 ± 0.003 | ... | ... | -0.190 ± 0.003 |
| 319 | CGCG 133-083 | 8.825 ± 0.006 | 8.754 ± 0.002 | ... | ... | 1.067 ± 0.003 |
| 320 | MCG 7-30-028 | 8.820 ± 0.011 | 8.699 ± 0.003 | ... | ... | 0.281 ± 0.003 |
| 321 | MCG 6-32-070 | 8.766 ± 0.023 | 8.662 ± 0.010 | 8.713 ± 0.193 | 8.901 ± 0.011 | -0.189 ± 0.004 |
| 323 | NGC 5698 | 8.870 ± 0.020 | 8.735 ± 0.007 | 8.715 ± 0.028 | 8.890 ± 0.011 | -0.186 ± 0.003 |
| 324 | NGC 5691 | 8.595 ± 0.005 | 8.597 ± 0.004 | 8.792 ± 0.005 | 9.000 ± 0.005 | -1.946 ± 0.003 |
| 325 | MCG 9-24-035 | 8.790 ± 0.009 | 8.837 ± 0.003 | ... | ... | 0.754 ± 0.004 |
| 326 | MCG 9-24-038 | 8.679 ± 0.017 | 8.720 ± 0.005 | ... | ... | 0.486 ± 0.005 |
| 327 | UGC 9560 | 8.127 ± 0.007 | 8.146 ± 0.008 | 8.708 ± 0.010 | 8.864 ± 0.012 | -0.925 ± 0.003 |
| 328 | IC 1076 | 8.719 ± 0.008 | 8.638 ± 0.004 | ... | ... | -0.651 ± 0.004 |
| 329 | IRAS 14538+1730 | 8.716 ± 0.011 | 8.850 ± 0.003 | ... | ... | 1.378 ± 0.004 |
| 330 | NGC 5795 | 8.700 ± 0.015 | 8.649 ± 0.006 | 9.003 ± 0.016 | 9.372 ± 0.008 | -1.668 ± 0.004 |

**Table 7.A.3:** Continued

| SFRS | Galaxy | Nuclear Metallicity | | Host Galaxy Metallicity | | log SFR |
|---|---|---|---|---|---|---|
| | | O3N2 | N2 | O3N2 | N2 | (Nuclear) |
| 333 | MCG 6-33-022 | 8.613 ± 0.023 | 8.710 ± 0.007 | ... | 9.193 ± 0.041 | 2.438 ± 0.006 |
| 335 | MCG 9-25-036 | 8.766 ± 0.016 | 8.699 ± 0.005 | ... | ... | -0.237 ± 0.004 |
| 337 | NGC 5905 | 8.705 ± 0.005 | 8.661 ± 0.002 | 8.831 ± 0.024 | 9.058 ± 0.020 | -0.009 ± 0.001 |
| 338 | MK 848 | 8.649 ± 0.002 | 8.723 ± 0.002 | ... | ... | 1.202 ± 0.002 |
| 340 | UGC 9922_NED02 | 8.657 ± 0.003 | 8.605 ± 0.003 | ... | ... | -0.363 ± 0.029 |
| 341 | IC 4567 | 8.649 ± 0.009 | 8.700 ± 0.006 | ... | ... | -0.636 ± 0.005 |
| 342 | MCG 4-37-016 | 8.796 ± 0.007 | 8.787 ± 0.004 | 8.800 ± 0.021 | 9.078 ± 0.031 | -1.169* ± 0.004 |
| 344 | NGC 5980 | 8.691 ± 0.048 | 8.756 ± 0.017 | 8.758 ± 0.050 | 8.890 ± 0.018 | -0.592 ± 0.015 |
| 345 | NGC 5992 | 8.632 ± 0.005 | 8.640 ± 0.003 | 8.750 ± 0.007 | 8.958 ± 0.005 | 0.126 ± 0.002 |
| 346 | NGC 5996 | 8.784 ± 0.003 | 8.666 ± 0.002 | ... | ... | -0.027 ± 0.003 |
| 347 | IRAS 15519+3537 | 8.649 ± 0.040 | 8.660 ± 0.027 | 8.743 ± 0.049 | 8.879 ± 0.033 | 1.103 ± 0.014 |
| 348 | UGC 10099 | 8.624 ± 0.003 | 8.710 ± 0.003 | ... | ... | 0.407 ± 0.003 |
| 349 | MCG 5-38-006 | 8.786 ± 0.009 | 8.740 ± 0.002 | 8.796 ± 0.013 | 9.014 ± 0.006 | 0.517 ± 0.002 |
| 351 | NGC 6027A | 8.700 ± 0.014 | 8.712 ± 0.009 | 8.732 ± 0.018 | 8.946 ± 0.011 | -0.903 ± 0.007 |
| 353 | UGC 10200 | 8.265 ± 0.004 | 8.332 ± 0.005 | 8.936 ± 0.006 | 9.211 ± 0.007 | -0.719 ± 0.003 |
| 354 | IRAS 16052+5334 | 8.723 ± 0.022 | 8.750 ± 0.005 | 8.687 ± 0.094 | 8.919 ± 0.026 | 0.880 ± 0.006 |
| 355 | IRAS 16053+1836 | 8.766 ± 0.008 | 8.772 ± 0.003 | ... | ... | 0.913 ± 0.003 |
| 356 | NGC 6090_NED01 | 8.738 ± 0.003 | 8.728 ± 0.003 | 8.721 ± 0.004 | 8.890 ± 0.004 | -0.052 ± 0.003 |
| 357 | UGC 10273_NED01 | 8.527 ± 0.003 | 8.523 ± 0.003 | 8.762 ± 0.004 | 9.000 ± 0.004 | -0.138 ± 0.002 |
| 359 | UGC 10322 | 8.741 ± 0.026 | 8.608 ± 0.011 | 8.796 ± 0.049 | 9.080 ± 0.062 | -0.515 ± 0.003 |
| 360 | NGC 6120 | 8.880 ± 0.027 | 8.765 ± 0.009 | 8.701 ± 0.031 | 8.894 ± 0.011 | -1.458* ± 0.008 |
| 361 | MCG 3-42-004 | 8.838 ± 0.015 | 8.702 ± 0.003 | 8.802 ± 0.099 | 9.033 ± 0.094 | 0.540 ± 0.003 |

**Table 7.A.3:** Continued

| SFRS | Galaxy | Nuclear Metallicity | | Host Galaxy Metallicity | | log SFR |
|---|---|---|---|---|---|---|
| | | O3N2 | N2 | O3N2 | N2 | (Nuclear) |
| 362 | UGC 10407 | 8.502 ± 0.002 | 8.504 ± 0.003 | 8.772 ± 0.003 | 8.959 ± 0.004 | -0.138 ± 0.001 |
| 364 | NGC 6186 | 8.808 ± 0.010 | 8.699 ± 0.004 | ... | ... | 0.371 ± 0.004 |
| 365 | MCG 9-27-053 | 8.773 ± 0.040 | 8.822 ± 0.011 | 8.578 ± 0.055 | 8.926 ± 0.014 | -0.696 ± 0.011 |
| 366 | UGC 10514 | 8.413 ± 0.003 | 8.510 ± 0.003 | ... | ... | -0.160 ± 0.003 |
| 367 | IRAS 16435+2154 | 8.775 ± 0.008 | 8.686 ± 0.003 | ... | ... | 0.485 ± 0.003 |
| 368 | IC 4623 | 8.820 ± 0.058 | 8.680 ± 0.012 | 8.714 ± 0.087 | 8.925 ± 0.070 | 0.458 ± 0.003 |

**Table 7.A.3:** Host galaxy and nuclear metallicities and SFRs for the SFRS SFGs. Host-galaxy metallicities are given only for galaxies observed with long-slit spectroscopy, with their nuclear contribution subtracted. SFR values flagged with a * symbol indicate uncertain measurements due to differences in the flux calibration between the blue and red spectral regions of galaxies observed with the 600 l mm$^{-1}$ grating configuration (Section 4.3.6).

**Table 7.A.4:** Host galaxy metallicities of the non-star-forming SFRS galaxies.

| SFRS | Galaxy | Host Galaxy Metallicity | | Classification |
|---|---|---|---|---|
| | | O3N2 | N2 | |
| 3 | NGC 2500 | 8.789 ± 0.033 | 8.914 ± 0.033 | LINER |
| 36 | IRAS 08572+3915NW | 8.716 ± 0.025 | 8.905 ± 0.013 | TO |
| 42 | IC 2434 | 8.755 ± 0.024 | 8.891 ± 0.017 | TO |
| 47 | NGC 2824 | 8.689 ± 0.032 | 8.924 ± 0.015 | LINER |
| 51 | IRAS 09197+2210 | 8.719 ± 0.071 | 8.895 ± 0.032 | TO |
| 61 | CGCG 181-068 | 8.676 ± 0.058 | 8.885 ± 0.021 | TO |
| 62 | NGC 2936 | 8.669 ± 0.052 | 8.714 ± 0.033 | LINER |
| 79 | IRAS 10120+1653 | 8.743 ± 0.064 | 8.891 ± 0.029 | LINER |
| 117 | IRAS 11102+3026 | 8.523 ± 0.241 | 8.960 ± 0.044 | Sy |
| 108 | IRAS 10565+2448W | 8.761 ± 0.012 | 9.031 ± 0.003 | Sy |
| 120 | 7ZW384 | 8.762 ± 0.008 | 8.949 ± 0.010 | TO |
| 131 | NGC3690 | 8.82 ± 0.003 | 9.024 ± 0.004 | Sy |
| 134 | NGC 3705 | 8.577 ± 0.036 | 8.824 ± 0.013 | LINER |
| 139 | NGC 3758 | 8.973 ± 0.013 | 8.833 ± 0.009 | Sy |
| 145 | UGC 6625 | 8.769 ± 0.017 | 8.948 ± 0.018 | TO |
| 148 | NGC 3822 | 8.857 ± 0.008 | 8.973 ± 0.006 | Sy |
| 152 | UGC 6732 | 8.741 ± 0.033 | 8.903 ± 0.013 | Sy |
| 157 | NGC 3934 | 8.727 ± 0.025 | 8.902 ± 0.011 | LINER |
| 169 | UGC 7016 | 8.770 ± 0.278 | 8.878 ± 0.034 | Sy |
| 176 | NGC 4150 | 8.779 ± 0.044 | 8.917 ± 0.020 | Sy |
| 193 | NGC 4314 | 8.773 ± 0.023 | 8.859 ± 0.015 | LINER |
| 197 | NGC 4412 | 8.897 ± 0.007 | 8.874 ± 0.005 | Sy |
| 201 | NGC 4435 | 8.585 ± 0.155 | 8.917 ± 0.036 | TO |
| 202 | NGC 4438 | 8.677 ± 0.087 | 8.801 ± 0.021 | LINER |
| 213 | NGC 4548 | 8.570 ± 0.075 | 8.841 ± 0.025 | Sy |
| 229 | NGC 4704 | 8.768 ± 0.022 | 8.693 ± 0.014 | Sy |
| 231 | IRAS 12468+3436 | 8.778 ± 0.246 | 8.912 ± 0.029 | Sy |
| 233 | MCG 8-23-097 | 8.723 ± 0.050 | 8.885 ± 0.013 | TO |
| 235 | UGC 8017 | 8.814 ± 0.281 | 9.003 ± 0.021 | TO |
| 248 | UGC 8269 | 8.578 ± 1.864 | 8.925 ± 0.025 | TO |
| 255 | UGC 8357_NED01 | 8.645 ± 0.023 | 8.875 ± 0.010 | TO |
| 258 | NGC 5100_NED02 | 8.705 ± 0.022 | 8.859 ± 0.009 | TO |
| 275 | IC 910 | 8.742 ± 0.009 | 8.805 ± 0.005 | Sy |
| 282 | NGC 5297 | 8.731 ± 0.033 | 8.762 ± 0.021 | LINER |
| 303 | CGCG 74-129 | 8.736 ± 0.020 | 8.882 ± 0.018 | Sy |
| 305 | NGC 5515 | 8.742 ± 0.033 | 8.828 ± 0.035 | Sy |
| 308 | NGC 5541 | 8.790 ± 0.055 | 8.873 ± 0.022 | TO |
| 322 | UGC 9412 | 8.665 ± 0.008 | 8.860 ± 0.009 | Sy |
| 331 | UGC 9618_NED02 | 9.040 ± 0.014 | 9.398 ± 0.016 | TO |
| 332 | UGC 9639 | 8.845 ± 0.065 | 8.971 ± 0.115 | Sy |
| 336 | NGC 5899 | 8.849 ± 0.011 | 8.796 ± 0.012 | Sy |

**Table 7.A.4:** Continued

| SFRS | Galaxy | Host Galaxy Metallicity | | Classification |
|---|---|---|---|---|
| | | O3N2 | N2 | |
| 339 | IC 4553 | 8.744 ± 0.086 | 8.768 ± 0.024 | Sy |
| 350 | UGC10120 | 8.697 ± 0.013 | 8.868 ± 0.019 | Sy |
| 352 | NGC 6040B | 8.959 ± 0.103 | 9.244 ± 0.126 | LINER |
| 369 | IRAS 16516+3030 | 8.426 ± 0.048 | 8.376 ± 0.026 | LINER |

**Table 7.A.4:** Host-galaxy metallicities for the non-star-forming SFRS galaxies with available long-slit spectroscopy.

**Table 7.A.5:** Probabilistic Activity Classification.

| SFRS | Galaxy | [N II]/H$\alpha$ | | | [S II]/H$\alpha$ | | | [O I]/H$\alpha$ | | |
|---|---|---|---|---|---|---|---|---|---|---|
| | | H II | TO | Sy/LINER | H II | LINER | Sy | H II | LINER | Sy |
| 1 | IC 486 | 0.000 | 0.000 | 1.000 | 0.000 | 0.000 | 1.000 | 0.000 | 0.000 | 1.000 |
| 2 | IC 2217 | 1.000 | 0.000 | 0.000 | 1.000 | 0.000 | 0.000 | 1.000 | 0.000 | 0.000 |
| 3 | NGC 2500 | 0.334 | 0.666 | 0.000 | 0.326 | 0.573 | 0.101 | 0.000 | 1.000 | 0.000 |
| 4 | NGC 2512 | 1.000 | 0.000 | 0.000 | 1.000 | 0.000 | 0.000 | 1.000 | 0.000 | 0.000 |
| 5 | MCG 6-18-009 | 0.729 | 0.271 | 0.000 | 1.000 | 0.000 | 0.000 | 1.000 | 0.000 | 0.000 |
| 6 | MK 1212 | 0.000 | 1.000 | 0.000 | 1.000 | 0.000 | 0.000 | 1.000 | 0.000 | 0.000 |
| 7 | IRAS 08072+1847 | 0.000 | 1.000 | 0.000 | 1.000 | 0.000 | 0.000 | 1.000 | 0.000 | 0.000 |
| 8 | NGC 2532 | 1.000 | 0.000 | 0.000 | 1.000 | 0.000 | 0.000 | 1.000 | 0.000 | 0.000 |
| 9 | UGC 4261 | 1.000 | 0.000 | 0.000 | 1.000 | 0.000 | 0.000 | 1.000 | 0.000 | 0.000 |
| 10 | NGC 2535 | 1.000 | 0.000 | 0.000 | 1.000 | 0.000 | 0.000 | 1.000 | 0.000 | 0.000 |
| 11 | NGC 2543 | 1.000 | 0.000 | 0.000 | 1.000 | 0.000 | 0.000 | 1.000 | 0.000 | 0.000 |
| 12 | NGC 2537 | 0.998 | 0.002 | 0.000 | 0.902 | 0.098 | 0.000 | 0.852 | 0.144 | 0.004 |
| 13 | IC 2233 | 1.000 | 0.000 | 0.000 | 1.000 | 0.000 | 0.000 | 1.000 | 0.000 | 0.000 |
| 14 | IC 2239 | 0.000 | 1.000 | 0.000 | 1.000 | 0.000 | 0.000 | 0.962 | 0.038 | 0.000 |
| 15 | UGC 4286 | 0.164 | 0.836 | 0.000 | 1.000 | 0.000 | 0.000 | 0.727 | 0.261 | 0.012 |
| 16 | UGC 4306 | 1.000 | 0.000 | 0.000 | 1.000 | 0.000 | 0.000 | 1.000 | 0.000 | 0.000 |
| 17 | NGC 2552 | 1.000 | 0.000 | 0.000 | 1.000 | 0.000 | 0.000 | 1.000 | 0.000 | 0.000 |
| 18 | UGC 4383 | 1.000 | 0.000 | 0.000 | 1.000 | 0.000 | 0.000 | 1.000 | 0.000 | 0.000 |
| 19 | IRAS 08234+1054 | 0.000 | 1.000 | 0.000 | 1.000 | 0.000 | 0.000 | 0.954 | 0.046 | 0.000 |
| 20 | IRAS 08269+1514 | 0.000 | 1.000 | 0.000 | 1.000 | 0.000 | 0.000 | 1.000 | 0.000 | 0.000 |
| 21 | NGC 2604 | 1.000 | 0.000 | 0.000 | 1.000 | 0.000 | 0.000 | 1.000 | 0.000 | 0.000 |

**Table 7.A.5:** Continued

| SFRS | Galaxy | [N II]/H$\alpha$ | | | [S II]/H$\alpha$ | | | [O I]/H$\alpha$ | | |
|---|---|---|---|---|---|---|---|---|---|---|
| | | H II | TO | Sy/LINER | H II | LINER | Sy | H II | LINER | Sy |
| 22 | NGC 2608 | 1.000 | 0.000 | 0.000 | 1.000 | 0.000 | 0.000 | 1.000 | 0.000 | 0.000 |
| 23 | MK 92 | 1.000 | 0.000 | 0.000 | 1.000 | 0.000 | 0.000 | 1.000 | 0.000 | 0.000 |
| 24 | NGC 2623 | 0.000 | 0.000 | 1.000 | 0.000 | 0.000 | 1.000 | 0.000 | 0.005 | 0.995 |
| 25 | CGCG 120-018 | 0.000 | 1.000 | 0.000 | 1.000 | 0.000 | 0.000 | 1.000 | 0.000 | 0.000 |
| 26 | NGC 2644 | 1.000 | 0.000 | 0.000 | 1.000 | 0.000 | 0.000 | 1.000 | 0.000 | 0.000 |
| 27 | UGC 4572 | 0.000 | 1.000 | 0.000 | 0.927 | 0.073 | 0.000 | 0.482 | 0.518 | 0.000 |
| 28 | UGC 4653 | 0.000 | 1.000 | 0.000 | 1.000 | 0.000 | 0.000 | 0.647 | 0.353 | 0.000 |
| 29 | IRAS 08512+2727 | 1.000 | 0.000 | 0.000 | 1.000 | 0.000 | 0.000 | 1.000 | 0.000 | 0.000 |
| 31 | IRAS 08538+4256 | 0.018 | 0.982 | 0.000 | 1.000 | 0.000 | 0.000 | 1.000 | 0.000 | 0.000 |
| 32 | IRAS 08550+3908 | 0.000 | 0.000 | 1.000 | 0.000 | 1.000 | 0.000 | 0.000 | 0.025 | 0.975 |
| 33 | NGC 2718 | 1.000 | 0.000 | 0.000 | 1.000 | 0.000 | 0.000 | 1.000 | 0.000 | 0.000 |
| 34 | NGC 2712 | 0.000 | 1.000 | 0.000 | 1.000 | 0.000 | 0.000 | 0.951 | 0.049 | 0.000 |
| 35 | NGC 2719 | 1.000 | 0.000 | 0.000 | 1.000 | 0.000 | 0.000 | 1.000 | 0.000 | 0.000 |
| 36 | IRAS 08572+3915NW | 0.007 | 0.993 | 0.000 | 1.000 | 0.000 | 0.000 | 0.426 | 0.141 | 0.433 |
| 37 | IRAS 08579+3447 | 1.000 | 0.000 | 0.000 | 1.000 | 0.000 | 0.000 | 0.975 | 0.025 | 0.000 |
| 38 | NGC 2731 | 1.000 | 0.000 | 0.000 | 1.000 | 0.000 | 0.000 | 1.000 | 0.000 | 0.000 |
| 39 | NGC 2730 | 1.000 | 0.000 | 0.000 | 1.000 | 0.000 | 0.000 | 0.458 | 0.542 | 0.000 |
| 40 | IC 2431 | 1.000 | 0.000 | 0.000 | 1.000 | 0.000 | 0.000 | 1.000 | 0.000 | 0.000 |
| 41 | NGC 2750 | 1.000 | 0.000 | 0.000 | 1.000 | 0.000 | 0.000 | 1.000 | 0.000 | 0.000 |
| 42 | IC 2434 | 0.000 | 1.000 | 0.000 | 1.000 | 0.000 | 0.000 | 0.073 | 0.849 | 0.078 |
| 43 | NGC 2761 | 0.000 | 1.000 | 0.000 | 1.000 | 0.000 | 0.000 | 1.000 | 0.000 | 0.000 |
| 44 | NGC 2773 | 1.000 | 0.000 | 0.000 | 1.000 | 0.000 | 0.000 | 1.000 | 0.000 | 0.000 |

**Table 7.A.5:** Continued

| SFRS | Galaxy | [N II]/H$\alpha$ | | | [S II]/H$\alpha$ | | | [O I]/H$\alpha$ | | |
|---|---|---|---|---|---|---|---|---|---|---|
| | | H II | TO | Sy/LINER | H II | LINER | Sy | H II | LINER | Sy |
| 45 | NGC 2776 | 0.275 | 0.725 | 0.000 | 1.000 | 0.000 | 0.000 | 0.994 | 0.006 | 0.000 |
| 46 | NGC 2789 | 0.000 | 1.000 | 0.000 | 1.000 | 0.000 | 0.000 | 1.000 | 0.000 | 0.000 |
| 47 | NGC 2824 | 0.000 | 0.014 | 0.986 | 0.000 | 1.000 | 0.000 | 0.000 | 0.930 | 0.070 |
| 48 | IRAS 09121+3908 | 0.000 | 1.000 | 0.000 | 1.000 | 0.000 | 0.000 | 0.956 | 0.044 | 0.000 |
| 49 | IRAS 09184+4356 | 0.941 | 0.059 | 0.000 | 1.000 | 0.000 | 0.000 | 1.000 | 0.000 | 0.000 |
| 50 | CGCG 238-041 | 1.000 | 0.000 | 0.000 | 1.000 | 0.000 | 0.000 | 1.000 | 0.000 | 0.000 |
| 51 | IRAS 09197+2210 | 0.008 | 0.786 | 0.206 | 0.830 | 0.002 | 0.168 | 0.306 | 0.147 | 0.547 |
| 52 | NGC 2854 | 0.000 | 1.000 | 0.000 | 1.000 | 0.000 | 0.000 | 0.141 | 0.859 | 0.000 |
| 53 | UGC 5046 | 1.000 | 0.000 | 0.000 | 1.000 | 0.000 | 0.000 | 1.000 | 0.000 | 0.000 |
| 54 | UGC 5055 | 1.000 | 0.000 | 0.000 | 1.000 | 0.000 | 0.000 | 1.000 | 0.000 | 0.000 |
| 55 | NGC 2893 | 0.876 | 0.124 | 0.000 | 1.000 | 0.000 | 0.000 | 1.000 | 0.000 | 0.000 |
| 56 | MCG 3-24-062 | 0.920 | 0.080 | 0.000 | 1.000 | 0.000 | 0.000 | 0.998 | 0.002 | 0.000 |
| 57 | CGCG 238-066 | 0.000 | 0.474 | 0.526 | 1.000 | 0.000 | 0.000 | 0.000 | 0.000 | 1.000 |
| 58 | UGC 5097 | 1.000 | 0.000 | 0.000 | 1.000 | 0.000 | 0.000 | 1.000 | 0.000 | 0.000 |
| 59 | CGCG 289-012 | 1.000 | 0.000 | 0.000 | 1.000 | 0.000 | 0.000 | 1.000 | 0.000 | 0.000 |
| 60 | MCG 8-18-013 | 0.000 | 1.000 | 0.000 | 1.000 | 0.000 | 0.000 | 0.987 | 0.013 | 0.000 |
| 61 | CGCG 181-068 | 0.000 | 0.999 | 0.001 | 1.000 | 0.000 | 0.000 | 0.473 | 0.508 | 0.019 |
| 62 | NGC 2936 | 0.000 | 0.270 | 0.730 | 0.000 | 1.000 | 0.000 | 0.122 | 0.847 | 0.031 |
| 63 | NGC 2955 | 0.821 | 0.179 | 0.000 | 0.000 | 1.000 | 0.000 | 0.964 | 0.036 | 0.000 |
| 64 | CGCG 182-010 | 1.000 | 0.000 | 0.000 | 1.000 | 0.000 | 0.000 | 1.000 | 0.000 | 0.000 |
| 65 | UGC 5228 | 1.000 | 0.000 | 0.000 | 1.000 | 0.000 | 0.000 | 1.000 | 0.000 | 0.000 |
| 66 | IRAS 09438+1141 | 1.000 | 0.000 | 0.000 | 1.000 | 0.000 | 0.000 | 1.000 | 0.000 | 0.000 |

**Table 7.A.5:** Continued

| SFRS | Galaxy | [N II]/H$\alpha$ | | | [S II]/H$\alpha$ | | | [O I]/H$\alpha$ | | |
|---|---|---|---|---|---|---|---|---|---|---|
| | | H II | TO | Sy/LINER | H II | LINER | Sy | H II | LINER | Sy |
| 67 | NGC 3015 | 0.000 | 1.000 | 0.000 | 1.000 | 0.000 | 0.000 | 0.141 | 0.859 | 0.000 |
| 68 | MCG 2-25-039 | 1.000 | 0.000 | 0.000 | 1.000 | 0.000 | 0.000 | 1.000 | 0.000 | 0.000 |
| 69 | NGC 3020 | 1.000 | 0.000 | 0.000 | 1.000 | 0.000 | 0.000 | 0.999 | 0.000 | 0.001 |
| 70 | NGC 3049 | 1.000 | 0.000 | 0.000 | 1.000 | 0.000 | 0.000 | 1.000 | 0.000 | 0.000 |
| 71 | NGC 3055 | 0.000 | 1.000 | 0.000 | 1.000 | 0.000 | 0.000 | 1.000 | 0.000 | 0.000 |
| 72 | IC 2520 | 0.991 | 0.009 | 0.000 | 1.000 | 0.000 | 0.000 | 1.000 | 0.000 | 0.000 |
| 73 | UGC 5403 | 1.000 | 0.000 | 0.000 | 1.000 | 0.000 | 0.000 | 1.000 | 0.000 | 0.000 |
| 74 | UGC 5459 | 1.000 | 0.000 | 0.000 | 1.000 | 0.000 | 0.000 | 0.963 | 0.037 | 0.000 |
| 75 | MCG 5-24-022 | 1.000 | 0.000 | 0.000 | 1.000 | 0.000 | 0.000 | 0.997 | 0.003 | 0.000 |
| 76 | IC 2551 | 0.000 | 1.000 | 0.000 | 1.000 | 0.000 | 0.000 | 1.000 | 0.000 | 0.000 |
| 77 | IRAS 10106+2745 | 1.000 | 0.000 | 0.000 | 1.000 | 0.000 | 0.000 | 1.000 | 0.000 | 0.000 |
| 78 | NGC 3162 | 1.000 | 0.000 | 0.000 | 1.000 | 0.000 | 0.000 | 0.498 | 0.502 | 0.000 |
| 79 | IRAS 10120+1653 | 0.000 | 0.272 | 0.728 | 0.000 | 1.000 | 0.000 | 0.301 | 0.506 | 0.193 |
| 81 | IC 602 | 1.000 | 0.000 | 0.000 | 1.000 | 0.000 | 0.000 | 1.000 | 0.000 | 0.000 |
| 82 | NGC 3191 | 0.998 | 0.002 | 0.000 | 1.000 | 0.000 | 0.000 | 0.498 | 0.502 | 0.000 |
| 83 | NGC 3206 | 1.000 | 0.000 | 0.000 | 1.000 | 0.000 | 0.000 | 1.000 | 0.000 | 0.000 |
| 84 | UGC 5613 | 0.000 | 1.000 | 0.000 | 1.000 | 0.000 | 0.000 | 1.000 | 0.000 | 0.000 |
| 85 | UGC 5644 | 0.000 | 0.000 | 1.000 | 0.000 | 0.996 | 0.004 | 0.000 | 1.000 | 0.000 |
| 86 | NGC 3245 | 0.000 | 1.000 | 0.000 | 1.000 | 0.000 | 0.000 | 1.000 | 0.000 | 0.000 |
| 87 | IRAS 10246+2042 | 0.000 | 1.000 | 0.000 | 1.000 | 0.000 | 0.000 | 1.000 | 0.000 | 0.000 |
| 88 | MCG 7-22-012 | 1.000 | 0.000 | 0.000 | 1.000 | 0.000 | 0.000 | 0.991 | 0.009 | 0.000 |
| 89 | IRAS 10276+1119 | 0.011 | 0.989 | 0.000 | 1.000 | 0.000 | 0.000 | 1.000 | 0.000 | 0.000 |

**Table 7.A.5:** Continued

| SFRS | Galaxy | [N II]/H$\alpha$ | | | [S II]/H$\alpha$ | | | [O I]/H$\alpha$ | | |
|---|---|---|---|---|---|---|---|---|---|---|
| | | H II | TO | Sy/LINER | H II | LINER | Sy | H II | LINER | Sy |
| 90 | NGC 3265 | 1.000 | 0.000 | 0.000 | 1.000 | 0.000 | 0.000 | 1.000 | 0.000 | 0.000 |
| 91 | UGC 5713 | 0.000 | 0.000 | 1.000 | 0.000 | 0.372 | 0.628 | 0.000 | 0.001 | 0.999 |
| 92 | NGC 3274 | 1.000 | 0.000 | 0.000 | 0.071 | 0.000 | 0.929 | 0.887 | 0.000 | 0.113 |
| 94 | KUG 1031+351 | 1.000 | 0.000 | 0.000 | 1.000 | 0.000 | 0.000 | 1.000 | 0.000 | 0.000 |
| 95 | NGC 3306 | 1.000 | 0.000 | 0.000 | 1.000 | 0.000 | 0.000 | 1.000 | 0.000 | 0.000 |
| 96 | NGC 3323 | 1.000 | 0.000 | 0.000 | 1.000 | 0.000 | 0.000 | 1.000 | 0.000 | 0.000 |
| 97 | IC 2598 | 1.000 | 0.000 | 0.000 | 1.000 | 0.000 | 0.000 | 1.000 | 0.000 | 0.000 |
| 98 | NGC 3338 | 0.000 | 0.297 | 0.703 | 0.858 | 0.133 | 0.009 | 0.000 | 1.000 | 0.000 |
| 99 | NGC 3353 | 1.000 | 0.000 | 0.000 | 1.000 | 0.000 | 0.000 | 1.000 | 0.000 | 0.000 |
| 100 | UGC 5881 | 0.000 | 1.000 | 0.000 | 1.000 | 0.000 | 0.000 | 1.000 | 0.000 | 0.000 |
| 101 | NGC 3370 | 1.000 | 0.000 | 0.000 | 1.000 | 0.000 | 0.000 | 0.925 | 0.075 | 0.000 |
| 102 | NGC 3381 | 1.000 | 0.000 | 0.000 | 1.000 | 0.000 | 0.000 | 1.000 | 0.000 | 0.000 |
| 103 | UGC 5941_NED02 | 1.000 | 0.000 | 0.000 | 1.000 | 0.000 | 0.000 | 1.000 | 0.000 | 0.000 |
| 104 | NGC 3413 | 1.000 | 0.000 | 0.000 | 1.000 | 0.000 | 0.000 | 1.000 | 0.000 | 0.000 |
| 105 | NGC 3408 | 1.000 | 0.000 | 0.000 | 1.000 | 0.000 | 0.000 | 1.000 | 0.000 | 0.000 |
| 106 | NGC 3430 | 1.000 | 0.000 | 0.000 | 1.000 | 0.000 | 0.000 | 0.601 | 0.399 | 0.000 |
| 107 | CGCG 95-055 | 0.000 | 0.000 | 1.000 | 0.000 | 0.000 | 1.000 | 0.000 | 0.000 | 1.000 |
| 108 | IRAS 10565+2448W | 0.000 | 1.000 | 0.000 | 1.000 | 0.000 | 0.000 | 1.000 | 0.000 | 0.000 |
| 109 | UGC 6074 | 0.000 | 1.000 | 0.000 | 1.000 | 0.000 | 0.000 | 1.000 | 0.000 | 0.000 |
| 110 | NGC 3495 | 0.656 | 0.344 | 0.000 | 0.991 | 0.009 | 0.000 | 0.000 | 1.000 | 0.000 |
| 111 | UGC 6103 | 0.000 | 1.000 | 0.000 | 1.000 | 0.000 | 0.000 | 1.000 | 0.000 | 0.000 |
| 112 | MCG 7-23-019 | 0.029 | 0.971 | 0.000 | 1.000 | 0.000 | 0.000 | 0.821 | 0.159 | 0.020 |

**Table 7.A.5:** Continued

| SFRS | Galaxy | [N II]/H$\alpha$ | | | [S II]/H$\alpha$ | | | [O I]/H$\alpha$ | | |
|---|---|---|---|---|---|---|---|---|---|---|
| | | H II | TO | Sy/LINER | H II | LINER | Sy | H II | LINER | Sy |
| 113 | UGC 6135 | 0.000 | 0.000 | 1.000 | 0.000 | 0.998 | 0.002 | 0.000 | 0.998 | 0.002 |
| 114 | CGCG 241-078 | 0.000 | 1.000 | 0.000 | 1.000 | 0.000 | 0.000 | 1.000 | 0.000 | 0.000 |
| 115 | IRAS 11069+2711 | 1.000 | 0.000 | 0.000 | 1.000 | 0.000 | 0.000 | 1.000 | 0.000 | 0.000 |
| 116 | IC 676 | 1.000 | 0.000 | 0.000 | 1.000 | 0.000 | 0.000 | 1.000 | 0.000 | 0.000 |
| 117 | IRAS 11102+3026 | 0.000 | 0.451 | 0.549 | 0.666 | 0.030 | 0.304 | 0.304 | 0.266 | 0.430 |
| 118 | IC 2637 | 0.000 | 0.000 | 1.000 | 0.000 | 0.000 | 1.000 | 0.000 | 0.000 | 1.000 |
| 119 | MCG 9-19-013 | 0.000 | 1.000 | 0.000 | 1.000 | 0.000 | 0.000 | 0.218 | 0.741 | 0.041 |
| 120 | 7ZW384 | 0.000 | 1.000 | 0.000 | 1.000 | 0.000 | 0.000 | 0.000 | 1.000 | 0.000 |
| 121 | 2MASX J11193404+5335181 | 0.000 | 1.000 | 0.000 | 1.000 | 0.000 | 0.000 | 0.000 | 0.000 | 1.000 |
| 122 | NGC 3633 | 1.000 | 0.000 | 0.000 | 1.000 | 0.000 | 0.000 | 1.000 | 0.000 | 0.000 |
| 123 | NGC 3652 | 1.000 | 0.000 | 0.000 | 1.000 | 0.000 | 0.000 | 1.000 | 0.000 | 0.000 |
| 124 | NGC 3656 | 0.000 | 1.000 | 0.000 | 0.396 | 0.604 | 0.000 | 0.000 | 0.861 | 0.139 |
| 125 | NGC 3659 | 1.000 | 0.000 | 0.000 | 1.000 | 0.000 | 0.000 | 1.000 | 0.000 | 0.000 |
| 126 | NGC 3664 | 1.000 | 0.000 | 0.000 | 1.000 | 0.000 | 0.000 | 0.998 | 0.000 | 0.002 |
| 127 | NGC 3666 | 0.979 | 0.021 | 0.000 | 1.000 | 0.000 | 0.000 | 0.999 | 0.001 | 0.000 |
| 128 | IC 691 | 1.000 | 0.000 | 0.000 | 1.000 | 0.000 | 0.000 | 1.000 | 0.000 | 0.000 |
| 129 | NGC 3686 | 1.000 | 0.000 | 0.000 | 1.000 | 0.000 | 0.000 | 0.932 | 0.068 | 0.000 |
| 130 | UGC 6469 | 1.000 | 0.000 | 0.000 | 1.000 | 0.000 | 0.000 | 1.000 | 0.000 | 0.000 |
| 131 | NGC 3690 | 0.000 | 1.000 | 0.000 | 1.000 | 0.000 | 0.000 | 1.000 | 0.000 | 0.000 |
| 132 | IC 698 | 0.993 | 0.007 | 0.000 | 1.000 | 0.000 | 0.000 | 1.000 | 0.000 | 0.000 |
| 133 | IRAS 11267+1558 | 0.002 | 0.998 | 0.000 | 1.000 | 0.000 | 0.000 | 0.997 | 0.003 | 0.000 |
| 134 | NGC 3705 | 0.000 | 0.001 | 0.999 | 0.000 | 0.953 | 0.047 | 0.000 | 0.525 | 0.475 |

**Table 7.A.5:** Continued

| SFRS | Galaxy | [N II]/H$\alpha$ | | | [S II]/H$\alpha$ | | | [O I]/H$\alpha$ | | |
|---|---|---|---|---|---|---|---|---|---|---|
| | | H II | TO | Sy/LINER | H II | LINER | Sy | H II | LINER | Sy |
| 135 | MCG 3-29-061 | 0.000 | 1.000 | 0.000 | 1.000 | 0.000 | 0.000 | 1.000 | 0.000 | 0.000 |
| 136 | NGC 3720 | 1.000 | 0.000 | 0.000 | 1.000 | 0.000 | 0.000 | 1.000 | 0.000 | 0.000 |
| 137 | NGC 3729 | 0.000 | 1.000 | 0.000 | 1.000 | 0.000 | 0.000 | 1.000 | 0.000 | 0.000 |
| 138 | MCG 10-17-019 | 1.000 | 0.000 | 0.000 | 1.000 | 0.000 | 0.000 | 1.000 | 0.000 | 0.000 |
| 139 | NGC 3758 | 0.000 | 0.000 | 1.000 | 1.000 | 0.000 | 0.000 | 0.319 | 0.000 | 0.681 |
| 140 | UGC 6583 | 1.000 | 0.000 | 0.000 | 1.000 | 0.000 | 0.000 | 1.000 | 0.000 | 0.000 |
| 141 | MCG 1-30-003 | 1.000 | 0.000 | 0.000 | 1.000 | 0.000 | 0.000 | 1.000 | 0.000 | 0.000 |
| 142 | NGC 3769 | 0.999 | 0.001 | 0.000 | 1.000 | 0.000 | 0.000 | 1.000 | 0.000 | 0.000 |
| 143 | NGC 3773 | 1.000 | 0.000 | 0.000 | 1.000 | 0.000 | 0.000 | 1.000 | 0.000 | 0.000 |
| 144 | NGC 3781 | 0.000 | 0.000 | 1.000 | 0.000 | 0.000 | 1.000 | 0.000 | 0.001 | 0.999 |
| 145 | UGC 6625 | 0.000 | 1.000 | 0.000 | 1.000 | 0.000 | 0.000 | 0.187 | 0.813 | 0.000 |
| 146 | NGC 3808_NED02 | 1.000 | 0.000 | 0.000 | 1.000 | 0.000 | 0.000 | 1.000 | 0.000 | 0.000 |
| 148 | NGC 3822 | 0.000 | 0.000 | 1.000 | ... | ... | ... | 0.000 | 0.000 | 1.000 |
| 147 | NGC 3811 | 1.000 | 0.000 | 0.000 | 1.000 | 0.000 | 0.000 | 1.000 | 0.000 | 0.000 |
| 149 | UGC 6665 | 1.000 | 0.000 | 0.000 | 1.000 | 0.000 | 0.000 | 1.000 | 0.000 | 0.000 |
| 150 | MCG 3-30-051 | 1.000 | 0.000 | 0.000 | 1.000 | 0.000 | 0.000 | 1.000 | 0.000 | 0.000 |
| 151 | NGC 3839 | 1.000 | 0.000 | 0.000 | 1.000 | 0.000 | 0.000 | 1.000 | 0.000 | 0.000 |
| 152 | UGC 6732 | 0.000 | 0.000 | 1.000 | 0.000 | 0.000 | 1.000 | 0.000 | 0.000 | 1.000 |
| 153 | IC 730 | 1.000 | 0.000 | 0.000 | 1.000 | 0.000 | 0.000 | 1.000 | 0.000 | 0.000 |
| 154 | IC 732_NED01 | 0.144 | 0.856 | 0.000 | 1.000 | 0.000 | 0.000 | 0.999 | 0.001 | 0.000 |
| 155 | NGC 3912 | 1.000 | 0.000 | 0.000 | 1.000 | 0.000 | 0.000 | 1.000 | 0.000 | 0.000 |
| 156 | NGC 3928 | 0.000 | 1.000 | 0.000 | 1.000 | 0.000 | 0.000 | 1.000 | 0.000 | 0.000 |

**Table 7.A.5:** Continued

| SFRS | Galaxy | [N II]/H$\alpha$ | | | [S II]/H$\alpha$ | | | [O I]/H$\alpha$ | | |
|---|---|---|---|---|---|---|---|---|---|---|
| | | H II | TO | Sy/LINER | H II | LINER | Sy | H II | LINER | Sy |
| 157 | NGC 3934 | 0.000 | 1.000 | 0.000 | 0.093 | 0.907 | 0.000 | 0.000 | 0.949 | 0.051 |
| 158 | UGC 6865 | 1.000 | 0.000 | 0.000 | 1.000 | 0.000 | 0.000 | 1.000 | 0.000 | 0.000 |
| 159 | UGC 6901 | 1.000 | 0.000 | 0.000 | 1.000 | 0.000 | 0.000 | 1.000 | 0.000 | 0.000 |
| 160 | CGCG 013-010 | 0.000 | 1.000 | 0.000 | 1.000 | 0.000 | 0.000 | 0.571 | 0.351 | 0.078 |
| 161 | NGC 3991 | 1.000 | 0.000 | 0.000 | 1.000 | 0.000 | 0.000 | 1.000 | 0.000 | 0.000 |
| 162 | NGC 4004 | 1.000 | 0.000 | 0.000 | 1.000 | 0.000 | 0.000 | 1.000 | 0.000 | 0.000 |
| 163 | NGC 4014 | 0.000 | 1.000 | 0.000 | 0.999 | 0.001 | 0.000 | 0.787 | 0.164 | 0.049 |
| 164 | NGC 4010 | 1.000 | 0.000 | 0.000 | 1.000 | 0.000 | 0.000 | 1.000 | 0.000 | 0.000 |
| 165 | NGC 4018 | 0.991 | 0.009 | 0.000 | 1.000 | 0.000 | 0.000 | 0.947 | 0.053 | 0.000 |
| 166 | NGC 4020 | 1.000 | 0.000 | 0.000 | 0.053 | 0.947 | 0.000 | 0.133 | 0.849 | 0.018 |
| 167 | IRAS 11571+3003 | 0.984 | 0.016 | 0.000 | 1.000 | 0.000 | 0.000 | 1.000 | 0.000 | 0.000 |
| 168 | UGC 7017 | 1.000 | 0.000 | 0.000 | 1.000 | 0.000 | 0.000 | 1.000 | 0.000 | 0.000 |
| 169 | UGC 7016 | 0.000 | 0.000 | 1.000 | 0.000 | 0.000 | 1.000 | 0.000 | 0.000 | 1.000 |
| 170 | MCG 3-31-030 | 1.000 | 0.000 | 0.000 | 1.000 | 0.000 | 0.000 | 1.000 | 0.000 | 0.000 |
| 171 | NGC 4062 | 0.622 | 0.378 | 0.000 | 1.000 | 0.000 | 0.000 | 0.156 | 0.844 | 0.000 |
| 172 | NGC 4064 | 1.000 | 0.000 | 0.000 | 1.000 | 0.000 | 0.000 | 1.000 | 0.000 | 0.000 |
| 173 | CGCG 098-059 | 1.000 | 0.000 | 0.000 | 1.000 | 0.000 | 0.000 | 1.000 | 0.000 | 0.000 |
| 174 | NGC 4116 | 1.000 | 0.000 | 0.000 | 1.000 | 0.000 | 0.000 | 1.000 | 0.000 | 0.000 |
| 175 | NGC 4136 | 1.000 | 0.000 | 0.000 | 1.000 | 0.000 | 0.000 | 0.000 | 0.000 | 0.000 |
| 176 | NGC 4150 | 0.000 | 0.000 | 1.000 | 0.000 | 0.865 | 0.135 | 0.000 | 0.132 | 0.868 |
| 177 | IRAS 12086+1441 | 1.000 | 0.000 | 0.000 | 1.000 | 0.000 | 0.000 | 1.000 | 0.000 | 0.000 |
| 178 | NGC 4162 | 0.000 | 1.000 | 0.000 | 1.000 | 0.000 | 0.000 | 0.988 | 0.010 | 0.002 |

**Table 7.A.5:** Continued

| SFRS | Galaxy | [N II]/Hα | | | [S II]/Hα | | | [O I]/Hα | | |
|---|---|---|---|---|---|---|---|---|---|---|
| | | H II | TO | Sy/LINER | H II | LINER | Sy | H II | LINER | Sy |
| 179 | NGC 4178 | 0.988 | 0.012 | 0.000 | 0.980 | 0.014 | 0.006 | 0.924 | 0.071 | 0.005 |
| 180 | IRAS 12112+0305 | 0.000 | 1.000 | 0.000 | 0.000 | 0.001 | 0.999 | 0.000 | 0.019 | 0.981 |
| 181 | NGC 4189 | 1.000 | 0.000 | 0.000 | 1.000 | 0.000 | 0.000 | 1.000 | 0.000 | 0.000 |
| 183 | NGC 4204 | 1.000 | 0.000 | 0.000 | 0.931 | 0.069 | 0.000 | 0.682 | 0.310 | 0.008 |
| 184 | NGC 4207 | 1.000 | 0.000 | 0.000 | 1.000 | 0.000 | 0.000 | 1.000 | 0.000 | 0.000 |
| 185 | UGC 7286 | 0.120 | 0.880 | 0.000 | 1.000 | 0.000 | 0.000 | 0.902 | 0.091 | 0.007 |
| 186 | NGC 4234 | 1.000 | 0.000 | 0.000 | 1.000 | 0.000 | 0.000 | 1.000 | 0.000 | 0.000 |
| 187 | NGC 4237 | 0.005 | 0.995 | 0.000 | 1.000 | 0.000 | 0.000 | 0.495 | 0.505 | 0.000 |
| 188 | NGC 4244 | 1.000 | 0.000 | 0.000 | 1.000 | 0.000 | 0.000 | 0.765 | 0.234 | 0.001 |
| 189 | NGC 4253 | 0.598 | 0.402 | 0.000 | 1.000 | 0.000 | 0.000 | 1.000 | 0.000 | 0.000 |
| 190 | MCG 3-32-005 | 1.000 | 0.000 | 0.000 | 1.000 | 0.000 | 0.000 | 1.000 | 0.000 | 0.000 |
| 191 | NGC 4290 | 1.000 | 0.000 | 0.000 | 1.000 | 0.000 | 0.000 | 1.000 | 0.000 | 0.000 |
| 192 | NGC 4294 | 1.000 | 0.000 | 0.000 | 1.000 | 0.000 | 0.000 | 1.000 | 0.000 | 0.000 |
| 193 | NGC 4314 | 0.000 | 0.003 | 0.997 | 0.056 | 0.944 | 0.000 | 0.000 | 1.000 | 0.000 |
| 194 | NGC 4385 | 0.000 | 1.000 | 0.000 | 1.000 | 0.000 | 0.000 | 1.000 | 0.000 | 0.000 |
| 195 | NGC 4395 | 0.000 | 0.000 | 1.000 | 0.000 | 0.000 | 1.000 | 0.000 | 0.000 | 1.000 |
| 196 | NGC 4396 | 1.000 | 0.000 | 0.000 | 1.000 | 0.000 | 0.000 | 1.000 | 0.000 | 0.000 |
| 197 | NGC 4412 | 0.000 | 0.000 | 1.000 | 0.000 | 0.000 | 1.000 | 0.000 | 0.000 | 1.000 |
| 198 | NGC 4418 | 0.000 | 0.512 | 0.488 | 0.000 | 1.000 | 0.000 | 0.000 | 1.000 | 0.000 |
| 199 | NGC 4420 | 1.000 | 0.000 | 0.000 | 1.000 | 0.000 | 0.000 | 1.000 | 0.000 | 0.000 |
| 200 | NGC 4424 | 1.000 | 0.000 | 0.000 | 1.000 | 0.000 | 0.000 | 0.498 | 0.502 | 0.000 |
| 201 | NGC 4435 | 0.085 | 0.549 | 0.366 | 0.812 | 0.000 | 0.188 | 0.000 | 0.951 | 0.049 |

**Table 7.A.5:** Continued

| SFRS | Galaxy | [N II]/H$\alpha$ | | | [S II]/H$\alpha$ | | | [O I]/H$\alpha$ | | |
|---|---|---|---|---|---|---|---|---|---|---|
| | | H II | TO | Sy/LINER | H II | LINER | Sy | H II | LINER | Sy |
| 202 | NGC 4438 | 0.000 | 0.000 | 1.000 | 0.000 | 1.000 | 0.000 | 0.000 | 1.000 | 0.000 |
| 203 | NGC 4448 | 0.582 | 0.270 | 0.148 | 0.880 | 0.000 | 0.120 | 0.000 | 0.000 | 0.000 |
| 205 | NGC 4470 | 1.000 | 0.000 | 0.000 | 1.000 | 0.000 | 0.000 | 1.000 | 0.000 | 0.000 |
| 206 | IRAS 12274+0018 | 1.000 | 0.000 | 0.000 | 1.000 | 0.000 | 0.000 | 1.000 | 0.000 | 0.000 |
| 207 | NGC 4491 | 1.000 | 0.000 | 0.000 | 1.000 | 0.000 | 0.000 | 0.498 | 0.502 | 0.000 |
| 208 | NGC 4500 | 0.000 | 1.000 | 0.000 | 1.000 | 0.000 | 0.000 | 0.988 | 0.000 | 0.012 |
| 209 | NGC 4495 | 0.000 | 1.000 | 0.000 | 1.000 | 0.000 | 0.000 | 1.000 | 0.000 | 0.000 |
| 210 | IC 3476 | 1.000 | 0.000 | 0.000 | 1.000 | 0.000 | 0.000 | 0.999 | 0.001 | 0.000 |
| 211 | NGC 4509 | 1.000 | 0.000 | 0.000 | 0.962 | 0.000 | 0.038 | 0.606 | 0.137 | 0.257 |
| 212 | NGC 4519 | 1.000 | 0.000 | 0.000 | 1.000 | 0.000 | 0.000 | 1.000 | 0.000 | 0.000 |
| 213 | NGC 4548 | 0.000 | 0.000 | 1.000 | 0.000 | 0.833 | 0.167 | 0.000 | 0.338 | 0.662 |
| 214 | IRAS 12337+5044 | 1.000 | 0.000 | 0.000 | 1.000 | 0.000 | 0.000 | 1.000 | 0.000 | 0.000 |
| 215 | IC 3581 | 0.000 | 1.000 | 0.000 | 1.000 | 0.000 | 0.000 | 1.000 | 0.000 | 0.000 |
| 216 | NGC 4592 | 1.000 | 0.000 | 0.000 | 1.000 | 0.000 | 0.000 | 0.963 | 0.011 | 0.026 |
| 217 | NGC 4607 | 0.000 | 1.000 | 0.000 | 0.000 | 1.000 | 0.000 | 0.002 | 0.582 | 0.416 |
| 218 | NGC 4625 | 0.635 | 0.365 | 0.000 | 0.990 | 0.010 | 0.000 | 0.614 | 0.380 | 0.006 |
| 219 | NGC 4630 | 1.000 | 0.000 | 0.000 | 1.000 | 0.000 | 0.000 | 1.000 | 0.000 | 0.000 |
| 220 | IC 3690 | 0.000 | 1.000 | 0.000 | 1.000 | 0.000 | 0.000 | 0.752 | 0.248 | 0.000 |
| 221 | UGC 7905_NED01 | 1.000 | 0.000 | 0.000 | 1.000 | 0.000 | 0.000 | 0.988 | 0.000 | 0.012 |
| 222 | MCG 5-30-069 | 1.000 | 0.000 | 0.000 | 1.000 | 0.000 | 0.000 | 1.000 | 0.000 | 0.000 |
| 223 | IC 3721 | 0.347 | 0.653 | 0.000 | 1.000 | 0.000 | 0.000 | 1.000 | 0.000 | 0.000 |
| 224 | NGC 4670 | 1.000 | 0.000 | 0.000 | 1.000 | 0.000 | 0.000 | 1.000 | 0.000 | 0.000 |

**Table 7.A.5:** Continued

| SFRS | Galaxy | [N II]/Hα | | | [S II]/Hα | | | [O I]/Hα | | |
|---|---|---|---|---|---|---|---|---|---|---|
| | | H II | TO | Sy/LINER | H II | LINER | Sy | H II | LINER | Sy |
| 225 | NGC 4675 | 0.000 | 1.000 | 0.000 | 1.000 | 0.000 | 0.000 | 1.000 | 0.000 | 0.000 |
| 226 | MCG 7-26-051 | 0.000 | 1.000 | 0.000 | 1.000 | 0.000 | 0.000 | 0.757 | 0.053 | 0.190 |
| 227 | NGC 4689 | 0.000 | 1.000 | 0.000 | 1.000 | 0.000 | 0.000 | 0.382 | 0.617 | 0.001 |
| 228 | NGC 4688 | 0.838 | 0.161 | 0.001 | 0.458 | 0.335 | 0.207 | 0.498 | 0.502 | 0.000 |
| 229 | NGC 4704 | 0.000 | 0.000 | 1.000 | 0.000 | 0.971 | 0.029 | 0.000 | 0.379 | 0.621 |
| 230 | NGC 4701 | 1.000 | 0.000 | 0.000 | 1.000 | 0.000 | 0.000 | 1.000 | 0.000 | 0.000 |
| 231 | IRAS 12468+3436 | 0.000 | 0.956 | 0.044 | 0.478 | 0.034 | 0.488 | 0.000 | 0.422 | 0.578 |
| 232 | IRAS 12470+1404 | 0.000 | 1.000 | 0.000 | 1.000 | 0.000 | 0.000 | 1.000 | 0.000 | 0.000 |
| 233 | MCG 8-23-097 | 0.000 | 0.536 | 0.464 | 0.986 | 0.000 | 0.014 | 0.770 | 0.036 | 0.194 |
| 234 | NGC 4747 | 0.945 | 0.054 | 0.001 | 0.799 | 0.135 | 0.066 | 0.000 | 0.000 | 0.000 |
| 235 | UGC 8017 | 0.000 | 1.000 | 0.000 | 1.000 | 0.000 | 0.000 | 0.010 | 0.990 | 0.000 |
| 236 | NGC 4765 | 1.000 | 0.000 | 0.000 | 1.000 | 0.000 | 0.000 | 1.000 | 0.000 | 0.000 |
| 237 | VCC 2096 | 0.024 | 0.976 | 0.000 | 1.000 | 0.000 | 0.000 | 1.000 | 0.000 | 0.000 |
| 238 | UGC 8041 | 1.000 | 0.000 | 0.000 | 1.000 | 0.000 | 0.000 | 1.000 | 0.000 | 0.000 |
| 240 | NGC 4837_NED01 | 0.000 | 1.000 | 0.000 | 1.000 | 0.000 | 0.000 | 0.927 | 0.073 | 0.000 |
| 241 | UM 530 | 1.000 | 0.000 | 0.000 | 1.000 | 0.000 | 0.000 | 1.000 | 0.000 | 0.000 |
| 242 | NGC 4861 | 1.000 | 0.000 | 0.000 | 1.000 | 0.000 | 0.000 | 1.000 | 0.000 | 0.000 |
| 243 | NGC 4868 | 1.000 | 0.000 | 0.000 | 1.000 | 0.000 | 0.000 | 1.000 | 0.000 | 0.000 |
| 244 | NGC 4922_NED02 | 0.000 | 0.000 | 1.000 | 0.000 | 0.000 | 1.000 | 0.000 | 0.000 | 1.000 |
| 245 | UGC 8179 | 0.570 | 0.430 | 0.000 | 1.000 | 0.000 | 0.000 | 0.666 | 0.334 | 0.000 |
| 246 | NGC 5001 | 0.000 | 1.000 | 0.000 | 1.000 | 0.000 | 0.000 | 0.792 | 0.154 | 0.054 |
| 247 | IC 856 | 1.000 | 0.000 | 0.000 | 1.000 | 0.000 | 0.000 | 1.000 | 0.000 | 0.000 |

**Table 7.A.5:** Continued

| SFRS | Galaxy | [N II]/H$\alpha$ | | | [S II]/H$\alpha$ | | | [O I]/H$\alpha$ | | |
|---|---|---|---|---|---|---|---|---|---|---|
| | | H II | TO | Sy/LINER | H II | LINER | Sy | H II | LINER | Sy |
| 248 | UGC 8269 | 0.000 | 0.999 | 0.001 | 1.000 | 0.000 | 0.000 | 0.046 | 0.954 | 0.000 |
| 249 | NGC 5014 | 1.000 | 0.000 | 0.000 | 1.000 | 0.000 | 0.000 | 1.000 | 0.000 | 0.000 |
| 250 | NGC 5012 | 0.000 | 0.000 | 1.000 | 0.010 | 0.982 | 0.008 | 0.000 | 0.953 | 0.047 |
| 251 | IRAS 13116+4508 | 1.000 | 0.000 | 0.000 | 1.000 | 0.000 | 0.000 | 1.000 | 0.000 | 0.000 |
| 252 | IC 860 | 0.000 | 0.000 | 1.000 | 0.000 | 1.000 | 0.000 | 0.000 | 1.000 | 0.000 |
| 253 | IRAS 13144+4508 | 0.000 | 0.000 | 1.000 | 0.000 | 0.000 | 1.000 | 0.000 | 0.000 | 1.000 |
| 254 | NGC 5060 | 0.945 | 0.055 | 0.000 | 0.000 | 0.000 | 0.000 | 1.000 | 0.000 | 0.000 |
| 255 | UGC 8357_NED01 | 0.000 | 1.000 | 0.000 | 1.000 | 0.000 | 0.000 | 0.333 | 0.667 | 0.000 |
| 256 | UGC 8361 | 0.000 | 1.000 | 0.000 | 1.000 | 0.000 | 0.000 | 1.000 | 0.000 | 0.000 |
| 257 | IC 883 | 0.000 | 1.000 | 0.000 | 1.000 | 0.000 | 0.000 | 0.002 | 0.998 | 0.000 |
| 258 | NGC 5100_NED02 | 0.000 | 0.998 | 0.002 | 1.000 | 0.000 | 0.000 | 0.915 | 0.008 | 0.077 |
| 259 | NGC 5104 | 0.000 | 0.031 | 0.969 | 1.000 | 0.000 | 0.000 | 0.076 | 0.001 | 0.923 |
| 260 | NGC 5107 | 1.000 | 0.000 | 0.000 | 0.863 | 0.000 | 0.137 | 0.479 | 0.016 | 0.505 |
| 261 | NGC 5112 | 0.013 | 0.987 | 0.000 | 0.437 | 0.547 | 0.016 | 0.451 | 0.168 | 0.381 |
| 262 | NGC 5123 | 0.928 | 0.072 | 0.000 | 0.000 | 0.000 | 0.000 | 0.000 | 0.000 | 0.000 |
| 264 | IRAS 13232+1731 | 1.000 | 0.000 | 0.000 | 1.000 | 0.000 | 0.000 | 1.000 | 0.000 | 0.000 |
| 265 | NGC 5147 | 0.989 | 0.011 | 0.000 | 0.998 | 0.001 | 0.001 | 0.498 | 0.502 | 0.000 |
| 266 | NGC 5204 | 1.000 | 0.000 | 0.000 | 0.000 | 1.000 | 0.000 | 0.498 | 0.502 | 0.000 |
| 267 | UGC 8502_NED02 | 1.000 | 0.000 | 0.000 | 1.000 | 0.000 | 0.000 | 1.000 | 0.000 | 0.000 |
| 268 | UGC 8561 | 0.994 | 0.006 | 0.000 | 1.000 | 0.000 | 0.000 | 1.000 | 0.000 | 0.000 |
| 269 | NGC 5230 | 0.927 | 0.073 | 0.000 | ... | ... | ... | ... | ... | ... |
| 271 | NGC 5256 | 0.000 | 0.000 | 1.000 | 0.000 | 0.000 | 1.000 | 0.000 | 0.000 | 1.000 |

**Table 7.A.5:** Continued

| SFRS | Galaxy | [N II]/Hα | | | [S II]/Hα | | | [O I]/Hα | | |
|---|---|---|---|---|---|---|---|---|---|---|
| | | H II | TO | Sy/LINER | H II | LINER | Sy | H II | LINER | Sy |
| 272 | UGC 8626 | 0.999 | 0.001 | 0.000 | 1.000 | 0.000 | 0.000 | 1.000 | 0.000 | 0.000 |
| 273 | NGC 5263 | 0.398 | 0.602 | 0.000 | 1.000 | 0.000 | 0.000 | 1.000 | 0.000 | 0.000 |
| 274 | MCG 1-35-028 | 0.000 | 1.000 | 0.000 | 1.000 | 0.000 | 0.000 | 1.000 | 0.000 | 0.000 |
| 275 | IC 910 | 0.000 | 0.000 | 1.000 | 0.000 | 0.000 | 1.000 | 0.000 | 0.000 | 1.000 |
| 276 | MK 268 | 0.000 | 0.000 | 1.000 | 0.000 | 1.000 | 0.000 | 0.000 | 0.140 | 0.860 |
| 277 | NGC 5278 | 0.000 | 0.045 | 0.955 | 0.000 | 1.000 | 0.000 | 0.000 | 0.868 | 0.132 |
| 278 | NGC 5273 | 0.000 | 0.000 | 1.000 | 0.000 | 0.000 | 1.000 | 0.000 | 0.000 | 1.000 |
| 279 | UGC 8685 | 0.026 | 0.974 | 0.000 | 1.000 | 0.000 | 0.000 | 1.000 | 0.000 | 0.000 |
| 280 | UGC 8686 | 0.000 | 1.000 | 0.000 | 1.000 | 0.000 | 0.000 | 0.880 | 0.093 | 0.027 |
| 281 | UGC 8696 | 0.000 | 0.000 | 1.000 | 0.000 | 0.000 | 1.000 | 0.000 | 0.000 | 1.000 |
| 282 | NGC 5297 | 0.000 | 0.000 | 1.000 | 0.000 | 1.000 | 0.000 | 0.000 | 1.000 | 0.000 |
| 283 | MK 796 | 0.000 | 1.000 | 0.000 | 1.000 | 0.000 | 0.000 | 1.000 | 0.000 | 0.000 |
| 284 | IRAS 13446+1121 | 0.000 | 0.000 | 1.000 | 0.000 | 0.000 | 1.000 | 0.000 | 0.000 | 1.000 |
| 285 | NGC 5303 | 1.000 | 0.000 | 0.000 | 1.000 | 0.000 | 0.000 | 0.776 | 0.223 | 0.001 |
| 286 | NGC 5313 | 0.000 | 0.000 | 1.000 | 0.000 | 1.000 | 0.000 | 0.000 | 1.000 | 0.000 |
| 287 | MCG 3-35-034_NED01 | 0.000 | 1.000 | 0.000 | 1.000 | 0.000 | 0.000 | 0.000 | 1.000 | 0.000 |
| 288 | NGC 5347 | 0.000 | 0.000 | 1.000 | 0.000 | 0.000 | 1.000 | 0.000 | 0.000 | 1.000 |
| 289 | NGC 5350 | 0.000 | 1.000 | 0.000 | 1.000 | 0.000 | 0.000 | 1.000 | 0.000 | 0.000 |
| 290 | NGC 5368 | 0.000 | 1.000 | 0.000 | 1.000 | 0.000 | 0.000 | 0.995 | 0.005 | 0.000 |
| 291 | UGC 8827 | 0.000 | 1.000 | 0.000 | 1.000 | 0.000 | 0.000 | 1.000 | 0.000 | 0.000 |
| 292 | UGC 8850 | 0.000 | 0.000 | 1.000 | 0.000 | 0.000 | 1.000 | 0.000 | 0.000 | 1.000 |
| 293 | UGC 8856_NED01 | 0.000 | 1.000 | 0.000 | 1.000 | 0.000 | 0.000 | 1.000 | 0.000 | 0.000 |

**Table 7.A.5:** Continued

| SFRS | Galaxy | [N II]/H$\alpha$ | | | [S II]/H$\alpha$ | | | [O I]/H$\alpha$ | | |
|---|---|---|---|---|---|---|---|---|---|---|
| | | H II | TO | Sy/LINER | H II | LINER | Sy | H II | LINER | Sy |
| 294 | NGC 5374 | 1.000 | 0.000 | 0.000 | 1.000 | 0.000 | 0.000 | 0.193 | 0.807 | 0.000 |
| 295 | UGC 8902 | 0.000 | 1.000 | 0.000 | 1.000 | 0.000 | 0.000 | 0.239 | 0.743 | 0.018 |
| 296 | NGC 5403 | 0.000 | 1.000 | 0.000 | 1.000 | 0.000 | 0.000 | ... | ... | ... |
| 297 | MCG 7-29-036 | 0.378 | 0.622 | 0.000 | 1.000 | 0.000 | 0.000 | 1.000 | 0.000 | 0.000 |
| 298 | NGC 5414 | 1.000 | 0.000 | 0.000 | 1.000 | 0.000 | 0.000 | 1.000 | 0.000 | 0.000 |
| 299 | MCG 5-33-046 | 0.000 | 1.000 | 0.000 | 1.000 | 0.000 | 0.000 | 1.000 | 0.000 | 0.000 |
| 300 | NGC 5474 | 1.000 | 0.000 | 0.000 | 1.000 | 0.000 | 0.000 | 0.944 | 0.001 | 0.055 |
| 301 | NGC 5480 | 1.000 | 0.000 | 0.000 | 1.000 | 0.000 | 0.000 | 0.995 | 0.005 | 0.000 |
| 302 | MCG 6-31-070 | 0.000 | 1.000 | 0.000 | 1.000 | 0.000 | 0.000 | 0.938 | 0.062 | 0.000 |
| 303 | CGCG 74-129 | 0.000 | 0.000 | 1.000 | 0.000 | 0.000 | 1.000 | 0.000 | 0.026 | 0.974 |
| 304 | NGC 5520 | 0.412 | 0.588 | 0.000 | 1.000 | 0.000 | 0.000 | 0.977 | 0.023 | 0.000 |
| 305 | NGC 5515 | 0.000 | 0.006 | 0.994 | 0.710 | 0.012 | 0.278 | 0.069 | 0.324 | 0.607 |
| 306 | NGC 5526_NED02 | 1.000 | 0.000 | 0.000 | 1.000 | 0.000 | 0.000 | 1.000 | 0.000 | 0.000 |
| 307 | NGC 5522 | 0.000 | 1.000 | 0.000 | 0.502 | 0.498 | 0.000 | 0.577 | 0.422 | 0.001 |
| 308 | NGC 5541 | 0.002 | 0.984 | 0.014 | 0.998 | 0.000 | 0.002 | 0.496 | 0.411 | 0.093 |
| 309 | IC 4395 | 0.000 | 1.000 | 0.000 | 1.000 | 0.000 | 0.000 | 1.000 | 0.000 | 0.000 |
| 310 | UGC 9165 | 0.436 | 0.563 | 0.001 | 0.969 | 0.015 | 0.016 | 0.788 | 0.167 | 0.045 |
| 311 | MK 1490 | 0.000 | 1.000 | 0.000 | 1.000 | 0.000 | 0.000 | 1.000 | 0.000 | 0.000 |
| 312 | NGC 5585 | 1.000 | 0.000 | 0.000 | 1.000 | 0.000 | 0.000 | 0.288 | 0.004 | 0.708 |
| 313 | IC 4408 | 0.000 | 1.000 | 0.000 | 1.000 | 0.000 | 0.000 | 1.000 | 0.000 | 0.000 |
| 314 | NGC 5584 | 1.000 | 0.000 | 0.000 | 1.000 | 0.000 | 0.000 | ... | ... | ... |
| 315 | NGC 5633 | 1.000 | 0.000 | 0.000 | 1.000 | 0.000 | 0.000 | 1.000 | 0.000 | 0.000 |

**Table 7.A.5:** Continued

| SFRS | Galaxy | [N II]/Hα | | | [S II]/Hα | | | [O I]/Hα | | |
|---|---|---|---|---|---|---|---|---|---|---|
| | | H II | TO | Sy/LINER | H II | LINER | Sy | H II | LINER | Sy |
| 316 | NGC 5660 | 1.000 | 0.000 | 0.000 | 1.000 | 0.000 | 0.000 | 0.995 | 0.005 | 0.000 |
| 317 | NGC 5656 | 0.000 | 0.129 | 0.871 | 0.106 | 0.498 | 0.396 | 0.000 | 0.994 | 0.006 |
| 318 | NGC 5657 | 1.000 | 0.000 | 0.000 | 1.000 | 0.000 | 0.000 | 1.000 | 0.000 | 0.000 |
| 319 | CGCG 133-083 | 0.000 | 1.000 | 0.000 | 1.000 | 0.000 | 0.000 | 1.000 | 0.000 | 0.000 |
| 320 | MCG 7-30-028 | 1.000 | 0.000 | 0.000 | 1.000 | 0.000 | 0.000 | 1.000 | 0.000 | 0.000 |
| 321 | MCG 6-32-070 | 1.000 | 0.000 | 0.000 | 1.000 | 0.000 | 0.000 | 1.000 | 0.000 | 0.000 |
| 322 | UGC 9412 | 0.000 | 0.000 | 1.000 | 0.000 | 0.000 | 1.000 | 0.000 | 0.000 | 1.000 |
| 323 | NGC 5698 | 0.990 | 0.010 | 0.000 | 1.000 | 0.000 | 0.000 | 1.000 | 0.000 | 0.000 |
| 324 | NGC 5691 | 1.000 | 0.000 | 0.000 | 1.000 | 0.000 | 0.000 | 1.000 | 0.000 | 0.000 |
| 325 | MCG 9-24-035 | 0.000 | 1.000 | 0.000 | 1.000 | 0.000 | 0.000 | 1.000 | 0.000 | 0.000 |
| 326 | MCG 9-24-038 | 0.001 | 0.999 | 0.000 | 1.000 | 0.000 | 0.000 | 1.000 | 0.000 | 0.000 |
| 327 | UGC 9560 | 1.000 | 0.000 | 0.000 | 1.000 | 0.000 | 0.000 | 1.000 | 0.000 | 0.000 |
| 328 | IC 1076 | 1.000 | 0.000 | 0.000 | 1.000 | 0.000 | 0.000 | 1.000 | 0.000 | 0.000 |
| 329 | IRAS 14538+1730 | 0.000 | 1.000 | 0.000 | 1.000 | 0.000 | 0.000 | 0.698 | 0.204 | 0.098 |
| 330 | NGC 5795 | 1.000 | 0.000 | 0.000 | 1.000 | 0.000 | 0.000 | 1.000 | 0.000 | 0.000 |
| 331 | UGC 9618_NED02 | 0.000 | 0.979 | 0.021 | 1.000 | 0.000 | 0.000 | 0.501 | 0.005 | 0.494 |
| 332 | UGC 9639 | 0.000 | 0.000 | 1.000 | 0.000 | 0.326 | 0.674 | 0.000 | 0.097 | 0.903 |
| 333 | MCG 6-33-022 | 0.000 | 1.000 | 0.000 | 1.000 | 0.000 | 0.000 | 0.630 | 0.128 | 0.242 |
| 334 | NGC 5879 | 0.000 | 0.000 | 1.000 | 0.000 | 1.000 | 0.000 | 0.000 | 1.000 | 0.000 |
| 335 | MCG 9-25-036 | 1.000 | 0.000 | 0.000 | 1.000 | 0.000 | 0.000 | 1.000 | 0.000 | 0.000 |
| 337 | NGC 5905 | 1.000 | 0.000 | 0.000 | 1.000 | 0.000 | 0.000 | 1.000 | 0.000 | 0.000 |
| 336 | NGC 5899 | 0.000 | 0.000 | 1.000 | 0.000 | 0.000 | 1.000 | 0.000 | 0.000 | 1.000 |

**Table 7.A.5:** Continued

| SFRS | Galaxy | [N II]/H$\alpha$ | | | [S II]/H$\alpha$ | | | [O I]/H$\alpha$ | | |
|---|---|---|---|---|---|---|---|---|---|---|
| | | H II | TO | Sy/LINER | H II | LINER | Sy | H II | LINER | Sy |
| 338 | MK 848 | 0.000 | 1.000 | 0.000 | 1.000 | 0.000 | 0.000 | 1.000 | 0.000 | 0.000 |
| 339 | IC 4553 | 0.000 | 0.000 | 1.000 | 0.000 | 1.000 | 0.000 | 0.000 | 0.150 | 0.850 |
| 340 | UGC 9922_NED02 | 1.000 | 0.000 | 0.000 | 1.000 | 0.000 | 0.000 | 1.000 | 0.000 | 0.000 |
| 341 | IC 4567 | 0.003 | 0.997 | 0.000 | 1.000 | 0.000 | 0.000 | 0.657 | 0.343 | 0.000 |
| 342 | MCG 4-37-016 | 0.000 | 1.000 | 0.000 | 1.000 | 0.000 | 0.000 | 1.000 | 0.000 | 0.000 |
| 343 | NGC 5975 | 0.000 | 0.069 | 0.931 | 1.000 | 0.000 | 0.000 | 0.000 | 0.971 | 0.029 |
| 344 | NGC 5980 | 0.007 | 0.992 | 0.001 | 0.992 | 0.003 | 0.005 | 0.627 | 0.330 | 0.043 |
| 345 | NGC 5992 | 1.000 | 0.000 | 0.000 | 1.000 | 0.000 | 0.000 | 1.000 | 0.000 | 0.000 |
| 346 | NGC 5996 | 1.000 | 0.000 | 0.000 | 1.000 | 0.000 | 0.000 | 1.000 | 0.000 | 0.000 |
| 347 | IRAS 15519+3537 | 0.816 | 0.184 | 0.000 | 1.000 | 0.000 | 0.000 | 0.526 | 0.472 | 0.002 |
| 348 | UGC 10099 | 0.000 | 1.000 | 0.000 | 1.000 | 0.000 | 0.000 | 1.000 | 0.000 | 0.000 |
| 349 | MCG 5-38-006 | 0.000 | 1.000 | 0.000 | 1.000 | 0.000 | 0.000 | 1.000 | 0.000 | 0.000 |
| 350 | UGC 10120 | 1.000 | 0.000 | 0.000 | 1.000 | 0.000 | 0.000 | 1.000 | 0.000 | 0.000 |
| 351 | NGC 6027A | 0.158 | 0.842 | 0.000 | 1.000 | 0.000 | 0.000 | 0.997 | 0.003 | 0.000 |
| 352 | NGC 6040B | 0.000 | 0.000 | 1.000 | 0.000 | 0.974 | 0.026 | 0.000 | 0.861 | 0.139 |
| 353 | UGC 10200 | 1.000 | 0.000 | 0.000 | 1.000 | 0.000 | 0.000 | 1.000 | 0.000 | 0.000 |
| 354 | IRAS 16052+5334 | 0.000 | 1.000 | 0.000 | 1.000 | 0.000 | 0.000 | 0.879 | 0.121 | 0.000 |
| 355 | IRAS 16053+1836 | 0.000 | 1.000 | 0.000 | 1.000 | 0.000 | 0.000 | 1.000 | 0.000 | 0.000 |
| 356 | NGC 6090_NED01 | 0.000 | 1.000 | 0.000 | 1.000 | 0.000 | 0.000 | 1.000 | 0.000 | 0.000 |
| 357 | UGC 10273_NED01 | 1.000 | 0.000 | 0.000 | 1.000 | 0.000 | 0.000 | 1.000 | 0.000 | 0.000 |
| 358 | P 16150+2233 | 0.000 | 0.000 | 1.000 | 0.000 | 0.000 | 1.000 | 0.000 | 0.000 | 1.000 |
| 359 | UGC 10322 | 1.000 | 0.000 | 0.000 | 1.000 | 0.000 | 0.000 | 1.000 | 0.000 | 0.000 |

**Table 7.A.5:** Continued

| SFRS | Galaxy | [N II]/H$\alpha$ | | | [S II]/H$\alpha$ | | | [O I]/H$\alpha$ | | |
|---|---|---|---|---|---|---|---|---|---|---|
| | | H II | TO | Sy/LINER | H II | LINER | Sy | H II | LINER | Sy |
| 360 | NGC 6120 | 0.167 | 0.833 | 0.000 | 1.000 | 0.000 | 0.000 | 0.975 | 0.025 | 0.000 |
| 361 | MCG 3-42-004 | 0.957 | 0.043 | 0.000 | ... | ... | ... | 0.005 | 0.995 | 0.000 |
| 362 | UGC 10407 | 1.000 | 0.000 | 0.000 | 1.000 | 0.000 | 0.000 | 1.000 | 0.000 | 0.000 |
| 363 | IRAS 16320+3922 | 0.000 | 1.000 | 0.000 | 0.284 | 0.716 | 0.000 | 0.000 | 1.000 | 0.000 |
| 364 | NGC 6186 | 1.000 | 0.000 | 0.000 | 1.000 | 0.000 | 0.000 | 1.000 | 0.000 | 0.000 |
| 365 | MCG 9-27-053 | 0.000 | 1.000 | 0.000 | 1.000 | 0.000 | 0.000 | 0.667 | 0.327 | 0.006 |
| 366 | UGC 10514 | 1.000 | 0.000 | 0.000 | 1.000 | 0.000 | 0.000 | 1.000 | 0.000 | 0.000 |
| 367 | IRAS 16435+2154 | 1.000 | 0.000 | 0.000 | 1.000 | 0.000 | 0.000 | 1.000 | 0.000 | 0.000 |
| 368 | IC 4623 | 0.998 | 0.002 | 0.000 | 1.000 | 0.000 | 0.000 | 0.966 | 0.034 | 0.000 |
| 369 | IRAS 16516+3030 | 0.000 | 0.000 | 1.000 | 0.000 | 1.000 | 0.000 | 0.019 | 0.981 | 0.000 |

**Table 7.A.5:** Probability classification for the different activity types based on the uncertainties of line measurements and following the methods outlined in Section 4.A.1.

# 8 Nuclear spectra

## 8.A Summary of plots

The nuclear plots of the SFRS galaxies as observed from the FAST long-slit spectrograph and the SDSS 3″ fibers. The observed spectrum is shown with a black line, the STARLIGHT fit with a red line, and the starlight subtracted spectrum with a blue line. For galaxies observed with the 600 l mm$^{-1}$ grating, the two separate exposures at the 3800 – 5700 Å and 5500 – 7800Å wavelength range are over-plotted in the same figure.

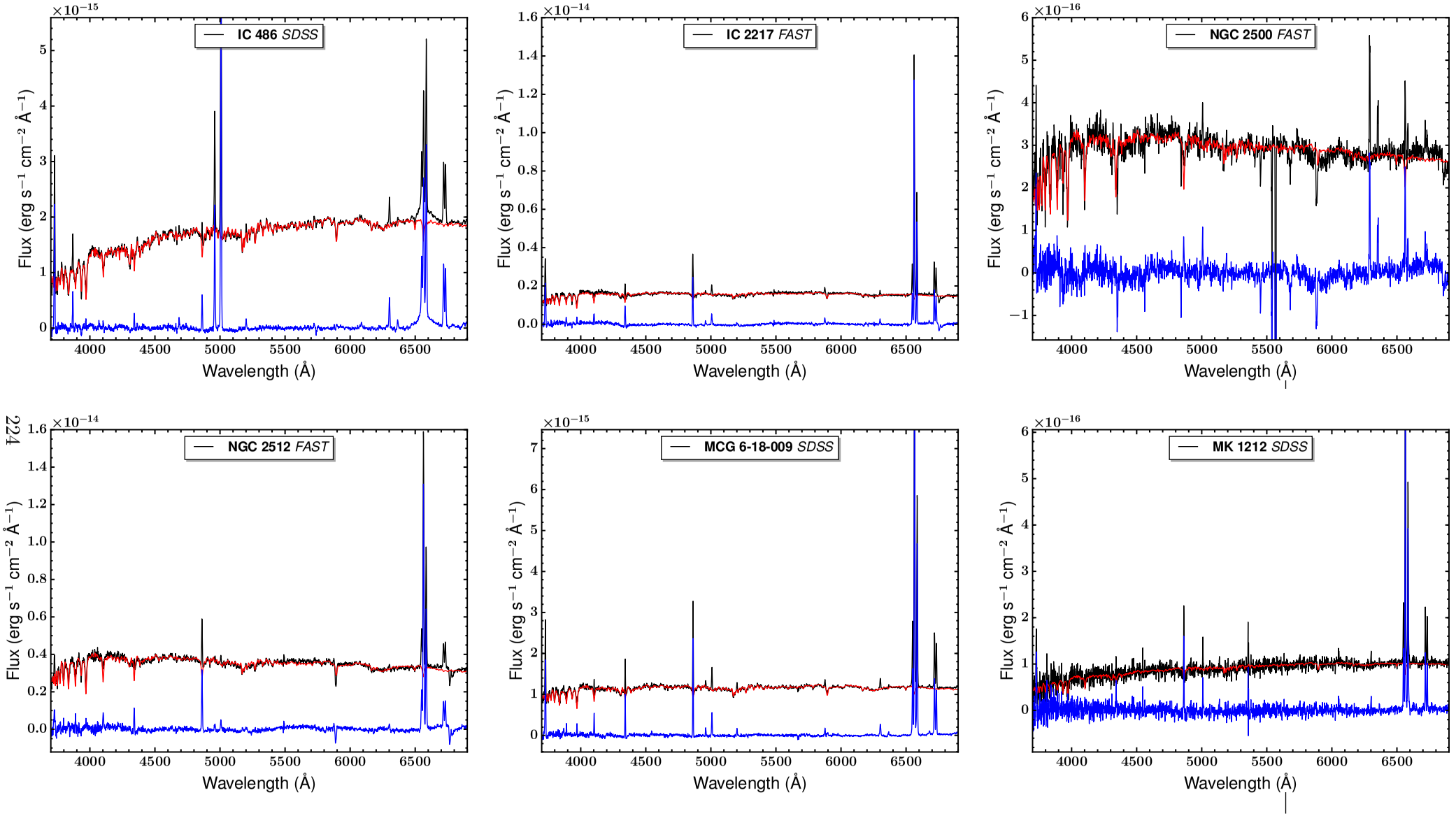


**Figure 8.A.1:** The nuclear spectra of IC 486, IC 2217, NGC 2500, NGC 2512, MCG 6-18-009, MK 1212. The observed spectrum is shown with a black line, the STARLIGHT fit with a red line, and the starlight subtracted spectrum with a blue line.

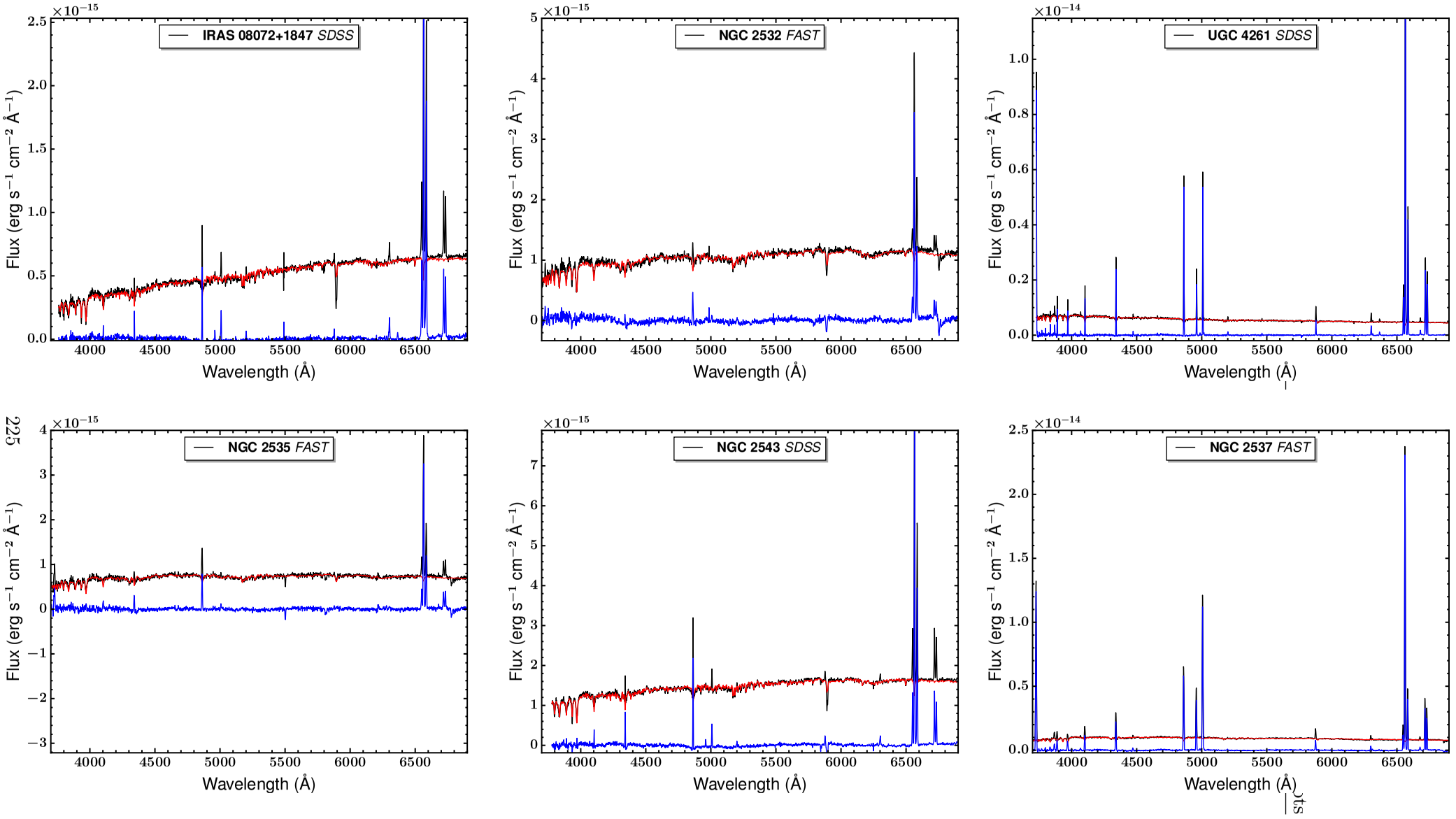


**Figure 8.A.2:** The nuclear spectra of IRAS 08072+1847, NGC 2532, UGC 4261, NGC 2535, NGC 2543, NGC 2537. The observed spectrum is shown with a black line, the STARLIGHT fit with a red line, and the starlight subtracted spectrum with a blue line.

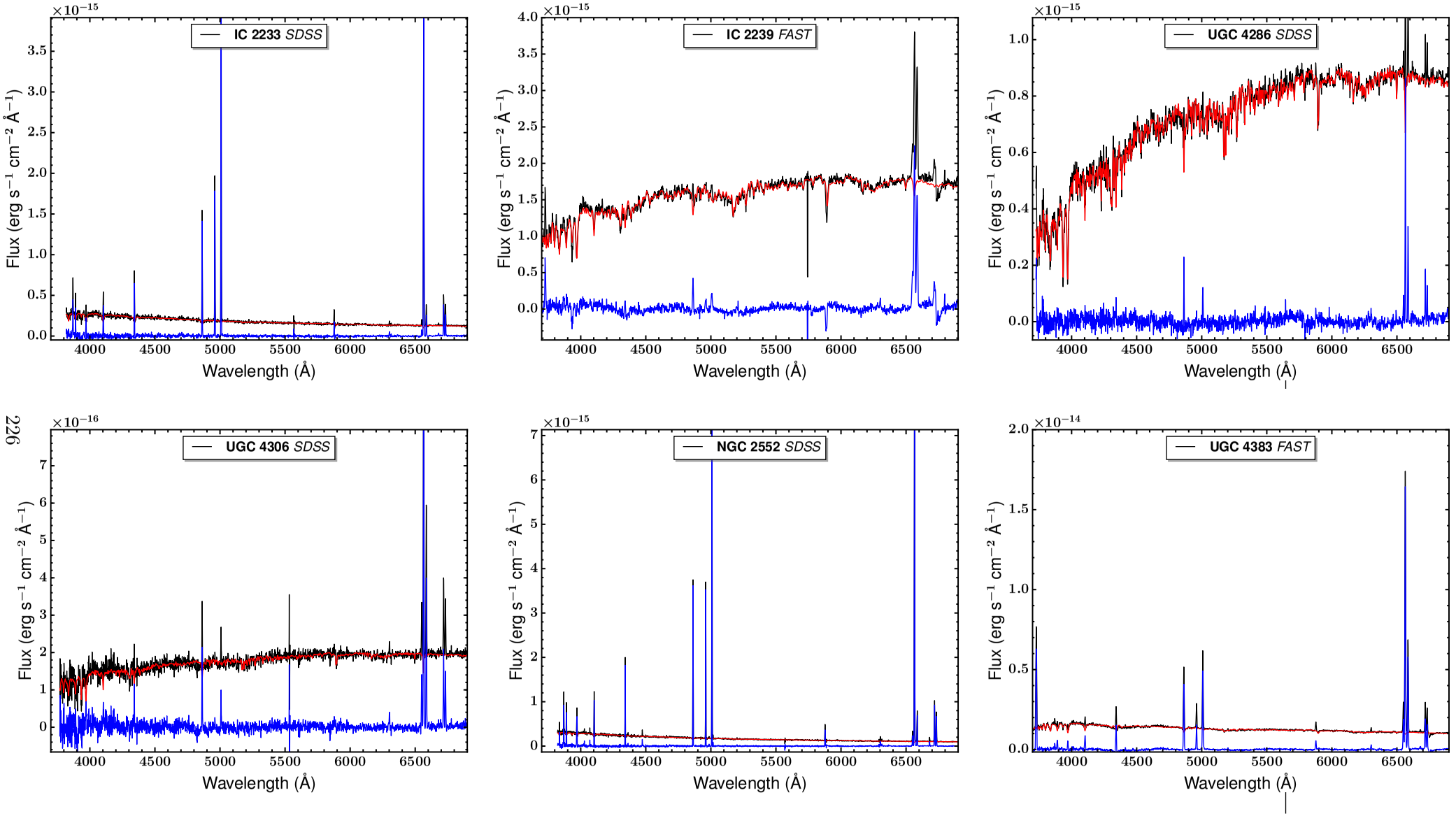


**Figure 8.A.3:** The nuclear spectra of IC 2233, IC 2239, UGC 4286, UGC 4306, NGC 2552, UGC 4383. The observed spectrum is shown with a black line, the STARLIGHT fit with a red line, and the starlight subtracted spectrum with a blue line.

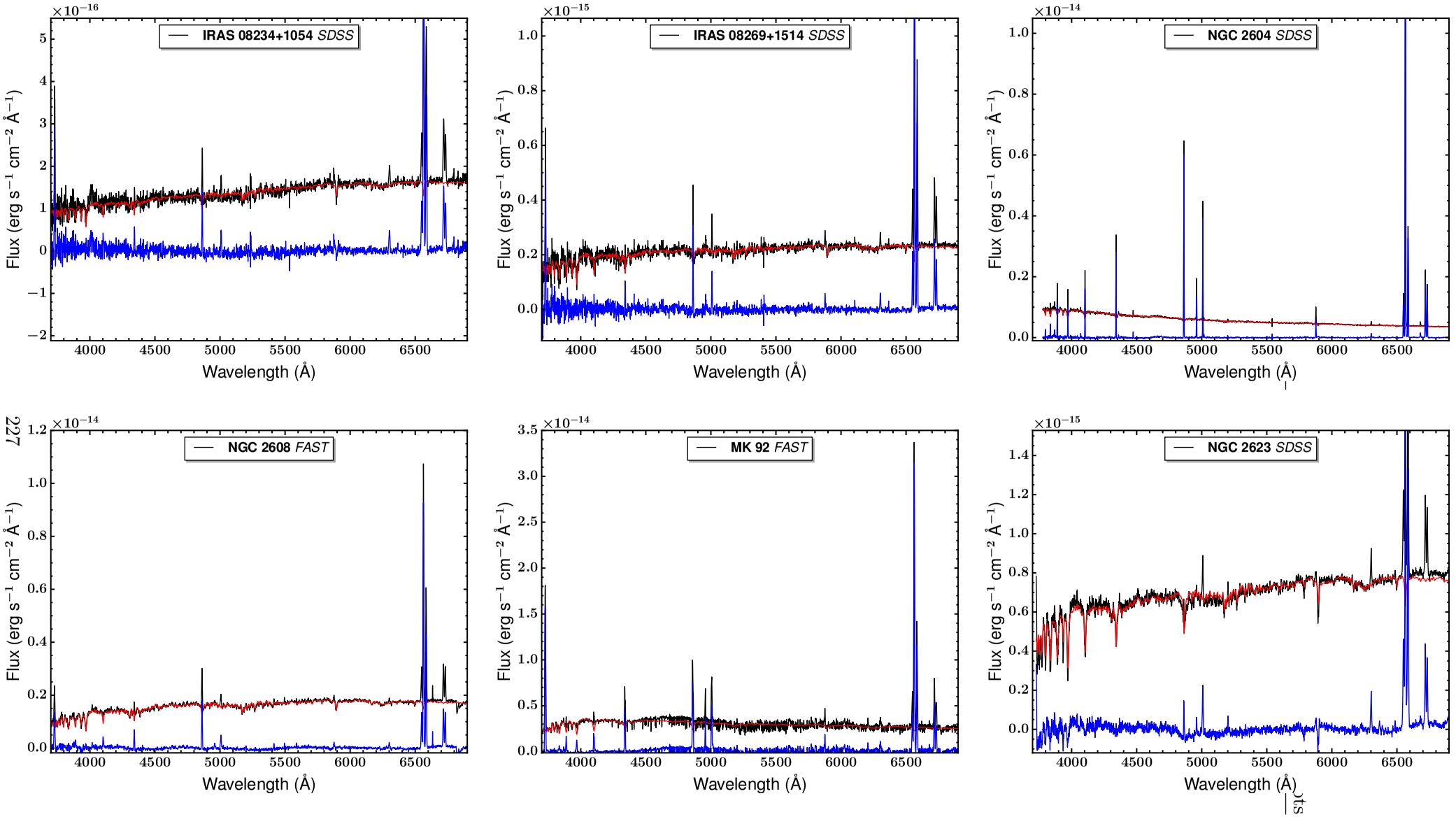


**Figure 8.A.4:** The nuclear spectra of IRAS 08234+1054, IRAS 08269+1514, NGC 2604, NGC 2608, MK 92, NGC 2623. The observed spectrum is shown with a black line, the STARLIGHT fit with a red line, and the starlight subtracted spectrum with a blue line.

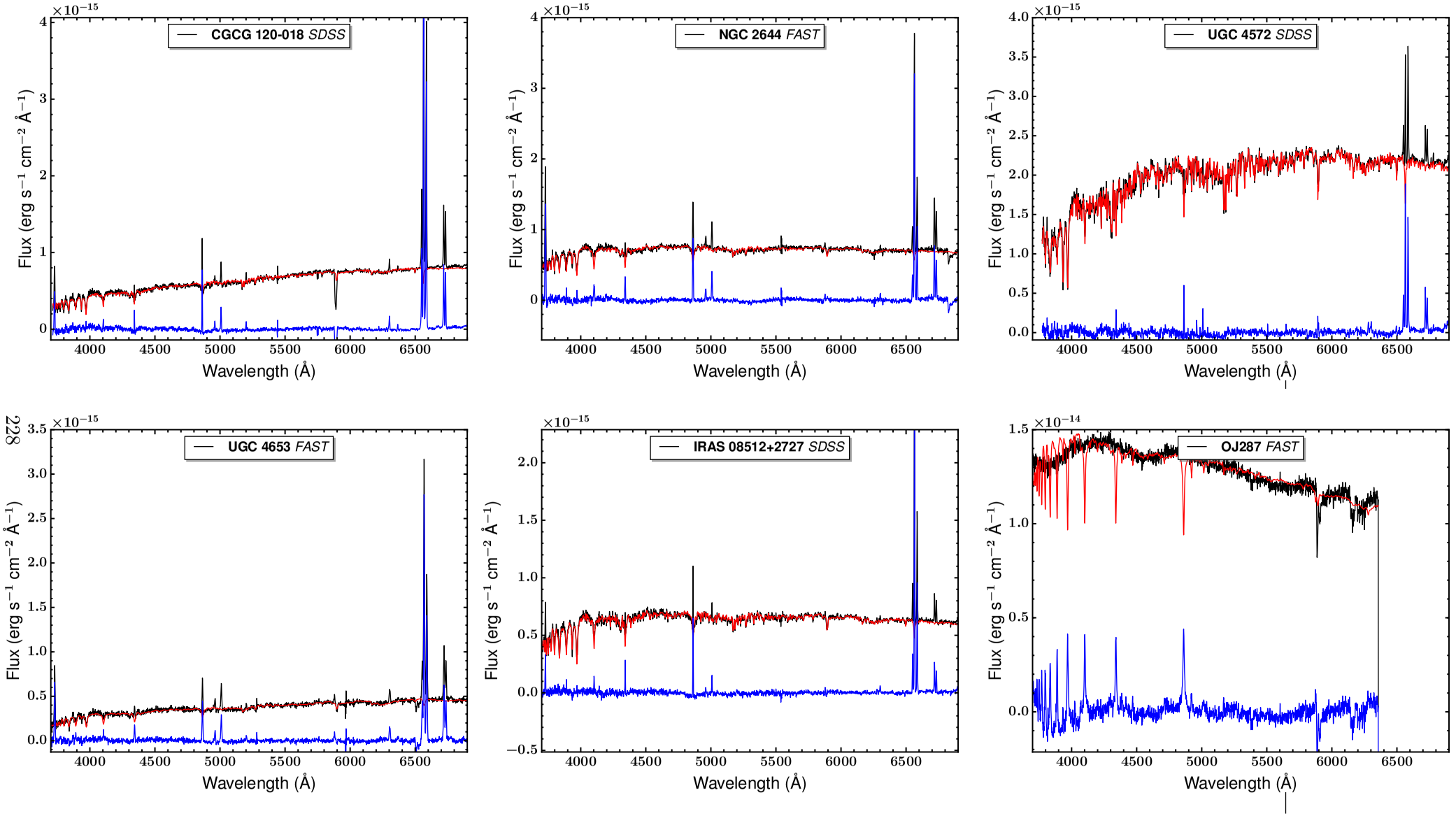


**Figure 8.A.5:** The nuclear spectra of CGCG 120-018, NGC 2644, UGC 4572, UGC 4653, IRAS 08512+2727, OJ 287. The observed spectrum is shown with a black line, the STARLIGHT fit with a red line, and the starlight subtracted spectrum with a blue line.

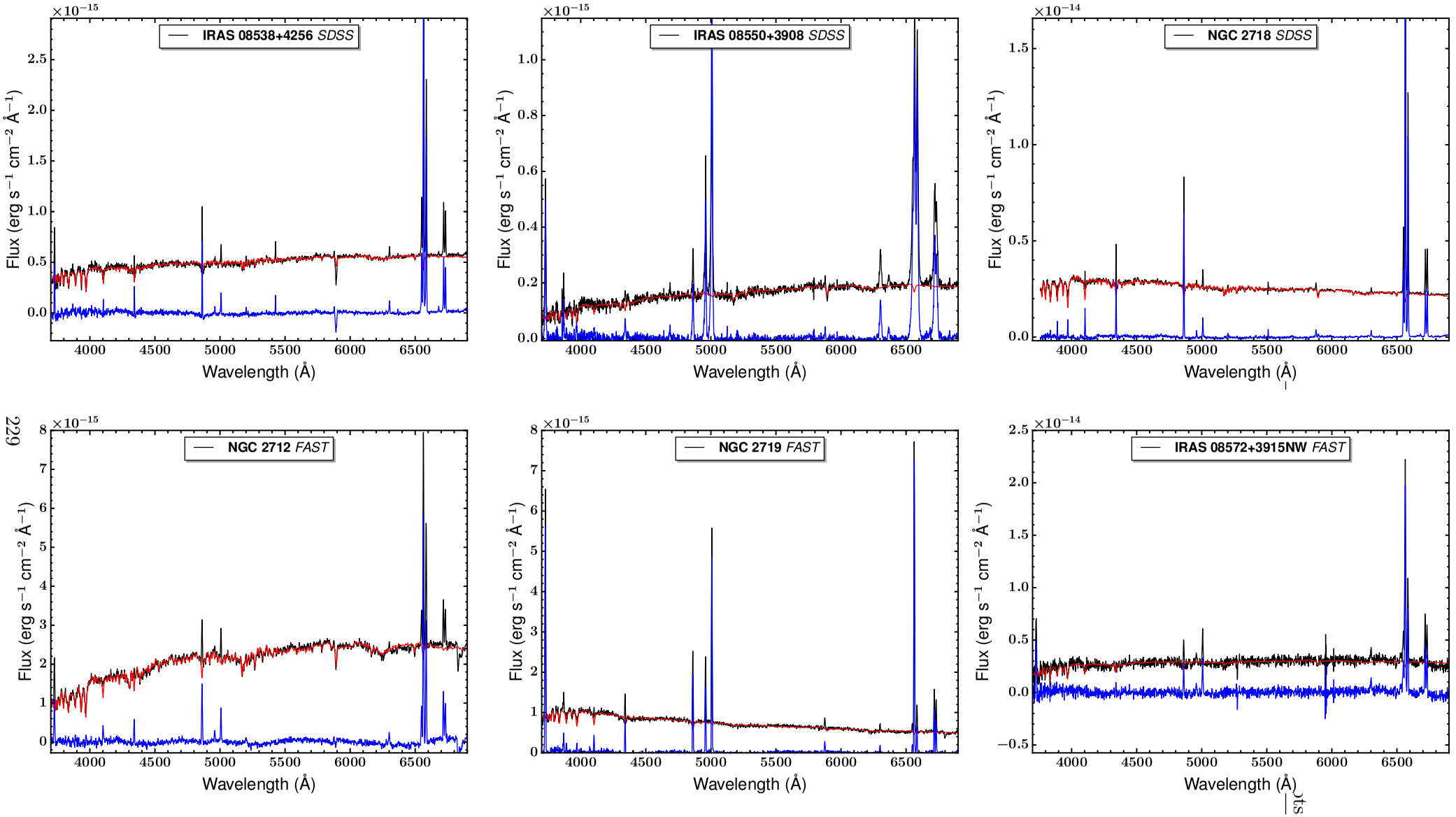


**Figure 8.A.6:** The nuclear spectra of IRAS 08538+4256, IRAS 08550+3908, NGC 2718, NGC 2712, NGC 2719, IRAS 08572+3915NW. The observed spectrum is shown with a black line, the STARLIGHT fit with a red line, and the starlight subtracted spectrum with a blue line.

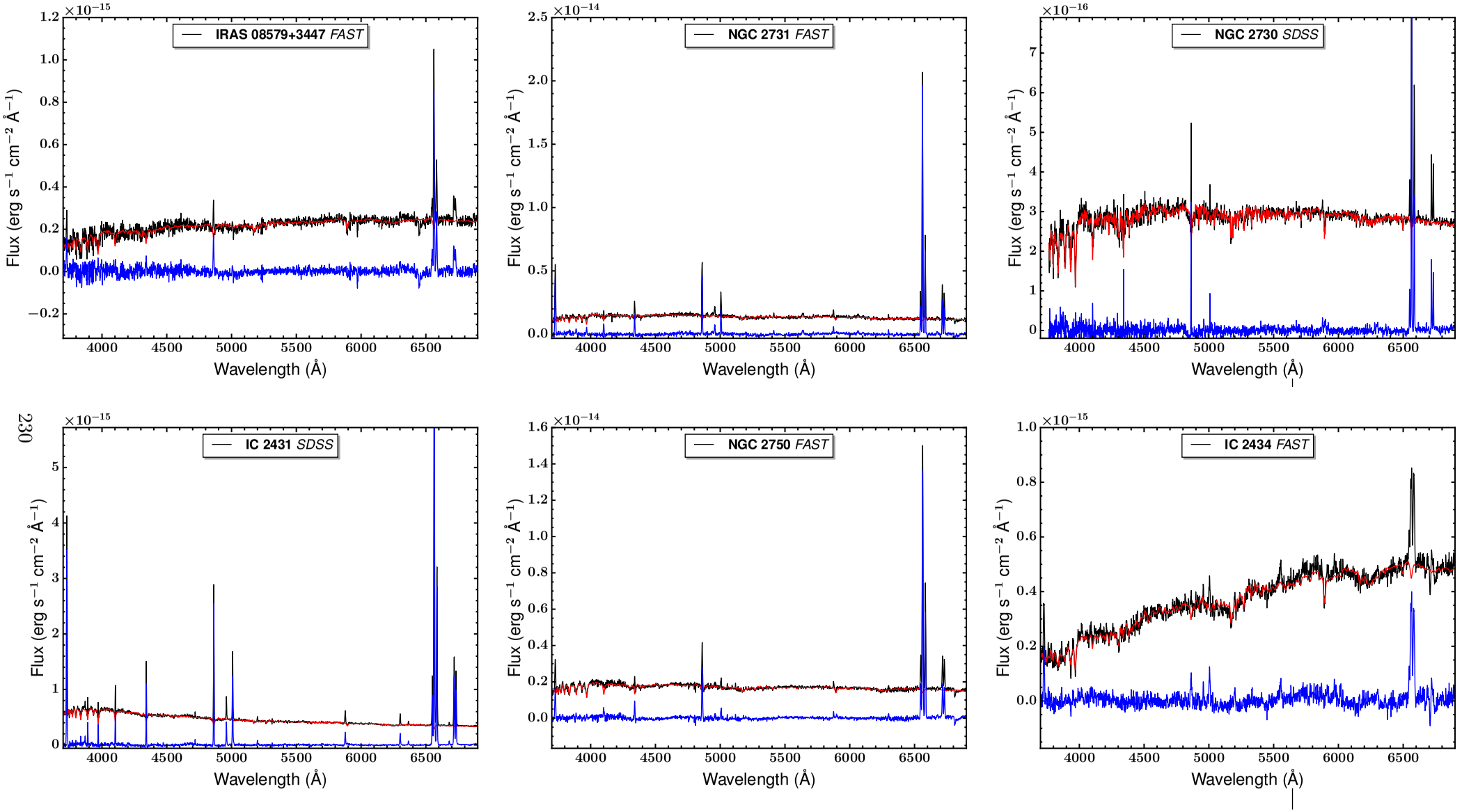


**Figure 8.A.7:** The nuclear spectra of IRAS 08579+3447, NGC 2731, NGC 2730, IC 2431, NGC 2750, IC 2434. The observed spectrum is shown with a black line, the STARLIGHT fit with a red line, and the starlight subtracted spectrum with a blue line.

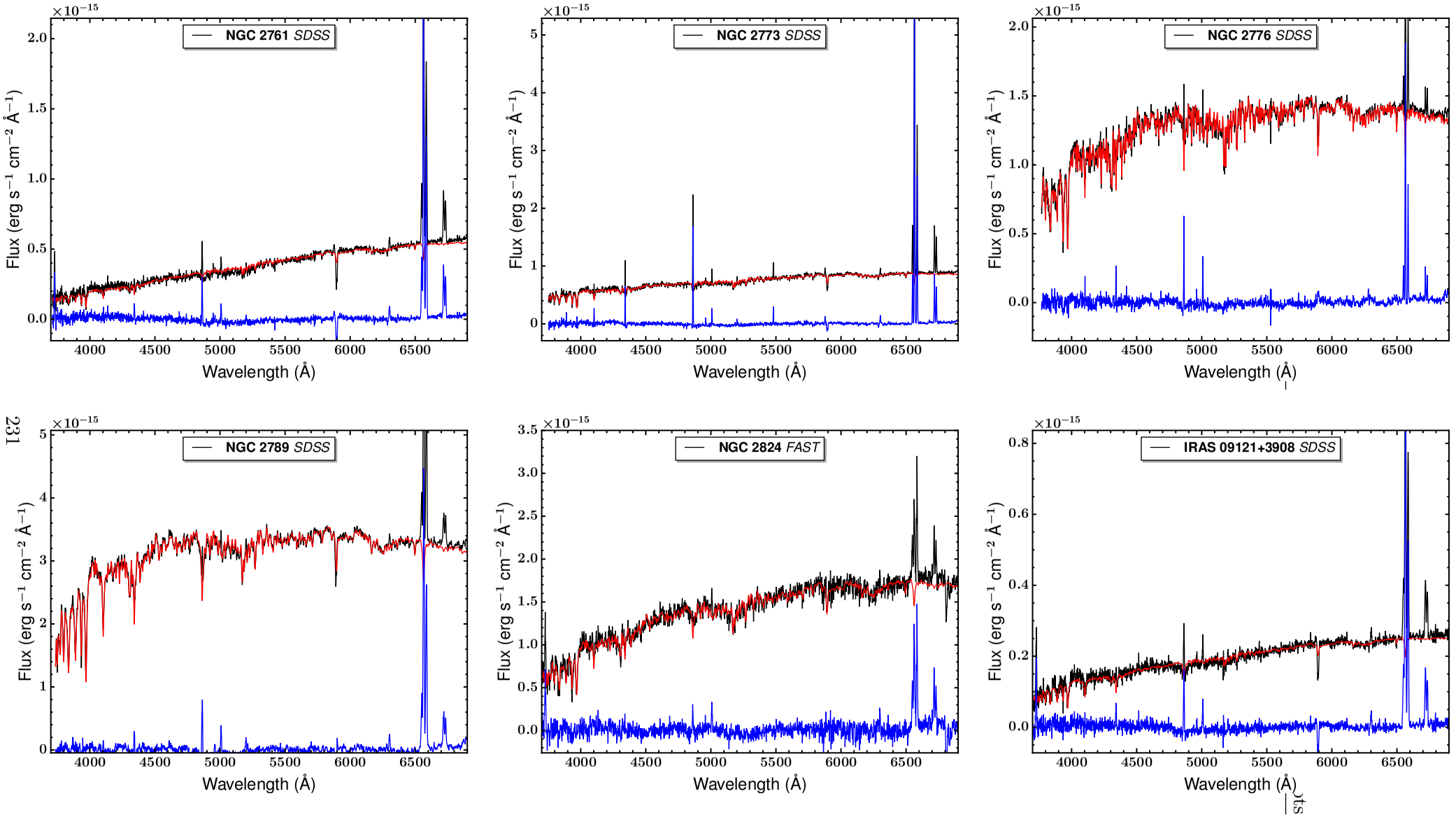


**Figure 8.A.8:** The nuclear spectra of NGC 2761, NGC 2773, NGC 2776, NGC 2789, NGC 2824, IRAS 09121+3908. The observed spectrum is shown with a black line, the STARLIGHT fit with a red line, and the starlight subtracted spectrum with a blue line.

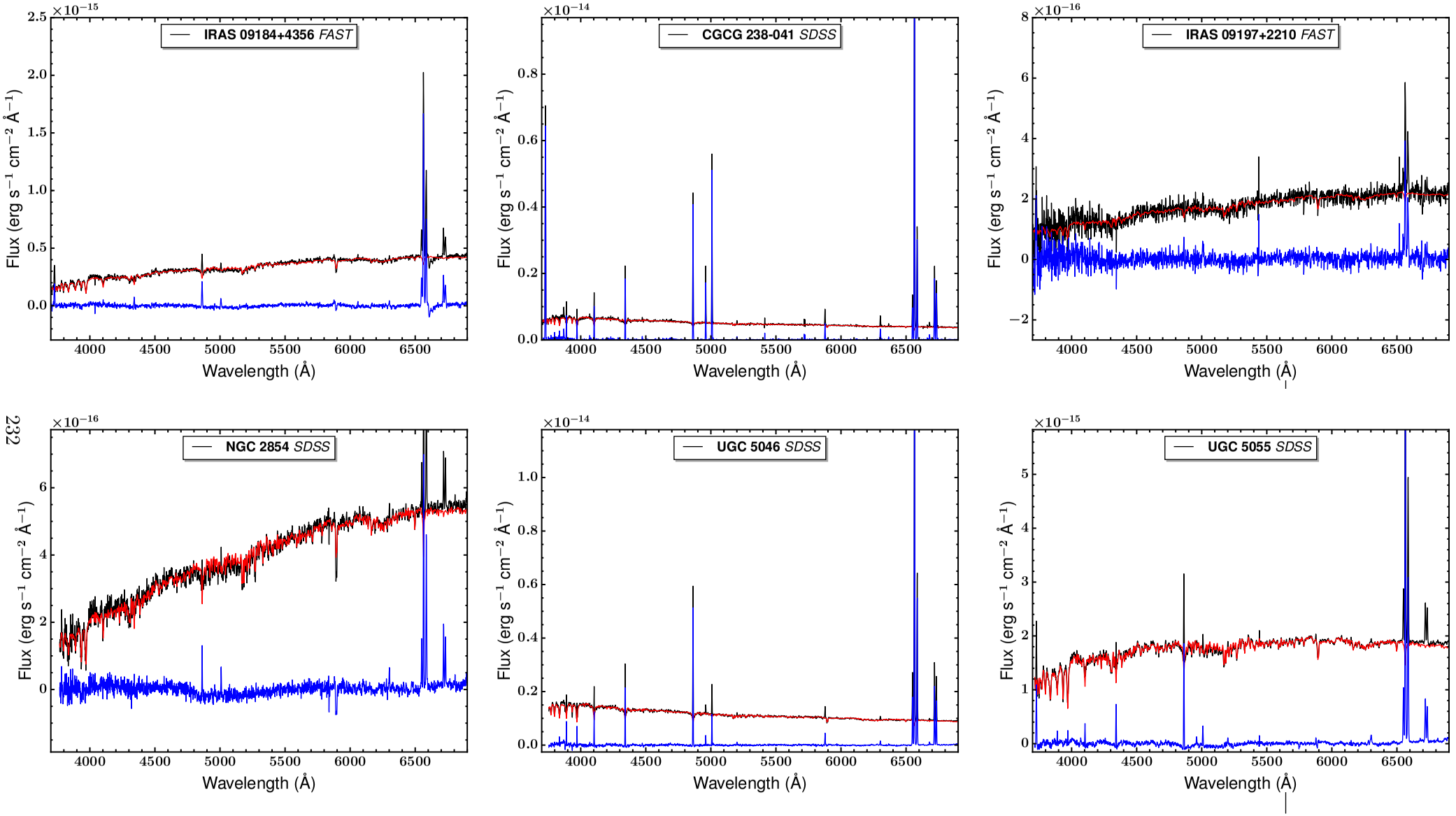


**Figure 8.A.9:** The nuclear spectra of IRAS 09184+4356, CGCG 238-041, IRAS 09197+2210, NGC 2854, UGC 5046, UGC 5055. The observed spectrum is shown with a black line, the STARLIGHT fit with a red line, and the starlight subtracted spectrum with a blue line.

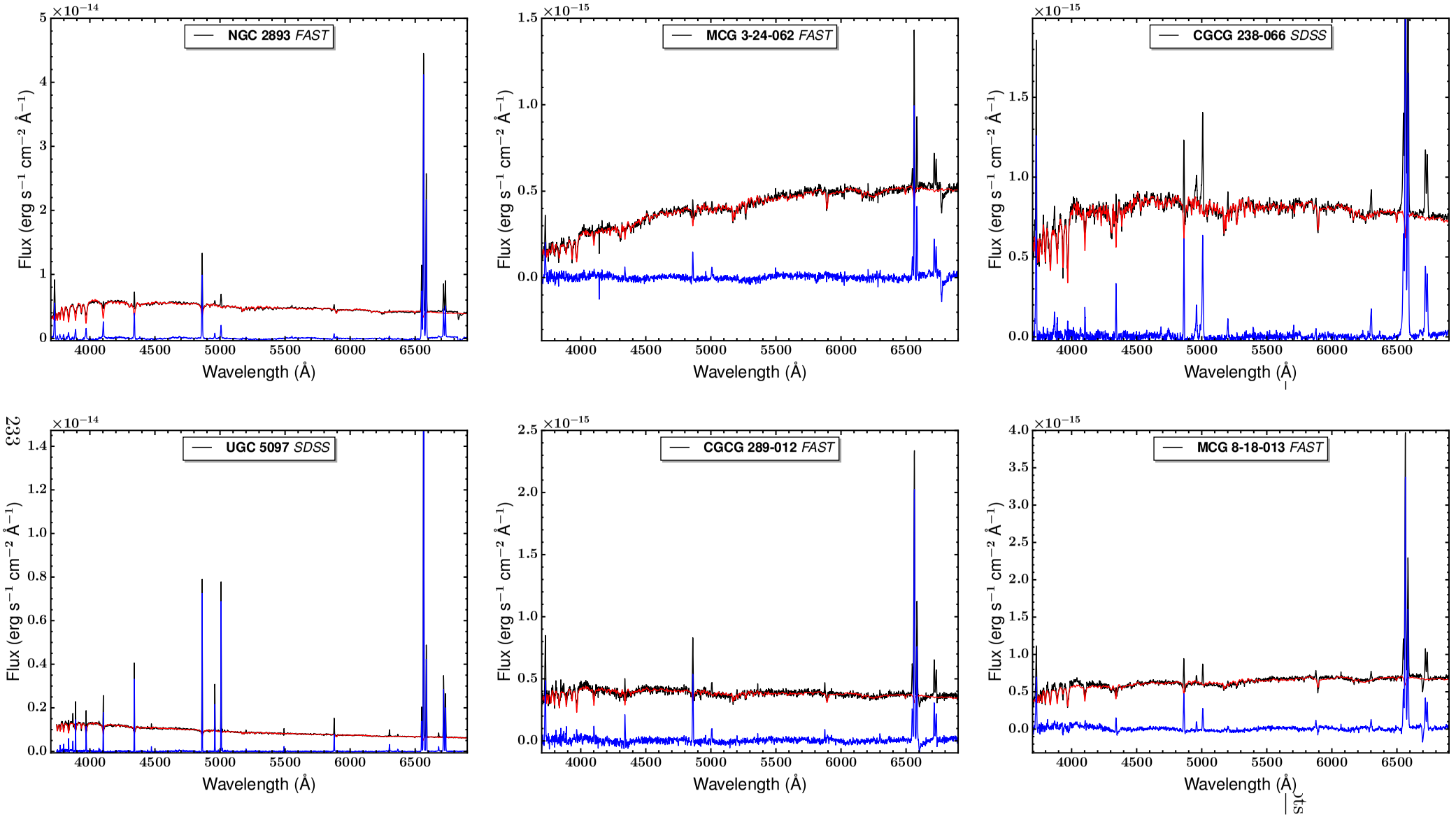


**Figure 8.A.10:** The nuclear spectra of NGC 2893, MCG 3-24-062, CGCG 238-066, UGC 5097, CGCG 289-012, MCG 8-18-013. The observed spectrum is shown with a black line, the STARLIGHT fit with a red line, and the starlight subtracted spectrum with a blue line.

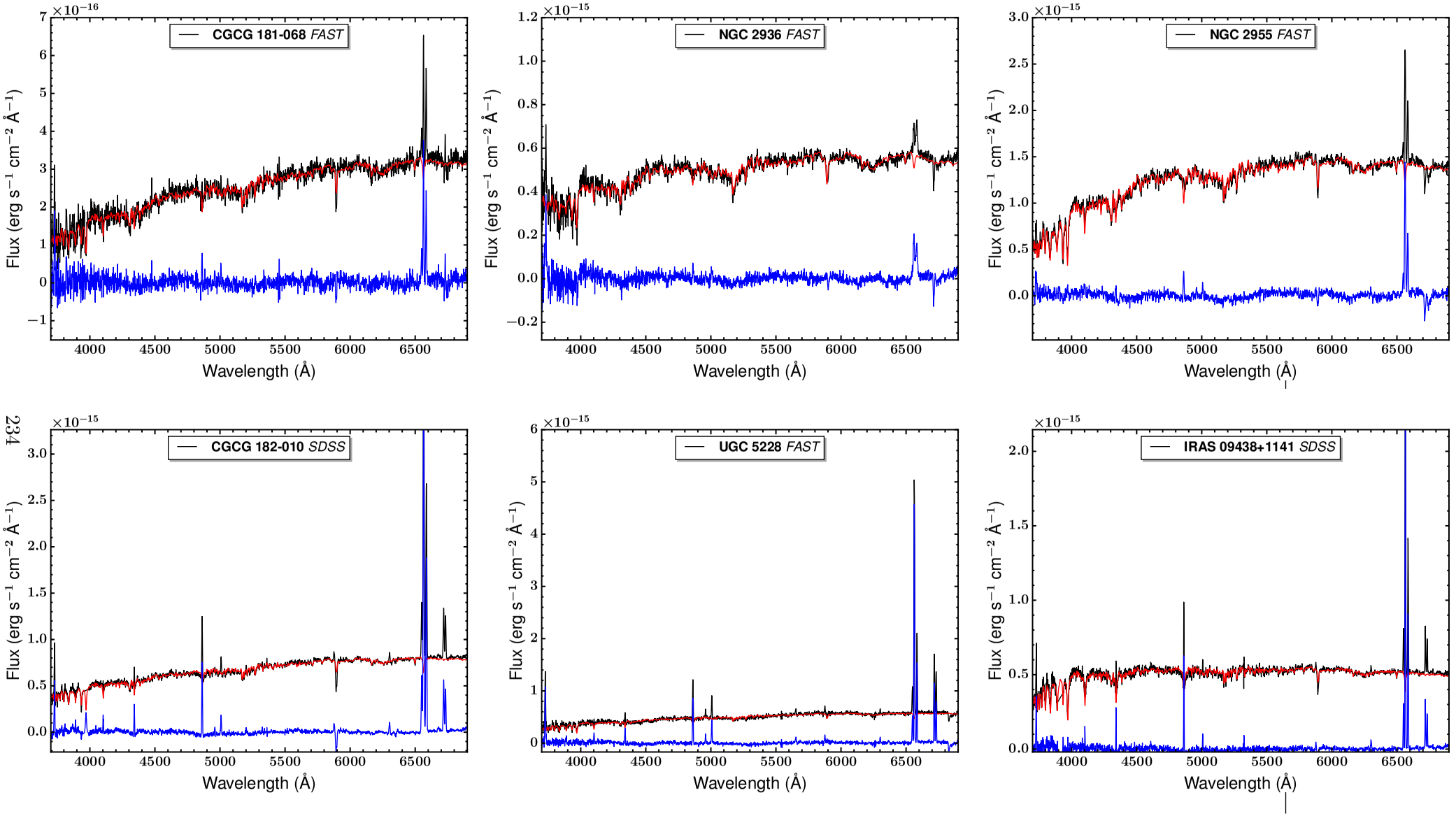


**Figure 8.A.11:** The nuclear spectra of CGCG 181-068, NGC 2936, NGC 2955, CGCG 182-010, UGC 5228, IRAS 09438+1141. The observed spectrum is shown with a black line, the STARLIGHT fit with a red line, and the starlight subtracted spectrum with a blue line.

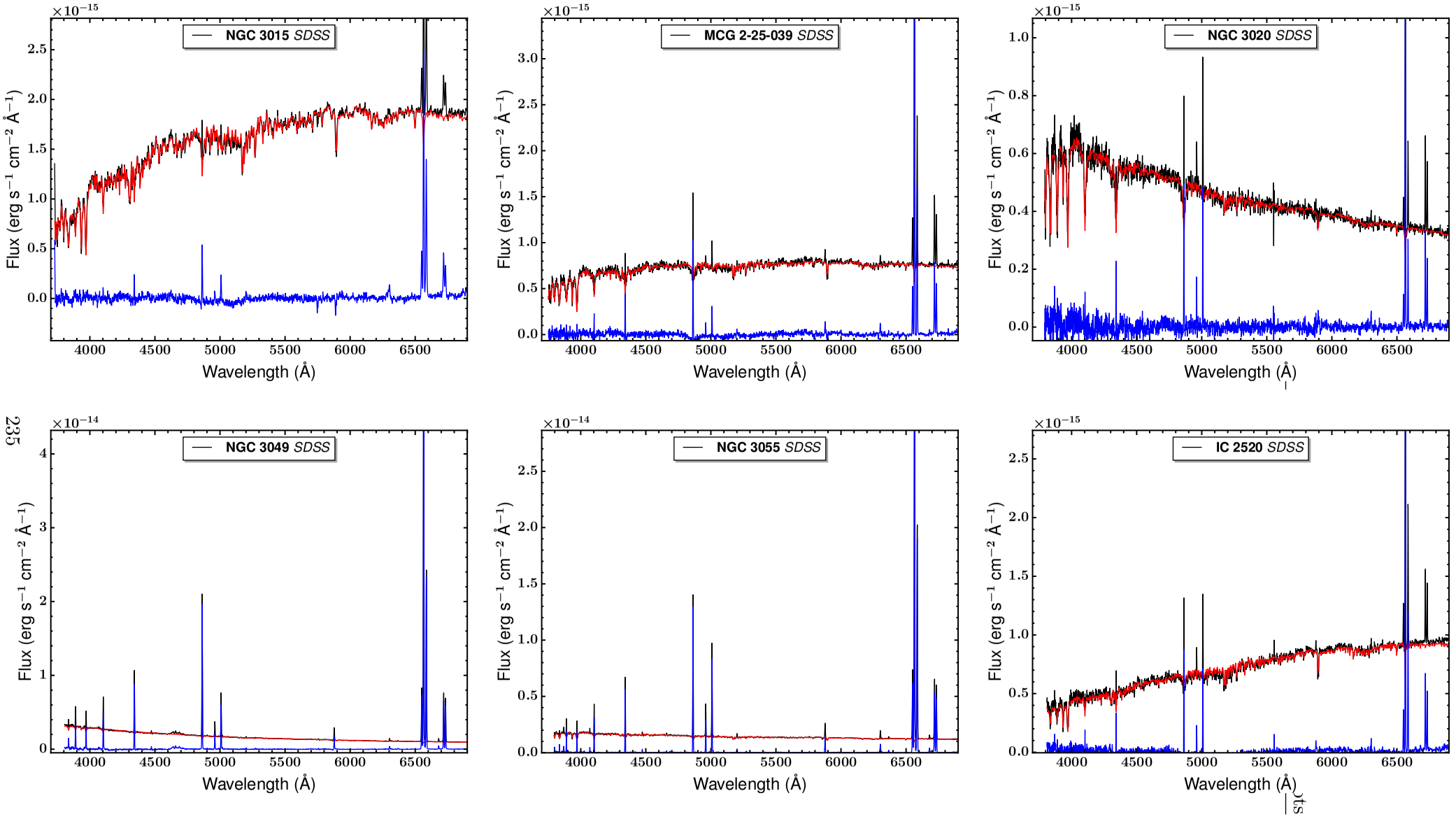


**Figure 8.A.12:** The nuclear spectra of NGC 3015, MCG 2-25-039, NGC 3020, NGC 3049, NGC 3055, IC 2520. The observed spectrum is shown with a black line, the STARLIGHT fit with a red line, and the starlight subtracted spectrum with a blue line.

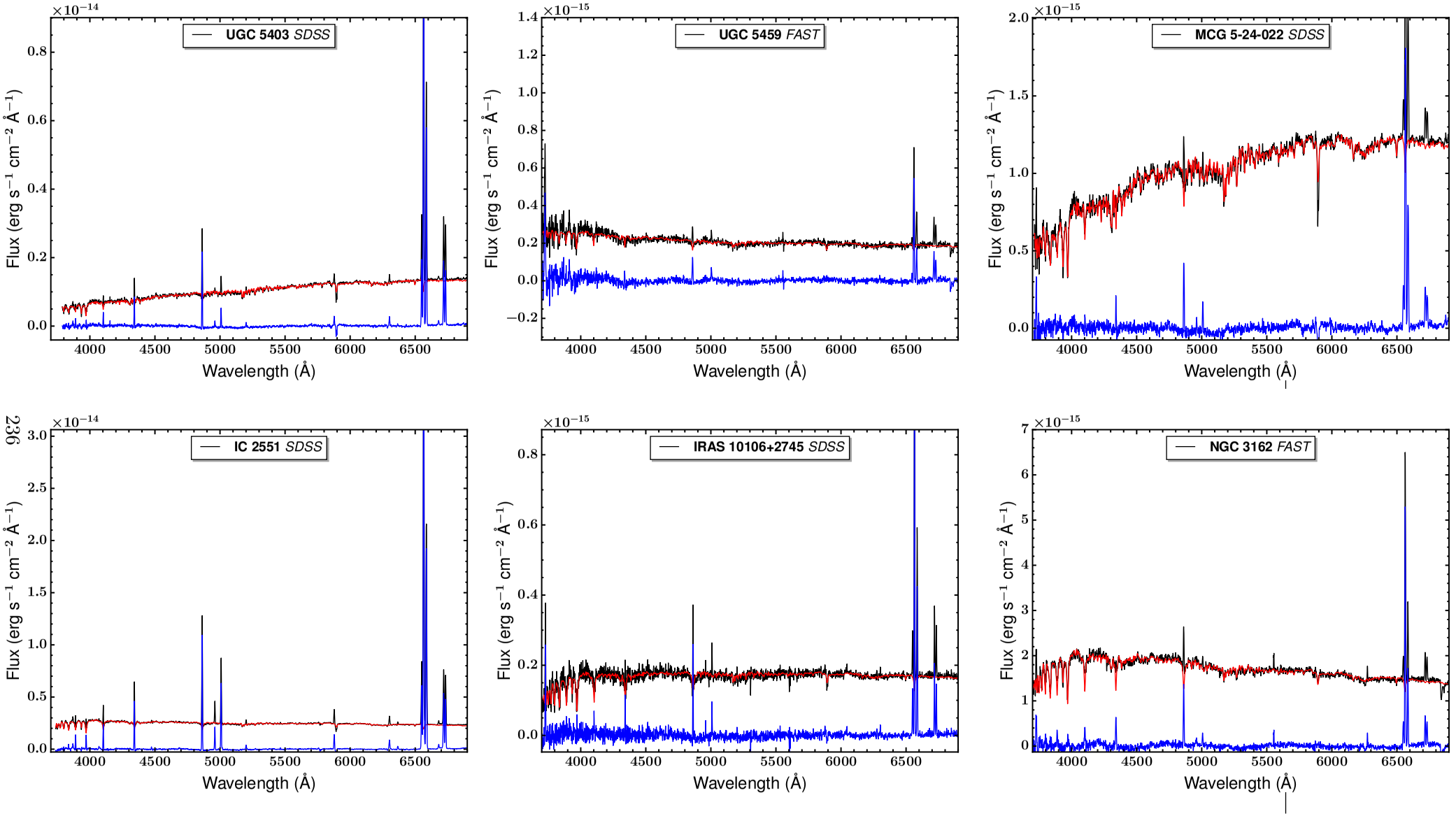




**Figure 8.A.13:** The nuclear spectra of UGC 5403, UGC 5459, MCG 5-24-022, IC 2551, IRAS 10106+2745, NGC 3162. The observed spectrum is shown with a black line, the STARLIGHT fit with a red line, and the starlight subtracted spectrum with a blue line.

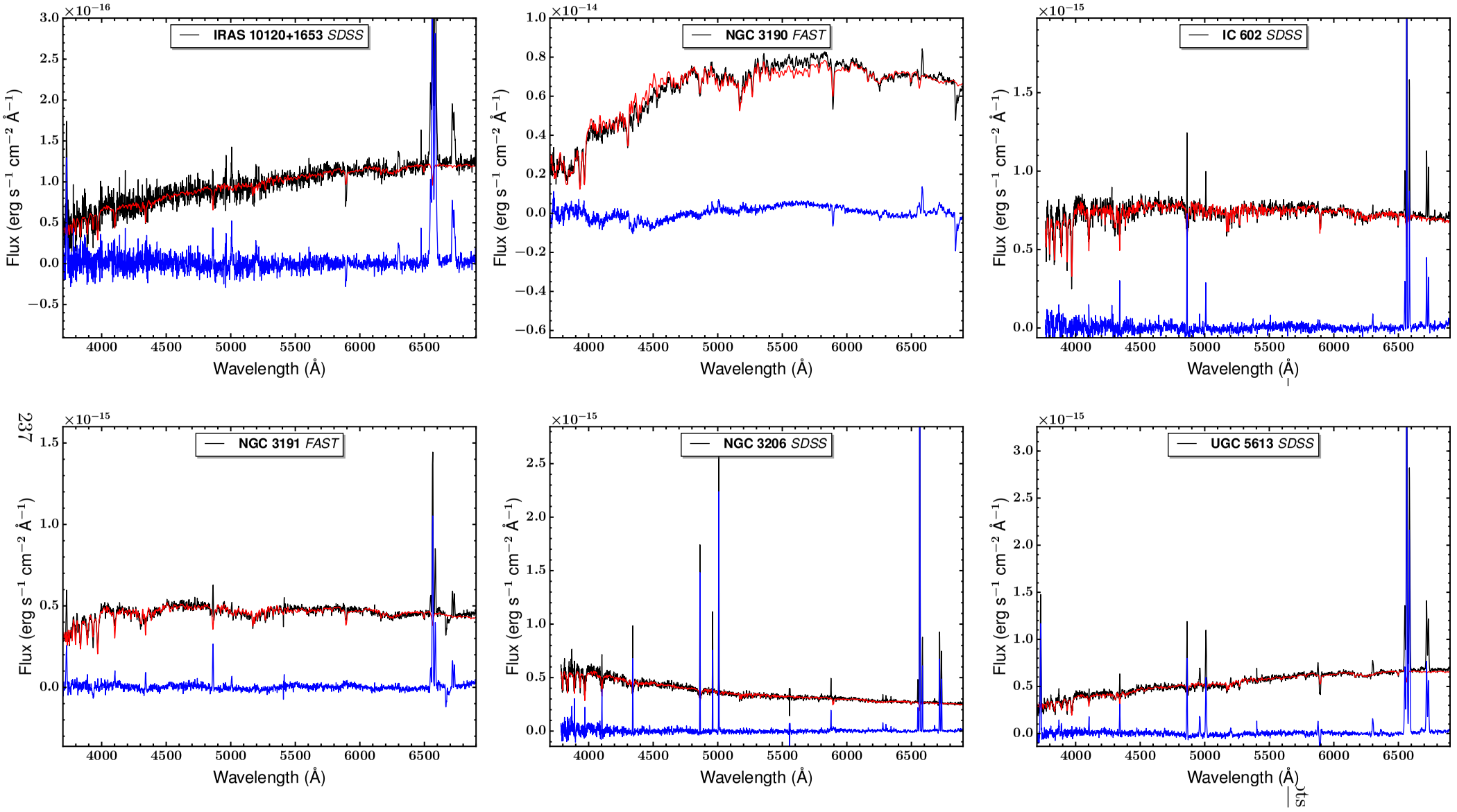




**Figure 8.A.14:** The nuclear spectra of IRAS 10120+1653, NGC 3190, IC 602, NGC 3191, NGC 3206, UGC 5613. The observed spectrum is shown with a black line, the STARLIGHT fit with a red line, and the starlight subtracted spectrum with a blue line.

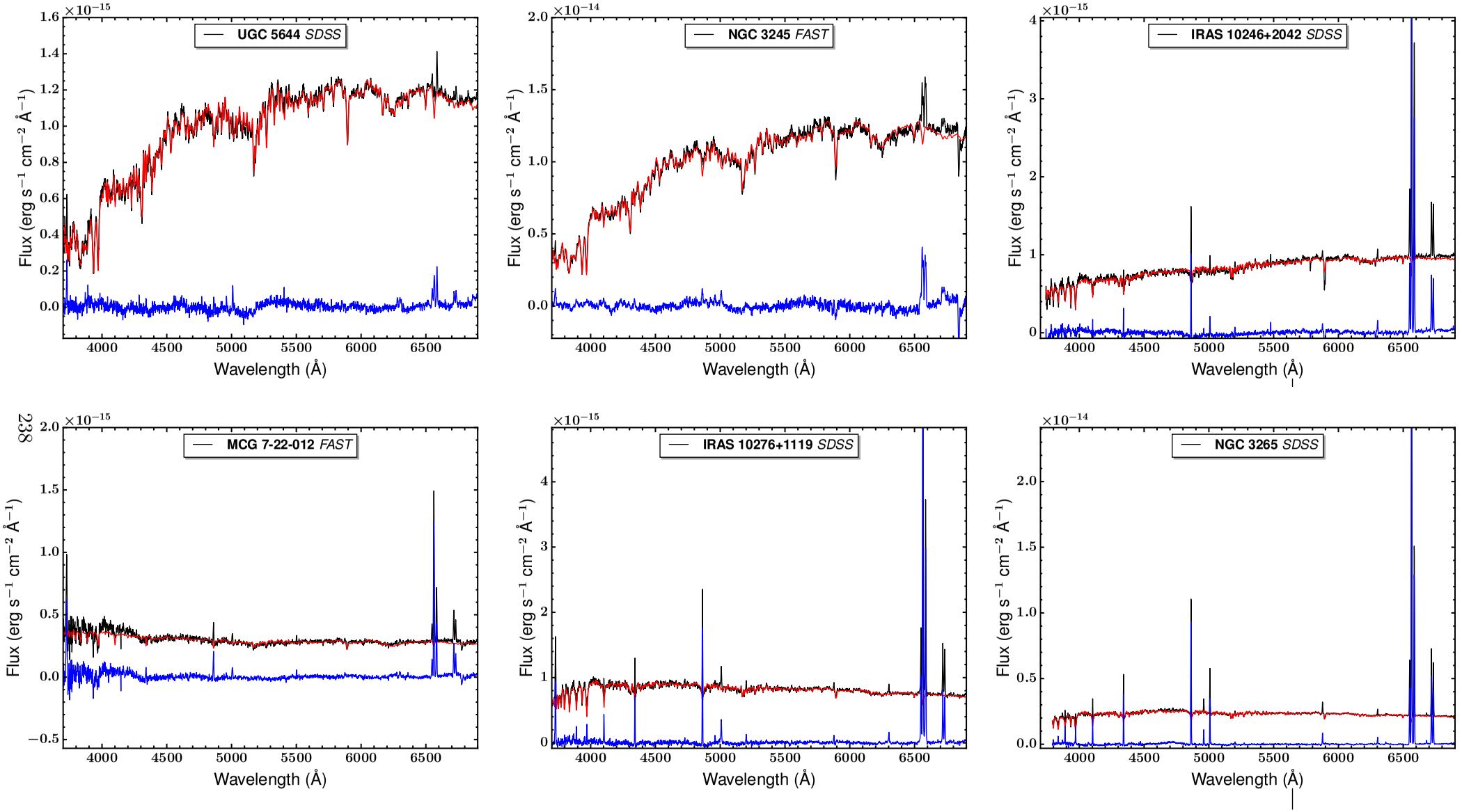


**Figure 8.A.15:** The nuclear spectra of UGC 5644, NGC 3245, IRAS 10246+2042, MCG 7-22-012, IRAS 10276+1119, NGC 3265. The observed spectrum is shown with a black line, the STARLIGHT fit with a red line, and the starlight subtracted spectrum with a blue line.

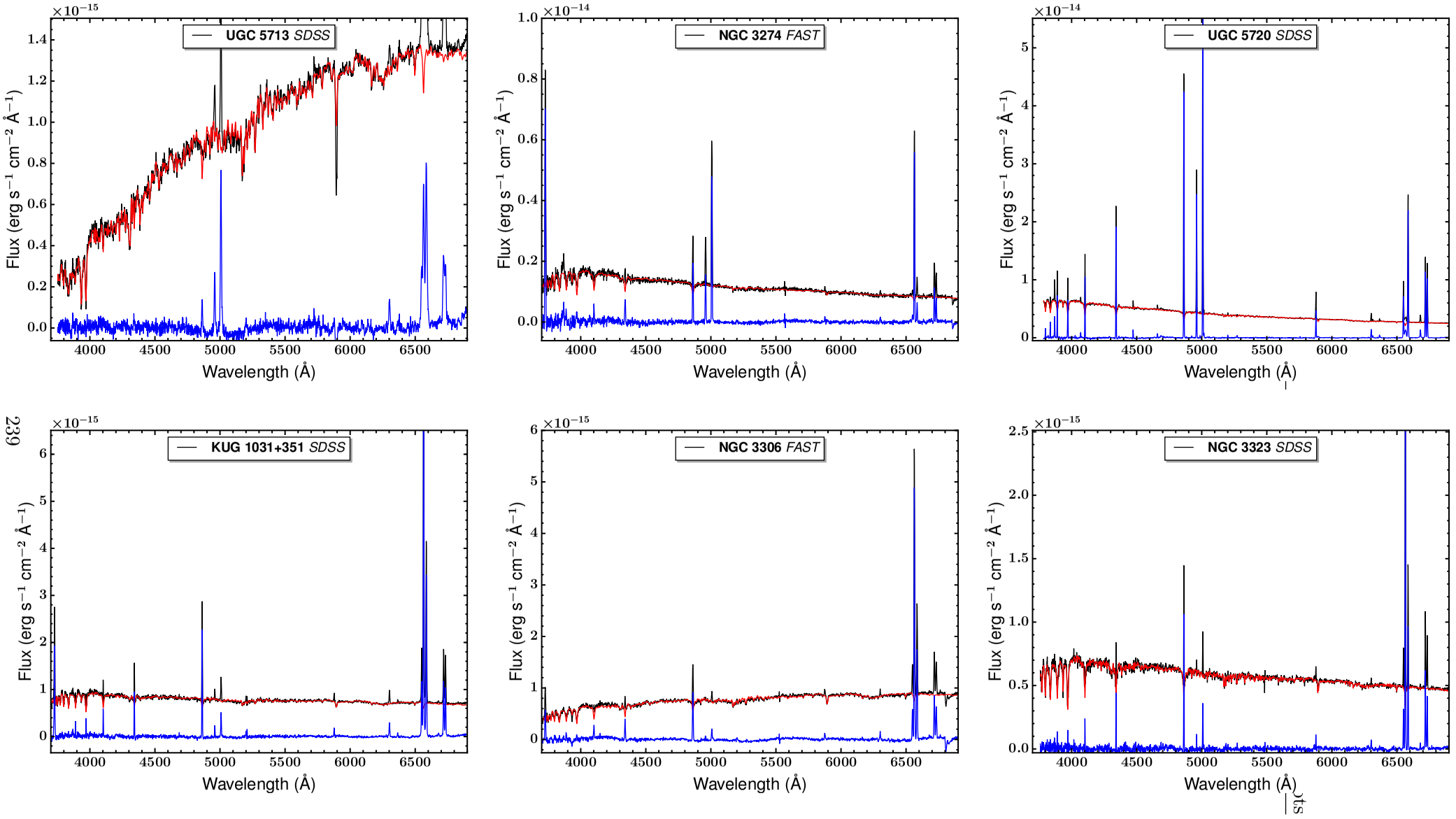


**Figure 8.A.16:** The nuclear spectra of UGC 5713, NGC 3274, UGC 5720, KUG 1031+351, NGC 3306, NGC 3323. The observed spectrum is shown with a black line, the STARLIGHT fit with a red line, and the starlight subtracted spectrum with a blue line.

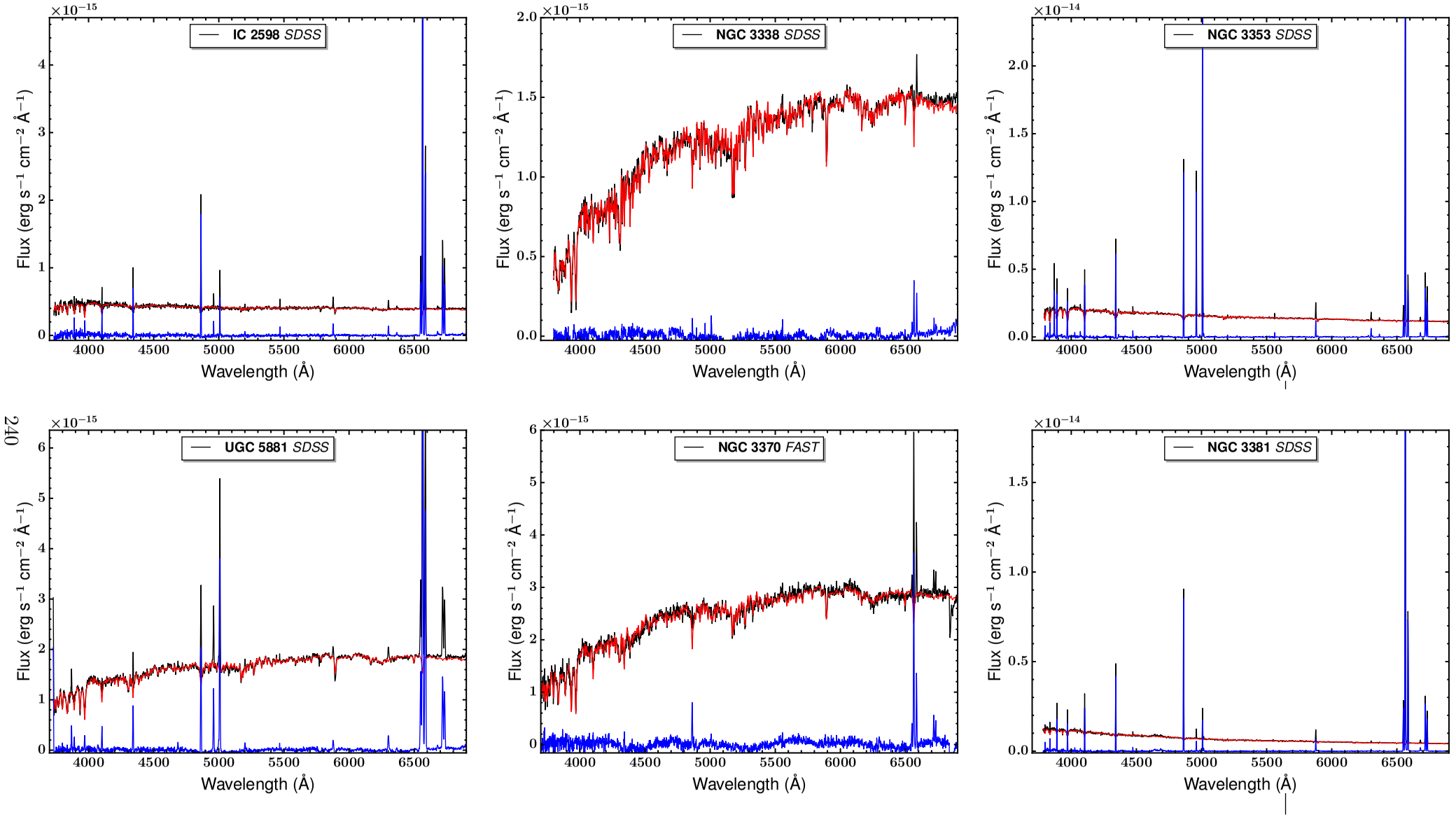


**Figure 8.A.17:** The nuclear spectra of IC 2598, NGC 3338, NGC 3353, UGC 5881, NGC 3370, NGC 3381. The observed spectrum is shown with a black line, the STARLIGHT fit with a red line, and the starlight subtracted spectrum with a blue line.

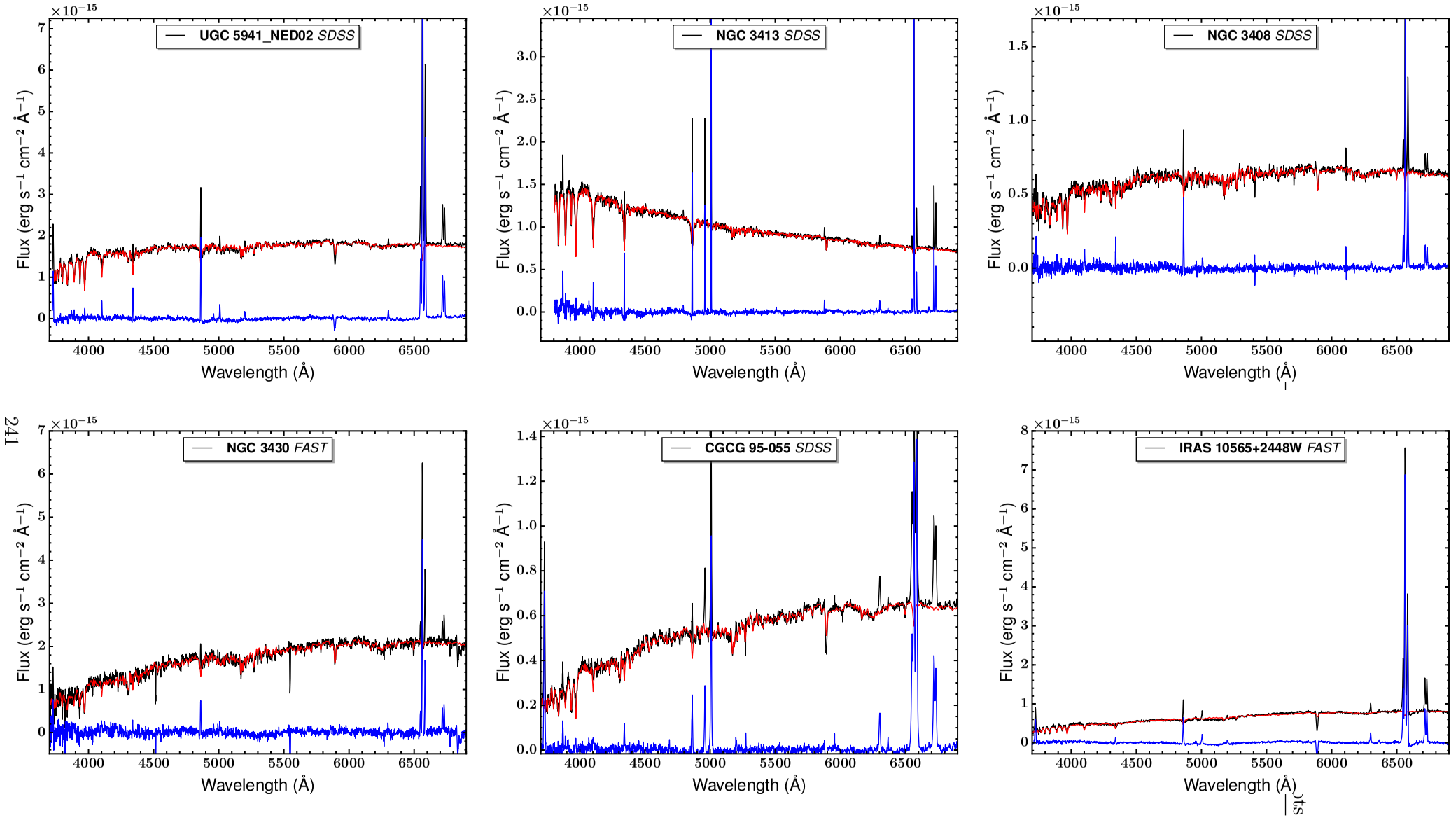


**Figure 8.A.18:** The nuclear spectra of UGC 5941_NED02, NGC 3413, NGC 3408, NGC 3430, CGCG 95-055, IRAS 10565+2448W. The observed spectrum is shown with a black line, the STARLIGHT fit with a red line, and the starlight subtracted spectrum with a blue line.

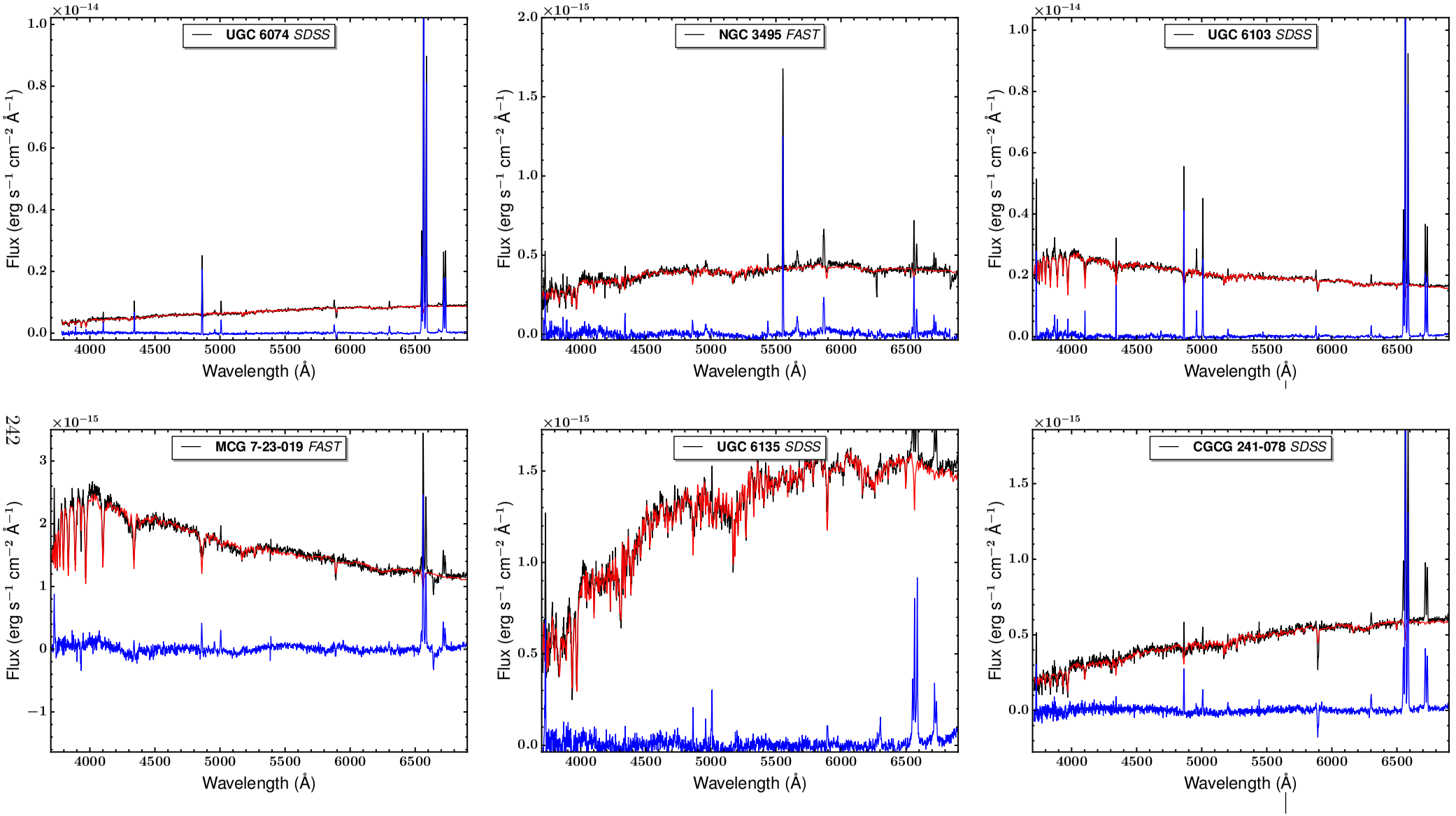


**Figure 8.A.19:** The nuclear spectra of UGC 6074, NGC 3495, UGC 6103, MCG 7-23-019, UGC 6135, CGCG 241-078. The observed spectrum is shown with a black line, the STARLIGHT fit with a red line, and the starlight subtracted spectrum with a blue line.

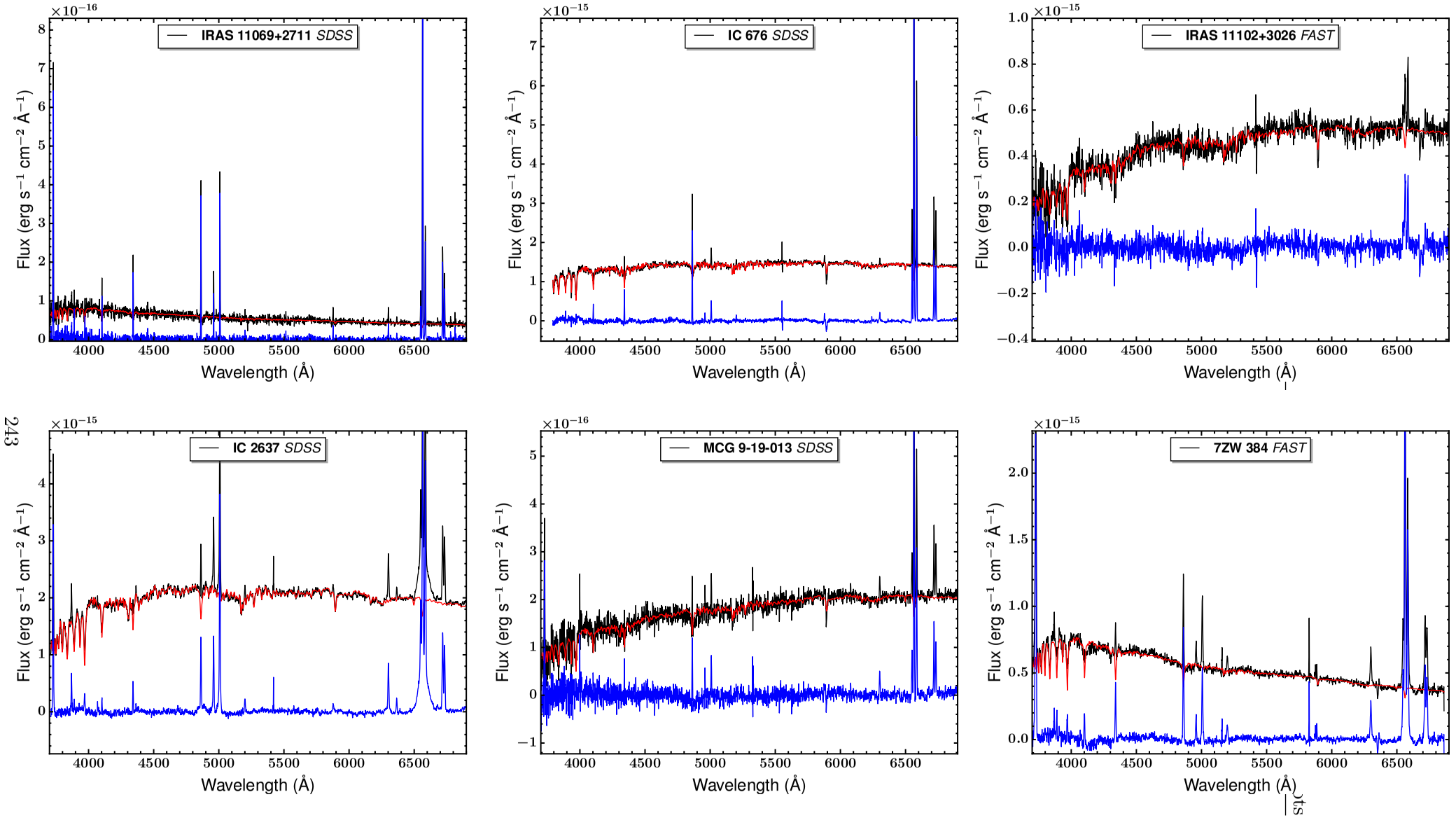


**Figure 8.A.20:** The nuclear spectra of IRAS 11069+2711, IC 676, IRAS 11102+3026, IC 2637, MCG 9-19-013, 7ZW384. The observed spectrum is shown with a black line, the STARLIGHT fit with a red line, and the starlight subtracted spectrum with a blue line.

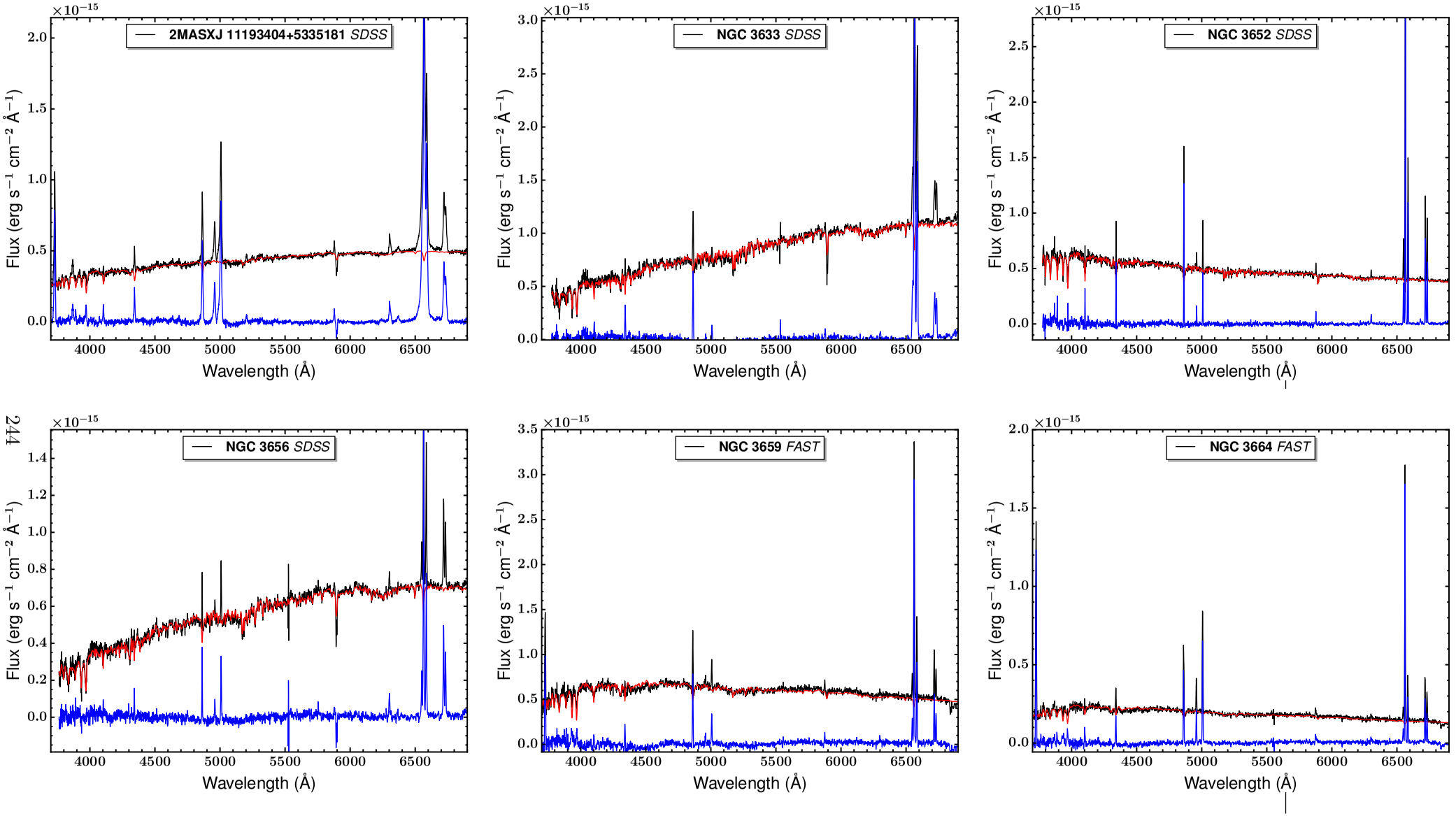




**Figure 8.A.21:** The nuclear spectra of 2MASX J11193404+5335181, NGC 3633, NGC 3652, NGC 3656, NGC 3659, NGC 3664. The observed spectrum is shown with a black line, the STARLIGHT fit with a red line, and the starlight subtracted spectrum with a blue line.

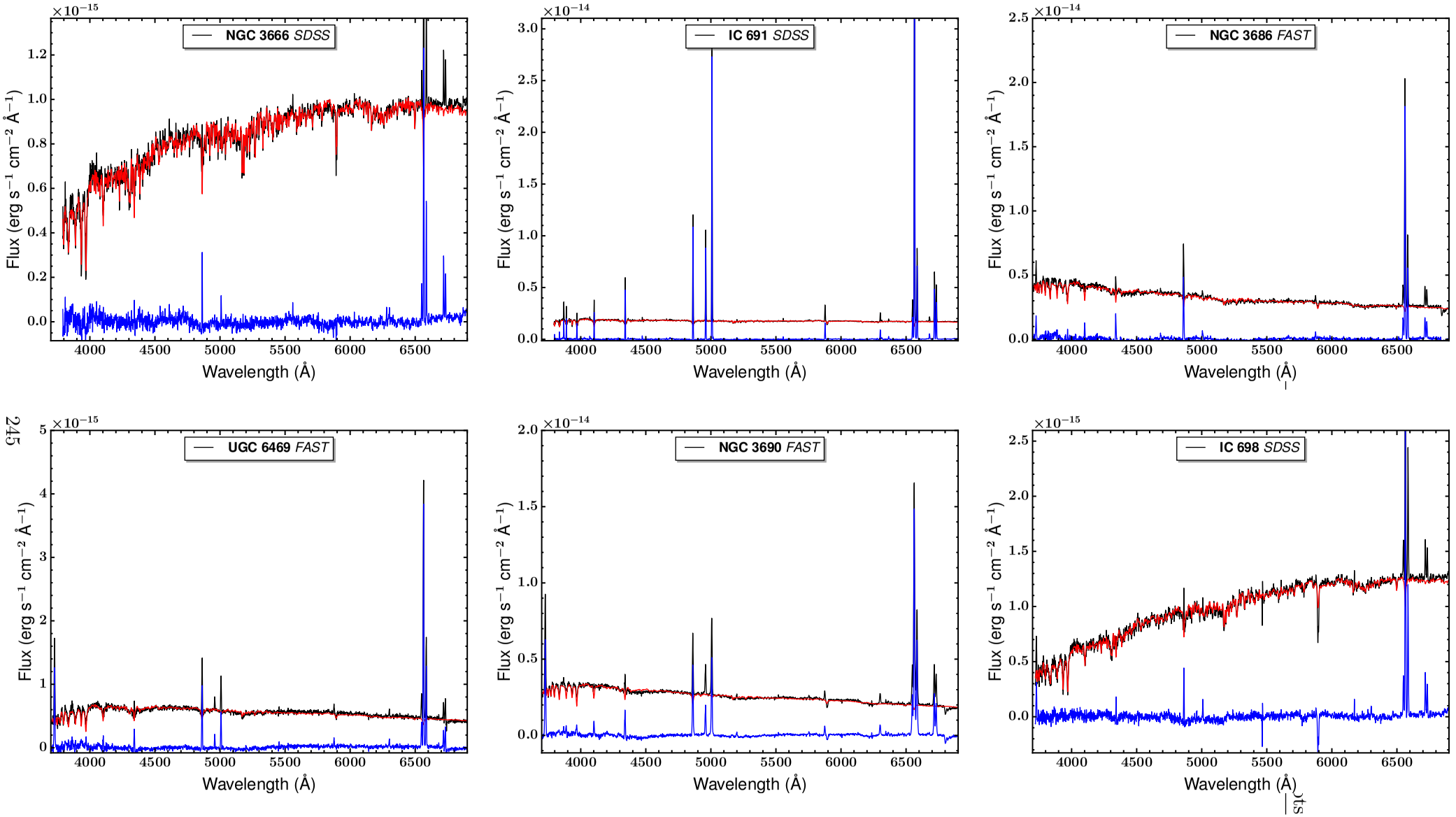


**Figure 8.A.22:** The nuclear spectra of NGC 3666, IC 691, NGC 3686, UGC 6469, NGC 3690, IC 698. The observed spectrum is shown with a black line, the STARLIGHT fit with a red line, and the starlight subtracted spectrum with a blue line.

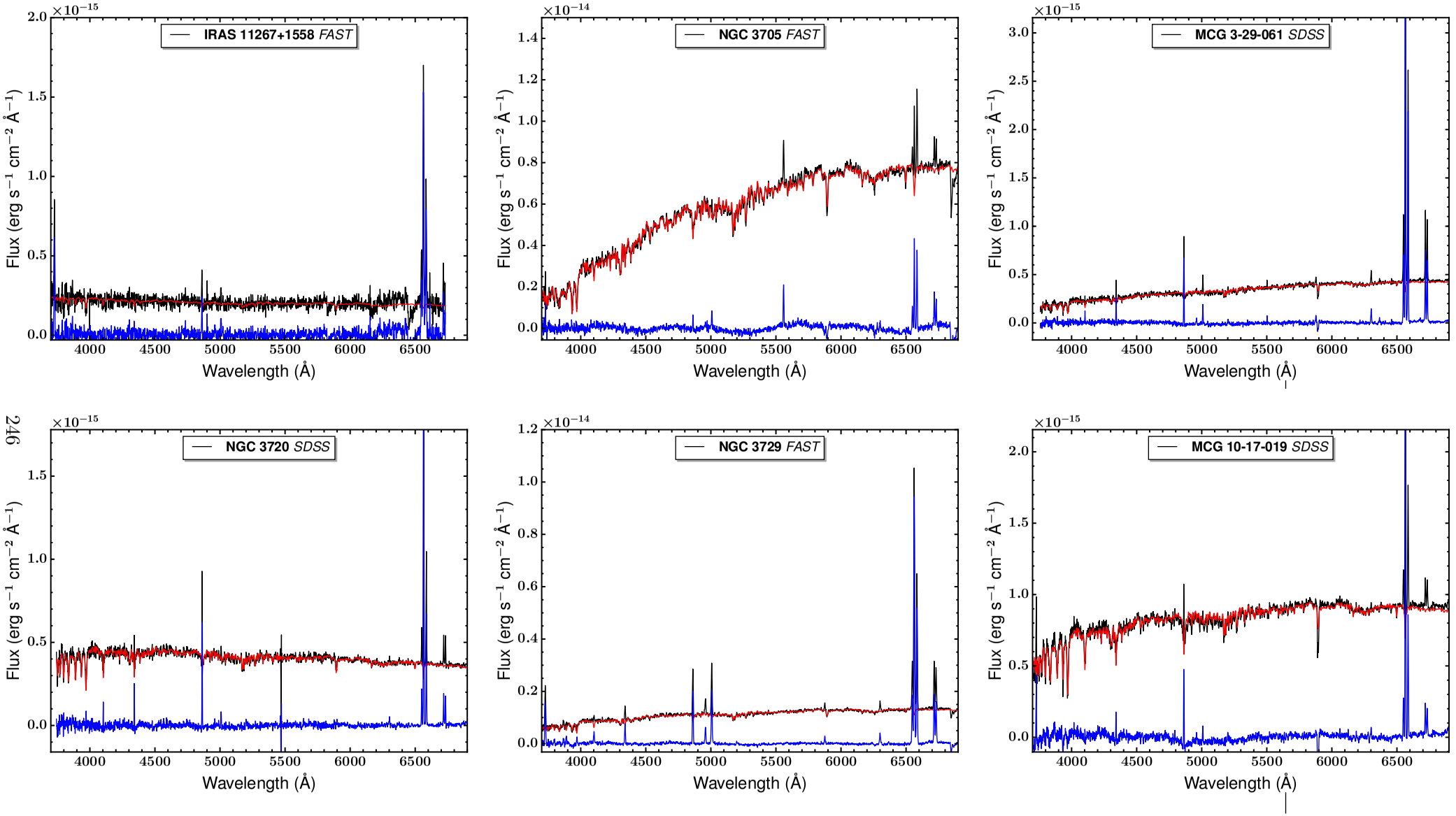


**Figure 8.A.23:** The nuclear spectra of IRAS 11267+1558, NGC 3705, MCG 3-29-061, NGC 3720, NGC 3729, MCG 10-17-019. The observed spectrum is shown with a black line, the STARLIGHT fit with a red line, and the starlight subtracted spectrum with a blue line.

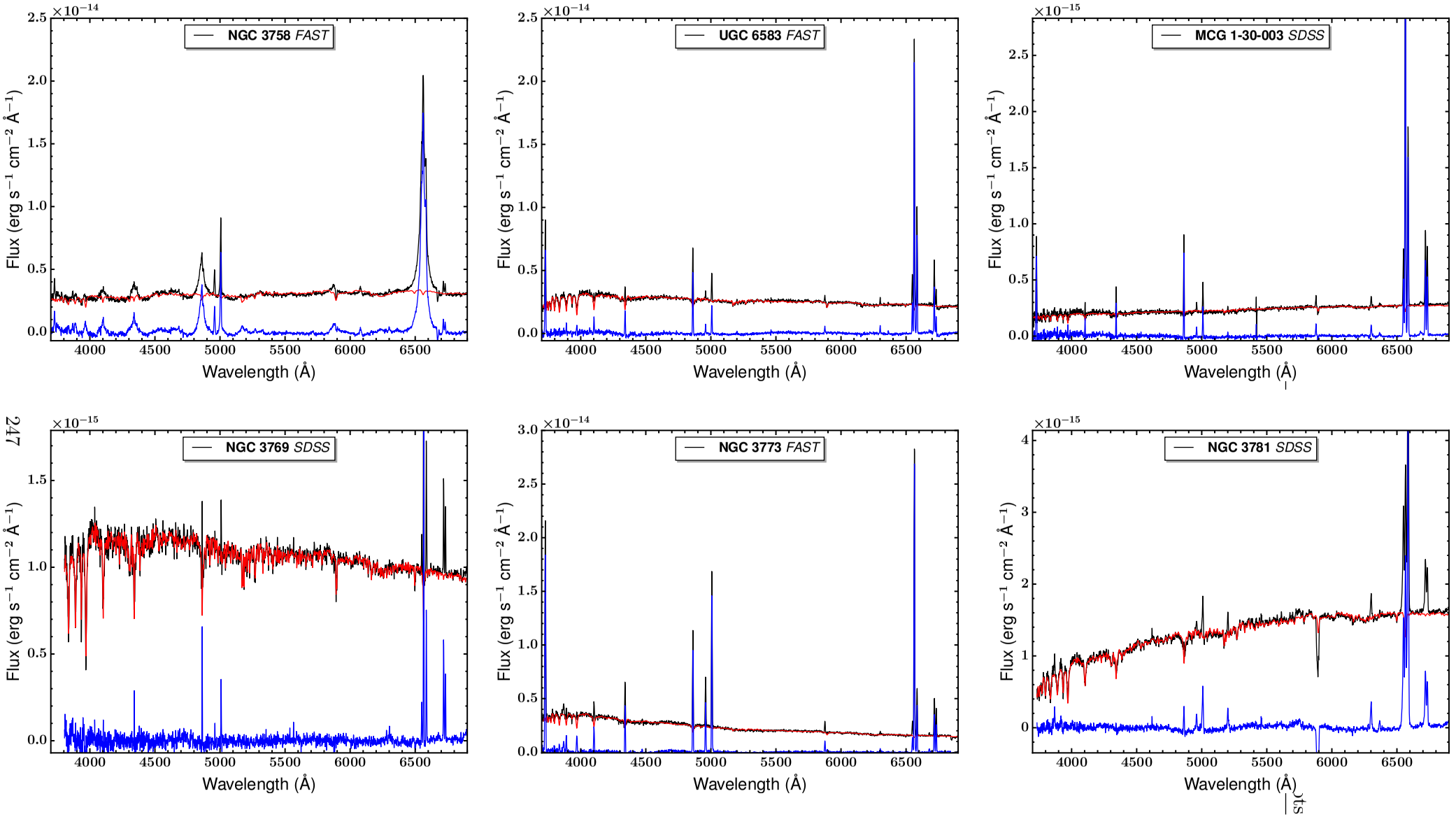




**Figure 8.A.24:** The nuclear spectra of NGC 3758, UGC 6583, MCG 1-30-003, NGC 3769, NGC 3773, NGC 3781. The observed spectrum is shown with a black line, the STARLIGHT fit with a red line, and the starlight subtracted spectrum with a blue line.

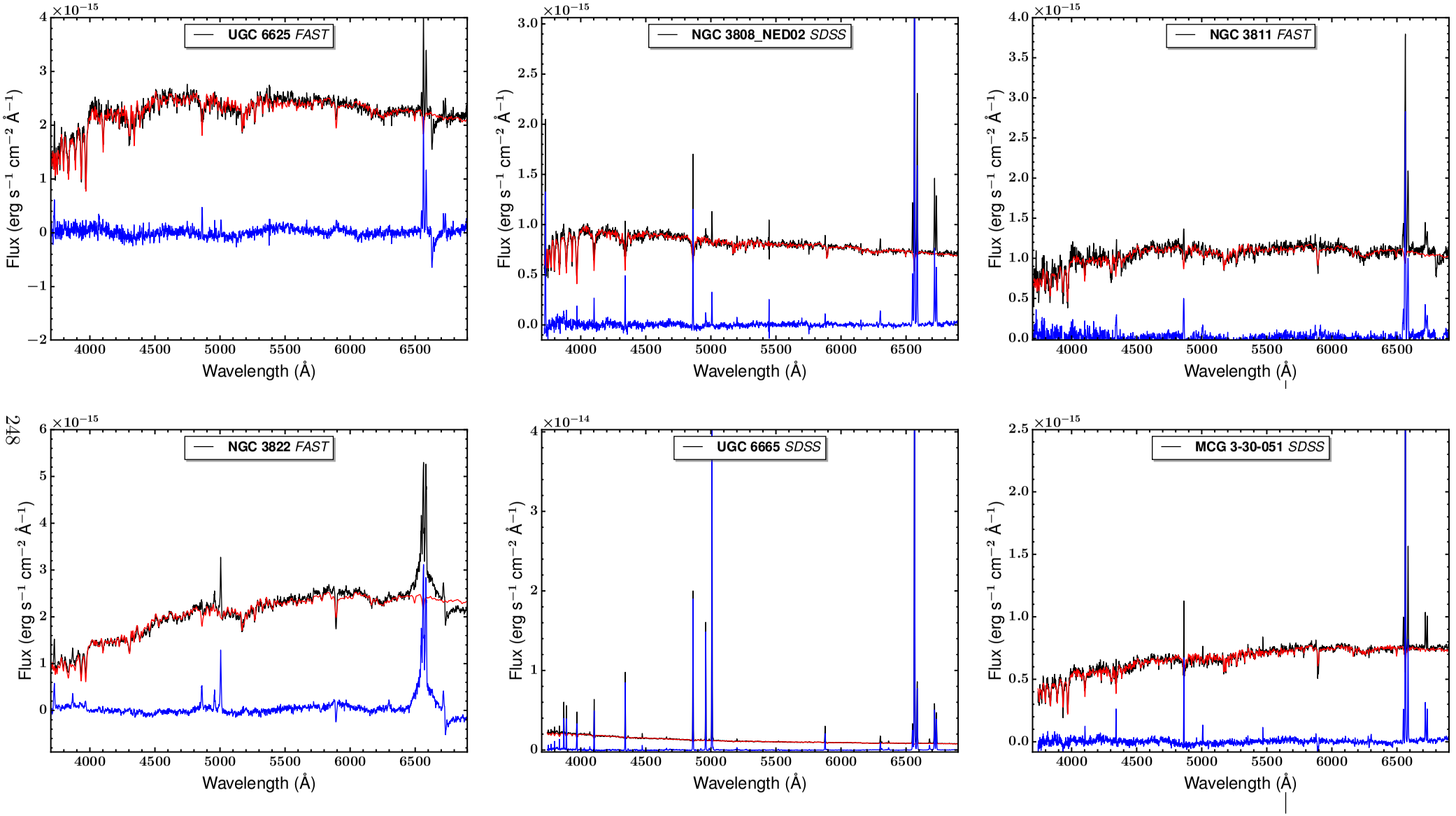




**Figure 8.A.25:** The nuclear spectra of UGC 6625, NGC 3808_NED02, NGC 3811, NGC 3822, UGC 6665, MCG 3-30-051. The observed spectrum is shown with a black line, the STARLIGHT fit with a red line, and the starlight subtracted spectrum with a blue line.

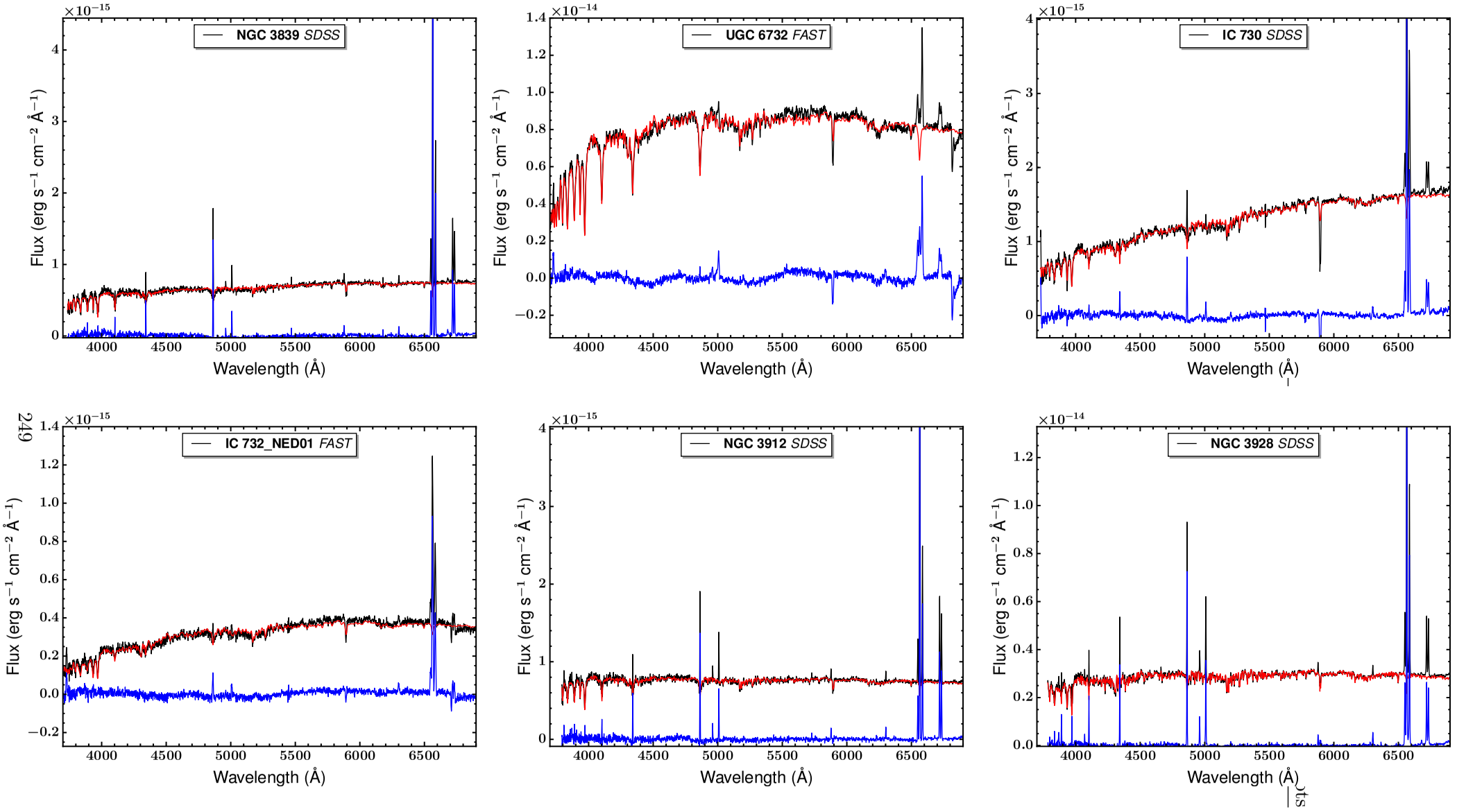




**Figure 8.A.26:** The nuclear spectra of NGC 3839, UGC 6732, IC 730, IC 732_NED01, NGC 3912, NGC 3928. The observed spectrum is shown with a black line, the STARLIGHT fit with a red line, and the starlight subtracted spectrum with a blue line.

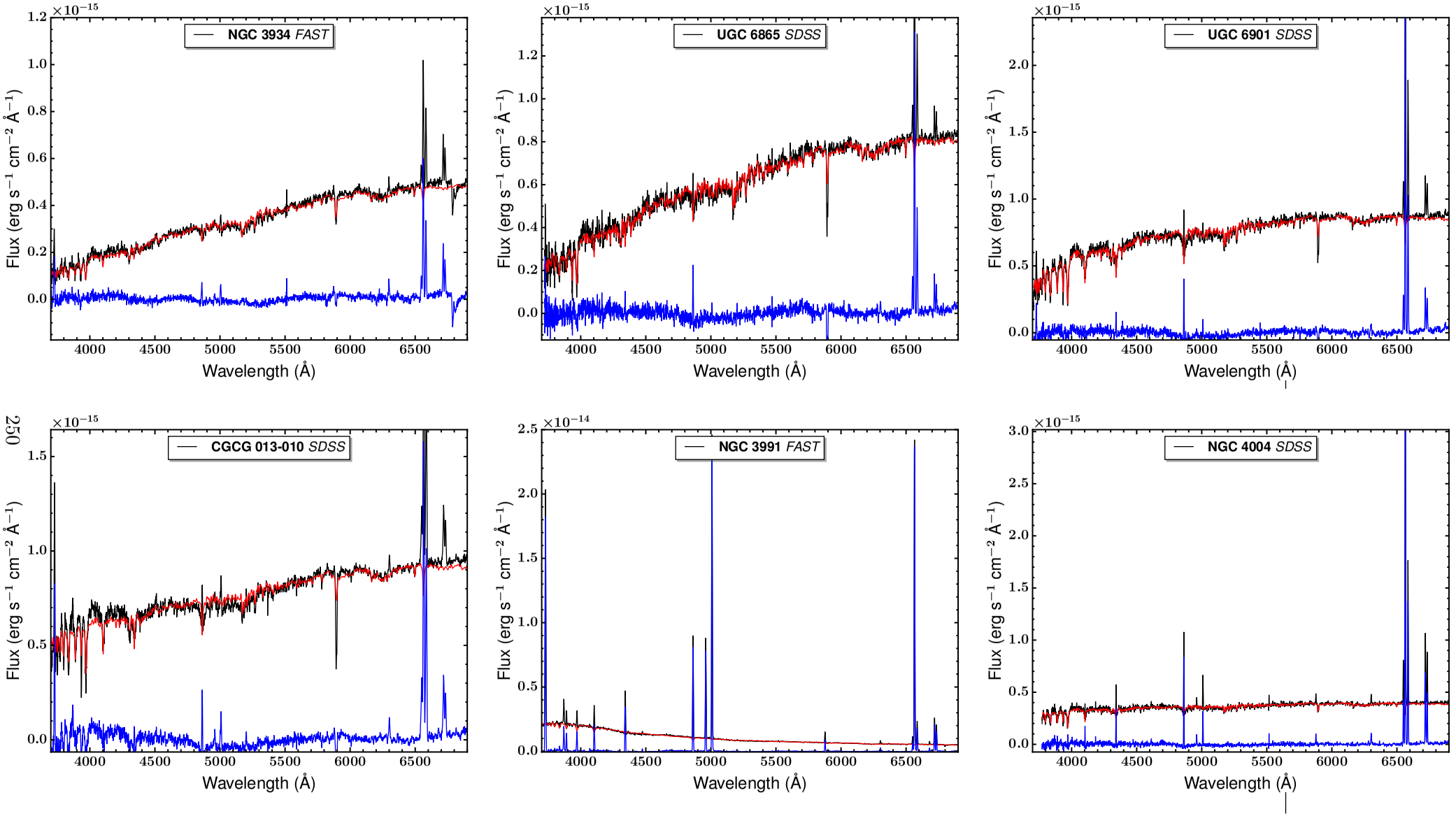


**Figure 8.A.27:** The nuclear spectra of NGC 3934, UGC 6865, UGC 6901, CGCG 013-010, NGC 3991, NGC 4004. The observed spectrum is shown with a black line, the STARLIGHT fit with a red line, and the starlight subtracted spectrum with a blue line.

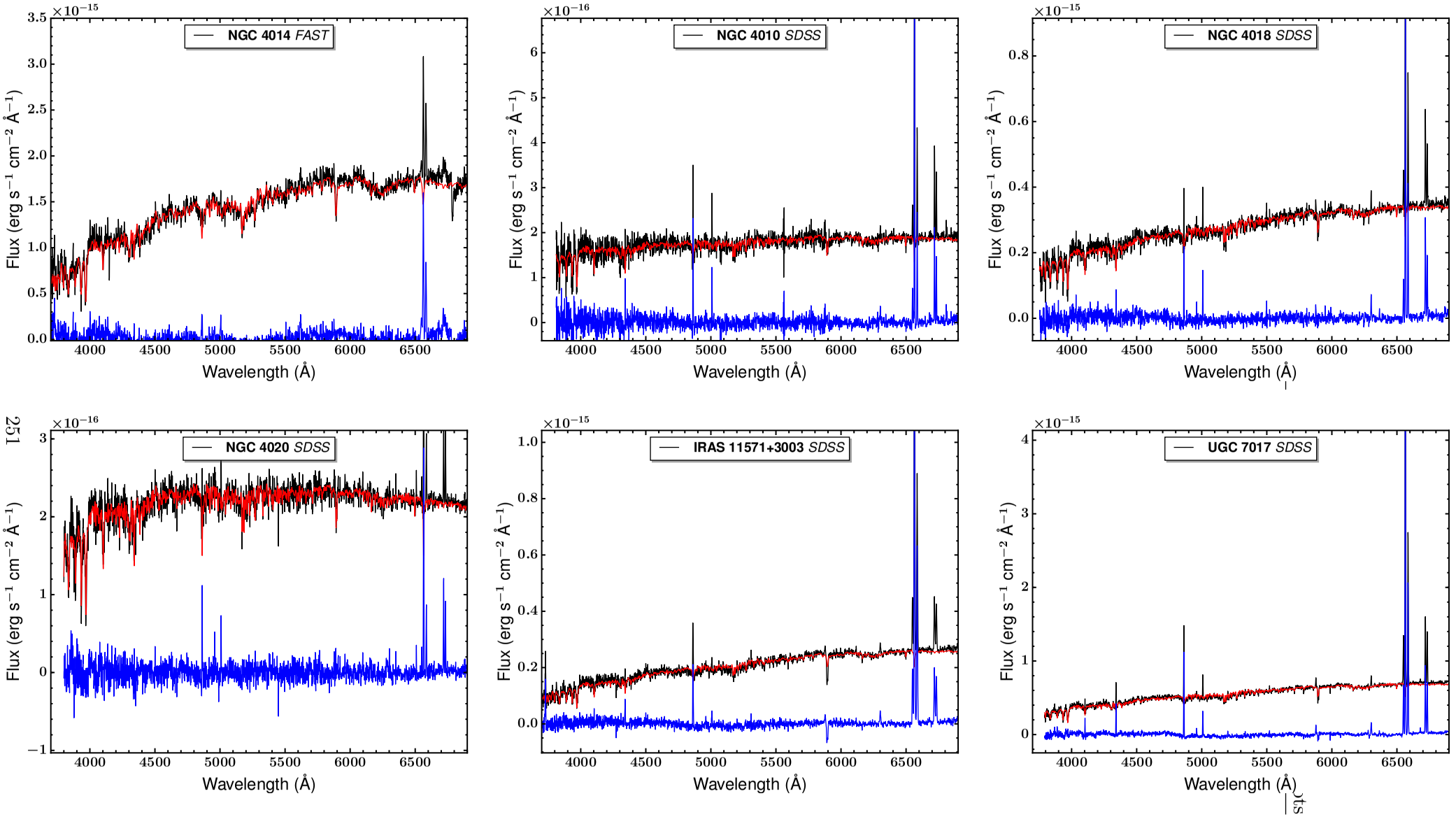


**Figure 8.A.28:** The nuclear spectra of NGC 4014, NGC 4010, NGC 4018, NGC 4020, IRAS 11571+3003, UGC 7017. The observed spectrum is shown with a black line, the STARLIGHT fit with a red line, and the starlight subtracted spectrum with a blue line.

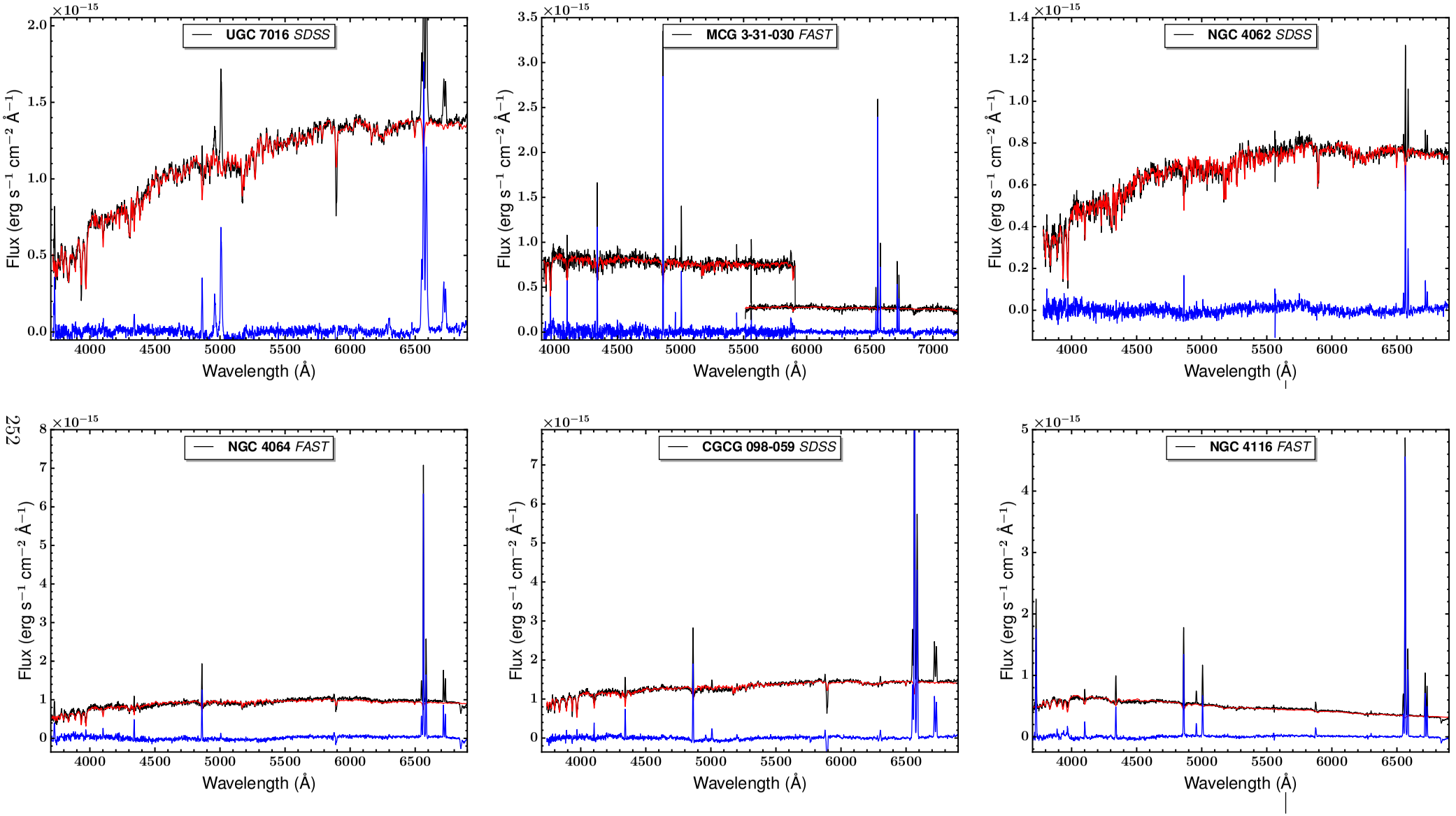


**Figure 8.A.29:** The nuclear spectra of UGC 7016, MCG 3-31-030, NGC 4062, NGC 4064, CGCG 098-059, NGC 4116. The observed spectrum is shown with a black line, the STARLIGHT fit with a red line, and the starlight subtracted spectrum with a blue line.

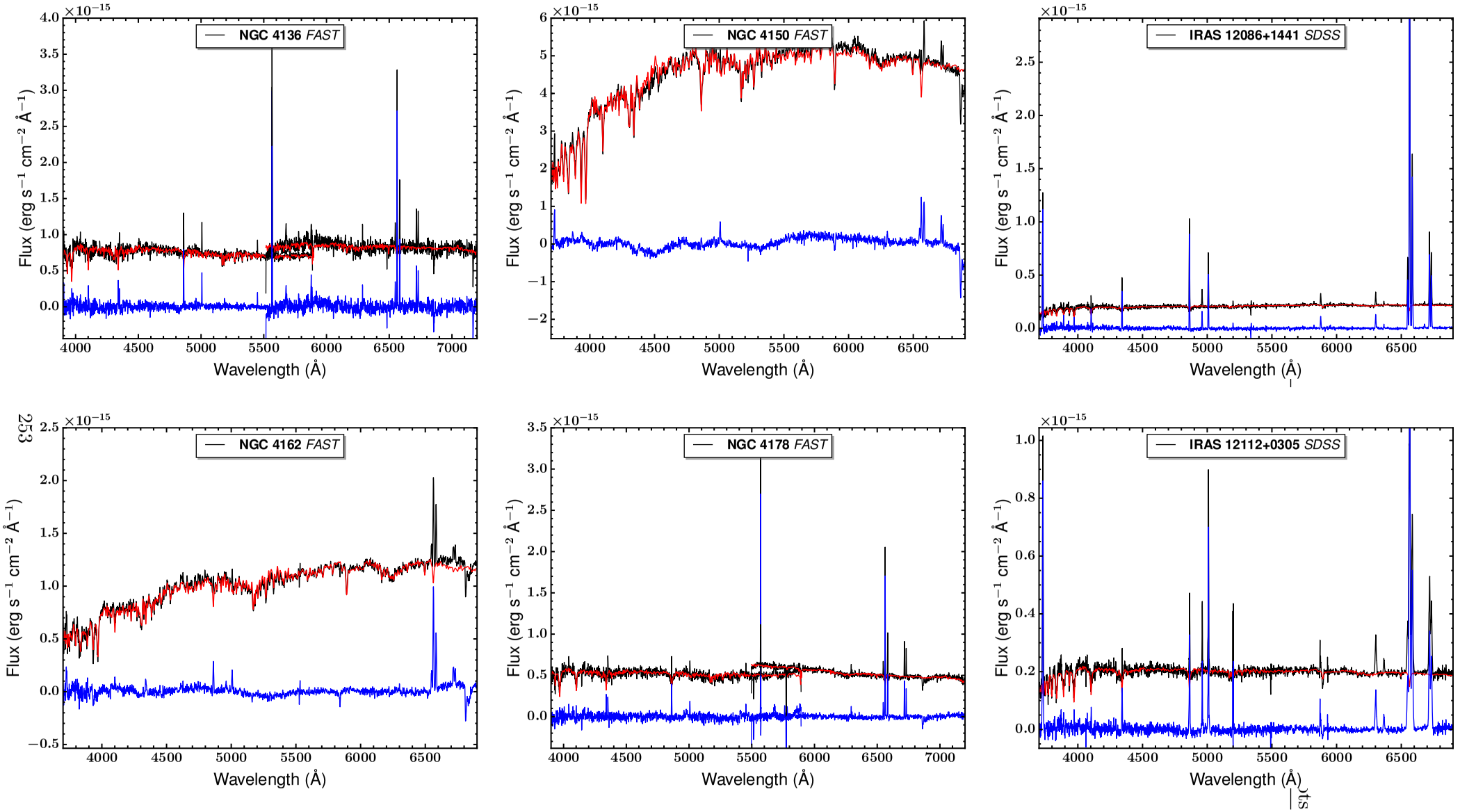


**Figure 8.A.30:** The nuclear spectra of NGC 4136, NGC 4150, IRAS 12086+1441, NGC 4162, NGC 4178, IRAS 12112+0305. The observed spectrum is shown with a black line, the STARLIGHT fit with a red line, and the starlight subtracted spectrum with a blue line.

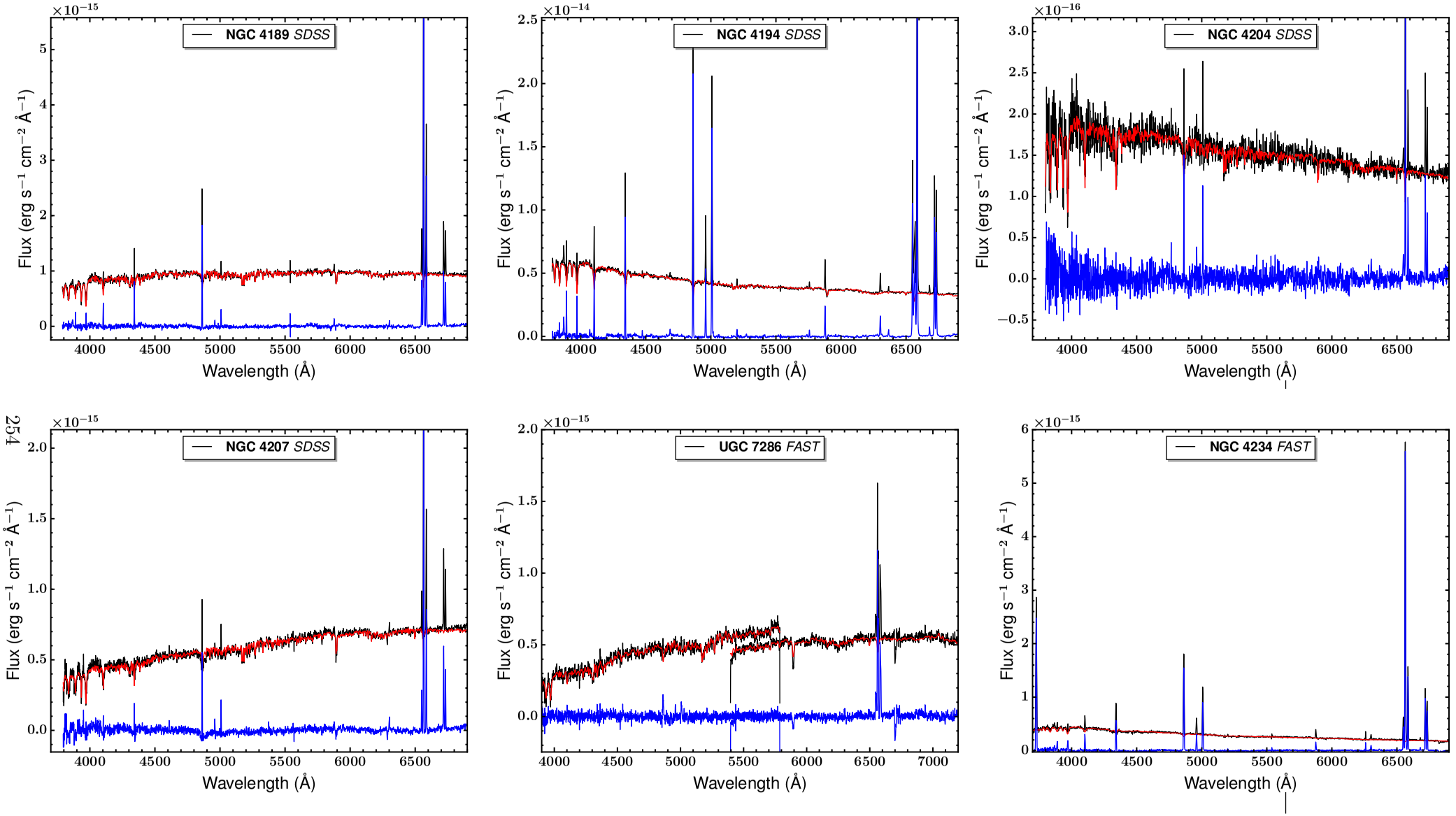


**Figure 8.A.31:** The nuclear spectra of NGC 4189, NGC 4194, NGC 4204, NGC 4207, UGC 7286, NGC 4234. The observed spectrum is shown with a black line, the STARLIGHT fit with a red line, and the starlight subtracted spectrum with a blue line.

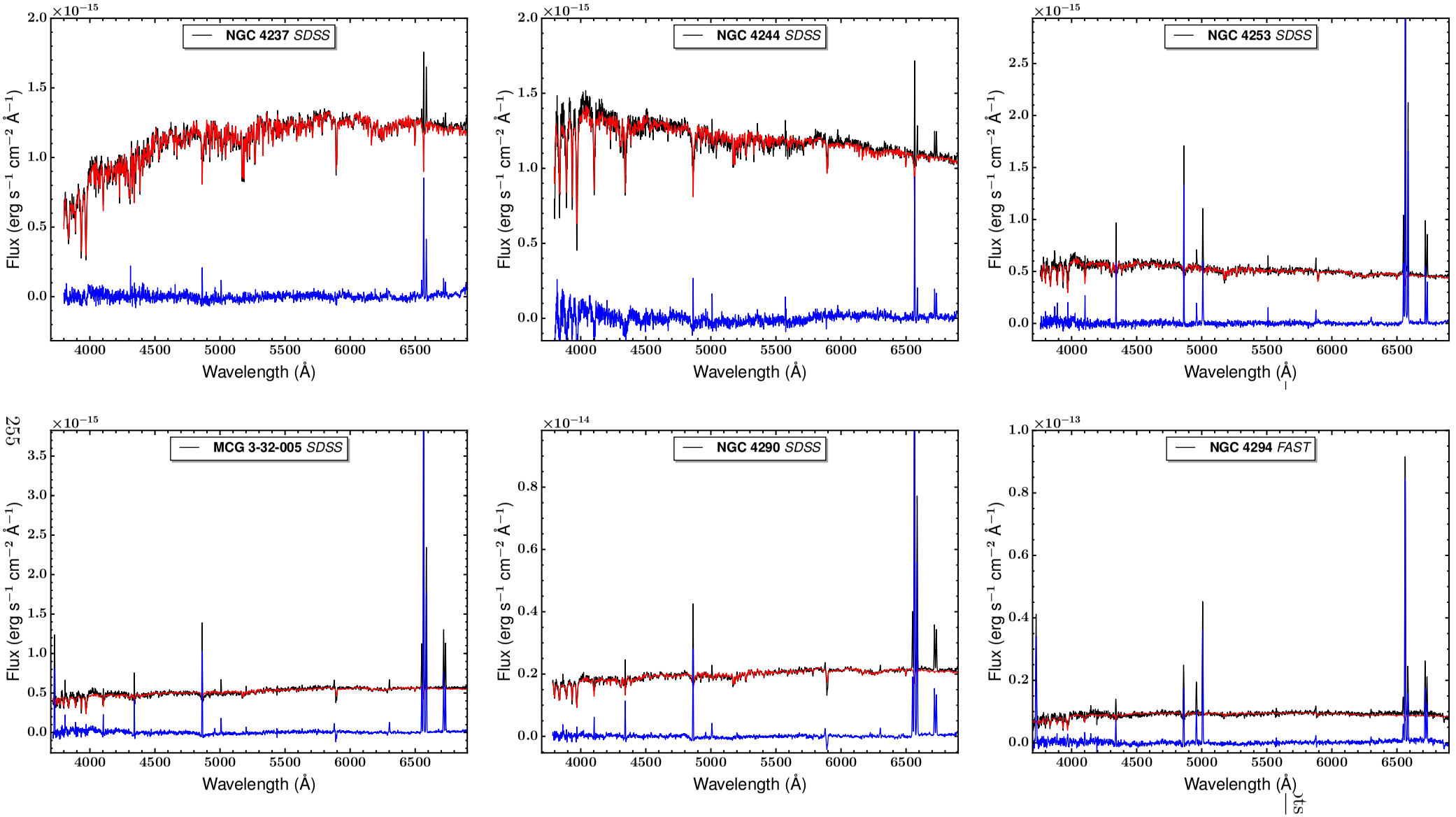


**Figure 8.A.32:** The nuclear spectra of NGC 4237, NGC 4244, NGC 4253, MCG 3-32-005, NGC 4290, NGC 4294. The observed spectrum is shown with a black line, the STARLIGHT fit with a red line, and the starlight subtracted spectrum with a blue line.

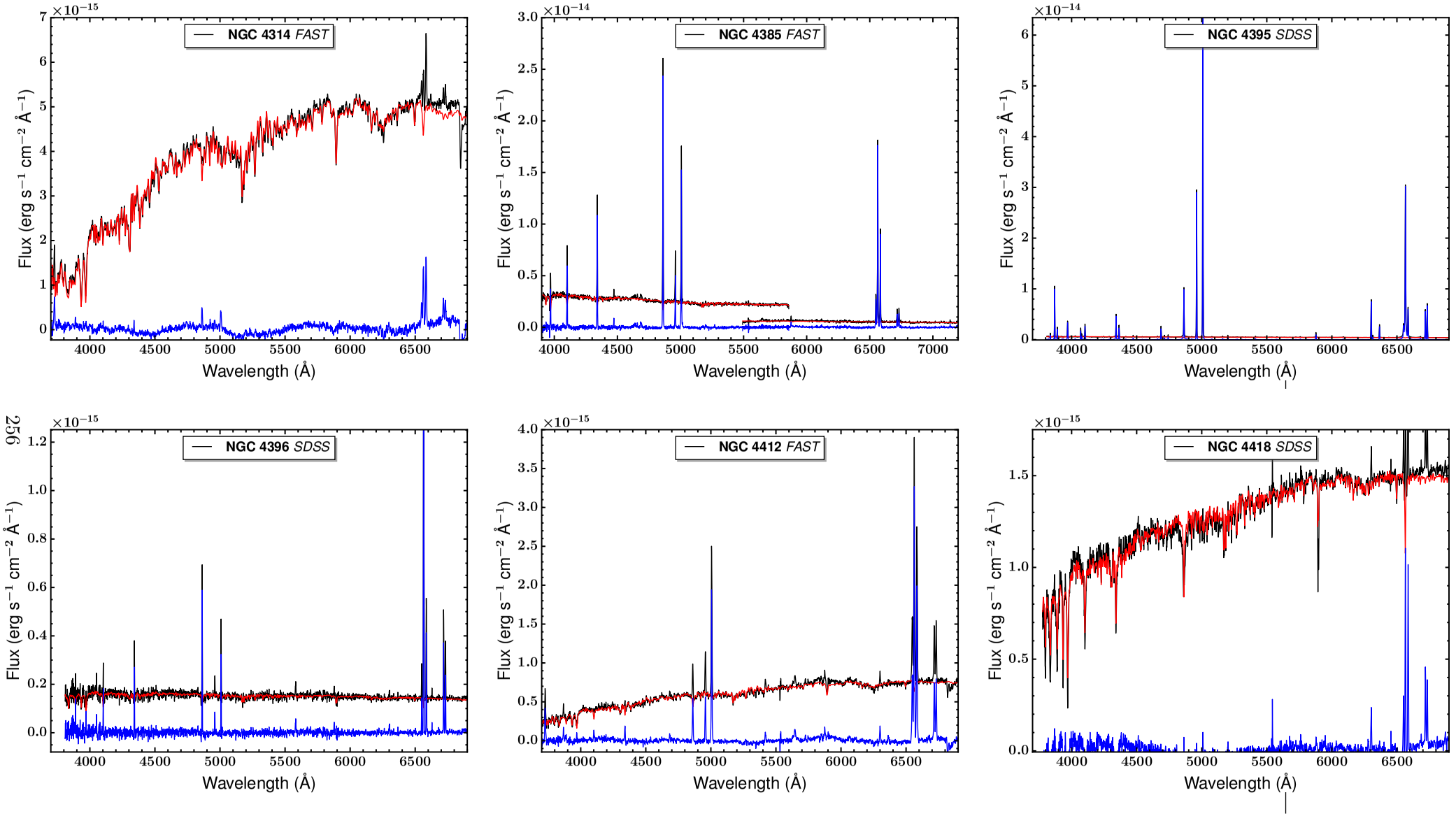


**Figure 8.A.33:** The nuclear spectra of NGC 4314, NGC 4385, NGC 4395, NGC 4396, NGC 4412, NGC 4418. The observed spectrum is shown with a black line, the STARLIGHT fit with a red line, and the starlight subtracted spectrum with a blue line.

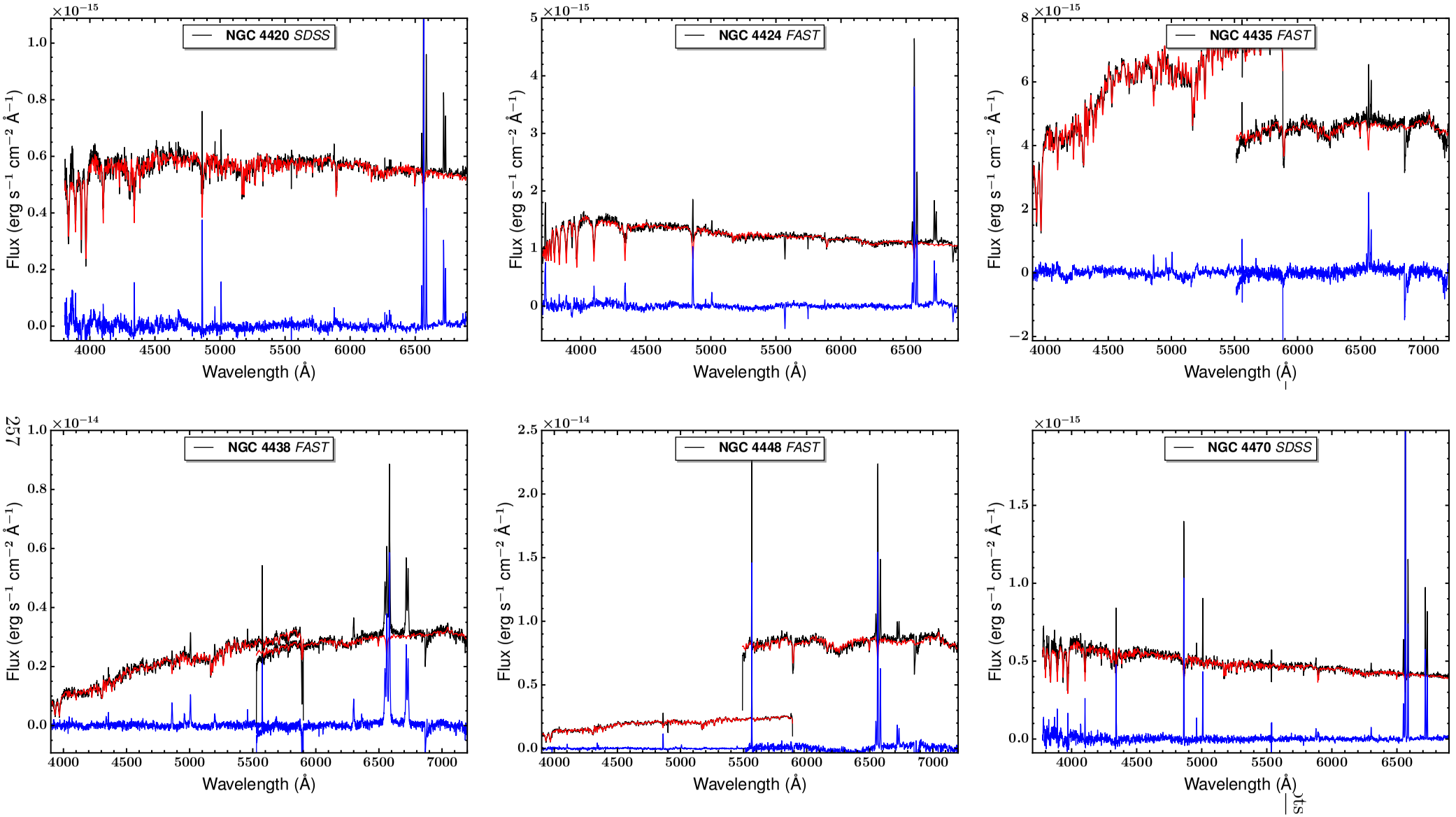


**Figure 8.A.34:** The nuclear spectra of NGC 4420, NGC 4424, NGC 4435, NGC 4438, NGC 4448, NGC 4470. The observed spectrum is shown with a black line, the STARLIGHT fit with a red line, and the starlight subtracted spectrum with a blue line.

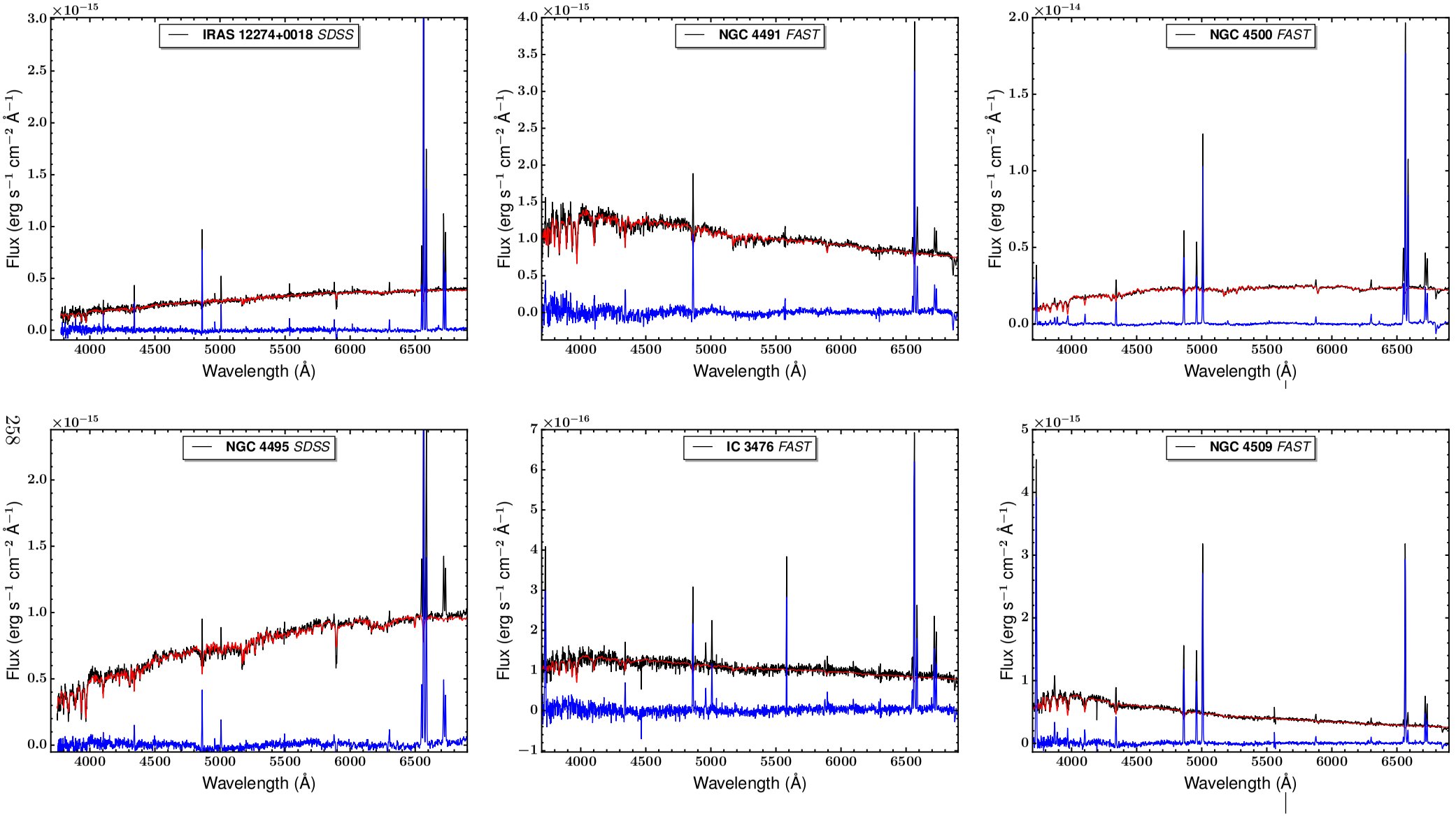


**Figure 8.A.35:** The nuclear spectra of IRAS 12274+0018, NGC 4491, NGC 4500, NGC 4495, IC 3476, NGC 4509. The observed spectrum is shown with a black line, the STARLIGHT fit with a red line, and the starlight subtracted spectrum with a blue line.

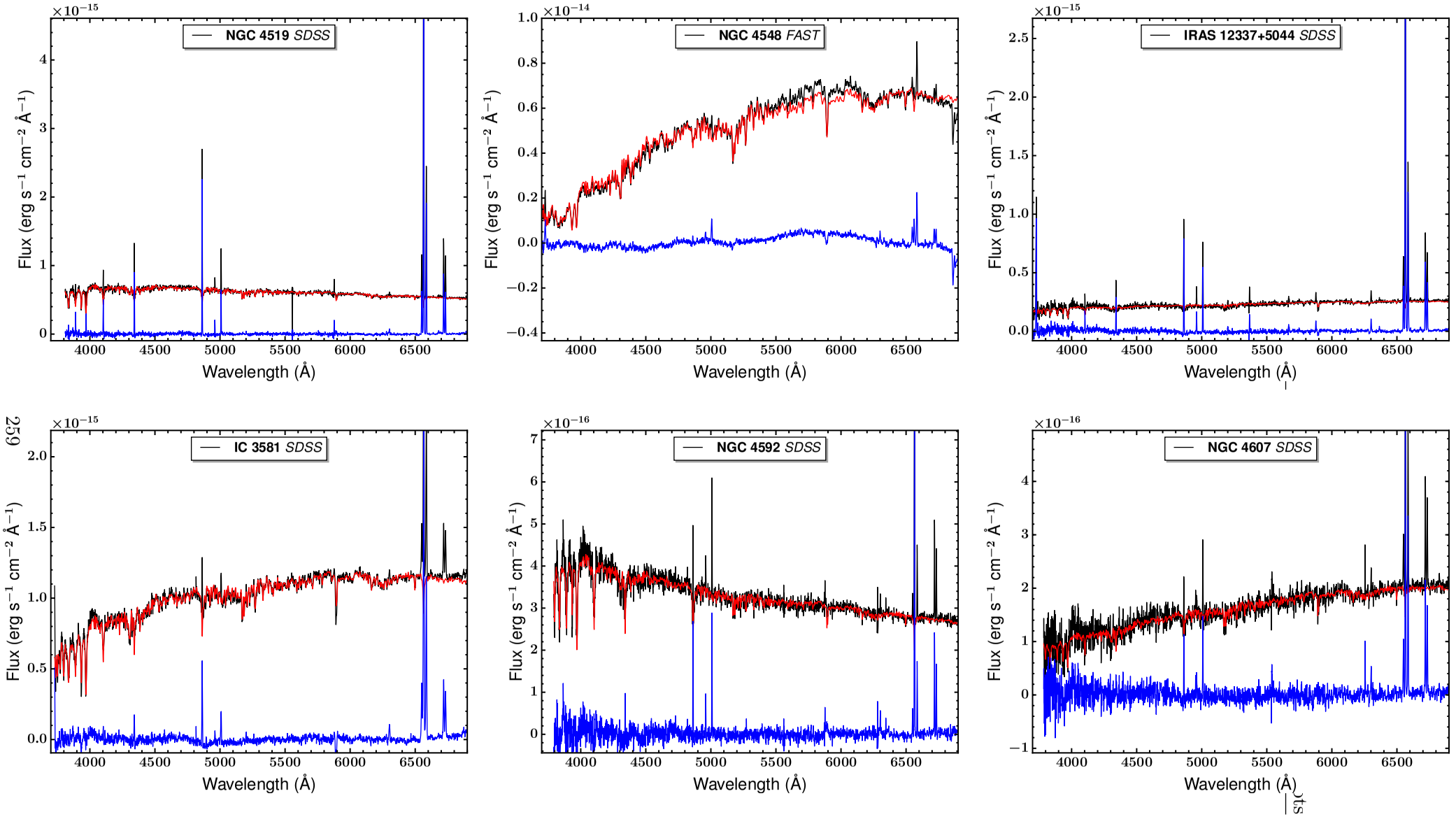


**Figure 8.A.36:** The nuclear spectra of NGC 4519, NGC 4548, IRAS 12337+5044, IC 3581, NGC 4592, NGC 4607. The observed spectrum is shown with a black line, the STARLIGHT fit with a red line, and the starlight subtracted spectrum with a blue line.

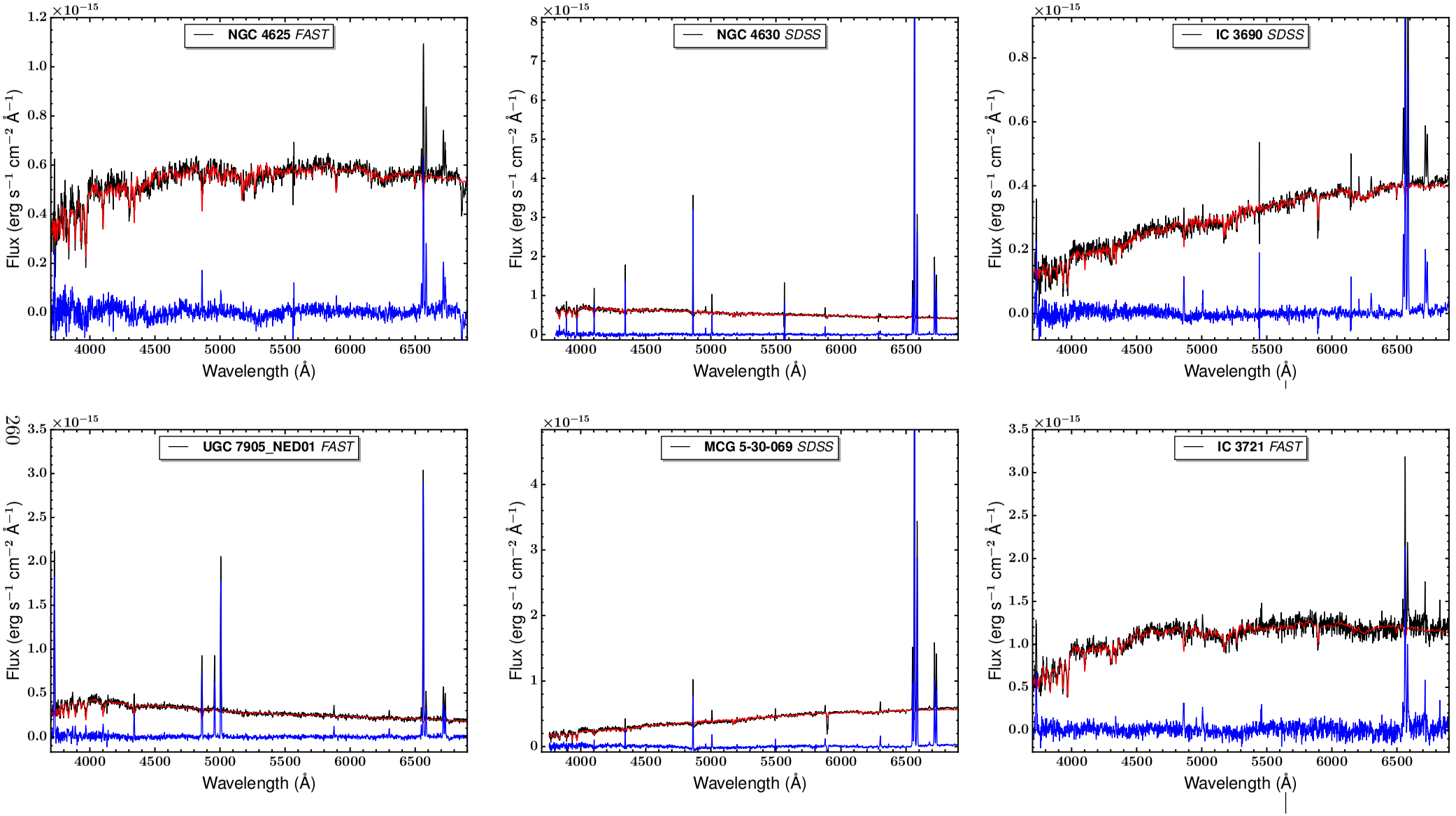


**Figure 8.A.37:** The nuclear spectra of NGC 4625, NGC 4630, IC 3690, UGC 7905_NED01, MCG 5-30-069, IC 3721. The observed spectrum is shown with a black line, the STARLIGHT fit with a red line, and the starlight subtracted spectrum with a blue line.

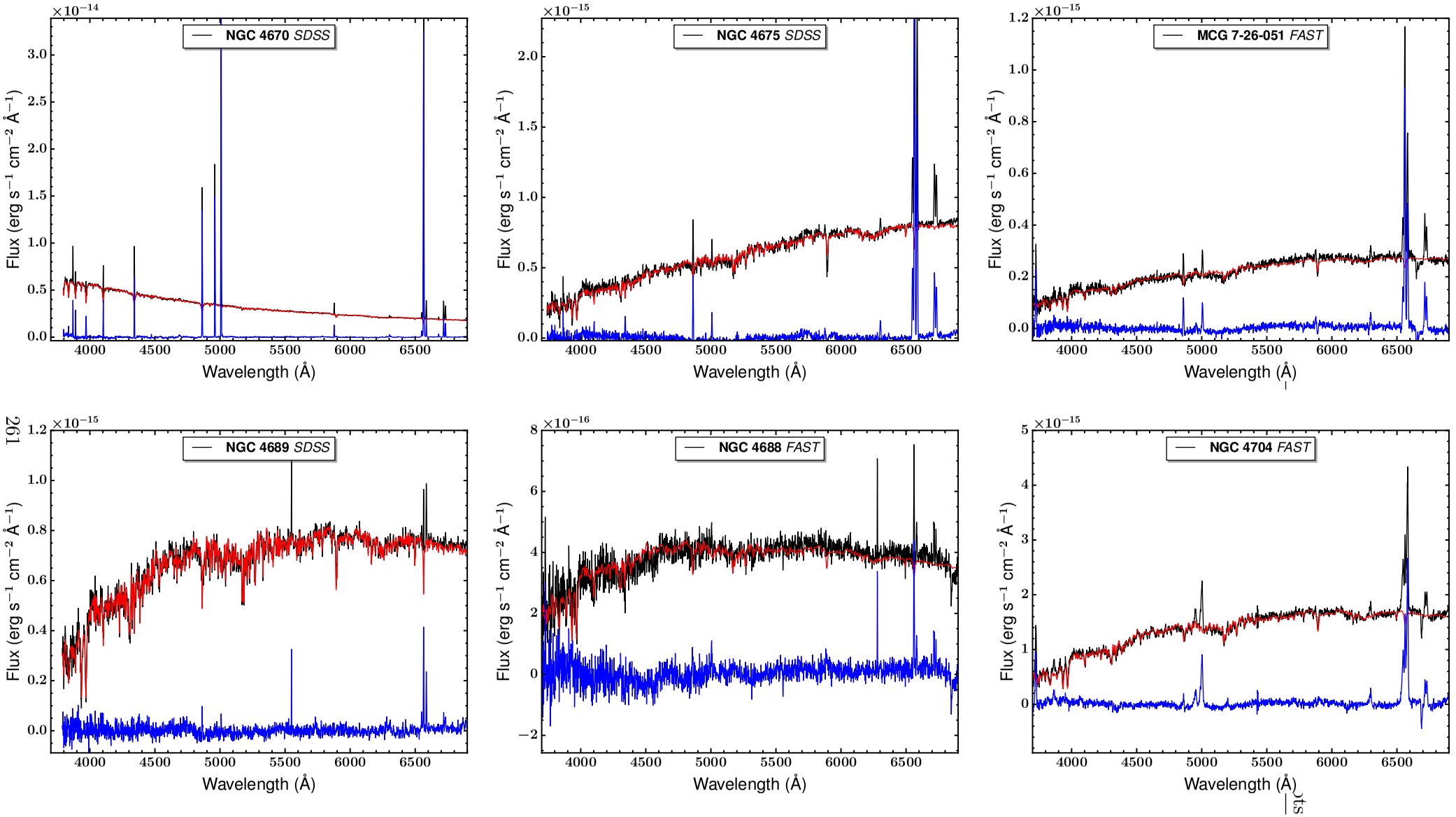




**Figure 8.A.38:** The nuclear spectra of NGC 4670, NGC 4675, MCG 7-26-051, NGC 4689, NGC 4688, NGC 4704. The observed spectrum is shown with a black line, the STARLIGHT fit with a red line, and the starlight subtracted spectrum with a blue line.

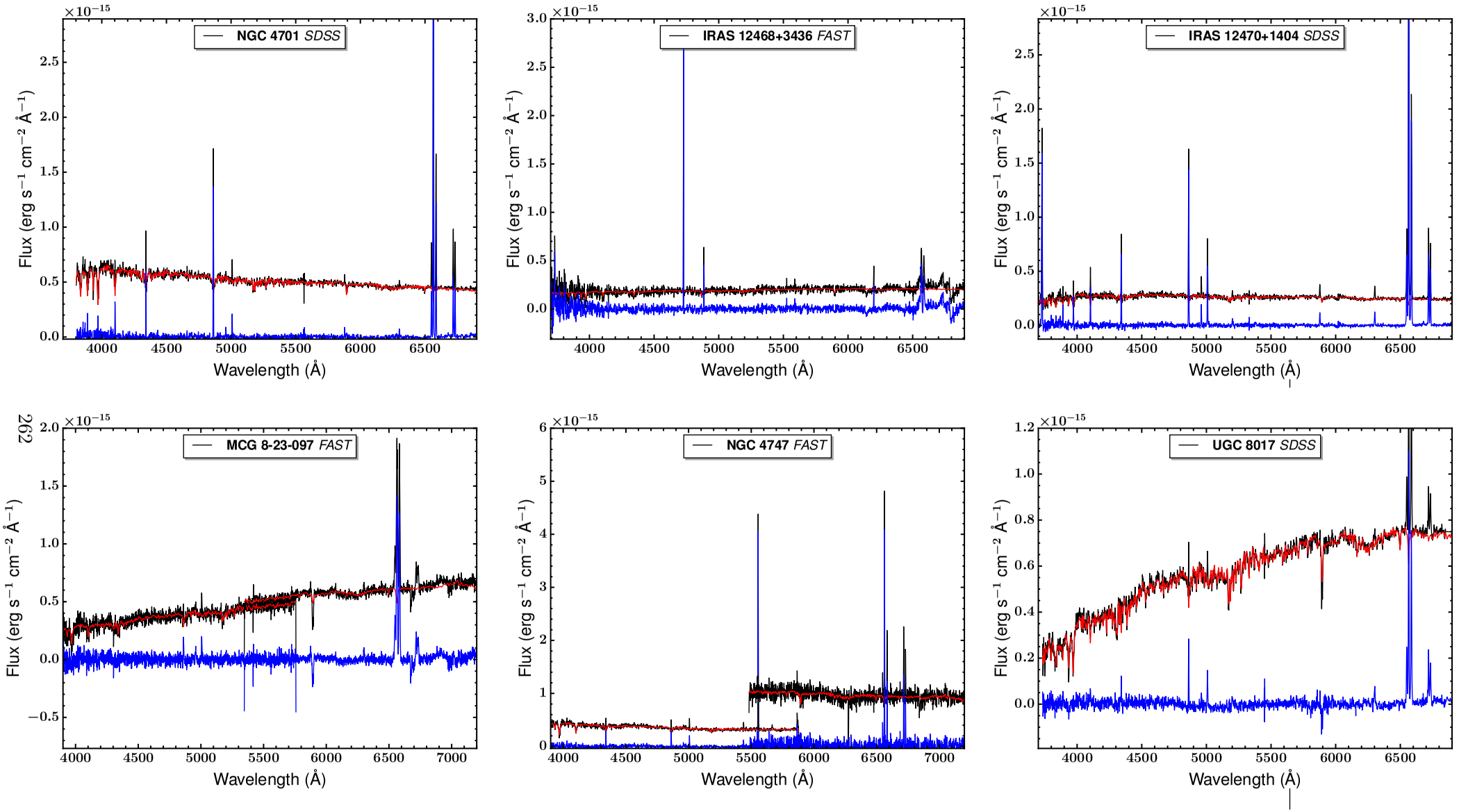


**Figure 8.A.39:** The nuclear spectra of NGC 4701, IRAS 12468+3436, IRAS 12470+1404, MCG 8-23-097, NGC 4747, UGC 8017. The observed spectrum is shown with a black line, the STARLIGHT fit with a red line, and the starlight subtracted spectrum with a blue line.

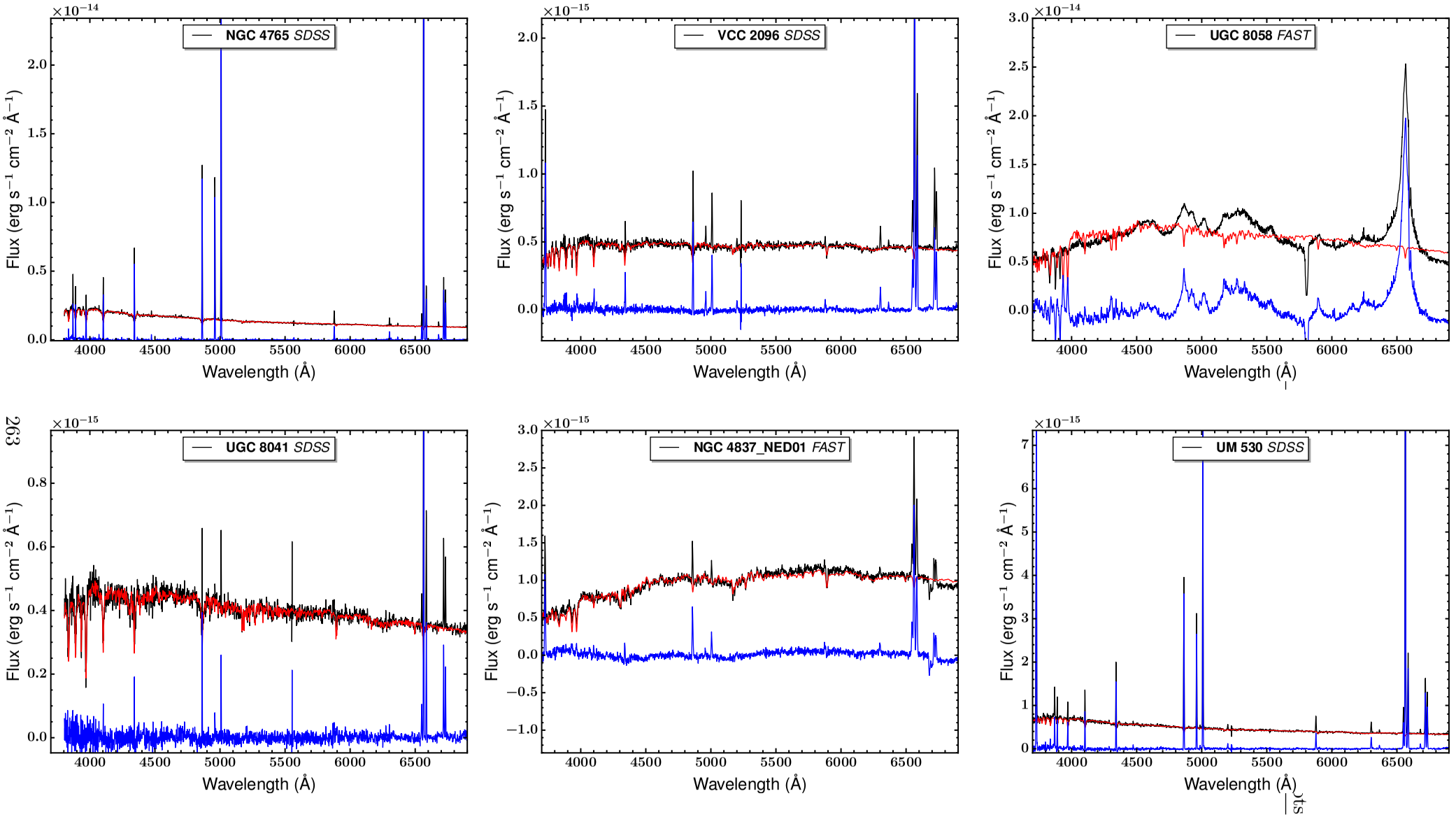


**Figure 8.A.40:** The nuclear spectra of NGC 4765, VCC 2096, UGC 8058, UGC 8041, NGC 4837_NED01, UM 530. The observed spectrum is shown with a black line, the STARLIGHT fit with a red line, and the starlight subtracted spectrum with a blue line.

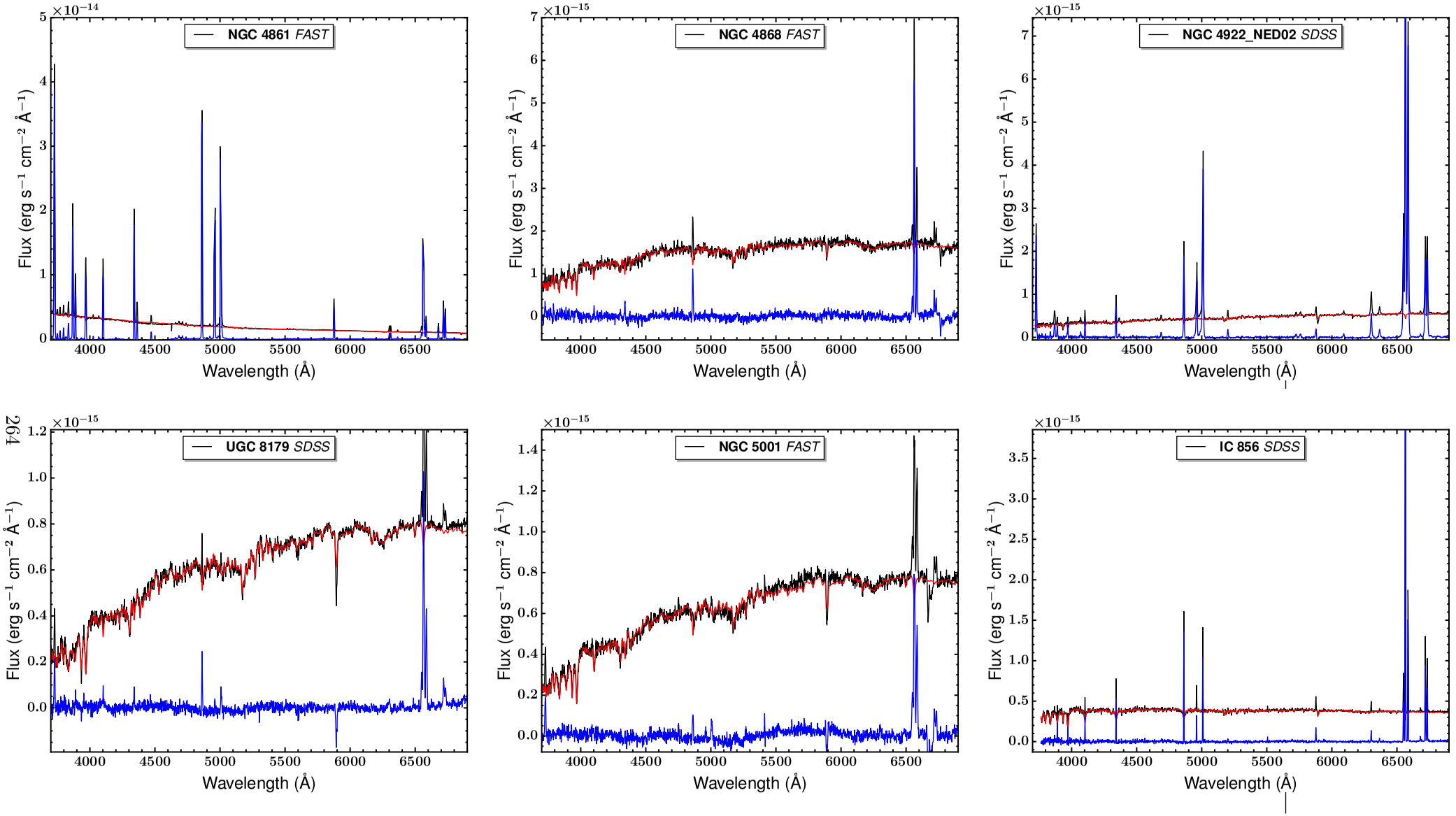




**Figure 8.A.41:** The nuclear spectra of NGC 4861, NGC 4868, NGC 4922_NED02, UGC 8179, NGC 5001, IC 856. The observed spectrum is shown with a black line, the STARLIGHT fit with a red line, and the starlight subtracted spectrum with a blue line.

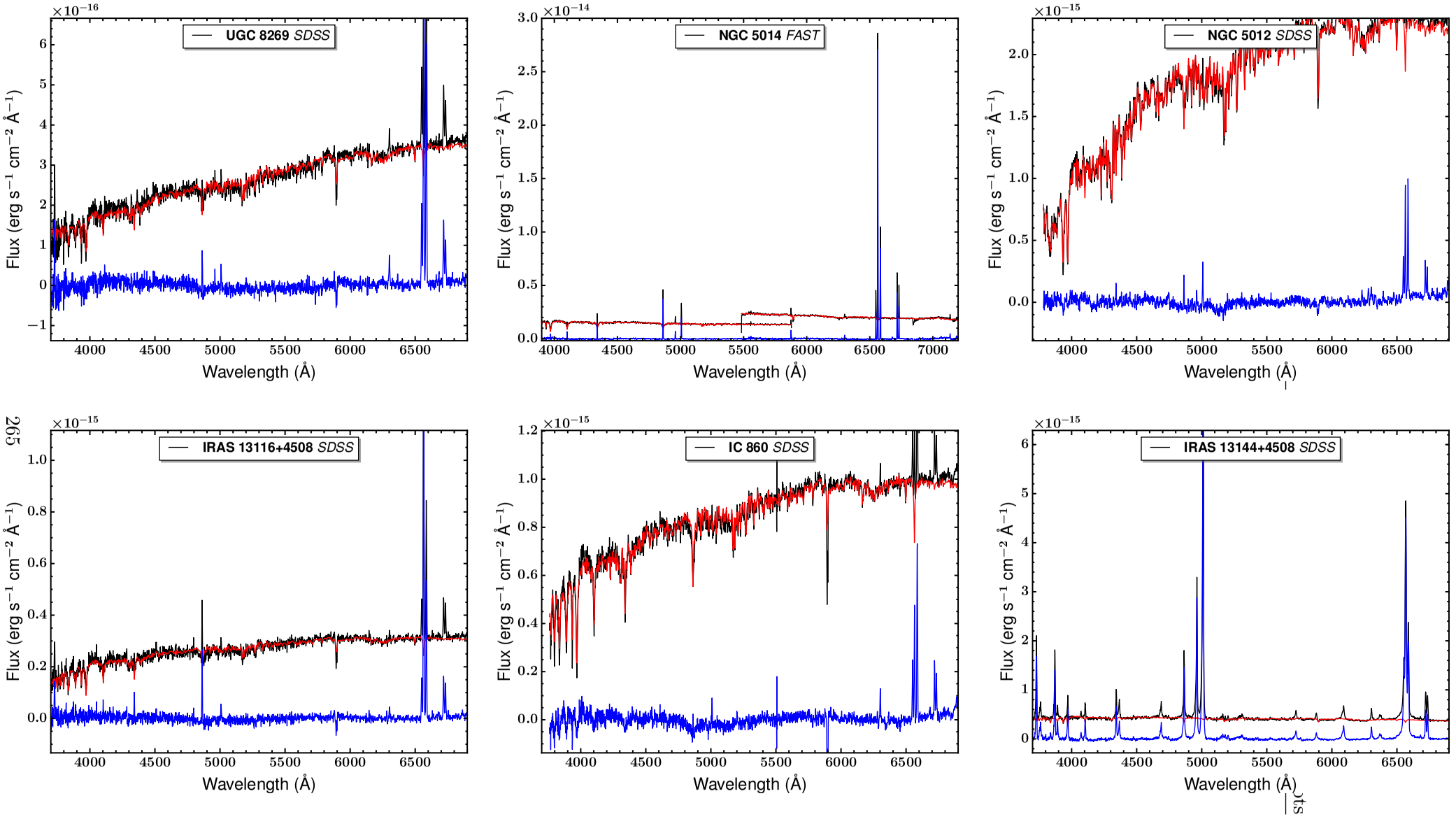


**Figure 8.A.42:** The nuclear spectra of UGC 8269, NGC 5014, NGC 5012, IRAS 13116+4508, IC 860, IRAS 13144+4508. The observed spectrum is shown with a black line, the STARLIGHT fit with a red line, and the starlight subtracted spectrum with a blue line.

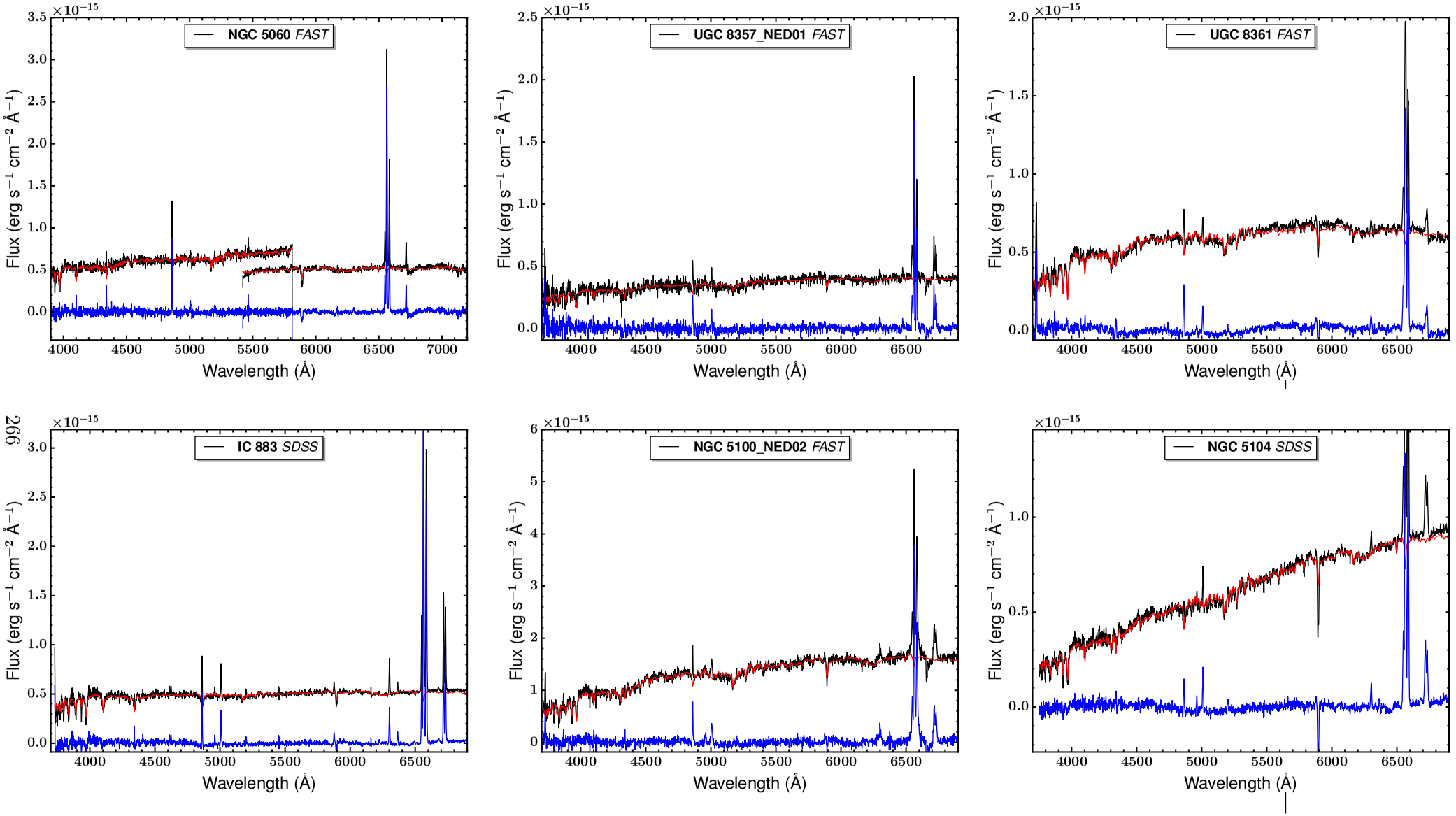




**Figure 8.A.43:** The nuclear spectra of NGC 5060, UGC 8357_NED01, UGC 8361, IC 883, NGC 5100_NED02, NGC 5104. The observed spectrum is shown with a black line, the STARLIGHT fit with a red line, and the starlight subtracted spectrum with a blue line.

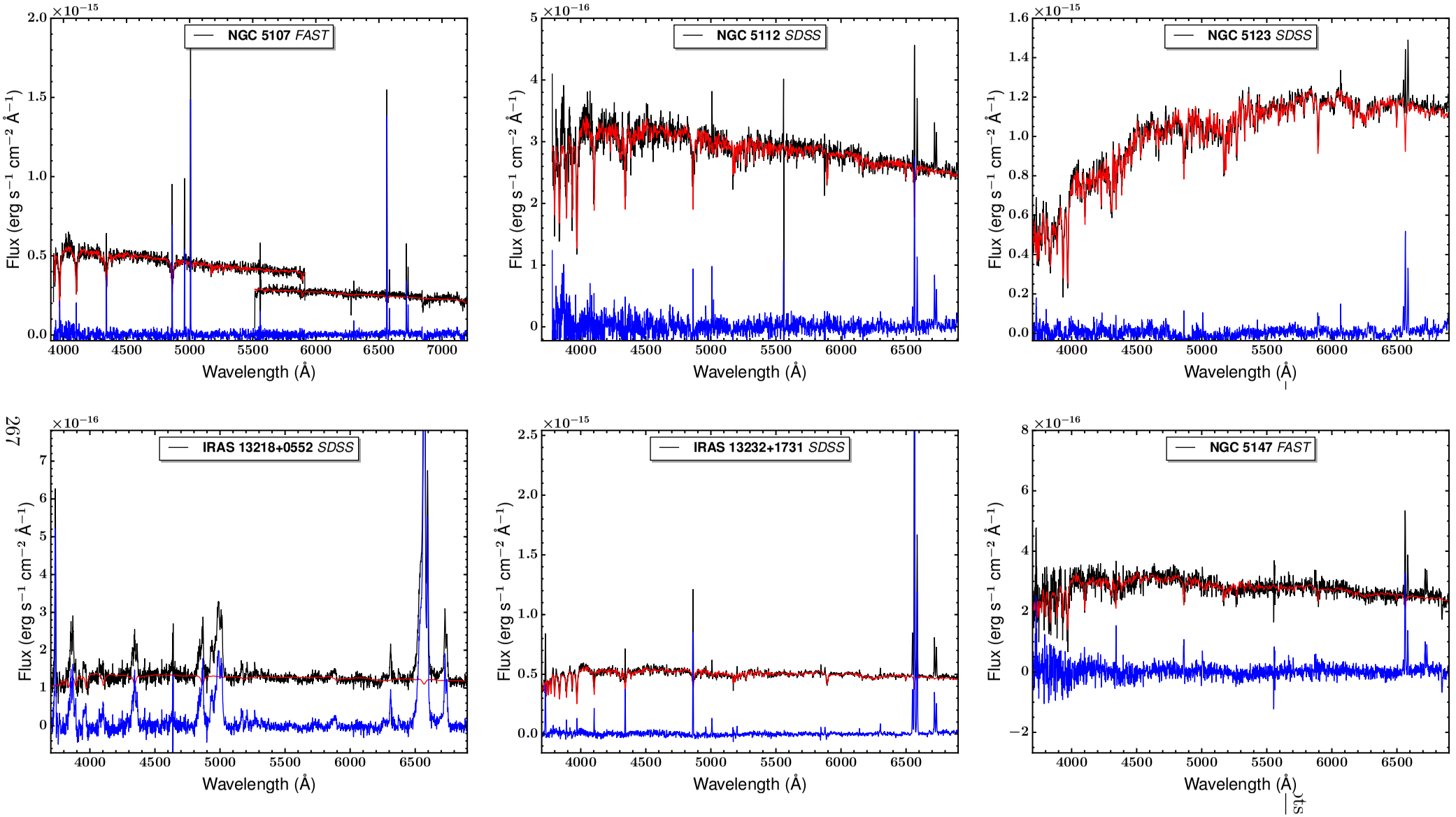




**Figure 8.A.44:** The nuclear spectra of NGC 5107, NGC 5112, NGC 5123, IRAS 13218+0552, IRAS 13232+1731, NGC 5147. The observed spectrum is shown with a black line, the STARLIGHT fit with a red line, and the starlight subtracted spectrum with a blue line.

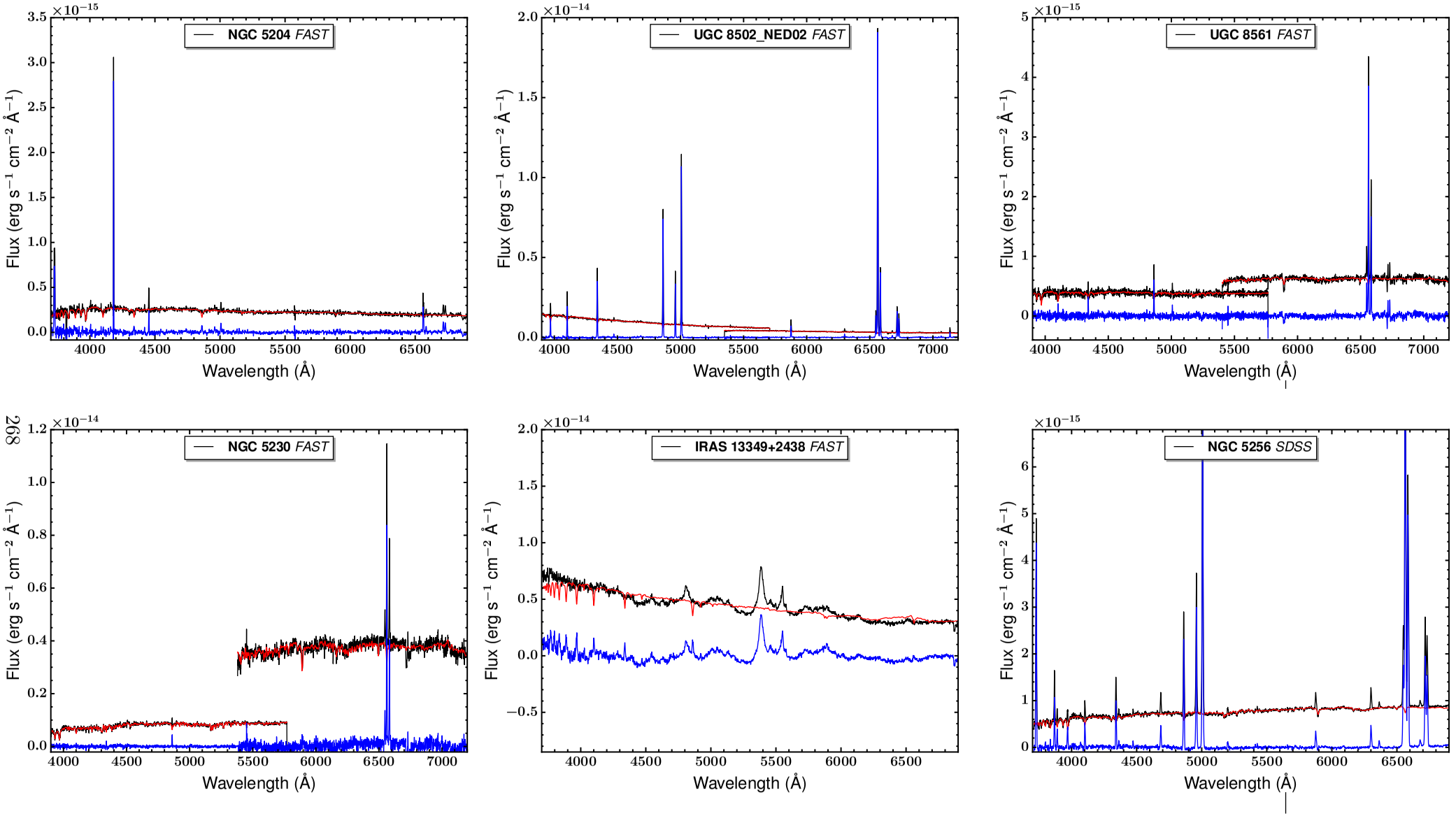


**Figure 8.A.45:** The nuclear spectra of NGC 5204, UGC 8502_NED02, UGC 8561, NGC 5230, IRAS 13349+2438, NGC 5256. The observed spectrum is shown with a black line, the STARLIGHT fit with a red line, and the starlight subtracted spectrum with a blue line.

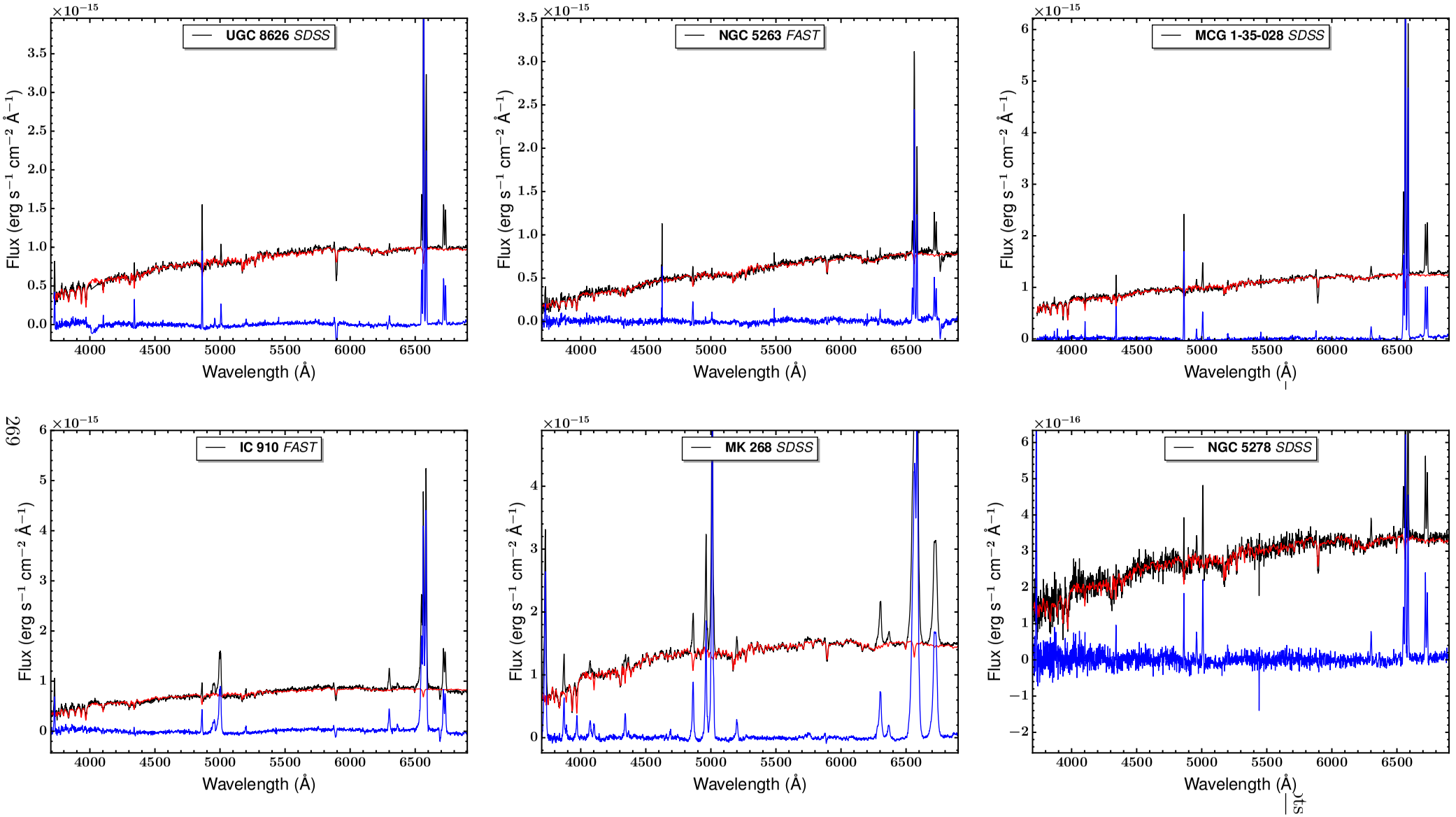




**Figure 8.A.46:** The nuclear spectra of UGC 8626, NGC 5263, MCG 1-35-028, IC 910, MK 268, NGC 5278. The observed spectrum is shown with a black line, the STARLIGHT fit with a red line, and the starlight subtracted spectrum with a blue line.

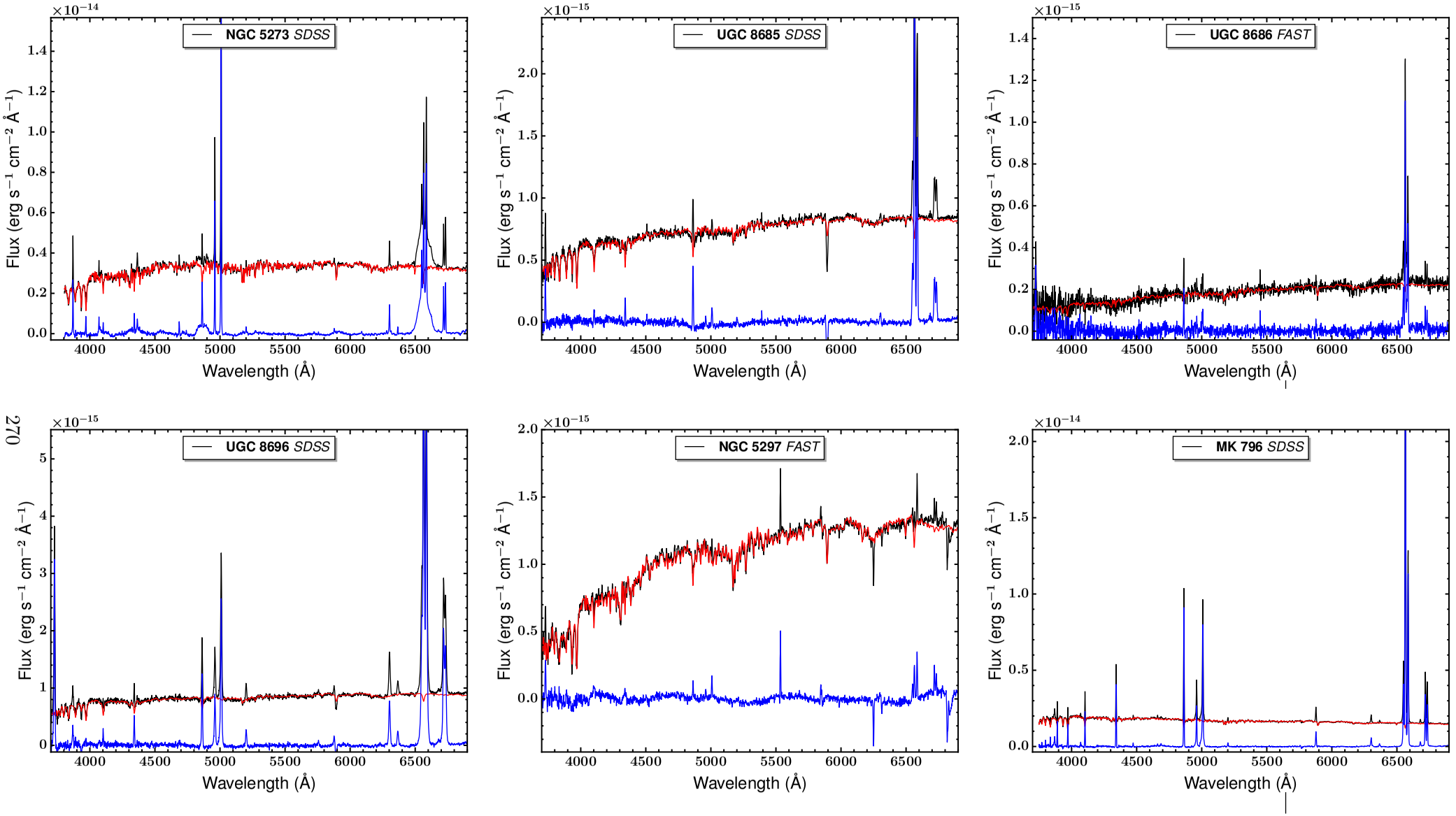




**Figure 8.A.47:** The nuclear spectra of NGC 5273, UGC 8685, UGC 8686, UGC 8696, NGC 5297, MK 796. The observed spectrum is shown with a black line, the STARLIGHT fit with a red line, and the starlight subtracted spectrum with a blue line.

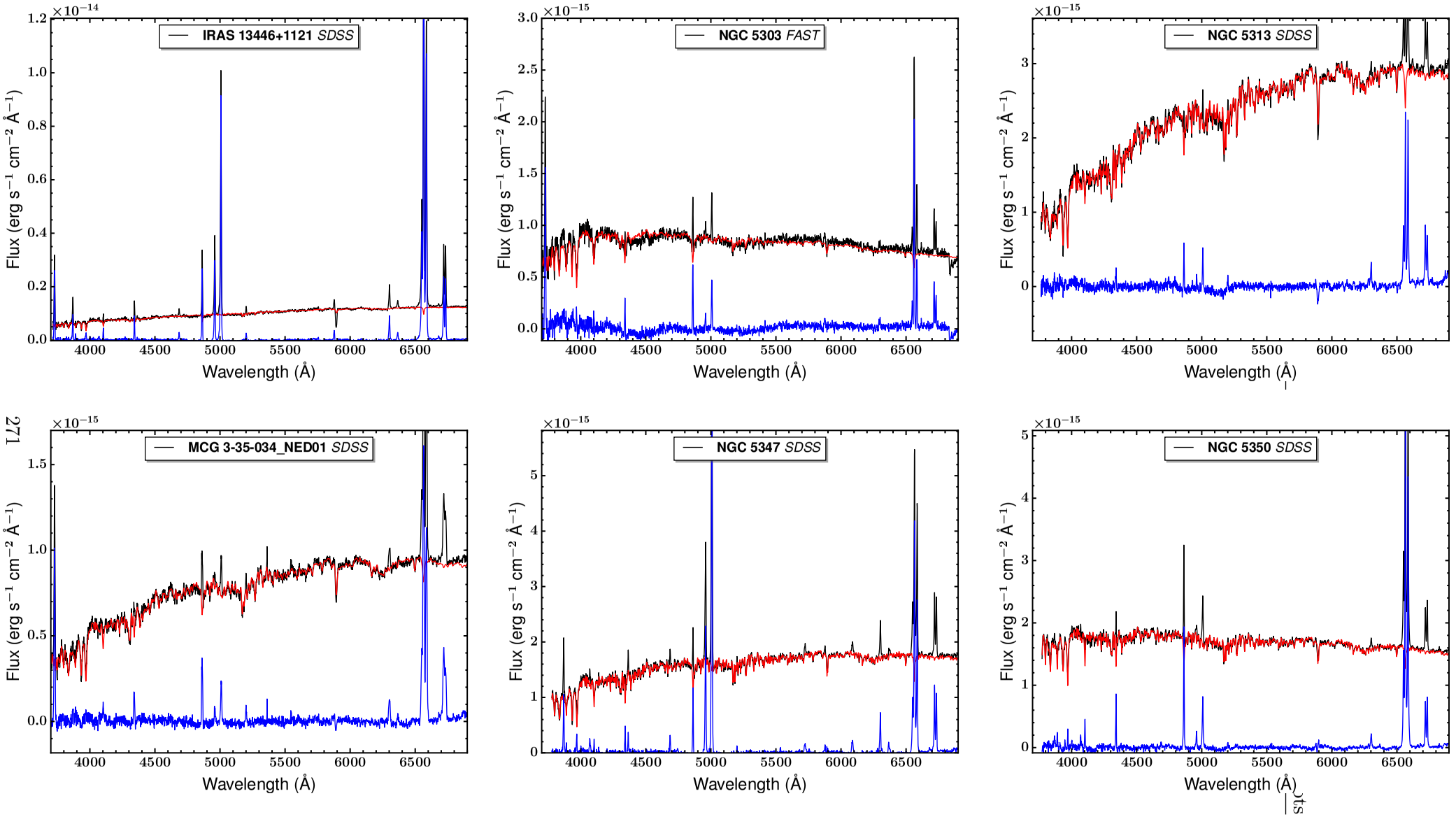


**Figure 8.A.48:** The nuclear spectra of IRAS 13446+1121, NGC 5303, NGC 5313, MCG 3-35-034_NED01, NGC 5347, NGC 5350. The observed spectrum is shown with a black line, the STARLIGHT fit with a red line, and the starlight subtracted spectrum with a blue line.

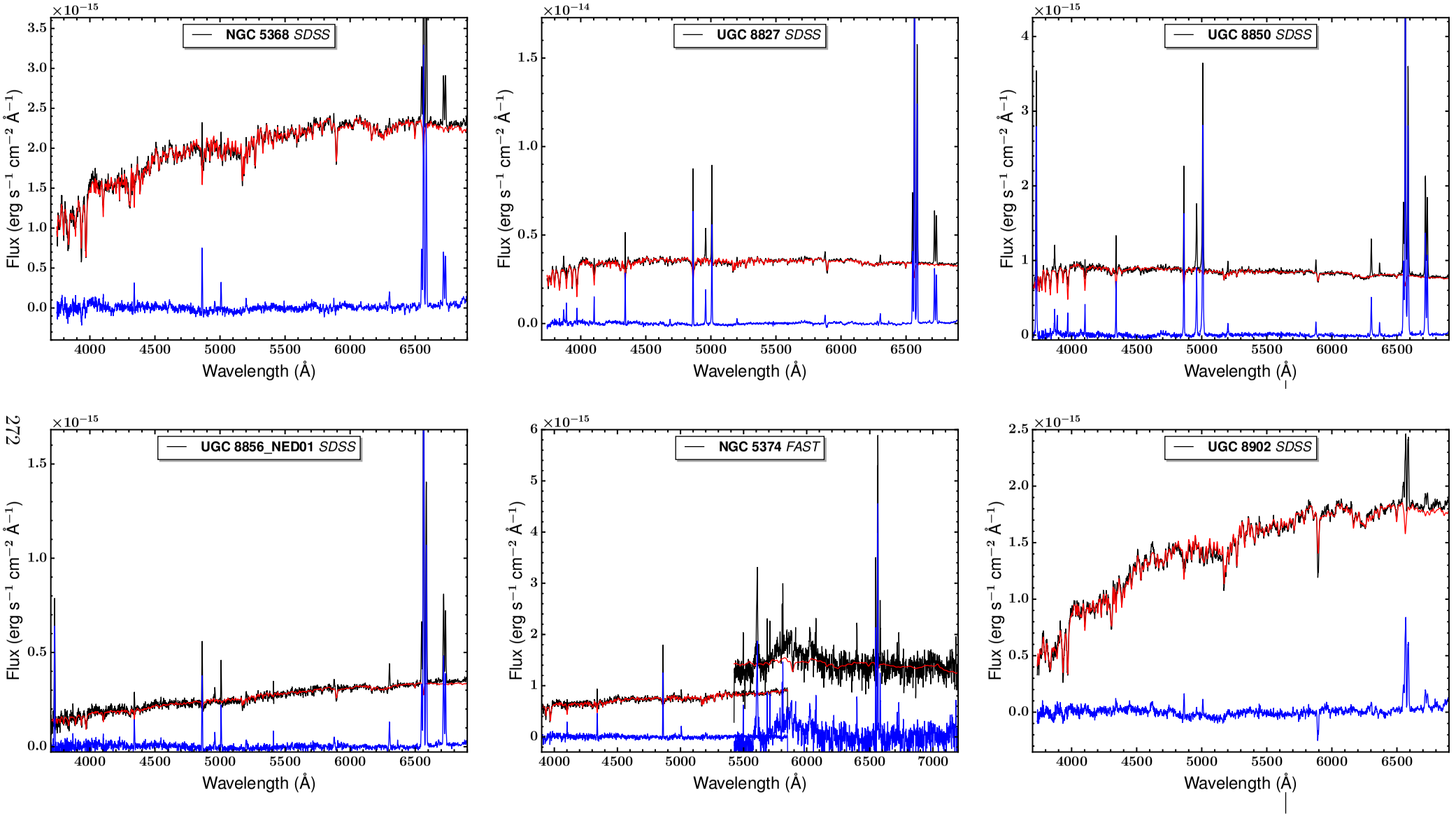


**Figure 8.A.49:** The nuclear spectra of NGC 5368, UGC 8827, UGC 8850, UGC 8856_NED01, NGC 5374, UGC 8902. The observed spectrum is shown with a black line, the STARLIGHT fit with a red line, and the starlight subtracted spectrum with a blue line.

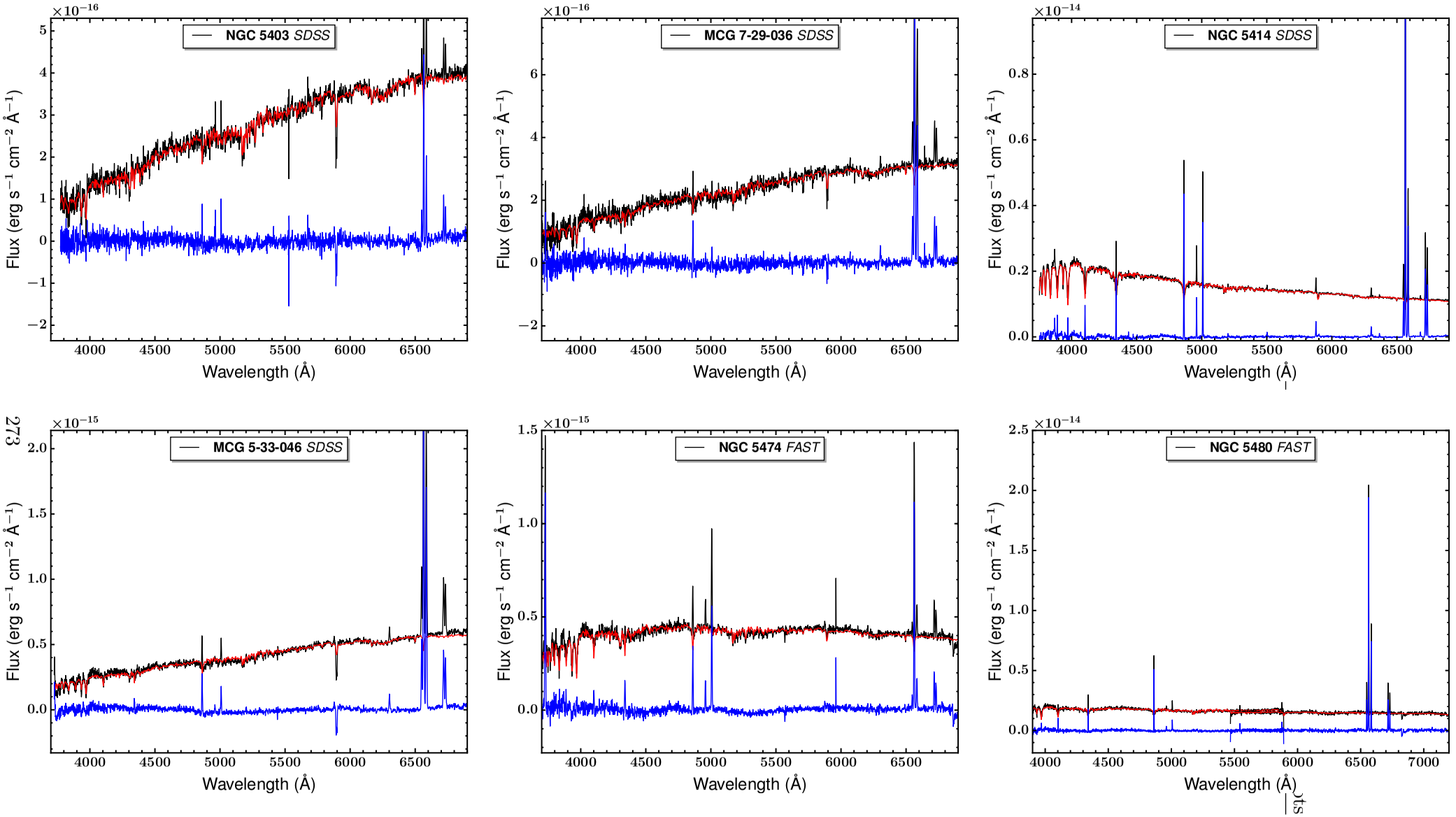


**Figure 8.A.50:** The nuclear spectra of NGC 5403, MCG 7-29-036, NGC 5414, MCG 5-33-046, NGC 5474, NGC 5480. The observed spectrum is shown with a black line, the STARLIGHT fit with a red line, and the starlight subtracted spectrum with a blue line.

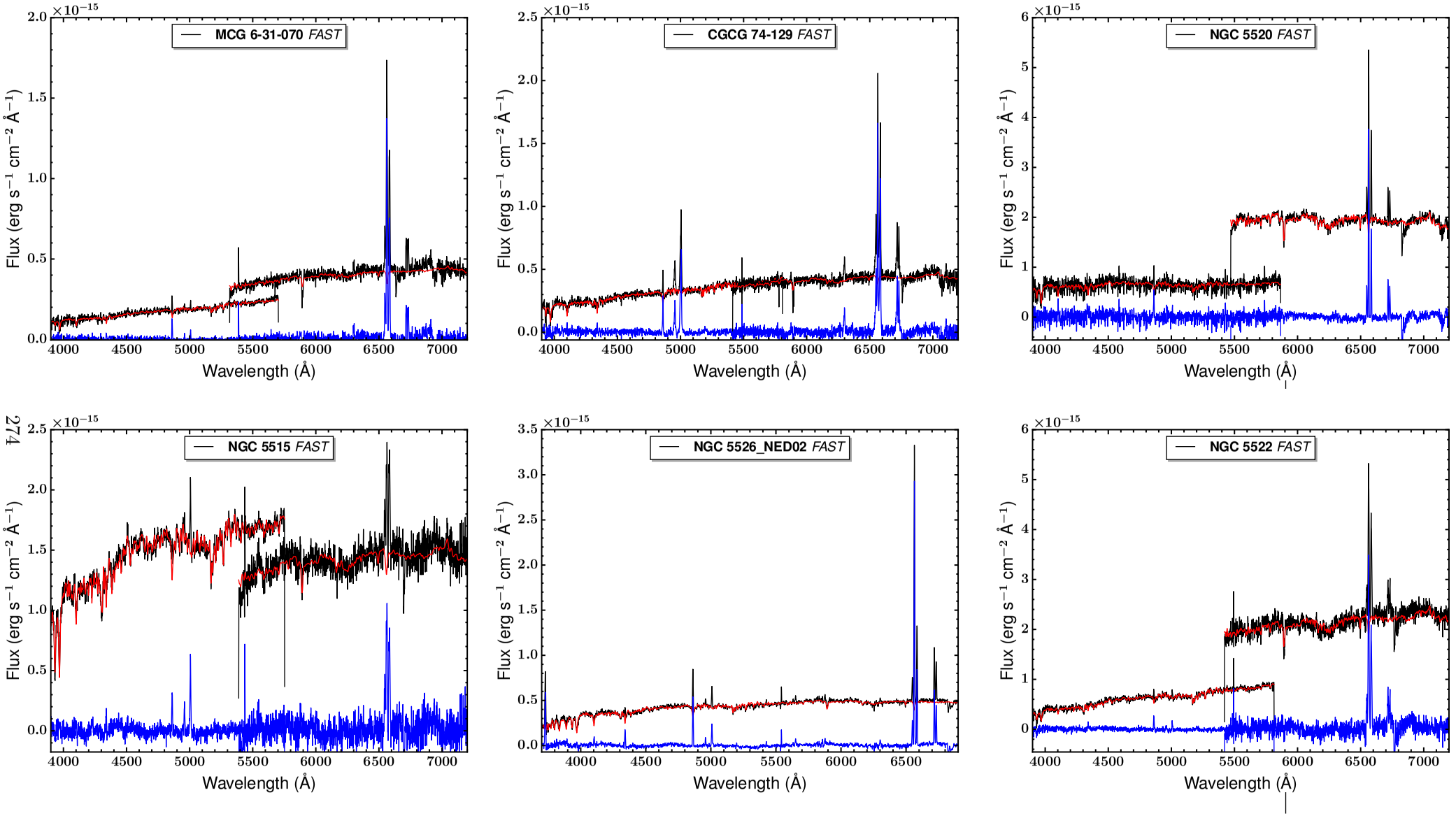


**Figure 8.A.51:** The nuclear spectra of MCG 6-31-070, CGCG 74-129, NGC 5520, NGC 5515, NGC 5526_NED02, NGC 5522. The observed spectrum is shown with a black line, the STARLIGHT fit with a red line, and the starlight subtracted spectrum with a blue line.

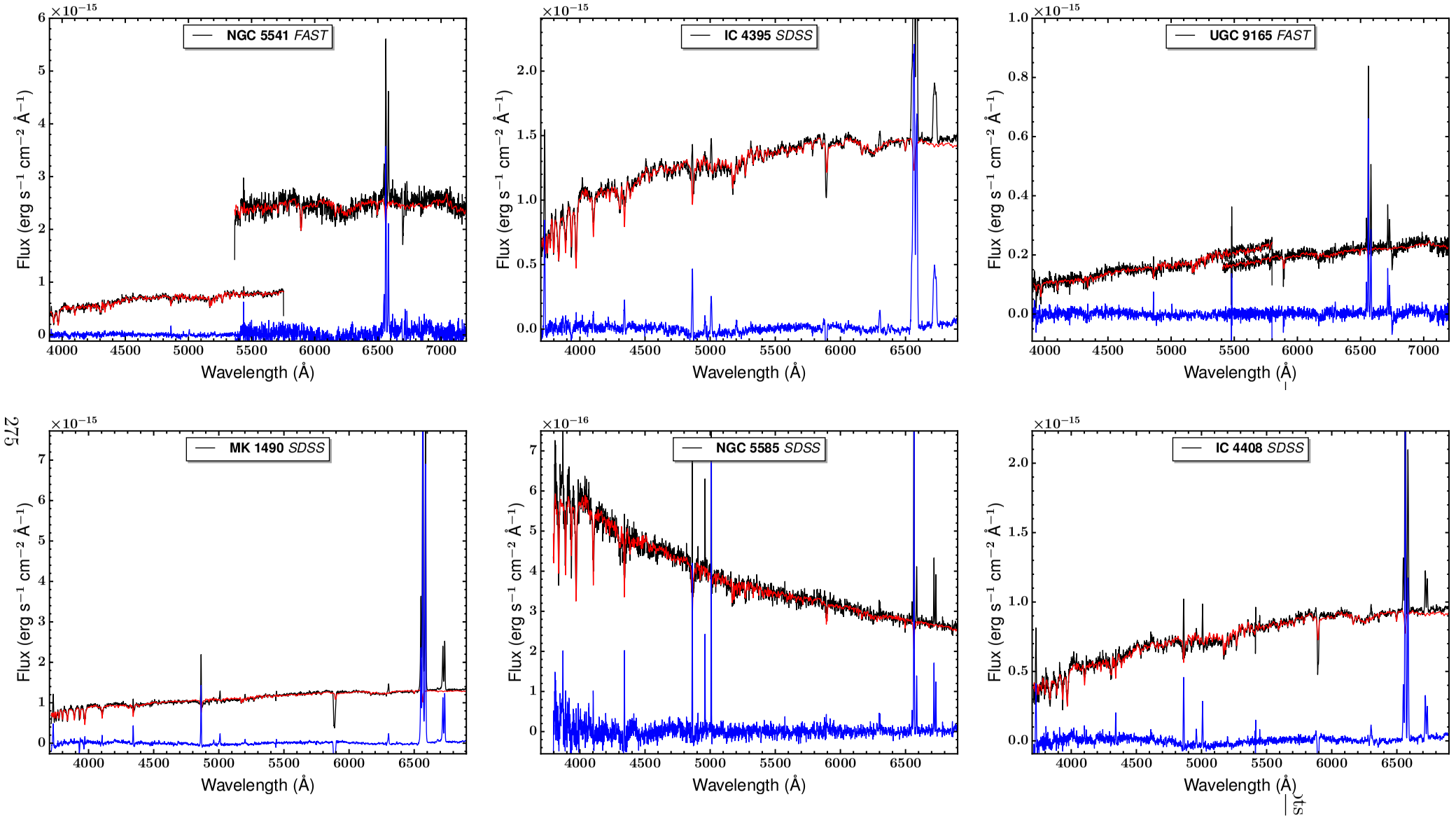


**Figure 8.A.52:** The nuclear spectra of NGC 5541, IC 4395, UGC 9165, MK 1490, NGC 5585, IC 4408. The observed spectrum is shown with a black line, the STARLIGHT fit with a red line, and the starlight subtracted spectrum with a blue line.

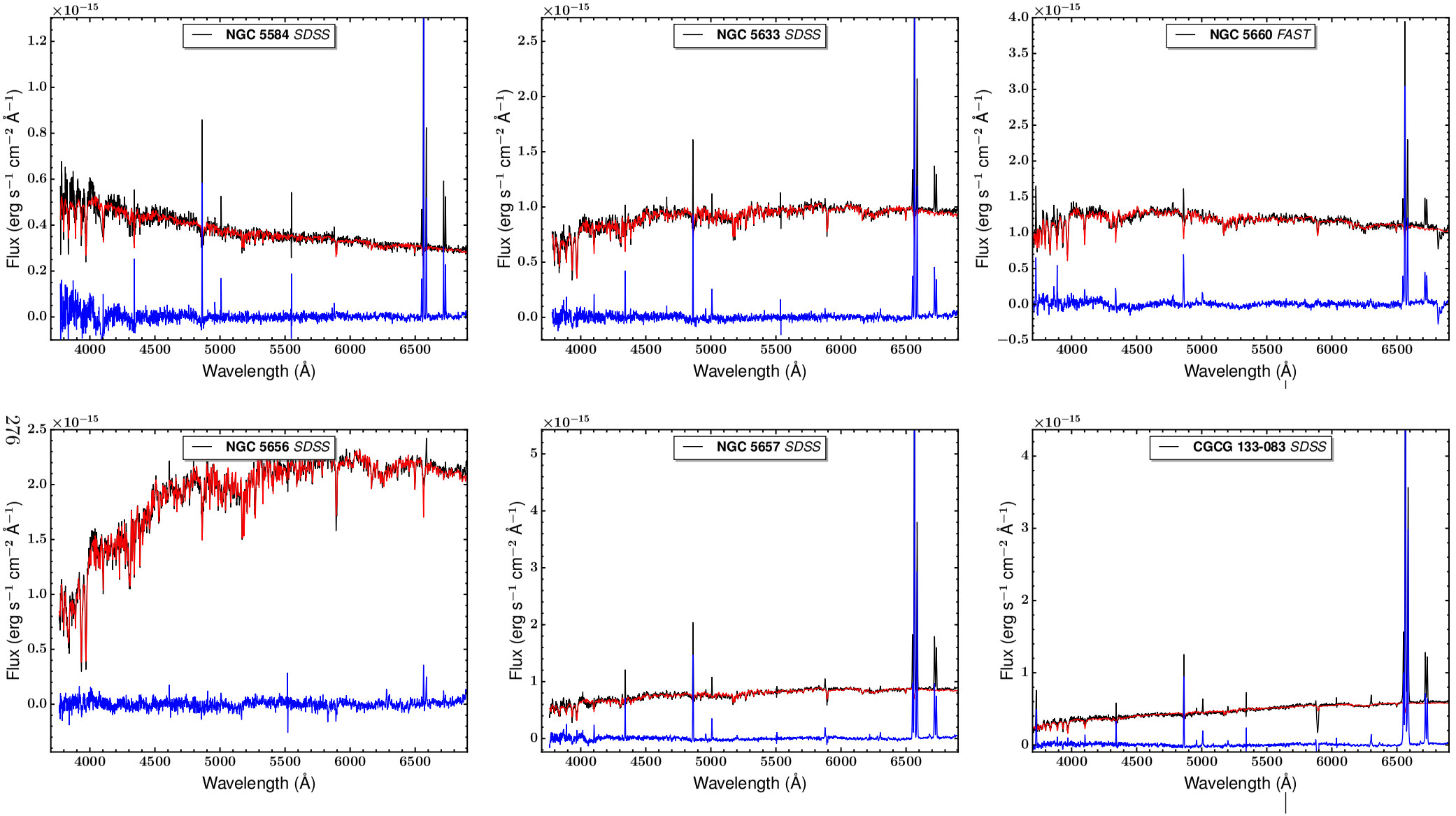




**Figure 8.A.53:** The nuclear spectra of NGC 5584, NGC 5633, NGC 5660, NGC 5656, NGC 5657, CGCG 133-083. The observed spectrum is shown with a black line, the STARLIGHT fit with a red line, and the starlight subtracted spectrum with a blue line.

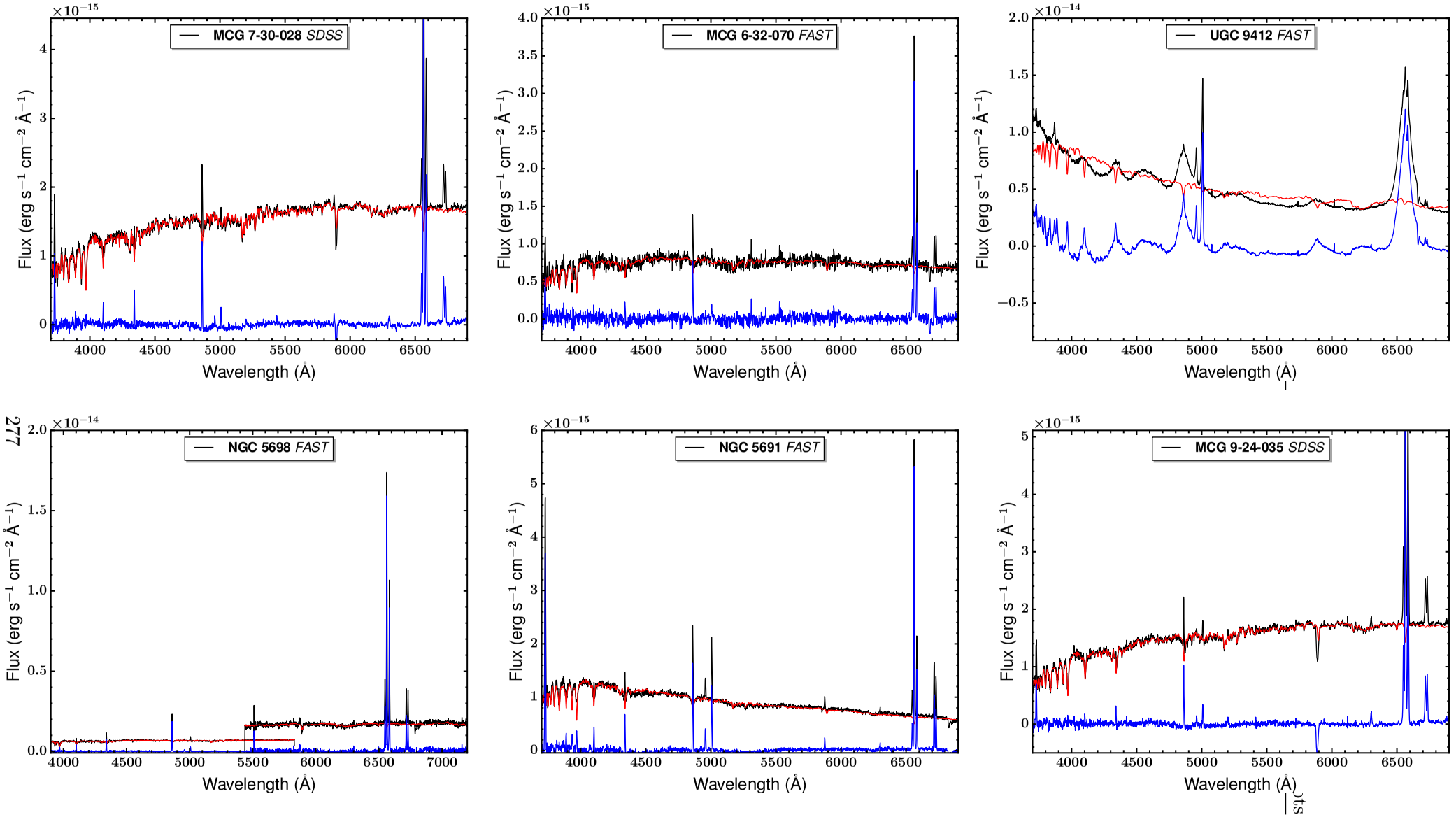




**Figure 8.A.54:** The nuclear spectra of MCG 7-30-028, MCG 6-32-070, UGC 9412, NGC 5698, NGC 5691, MCG 9-24-035. The observed spectrum is shown with a black line, the STARLIGHT fit with a red line, and the starlight subtracted spectrum with a blue line.

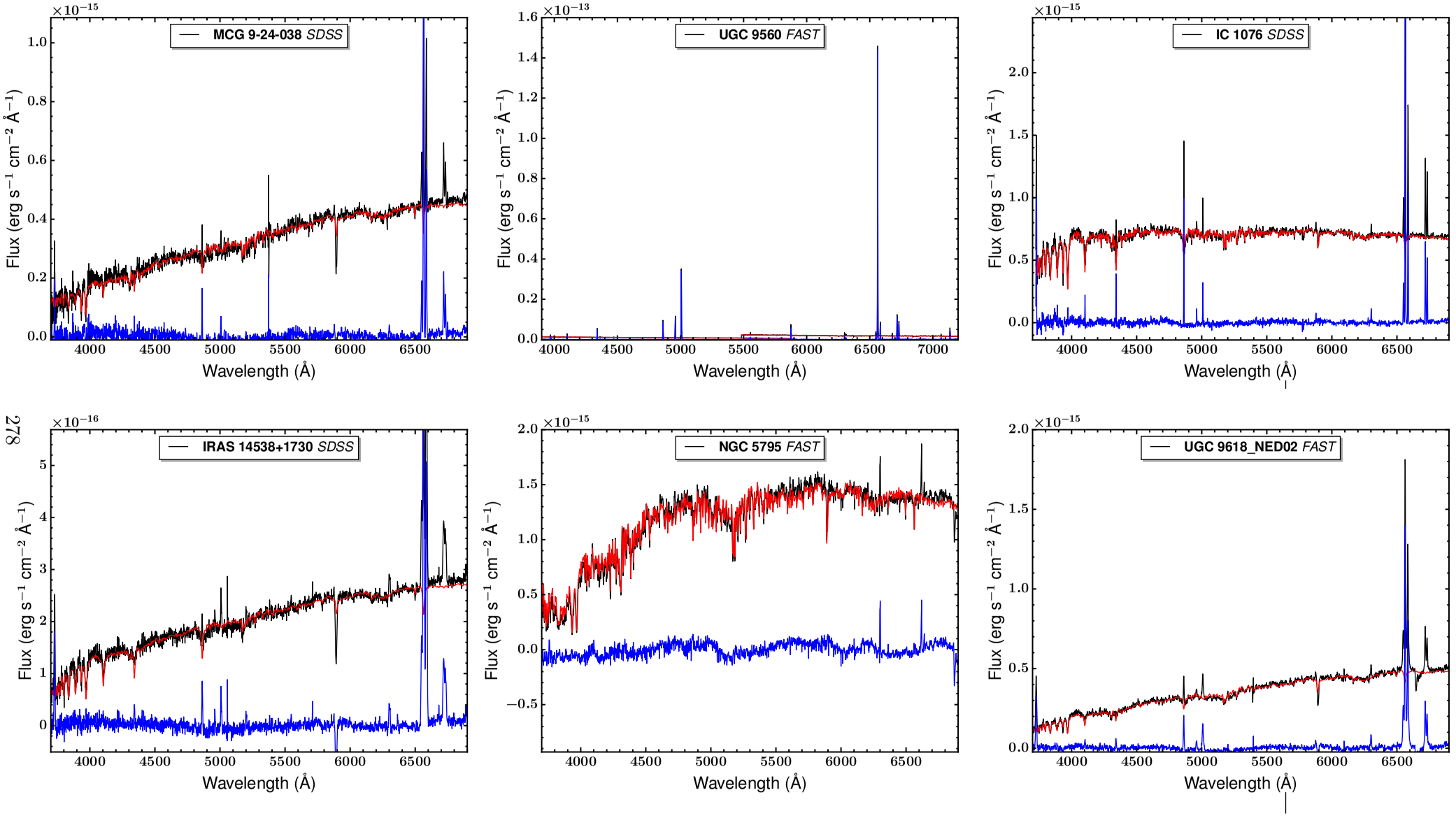




**Figure 8.A.55:** The nuclear spectra of MCG 9-24-038, UGC 9560, IC 1076, IRAS 14538+1730, NGC 5795, UGC 9618_NED02. The observed spectrum is shown with a black line, the STARLIGHT fit with a red line, and the starlight subtracted spectrum with a blue line.

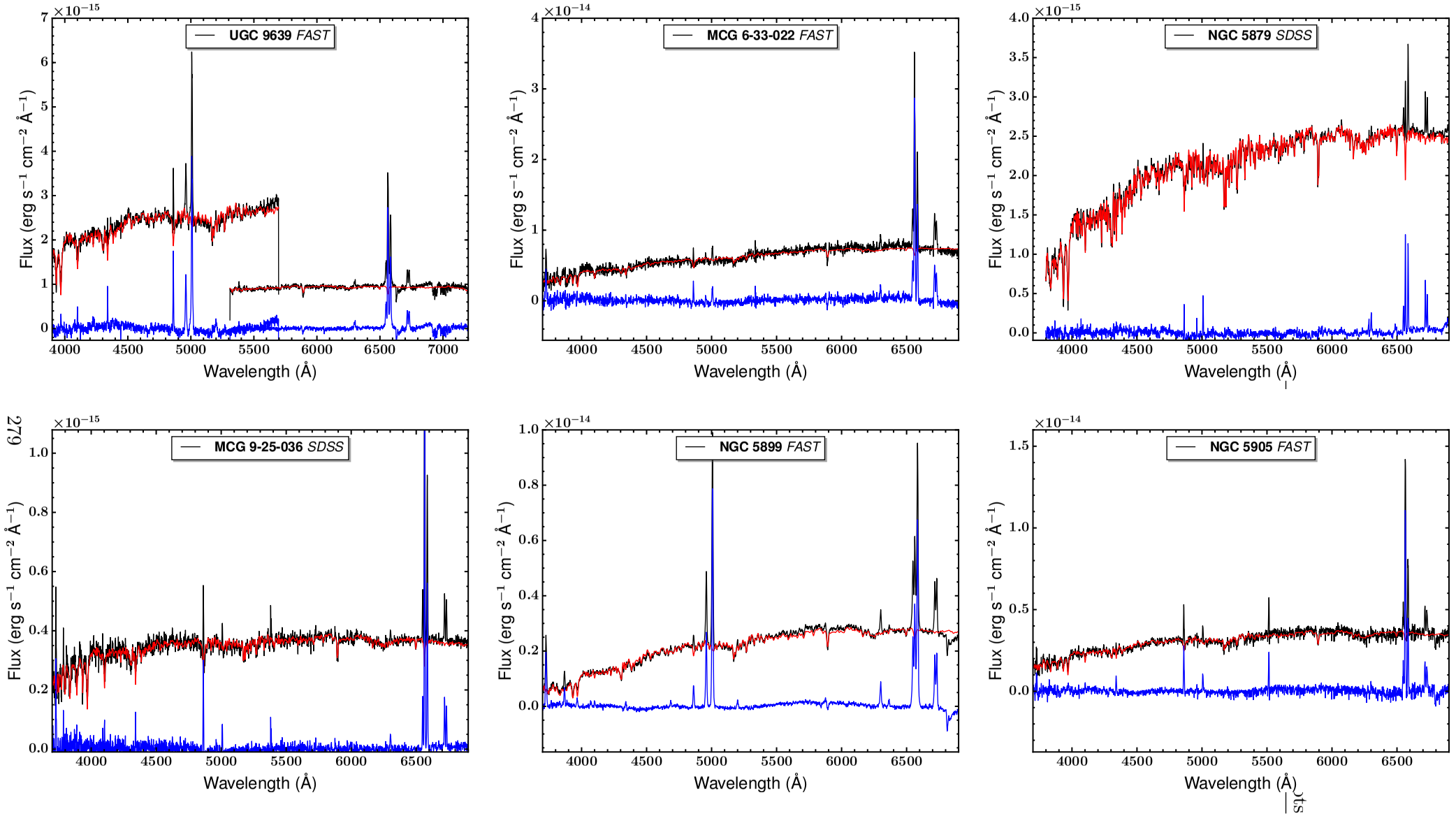




**Figure 8.A.56:** The nuclear spectra of UGC 9639, MCG 6-33-022, NGC 5879, MCG 9-25-036, NGC 5899, NGC 5905. The observed spectrum is shown with a black line, the STARLIGHT fit with a red line, and the starlight subtracted spectrum with a blue line.

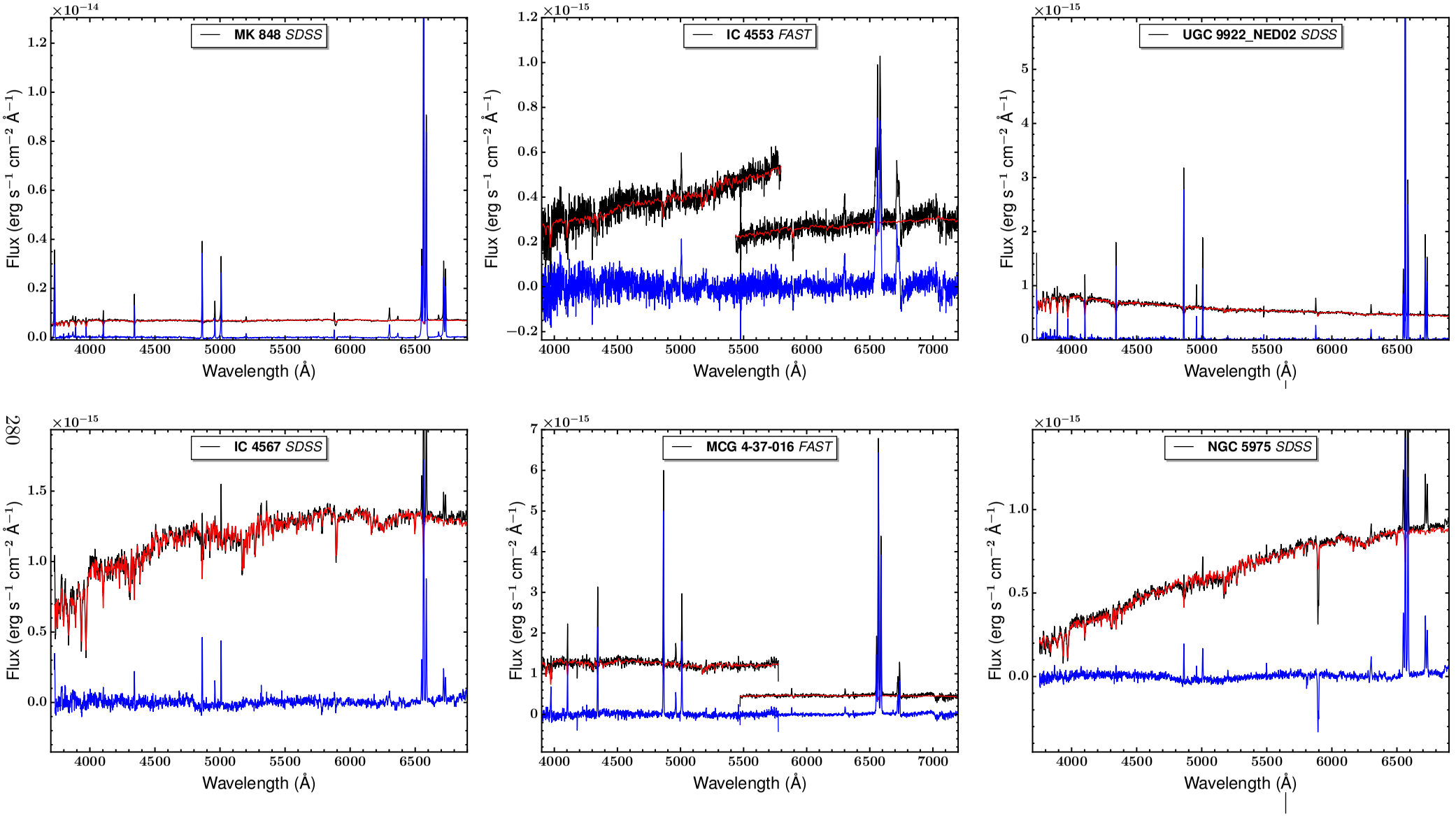


**Figure 8.A.57:** The nuclear spectra of MK 848, IC 4553, UGC 9922_NED02, IC 4567, MCG 4-37-016, NGC 5975. The observed spectrum is shown with a black line, the STARLIGHT fit with a red line, and the starlight subtracted spectrum with a blue line.

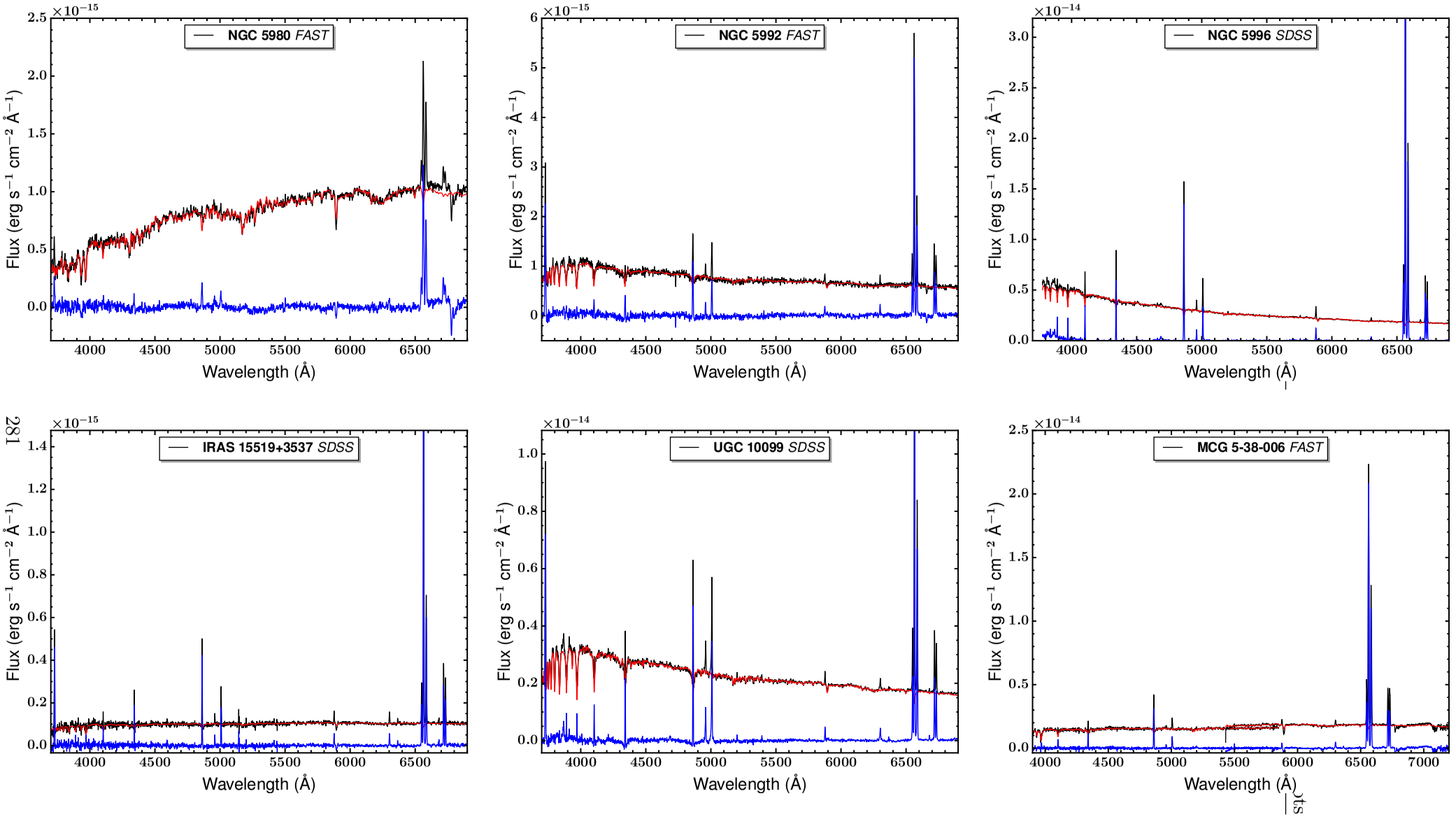




**Figure 8.A.58:** The nuclear spectra of NGC 5980, NGC 5992, NGC 5996, IRAS 15519+3537, UGC 10099, MCG 5-38-006. The observed spectrum is shown with a black line, the STARLIGHT fit with a red line, and the starlight subtracted spectrum with a blue line.

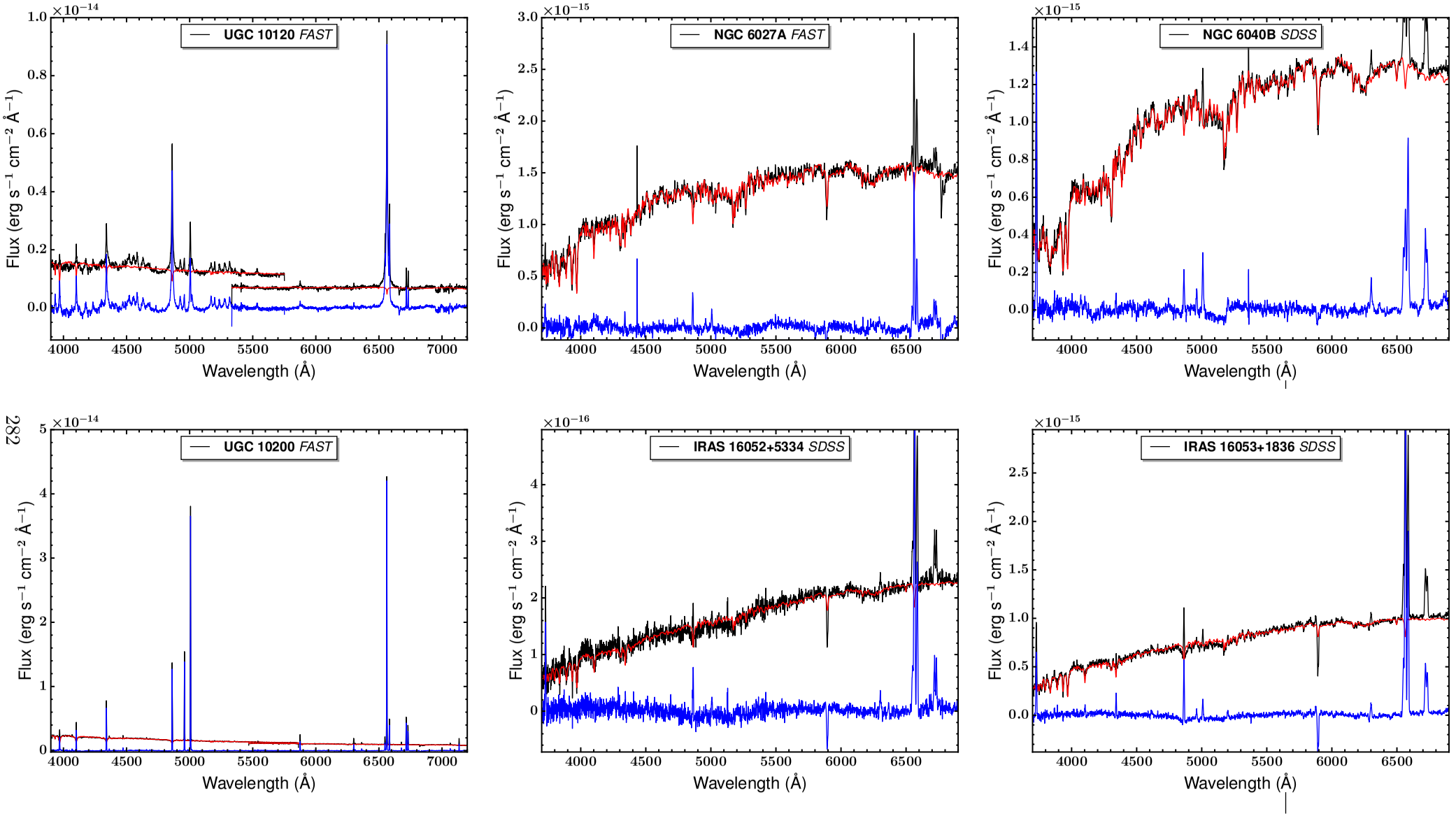




**Figure 8.A.59:** The nuclear spectra of UGC 10120, NGC 6027A, NGC 6040B, UGC 10200, IRAS 16052+5334, IRAS 16053+1836. The observed spectrum is shown with a black line, the STARLIGHT fit with a red line, and the starlight subtracted spectrum with a blue line.

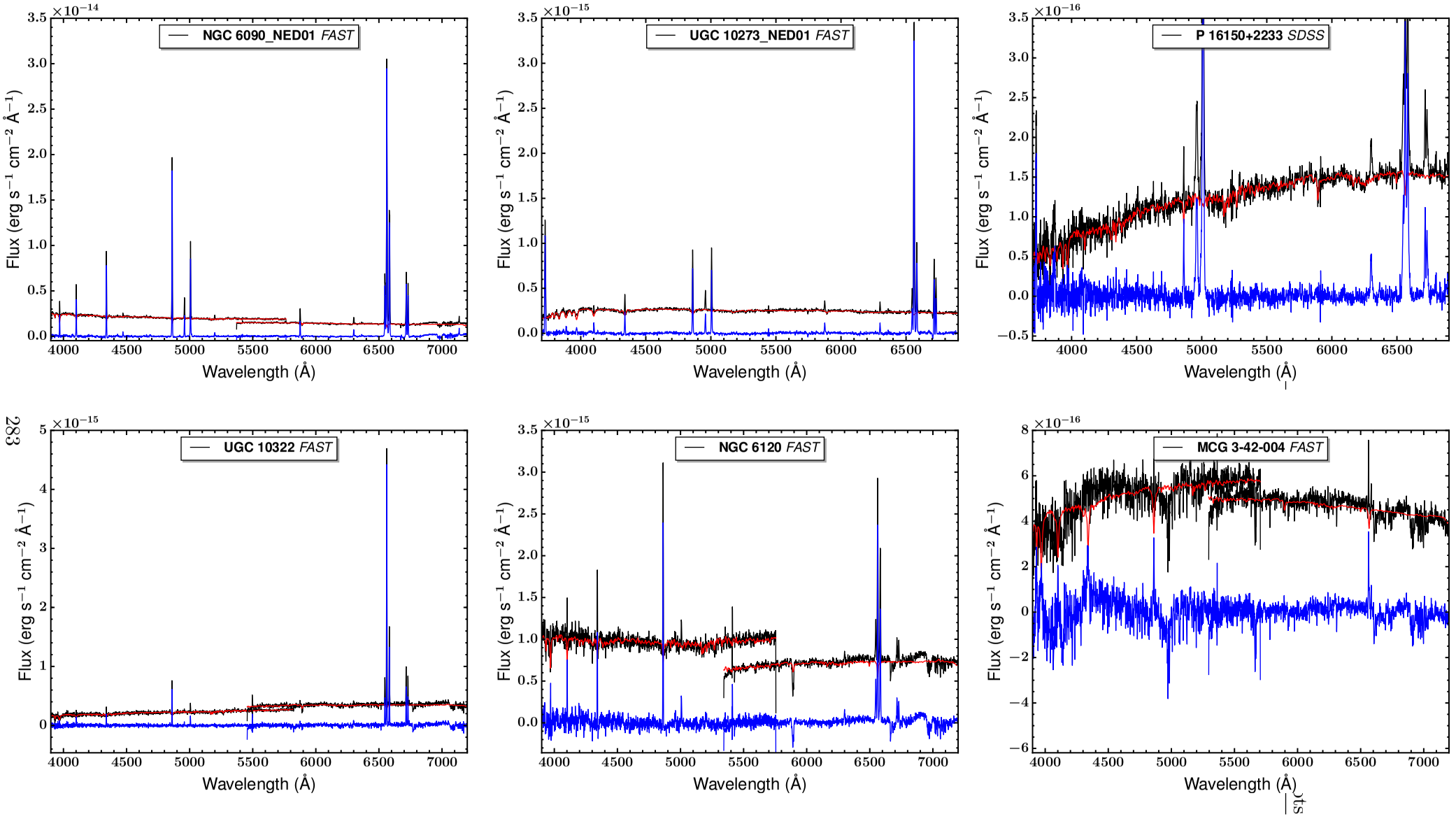




**Figure 8.A.60:** The nuclear spectra of NGC 6090_NED01, UGC 10273_NED01, P 16150+2233, UGC 10322, NGC 6120, MCG 3-42-004. The observed spectrum is shown with a black line, the STARLIGHT fit with a red line, and the starlight subtracted spectrum with a blue line.

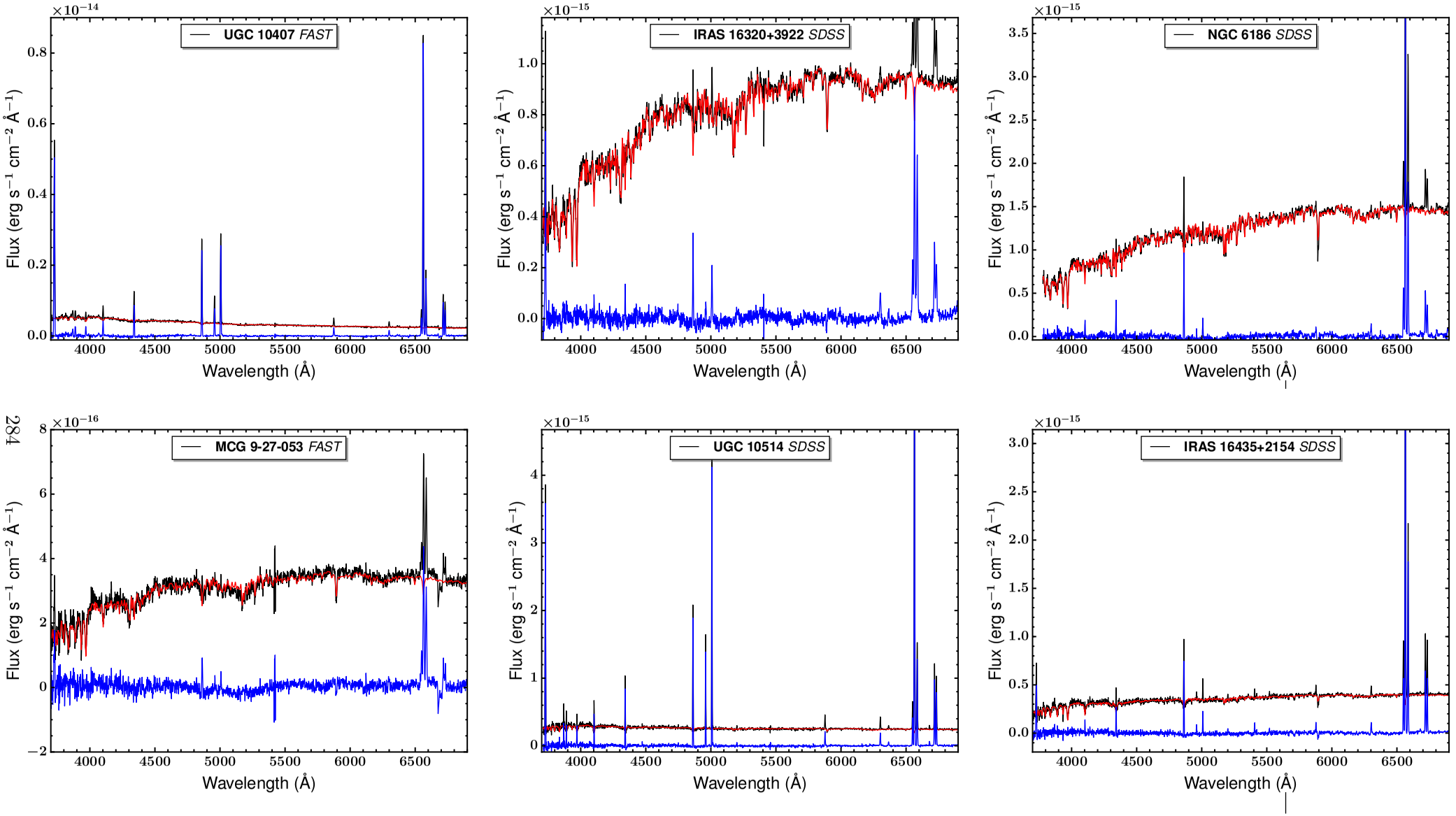


**Figure 8.A.61:** The nuclear spectra of UGC 10407, IRAS 16320+3922, NGC 6186, MCG 9-27-053, UGC 10514, IRAS 16435+2154. The observed spectrum is shown with a black line, the STARLIGHT fit with a red line, and the starlight subtracted spectrum with a blue line.

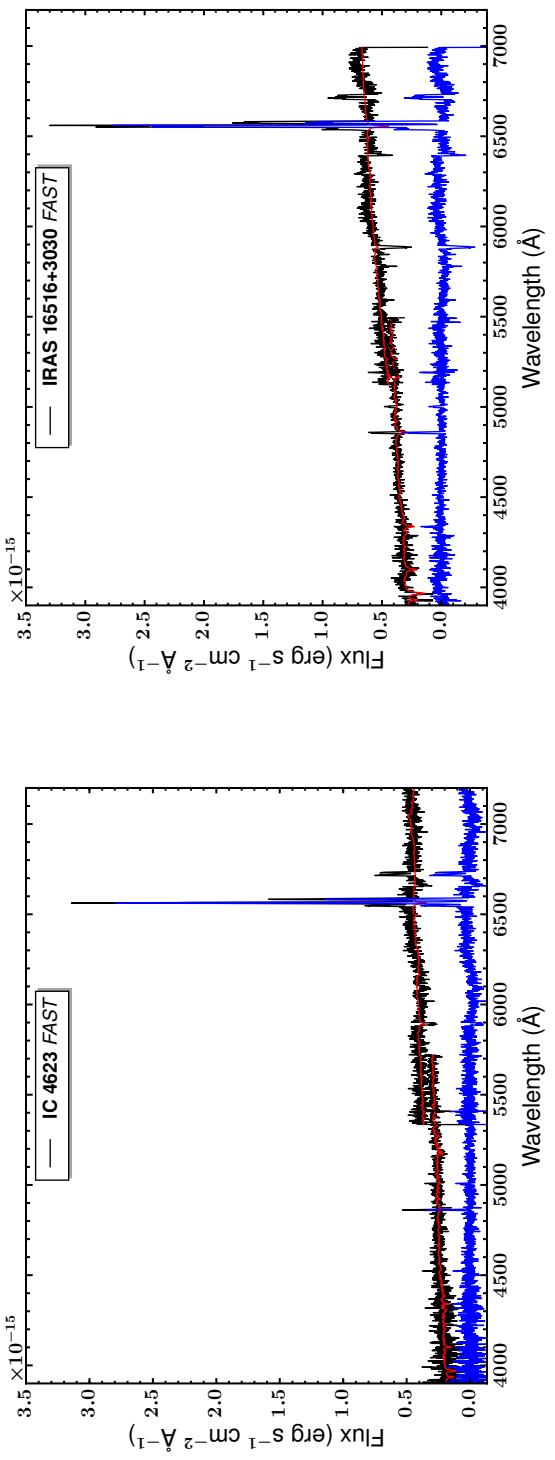


**Figure 8.A.62:** The nuclear spectra of IC 4623 and IRAS 16516+3030. The observed spectrum is shown with a black line, the STARLIGHT fit with a red line, and the starlight subtracted spectrum with a blue line.